

HZDR-126

PRIMORDIAL NUCLIDES AND LOW-LEVEL COUNTING AT FELSENKELLER

Steffen Turkat

Wissenschaftlich-Technische Berichte
HZDR-126 · 2023 · ISSN 2191-8708

**WISSENSCHAFTLICH-
TECHNISCHE BERICHTE**

hZDR

HELMHOLTZ ZENTRUM
DRESDEN ROSSENDORF

Wissenschaftlich-Technische Berichte
HZDR-126

Steffen Turkat

**PRIMORDIAL NUCLIDES
AND LOW-LEVEL COUNTING AT FELSENKELLER**

Druckausgabe: ISSN 2191-8708

Elektronische Ausgabe: ISSN 2191-8716

Die elektronische Ausgabe erscheint unter Creative Commons License (CC BY 4.0):

<https://www.hzdr.de/publications/Publ-37600>

<urn:nbn:de:bsz:d120-qucosa2-872765>

Die vorliegende Arbeit wurde sowohl als Dissertation an der Fakultät Mathematik und Naturwissenschaften der Technischen Universität Dresden sowie als Wissenschaftlich-Technischer Bericht des Helmholtz-Zentrum Dresden – Rossendorf mit der Berichtsnummer **HZDR-126** veröffentlicht.

2023

Herausgegeben vom

Helmholtz-Zentrum Dresden - Rossendorf

Bautzner Landstraße 400

01328 Dresden

Germany



TECHNISCHE
UNIVERSITÄT
DRESDEN

Primordial nuclides and low-level counting at Felsenkeller

Dissertation

zur Erlangung des Hochschulgrades

Doctor rerum naturalium

(Dr. rer. nat.)

vorgelegt von

Steffen Turkat

geboren am 07.09.1992 in Magdeburg

Institut für Kern- und Teilchenphysik
Technische Universität Dresden

2023

Eingereicht am 05.04.2023

1. Gutachter: Prof. Dr. Kai Zuber
2. Gutachter: Prof. Dr. Daniel Bemmerer
3. Gutachter: Prof. Dr. René Reifarth

Abstract

Within cosmology, there are two entirely independent pillars which can jointly drive this field towards precision: Astronomical observations of primordial element abundances and the detailed surveying of the cosmic microwave background. However, the comparatively large uncertainty stemming from the nuclear physics input is currently still hindering this effort, i.e. stemming from the ${}^2\text{H}(p,\gamma){}^3\text{He}$ reaction. An accurate understanding of this reaction is required for precision data on primordial nucleosynthesis and an independent determination of the cosmological baryon density.

Elsewhere, our Sun is an exceptional object to study stellar physics in general. While we are now able to measure solar neutrinos live on earth, there is a lack of knowledge regarding theoretical predictions of solar neutrino fluxes due to the limited precision (again) stemming from nuclear reactions, i.e. from the ${}^3\text{He}(\alpha,\gamma){}^7\text{Be}$ reaction. This thesis sheds light on these two nuclear reactions, which both limit our understanding of the universe. While the investigation of the ${}^2\text{H}(p,\gamma){}^3\text{He}$ reaction will focus on the determination of its cross-section in the vicinity of the Gamow window for the Big Bang nucleosynthesis, the main aim for the ${}^3\text{He}(\alpha,\gamma){}^7\text{Be}$ reaction will be a measurement of its γ -ray angular distribution at astrophysically relevant energies.

In addition, the installation of an ultra-low background counting setup will be reported which further enables the investigation of the physics of rare events. This is essential for modern nuclear astrophysics, but also relevant for double beta decay physics and the search for dark matter. The presented setup is now the most sensitive in Germany and among the most sensitive ones worldwide.

Zusammenfassung

Innerhalb der Kosmologie gibt es zwei völlig unabhängige Ansätze, die gemeinsam die Präzision in diesem Gebiet weiter vorantreiben können: Astronomische Beobachtungen der primordialen Elementhäufigkeiten und die detaillierte Vermessung des kosmischen Mikrowellenhintergrunds. Dieses Vorhaben wird derzeit allerdings noch durch die vergleichsweise große Unsicherheit des kernphysikalischen Inputs verhindert, vor allem bedingt durch das limitierte Verständnis der ${}^2\text{H}(p,\gamma){}^3\text{He}$ -Reaktion. Eine präzise Vermessung dieser Reaktion ist sowohl für die Präzisionsdaten zur primordialen Nukleosynthese erforderlich, als auch für die damit einhergehende unabhängige Bestimmung der kosmologischen Baryondichte.

Des Weiteren ist unsere Sonne ein exzellent geeignetes Objekt, um unser theoretisches Verständnis über die Physik von Sternen mit experimentellen Messungen abgleichen zu können. Während wir heutzutage in der Lage sind, solare Neutrinos in Echtzeit auf der Erde messen können, mangelt es noch an der theoretischen Vorhersagekraft von solaren Neutrinoströmen. Auch hier ist die Präzision (erneut) begrenzt durch das limitierte Verständnis der beteiligten Kernreaktionen, vor allem bedingt durch mangelnde Kenntnis über die ${}^3\text{He}(\alpha,\gamma){}^7\text{Be}$ -Reaktion. Die vorliegende Arbeit beleuchtet diese zwei Kernreaktionen, die beide unser Verständnis des Universums auf verschiedene Weise einschränken. Während sich die Untersuchung der ${}^2\text{H}(p,\gamma){}^3\text{He}$ -Reaktion auf die Bestimmung ihres Wirkungsquerschnitts in der Nähe des Gamow-Fensters für die Urknall-Nukleosynthese konzentriert, ist das Hauptanliegen für die ${}^3\text{He}(\alpha,\gamma){}^7\text{Be}$ -Reaktion eine Messung der Winkelverteilung der dabei emittierten γ -Strahlung bei astrophysikalisch relevanten Energien.

Darüber hinaus wird über die Installation eines Messaufbaus zur Untersuchung niedriger Aktivitäten berichtet, das sich durch seine äußerst geringe Untergrundzählrate auszeichnet. Bedingt durch seine hohe Sensitivität kann dieser Aufbau in Zukunft bedeutende Beiträge für die moderne nukleare Astrophysik leisten und ist darüber hinaus beispielsweise auch relevant für die Untersuchung von Doppel-Betazerfällen oder die Suche nach dunkler Materie. Der präsentierte Aufbau ist nun der Sensitivste seiner Art in Deutschland und gehört zu den Sensitivsten weltweit.

Contents

Funding, publications and teaching accomplishments	12
List of Figures	18
List of Tables	19
Acronyms	20
1 Introduction	21
1.1 Evolution of the universe	21
1.1.1 Big Bang nucleosynthesis	22
1.1.2 Cosmological concordance from BBN	24
1.2 Stellar nucleosynthesis	26
1.3 The ${}^2\text{H}(p,\gamma){}^3\text{He}$ reaction	28
1.3.1 Review on previous work	29
1.4 The ${}^3\text{He}(\alpha,\gamma){}^7\text{Be}$ reaction	32
1.4.1 Review on previous work	33
1.4.2 The γ -ray angular distribution	34
1.5 The physics of rare event searches	38
1.6 Structure of this thesis and general comments	39
2 Physics background and analysis techniques	41
2.1 Interaction of photons with matter	41
2.2 Detection mechanisms	43
2.2.1 HPGe detectors	43
2.2.2 Scintillation detectors	44
2.2.3 Particle detectors	45
2.3 Data acquisition and pulse processing	46
2.4 γ -ray spectrometry	48
2.4.1 Energy calibrations	48
2.4.2 Efficiencies in γ -ray spectrometry	48
2.4.3 Evaluation of peaks and determination of their net counts	51
2.4.4 Peak widths in γ -ray spectrometry	52
2.4.5 Coincidences in γ -ray spectrometry	53
2.5 Dead time	54
2.6 Reaction kinematics of radiative capture reactions	55
2.6.1 Determination of the laboratory energy for the IBC campaigns	55
2.6.2 Determination of the laboratory energy for the FK campaigns	56
2.6.3 Determination of the effective energy and the center-of-mass energy	56

2.6.4	Determination of the γ -ray energy in radiative capture reactions	57
2.6.5	Relativistic angle correction in radiative capture reactions	59
2.7	Determination techniques for target areal densities	60
2.7.1	Nuclear reaction analysis - NRA	60
2.7.2	Elastic recoil detection analysis - ERDA	61
2.8	Reaction rates and the astrophysical S -factor	62
3	Setup of the experimental campaigns on nuclear astrophysics	64
3.1	Overview and categorization of the experimental campaigns	64
3.1.1	Overview of the implantation characteristics of the samples	65
3.1.2	Overview of the irradiation parameters of the samples	66
3.1.3	Overview of calibration sources	67
3.1.4	Overview of in-beam HPGe detectors	68
3.1.5	Overview of target holder designs	69
3.1.6	Overview of additional beam line elements in proximity to the target	72
3.2	Sample production for the experimental campaigns	75
3.2.1	Cleaning procedures of the backings prior to implantation/deuteration	76
3.2.2	Evaporation procedures for the backings	77
3.2.3	Sample production for the ${}^2\text{H}(p,\gamma){}^3\text{He}$ campaign	77
3.2.4	Sample production for the ${}^3\text{He}(\alpha,\gamma){}^7\text{Be}$ campaigns	78
3.3	The 3 MV Tandetron at the Ion Beam Center of HZDR	79
3.3.1	Setup for the ${}^2\text{H}(p,\gamma){}^3\text{He}$ campaign (IBC-I) at the 3 MV Tandetron .	79
3.3.2	Setup for ${}^3\text{He}(\alpha,\gamma){}^7\text{Be}$ campaign (IBC-II) at the 3 MV Tandetron .	82
3.4	The Felsenkeller shallow-underground laboratory	84
3.4.1	Development and construction of an extended solid target setup . . .	85
3.4.2	Setup for the ${}^3\text{He}(\alpha,\gamma){}^7\text{Be}$ campaigns FK-I and FK-II at Felsenkeller	86
3.4.3	Setup for the ${}^3\text{He}(\alpha,\gamma){}^7\text{Be}$ campaign FK-III at Felsenkeller	88
3.4.4	Setup for the ${}^3\text{He}(\alpha,\gamma){}^7\text{Be}$ campaign FK-IV at Felsenkeller	89
3.4.5	Setup for the ${}^3\text{He}(\alpha,\gamma){}^7\text{Be}$ campaign FK-V at Felsenkeller	89
3.5	The TU bunker at Felsenkeller	91
3.5.1	The current status of detectors in the TU bunker	91
3.5.2	The setup of the TU1 detector	93
3.5.2.1	Passive shielding	93
3.5.2.2	Anti-radon box	94
3.5.2.3	Active shielding	95
3.5.2.4	Hardware and data acquisition	97
4	Development of an ultra-low background γ-ray spectrometer at Felsenkeller	99
4.1	Characteristics and anomalies in the signal of TU1	100
4.1.1	Noise level in the preamplified signal	100

4.1.2	Remaining noise of unknown origin	100
4.1.3	Remaining noise due to LN2 filling of the dewar	101
4.1.4	Non-linearity in the energy calibration	102
4.1.5	Occurrence of signals with the opposite (positive) polarity	103
4.2	Investigation of the radon concentration	109
4.3	The passively shielded TU1 detector	112
4.4	Measurements and analysis of the scintillation panels	114
4.4.1	Energy calibration of the panels	115
4.4.2	Light collection efficiency of the panels	117
4.4.3	Interpretation of energy calibrated spectra	119
4.4.4	Coincidence spectra between panels and TU1	122
4.4.5	Definition of the cut criteria for the active veto	126
4.4.6	Optimization of the cut criteria for the active veto	127
4.4.7	Origin of prompt and delayed coincidences in TU1	132
4.4.7.1	Prompt coincidences: The timing interval of $[-5 \mu\text{s}, 0 \mu\text{s}]$. . .	132
4.4.7.2	Delayed coincidences: The timing interval of $[-50 \mu\text{s}, -5 \mu\text{s}]$.	134
4.4.7.3	Delayed coincidences: The timing interval of $[-150 \mu\text{s}, -50 \mu\text{s}]$	135
4.4.7.4	Time delay dependency of energy depositions in TU1	135
4.5	The actively shielded TU1 detector	139
4.5.1	The pulse-height spectrum of a long-term background measurement .	139
4.5.2	Analysis on the remaining background components	141
4.5.3	Treatment of remaining oscillation events within TU1	143
4.5.4	Effective half-life of the radon-induced rate	146
4.5.5	Annual modulation and long-term development of the counting rate .	147
4.6	Determination of losses in the full energy peaks	149
4.6.1	Determination of the dead time	150
4.6.2	Determination of the veto efficiency	151
4.7	Design of an appropriate sample holder	154
4.7.1	First attempt: Sample holders from aluminum	154
4.7.2	Final attempt: Sample holder from OFRP copper	154
4.8	Comparison to other underground γ -ray counting setups	157
4.9	Sensitivity for future measurements	158
4.10	Comments on further improvements	162
5	Experimental campaign on the ${}^2\text{H}(p, \gamma){}^3\text{He}$ reaction	164
5.1	Results of previous work on the data of this campaign	165
5.1.1	Statements on the stability of the targets	165
5.1.2	Absolute full-energy peak efficiency of the HPGe detectors	165
5.1.3	Laboratory and beam-induced background	166

5.2	Evaluation of the in-beam spectra	167
5.3	Theoretical ab initio γ -ray angular distribution	169
5.3.1	Yield correction using the theoretical γ -ray angular distribution	171
5.4	Determination of the target areal density	172
5.4.1	Nuclear reaction analysis	172
5.4.1.1	Energy calibration of the silicon detector	173
5.4.1.2	Solid angle of the silicon detector	176
5.4.1.3	Determination of the areal density	177
5.4.2	Elastic recoil detection analysis	180
5.4.3	Summary	184
5.5	Evaluation of the cross section and the S -factor	185
5.5.1	Discussion on the resulting S -factor	186
5.5.2	Discrepancy with the new data set from LUNA	188
5.5.3	Treatment of uncertainties	189
6	Experimental campaigns on the ${}^3\text{He}(\alpha, \gamma){}^7\text{Be}$ reaction	190
6.1	General considerations in advance	191
6.1.1	Optimization of the implantation depth	191
6.1.2	Optimization of the areal density	193
6.1.3	Calculation of the implantation fluence	194
6.1.4	Reliability of the quoted effective energies	197
6.1.5	Suitable irradiation energies	198
6.2	In-beam analysis of FK-I to FK-IV	199
6.2.1	Results for the in-beam analysis during the FK-I campaign	199
6.2.2	Results for the in-beam analysis during the FK-II campaign	202
6.2.3	Angular uncertainty for full-energy events deposition in the HPGe	204
6.2.4	Results for the in-beam analysis during the FK-III campaign	205
6.2.5	Results for the in-beam analysis during the FK-IV campaign	207
6.3	In-beam analysis of FK-V	209
6.3.1	Target stability	210
6.3.2	Prompt γ -ray analysis	212
6.3.3	Absolute full-energy peak efficiency	217
6.3.4	Resulting γ -ray angular distribution	218
6.3.5	Treatment of uncertainties	221
6.3.6	Deduction of Legendre polynomials	224
6.4	In-beam analysis of IBC-II	227
6.4.1	Nuclear reaction analysis - NRA	228
6.4.2	Prompt γ -ray analysis	230
6.4.3	Absolute full-energy peak efficiency	232

6.4.4	Resulting γ -ray angular distribution	233
6.5	Activation analyses	235
6.5.1	General procedure	235
6.5.2	Activation analyses for IBC-II	237
6.5.3	Activation analyses for FK-I to FK-IV	237
6.5.4	Activation analyses for FK-V	238
6.5.5	Deductions from the activation analyses	239
6.5.6	Cross section analysis for target Ta502	245
7	Discussion	248
	References	251
A	General appendix	266
A.1	Coincidences between detectors	266
A.1.1	Anti-Compton suppression	267
A.1.2	Add-back techniques	268
A.1.3	Approach for ACS and add-back	269
A.2	Radon concentration at Felsenkeller	271
B	Appendix regarding the TU1 setup	272
B.1	Panel spectra and their coincidences with TU1	272
B.2	Delayed coincidences in TU1	273
B.3	Time delay dependency for each panel	275
B.4	Time delay dependency for energy depositions in the panels	276
B.5	Technical drawings of the final target holder for TU1	277
C	Appendix regarding the ${}^2\text{H}(\text{p},\gamma){}^3\text{He}$ reaction	278
C.1	The S -factor fit for ${}^2\text{H}(\text{p},\gamma){}^3\text{He}$ with Mossa et al.	278
C.2	Pulse height spectra for the ${}^2\text{H}(\text{p},\gamma){}^3\text{He}$ campaign	279
D	Appendix regarding the ${}^3\text{He}(\alpha,\gamma){}^7\text{Be}$ reaction	283
D.1	Photos of irradiated targets and targets setups	283
D.2	New dewar design for in-beam experiments at FK	286
D.3	Tests for improving the thermal conductivity	287
D.4	Resulting depth distributions during ion implantation	289
D.5	The effective opening angle of HPGe	291
D.6	Utilized runs for the analysis of FK-V	294
D.7	Residua for the analysis of prompt γ -rays in FK-V	295
D.8	Fits for the ${}^3\text{He}(\alpha,\gamma){}^7\text{Be}$ γ -ray angular distribution	302
D.9	The γ -ray angular distribution for ${}^3\text{He}(\alpha,\gamma){}^7\text{Be}$	305

Funding, publications and teaching accomplishments

Funding and support

This dissertation was supported in part by Konrad-Adenauer-Stiftung, and Deutsche Forschungsgemeinschaft DFG (ZU123/21-1).

List of publications which are directly related to this thesis

Parts of the present thesis have been published previously in peer-reviewed papers:

- S. Turkat, S. Hammer, E. Masha, S. Akhmadaliev, D. Bemmerer, M. Grieger, T. Hensel, J. Julin, M. Koppitz, F. Ludwig, C. Möckel, S. Reinicke, R. Schwengner, K. Stöckel, T. Szücs, L. Wagner, and K. Zuber. “Measurement of the ${}^2\text{H}(p,\gamma){}^3\text{He}$ S factor at 265–1094 keV.” in: *Physical Review C* 103.4 (2021). DOI: 10.1103/physrevc.103.045805
- S. Turkat, D. Bemmerer, A. Boeltzig, A. Domula, J. Koch, T. Lossin, M. Osswald, K. Schmidt, and K. Zuber. “A new ultra low-level HPGe activity counting setup in the Felsenkeller shallow-underground laboratory.” In: *Astroparticle Physics* (2023), p. 102816. DOI: 10.1016/j.astropartphys.2023.102816

List of other publications with first authorship

- S. Turkat, X. Mougeot, B. Singh, and K. Zuber. “Systematics of $\log ft$ values for β^- , and EC/β^+ transitions.” In: *At. Data Nucl. Data Tables* (in review)

List of publications with co-authorship

- T. Szücs, D. Bemmerer, D. Degering et al. “Background in γ -ray detectors and carbon beam tests in the Felsenkeller shallow-underground accelerator laboratory.” In: *The European Physical Journal A* 55.10 (2019). DOI: 10.1140/epja/i2019-12865-4
- J. Wilhelmy, M. Müscher, G. Rusev, et al. “Dipole response of ${}^{87}\text{Rb}$ and its impact on the ${}^{86}\text{Rb}(n,\gamma){}^{87}\text{Rb}$ cross section.” In: *Physical Review C* 102.4 (2020). DOI: 10.1103/physrevc.102.044327
- R. Schwengner, R. Massarczyk, M. Scheck, et al., “Electric and magnetic dipole strength in ${}^{66}\text{Zn}$.” In: *Physical Review C* 103.2 (2021). DOI: 10.1103/physrevc.103.024312
- R. Schwengner, R. Massarczyk, K. Schmidt, et al., “Photoexcitation of ${}^{76}\text{Ge}$.” In: *Physical Review C* 105.2 (2022). DOI: 10.1103/physrevc.105.024303
- T. Shizuma, S. Endo, A. Kimura, et al., “Low-lying dipole strength distribution in ${}^{204}\text{Pb}$.” In: *Physical Review C* 106.4 (2022). DOI: 10.1103/physrevc.106.044326

Lecture duties

- Seminar “Nukleare Astrophysik” in SS2017, and SS2021
- Seminar “Kosmologie und Astroteilchenphysik” in SS2017
- Seminar “Moderne Kosmologie” in SS2021
- Seminar “Physics beyond the Standard Model and Astroparticle Physics” in SS2019
- Seminar “Experimental Nuclear and Particle Physics” in SS2019, and WS2019/20
- Seminar “Wechselwirkung Strahlung Stoff” in WS2019/20, and WS2020/21
- Seminar “Recent findings in nuclear astrophysics and beyond” in WS2019/20
- Lab course “Radiometrie 3” in SS2017, SS2018, and SS2019
- Lab course “Aktivitätskonzentration” in WS2017/18, and WS2018/19
- Lab course “Gammaskopie” in WS2017/18, and WS2018/19

List of co-supervised theses

- L. Hübinger. “Investigation of the ${}^3\text{He}(\alpha, \gamma){}^7\text{Be}$ reaction at $E_{\text{com}} = 1.5 \text{ MeV}$.” Bachelor Thesis. TU Dresden, 2018. URL: https://iktp.tu-dresden.de/IKTP/pub/18/Lisa_Huebinger_Bachelor.pdf
- S. Hammer. “Study of the ${}^2\text{H}(p, \gamma){}^3\text{He}$ cross section at $E_p = 400 \text{ keV} - 800 \text{ keV}$.” Master Thesis. TU Dresden, 2019. URL: https://iktp.tu-dresden.de/IKTP/pub/19/Sebastian_Hammer_Master.pdf
- J. Koch. “Untergrund und Test der Offline Gammadetektoren am Felsenkeller.” Bachelor Thesis. TU Dresden, 2020. URL: https://iktp.tu-dresden.de/IKTP/pub/20/Jonas_Koch_Bachelor.pdf
- M. Müller. “Monte-Carlo-Simulation des in-beam- γ -Spektroskopie-Aufbaus im Felsenkeller.” Bachelor Thesis. TU Dresden, 2020
- P. Hempel. “Studien zur Bestimmung der Halbwertszeiten von ${}^{139}\text{Ce}$, ${}^{143}\text{Pm}$, ${}^{144}\text{Pm}$, ${}^{146}\text{Pm}$.” Bachelor Thesis. TU Dresden, 2020
- M. Osswald. “Test und Kalibrierung der Reinstgermaniumdetektoren für die ${}^3\text{He}(\alpha, \gamma){}^7\text{Be}$ -Messung am Felsenkeller.” Bachelor Thesis. TU Dresden, 2020. URL: https://iktp.tu-dresden.de/IKTP/pub/20/Max_Osswald_Bachelor.pdf
- M. Pichotta. “Investigating the background of the GERDA experiment by ${}^{76}\text{Ge}(n, p){}^{76}\text{Ga}$ reaction studies.” Master Thesis. TU Dresden, 2021
- J. Michaelis. “In-beam γ -spektroskopische Untersuchung der ${}^3\text{He}(\alpha, \gamma){}^7\text{Be}$ -Reaktion.” Bachelor Thesis. TU Dresden, 2021
- C. Seibt. “Operation of the X-Ray Detector at Felsenkeller Dresden and First Measurements.” Bachelor Thesis. TU Dresden, 2021
- B. Vergoosen. “X-ray Spectrometry: Attenuation of the background components in a silicon drift detector.” Bachelor Thesis. TU Dresden, 2022
- M. Wolf. “Study on the emission probability of gamma-rays from ${}^{74}\text{Ga}$ and ${}^{76}\text{Ga}$ in the ROI of GERDA/LEGEND.” Bachelor Thesis. TU Dresden, 2022
- S. Vincent. “In-Beam-Experimente am Felsenkeller zur komischen Lithium-7-Produktion.” Bachelor Thesis. TU Dresden, 2022

List of Figures

1.1	Evolution of elemental abundances in the early universe.	22
1.2	Relevant reactions for BBN and stellar nucleosynthesis.	24
1.3	Concordance plot for Big Bang nucleosynthesis.	25
1.4	Schematic energy level diagram of the ${}^2\text{H}(p,\gamma){}^3\text{He}$ and ${}^3\text{He}(\alpha,\gamma){}^7\text{Be}$ reaction.	29
1.5	S -factor for the ${}^2\text{H}(p,\gamma){}^3\text{He}$ reaction until mid of 2020.	30
1.6	S -factor for the ${}^3\text{He}(\alpha,\gamma){}^7\text{Be}$ reaction with data sets used by Solar Fusion II.	33
1.7	Theoretical Legendre coefficients for the ${}^3\text{He}(\alpha,\gamma){}^7\text{Be}$ reaction (Tombrello)	35
1.8	Theoretical γ -ray angular distribution for the ${}^3\text{He}(\alpha,\gamma){}^7\text{Be}$ reaction (Tombrello)	36
1.9	Theoretical Legendre coefficients for the ${}^3\text{He}(\alpha,\gamma){}^7\text{Be}$ reaction (Zhang)	37
1.10	Theoretical γ -ray angular distribution for the ${}^3\text{He}(\alpha,\gamma){}^7\text{Be}$ reaction (Zhang)	38
2.1	Attenuation and mean free path of photons in lead.	42
2.2	Reconstruction of HPGe signals with the utilized software.	46
2.3	Determination of peak areas with continuous backgrounds.	51
2.4	Contributions to E_γ in case of the ${}^3\text{He}(\alpha,\gamma){}^7\text{Be}$ reaction in linear scale.	58
2.5	Contributions to E_γ in case of the ${}^3\text{He}(\alpha,\gamma){}^7\text{Be}$ reaction in log scale.	58
2.6	Correction regarding relativistic angles for the ${}^3\text{He}(\alpha,\gamma){}^7\text{Be}$ reaction.	60
3.1	Schematic drawing of the target holder design I.	69
3.2	Schematic drawing of the target holder design II.	70
3.3	Schematic drawing of the target holder design III.	71
3.4	Schematic drawing of copper pipe cold trap.	73
3.5	Schematic drawing of the particle detector for IBC-I and IBC-II.	74
3.6	Photographs of the beam spot on the target	75
3.7	Irradiated targets from the investigation of the ${}^2\text{H}(p,\gamma){}^3\text{He}$ reaction.	78
3.8	Schematic view of the 3 MV Tandetron accelerator at HZDR.	79
3.9	Setup of the ${}^2\text{H}(p,\gamma){}^3\text{He}$ campaign (IBC-I) at the IBC.	80
3.10	Setup of the ${}^3\text{He}(\alpha,\gamma){}^7\text{Be}$ campaign (IBC-II) at the IBC.	82
3.11	Scheme of the tunnel system at Felsenkeller.	84
3.12	Schematic drawing of the in-beam target chamber at Felsenkeller.	85
3.13	Scheme of the target area at Felsenkeller.	87
3.14	Photos of the in-beam collimator and its water-cooled holder.	88
3.15	Scheme of the target area at Felsenkeller during FK-V.	90
3.16	Schematic drawing of TU1.	93
3.17	Schematic drawing of the five scintillation panels of TU1.	96
4.1	Pulse height spectrum of a ${}^{133}\text{Ba}$ source on TU1 for low energies.	101
4.2	Non-linearity in the energy calibration of TU1.	102
4.3	Corrections for the energy calibration in TU1.	103
4.4	Typical signal with correct polarity in TU1.	104

4.5	Typical signal with opposite polarity in TU1.	104
4.6	Coincident events of negative pulses with positive pulses in TU1.	105
4.7	Coincident events of positive pulses with negative pulses in TU1.	105
4.8	Non-coincident events of negative pulses with positive pulses in TU1.	108
4.9	Non-coincident events of positive pulses with negative pulses in TU1.	108
4.10	Positions of RadonScouts at Felsenkeller.	110
4.11	Radon concentration in bunker 110 at Felsenkeller.	110
4.12	Counting rates for different stages of passive shielding for TU1.	113
4.13	Counting rates of scintillation panel #45.	116
4.14	Energy calibration of scintillation panel #45.	117
4.15	Spectrum for ^{90}Sr source with scintillation panel #45.	118
4.16	Light collection efficiency for a scintillation panel.	119
4.17	Background spectrum of panel #45 and its components.	120
4.18	Coincidence plots between two detectors of the setup in TU1.	124
4.19	Fit of the minimum in the spectrum of panel #45.	127
4.20	Remaining events in TU1 for certain cut combinations.	129
4.21	Loss of full energy events in TU1 for certain cut combinations.	129
4.22	Pulse height spectrum of panel #45 with final cut conditions.	130
4.23	Time difference plot of panel #45 with final cut conditions.	130
4.24	Delayed coincidences between events of TU1 and panel #45.	133
4.25	Coincident events in TU1 with $[-5\ \mu\text{s}, 0\ \mu\text{s}]$ in panel #45.	133
4.26	Coincident events in panel #45 with $[-5\ \mu\text{s}, 0\ \mu\text{s}]$ in TU1.	133
4.27	Coincident events in TU1 with $[-50\ \mu\text{s}, -5\ \mu\text{s}]$ in panel #45.	134
4.28	Coincident events in panel #45 with $[-50\ \mu\text{s}, -5\ \mu\text{s}]$ in TU1.	134
4.29	Coincident events in TU1 with $[-150\ \mu\text{s}, -50\ \mu\text{s}]$ in panel #45.	136
4.30	Coincident events in panel #45 with $[-150\ \mu\text{s}, -50\ \mu\text{s}]$ in TU1.	136
4.31	Energy dependent time delay of coincident events in TU1.	137
4.32	Passively and actively shielded background of TU1.	140
4.33	Background counting rate of the actively vetoed TU1.	142
4.34	Rate of TU1 showing some rare oscillation events.	143
4.35	Spectrum of TU1 showing some rare oscillation events.	144
4.36	First example of an oscillation event in TU1.	145
4.37	Second example of an oscillation event in TU1.	145
4.38	Effect of radon on the counting rate in TU1 for 7h.	146
4.39	Effect of radon on the counting rate in TU1 for 2d.	147
4.40	Long-term counting rate of the background in the TU1 detector.	148
4.41	Pulse height spectrum of a ^7Be sample on TU1.	152
4.42	Veto efficiency of TU1 using the final cut conditions.	153
4.43	Pulse height spectrum of the first sample holder on TU1.	155

4.44	First sample holder for TU1 made of aluminum.	155
4.45	Schematic drawing of the final sample holder.	156
4.46	Integrated counting rate for several underground HPGeS.	157
4.47	Detection limit for the TU1 setup.	160
4.48	Half-life sensitivity for the TU1 setup.	161
5.1	Absolute full-energy peak efficiency of the HPGe detectors for ${}^2\text{H}(p,\gamma){}^3\text{He}$	166
5.2	Exemplary pulse height spectrum for ${}^2\text{H}(p,\gamma){}^3\text{He}$	168
5.3	Theoretical γ -ray angular distribution of the ${}^2\text{H}(p,\gamma){}^3\text{He}$ reaction.	170
5.4	Energy-dependent relativistic angle for the ${}^2\text{H}(p,\gamma){}^3\text{He}$ reaction.	171
5.5	Energy calibration of the Si detector using the triple alpha source EC221.	174
5.6	Calibration of the Si-detector with an ${}^{241}\text{Am}$ source.	176
5.7	Pulse height spectra of all three NRA runs during the ${}^2\text{H}(p,\gamma){}^3\text{He}$ campaign.	178
5.8	ROI and residuum for the three NRA runs during the ${}^2\text{H}(p,\gamma){}^3\text{He}$ campaign.	179
5.9	ERDA plot for IBC-I using a BIC detector and a solid state detector.	181
5.10	Resulting depth distribution of TiD2-2-4 from the ERDA analysis.	182
5.11	Simulation of the heat transfer in the target.	184
5.12	Astrophysical S -factor for the ${}^2\text{H}(p,\gamma){}^3\text{He}$ reaction without Mossa et al.	187
5.13	Residuum of the S -factor for the ${}^2\text{H}(p,\gamma){}^3\text{He}$ reaction without Mossa et al.	188
6.1	Relative loss of ${}^4\text{He}$ due to different implantation depths.	192
6.2	Loss of E_{cm} for ${}^4\text{He}$ due to different implantation depths.	192
6.3	Ion depth distribution based on ${}^3\text{He}$ ions with 45 keV and 15 keV in tantalum.	194
6.4	Ratio of backscattered ${}^3\text{He}$ ions R during ion implantation.	195
6.5	Straggling of ${}^3\text{He}$ ions within gold and tantalum.	195
6.6	Energy loss of ${}^4\text{He}$ ions in tantalum for different implantation ratios.	197
6.7	Suitable irradiation energies based on the resulting in-beam spectrum	198
6.8	Photos of tantalum targets after irradiation.	200
6.9	Pulse height spectra from the irradiation of ST3 during the FK-I campaign.	201
6.10	Pulse height spectrum from the irradiation of ST5 during the FK-II campaign.	203
6.11	Spread on the effective detector angles.	205
6.12	Pulse height spectrum from the irradiation of ST6 during FK-III.	206
6.13	Pulse height spectrum from the irradiation of ST7 during FK-III.	208
6.14	Order, durations and target current of all irradiations during FK-V.	210
6.15	Net yield over time for all target during FK-V.	211
6.16	Pulse height spectra for the in-beam analysis of the FK-V campaign.	213
6.17	Residua resulting from the analysis of prompt γ -rays in the FK-V campaign.	216
6.18	Absolute full-energy peak efficiency for all detectors during FK-V.	218
6.19	Resulting γ -ray angular distributions for all FK-V irradiations.	220
6.20	Interpolation of angular uncertainties for FK-V based on earlier simulations.	221
6.21	Uncertainties for the yield of all detectors during FK-V.	223

6.22	Legendre polynomials for the ground state transition during FK-V.	226
6.23	Legendre polynomials for the excited state transition during FK-V.	227
6.24	Pulse height spectra from the Si detector during the IBC-II campaign.	229
6.25	Pulse height spectra from the irradiation of Ta100 during IBC-II.	231
6.26	Residua of the Can60 detector during the irradiation of Ta100 and Ta502.	232
6.27	Absolute full-energy peak efficiency for the HPGe detectors during IBC-II.	232
6.28	Resulting γ -ray angular distributions for both IBC-II irradiations.	233
6.29	Legendre polynomials for the ground state transition during IBC-II.	234
6.30	Procedure for the determination of an activity at the end of irradiation.	236
6.31	Activities at the end of irradiation for all relevant ${}^3\text{He}(\alpha,\gamma){}^7\text{Be}$ samples.	240
6.32	Target current and accumulated activity during the irradiation of ST9.	244
6.33	S -factor for ${}^3\text{He}(\alpha,\gamma){}^7\text{Be}$ with other data sets than Solar Fusion II.	247
A.1	Comparison of mean free path and size of the detector crystals.	266
A.2	Anti-Compton suppression based on ${}^{60}\text{Co}$	267
A.3	Timing for anti-Compton suppression based on ${}^{60}\text{Co}$	267
A.4	Radon concentration in the overground site of Felsenkeller.	271
A.5	Radon concentration in the open tunnel of Felsenkeller.	271
A.6	Radon concentration in bunker 111 of Felsenkeller.	271
B.1	Pulse height spectra of panel #15 from TU1.	272
B.2	Pulse height spectra of panel #16 from TU1.	272
B.3	Pulse height spectra of panel #17 from TU1.	272
B.4	Pulse height spectra of panel #44 from TU1.	273
B.5	Delayed coincidences in TU1 within $(-5\ \mu\text{s}, 0\ \mu\text{s})$	273
B.6	Delayed coincidences in TU1 within $(-50\ \mu\text{s}, -5\ \mu\text{s})$	274
B.7	Delayed coincidences in TU1 within $(-150\ \mu\text{s}, -50\ \mu\text{s})$	274
B.8	Energy dependent time delay in TU1 for each panel.	275
B.9	Energy dependent time delay with TU1 for each panel.	276
B.10	Technical drawings of the new target holder for TU1.	277
C.1	Astrophysical S -factor for the ${}^2\text{H}(\text{p},\gamma){}^3\text{He}$ reaction.	278
C.2	Residuum of the astrophysical S -factor for the ${}^2\text{H}(\text{p},\gamma){}^3\text{He}$ reaction.	278
C.3	Pulse height spectra from IBC-I campaign with $E_{\text{cm}} = 278.7\ \text{keV}$	279
C.4	Pulse height spectra from IBC-I campaign with $E_{\text{cm}} = 400.4\ \text{keV}$	279
C.5	Pulse height spectra from IBC-I campaign with $E_{\text{cm}} = 461.3\ \text{keV}$	279
C.6	Pulse height spectra from IBC-I campaign with $E_{\text{cm}} = 535.3\ \text{keV}$	279
C.7	Pulse height spectra from IBC-I campaign with $E_{\text{cm}} = 670.1\ \text{keV}$	280
C.8	Pulse height spectra from IBC-I campaign with $E_{\text{cm}} = 693.8\ \text{keV}$	280
C.9	Pulse height spectra from IBC-I campaign with $E_{\text{cm}} = 859.8\ \text{keV}$	280
C.10	Pulse height spectra from IBC-I campaign with $E_{\text{cm}} = 1033.4\ \text{keV}$	280
C.11	Pulse height spectra from IBC-I campaign with $E_{\text{cm}} = 1094.2\ \text{keV}$	281

C.12	Pulse height spectra from IBC-I campaign with $E_{\text{cm}} = 265.1$ keV	281
C.13	Pulse height spectra from IBC-I campaign with $E_{\text{cm}} = 332.8$ keV	281
C.14	Pulse height spectra from IBC-I campaign with $E_{\text{cm}} = 399.8$ keV	281
C.15	Pulse height spectra from IBC-I campaign with $E_{\text{cm}} = 467.8$ keV	282
C.16	Pulse height spectra from IBC-I campaign with $E_{\text{cm}} = 535.3$ keV	282
D.1	Photos of several targets after irradiation (#1).	283
D.2	Photos of several targets after irradiation (#2).	284
D.3	Photo from the setup of the target area during FK-I.	285
D.4	Photo from the setup of the target area during FK-V.	285
D.5	Upgraded cold trap design for the target area of the Felsenkeller lab.	286
D.6	Tests with thermal conductivity paste between target and holder.	287
D.7	Impact of a thermal pad on the conductivity of the target and its holder.	288
D.8	Depth distribution for ^3He ions with 45 keV into tantalum.	289
D.9	Depth distribution for ^3He ions with 45 keV, 15 keV and 5 keV into tantalum.	290
D.10	Effective opening angles for MB1, MB2 and Can60.	291
D.11	Effective opening angle for EB17.	292
D.12	Effective opening angle for EB18.	293
D.13	Residua for analysis into the first excited state with ST9.	295
D.14	Residua for analysis into the ground state with ST10.	296
D.15	Residua for analysis into the first excited state with ST10.	297
D.16	Residua for analysis into the ground state with ST11 and ST9B.	298
D.17	Residua for analysis into the first excited state with ST11 and ST9B.	299
D.18	Residua for analysis into the ground state with ST15.	300
D.19	Residua for analysis into the first excited state with ST15.	301
D.20	Resulting γ -ray angular distributions for all irradiations.	302
D.21	Legendre polynomials for the ground state transition using approach 2.	303
D.22	Legendre polynomials for the excited state transition using approach 2.	303
D.23	Legendre polynomials for the ground state transition using approach 3.	304
D.24	Legendre polynomials for the excited state transition using approach 3.	304
D.25	Comprehensive γ -ray angular distribution for the ground state transition.	305
D.26	Comprehensive γ -ray angular distribution for the first excited state transition.	306

List of Tables

2.1	Various properties of the two utilized scintillation materials.	45
3.1	List of all experimental campaigns and utilized samples	64
3.2	Implantation parameters for all samples used during the in-beam campaigns.	65
3.3	Parameters for all samples during their irradiation.	66
3.4	List of utilized α -, and γ -calibration sources and their relevant information.	67
3.5	List of all utilized HPGe detectors and there characteristics.	68
3.6	List of all HPGe detectors and their utilization during the various campaigns.	68
3.7	List of detector distances and angles during the IBC-I campaign.	81
3.8	List of detector distances and angles during the FK-I campaign.	87
3.9	List of detector distances and angles during the FK-V campaign.	90
3.10	Specifications for the offline counting detectors at Felsenkeller	92
3.11	Channel assignment for the digitizer of TU1.	98
4.1	Radon concentration at various positions of the Felsenkeller laboratory.	111
4.2	Comparison of different shielding stages for TU1.	140
4.3	Remaining γ -ray lines in the actively vetoed background spectrum of TU1.	141
4.4	Specifications for all sample holder possibilities with TU1.	156
4.5	Integral background count rates for selected underground HPGe detectors.	158
5.1	Beam energies and γ -ray energies for all campaigns on ${}^2\text{H}(p,\gamma){}^3\text{He}$	167
5.2	Ratio between peak and satellite during the NRA runs.	180
5.3	Areal densities from the ERDA analysis during IBC-I.	183
5.4	Average areal densities from the ERDA analysis.	183
5.5	Areal densities from ERDA and NRA during IBC-I.	185
5.6	Resulting astrophysical S -factor for the ${}^2\text{H}(p,\gamma){}^3\text{He}$ reaction.	186
6.1	Predictions for the Legendre polynomials of the ground state transition.	225
6.2	Resulting Legendre polynomials of the ground state transition.	226
6.3	Predictions of the Legendre polynomials for the first excited state transition.	227
6.4	Resulting Legendre polynomials of the first excited state transition.	228
6.5	Areal densities from the NRA during the IBC-II campaign.	230
6.6	Absolute full-energy peak efficiencies during IBC-II.	233
6.7	Legendre polynomials of the ground state transition during IBC-II.	235
6.8	Resulting activities at the end of irradiation during IBC-II.	237
6.9	Resulting activities at the end of irradiation during FK-I to FK-IV.	238
6.10	Resulting activities at the end of the respective irradiations during FK-V.	239
6.11	Mean activities at the end of each irradiation campaign.	241
6.12	Influencing causes for the quality of a target.	243
D.1	Utilized runs for the analysis of the FK-V campaign.	294

Acronyms

BBN	Big Bang nucleosynthesis
BG	Background
BGO	Bismuthe germanate ($\text{Bi}_4\text{Ge}_3\text{O}_{12}$)
BSD	Bias shutdown
CDM	Cold dark matter
C.L.	Confidence level
CM	Center of mass
CFD	Constant fraction discrimination
CMB	Cosmic microwave background
DAQ	Data acquisition
ENSDF	Evaluated Nuclear Structure Data File
ERDA	Elastic recoil detection analysis
EFT	Effective field theory
FWHM	Full width at half maximum
HG	Hadron gas
HPGe	High purity germanium
HV	High voltage
HZDR	Helmholtz-Zentrum Dresden-Rossendorf
IBC	Ion beam center
KAS	Konrad-Adenauer-Stiftung
LCE	Light collection efficiency
LN2	Liquid nitrogen
MIP	Minimal ionizing particle
NDF	Number of degrees of freedom
NRA	Nuclear reaction analysis
OFRP	Oxygen-free radiopure
PHA	Pulse height analysis
PMT	Photomultiplier
PSD	Pulse shape discrimination
PSD	Physikalisch Technische Bundesanstalt
PVT	Polyvinyltoluene
QCD	Quantum chromodynamics
ROI	Region of interest
SATP	Standard ambient temperature and pressure
SDD	Silicon drift detector
SSB	Silicon surface barrier
SBBN	Standard Big Bang nucleosynthesis
SES	Secondary electron suppression
SHV	Safe high voltage
VKTA	Verein für Kernverfahrenstechnik und Analytik
ULB	Ultra-low background

1 Introduction

While the subtopics within this thesis might seem to illuminate a broad variety of physics fields, the general aim of this thesis can be summarized by the demand to further improve our understanding of primordial nuclides, i.e. based on the investigation of the nuclear physics input. This first chapter is dedicated to give an insight into the main concepts which are important for the further investigations throughout this work. One of the key elements of this thesis is to tackle our understanding of the evolution of chemical elements in both the early Universe (cf. chapter 1.1) and stellar environments (cf. chapter 1.2). Within both of these topics, the ${}^2\text{H}(p,\gamma){}^3\text{He}$ reaction and the ${}^3\text{He}(\alpha,\gamma){}^7\text{Be}$ reaction play a major role. Their relevance, as well as our current understanding of both of them will be discussed in section 1.3 and section 1.4, respectively.

However, studying the early universe and stellar environments here on earth (e.g. via the two mentioned reactions) often requires the ability to measure rarely occurring events. Its concept will be discussed in section 1.5.

1.1 Evolution of the universe

Our current understanding for the expansion of the universe is based on the Einstein field equations of general relativity. By applying the cosmological principle¹ to them, an exact solution for these Einsteins field equations is the Friedmann-Lemaître-Robertson-Walker metric. The resulting so-called Friedmann equations subsequently describe the expansion of the universe based on its spatial curvature k . Assuming both a thermal equilibrium between interacting particles and an adiabatic expansion of the universe, a direct correlation between the thermal development of the universe and its time dimension can be inferred, as e.g. applied in figure 1.1. Along with some extensions, this widely accepted standard model of Big Bang cosmology is called Λ CDM model with Λ being the cosmological constant, and CDM being cold dark matter.

The following section will give an introduction into the formation of the first elements in the early universe based on the model of standard Big Bang nucleosynthesis (SBBN). This theory is using the Λ CDM model with three neutrino flavors, as well as the Standard Model of particle physics, as well as implications from nuclear physics, i.e. fusion processes. While direct citations within the subsections will only be used for specific statements and measurements, a general overview into the field of the standard model of cosmology and the BBN can be found in [21], but also in [22–24]. Highly reputable introductions of both a historic and a modern understanding of stellar nucleosynthesis can be found in [25, 26].

¹At sufficiently large scales, the cosmological principle states, that the universe is isotropic and homogeneous in both space and time.

1.1.1 Big Bang nucleosynthesis

Neutrons and protons are able to condense out of the quark-gluon plasma within a crossover from quantum chromodynamics (QCD) into a hadron gas (HG) as soon as the thermal energy within the early universe drops below $k_B T \approx 170$ MeV (subsequently lower energies in case of a 1st order phase transition). Their subsequent ratio after the cosmological QCD transition is approximately $n_n/n_p = 1$. While both are still within a thermal equilibrium, the further development of their ratio now depends on the temperature (thermal energy) and gets shifted in favor of protons as the universe is expanding and cooling down (cf. figure 1.1 and equation 1).

$$\frac{n_n}{n_p} = \left(\frac{m_n}{m_p}\right)^{3/2} \cdot \exp\left[-\frac{m_n - m_p}{k_B T}\right] \approx \exp\left[-\frac{1.3\text{MeV}}{k_B T}\right] \stackrel{k_B T \approx 0.7\text{MeV}}{\approx} \frac{1}{6} \quad (1)$$

At thermal energies of $k_B T \approx 0.7$ MeV, neutrons and protons also decouple from each other, and their ratio subsequently freezes out². Further changes in this ratio are dominated by the decay of free neutrons.

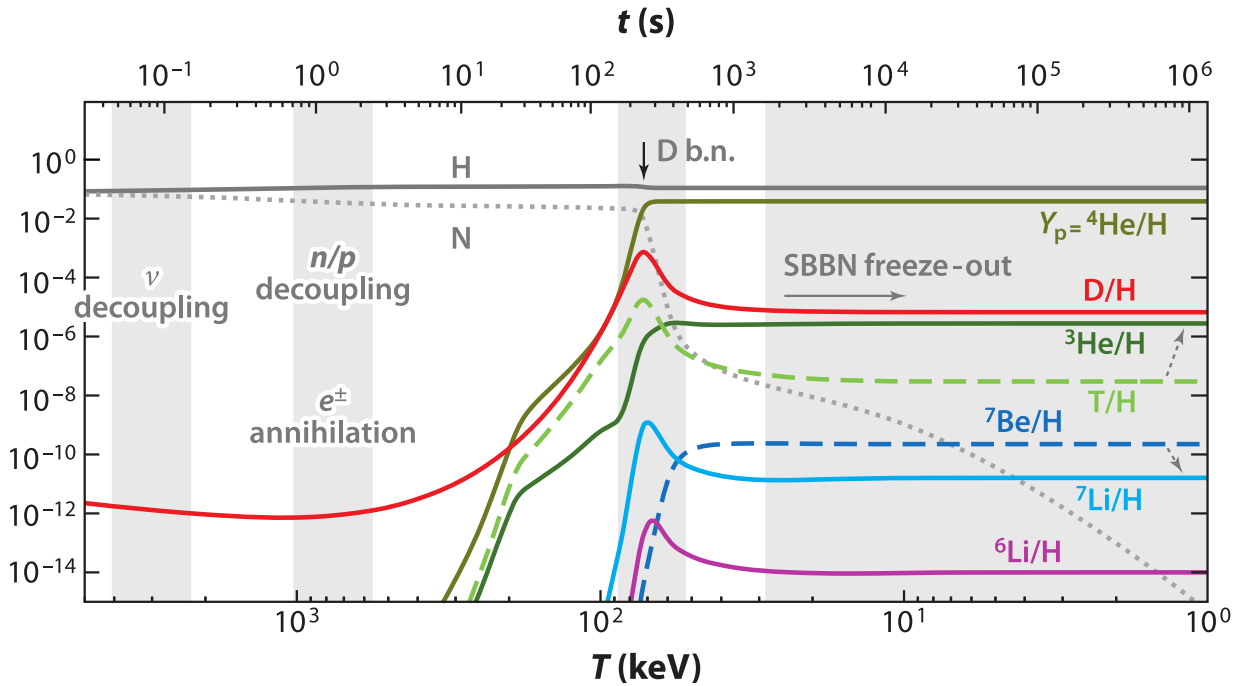


Figure 1.1: Evolution of temperature and time in the early universe with the corresponding development of the BBN-relevant light elements. In addition, relevant other events are indicated by grey vertical bands, i.e. the neutrino decoupling, the n/p freeze-out and e^-/e^+ annihilation, the ^2H bottleneck, and the freeze-out of the BBN. Taken and adapted from [28].

Within the following time period (starting at $t \approx 1$ s after the Big Bang), the universe enters an entirely unique era of its life time: As just discussed, the temperature in the universe is

²The stated energies, temperatures and times are certainly only of an approximate nature, since each particle species actually follows an entire Maxwell-Boltzmann distribution in energies. Furthermore, especially for the weak decoupling, there are also multiple subsequently involved charged current processes [27]

already low enough for the existence of condensed hadrons (i.e. proton & neutron). However, its energy density is also still high enough during the next minutes to let protons and neutrons undergo the first nuclear fusion processes. This stage during the early universe is called the era of Big Bang nucleosynthesis (BBN).

Despite perfect conditions for the subsequent fusion of the first possible nuclide (deuteron), a significant deuteron abundance does not form until $t \approx 100$ s after the Big Bang, as shown in figure 1.1. This is due to the fact, that the binding energy of deuteron is only $E_B = 2.2$ MeV, i.e. it is the lowest of all stable nuclei in the entire nuclide chart. Hence, while every other nucleus in the nuclide chart would already be able to exist with higher abundances, it is the fate of the deuteron nuclei to be constantly photodissociated via ${}^2\text{H}(\gamma, n){}^1\text{H}$.

It is worthwhile noticing, that (according to figure 1.1) the temperature at $t \approx 100$ s is already below the binding energy of deuteron, hence its dissociation up to this point seems unintuitive. However, the photons are following a Maxwell-Boltzmann distribution, so there are high energetic photons with $E > 2.2$ MeV in the universe even at $t \approx 100$ s. In fact, the number of baryons per photon above $k_B T = 2.2$ MeV becomes equal at approximately this point in time. This photodissociation of deuteron nuclei and their hindrance of being formed in significant abundances is also supported by the overwhelming general amount of photons with respect to baryons (baryon-to-photon ratio: $\eta = n_b/n_\gamma \approx 6 \text{ E-}10$). This circumstance, that the entire BBN in the early universe had to ‘wait’ and cool down further until deuteron is not instantaneously dissociated anymore, is also called the deuterium bottle neck³. Until the BBN can finally ignite efficiently, the neutron-to-proton-ratio already decreased further down to $n_n/n_p \approx 1/7$.

As soon as deuteron is not energetically disfavored anymore, other heavy nuclei, i.e. ${}^4\text{He}$ can be formed quickly, as shown in figure 1.1. While there are more than sufficient protons for the subsequent nuclear fusion processes, the major limitation now becomes the low number of neutrons, which are ‘cooked-up’ first. The initial neutron-to-proton-ratio is therefore a crucial measure for the final abundance of ${}^4\text{He}$ in the universe. All of the other nuclei up to $A = 7$ can be understood as insufficiently fused left-overs within the main process of merging protons and neutrons into ${}^4\text{He}$. This way of interpretation of the BBN can also be seen in the left panel of figure 1.2, which shows the involved nuclides, as well as the most important reactions during BBN in terms of the nuclide chart. As indicated by the arrows, all of the most important reactions during BBN end at ${}^4\text{He}$. In addition, this figure also emphasizes the fact, that there are no stable nuclides with $A = 5$, and $A = 8$ in the universe, which acted as a natural border for the merging of heavier nuclei during the early universe.

³In fact, the term ‘deuterium bottle neck’ is misleading and should actually be called ‘deuteron bottle neck’. This is due to the fact that nuclei were being perfectly ionized during the early Big Bang. However, the scientifically accepted term of ‘deuterium bottle neck’ will be used within the scope of this thesis.

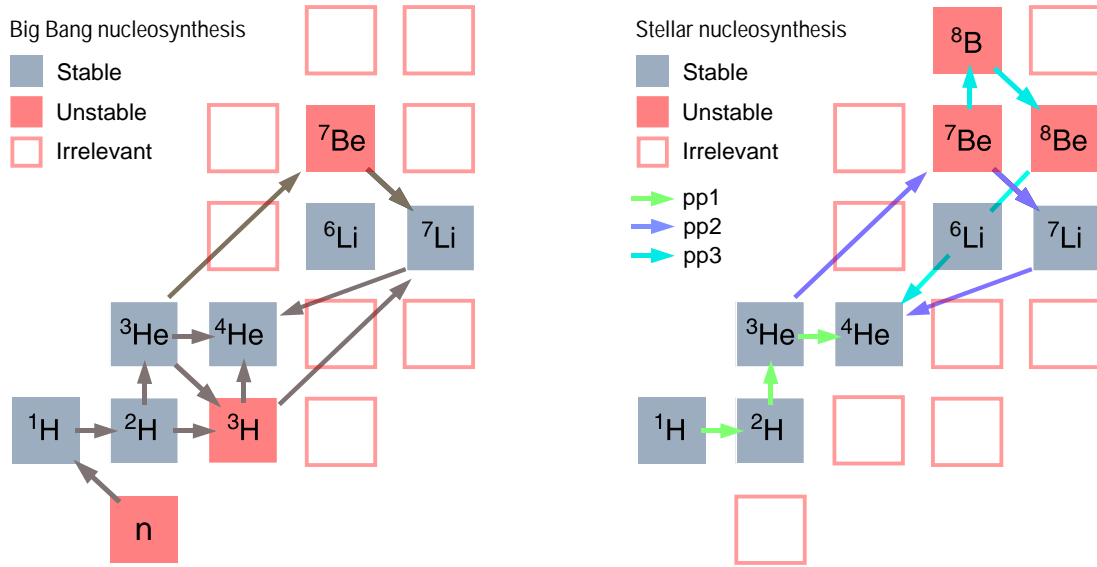


Figure 1.2: Relevant reactions for the BBN (left) and stellar nucleosynthesis (right) are indicated by arrows. The relevant nuclides are labeled and have filled boxes. Stable nuclides are shown in grey and unstable nuclides are shown in red. Furthermore, the right panel also shows the three pp-chains with green (pp1), dark blue (pp2) and light blue (pp3) arrows.

Approximately ten minutes after the Big Bang, the energy density becomes too low for nuclides to overcome each others Coulomb barriers, and the BBN slowly ends. The only abundances, which will still change significantly over the next couple of years are the unstable nuclei (neutrons, ^3H , and ^7Be), subsequently leading to an additional enhancement of ^1H , ^3He , and ^7Li , respectively⁴.

1.1.2 Cosmological concordance from BBN

The abundance of each light nuclide after the BBN solely depends on one free parameter: the baryon-to-photon ratio $\eta = n_b/n_\gamma$. In case of large values for η (which means less photons and more baryons, i.e. nucleons), it is possible to overcome the deuterium bottleneck even earlier in time. The total available time for BBN therefore becomes longer. However, in case of e.g. ^2H and ^3He it is counterproductive to have a longer BBN phase since they will be subsequently fused in larger amounts. Hence, large value for η will therefore result in lower expected abundances of ^2H and ^3He after BBN, but will lead to a (slightly) larger amount of ^4He . This correlation is also shown in figure 1.3. In case of ^7Li it is a little bit more complex due to the fact, that there are two possible reaction channels to produce it. For the first channel, which is the $^3\text{H}(\alpha, \gamma)^7\text{Li}$ reaction, its rate becomes enhanced for low values of η . The second possibility of undergoing a $^3\text{He}(\alpha, \gamma)^7\text{Li}$ reaction with a subsequent

⁴The nuclide ^7Be will play an important role within this thesis. It is crucial to keep in mind, that the half-life of ^7Be at earth will differ with respect to BBN or stellar environments. This is due to the fact, that ^7Be decays via electron capture, which will certainly be distorted in a plasma environment [29].

electron capture into ${}^7\text{Li}$ becomes enhanced for large values of η . Hence, in case of the ${}^7\text{Li}$ abundance, the dependency on η has a minimum, as also shown in figure 1.3.

While the theoretical abundances of the light elements solely rely on the baryon-to-photon ratio η and the reaction rates, the shape of each single curve also depends on the cross sections of all reactions shown in the left panel of figure 1.2. By measuring the elemental abundances, both astronomy and BBN can be used to make multiple statements on the baryon-to-photon ratio, i.e. one for each primordial abundance. However, astronomical observations on primordial abundances are not trivial, simply due to the fact, that almost 13.8 billion years passed, since these primordial elements have been formed.

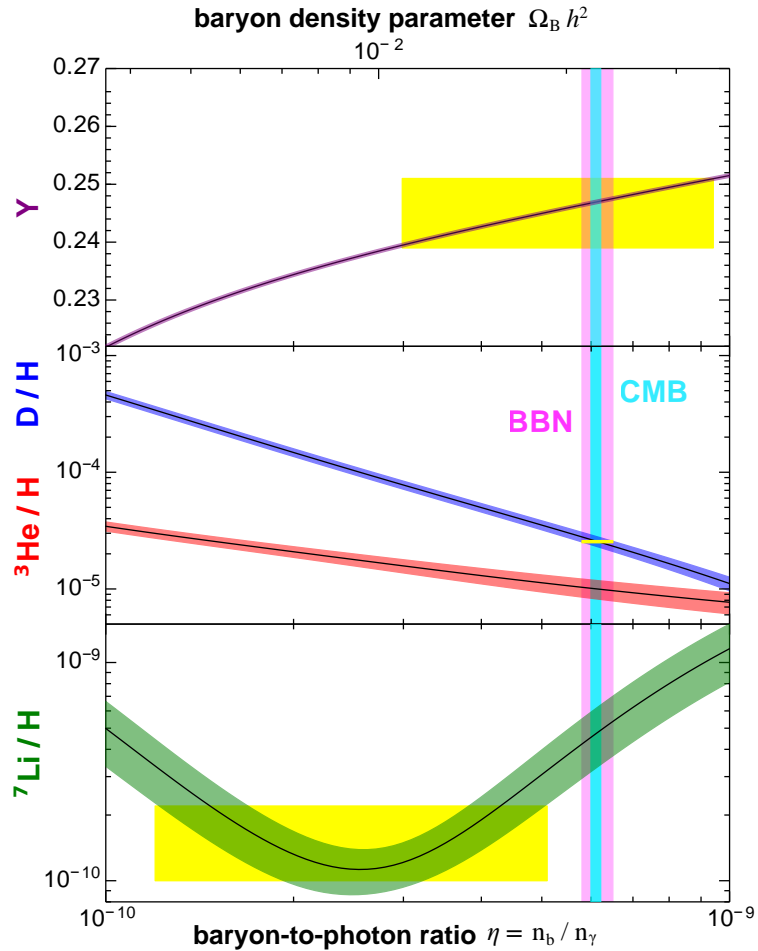


Figure 1.3: Concordance plot for the BBN with the relative abundance of ${}^4\text{He}$ ($Y = {}^4\text{He}/\text{H}$), ${}^2\text{H}$, ${}^3\text{He}$, and ${}^7\text{Li}$ plotted with respect to the baryon-to-photon ratio $\eta = n_b/n_\gamma$. The corresponding predictions of these correlations (stemming from BBN) are shown in purple, blue, red and green, respectively. Their precision on astronomical observations are shown as yellow band. The two vertical lines represent the current predictions of η for BBN and CMB, respectively. The data is based on the 2020 update by the Particle Data Group [24].

Hence, there is a broad variety of scientists working on the precise determination of these abundances. Summing up their legacy in a dangerously brief way, the best observational values for $Y = {}^4\text{He}/\text{H}$, D/H , and ${}^7\text{Li}/\text{H}$ stem from emission lines of H II regions in metal-poor galaxies [23, 30, 31], quasars back-lighting pristine gas clouds [31] and very metal-poor stars

in the halo of our galaxy [23, 31, 32], respectively. Considering the ten orders of magnitude for their differences in observed abundance (yellow boxes in figure 1.2), it is worthwhile emphasizing the overall agreement for the resulting values of η . However, especially the role of the deuterium abundance, which has the most precisely observed primordial element abundances, will be further discussed in section 1.3.

The so-called cosmological concordance from BBN therefore describes the prediction (and the accordance) of the baryon-to-photon ratio η from different primordial abundances based on the standard BBN theory. In addition, there is also an entirely independent field of physics, which can also be used to predict the baryon-to-photon ratio, namely the cosmic microwave background (CMB) [33]. The current constraint on η is plotted as a blue vertical line in figure 1.3 and amazingly, also agrees very well with BBN and observations.

In summary, the direct implications of the cosmological concordance plot shown in figure 1.3 are, that entirely different field of (astro-)physics lead to a comparable result for one of the basic quantities in modern cosmology. This is a great success for the credibility of this broad field and clearly points towards the existence of a Big Bang. However, comparing the resulting uncertainties stemming from the different field of physics, there is a clear mandate to improve the BBN predictions, especially for the ^2H abundance, as discussed later [31].

1.2 Stellar nucleosynthesis

After the completion of the BBN, the universe itself did not have the temperature anymore to overcome Coulomb barriers of nuclei. Hence, it was impossible for the universe to intrinsically change anything in the elemental abundances, neither via fusion processes, nor dissociation processes. Neutrons, which potentially could change the abundance pattern due to their missing electrical charge, either decayed or got bound into light elements. Hence, the universe within the next ≈ 100 Myr became rather unspectacular from a nuclear physics perspective. This drastically changed due to the inevitable consequences from the laws of general relativity. While the universe was assumed to be homogeneous and isotropic (cf. section 1.1), this is only true on considerably large scales. On subsequently smaller scales, inhomogeneous mass distributions lead to significant curvatures in space time, which will then lead to the attraction of more mass. It is the birth of large gas clouds, nebulae, dense cores, protoplanetary disks, and finally the formation of protostars. The continuous accumulation of mass leads to a gravitational pressure, which effectively increases the temperature within the center of these objects. Ionization energies are rather quickly overcome, which leads to a plasma within these protostars [26, 34].

However, during the further in-fall of matter, in the majority of protostars, the central density does not even reach $\rho = 100 \text{ g/cm}^3$ in order to (re-)ignite the first fusion process. This is a considerably low density, especially when compared to the earth's element with the highest density: Osmium with $\rho = 22.6 \text{ g/cm}^3$. This star will subsequently start to fuse hydrogen,

as further discussed in the next paragraph. These overwhelmingly exothermic reactions will soon stop the in-fall of matter and create a hydrostatic equilibrium. This means, that each layer of the star equals out the outgoing radiation pressure stemming from lower layers and the ingoing gravitational pressure from outer layers. As long as both driving forces remain similar, the star will also keep its size.

Hydrostatic hydrogen burning

The overall elemental fuel, which can be burned in nuclear fusion processes within stars essentially consists of 75% protons and 25% of ^4He (i.e. the relic of the BBN). Furthermore, the necessary core temperature for a nucleus within a star to be fused to a larger nucleus strongly depends on its atomic number. The higher the atomic number, the larger the Coulomb barrier and the larger the necessary core temperature of the star [26].

In summary, each protostar mainly consists of ^1H and ^4He and protons can already undergo fusion reactions at these low core temperatures. Hence, the first burning processes of stars concentrates solely on the fusion of hydrogen to helium. This era of the star usually also takes far more than 90% of its entire life time (depending on the initial mass).

There are two main known processes to effectively merge protons into ^4He , namely the pp-chain and the CNO cycle⁵. The most important reactions of the pp-chain are shown in the right panel of figure 1.2, which is also indicating three subchains pp1, pp2 and pp3. It is worthwhile mentioning, that the color of the arrow for each subchain only shows the breakout reactions with respect to the previous chain. For example, the pp2-chain and pp3-chain also undergo the first p+p (or p+e+p) reaction in the network, but break out at a later stage. The other known process within the hydrostatic hydrogen burning is the CNO cycle, which can also be divided into sub-cycles. The first cycle (the CNO-I cycle) uses proton captures and weak decays to fuse the nuclide ^{12}C piece-wise into ^{15}N . This undergoes a $^{15}\text{N}(p,\alpha)^{12}\text{C}$ reaction, and hence also effectively transformed four protons into ^4He . Alternatively, ^{15}N could also undergo another proton capture to result in ^{16}O , hence breaking out of CNO-I and starting the CNO-II cycle, and so on and so forth.

Higher burning states

While the hydrostatic hydrogen burning lasts for the majority of the entire life span of the star, eventually it will have burned its available fuel considerably. The radiation pressure will therefore also decrease, so the star will inevitably shrink in order to maintain hydrostatic equilibrium. If the mass of the star is large enough, the resulting core temperature during collapse will ignite the next burning cycle, which is called helium burning [26].

Due to its abundance in the universe (especially in stars after hydrogen burning), ^4He is the most suitable candidate to dominate the further fate of a star. Its large abundance,

⁵Stars of the first generation were only able to fuse via the pp-chain due to their lack of carbon, nitrogen and oxygen.

together with the argument of preferred reactions with low atomic number (due to Coulomb barriers), leads to the so-called triple- α process, which is the (almost) simultaneous fusion of three alpha particles to ^{12}C . In fact, the product of the fusion of two alpha particles (^8Be) is highly unstable. Nevertheless, depending on the temperature, a certain amount of nuclides in the star will always be in the state of ^8Be and subsequently enable another alpha capture process to form the energetically preferred ^{12}C . The reaction rate of this process is greatly enhanced by the so-called Hoyle-state in ^{12}C and opens the further burning cycles of subsequent alpha captures ($^{12}\text{C}(\alpha, \gamma)^{16}\text{O}$, $^{16}\text{O}(\alpha, \gamma)^{20}\text{Ne}$ etc.). These, and many more break-out reactions will subsequently fuse heavier elements within various burning cycles until the nuclides with the largest binding energy per nucleon are formed in the core (namely ^{62}Ni , ^{58}Fe and ^{56}Fe). The production of these nuclides will mark the final stage and initiate the inevitable death of massive stars.

1.3 The $^2\text{H}(\text{p}, \gamma)^3\text{He}$ reaction

As indicated before, deuterium has an outstanding position considering all nuclei in the universe. On the one hand, it is the nuclide with the lowest binding energy of all stable nuclides, and on the other hand, it is always the first one which can be formed within a hot proton/neutron plasma (i.e. BBN and stellar environments etc.). During the early universe, this resulted in the deuterium bottle neck, as elaborated in section 1.1.1.

Due to the comparatively ‘large’ amount of deuterium during certain phases of the BBN, all three possible destruction channels ($^2\text{H}(\text{p}, \gamma)^3\text{He}$, $^2\text{H}(^2\text{H}, \text{n})^3\text{He}$, and $^2\text{H}(^2\text{H}, \text{p})^3\text{H}$) play a significant role there (cf. section 1.1.1 and figure 1.2). However, for stellar hydrogen burning processes, usually only the destruction via $^2\text{H}(\text{p}, \gamma)^3\text{He}$ is considered (cf. figure 1.2). This can be explained as follows: Compared to the other two destruction channels its cross section might not be the largest, but one of its two necessary nuclides (namely ^1H) makes up approximately 75% of protostar. Meanwhile, the other two channels ($\text{d}+\text{d}\rightarrow\text{n}+^3\text{He}$ and $\text{d}+\text{d}\rightarrow\text{p}+\text{t}$) rely in their entirety on the comparatively negligible amount of deuterium [26]. Additionally, the scientific significance of the $^2\text{H}(\text{p}, \gamma)^3\text{He}$ reaction has been boosted during the last years. One reason is the recent precise determination of the primordial deuterium abundance from astronomical observations [31]. The underlying measurements are based on quasars shining through pristine gas clouds (very low metallicity, hence as primordial as possible) [31]. This leads to a determination of the primordial deuterium abundance with an accuracy of 1.2%, which is unprecedented for primordial abundances.

As elaborated in section 1.1.2, the determination of the cosmological baryon density Ω_b is based on three entirely independent pillars, namely astronomical observations, the CMB and the BBN. Furthermore, the primordial deuterium abundance is unprecedented for both its known precision and its highest sensitivity to Ω_b among all relevant nuclei (cf. figure 1.3). While the latest results of astronomical observations and the CMB lead to precisions of Ω_b

in the order of 1%, the BBN has been lacking behind with almost 3% uncertainty on Ω_b . Its corresponding error budget for a precise prediction of the primordial deuterium abundance (and subsequently Ω_b) stemming from BBN can be divided into the contributions of the three main destruction reactions of deuterium [35]. These reactions are (in order of significance to the total error budget) ${}^2\text{H}(p,\gamma){}^3\text{He}$ with 49%, ${}^2\text{H}({}^2\text{H},n){}^3\text{He}$ with 37%, and ${}^2\text{H}({}^2\text{H},p){}^3\text{H}$ with 14%.

In order to drive modern cosmology further towards a precision science, one essential step is therefore to precisely understand the ${}^2\text{H}(p,\gamma){}^3\text{He}$ reaction, namely its cross section and its astrophysical S -factor (see also section 2.8 for a more thorough introduction).

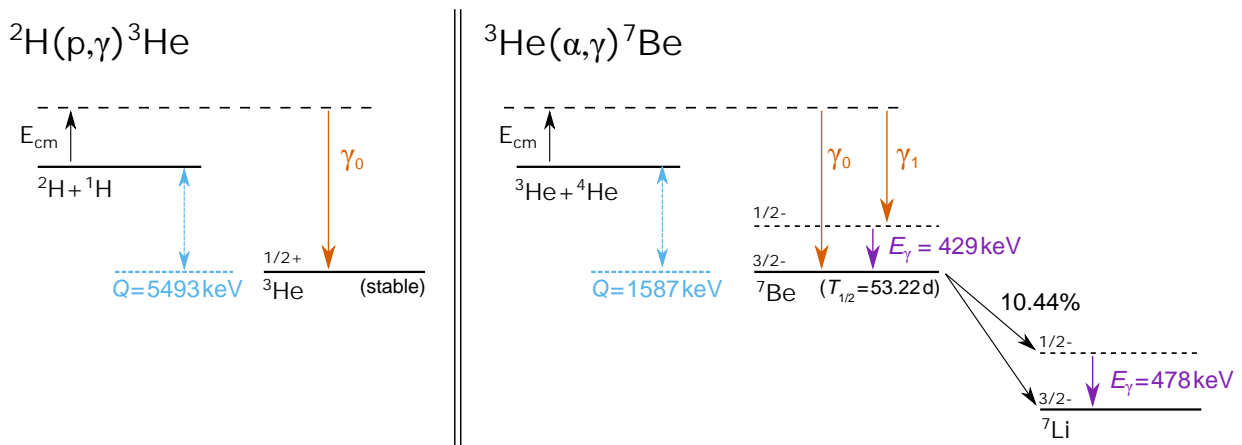


Figure 1.4: Schematic energy level diagram of the ${}^2\text{H}(p,\gamma){}^3\text{He}$ reaction (left) and ${}^3\text{He}(\alpha,\gamma){}^7\text{Be}$ reaction (right). Their corresponding Q -values are marked in light blue. The resulting prompt γ -rays stemming from the direct capture are shown in orange. Fixed γ -ray energies due to the de-excitation of excited states are shown in purple. In case of ${}^7\text{Be}$, the subsequent electron capture to ${}^7\text{Li}$ is also shown. These figures are not true to scale.

Course of this reaction

Due to the ejectile being a γ -ray, the ${}^2\text{H}(p,\gamma){}^3\text{He}$ reaction is a so-called radiative capture reaction. The projectile gets absorbed by the target, and there is no ejected nucleon. Furthermore, this reaction is exothermic with a Q -value of $Q = 5493$ keV. Despite this large Q -value, there is no available excited state in ${}^3\text{He}$, which could be populated. Hence, this reaction solely relies on a direct capture, as shown in the left panel of figure 1.4. The underlying kinematics of direct capture reactions will be introduced in chapter 2.6, but it's already apparent that the energy of the emitted γ -ray strongly depends on the center-of-mass energy E_{CM} .

1.3.1 Review on previous work

The current status of the S -factor for the ${}^2\text{H}(p,\gamma){}^3\text{He}$ reaction during mid 2020 is shown in figure 1.5. While the available data sets, and the resulting S -factor are shown in the upper panel, the lower panel provides the BBN sensitivity window. It is apparent, that the

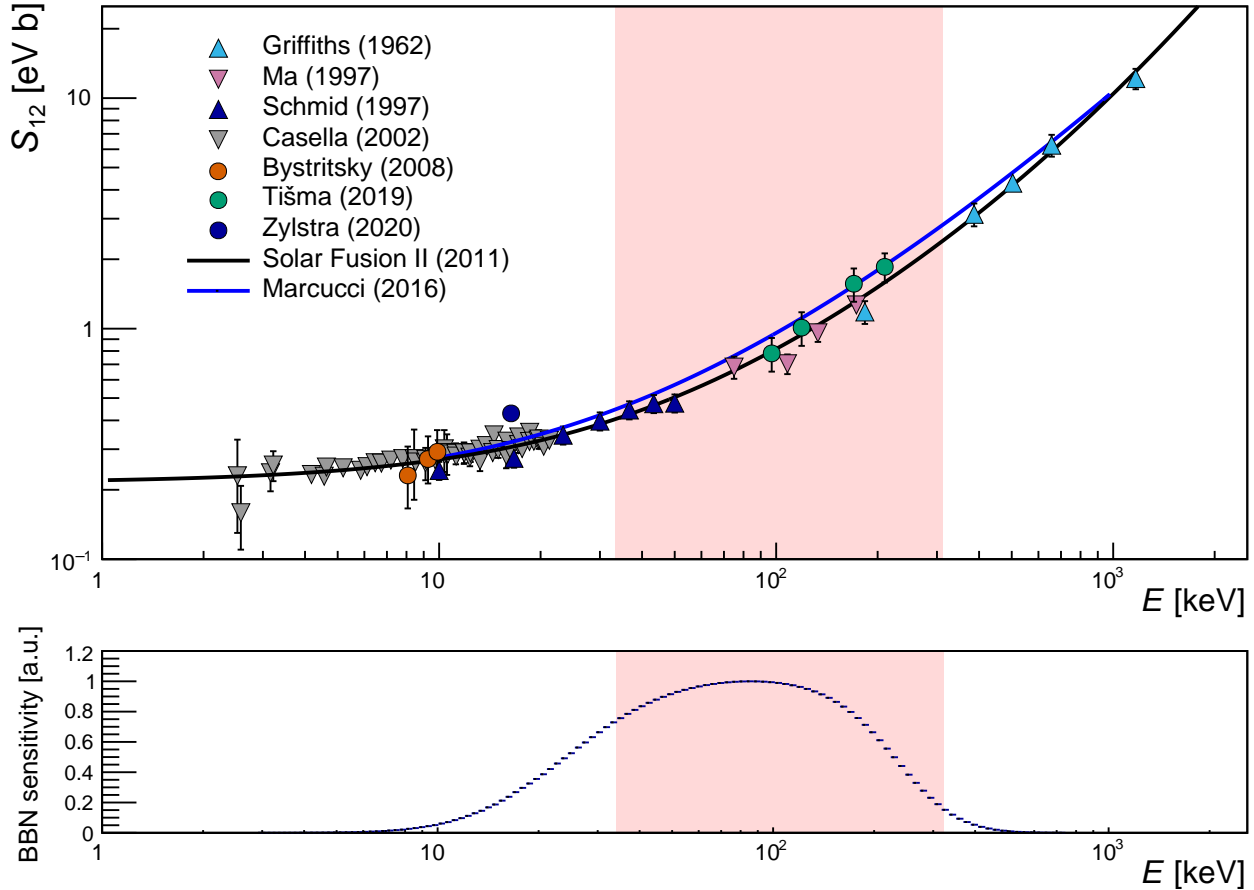


Figure 1.5: Top: Experimental campaigns on the astrophysical S -factor of the ${}^2\text{H}(p,\gamma){}^3\text{He}$ reaction, which have been performed past 1990 and until the mid of 2020, are shown with respect to the energy [36–42]. In addition, the result of the Solar Fusion II fit [43] and an ab initio theory curve [44] is shown as black line, and blue line, respectively. The triangles represent the data sets, which have been used for the Solar Fusion II fit. Bottom: Sensitivity of this reaction for BBN in arbitrary units. The red shaded area marks the central 90% of the sensitivity (note the phenomenologically linear binning on the otherwise logarithmic x-scale). The corresponding figure including datasets after mid 2020 can be found in chapter 5.5.

majority of precise data sets is located at lower energies, i.e. closer to the Gamow window of the Sun. A lack of precision for this reaction as input for BBN is evident.

During the Solar Fusion II workshop held at the Institute for Nuclear Theory, Seattle, in January 2009, this reaction has been evaluated along with its available data sets in order to agree on an accepted fit curve for its S -factor. The experimental data sets found to be valid for this fit curve stem from Griffiths et al. (1962), Schmid et al. (1997), Ma et al. (1997), and Casella et al. (2002) [36–39].

The first reliable measurement was published by Griffiths et al. in 1962. They used both ice targets, and a gas target made of deuterated water (D_2O), irradiated them with a proton beam and measured both the cross section and the angular distribution using two sodium iodide scintillation counters. Together with two publications from Griffiths et al. (1963), and Bailey et al. (1970), a more or less coherent picture of this reaction arose, which held

until the late 1990's [45, 46].

Within 1996, and 1997, the two independent groups of Schmid et al. and Ma et al. published their data using the same accelerator at the Triangle Universities Nuclear Laboratory (TUNL) at Duke University [37, 47]. Both collaborations reported coherently lower astrophysical S -factors than previously assumed and claimed that both data sets from Griffiths et al. (1963), and Bailey et al. (1970) suffer from the use of incorrect stopping powers, which systematically increased their cross section [45]. Due to the fact, that the Solar Fusion II workshop also excluded these two publications, they are also not further considered within this thesis.

However, in 1996 Schmid et al. published their data based on a similar experimental approach than Griffiths et al. in 1962⁶. They investigated this reaction both in direct and indirect kinematics using D_2O and H_2O ice targets and a HPGe γ -ray detector. Also Ma et al. were using a similar approach, which was published in 1997 by working with thick ice or heavy ice targets. They also investigated this reaction both in direct and indirect kinematics by using deuterated water (D_2O) and deuterium depleted H_2O as targets, respectively. Furthermore, they used two large-volume, HPGe γ -ray detectors.

An extensive study by the LUNA collaboration was published in 2002, which covers the low energetic region, i.e. the solar Gamow window (approximately lying at 3-10 keV in case of our Sun) [39]. They used a windowless gas target with three differentially pumped stages and the signal detection was done using a segmented BGO detector.

In addition to the four studies included in the Solar Fusion II fit (Griffiths in 1962, Schmid in 1996, Ma in 1997, and Casella in 2002), there are also three further measurements, which will be briefly discussed in the following, namely the publications by Bystritsky et al. in 2008 [40], Tišma et al. in 2019 [41] and Zylstra et al. in 2020 [42].

Bystritsky et al. published their data in 2008 based on using the Hall accelerator at Tomsk Polytechnic University and frozen targets of heavy water D_2O . The γ -ray detection was performed using six plastic scintillators and one NaI(Tl) crystal. Tišma et al. published their data in 2019 using two deuterated titanium targets. They investigated both the S -factor and the γ -ray angular distribution using two HPGe detectors. Zylstra et al. reported on their measurement of the ${}^2\text{H}(p,\gamma){}^3\text{He}$ cross section in 2020 using inertially confined plasmas at the OMEGA laser facility. Their measurement seems to result in a larger S -factor, but is also not out of scope when considering their systematic uncertainties. All of these available data sets are shown in figure 1.5 with triangles for the data used by Solar Fusion II, and circles for additional data sets.

While the previously described data sets provide a crucial experimental insight into this reaction, an important theoretical contribution has been provided by Marcucci et al. in 2016 [44]. They calculated the astrophysical S -factor using a microscopic ab initio approach. This approach is based on the hyperspherical harmonics technique in order to solve for the $A=3$

⁶The PRL was published in 1996 [47], and the subsequent PRC was published in 1997 [38].

nuclear wave functions including both two- and three-nucleon interactions. Their result is plotted as a blue curve in figure 1.5 and pointed towards a more severe destruction of deuteron during the Big Bang.

The most influential recently published data set has been acquired by the LUNA collaboration [48]. Their experiment and the subsequent analysis has been performed almost simultaneously to the analysis of the group by HZDR and TU Dresden [1]. While this section only covered the publications until mid of 2020, both the work of LUNA, as well as the work of the group by HZDR and TU Dresden will be discussed in the dedicated section 5.

1.4 The ${}^3\text{He}(\alpha,\gamma){}^7\text{Be}$ reaction

Within section 1.1.1 it was mentioned, that the most important reactions during BBN end at ${}^4\text{He}$. In fact, this is only partly true, as there are also two destruction channels for ${}^4\text{He}$, namely ${}^3\text{He}(\alpha,\gamma){}^7\text{Be}$, and ${}^3\text{H}(\alpha,\gamma){}^7\text{Li}$. Due to the fact, that both starting nuclides are stable, especially the ${}^3\text{He}(\alpha,\gamma){}^7\text{Be}$ plays a major role in both BBN and stellar nucleosynthesis (cf. figure 1.2). Furthermore, the ${}^3\text{He}(\alpha,\gamma){}^7\text{Be}$ reaction currently limits our theoretical understanding of the otherwise precisely measured ${}^7\text{Be}$ neutrino flux [49] and ${}^8\text{B}$ neutrino fluxes [50] stemming from the Sun. The impact of the reaction onto the error budget of both theoretical fluxes has been estimated to be 4.6% and 4.3%, respectively [51]. In case of the ${}^7\text{Be}$ solar neutrino flux, the uncertainty stemming from the ${}^3\text{He}(\alpha,\gamma){}^7\text{Be}$ reaction is even the largest uncertainty among all contributions.

Course of this reaction

While the ${}^2\text{H}(\text{p},\gamma){}^3\text{He}$ reaction (within BBN and stellar environments) is a radiative capture reaction, which is simply based on a direct capture and a subsequent de-excitation into the ground state of ${}^3\text{He}$, the situation is more complex in case of the ${}^3\text{He}(\alpha,\gamma){}^7\text{Be}$ reaction.

Due to the ejectile being a γ -ray, the ${}^3\text{He}(\alpha,\gamma){}^7\text{Be}$ reaction is also a radiative capture reaction. The projectile gets absorbed by the target, and there is no ejected nucleon. Furthermore, this reaction is also exothermic with a Q -value of $Q = 1587$ keV. In contrast to the ${}^2\text{H}(\text{p},\gamma){}^3\text{He}$ reaction, the resulting ${}^7\text{Be}$ nucleus has an important first excited state (cf. right panel in figure 1.4), i.e. an excited state at $E = 429$ keV. While this reaction itself also solely relies on a direct capture (cf. chapter 2.6 for a kinematic introduction), the resulting nucleus can now deexcite either directly into the ground state via the emission of γ_0 , or it deexcite into the first excited state, hence populating it and leading to a subsequent emission of a $E = 429$ keV γ -ray. The resulting ${}^7\text{Be}$ nucleus is radioactive and decays via an electron capture ($T_{1/2} = 53.22$ d) into ${}^7\text{Li}$. In $\eta = 10.44\%$ of these transitions, the first excited state of ${}^7\text{Li}$ is populated, leading to a subsequent emission of a γ -ray with $E = 478$ keV.

1.4.1 Review on previous work

The previous investigations on the ${}^3\text{He}(\alpha,\gamma){}^7\text{Be}$ reaction can be categorized into three major experimental approaches: Publications on the cross section by measuring the prompt γ -rays (further called ‘in-beam experiments’), experiments based on an activation analysis of the subsequently activated ${}^7\text{Be}$ (further called ‘offline experiments’), and ERNA measurements based on the detection of ${}^7\text{Be}$ recoil nuclei (further called ‘recoil measurements’).

However, the first two approaches seem to be somehow discrepant in a way, that offline experiment tend to result in a slightly lower S -factor, than in-beam experiments (cf. figure 1.6 and figure 6.33). Intuitive attempts of explanation could either points towards an overestimation of the ${}^7\text{Be}$ activity in offline experiments due to ${}^7\text{Be}$ being also produced via contaminant reactions during the irradiation of the targets [43].

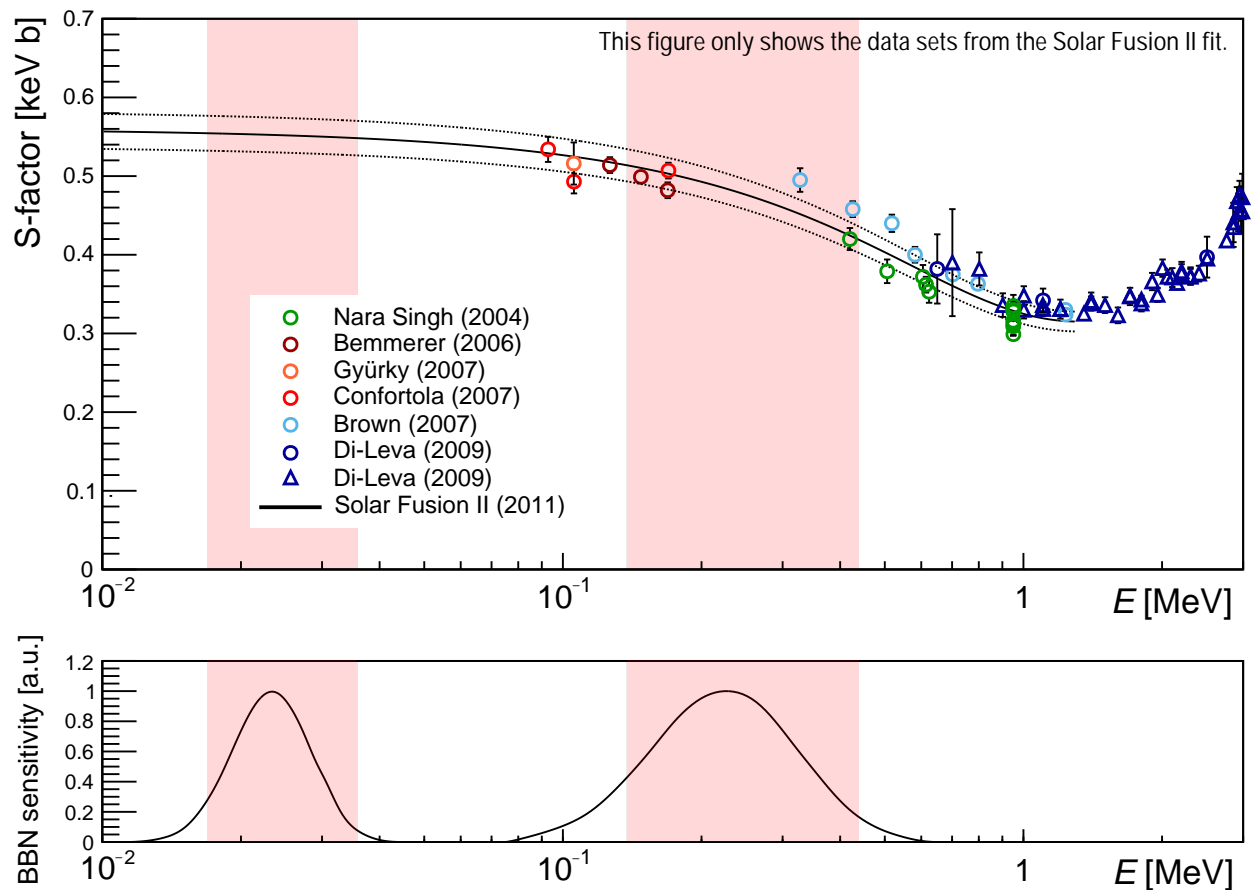


Figure 1.6: Top: Experimental campaigns on the astrophysical S -factor for the ${}^3\text{He}(\alpha,\gamma){}^7\text{Be}$ reaction with the data sets used by Solar Fusion II workshop are shown with respect to the energy [52–57]. In addition, the result of the Solar Fusion II fit [43] and its uncertainty band is shown as a black line and dotted lines up to $E = 1.3\text{ MeV}$, respectively. The circles represent the data sets based on offline measurements. The triangles show the data set based on ERDA. Bottom: Sensitivity of this reaction for nucleosynthesis within our Sun, and during the BBN, respectively [58, 59]. The red shaded areas mark the central 90% of these sensitivities. The corresponding figure with more data sets is shown in figure 6.33.

Alternatively, the issue could also be explained by the lack of data on the γ -ray angular distribution in in-beam experiments (cf. section 1.4.2). This distribution is only theoretically predicted and may introduce inaccuracies, when correcting the data of an in-beam detector to the anisotropy at this certain angle.

For the Solar Fusion II fit, this discussion lead to the exclusion of any prompt data for their analysis [43]. It has been argued, that cross contaminations in offline experiments are highly disfavored by choosing ^3He as a target and ^4He as projectile (which also has been done for all new measurements besides [52]), and are therefore trustworthy. In addition, the inclusion of the in-beam experiments into the fit would not have been affected the resulting precision very much. The current Solar Fusion II fit is therefore only based on offline experiments and recoil experiments.

Due to the importance of this reaction, there is a broad variety of data sets available. In order to coherently introduce the previous work on this reaction, figure 1.6 **only** shows the data, which has been used for the fit of the Solar Fusion II workshop [43], namely offline experiments (circles) and recoil measurements (triangles). Additional data sets, which were either excluded by the Solar Fusion II workshop (e.g. online experiments), or not yet existing in 2011, are shown in figure 6.33.

1.4.2 The γ -ray angular distribution

As previously mentioned, there is no experimental data on the γ -ray angular distribution of the $^3\text{He}(\alpha,\gamma)^7\text{Be}$ reaction. However, there are theoretical approaches mainly based on effective field theory (EFT). In the following, there are two theoretically predicted distributions, which will be briefly introduced. The first one is the prediction by Tombrello et al. [60], which is from 1963 and widely used in the scientific community in order to correct the in-beam experiments investigating the cross section of this reaction. The second theoretical approach, which will be shortly discussed is the work by Zhang et al. [61]. This publication is more contemporary, and mainly focusing on the energy region well below the $7/2^-$ resonance. However, both groups quote their results in terms of both the ground state transition, as well as the transition into the first excited state.

Due to the fact, that both works are using slightly different interpretations of Legendre polynomials and their coefficients, the coefficients a_i of Tombrello et al. will be quoted in lower case letters, while the coefficients A_i by Zhang et al. will be quoted using upper case letters.

It is worthwhile mentioning, that the γ -ray angular distribution of the $^3\text{He}(\alpha,\gamma)^7\text{Be}$ reaction is investigated also by multiple other groups in the scientific community [62–66]. However, the focus in the following will be on the two mentioned investigations.

Distribution by Tombrello et al.

The data, which is shown in this paragraph (i.e. the data in figure 1.7) is extracted from figure 3 and figure 4 in [60] using a digitizing software. The underlying approach by Tombrello et al. is based on first-order perturbation theory with contributions to the capture matrix element only from outside the nuclear surface. The resulting differential cross section is given in terms of the five coefficients σ_0 , a_1 , a_2 , a_3 , and a_4 , as shown in equation 2.

$$\frac{d\sigma}{d\Omega} = \sigma_0(E_{\text{cm}}) [1 + a_1(E_{\text{cm}}) \cos(\theta) + a_2(E_{\text{cm}}) \cos^2(\theta) + a_3(E_{\text{cm}}) \cos^3(\theta) + a_4(E_{\text{cm}}) \cos^4(\theta)] \quad (2)$$

While σ_0 is an energy dependent factor, which determines the general strength of the cross section, the four other constants are giving an insight into the angular distribution at each center-of-mass energy E_{cm} . The theoretical prediction of these energy dependent coefficients is shown in figure 1.7 for both the ground state transition and the first excited state transition, respectively.

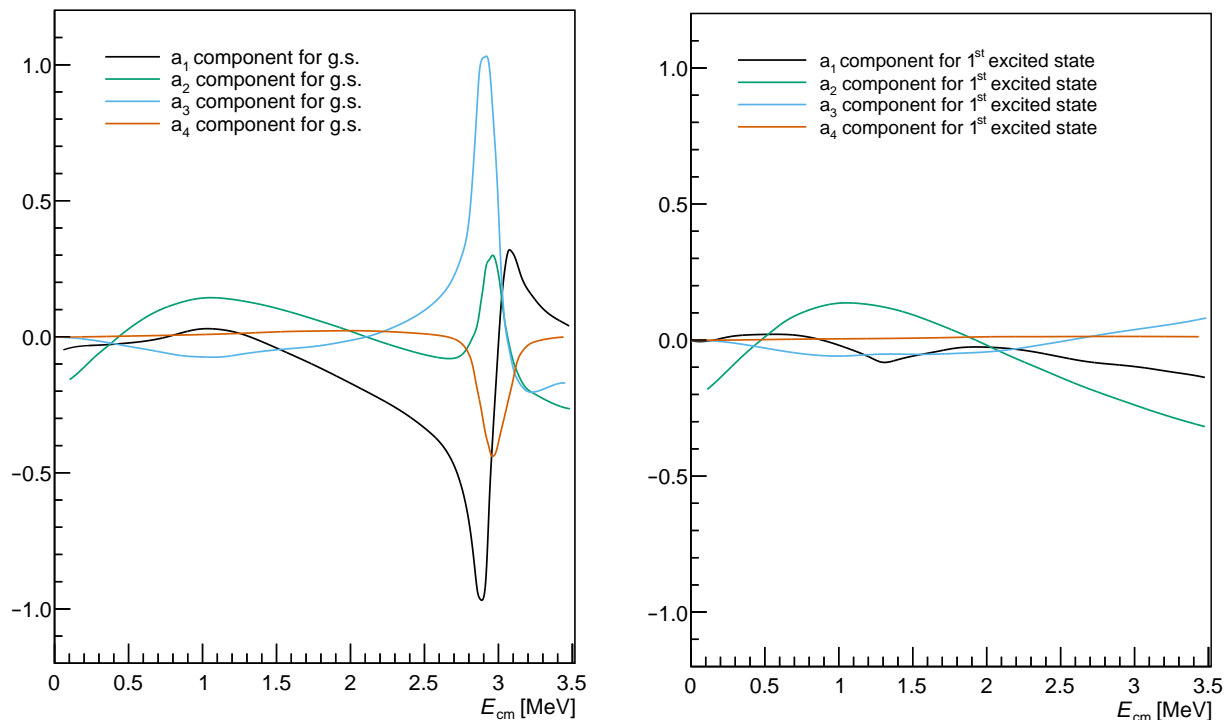


Figure 1.7: Theoretical coefficients for the γ -ray angular distribution of the ${}^3\text{He}(\alpha,\gamma){}^7\text{Be}$ reaction based on Tombrello et al. [60]. Both y-axes are identical for sake of comparability. Their x-axes span a broader energy interval than their resulting distributions in figure 1.8, but cover the same as in figure D.25 and figure D.26. Left: Coefficients for the ground state transition. Right: Coefficients for the transition into the first excited state (see appendix D.9).

The resulting prediction for the γ -ray angular distributions of the ${}^3\text{He}(\alpha,\gamma){}^7\text{Be}$ reaction within the energy region of interest is shown in figure 1.8 for both the transition into the

ground state (left) and the transition into the first excited state (right). For the corresponding distributions spanning a broader energy range, see the appendix D.9.

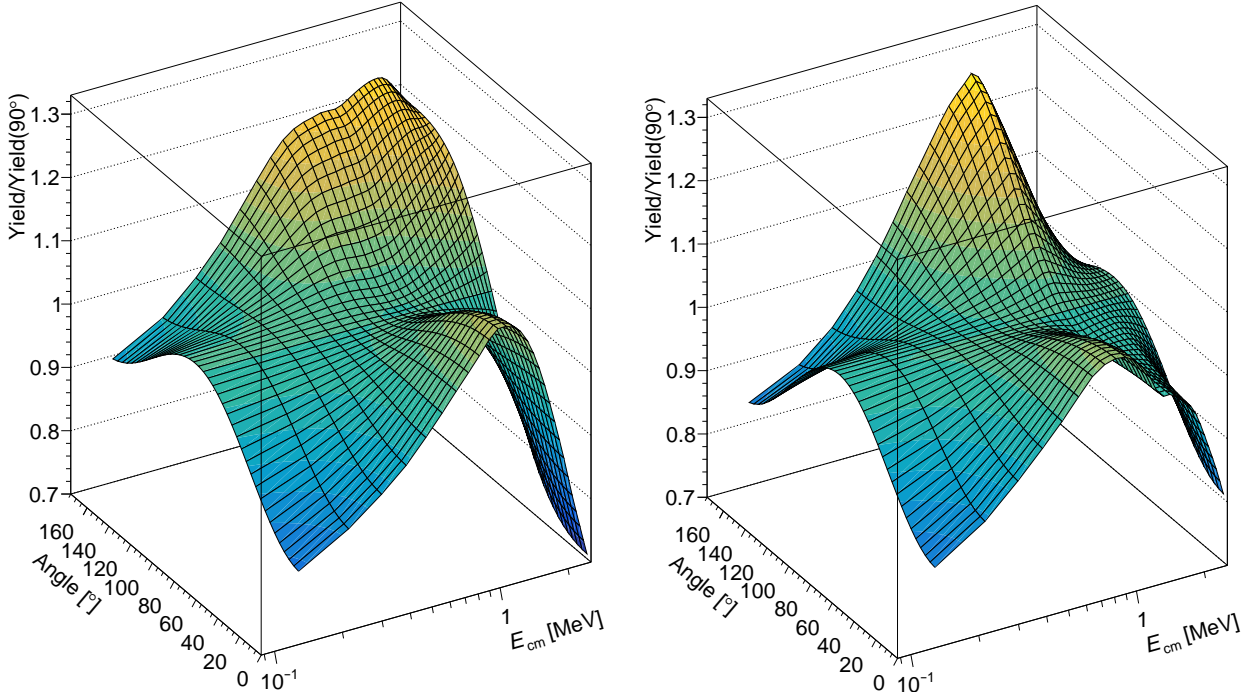


Figure 1.8: Theoretical γ -ray angular distribution for the ${}^3\text{He}(\alpha,\gamma){}^7\text{Be}$ reaction based on Tombrello et al. [60]. Left: Normalized yield with respect to E_{cm} of the reaction (log scale) and the angle of the emitted photon from the ground state transition. Right: Normalized yield with respect to E_{cm} of the reaction (log scale) and the angle of the emitted photon from the transition into the first excited state. For the sake of clarity, these plots only show energies up to $E_{\text{cm}} = 2.5$ MeV, while more detailed figures can be found in the appendix D.9.

In these energy regions of interest, particularly the region well below the $7/2^-$ resonance at approximately $E_{\text{cm}} = 2.7$ MeV (not shown here and stemming from the second excited state of ${}^7\text{Be}$ at $E = 4570(50)$ keV), both theoretical angular distributions are dominated by the comparatively strong variations in the a_2 component.

This a_2 component is positive at around $E_{\text{cm}} = 1$ MeV, and becomes negative above and below. Hence, this component is responsible for the overall underlying quasi-symmetric shape with a minimum in the yield at 90° around $E_{\text{cm}} = 1$ MeV, which would subsequently develop into a maximum at 90° for corresponding lower and higher energies. However, this maximum only develops at lower energies ($E_{\text{cm}} \lesssim 0.3$ MeV) and is covered for higher energies by non-negligible a_1 , a_3 , and a_4 components, respectively. The forward/backward asymmetry from the a_1 and a_3 components, as well as the general complexity of the distribution becomes even more prominent when approaching the $7/2^-$ resonance at $E_{\text{cm}} \approx 2.7$ MeV (cf. appendix D.9).

The general behavior for the distribution of the ground state transition in the region of interest can briefly be summarized as follows:

- $E_{\text{cm}} < 0.3 \text{ MeV}$: Mainly dominated by the negative a_2 component.
- $E_{\text{cm}} \approx 0.4 \text{ MeV}$: All components comparatively small (approx. isotropic emission).
- $0.5 \text{ MeV} < E_{\text{cm}} < 1.5 \text{ MeV}$: Mainly dominated by the positive a_2 component.
- $2.0 \text{ MeV} < E_{\text{cm}} < 2.5 \text{ MeV}$: Mainly dominated by the negative a_3 component.
- $E_{\text{cm}} > 2.5 \text{ MeV}$: Resonant region with dominance of odd components.

Distribution by Zhang et al.

The data, which is shown in this paragraph is based on figure 5 in [61] and was kindly provided by X. Zhang. The underlying approach is using a next-to-leading-order (NLO) amplitude in an Halo EFT. However, they are mainly focusing on the angular distribution in the region below 2 MeV, which is dominated by the anisotropy due to the A_2 component [61]. This anisotropy therefore can be expressed by the differential S -factor $dS/d\Omega$, as shown in equation 3.

$$\frac{dS}{d\Omega} \propto 1 + A_2(E_{\text{cm}}) \cos^2(\theta) \quad (3)$$

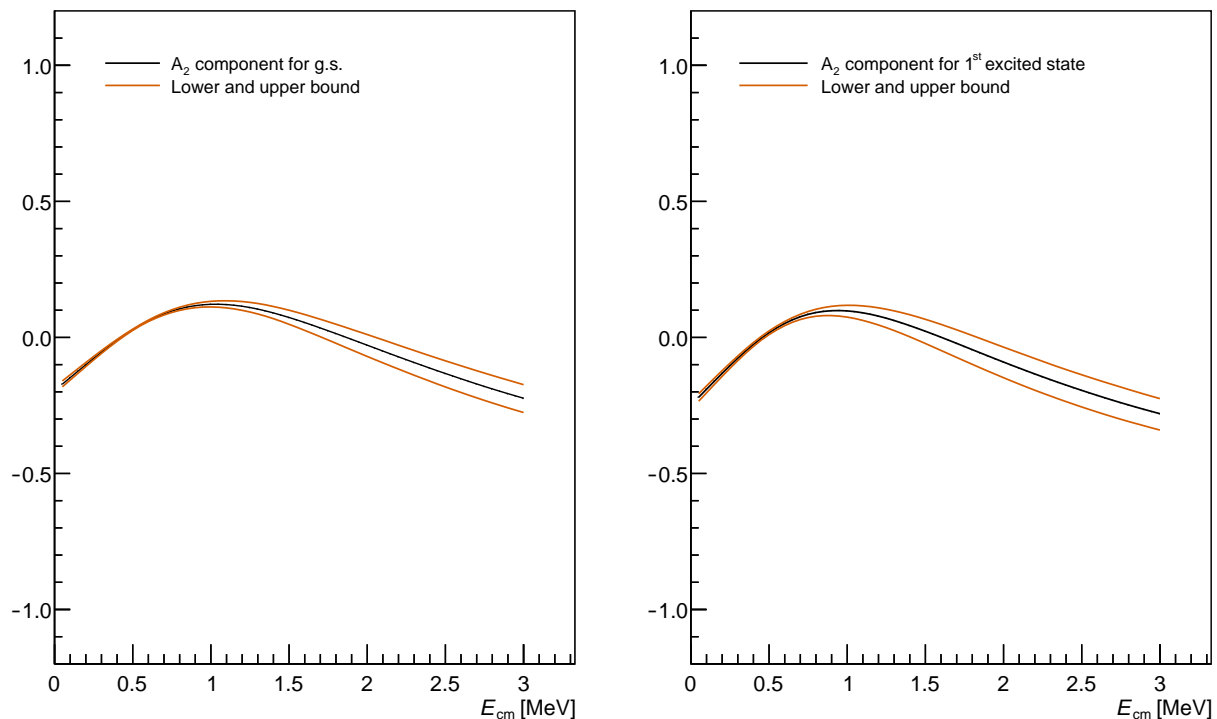


Figure 1.9: Theoretical coefficient A_2 for the γ -ray angular distribution of the ${}^3\text{He}(\alpha,\gamma){}^7\text{Be}$ reaction based on Zhang et al. [61]. For sake of comparability, both figures are showing the same axis ranges as in figure 1.7 despite the data is actually only meant for energies up to 2 MeV [61]. The A_2 coefficient (black) and its lower and upper bounds (orange) are shown in the left and the right panel for the ground state transition and the first excited state transition, respectively.

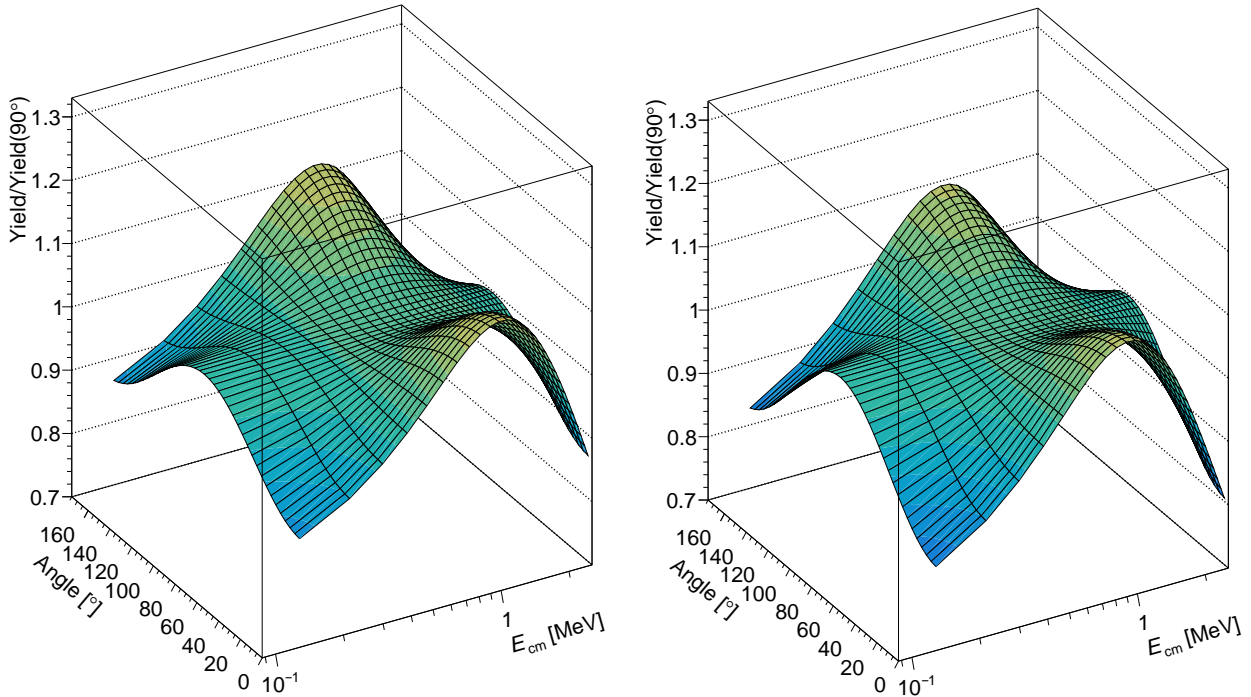


Figure 1.10: Theoretical γ -ray angular distribution for the ${}^3\text{He}(\alpha,\gamma){}^7\text{Be}$ reaction based on Zhang et al. [61]. For sake of comparability, both figures are showing the same axis ranges as in figure 1.8 despite the data is actually only meant for energies up to 2 MeV [61]. Left: Normalized yield with respect to E_{cm} of the reaction (log scale) and the angle of the emitted photon from the ground state transition. Right: Normalized yield with respect to E_{cm} of the reaction (log scale) and the angle of the emitted photon from the transition into the first excited state.

The theoretical prediction of the A_2 coefficients is shown in figure 1.9 for both the ground state transition and the first excited state transition, respectively. The resulting prediction for the γ -ray angular distributions of the ${}^3\text{He}(\alpha,\gamma){}^7\text{Be}$ reaction within the energy region of interest is shown in figure 1.10 for both the transition into the ground state (left) and the transition into the first excited state (right), respectively.

1.5 The physics of rare event searches

In addition to low systematic uncertainties, the quality of any measurement in science is based on the accumulation of enough data in order to minimize statistical uncertainties. The appropriate design of an experiment, which guarantees a sufficiently large signal rate is therefore the foundation of any feasibility study.

However, there are also numerous cases, where comparatively large signal rates are impossible (literally) by nature. Especially in modern physics, experimentalists are more and more often confronted with the need of measuring rare events. A list of examples (which does not claim to be complete, see also [67]) includes the field of **neutrino physics** (double-beta decay, solar

neutrinos, sterile neutrinos, neutrino coherent scattering, etc. [68]), as well as **dark matter** (search for WIMPs, axions, axion-like particles, and also indirect detection approaches [69, 70]), and **high energy physics** (Higgs physics and investigations at LHC in general, cosmic rays, physics beyond the Standard Model etc. [71]).

Further examples, where the search for rare events is a frequently faced challenge are the fields of nuclear physics, and nuclear astrophysics (cf. also the analysis chapters of this work, i.e. chapter 4, chapter 5 and chapter 6). Especially in nuclear physics, the signal rate in a detector is (in first order) proportional to the activity of the sample. However, by investigating nuclides with low decay constants λ and/or low number of nuclei N within the sample, the activity will automatically also suffer. Hence, as soon as the experiment faces samples with long half-lives or very low masses (i.e. due to rarely abundant materials), the obtained signal rate is expected to be small. In nuclear astrophysics (especially accelerator-based experiments), the resulting signal strength strongly depends on the beam current, the target's areal density and the reaction cross section. Hence, it is inevitable to deal with searches of rare events, whenever the reaction cross section in nuclear astrophysical experiments becomes considerably low, no matter whether the reaction is examined with an offline counting setup (see e.g. [53, 72, 73]), or investigated in an in-beam measurement (see e.g. [74]).

Whenever dealing with physics experiments for detecting rare events, the crucial fact for its feasibility is the background counting rate in the detector stemming from cosmic radiation, environmental radionuclides, intrinsic contaminations, etc.

The ability to measure rare events is closely connected to the attenuation of external background events in a detector. Any improvement in the sensitivity of a detector (in first order) is proportional to a drop in necessary activity of the sample. Hence, decreasing the background rate in any detector further enables measurements of lower mass, larger half-life or even reduces the necessary beam time in an in-beam activation of a sample. In case of long-living nuclides (half-life much longer than irradiation time), a factor of ten in sensitivity of an offline counting setup can therefore rapidly be the reason why an experiment will only need one week of precious beam time, instead of three months. This will also be further discussed in chapter 4 and chapter 6.

1.6 Structure of this thesis and general comments

This thesis is structured as follows: In order to avoid duplications within the analysis chapters, the vast majority of necessary analysis techniques will be described in chapter 2. Afterwards, chapter 3 will then introduce all setups, as well as their components, which were used during the experimental campaigns. Furthermore, all utilized samples, detectors and important parameters of the campaigns will be discussed here.

The three following chapters will focus on three distinct projects and their analysis. Chapter

4 will introduce the implementation of a new ultra low-level γ -ray counting setup within the Felsenkeller shallow-underground laboratory. The other two chapters, namely chapter 5 and chapter 6 will be dedicated to two experimental campaigns on the investigation of the ${}^2\text{H}(p,\gamma){}^3\text{He}$ reaction and ${}^3\text{He}(\alpha,\gamma){}^7\text{Be}$ reaction, respectively. A discussion on the entire work will be provided in chapter 7.

Comment on usage of nuclear data If it is not stated otherwise, all properties of nuclei such as half-lives, emission probabilities or level energies are based on the ENSDF database and its subsequent nuclear data sheets [75, 76].

2 Physics background and analysis techniques

The subsequent analysis chapters 4, 5, and 6 are essentially relying on very similar physical principles and analysis techniques. Their context will be introduced within the following in order to avoid duplications in various subsequent sections.

The most relevant analysis technique within this thesis concerns the evaluation of γ -ray spectra obtained with a variety of detectors. The first section is therefore providing a general understanding of how photons (i.e. X-rays and γ -rays) interact with matter (cf. section 2.1). This will be crucial to coherently introduce and elaborate on the analysis techniques provided in the sections 2.2 to A.1, which will discuss the energy-dispersive detection of photons, and the subsequent processing of their information. While the basic detection of γ -rays from radioactive nuclides will be introduced more or less straight forward, there is another level of complexity, when it comes to accelerator-based investigations of nuclear reactions. Hence, the last three sections 2.6 to 2.8 will give an insight into reaction kinematics of radiative capture reactions, determination techniques for the characterization of in-beam targets, and the subsequent determination of cross sections and the astrophysical S -factor.

2.1 Interaction of photons with matter

The interesting energy range of photons for the scope of this thesis spans roughly from $E = 100$ keV to $E = 10$ MeV. Within this range there are four relevant possibilities for photons to interact with their surrounding matter. While these are namely coherent scattering, photoelectric effect, incoherent scattering and pair production, their general working principle won't be part of this section (see e.g. [77, 78] for further details). As a rule of thumb, the photoelectric effect is dominant at comparatively lower energies (up to several hundreds of keV), the incoherent scattering is dominant in the order of $E = 1$ MeV, and the pair production becomes dominant in the order of $E = 10$ MeV. However, these numbers have to be treated carefully due to their strong dependency on the material of interest. In case of organic matter, for example, incoherent scattering is the dominating interaction within the entire interval. It is however worthwhile mentioning, that dominance of a certain effect may not be mistaken with negligibility of the other effects.

$$I(x) = I_0 \cdot e^{-\mu x} \tag{4}$$

$$= I_0 \cdot e^{-x/\lambda} \tag{5}$$

$$= I_0 \cdot e^{-\left(\frac{\mu}{\rho}\right) \rho x} \tag{6}$$

$$= I_0 \cdot e^{-\sigma n_a x} \tag{7}$$

$$= I_0 \cdot e^{-\sigma \frac{\rho}{M} N_A x} \tag{8}$$

Assuming a narrow, collimated, and monoenergetic beam of photons, its intensity $I(x)$ decreases exponentially with respect to the propagated depth x . This relation is independent of the specific interaction channel and expressed in equation 4.

The severity of this attenuation is both material dependent and energy dependent. The material dependency is expressed by the linear attenuation coefficient μ , but it is widely accepted to state the attenuation in terms of the so-called mass attenuation coefficient μ/ρ (cf. equation 6) with ρ being the mass density. Their energy dependent values are tabulated [79] and also shown in case of lead in the left plot of figure 2.1.

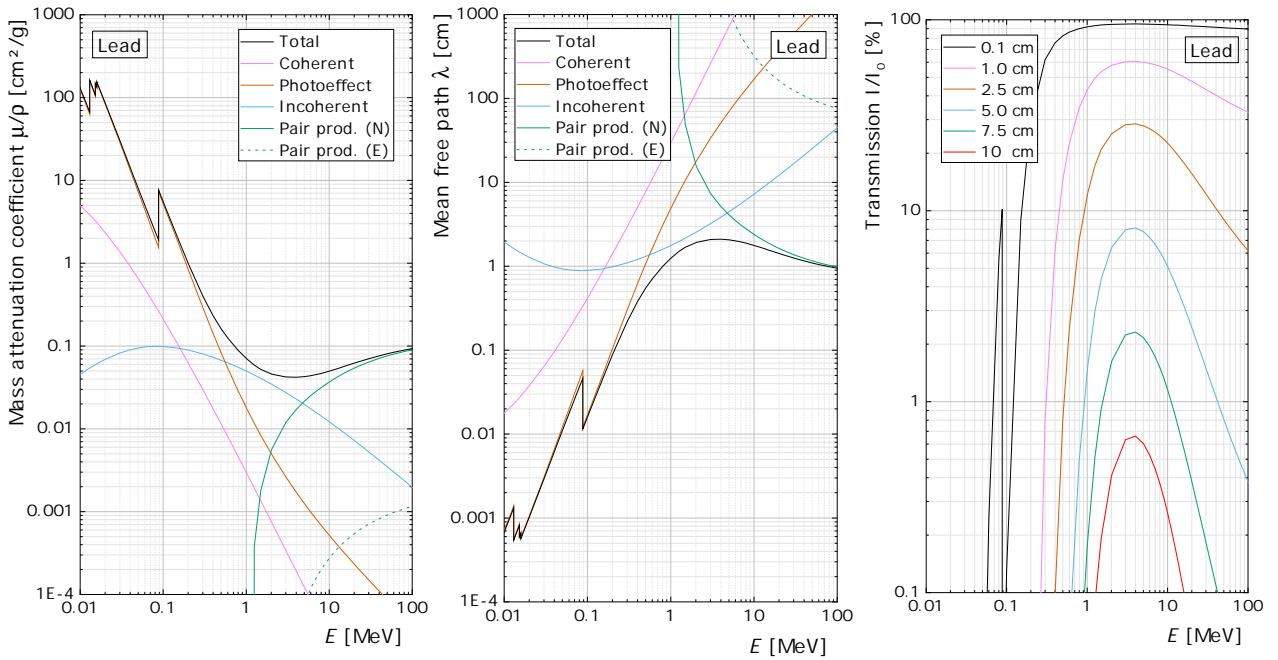


Figure 2.1: Details on crucial parameters for the interactions of photons ($E = 10 \text{ keV}$ to $E = 100 \text{ MeV}$) with lead. Left: The total mass attenuation coefficient μ/ρ is shown (black), as well as its decomposition into its constituents (see text for details). Middle: Total mean free path λ is again shown (black), as well as its decomposition into its constituents (see text for details). Right: The transmitted fraction of the initial photon intensity (I/I_0) is shown with respect to its energy in case of the propagation through different thicknesses of lead.

It is apparent, that the total mass attenuation coefficient μ/ρ , which a photon of energy E experiences, is the sum of all mass attenuation coefficients of the previously mentioned effects. To be more accurate, the total linear attenuation coefficient μ in equation 4 is therefore actually a sum over all its constituents $\mu = \sum_i \mu_i$.

Its reciprocal is the mean free path λ (cf. equation 5), which represents the average distance of a photon before undergoing an interaction. It is shown as the total mean free path λ in the middle plot of figure 2.1 together with its constituents. These constituents can be interpreted as the mean free path of a photon without undergoing this specific kind of interaction.

In addition to the mean free path λ , the linear attenuation coefficient can also be expressed in various other material specific parameters, which are all defined for different purposes in physics. As shown in equation 7 and 8, the attenuation of photons in matter can also be

expressed by combinations of the total interaction cross section σ , the number density n_a (number of atoms per volume), the molar mass M , and the Avogadro constant N_A . However, independent of the applied form of expression for equation 4: For the overwhelming majority of application purposes throughout this thesis, the resulting total attenuation is needed. An intuitive measure for the total attenuation is the remaining fraction of the transmitted photon intensity with respect to its initial intensity I/I_0 , which is shown in the right plot of figure 2.1. In a simplified way of interpretation, the transmission at low energies is strongly suppressed by the photoelectric effect and at high energies suppressed by pair production (cf. also left and middle plot in figure 2.1). The photon energy of maximal transmittance is typically in the order of MeV. However, for materials with lower mass numbers, the impact of incoherent scattering becomes significantly more relevant, as already mentioned before. For carbon, incoherent scattering is the dominating interaction of photons with matter in the range of approximately $E = 30 \text{ keV}$ to $E = 30 \text{ MeV}$, and also their maximal transmittance subsequently shifts to higher energies, respectively.

2.2 Detection mechanisms

The entire scope of conducted experiments within this thesis mainly depends on the detection of different types of radiation. Within this section, the utilized detection principles will be introduced and discussed. The main focus will be on HPGe detectors and scintillation detectors, with only a brief introduction into the utilized particle detectors.

2.2.1 HPGe detectors

A high-purity germanium detector is a reversly-biased diode with a p-i-n structure. An applied high voltage leads to an electric field, which is homogeneously distributed in the intrinsic region and sharply drops at its p- and n-junction, respectively. This intrinsic region is also called the ‘active volume’ of the detector. Whenever an ionizing particle (i.e. X-rays and γ -rays) enters this active volume, its subsequent energy depositions result in the production of electron-hole pairs, which are able to overcome the band-gap between valence and conduction band. The resulting cloud of freely movable charge carriers propagate along the field gradient to the anode and cathode, and induce a voltage, respectively. The final pulse height of this signal is proportional to the number of initially produced charge carriers [77, 78, 80].

Due to the stochastic nature of absorption processes, the number of produced charge carriers statistically varies for a certain amount of energy deposition. Hence, it is favorable to maximize the number of overall charge carriers given a certain energy deposition. In this way, this unavoidable relative fluctuation in pulse height due to statistical fluctuations in the production of charge carriers can be minimized. As a consequence, detectors like HPGe detectors need to have a very small band gap in order to achieve an excellent energy resolu-

tion. In other words, the number of produced electron-hole pairs for each energy deposition is subsequently larger for considerably low band-gaps, which increases the over-all energy resolution.

The disadvantage of low band-gaps however are thermally induced leakage currents based on excitations of valence electrons. If not operated at reasonably low temperatures, the electric noise due to these leakage currents would significantly worsen the energy resolution.

In summary, the overall solution for modern semiconductor detectors are materials with small band-gaps, which are operated at low temperatures. In case of germanium (assuming $T = 77$ K), the band gap is $\Delta = 0.67$ eV, which leads to an average needed energy for the creation of one electron-hole pair of $\varepsilon = 2.96$ eV. If a photon from ^{60}Co ($E = 1332$ keV) deposits its full energy in the active volume, it should in theory therefore create approximately $N = 450000 \pm 671$ electron-hole pairs (with $\Delta N/N = 0.15\%$ according to Poisson statistics). This is however not the case. Otherwise, the resulting peak in the spectrum would already inevitably suffer from a band-gap-induced peak width of $\sigma = 0.0015 \cdot 1332 \text{ keV} = 2 \text{ keV}$ (FWHM $\approx 4.7 \text{ keV}$). However, the actual uncertainty of electron-hole pairs is smaller than predicted by Poisson statistics. This is due to the highly restricted amount of possibilities during ionization based on quantum mechanical considerations. This is taken into account by the so-called Fano factor F . While the literature is stating a broad variety in case of germanium even in more recent investigations ($F = 0.06 - 0.12$ for [81, 82]), it is assumed here to be approximately $F = 0.11$ (as quoted in [77, 83]). In this case, the respective uncertainty would be quenched down to $\sqrt{F} \approx 33\%$). This subsequently results in an actual inevitable peak width of $\sigma = 0.33 \cdot 0.0015 \cdot 1332 \text{ keV} = 0.66 \text{ keV}$ (FWHM $\approx 1.5 \text{ keV}$).

2.2.2 Scintillation detectors

Whenever an ionizing particle propagates through a scintillating material, it ionizes the surrounding atoms and molecules. The resulting vacancies of their electron orbitals will almost instantaneously be refilled, which effectively leads to the emission of prompt fluorescence photons. The total number of emitted photons (light yield) is intended to be both as large as possible, as well as highly proportional to the deposited energy. In the ideal case, the scintillation material has a long mean free path for these fluorescence photons (wave length typically 300 nm to 600 nm) in order to increase the amount of photons reaching the attached photo detector.

This photo detector (usually a photomultiplier tube or a photodiode) converts the photon-induced signal into an amplified electrical pulse, whose height is again proportional to the deposited energy. Compared to HPGe detectors, scintillation detectors have the advantage of comparatively lower costs, considerably faster signal processing chains and they can be operated at room temperature. However, their main disadvantage concerns the comparatively worse energy resolution.

There is a huge variety of scintillation detector materials, which all differ in costs, density,

Table 2.1: Various properties of the two utilized scintillation materials, namely bismuth germanate (BGO) and polyvinyl toluene (PVT). The information is collected from [77, 78, 84].

Property	Bismuth germanate	Polyvinyl toluene
Category	Inorganic non-alkali crystal	Plastic scintillator
Structural formula	$\text{Bi}_4\text{Ge}_3\text{O}_{12}$	$\text{CH}_2\text{CH}(\text{C}_6\text{H}_4\text{CH}_3)$
Density	7.12 g/cm^3	1.023 g/cm^3
Light yield	$8200 \gamma/\text{MeV}_{ee}$	$10000 \gamma/\text{MeV}_{ee}$
Decay time	300 ns	2.1 ns
Wavelength of max. emission	480 nm	425 nm
Wavelength range	375 nm - 650 nm	400 nm - 500 nm
Attenuation length	700 cm - 1500 cm	380 cm
Refractive index	2.15	1.58

light yield, optical properties, suitability for different kinds of radiation, and pulse processing time. Their scope of application ranges from α -, β -, and γ -detectors, up to neutron and even muon detectors.

However, within this thesis, mainly two different types of scintillation detectors will be important. As discussed in section 3.1.4 and section 3.5.2, the utilized HPGe detectors in the in-beam area are occasionally equipped with a surrounding bismuth germanate (BGO) detector and the TU1 detector is surrounded by large polyvinyl toluene (PVT) detectors. Their general properties are listed and compared in table 2.1.

The light yield, as well as the emission wave length ranges are rather similar between BGO and PVT. However, the advantages of PVT is the comparatively fast decay time of only 2.1 ns, as well as its ability to be shaped into almost any geometrical form without losing its performance abilities. In case of BGO, the main advantage is the comparatively large density. It therefore has a higher detection efficiency (lower mean free path) and also acts as an additional passive layer of shielding material.

2.2.3 Particle detectors

Both the HPGe detectors and scintillation detectors utilized within this thesis are comparatively large in size. This is due to the fact, that the mean free path of photons in matter is also comparatively large with respect to the mean free path of e.g. protons with a couple of MeV.

The design and working principle for a solid-state detector which aims to measure charged particles is therefore different from typical photon detectors. Dead layers and entrance windows need to be avoided as much as possible, as well as ambient air during the measurement [85].

The utilized particle detectors within this thesis are partially depleted silicon surface barrier (SSB) detectors with typical thicknesses in the order of $d = 1 \text{ mm}$. They are (similar to HPGe detectors) semiconductors, but are based on p-n type diode wafers. Surface barrier

detectors have (together with PIPS detectors) the thinnest dead layers of all semiconductor detectors (in the order of 100 nm), which minimizes the effects due to straggling. Whenever a charged particle enters the depleted area, it produces electron-hole pairs, which are migrating along the electric field (identical to HPGe detectors).

The ‘partially depleted’ SSB detector has an inactive entrance layer, while a ‘totally depleted’ SSB detector has no inactive layer.

2.3 Data acquisition and pulse processing

The vast majority of detection measurements throughout this thesis is dedicated to γ -ray spectrometry with HPGe detectors (cf. section 2.4). As a consequence, the focus of this chapter also lies on their signal processing and optimization. However, the hardware and software utilized for most of the measurements involving scintillation and particle detectors also rely on the same digitizers and software programs. Their pulse processing is therefore highly similar and only varies in the optimization of certain reconstruction parameters.

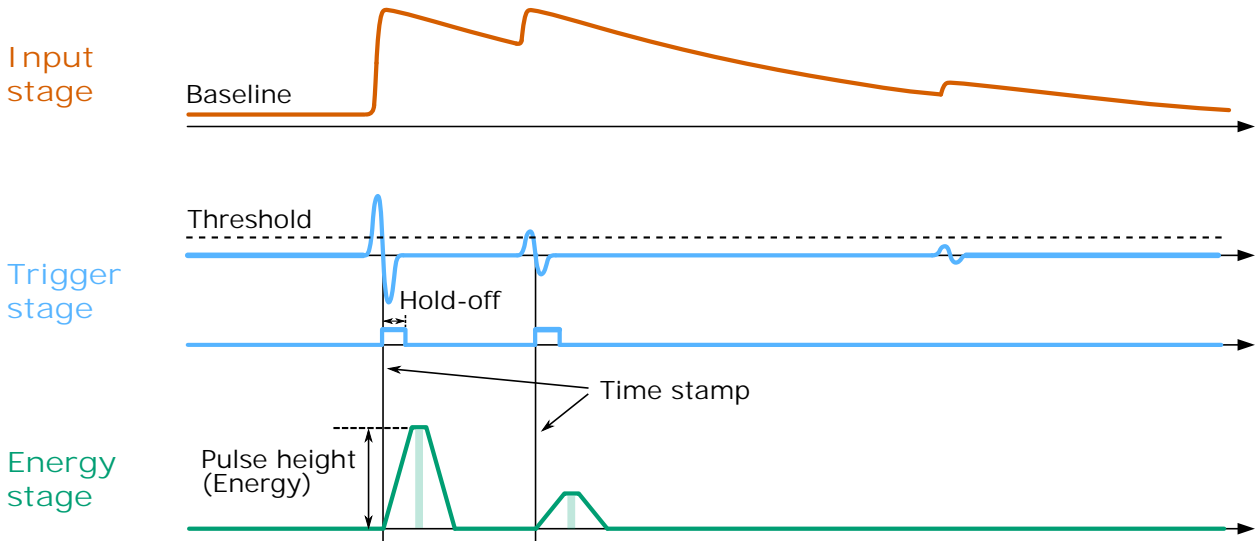


Figure 2.2: Reconstruction of HPGe signals with the utilized software from Caen [86]. Top: Input stage of the ingoing preamplified signal (orange). On top of the actual baseline, three subsequent events are shown. Middle: Trigger stage of the ingoing signal (blue). A signal is triggered, whenever it surpasses the chosen threshold (black dashed), which is true only for the first two signals. Bottom: Stage for the determination of the respective energy (or channel) of each triggered signal (green).

The entire thesis is based on signal reconstruction algorithms using a so-called pulse height analysis (PHA). In general, these algorithms take analog input signals, and digitize their pulse height. This energy information, its subsequently determined time stamp, as well as corresponding possible flags (e.g. ‘pile-up’) are stored for offline analyses.

To be more precisely, there are three main stages of pulse processing in case of the utilized digitizers from CAEN [86]. As shown in figure 2.2, these stages are further called the input

stage, the trigger stage, and the energy stage.

The input stage is mainly comparable to an oscilloscope, which shows the development of the signal baseline (voltage) over time. It can be used to identify noise, underlying oscillations, as well as polarity, rate and shape of the input signal.

For the trigger stage, an RC-CR2 filter is applied to the analog input signal, which converts it into its second derivative (upper blue). In this way, the height of the resulting signal is still proportional to the initially deposited energy, but the position for the crossing of the signal is independent of it. In this way, a reliable time stamp can be provided, similar to a constant fraction discriminator (CFD). However, the so-called triggering of the event only takes place, when the signal in the trigger stage surpasses a user-selected threshold (black dashed). As shown in figure 2.2, the third signal in the trigger stage is below the threshold and does not trigger the subsequent reconstruction chain below.

As it will be discussed thoroughly in section 2.5, each event needs a certain time to be processed. During this time, further called ‘trigger hold-off’, other trigger signals from this channel are not accepted, which subsequently will result in a so-called dead time. This hold-off time is shown in figure 2.2 in the lower blue line and shows, whether the trigger is armed or not. Actually, this arming already starts, when the RC-CR2 signal surpasses the threshold (hence resulting in a discrepancy between the ‘trigger hold-off’ and the ‘armed’ flag), but for reasons of consistency, only the hold-off time is plotted.

This trigger-hold off has a user-chosen length. It has to be set large enough in order to guarantee a proper reconstruction of the events of interest, but also as short as necessary in order to minimize the resulting dead time. Depending on the experiment (large energy depositions result in broader signals within the trigger stage) the trigger hold-off is typically in the order of $1\ \mu\text{s}$.

Whenever the signal in the trigger stage surpasses the threshold, it causes the initialization of the subsequent pulse height reconstruction in the energy stage (green). This reconstruction is based on a so-called trapezoidal filter, whose height is proportional to the deposited energy (similar to a Gaussian shaping in older, analog electronics). While the height of the trapezoid is therefore fixed by the deposited energy, its rise time, decay time, and the width of the flat top can be optimized by the user. The rise time corresponds to the shaping time of analog electronics ($3\ \mu\text{s}$ of shaping time corresponds to $7\text{--}8\ \mu\text{s}$ of rise time), and therefore influences the resolution.

It is worthwhile mentioning, that during an experiment, this rise time can not be chosen arbitrarily large due to its influence on pile-ups. The achievable resolution of the peaks in a pulse-height spectrum is therefore always a compromise between an experiment with high counting rate (rise time needs to be small in order to prevent pile-up) and an experiment with low counting rate (rise time can be chosen large in order to allow better resolutions).

However, the final pulse height will be determined by averaging over a user-selected number of samples within the flat top of the trapezoid (green shaded area).

2.4 γ -ray spectrometry

Within the previous sections, the focus was on the physical principles of detectors, the interaction of photons with these detectors, and the subsequent acquisition and processing of the resulting signals in a detection software. In addition, this section will now introduce the treatment of the acquired γ -ray data in offline analyses in order to extract the physical quantities of interest.

2.4.1 Energy calibrations

Most types of detectors are designed and optimized in a way, which guarantees a highly proportional correlation between the deposited energy and the resulting pulse height of its signal. This is usually ensured by providing the proportionality along all chains of pulse processing. In case of HPGe detectors, the number of produced charge carriers is highly proportional to the energy of the initial photon, and the induced signal height is proportional to the number of charge carriers. The subsequent amplification of the signal, as well as its software evaluation are designed to further maintain this proportionality.

While this linearity is certainly ensured for short-term measurements, some analyses throughout this thesis rely on the summation of data, which has been acquired over several months. In these cases, often it turned out to be unsuitable to perform one single energy calibration based on calibration sources and use it throughout the entire campaign. The resulting effective broadening of peak widths was frequently unacceptable. This lack of a long-term stability can e.g. be caused by internal calibrations of digitizers, which depend on the ambient room temperature [86]. Furthermore, the energy calibration also depends on the utilized cables, whose positioning could not be ensured to remain identical in long-term measurements due to frequent, inevitable (even if unintended) touching of cables during modifications on the setup.

A solution to this problem, which was proven to be reasonably robust throughout this thesis, is the execution of an energy calibration for each acquired run (typically 3 h duration) using precisely known, characteristic γ lines within the pulse height spectrum of the run itself. Dedicated tests of subsequently merging runs from several months and also several detector crystals (in case of cluster detectors), did not show any significant influence on the FWHM of the peaks, which would question this approach. This procedure is used in all analyses chapters without further notice. However, in some special cases, the energy calibration and resulting residua will be elaborated again in more detail.

2.4.2 Efficiencies in γ -ray spectrometry

A so-called efficiency in γ -ray spectrometry is usually connecting the activity of a radioactive sample with the number induced signals in a respective detector [77, 78, 80]. While there are multiple definitions of various different efficiencies in γ -ray spectrometry, only two of them

will be of importance within this thesis. Namely, these two are the relative efficiency ε_{rel} , and the absolute full-energy peak efficiency ε_{abs} . Whenever only ε is mentioned throughout the thesis, the latter one meant.

Definition of the relative efficiency ε_{rel}

The relative efficiency ε_{rel} is usually stated in order to judge the qualitative capabilities of a HPGe detector and is given in percent. It is measured by centrally placing a ^{60}Co source in 25 cm distance from the end cap of the detector. The resulting count rate of the peak at $E = 1332.5 \text{ keV}$, normalized by the activity of the source, results in an efficiency. This resulting value is compared to the efficiency of a standard 3" x 3" x 3" sodium iodine NaI(Tl) detector with $1.2 \cdot 10^{-3}$, which is used as a normalization and set to 100 %. Hence, relative efficiencies above 100 % are also possible.

Definition of the absolute full-energy peak efficiency ε_{abs}

While the relative efficiency is a fixed value for each detector, and usually is of help for comparing different HPGe detectors, the absolute full-energy peak efficiency ε_{abs} is both energy dependent, and strongly dependent on the specific experimental setup. For a certain emitted photon with the energy E_γ , it is defined as its probability to induce a signal in its corresponding full-energy peak within the pulse height spectrum after its initial nucleus in the source underwent a decay transition. This correlation is shown in equation 9

$$\varepsilon_{\text{abs}}(E) = \frac{N_\gamma}{A \cdot \nu \cdot t_{\text{live}}} \cdot C_{\text{sum}} \quad (9)$$

with N_γ being the net counts in the respective full-energy peak, A being the activity of the source, ν as the emission probability of the γ -ray of interest during a nuclear transition, and t_{live} being the live time of the measurement⁷. In case of negligible summation effects in the spectrum, the summation correction factor is $C_{\text{sum}} = 1$. In case of summing-in effects regarding the respective peak, this factor is $C_{\text{sum}} < 1$ in order to reduce the effective number of net counts appropriately. In case of summing-out effects, this factor is $C_{\text{sum}} > 1$ in order to enhance the net counts to their actual value of deposited full-energy events in the detector. An additional formalism for decomposing the absolute full-energy peak efficiency into multiple terms (e.g. used in chapter 5.4) is shown in equation 10.

$$\varepsilon_{\text{abs}}(E) = \varepsilon_{\text{s}}(E) \cdot \varepsilon_{\text{g}}(E) \cdot \varepsilon_{\text{d}}(E) \cdot C_{\text{sum}} \quad (10)$$

This formalism is deconvoluting ε_{abs} into multiple energy-dependent probabilities for a photon to propagate through matter without undergoing an energy-transferring scattering process. The first factor is the self-absorption term of the source ε_{s} . It describes the probability of a photon to leave the source volume without loss of energy due to photoelectric effect,

⁷The special case of considerably short half-lives (i.e. $A \neq \text{const.}$) will be elaborated in section 6.5.1.

incoherent scattering etc. While this gets more important for voluminous sources, it is approximately $\varepsilon_s = 1$ in case of γ -ray calibration sources. The second factor in equation 10 is a term, which takes into account the geometry of the setup. It represents the probability, that the photon is able to propagate into the active volume of the detector without energy loss after leaving the source geometry. The third factor describes the intrinsic detection efficiency $\varepsilon_d(E)$. It takes into account the probability of depositing its full-energy in the detector after entering the active detection volume [77].

Due to the complexity of source geometries, experimental setups, utilized materials and the physics of photons interacting with matter, there is no reasonable physically motivated equation, which takes all attenuation factors, propagated materials and detection efficiencies into account. However, in γ -ray spectrometry, there are multiple analytic approaches to fit the experimentally determined energy-dependent data points of ε_{abs} [80]. These fit functions are usually suitable only for certain energy region and proven to phenomenologically represent the underlying physics.

In general, an appropriate fit function has to fulfill two crucial purposes: One the one hand, it has to be suitable for a wide energy range (in case of this thesis at least 100 keV to 10 MeV). On the other hand, the fit function needs to be able to provide easily accessible analytic uncertainties at random energies within its fitting interval. Fit functions in general suffer from the fact, that their fit parameters become correlated during the fitting routine. This correlation results in a correlation matrix, which has to be taken into account, when properly propagating these energy-dependent uncertainties of all parameters into the uncertainty of the final efficiency at the energy of interest. This can be avoided by modeling the fit function in a way, which lets ε solely depend on one single parameter at this one specific energy of interest E_γ . This can be achieved by ensuring, that for this specific energy, all other parameters are canceled out. Such a function is shown in equation 11.

$$\varepsilon(E) = \prod_{i=0}^n \exp\left(C_i \ln\left(\frac{E}{E_\gamma}\right)^i\right) \stackrel{n=2}{=} \exp\left(C_0 + C_1 \ln\left(\frac{E}{E_\gamma}\right) + C_2 \ln\left(\frac{E}{E_\gamma}\right)^2\right) \quad (11)$$

By fitting this function using E_γ as the energy of interest, the correlated fit parameters C_i are obtained. However, the correlation of these parameters collapses at one single energy, which is $E = E_\gamma$ itself. At this energy, ε as well as its uncertainty, solely depends on C_0 . This advantageous relationship is used throughout this thesis and is shown in equation 12.

$$\Delta\varepsilon(E = E_\gamma) = \exp(C_0) \cdot \Delta C_0 \quad (12)$$

A comprehensive study on this approach, where the large amount of statistics allowed a staggering number of $n = 9$ parameters, is elaborated in [87]. For this thesis, the number of parameters is always chosen according to the results of the residuum and the values of the χ^2 -analysis. Throughout this thesis, the number of parameters is either $n = 1$ or $n = 2$.

2.4.3 Evaluation of peaks and determination of their net counts

The analysis of α -, and γ -ray pulse height spectra within this thesis mainly concentrates on the evaluation of full-energy peaks, as well as the subsequent determination of their net counts. Especially in γ -ray spectrometry, these peaks are usually located on top of some sort of background continuum. This continuum can have multiple origins, e.g. incoherently scattered photons or muon-induced events in the HPGe detector. In the ideal case, the sum of all these backgrounds can be treated as a linear continuum in close proximity to the peak. In case of non-continuous backgrounds within the region of interest (e.g. Compton-edges or different full-energy peaks), the analysis techniques, presented in the following, have to be adapted.

There are two main approaches regarding the determination of the net counts on top of a continuous BG, which will be discussed in the following. The first is a Gaussian fit procedure (cf. left and middle panel in figure 2.3) and the other one is a counting procedure (cf. right panel in figure 2.3), further called ‘cut and count’.

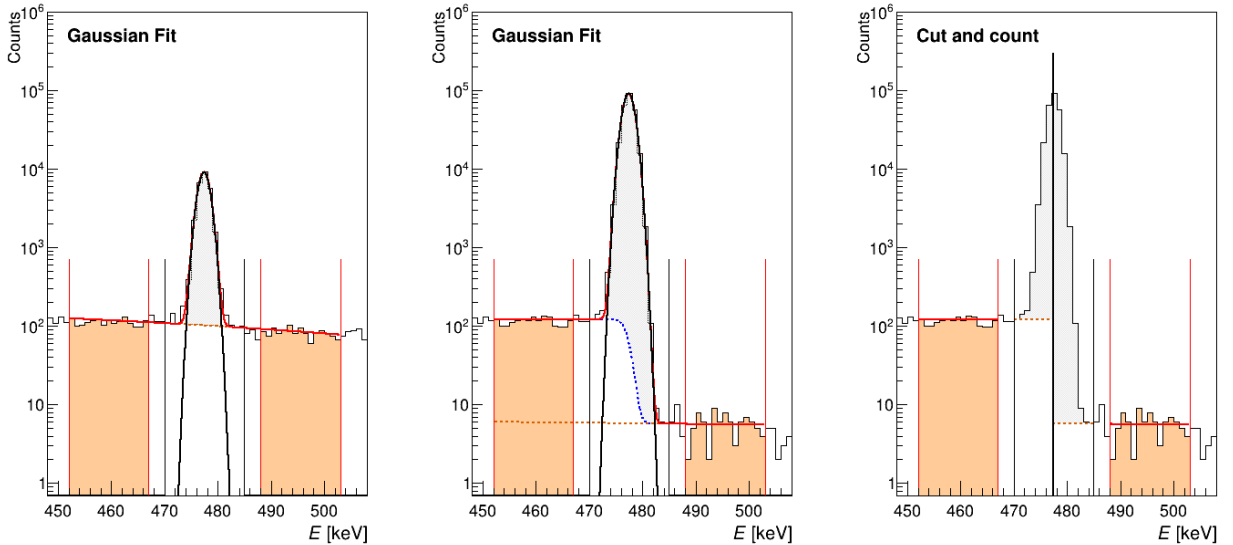


Figure 2.3: Determination of peak areas (${}^7\text{Be}$ with $E = 477.6$ keV) with continuous backgrounds (orange). Left: Comparatively small peak on top of a linear BG. Middle and right: Comparatively intense peaks on top of a linear BG. These large peak-to-BG ratios lead to a visible step function (blue) due to incoherently scattered photons. The left and right BGs are estimated within the red intervals. The transparent black area shows the result of all three net count determinations. The black fits (left & middle) show the resulting peak fits. See text for details.

The most simple fit routines usually take an approach of modeling the pulse height spectrum with a simple Gaussian and 1st order polynomial, as shown in the left panel of figure 2.3. This is convenient for a quick analysis of the net counts, as long as the peak-to-BG ratio is reasonably small. As soon as this ratio increases (as shown in the middle panel of figure

2.3), the peak-induced BG on the left side of the peak becomes non-negligible and has to be taken into account as well. So in addition to the fitted non-peak-induced BG (orange dashed), there is a peak-induced BG (blue dashed), which can be approximated with an error function using the same width σ , as for the peak.

While fit procedures provide a reasonably quick way to determine net counts, they are avoided within this thesis, whenever possible. This is due to the fact, that the distribution of counts in a peak is only reasonably similar to a Gaussian distribution. Due to effects like charge carrier losses (cf. section 2.4.4), surface effects, shape-effects in escape peaks, and others, peak shapes become distorted, and hence non-Gaussian. While there is a myriad of publications trying to include these effects by using more complex semi-empirical parameterized functions, like the Hypermet function (see [88] and citations therein), most of them are lacking of practicability, a reasonably low number of parameters, convincing fit residuals, easily determinable uncertainties and universal applicability. And even if there might be reasonable work-arounds, especially in nuclear astrophysics, they are definitely unsuitable, when it comes to the analysis of broader peak structures from e.g. radiative capture reactions in solid target experiments.

Therefore, the general procedure of determining net counts within this thesis is the method of ‘cut and count’ (cf. the right panel of figure 2.3). Within the region of interest, all counts are summed-up and subtracted by the number of underlying BG counts. These underlying BG counts are estimated by propagating the knowledge about the left and right BG, respectively. This procedure is highly similar to the one described in [77]. However, the procedure shown in the right panel of figure 2.3 neither relies on an equally wide left and right BGs, nor on a symmetrically chosen BG position around the ROI. Especially the benefit of not relying on equal distances of both BG regions to their ROI enables the avoidance of neighboring structures by choosing a subsequently smaller or shifted BG region on this particular side.

While any kind of Gaussian fit routines are highly avoided, they are however used in this thesis in order to determine both the central position of a peak for the ‘cut and count’ method (black vertical line in the right panel of figure 2.3) and, if needed, for the determination of the width of the peaks.

2.4.4 Peak widths in γ -ray spectrometry

Without going to much into detail, this section aims to complete the picture drawn in section 2.2.1 and section 2.4.3. During the introduction of HPGe detectors, one inevitable cause of the broadness of peaks in pulse height spectra was already motivated, which is the statistical fluctuation in the amount of produced charge carriers for a given energy deposition. Furthermore, it was derived, that this portion ω_P is proportional to the square root of the deposited energy E . As shown in equation 13, there are also two other effects contributing to the total width of a peak ω .

$$\omega(E)^2 = \omega_P^2 + \omega_C^2 + \omega_E^2 = p^2 E + c^2 E^2 + e^2 \quad (13)$$

The other two contributions are concerning the charge collection ω_C (which goes with $\omega_C \propto E$) and the electronic noise ω_E (which is energy independent). It was already discussed in section 2.2.1 and section 2.4.3, that the amounts of produced charge carriers is proportional to the resulting pulse height. However, this is only true in case of perfect collection of all charge carriers. Due to carrier-trapping crystal impurities, carrier-trapping neutron-induced damages or partially delayed charge collection for a certain integration time, there is an imperfect charge carrier collection, which leads to the statistical broadening ω_C to slightly lower energies (left tailing). It may be noticed here, that a left tailing can also be due to under-compensated pole-zero cancellation, which is way easier to remedy.

The last term in the explanation of peak widths concerns the width due to electronic noise ω_E . By attaching an oscilloscope to the signal cable of a HPGe detector, there will be clearly visible and unavoidable statistical fluctuation around the baseline. This fluctuation is mainly caused in the signal processing prior to the preamplifier stage, e.g. due to thermal noise (cf. section 2.2.1).

The significance of all three contributors crucially depends on the energy, but also on the size of the detector. Typically, at low energies, ω_E is dominating the total peak width due to its energy independence. At high energies ω_P and ω_C become more dominant and become either similar in significance or even surpassing ω_E [77, 78].

2.4.5 Coincidences in γ -ray spectrometry

Within the scope of this thesis, the resulting raw pulse height spectrum of a detector is only rarely used. Instead, during the post-processing of the raw data, so-called coincident events between different detectors (HPGe, BGO, PVT, cf. table 2.1) are identified and utilized in order to improve the resulting analysis. These coincident events can e.g. be due to a muon passing through several detectors or a photon, which is inelastically scattered with a subsequent energy deposition in two neighboring crystals.

The offline-identification of coincident events can either be used to eliminate them and hence improve the peak-to-background ratio (so called anti-Compton suppression) or to add up their respective energies in order to reconstruct the initial full energy (so called add-back). While these two techniques are one among the most important tools for the success of the subsequent offline analyses, they will only be further elaborated in the appendix A.1. It is however important to notice, that either an anti-Compton suppression or an add-back was used within the scope of this thesis, but certainly not both methods simultaneously. The general policy for their utilization is also discussed in the appendix A.1.3. It was avoided to discuss this topic hereafter due to the fact, that it also requires the information about the nomenclature of the utilized detectors, which however will be introduced later in section

3.1. Nevertheless, in order to perceive the analyses in their entirety, this chapter is certainly inevitable.

2.5 Dead time

During the subsequent data processing chain of a detected particle, a measurement system may not be able to simultaneously process another signal for a certain amount of time. This so-called dead time t_{dead} during the data acquisition therefore describes the discrepancy between the real time t_{real} of a measurement, and the effective time, where the detector was actually able to detect and process an incoming particle, further called ‘live time’ t_{live} . The corresponding correlation between these values is shown in equation 14.

$$t_{\text{dead}} = \frac{t_{\text{real}} - t_{\text{live}}}{t_{\text{real}}} = 1 - \frac{t_{\text{live}}}{t_{\text{real}}} \quad (14)$$

The dead time t_{dead} depends on a variety of parameters, most crucially on both the expected ‘real’ rate of potentially signal generating events in the detector, as well as on the time each signal needs for its processing until the system is armed for the next event. The complexity of experimentally accessing the dead time is extensively elaborated in a dedicated Bachelor thesis, which was assembled and supervised within the scope of this thesis [14].

However, a crucial point regarding dead times is, that common software programs are in fact not able to calculate the dead time during a measurement, but usually can only estimate it. Considering the fact, that the dead time impacts the final result in a proportional manner, its precise determination is a widely underestimated. Too often, the dead time is treated as a quantity, which is simply trusted and copied from the corresponding software in use. Especially taking into account the broad field of applications for a commonly available digitizer, it has to be treated with utmost caution, whether the underlying algorithm for estimating the dead time is at all entitled to meet the physics conditions of the particular experiment. A dedicated example, where the physics case vastly surpasses the capabilities of a commonly available software to determine an appropriate dead time will be elaborated in section 4.6.1.

The underlying assumption of typical digitizer softwares is based on the fact, that the signal inducing events in a detector occur entirely independent of each other, i.e. being randomly distributed in time and following a purely Poisson distribution. In this way, the total number of successfully processed events N_{out} of any kind (resulting in spectrum, flagged as ‘pile-up’, flagged as ‘saturated’), can be used to estimate the number of originally incoming signals N_{in} , which would be needed in order to achieve the resulting number of successfully processed events. The relationship between N_{in} , N_{out} , and t_{dead} is equivalent to equation 14 and shown in equation 15.

$$t_{\text{dead}} = 1 - \frac{N_{\text{out}}}{N_{\text{in}}} \quad (15)$$

The assumed Poisson nature of signal generating events further allows the following consideration: Time difference between two Poisson distributed events are known to follow an exponential probability density function $f_\lambda(t)$ with a random variable λ . This random variable is chosen in a way, that its reciprocal equals the expectation value regarding the time difference between two events. The probability F for an event to occur during a time span t_{hold} after the previous event took place can therefore be calculated according to eq. 16.

$$F(t_{\text{hold}}) = \int_0^{t_{\text{hold}}} f_\lambda(t) dt = \int_0^{t_{\text{hold}}} \lambda e^{-\lambda t} dt = \int_0^{t_{\text{hold}}} \dot{N}_{\text{in}} e^{-\dot{N}_{\text{in}} t} dt = 1 - e^{-\dot{N}_{\text{in}} t_{\text{hold}}} \quad (16)$$

This probability F can subsequently be used in an iterative procedure to estimate the rate of signal generating events \dot{N}_{in} , as shown in the following, with equation 17 being the first iteration step ($i = 1$) and equation 18 representing each subsequent iteration step ($i + 1$)⁸.

$$\dot{N}_{\text{in}}(i = 1) = \dot{N}_{\text{out}} + \dot{N}_{\text{out}} \cdot \left(1 - e^{-\dot{N}_{\text{out}} \cdot t_{\text{hold}}}\right) \quad (17)$$

$$\dot{N}_{\text{in}}(i + 1) = \dot{N}_{\text{out}} + \dot{N}_{\text{in}}(i) \cdot \left(1 - e^{-\dot{N}_{\text{in}}(i) \cdot t_{\text{hold}}}\right) \quad (18)$$

This procedure is based on the idea, that for each iteration, the rate of ‘lost’ events is reiterated and subsequently added to the assumed rate of signal generating events. Several tests with realistic scenarios show, that this procedure usually converges after 5 cycles.

2.6 Reaction kinematics of radiative capture reactions

In order to investigate nuclear fusion reactions, measuring and investigating the emitted radiation is a crucial experimental tool. All accelerator-based campaigns within this thesis are designed to investigate so-called radiative capture reactions, or more precisely: Direct capture reactions. In case of a direct capture reaction, the energy of the emitted photon relies on multiple quantities, stemming from both the underlying nuclear physics (Q -value, nuclear structure etc.), as well as experimentally chosen parameters (voltages to accelerate ions, detection angles etc.). Their relationship and influence on the energy of the emitted photon E_γ will be discussed in the following.

2.6.1 Determination of the laboratory energy for the IBC campaigns

During the campaigns at the Ion Beam Center (cf. table 3.1), the 3 MV Tandetron accelerator was used throughout all irradiations.

In case of the IBC-I campaign (cf. section 3.1), mainly the cesium sputter ion source was used to extract single charged hydrogen isotopes (cf. section 3.3). In this case, the laboratory

⁸It is worthwhile mentioning, that these equations treat the dead time as a relative measure, which can e.g. be stated as a percentage. The previous definition of the ‘inactive detector time’ needs to be also understood in a relative manner, and not as an absolute value.

energy of the ions $E_{\text{lab,IBC}}$ depends on the terminal voltage U_{TV} , the injection voltage U_{Inj} , a calibration factor C_{IBC} , the charge state of the ions Q and the elementary charge e , as shown in equation 19.

$$E_{\text{lab,IBC}} = (U_{\text{TV}} \cdot Q + U_{\text{Inj}}) \cdot C_{\text{IBC}} \cdot e \quad (19)$$

In case of the IBC-II campaign (cf. section 3.1), mainly the TORVIS He-ion source with a rubidium charge exchange cell from NEC was used to extract doubly charged helium isotopes (cf. section 3.3). In this case, the laboratory energy of the ions $E_{\text{lab,IBC}}$ can be calculated using a similar formula, as shown in equation 20.

$$E_{\text{lab,IBC}} = (U_{\text{TV}} \cdot (Q + 1) + U_{\text{Inj}}) \cdot C_{\text{IBC}} \cdot e \quad (20)$$

For both the IBC-I and the IBC-II campaign, the calibration factor C_{IBC} was determined to be $C_{\text{IBC}} = 1.0086 \pm 0.0004$. In addition, for the terminal voltage U_{TV} in case of the IBC-II campaign a recalibration was done between the old voltage display and a new (more precise) Terminal Voltmeter (Kethley 2000 Multimeter). This recalibration resulted in a conversion of $U_{\text{TV,new}} = 1.0059 \cdot U_{\text{TV,old}}$.

2.6.2 Determination of the laboratory energy for the FK campaigns

During the campaigns at Felsenkeller (cf. table 3.1), the internal radio frequency ion source was used throughout all irradiations. Therefore, the laboratory energy of the ions $E_{\text{lab,FK}}$ depends on the terminal voltage U_{TV} , the extractor voltage U_{Ex} , the anode voltage U_{An} , a calibration factor C_{FK} , the charge state of the ions Q and the elementary charge e .

$$E_{\text{lab,FK}} = (C_{\text{FK}} \cdot U_{\text{TV}} + U_{\text{An}} + U_{\text{Ex}}) \cdot Q \cdot e \quad (21)$$

For all in-beam campaigns at Felsenkeller (cf. section 3.1), this calibration factor is $C_{\text{FK}} = 0.957$. Its precise uncertainty is still under investigation, but will result in a value well below 1%. It is worthwhile mentioning, that the corresponding quantities at Felsenkeller are called ‘GVM_soll’, ‘Extraktor_soll’, and ‘Anode_soll’. They correspond to U_{TV} , U_{Ex} , and U_{An} , respectively.

2.6.3 Determination of the effective energy and the center-of-mass energy

The accelerator-based experiments within this thesis are based on the prior implantation of the target nucleus of interest into solid targets (cf. table 3.2). During the propagation of the ion beam through the implantation layer, the ions lose a certain amount of energy based on the Bethe-Bloch formula [89]. However, this energy loss ΔE_{loss} strongly depends on the respective ion energy. Due to the fact, that this energy loss is comparatively small with respect to the initial ion energy E_{lab} , it is assumed to be constant during the propa-

gation through the implantation layer. Assuming a homogeneous depth distribution for the implantation, an effective energy can therefore be determined using equation 22.

$$E_{\text{eff}} = E_{\text{lab}} - 0.5 \cdot \Delta E_{\text{loss}} \quad (22)$$

The assumption within this equation was verified by comparing the utilized approach of constant energy loss with the actual non-linear loss in energy while propagating through the implantation layer. Even with the worst combination of projectile, target, and energy, the discrepancy of the resulting E_{eff} is well below 1 keV. As it will be shown in the next paragraph, this value will be even less for the more important center-of-mass energy.

This effective energy corresponds to the mean laboratory energy of the ions, while propagating through the implantation layer. The individual energy loss for every experimental campaign is determined using the software SRIM [90].

Subsequently, this effective energy can be used to determine the so-called center-of-mass energy E_{CM} . While the laboratory energy, and the effective energy are both related to the inertial frame of the ‘resting’ laboratory, the center-of-mass energy is the equivalent energy for an inertial frame in which the total momentum of the reacting particles vanishes [26]. In case of a resting target nucleus (being in rest with respect to the laboratory frame), this energy E_{CM} solely depends on the projectile mass m_{p} , its laboratory energy E_{lab} , and the mass of the target nucleus m_{t} , as shown in equation 23.

$$E_{\text{CM}} = E_{\text{eff}} \cdot \frac{m_{\text{t}}}{m_{\text{p}} + m_{\text{t}}} \quad (23)$$

2.6.4 Determination of the γ -ray energy in radiative capture reactions

The proper calculation of the center-of-mass energy is certainly needed for the determination of the investigated energy of the particular reaction. However, in case of radiative capture reactions (the ejectile after collision of projectile and target nucleus is a photon), the energy of the emitted photon can also be calculated based on E_{CM} , as shown in equation 24 and equation 25. As it will become relevant for the experimental campaigns, it is worthwhile mentioning, that this relation only holds for transitions into the ground state of the particular recoil nucleus. In case of nuclear reaction processes with a recoil nucleus in an excited state, the Q -value has to be adjusted accordingly. In these equations, Q is the Q -value of the particular reaction, and ϑ is the angle between initial direction of the projectile and the direction of the emitted photon. The terms $\Delta E_{\text{Doppler}}$ and ΔE_{recoil} are taking into account the so-called Doppler shift and the recoil of the nucleus, respectively. The correction for the Doppler shift is necessary in case, that the emission of the photon takes place, while the recoil nucleus is still in motion. While this is always the case in direct capture reactions, this process can also occur during possible subsequent γ -ray accompanied de-excitations.

$$E_\gamma = Q + E_{\text{CM}} + \Delta E_{\text{Doppler}} - \Delta E_{\text{recoil}} \quad (24)$$

$$= Q + \frac{E_{\text{eff}} \cdot m_t}{m_p + m_t} + E_\gamma \cdot \frac{\sqrt{2m_p E_{\text{eff}}}}{m_p + m_t} \cdot \cos(\vartheta) - \frac{E_\gamma^2}{m_p + m_t} \quad (25)$$

$$\approx Q + \frac{E_{\text{eff}} \cdot m_t}{m_p + m_t} + \left(Q + \frac{E_{\text{eff}} \cdot m_t}{m_p + m_t} \right) \cdot \frac{\sqrt{2m_p E_{\text{eff}}}}{m_p + m_t} \cdot \cos(\vartheta) - \frac{\left(Q + \frac{E_{\text{eff}} \cdot m_t}{m_p + m_t} \right)^2}{m_p + m_t} \quad (26)$$

However, its occurrence depends on the half-life of the excited state and the time of the recoil nucleus to stop within the matter. The last term in the equation (ΔE_{recoil}) takes into account the fact, that due to momentum conservation, a small amount of energy will also be transferred to the recoil nucleus during the reaction. This term will however be the smallest contribution during the experimental campaigns.

The approximation in equation 26 takes into account, that its last two terms ($\Delta E_{\text{Doppler}}$ and ΔE_{recoil}) are only comparatively small corrections. This is why E_γ within these terms can be approximated by $E_\gamma \approx Q + E_{\text{CM}}$.

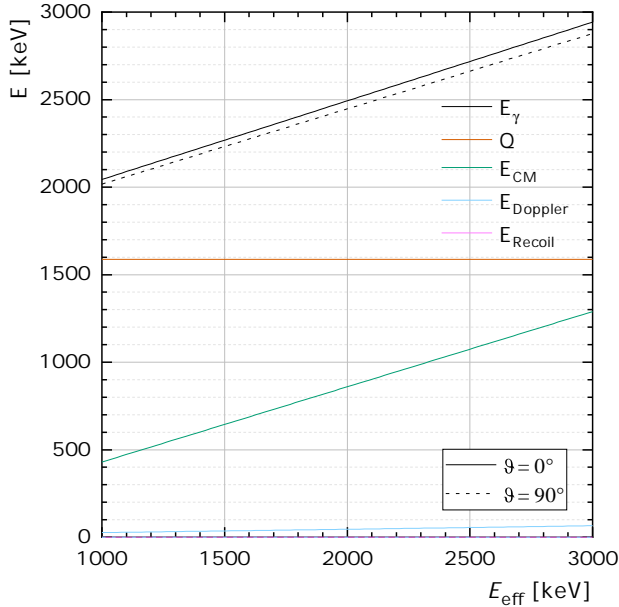


Figure 2.4: Contributions to the resulting E_γ in case of the ${}^3\text{He}(\alpha, \gamma){}^7\text{Be}$ reaction, shown in linear scale. The solid lines (dashed lines) represent the results for an emission angle of $\vartheta = 0^\circ$ ($\vartheta = 90^\circ$), respectively.

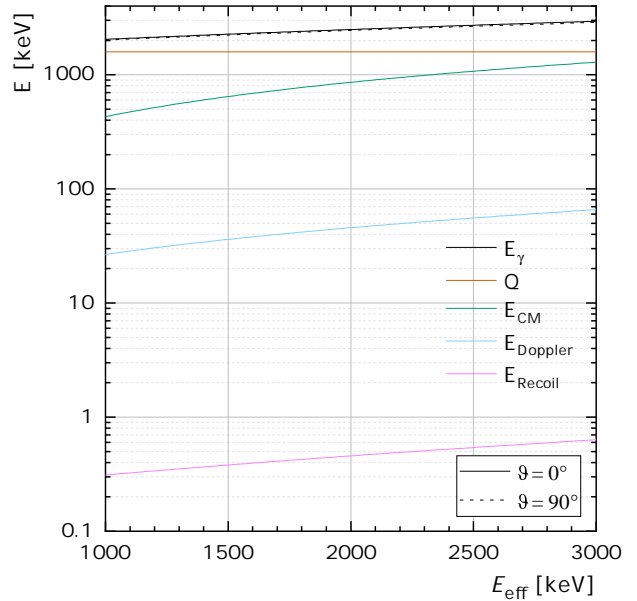


Figure 2.5: Contributions to the resulting E_γ in case of the ${}^3\text{He}(\alpha, \gamma){}^7\text{Be}$ reaction, shown in logarithmic scale. The solid lines (dashed lines) represent the results for an emission angle of $\vartheta = 0^\circ$ ($\vartheta = 90^\circ$), respectively.

These different contributions and their significance for the resulting γ -ray energy E_γ are shown for the ${}^3\text{He}(\alpha, \gamma){}^7\text{Be}$ reaction in figure 2.4 and figure 2.5, respectively. While the Q -value is independent of the energy, the other three contributions are increasing with increasing E_{eff} . However, the validation of the approximation ' $E_\gamma \approx Q + E_{\text{CM}}$ ' is also graphically

emphasized in these figures. While the linear scale in figure 2.4 gives a proper insight into the impact of different emission angles onto the resulting E_γ , the logarithmic scale in figure 2.5 also enables the visibility of the contribution of E_{recoil} . The Doppler contribution in case of $\vartheta = 90^\circ$ is not visible for either of the two cases, due to its vanishing contribution under this particular angle.

2.6.5 Relativistic angle correction in radiative capture reactions

For every experimental campaign, the positioning of all detectors was chosen and determined thoroughly. This includes both measuring their distance to the center of the target d_{det} , as well as the determining their alignment angle with respect to the beam direction ϑ_{lab} . However, the aimed angle in the laboratory frame may differ, when considering radiative capture reactions in relativistic regimes. Due to the fact, that the energy transfer of the projectile takes place prior to the emission of the photon, the virtual compound nucleus already has a momentum during the emission of the prompt γ -rays. Every detector angle therefore becomes distorted with respect to the projectile mass m_p , the target mass m_t , the angle of the detector in the laboratory frame ϑ_{lab} and the effective laboratory energy E_{eff} [26]. By introducing a relativistic parameter β , the correlation between the angle of the detector in the laboratory frame ϑ_{lab} , and the angle of the detector in the center-of-mass frame ϑ_{CM} can be expressed as shown in equation 27.

$$\cos(\vartheta_{\text{lab}}) = \frac{\cos(\vartheta_{\text{CM}}) + \beta}{1 + \beta \cos(\vartheta_{\text{CM}})} \Leftrightarrow \cos(\vartheta_{\text{CM}}) = \frac{\beta - \cos(\vartheta_{\text{lab}})}{\beta \cos(\vartheta_{\text{lab}}) - 1} \quad (27)$$

In case of heavy target nuclei, the relativistic parameter β becomes comparatively small, and both angles are equalizing. If e.g. the energy of the projectile becomes comparatively large, then the relativistic angle becomes more distorted. The definition of β is shown in equation 28.

$$\beta = \frac{\sqrt{E_{\text{eff}}(E_{\text{eff}} + 2m_p)}}{m_t + m_p + E_{\text{eff}}} \quad (28)$$

The resulting relation between the angle of the detector in the laboratory frame ϑ_{lab} , and the angle of the detector in the center-of-mass frame ϑ_{CM} is shown in figure 2.6. The difference of both angles is shown with respect to the effective laboratory energy E_{eff} for the ${}^3\text{He}(\alpha, \gamma){}^7\text{Be}$ reaction with ${}^4\text{He}$ as projectile. As expected, this relativistic effect becomes more severe for higher irradiation energies. While the angles of detectors under 0° and 180° remain undistorted independently of the projectile energy, the maximal distortion is found for detectors under 90° . Depending on the irradiation energy, the correction is in the order of $\vartheta_{\text{CM}} - \vartheta_{\text{lab}} = +1^\circ$. The relativistic angle of the detector is therefore effectively distorted towards a larger ‘more backward facing’ angle.

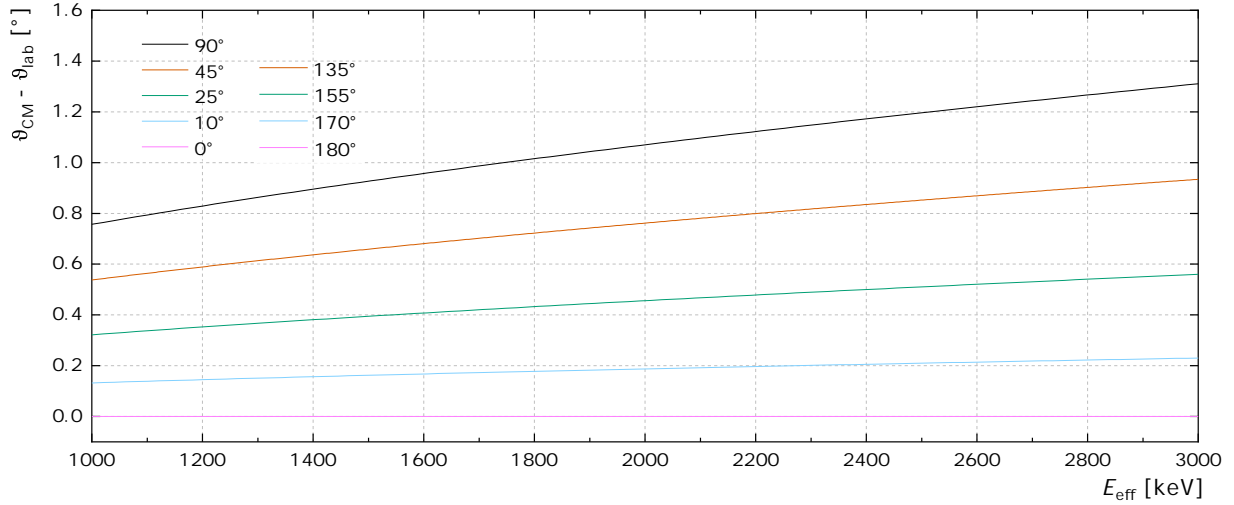


Figure 2.6: Correction regarding relativistic angles for investigating the ${}^3\text{He}(\alpha, \gamma){}^7\text{Be}$ reaction. The difference between the angle of the detector in the laboratory frame ϑ_{lab} , and the angle of the detector in the center-of-mass frame ϑ_{CM} is shown. The projectile is assumed to be ${}^4\text{He}$ and the angle is related to the emitted prompt γ -ray.

2.7 Determination techniques for target areal densities

In order to obtain information about a nuclear cross section in an in-beam experiment, the amount of involved projectiles, available target atoms and produced ejectiles (i.e. number of reactions) is needed. While the number projectiles will be measured via the current on the target, and the amount of ejectiles (or number reactions) will be measured using detectors, the missing quantity is the amount of involved target nuclei.

The two techniques, which are used throughout this thesis in order to analyze the areal density of target nuclei, are the so called nuclear reaction analysis (NRA) and the elastic recoil detection analysis (ERDA). Both of them rely on physics of material characterization, especially the characterization of surfaces and thin films. However, this topic spans a huge variety of techniques based on (among others) emission, transmission, absorption, reflection, diffraction, and scattering of various particles. While this section will only give a very brief introduction into two of these techniques, a broad overview into the topic itself can be found in [91].

2.7.1 Nuclear reaction analysis - NRA

The nuclear reaction analysis (NRA) is a spectroscopic method to determine the areal density of a chemical element in solid thin films. This technique can be performed in-situ by using an ion beam of typically 100 keV up to 10 MeV, which is suitable to undergo a nuclear reaction with the isotope of interest within the sample. By placing a detector close to the target and measuring the (live-time corrected) rate of full-energy events \dot{N} , the areal density of the target nuclei of interest ρ_T can be determined using information on the ion beam intensity

I , the cross section of the reaction σ , and detection efficiency of the ejectile ε , as shown in equation 29.

$$\begin{aligned} \dot{N} &= \dot{R} \cdot \varepsilon = \sigma \cdot \rho_T \cdot I \cdot \varepsilon \\ \frac{\text{events}}{\text{time}} &= \frac{\text{reactions}}{\text{time}} \cdot \varepsilon = \sigma \cdot \frac{\text{target atoms}}{\text{area}} \cdot \frac{\text{projectiles}}{\text{time}} \cdot \varepsilon \end{aligned} \quad (29)$$

It is worthwhile mentioning, that this basic formula will only be the foundation for further analyses. In case of non isotropic emission (i.e. whenever γ -ray angular distributions are involved), this equation has to be adapted, as e.g. shown in formula 48. A similar formula, which will be used in case of charged particles as ejectile will be introduced in equation 47. The underlying physics is the same, but the efficiency ε can be exchanged by the simplified opening angle Ω .

This approach of determining the areal density is particularly useful when dealing with non-resonant cross sections, which show a reasonably independent behavior in energy (within the energetic width of the target). Due to energy loss of the ion beam within the target layer of interest, the cross section will unavoidably vary. This has to be attenuated as much as possible by choosing appropriate irradiation energies, or properly taken into account, respectively.

However, with the so-called resonant NRA, it is also possible to obtain depth dependent information about the isotopic concentration. A resonance in a nuclear reaction at the resonance energy E_{res} is usually accompanied by a strong increase in cross section. Hence, by irradiating the material with an ion beam of $E = E_{\text{res}}$, most of the reactions will only take place directly on the surface of the material before subsequently losing energy within the material (facing an energy below $E = E_{\text{res}}$). By using initial irradiation energies above E_{res} , the majority of the ion beam will first lose energy while propagating through the material. At a certain depth, the energy of the ion beam will match E_{res} , which will subsequently lead to a strong increase in the number of reactions at this specific depth. Hence, an appropriate interval of irradiation energies will even lead to a scan of the depth profile for the chemical element of interest.

2.7.2 Elastic recoil detection analysis - ERDA

The elastic recoil detection analysis (ERDA) also uses an ion beam for determining the ion depth distribution or areal density, respectively. In case of ERDA however, the ion beam typically uses higher energies (2 MeV to 200 MeV) in order to kick out recoil nuclei out of the sample via elastic scattering. Given a fixed irradiation energy, the energy of these recoil nuclei depends on the depth from which they are emitted. In order to differentiate between different chemical elements, a Bragg Ionization Chamber can be used as a detector for the ejectiles. The Bragg Ionization Chamber is able to measure both the energy loss, and the

total energy of recoils, which are sputtered by the projectile atoms. Due to the fact, that the energy loss for nuclei of a certain energy depend on the respective element, the detector is able to assign nuclei to their nuclear charge Z . While this already enables the determination of the elemental abundance of a sample, the total energy of the incoming nucleus can subsequently be related to the depth from which it was sputtered out of the sample. The resulting 2D histograms of ‘energy loss versus total energy’ will be shown and further discussed later (e.g. figure 5.9).

As it will become evident later (e.g. in figure 5.9), the limitation of this technique is reached when trying to distinguish both very low nuclear charge numbers, and different isotopes from each other. In these particular cases, it is convenient to add a silicon detector to the setup, which precisely measures the respective light recoil nuclei.

It is worthwhile mentioning that the advantage of this technique is the simultaneous precise analysis of a variety of elements, as well as their depth profiles with one measurement. However, in contrast to the NRA, the ERD analyses within this thesis are not performed in-situ. These ERDA measurements are all executed before or after the experimental campaign at a different accelerator, which introduces different problems such as reliability and representativeness of the results with respect to the conditions during the actual measurement campaign.

2.8 Reaction rates and the astrophysical S -factor

The reaction rate $N_A \langle \sigma v \rangle$ between two sorts of nuclides refers to the number of reactions that occur per time and per volume (or i.e. per mol) at a given energy. It consists of the Avogadro constant N_A , as well as the average reaction rate $\langle \sigma v \rangle$ per particle pair. In stellar environments, the fusion reaction between two nuclei occurs due to their temperature-induced kinetic energy. This is why the corresponding rate is also called ‘thermonuclear’ reaction rate. This respective rate $\langle \sigma v \rangle$ depends on both the amount of available projectiles with this specific energy, as well as their cross section.

The amount of available projectiles per energy, or rather their velocity/energy distribution $P(v)dv$ or $P(E)dE$, can be approximated by a Maxwell-Boltzmann distribution. This is due to the fact, that plasma in astrophysical scenarios can be assumed to be in a thermodynamic equilibrium (cf. section 1.2). Hence, the thermonuclear reaction rate can be expressed, as shown in equation 30 with μ being the reduced mass, kT being the thermal energy, and N_A being the Avogadro constant [26, 92].

$$N_A \langle \sigma v \rangle = N_A \int_0^\infty v \sigma(E) P(E) dE = \left(\frac{8}{\pi \mu} \right)^{1/2} \frac{N_A}{(kT)^{3/2}} \int_0^\infty E \sigma(E) e^{-E/kT} dE \quad (30)$$

While the energy of available particles can be expressed by a Maxwell-Boltzmann distribution,

their cross section is also strongly energy dependent. In case of a (non-resonant) nuclear fusion reaction, this cross section rises exponentially with respect to the energy of the involved nuclei. This is due to the fact, that the penetrability through each others Coulomb barriers becomes significantly easier, the higher their energy is.

The energy dependency of the thermonuclear reaction rate (and therefore the question, at which energy the nuclear reactions actually take place) can therefore be understood by interpreting these two contributing energy dependencies: Taking both the flattening right tail of the Maxwell-Boltzmann distribution for the available particles (which usually peaks at energies in the order of ~ 1 keV within our Sun) and the cross section with its exponential increase into account, the integrand of equation 30 will result in a small window of non-negligible reaction rates, which is the so-called Gamow window or Gamow peak. Hence, the energy value of this window also indicates the energy region for a reaction in a certain astrophysical scenario (e.g. our Sun), where the reactions actually take place. They won't take place at subsequently lower energies due to the drop in cross section, and they also won't take place at larger energies due to the missing amount of particles. Its equivalent is also shown as in terms of sensitivity in figure 1.5 and figure 1.6.

In experimental nuclear astrophysics, the strong energy dependency of the cross section significantly complicates any fit and extrapolation of data sets. It is therefore convenient to introduce the so-called astrophysical S -factor (cf. equation 31), which is partly compensated for the energy dependency.

$$\sigma(E) = S(E) \frac{1}{E} e^{-2\pi\eta} \quad (31)$$

$$2\pi\eta = \frac{2\pi}{\hbar} \cdot Z_1 Z_2 e^2 \sqrt{\frac{\mu}{2E}} = 0.989510 \cdot Z_1 Z_2 \sqrt{\frac{M_1 M_2}{E(M_1 + M_2)}} \quad (32)$$

Both the $1/E$ dependency stemming from nuclear cross sections, as well as the exponential Coulomb barrier penetrability $e^{-2\pi\eta}$ (with η being the Sommerfeld parameter, cf. equation 32) gets eliminated. This penetrability acts as an approximation with Z_i as the nuclear charge number of both nuclei, E in MeV and M_i being their respective masses in atomic mass units.

$$N_A \langle \sigma v \rangle = \left(\frac{8}{\pi\mu} \right)^{1/2} \frac{N_A}{(kT)^{3/2}} \int_0^\infty S e^{-2\pi\eta} e^{-E/kT} dE \quad (33)$$

In summary, the astrophysical S -factor enables a more intuitive way to understand the behavior of a nuclear reaction by removing the influence of obvious energy dependencies. By combining both equation 30 and equation 31, the thermonuclear reaction rate can be stated in terms of the astrophysical S -factor, as shown in equation 33.

3 Setup of the experimental campaigns on nuclear astrophysics

The experimental campaigns for the investigation of the two main nuclear reactions of interest (cf. section 5 and section 6) were conducted in two experimental facilities, namely the Ion Beam Center (IBC) at HZDR, and the Felsenkeller shallow-underground laboratory in Dresden. While the ${}^2\text{H}(p,\gamma){}^3\text{He}$ reaction was investigated solely at the IBC, the ${}^3\text{He}(\alpha,\gamma){}^7\text{Be}$ reaction was studied both overground in the IBC, and underground in the Felsenkeller.

This chapter is organized as follows: Due to the comparatively large amount of seven distinct experimental campaigns, a variety of overview tables is offered in chapter 3.1 in order to provide a direct comparison of the most important experimental conditions. The different procedures regarding the target production for all in-beam campaigns will be discussed in section 3.2. The setup of each single campaign at the IBC and at Felsenkeller will be introduced in section 3.3 and section 3.4, respectively. The TU bunker for ultra-low background measurements at Felsenkeller will be discussed in section 3.5 with a special focus on the setup of the TU1 detector.

3.1 Overview and categorization of the experimental campaigns

Seven different experimental campaigns were conducted between the beginning of 2018 and the end of 2022 for the investigation of both the ${}^2\text{H}(p,\gamma){}^3\text{He}$ reaction and the ${}^3\text{He}(\alpha,\gamma){}^7\text{Be}$ reaction. Throughout these years, the design of these campaigns became increasingly more sophisticated, which subsequently also led to seven reasonably different experimental setups. While they all have in common, that they are in-beam experiments using cooled solid targets with surrounding HPGe detectors, the target production, the arrangement of the detectors and multiple subtleties were varying intensely over time.

A list regarding the main information of these seven campaigns is shown in table 3.1. It is noticeable, that all of these campaigns lasted for one or two weeks despite the last campaign (FK-V), which lasted for twelve contiguous weeks.

Table 3.1: List of all experimental campaigns with their investigated reaction, their location (Ion Beam Center at HZDR or Felsenkeller shallow-underground lab), their dates and their utilized samples, respectively.

Campaign	Reaction	Loc.	Date	Samples
IBC-I	${}^2\text{H}(p,\gamma){}^3\text{He}$	IBC	15.01. – 27.01.2018	TiD2-2-1 to TiD2-2-4
IBC-II	${}^3\text{He}(\alpha,\gamma){}^7\text{Be}$	IBC	23.05. – 06.06.2018	Au50, Au100, Ta100, Ta502
FK-I	${}^3\text{He}(\alpha,\gamma){}^7\text{Be}$	FK	13.11. – 27.11.2020	ST3, ST4
FK-II	${}^3\text{He}(\alpha,\gamma){}^7\text{Be}$	FK	28.02. – 07.03.2021	ST5
FK-III	${}^3\text{He}(\alpha,\gamma){}^7\text{Be}$	FK	21.09. – 29.09.2021	ST6
FK-IV	${}^3\text{He}(\alpha,\gamma){}^7\text{Be}$	FK	29.11. – 15.12.2021	ST7, ST8
FK-V	${}^3\text{He}(\alpha,\gamma){}^7\text{Be}$	FK	14.07. – 06.10.2022	ST9 - ST12, ST15, Ta51 - Ta54

3.1.1 Overview of the implantation characteristics of the samples

A total of 25 targets were produced within the scope of this thesis, with two of them being not irradiated (ST1 & ST2) and one of them being used twice (ST9 & ST9B). While the backing of these targets was always identical (pure tantalum disk with 27 mm diameter and 220 μm thickness), they all differed with respect to their cleaning procedures, possible evaporation layers, their implanted ions (blank, ^2H , ^3He), and the utilized fluence F during implantation. The total fluence was usually distributed to multiple implantation energies in order to obtain a more homogeneous depth profile. While the implantation/deuteration procedures itself will be described in section 3.2, a list of all targets is shown in table 3.2.

Table 3.2: Characteristics of all samples, which were produced for the $^2\text{H}(p,\gamma)^3\text{He}$ and the $^3\text{He}(\alpha,\gamma)^7\text{Be}$ campaign. Their cleaning procedures are elaborated in section 3.2.1, and the implantation procedure of the respective ion species will be introduced in section 3.2.2–3.2.4. The fluence is given as the applied fluence F_i , which differs from the areal density ρ_a (cf. section 6.1.3).

Camp.	Name ⁹	Backing	Clean. proc.	Ion	Fluence I [at/cm ²]	Fluence II [at/cm ²]
IBC-I	TiD2-2-1	100 nm Ti on Ta	I	^2H	Deuteration	—
	TiD2-2-2	100 nm Ti on Ta	I	^2H	Deuteration	—
	TiD2-2-3	100 nm Ti on Ta	I	^2H	Deuteration	—
	TiD2-2-4	100 nm Ti on Ta	I	^2H	Deuteration	—
IBC-II	Ta100	Ta	I	^3He	1.0E18 @ 40 keV	2.4E17 @ 10 keV
	Au100	200 nm Au on Ta	I	^3He	1.0E18 @ 40 keV	2.4E17 @ 10 keV
	Ta502	Ta	I	^3He	5.0E17 @ 40 keV	1.2E17 @ 10 keV
	Au50	200 nm Au on Ta	I	^3He	5.0E17 @ 40 keV	1.2E17 @ 10 keV
FK-I	ST1	180 nm Ta on Ta	I	^3He	1.0E18 @ 35 keV	2.5E17 @ 10 keV
	ST2	180 nm Nb on Ta	I	^3He	1.0E18 @ 35 keV	2.5E17 @ 10 keV
	ST3	Ta	I	^3He	1.0E18 @ 35 keV	2.5E17 @ 10 keV
	ST4	Ta	I	^3He	1.0E18 @ 35 keV	2.5E17 @ 10 keV
FK-II	ST5	Ta	I	^3He	1.0E18 @ 35 keV	2.5E17 @ 10 keV
FK-III	ST6	Ta	I	^3He	1.0E18 @ 35 keV	2.5E17 @ 10 keV
FK-IV	ST7	Ta	I	^3He	1.0E18 @ 35 keV	2.5E17 @ 10 keV
	ST8	Ta	I	^3He	1.0E18 @ 35 keV	2.5E17 @ 10 keV
FK-V	ST9	Ta	II	^3He	1.0E18 @ 35 keV	—
	Ta51	Ta	II	—	—	—
	ST12	Au on Ta	II	^3He	1.0E18 @ 35 keV	—
	ST10	Ta	II	^3He	1.0E18 @ 35 keV	—
	Ta52	Ta	II	—	—	—
	ST11	Ta	II	^3He	1.0E18 @ 35 keV	—
	ST9B	Ta	II	^3He	1.0E18 @ 35 keV	—
	Ta53	Ta	II	—	—	—
	ST15	Ta	II	^3He	1.0E18 @ 35 keV	—
Ta54	Ta	II	—	—	—	

⁹It is worthwhile mentioning, that ‘Ta’ during IBC-II was used to distinguish implanted tantalum targets from implanted gold targets, while during later campaigns, the term ‘Ta’ is always used for tantalum blanks.

3.1.2 Overview of the irradiation parameters of the samples

The irradiated samples can be classified according to important parameters of interest during their investigation. As elaborated in section 2.6, the applied energy of the projectiles can be stated in terms of the laboratory energy E_{lab} , the effective energy E_{eff} , and the center of mass energy E_{cm} . While the irradiations themselves will be described in the corresponding chapters 5 and 6, a list of the irradiation parameters for all samples used during the ${}^2\text{H}(p,\gamma){}^3\text{He}$ and the ${}^3\text{He}(\alpha,\gamma){}^7\text{Be}$ campaigns are shown in table 3.3.

Table 3.3: Overview of essential parameters during the irradiation of all samples. The irradiation energies are given in terms of the laboratory energy E_{lab} , the effective energy E_{eff} , and the center of mass energy E_{cm} (all calculations based on terminal voltage, cf. section 2.6). In case of ‘mult.’, multiple energies were investigated with this target, see e.g. table 5.1 in case of the ${}^2\text{H}(p,\gamma){}^3\text{He}$ reaction. Furthermore, the utilized target holder design is stated (cf. section 3.1.5), as well as the dates of the irradiation and the accumulated charge Q .

Camp.	Name ¹⁰	E_{lab} [keV]	E_{eff} ¹¹ [keV]	E_{cm} [keV]	Design of target holder	Begin of irradiation	End of irradiation	Q [C]
IBC-I	TiD2-2-1	mult.	mult.	mult.	I	17.01.18	19.01.18	0.4
	TiD2-2-2	mult.	mult.	mult.	I	19.01.18	22.01.18	0.2
	TiD2-2-3	mult.	mult.	mult.	I	23.01.18	25.01.18	0.5
	TiD2-2-4	mult.	mult.	mult.	I	25.01.18	27.01.18	0.4
IBC-II	Au50	mult.	mult.	mult.	II	23.05.18	24.05.18	0.1
	Au100	mult.	mult.	mult.	II	24.05.18	25.05.18	0.1
	Ta100	mult.	mult.	mult.	II	25.05.18	01.06.18	0.8
	Ta502	2881.6	2834.0	1217.7	II	04.06.18	06.06.18	0.2
FK-I	ST3	2773.0	2724.8	1170.8	II	16.11.20	19.11.20	2.4
	ST4	2773.0	2724.8	1170.8	II	23.11.20	25.11.20	0.8
FK-II	ST5	2772.4	2724.2	1170.5	II	02.03.21	07.03.21	0.9
FK-III	ST6	1884.8	1830.4	786.5	II	21.09.21	29.09.21	0.7
FK-IV	ST7	mult.	mult.	mult.	II	29.11.21	02.12.21	0.6
	ST8	mult.	mult.	mult.	II	06.12.21	15.12.21	2.4
FK-V	ST9	2880.0	2832.4	1217.1	III	14.07.22	18.07.22	2.7
	Ta51	2880.0	2832.4	1217.1	III	19.07.22	22.07.22	2.2
	ST12	2149.7	2097.3	901.2	III	22.07.22	25.07.22	1.9
	ST10	2149.7	2097.3	901.2	III	26.07.22	01.08.22	5.5
	Ta52	2149.7	2097.3	901.2	III	01.08.22	08.08.22	4.4
	ST11	1349.3	1290.8	554.6	III	16.08.22	21.08.22	4.7
	ST9B	1349.3	1290.8	554.6	III	24.08.22	29.08.22	4.6
	Ta53	1349.3	1290.8	554.6	III	30.08.22	03.09.22	4.2
	ST15	1101.2	1041.1	447.4	III	20.09.22	27.09.22	7.0
	Ta54	1101.2	1041.1	447.4	III	29.09.22	06.10.22	6.5

¹⁰It is worthwhile mentioning, that ‘Ta’ during IBC-II has been used to distinguish implanted tantalum targets from implanted gold targets, while during later campaigns, the term ‘Ta’ is used for tantalum blanks.

¹¹As elaborated in section 6.1.4 and 6.5.5, and also shown in figure 6.6, E_{eff} depends on the implantation ratio. In this case, a mean stoichiometric ratio of 1:3 between ${}^3\text{He}$ and tantalum was assumed.

3.1.3 Overview of calibration sources

Within the scope of this thesis multiple α -, and γ -ray calibration sources were used in order to test detection setups, optimize signal reconstructions, and calibrate detectors regarding their energy (cf. section 2.4.1) and their absolute full energy peak efficiency (cf. section 2.4.2). In order to avoid duplications within the analysis chapters, a list of all utilized calibration sources and their specifications is shown in table 3.4 .

Table 3.4: Assignment of all calibration sources to their ID, as well as their activity A (surface emission rate R_S in case of α sources), the reference date for the stated activity, the energies of their utilized α -, and γ -lines, and their subsequent emission probabilities. While the PTB usually states a 95 % C.L., for sake of consistency all uncertainties are stated with a confidence level of 68 %. If not stated otherwise, the activities of the reference dates are given for 00:00 CET. In case of missing uncertainties, these information are also not stated in the ENSDF data base as well.

ID	α/γ	Nuclide	A / R_S [kBq] / [ms^{-1}]	Reference date	Energy [keV]	Emis. prob. [%]
4696	γ	^7Be	8.34(12)	04.05.2021	477.6035(20)	10.44(4)
4697	γ	^7Be	18.09(24)	05.05.2021	477.6035(20)	10.44(4)
4698	γ	^7Be	1.726(24)	08.05.2021	477.6035(20)	10.44(4)
4659	γ	^{22}Na	49.30(25)	01.07.2020	1274.537(7)	99.940(14)
3394	γ	^{60}Co	9.12(4)	01.01.2005	1173.228(3)	99.85(3)
					1332.492(4)	99.9826(6)
3393	γ	^{60}Co	260.7(10)	01.01.2005	1173.228(3)	99.85(3)
					1332.492(4)	99.9826(6)
4433	γ	^{88}Y	133.2 (7)	01.03.2016	898.042(3)	93.7(3)
					1836.063(12)	99.2(3)
4753	γ	^{88}Y	103.2 (7)	12.01.2022	898.042(3)	93.7(3)
					1836.063(12)	99.2(3)
4621	γ	^{133}Ba	13.96(7)	01.06.2019	276.3989(12)	7.16(5)
					302.8508(5)	18.34(13)
					356.0129(7)	62.05(19)
					383.8485(12)	8.94(6)
3396	γ	^{137}Cs	11.30(6)	01.01.2005	661.657(3)	85.1(2)
4199	γ	^{137}Cs	59.7(3)	01.11.2012	661.657(3)	85.1(2)
AJ-5470 (Single α)	α	^{241}Am	5.38(11)	29.03.2018	5388	1.66(2)
					5442.80(13)	13.1(3)
					5485.56(12)	84.8(5)
					5544.5(16)	0.37(3)
EC221 (Triple α)	α	^{239}Pu	3.54(17)	14.10.1994	5105.5(8)	11.94(7)
					5156.59(14)	70.77(14)
		^{241}Am			5388	1.66(2)
					5442.80(13)	13.1(3)
					5485.56(12)	84.8(5)
		^{244}Cm			5544.5(16)	0.37(3)
					5762.64(3)	23.1(1)
					5804.77(5)	76.9(1)

3.1.4 Overview of in-beam HPGe detectors

During the experimental campaigns on the investigation of the ${}^2\text{H}(p,\gamma){}^3\text{He}$ and the ${}^3\text{He}(\alpha,\gamma){}^7\text{Be}$ reactions, a variety of high purity germanium (HPGe) detectors was used. A list of all utilized detectors along with their specifications is shown in table 3.5.

Table 3.5: List of all HPGe detectors, which were used for experimental campaigns. Their name, as well as their company, specification, type, number of capsules and their relative efficiency (cf. section 2.4.2) are stated. Abbreviations for ‘septuple’, ‘cluster’ and ‘hexagonal’ were used.

Name	Company	Specification	Type	# of caps.	Rel. eff. ¹² [%]
Can60	Mirion ¹³	Single crystal	Coax, p-type	1	60
Ortec90	Ortec	Single crystal	Coax, p-type	1	88
Ron100	Mirion ¹³	4-fold segmented	Coax, p-type	1	100
MB1	Mirion ¹³	MINIBALL triple cl.	Hexag. tapering, n-type	3	3 x 60
MB2	Mirion ¹³	MINIBALL triple cl.	Hexag. tapering, n-type	3	3 x 60
EB17	Mirion ¹³	EUROBALL sept. cl.	Hexag. tapering, n-type	7	7 x 60
EB18	Mirion ¹³	EUROBALL sept. cl.	Hexag. tapering, n-type	7	7 x 60

By far, not all detectors were used in all experimental campaigns. An overview of the usage of these detectors during the various campaigns is shown in table 3.6. As discussed in section A.1.1, the use of surrounding bismuth germanate (BGO) detectors may be useful in certain experiments to increase the peak-to-background ratio within the HPGe spectra. The usage of surrounding BGOs is also shown in table 3.6.

Table 3.6: List of all HPGe detectors, which were used for measurements. Their name is noted along with their use in the different campaigns. It is also listed, whether the HPGe detector was in use with or without a surrounding BGO.

Name	Ion Beam Center				Felsenkeller									
	IBC-I		IBC-II		FK-I		FK-II		FK-III		FK-IV		FK-V	
	Ge	BGO	Ge	BGO	Ge	BGO	Ge	BGO	Ge	BGO	Ge	BGO	Ge	BGO
Can60	X		X		X		X		X		X		X	X
Ortec90	X	X	X	X										
Ron100			X										X	
MB1			X	X	X	X	X	X	X	X	X	X	X	X
MB2					X	X	X	X	X	X	X	X	X	
EB17					X		X		X		X		X	
EB18					X	X	X	X	X	X	X	X	X	

¹²Relative efficiencies are stated as the ratio of the full energy peak efficiency relative to a 3”x3”x3” NaI(Tl) detector using a ${}^{60}\text{Co}$ source (1332 keV peak) measured at a distance of 25 cm to the detector. Relative efficiencies are stated without add-back factors (cf. section A.1.2).

¹³Mirion technologies, or formerly still produced under the companies ‘Canberra’ and ‘EURISYS Mesures’.

3.1.5 Overview of target holder designs

During the multiple experimental campaigns, a variety of target holders were designed and utilized, which is due to two main reasons. On the one hand, the investigations of both the ${}^2\text{H}(p,\gamma){}^3\text{He}$ and the ${}^3\text{He}(\alpha,\gamma){}^7\text{Be}$ reaction had to meet different specific requirements, which led to different designs. On the other hand these target holders were also upgraded subsequently over time in order to adapt them to the increasing awareness to weaknesses of the experimental setup.

The main evolution of target holder designs can be categorized into three main stages, which are further called target holder design I, II, and III (cf. table 3.2). While the targets in the target holder design I are water-cooled, in case of the target holder design II and III they are cooled with LN2.

Target holder design I

The target holder design I was adapted by prior experiments conducted by the working group for nuclear astrophysics at HZDR [73, 93, 94]. While this design leads to a target surface, which is perpendicular to the direction of the ion beam, prior experimental setups were usually designed in a way, that resulted in an inclination angle of 55° between target surface and the respective ion beam direction. Within this work, this target holder design was used solely for the investigation of the ${}^2\text{H}(p,\gamma){}^3\text{He}$ reaction (cf. table 3.2). The design of this target holder is shown in figure 3.1 and its unintuitive round shape will further be discussed in section 3.3.1.

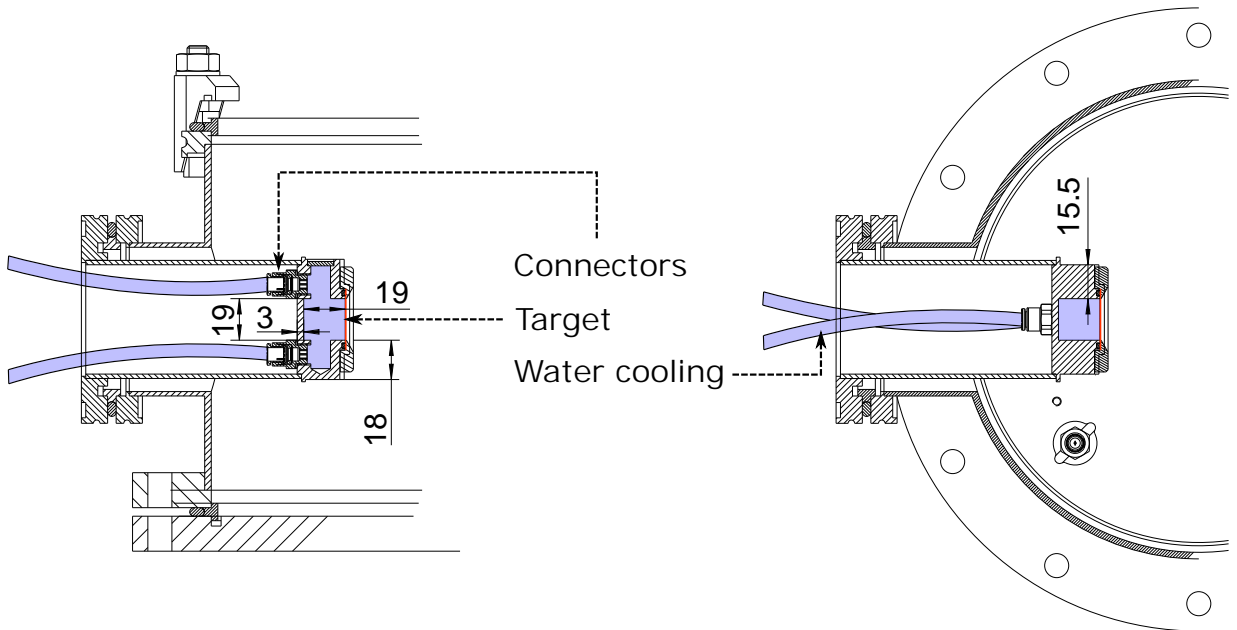


Figure 3.1: Schematic side view (left) and top view (right) of the target holder design I. The target itself is shown as a thin red vertical line. The water reservoir, as well as the supply pipes are shown in blue. The target holder is mounted with an ISO-K63 flange onto the target chamber.

It includes a water cooling with direct contact to the backside of the targets, which is realized by a reservoir of 19 mm width. This reservoir is continuously flushed with 20°C water using an entrance, and an exiting pipe system. The target itself is tightly fixed with help of an additional copper (formerly also aluminum) ring in order to prevent water from entering the vacuum chamber. This fixation, as well as its dimensions are identical to the one of target holder II, as shown in figure 3.2. An actual photo is shown in figure 3.9.

Target holder design II

The target holder design II is an entirely new concept, which was not used during any prior campaign. Its construction became necessary due to the fact, that the water cooling would have been insufficient for the investigation of the ${}^3\text{He}(\alpha, \gamma){}^7\text{Be}$ reaction. The ion-beam induced heat in the target subsequently would have led most likely to unacceptable diffusion processes or a possible deformation of the target.

The crucial elements of this target holder (cf. figure 3.2) consist entirely of copper, which has an excellent heat conductivity. Furthermore, it is designed with as few individual parts as possible in order to further optimize the heat transfer. The cooling itself is provided by a dewar ($d = 112\text{ mm}$, $h = 97\text{ mm}$) mounted from the top, which can be filled with LN2 ($\vartheta = -196^\circ\text{C}$). Each interface of two components along the LN2 reservoir and the target is filled with a thin layer of indium in order to optimize the heat conductivity even further.

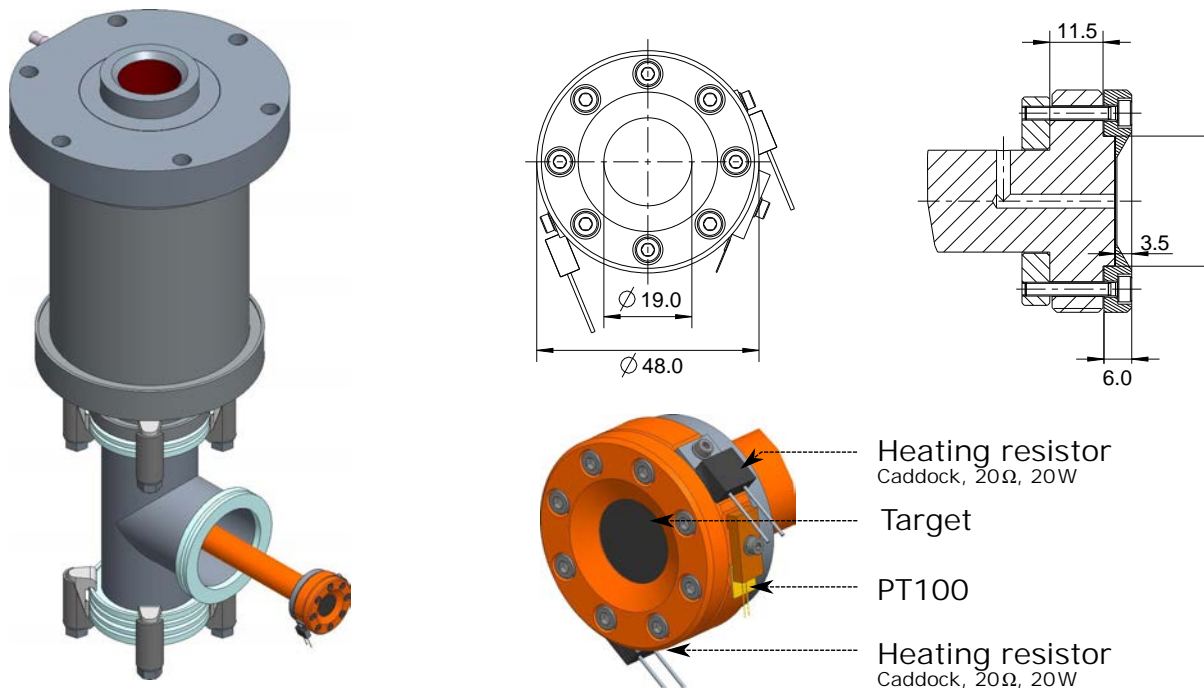


Figure 3.2: Schematic view of the target holder design II (left). The target itself is mounted between two copper elements (schematic drawings on the right). Its temperature is monitored using a PT100, and two heating resistors are used prior to target changes in order to effectively warm up the target. The construction of the LN2 dewar is identical to figure 3.4.

The target holder design was arranged in way, which guarantees a reasonably well insulated target, both regarding electrical currents, as well as against temperature gradients to the outside of the respective beam line element. In order to properly integrate the accumulated charge on the target, every connection other than the SHV connection to the current integrator is insulated with several $M\Omega$ or $G\Omega$ of resistance. This is realized, by putting the entire inner part of the LN2 dewar onto the same potential as the target holder, and insulated this inner part against the outer metal cylinder using teflon components and rubber O-rings. The temperature insulation is realized by evacuating the space between inner dewar and the outer cylinder. This vacuum is shared between LN2 dewar and target chamber (cf. construction of the LN2 dewar in figure 3.4).

Target holder design III

The holder design III is an upgrade of holder design II and was also optimized for the investigation of the ${}^3\text{He}(\alpha, \gamma){}^7\text{Be}$ reaction. The holder is once again entirely made of copper, but this new design is minimizing the utilized material towards the target, which reduces the γ -ray attenuation within the target area. However, its mounting is still compatible with the holding construction of the otherwise unchanged suspension frame. In addition, the entire structure is made of one piece of copper in order to optimize heat transfer.

The PT100 is mounted at the most representative position to indicate the temperature of the target itself, which is still feasible without geometrically influencing the detection efficiency of surrounding detectors, namely the bottom of the backside of the target holder. The resistors are mounted further to the back of the rod due to the irrelevance of their close proximity to the target.

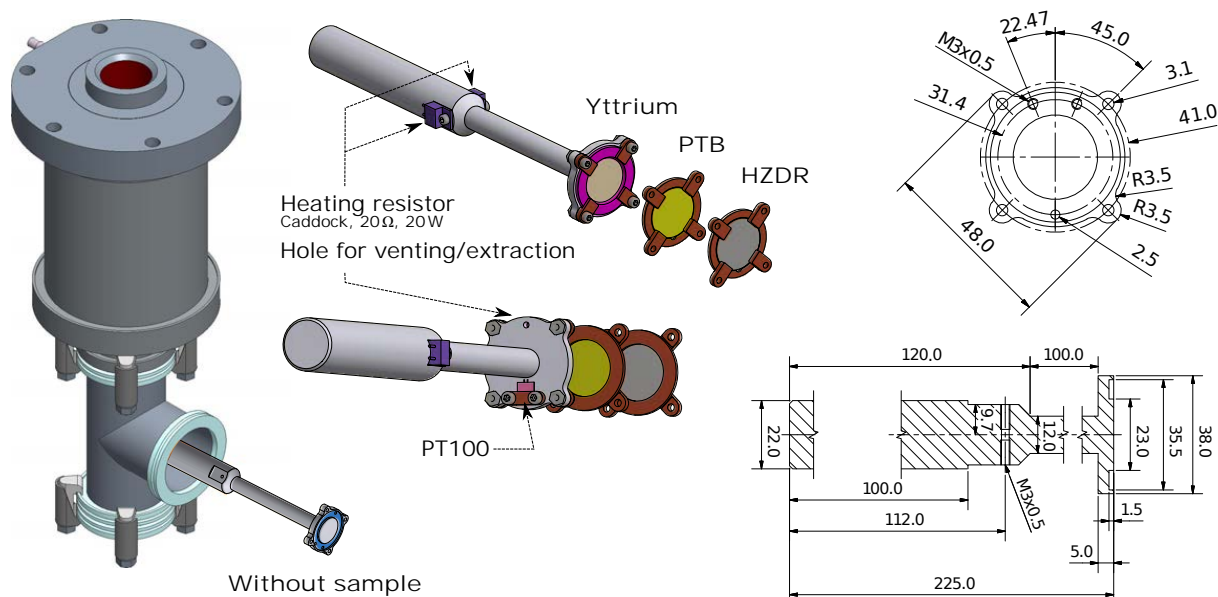


Figure 3.3: Schematic view of the target holder design III (left). The target holder can be precisely equipped with different target geometries, namely yttrium, PTB, and HZDR standards, respectively (middle). The construction of the dewar is identical to figure 3.4. See text for details.

Another crucial upgrade with respect to the target holder design II concerns the variety of mountable target geometries. All irradiation targets have a diameter of $d = 27$ mm and a thickness of $h = 220$ μm (further called ‘HZDR’ standard). However, the utilized γ -ray calibration sources (cf. section 3.1.3) are mainly provided by the ‘Physikalisch-Technische Bundesanstalt’ and they do have slightly different dimensions (further called ‘PTB’ standard). While these PTB sources can be dismounted from their frame, there is one calibration source (^{88}Y), which is provided by the Czech metrology institute, which can not be removed from its frame (further called ‘yttrium’ standard). The former target design II hindered a proper positioning of this yttrium standard, which subsequently led to complex offline corrections. Therefore, the new holder has a recess for the yttrium standard, so it can be properly mounted along with its frame. In case of using the PTB or HZDR standards (without frame), the empty recess can be filled with appropriate copper O-rings in order to equalize the attenuation for photons and subsequently valid full-energy peak efficiencies.

3.1.6 Overview of additional beam line elements in proximity to the target

In addition to the utilized target holders, targets, and detectors, there are some other elements, which are in proximity to the target and essential for a successful operation of the in-beam experiments. While their appearance in different setups, as well as their benefits, disadvantages and contributions to in-beam troubles will be discussed later, their introduction will be provided below.

Target cooling, cold trap and secondary electron suppression

As discussed in the section 3.1.5, the targets need to be actively cooled in order to prevent a beam-induced increase in target temperature, which subsequently could enhance diffusion processes of the implanted ions - either out of the target or into deeper layers than intended. However, an active cooling of the target has to be designed with utmost caution due to its accompanied inherent threats during operating. This is due to the fact, that during the cooling process of the target, remaining gas in the beam line would subsequently condensate onto its surface, which potentially leads to contaminations of carbon, oxygen, nitrogen and others, as well as time-dependent energy-loss effects of the beam during long-term campaigns. This has to be avoided under all circumstances.

Therefore, an additional so-called ‘cold trap’ is installed in close proximity prior to the target, which is shown in figure 3.4. Whenever a target needs to be cooled down, this large-surface cold trap is cooled down first (with ≈ 30 min delay), in order to act as the dominant catcher of remaining gas in the beam line, and also to increase the quality of the vacuum as a direct consequence. This procedure is turned around, whenever the target needs to be warmed up prior to a target change. First the target is warmed up, and thereafter the cold trap in order to prevent the condensated gas on the cold trap from being caught by the target. This delay in first warming up the target and then the cold trap is realized by using two

heating resistors on the target holder (cf. figure 3.2). In this way it is guaranteed (even when simultaneously stopping the operation of both coolings), that the target is always at a comparatively higher temperature, than the cold trap.

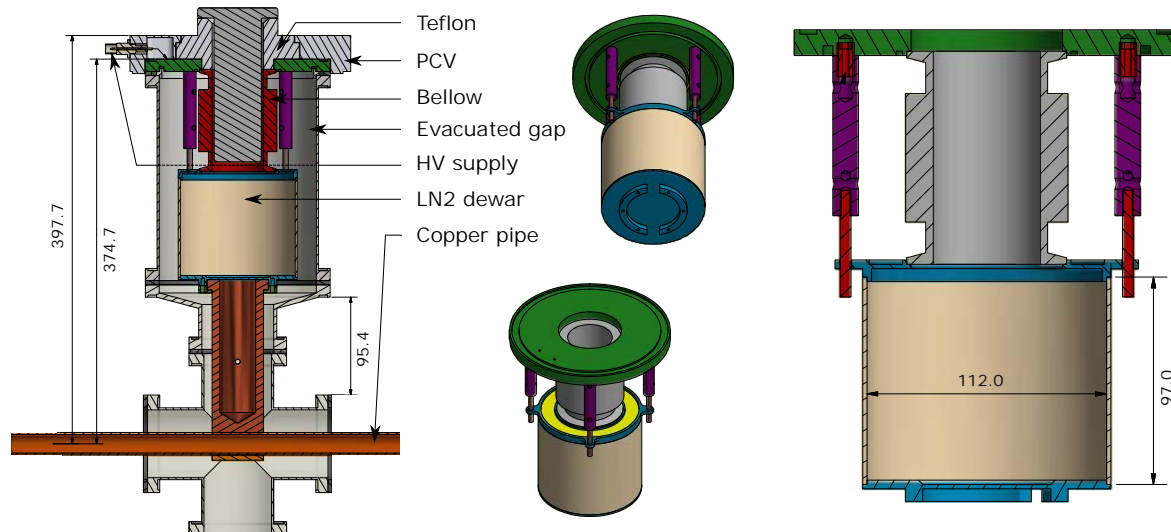


Figure 3.4: Schematic drawing of the cold trap, which simultaneously acts as secondary electron suppression. The same design was also used for the target cooling. All non-grey elements in the left figure are at the same potential and insulated from the outer metallic parts. The middle and right figures show the inner LN2 dewar and its mounting. The cap on top of the teflon also hosts a phase separator and a PT100, which are not shown here (cf. also figure D.5).

In addition to its purpose of acting as a cold trap, the copper pipe within the beam line (cf. figure 3.4) also acts as a so-called secondary electron suppression (SES). This copper pipe only ends a few millimeters in front of the installed target and (depending on the experimental campaign) is kept on a constant high voltage of $U = [-200 \text{ V}, -1500 \text{ V}]$.

In case of a target irradiation, the ion beam sputters out secondary electrons from the target surface, which subsequently lead to systematic distortions of the charge integration at the target. This electron emission can effectively be suppressed by applying the previously mentioned negative high voltage at the copper pipe, which is positioned in close proximity to the target surface and effectively ‘pushes’ the electrons back into the target.

Silicon detector, protection foil and holder

During the campaigns in the Ion Beam Center at HZDR (IBC-I and IBC-II), a partially depleted silicon surface barrier detector was used within the target chamber, and is further called silicon detector or particle detector. It has an active area of 300 mm^2 , and a sensitive thickness of $2000 \mu\text{m}$. A schematic drawing of the detector and its holder is shown in figure 3.5. In order to shield the detector from elastically scattered beam particles, two nickel foils with $25 \mu\text{m}$ thickness each were mounted in front of the sensitive area of the detector. This total thickness of $50 \mu\text{m}$ corresponds roughly to the range of 4 MeV protons within nickel. These foils were removed in case of calibration measurements with α sources.

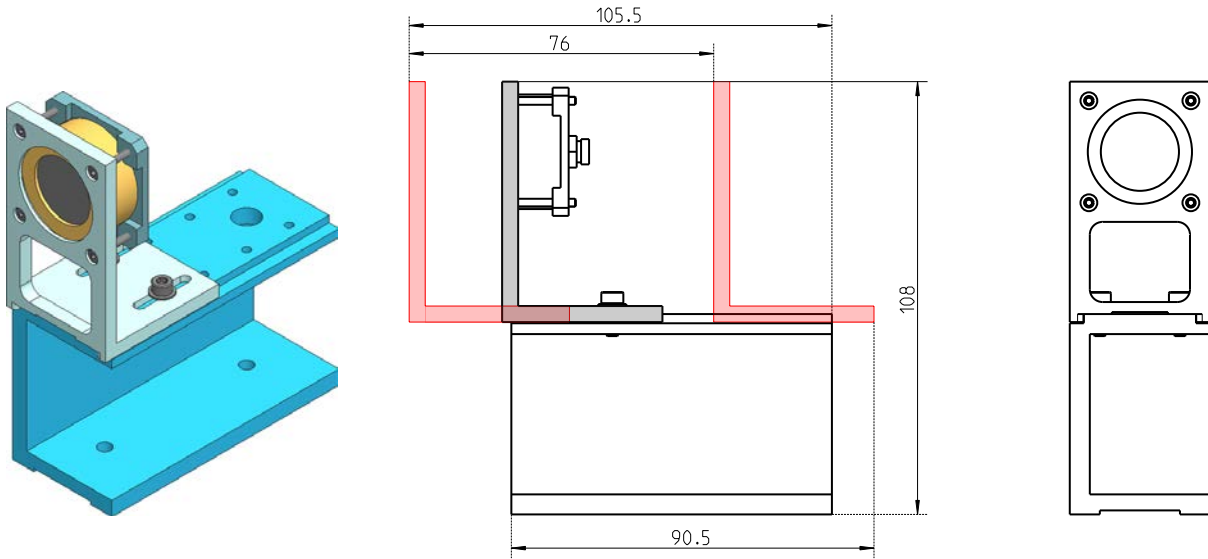


Figure 3.5: Schematic drawing of a partially depleted silicon surface barrier detector, and its holder in the target chambers for the IBC-I and IBC-II campaigns (cf. table 3.1). A photo of the detector in the target chamber is shown in figure 3.9. Left: 3D drawing of the detector on its holder. Middle: Side view of the detector on its holder with dimensions, and maximal positionings on the holder (red). Right: Front view of the detector on its holder.

The silicon detector (Model number BA-022-300-2000) is provided by Ortec and has a nominal alpha resolution of 20.6 keV at $E = 5.486$ MeV. The detector provides a Microdot connector on the rear of the can. Due to the fact that its not fabricated to be ‘ruggedized’, it is always operated in absence of air and ambient light[95].

Camera surveillance of the beam spot

In most accelerator-based experiments, the beam is supposed to hit the center of the target. This is even more important in target setups like the present ones, where parts of the targets are covered for the beam by their fixation ring. However, the irradiation of these materials has to be avoided due to the resulting accumulated charge without ions actually hitting the target itself. The possibility of a visual confirmation of the beam position on the target is highly uncommon, because indirect techniques are well-known. By steering the beam from left to right and from top to bottom, the minimum in beam-induced current on any kind of collimator can be used to center the beam.

However, for most of the presented experimental campaigns at Felsenkeller, a visual proof was implemented by using a camera and an ISO-KF40 window made of borosilicate glass. As shown in figure 3.6, this visual proof can be used to precisely shape the beam spot as necessary. This can be crucial in case of helium beams in order to delay so-called blistering effects by broadening the beam (cf. section 6.1.2). Furthermore, a visual target degradation (bursted blisters, beam-induced influences on the target surface, changes in color or local brightness, condensation-induced dullnesses etc.) can be monitored more effectively.

In addition, blistering effects were delayed by the use of wobbling techniques (continuous scanning of the beam spot along the target with help of additional magnets in order to reduce the implanted amount of ^4He per area). The necessary magnetic field strength was also optimized using the camera feedback of the beam spot position.

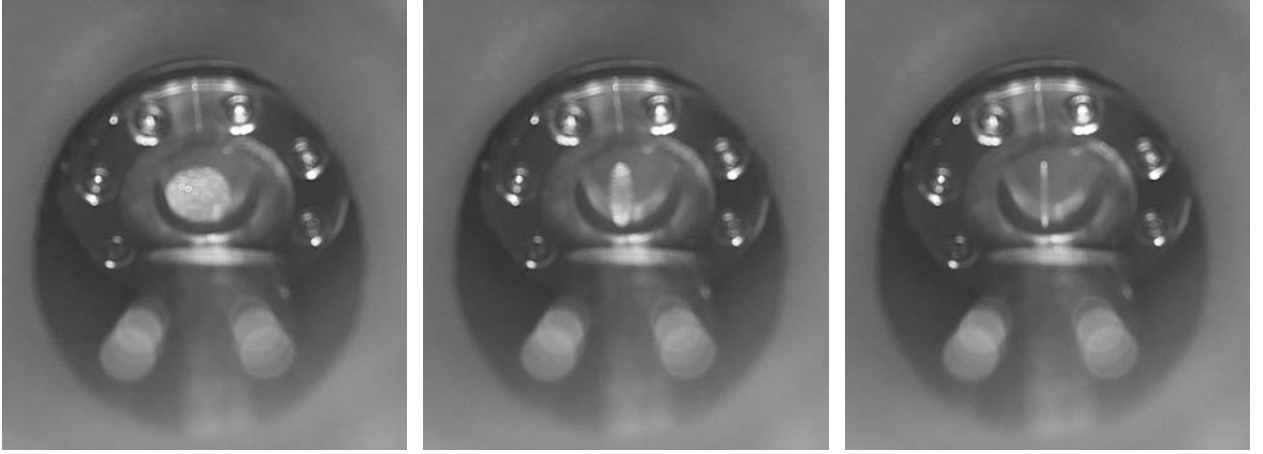


Figure 3.6: Photographs of different beam spot shapes on the target. All photos show the copper pipe of the secondary electron suppression in the lower part and the front of the target holder II on the upper part. The perspective is identical to the lower left picture in figure 3.9, when taking a photo from the position of the displayed silicon detector.

3.2 Sample production for the experimental campaigns

For the investigation of reactions with low cross sections, the production of the target is a crucial element. Both the selection of an appropriate backing material, as well as the optimization of the implantation process will therefore be discussed thoroughly in the following section.

The backings for all samples regarding the $^2\text{H}(p,\gamma)^3\text{He}$ campaign and the $^3\text{He}(\alpha,\gamma)^7\text{Be}$ campaigns are made of pure tantalum with a diameter of 27 mm and a thickness of 220 μm . Due to its high coulomb barrier, its resulting lack of contamination reactions at low irradiation energies and its reasonably high thermal conductivity and melting point, it is widely used in in-beam experiments for nuclear astrophysics [26] and also proved to be suitable in multiple experiments of the local science group [1, 73, 93, 96–99]. Nonetheless, it is worthwhile mentioning, that tantalum does have a well known disadvantage of hosting fluorine as a contaminant. Fluorine has a low ordering number, and therefore a low coulomb barrier. Hence, nuclear reactions on fluorine are one of the more important contributors to the in-beam background, and will be further elaborated in the subsequent analyses.

In addition, the backing material needs to fulfill another crucial task: It needs the ability to efficiently trap the ion of interest after their implantation. In case of the $^3\text{He}(\alpha,\gamma)^7\text{Be}$ reaction, this resulted in the occasional use of evaporation layers of different materials in order to optimize this quantity.

The implantation processes for the targets of both investigated reactions differ vastly from each other. However, there is one additional common consideration: On the one hand, the amount of occurring reactions is proportional to the amount of target nuclei, which gives rise to the necessity of maximizing the areal density. On the other hand, it is important (especially for direct capture reactions and surrounding HPGe detectors) to minimize the thickness of the target layer, which enables a more precise statement on the effective energy of the projectile. Furthermore, a thin target also unburdens the task of properly analyzing a broad peak in the resulting γ -ray spectrum. Therefore, the areal density needs to be as large as possible with a simultaneously acceptable energy loss of the projectiles in the target.

3.2.1 Cleaning procedures of the backings prior to implantation/deuteration

The proper cleaning of the backings prior to implantation is essential in order to minimize surface contaminations, and at least attempt to reduce contaminations in shallow depths as well [26]. Commonly applied procedures include the usage of acids, super sonic baths, and heat. All backings, which were used in the experimental campaigns underwent one of two different cleaning procedures (cf. table 3.2). Those are introduced below with α being the degree of dissociation for the acids. These procedures were always conducted prior to the evaporation (cf. section 3.2.2), implantation and/or deuteration, respectively.

Cleaning procedure I

- Supersonic bath with deionized water for 1 h at 20 kHz & 40 kHz
- Cleaning with 2-Propanol
- Drying with cleanroom wipers (100% polyester)
- Mounting in target holder

Cleaning procedure II

- Supersonic bath (60% deionized water, 40% 2-Propanol) for 30 min at 20 kHz & 40 kHz
- Heating of the backing to 200 °C under vacuum for 48 h
- Rinsing in 40°C warm 2-Propanol for 10 min, scrub as needed
- Drying with cleanroom wipers (100% polyester)
- Rinsing in 40°C warm 2-Propanol for 10 min, scrub as needed
- Rinsing in deionized water
- Bathing in acid [10% vol. HNO_3 ($\alpha = 0.7$) + 2% vol. HCl ($\alpha = 0.37$)] for 15 min (50°C)
- Rinsing in deionized water twice
- Drying with cleanroom wipers (100% polyester)
- Wrapping in filter paper & sealing in plastic bag under nitrogen/argon atmosphere
- Storage in freezer (-20°C)

3.2.2 Evaporation procedures for the backings

Regarding the purpose of in-beam experiments in nuclear astrophysics, there is no perfect evaporation layer. Evaporation layers with low atomic number are certainly unsuitable due to their low Coulomb barrier and their subsequent ability of undergoing undesired contamination reactions. On the other hand, elements with high atomic number have a higher stopping power compared to low atomic numbers. The higher the stopping power, the lower the effective number of target nuclei, which can be encountered without major loss in energy and subsequent inevitable change in cross section. In the following section, the focus will be on the evaporation of gold and titanium onto the tantalum backing due to their proven suitability in literature. For more information, see e.g. [100, 101].

The evaporation onto the tantalum backings in general may be beneficial due to two reasons with the first one being the use of potentially more suitable carriers for the implanted ion. The second reason is the lack of contaminants with low atomic number in the resulting surface layer (e.g. fluorine), due to the fact that evaporations can be performed using ultra pure elements. Unfortunately, as it will be shown in figure 6.1, the evaporation of some hundreds of nanometers (as done within the scope of this thesis) is not enough to prevent projectiles from propagating further into the potentially contaminated backing material. However, the projectiles are at least entering the backing with lower energy. In addition, surface contaminations can also accumulate after evaporation, which is why proper storage is also essential.

It may be noticed here, that the evaporation onto a backing can also have counter intuitive effects, as they are necessarily accompanied by an effective worsening of the target cooling due to the emerging interface between backing and evaporation layer.

All evaporations were conducted using a Leybold High Power Thermal Evaporator LAB500 with kind support of Claudia Neisser and Bernd Scheumann. Depending on the densities of the evaporated materials and the necessary thicknesses, the evaporation layers were applied onto the backing using an aimed areal density. An evaporation layer of 200 nm of gold ($\rho = 19.3 \text{ g/cm}^3$) results for instance in an areal density of $\rho_a = 390 \text{ } \mu\text{g/cm}^2$. The list of evaporated layers is shown in table 3.2.

3.2.3 Sample production for the ${}^2\text{H}(p,\gamma){}^3\text{He}$ campaign

While the production of the targets for the ${}^2\text{H}(p,\gamma){}^3\text{He}$ campaign also relies on group-internal experience [100], further information can be found in literature [102]. A list of irradiated targets for the investigation of the ${}^2\text{H}(p,\gamma){}^3\text{He}$ reaction is shown in table 3.2 and their corresponding photos are shown in figure 3.7. All of these four targets are based on a tantalum backing (27 mm diameter and 220 μm thickness), as well as an evaporation layer consisting of approximately 100 nm titanium (cf. section 3.2.2).

After conducting the cleaning and evaporation procedures, the targets were subsequently deuterated with help of Dr. Oliver Busse (Institute for Inorganic Molecular Chemistry at TU Dresden). They were exposed to a deuterium gas atmosphere (flow rate of 5 l/h D_2 and isotopic purity of 99.99 % at atmospheric pressure) and heated to 350 °C with $\Delta\dot{T} = 5$ K/min. The temperature was kept at 350 °C for 90 min and afterwards carefully cooled down to room temperature again. The aimed uptake should have resulted in TiD_2 targets. However, as shown in section 5.4, the actual areal density was reasonably smaller.

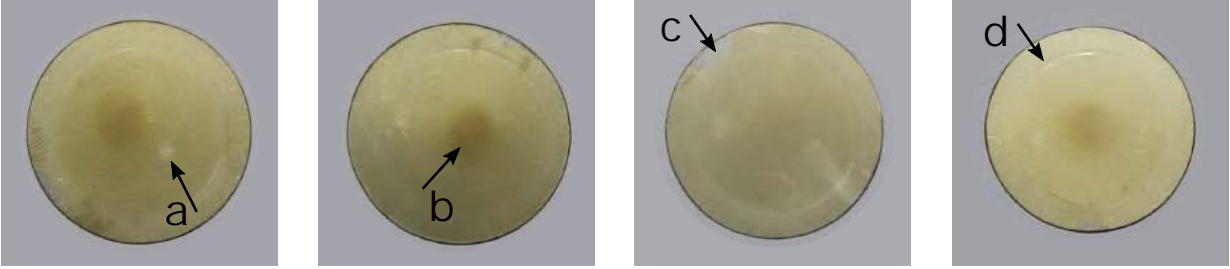


Figure 3.7: Irradiated targets from the investigation of the ${}^2H(p,\gamma){}^3He$ reaction. From left to right, the four photos correspond to TiD_2 -2-1, TiD_2 -2-2, TiD_2 -2-3, and TiD_2 -2-4, respectively (cf. table 3.2). The four arrows show four distinct characteristics of the targets. **a:** Beam spot from ERDA measurement. **b:** Beam spot from main irradiation. **c:** Position of the holder during titanium evaporation. **d:** Marker from the target holder during main irradiation. Only the area within this circle was potentially exposed to the 1H beam (cf. figure 3.2).

3.2.4 Sample production for the ${}^3He(\alpha,\gamma){}^7Be$ campaigns

There are multiple studies on the effectiveness of trapping helium in metals. Among others, the elements tantalum, gold, niobium and zirconium are discussed and evaluated to be promising [101, 103–105]. Within the scope of this thesis, only tantalum ($Z=73$) and (briefly) gold ($Z=79$) will be discussed, due to fact, that two materials were chosen for the subsequent evaporations (cf. table 3.2).

The implantation itself was conducted using the 40 kV ion implanter (Danfysik A/S, Denmark, Model 1050) at the IBC of HZDR. During the implantation, the targets are heated due to the ion beam, and simultaneously cooled with LN2. The effective target temperatures during implantation were approximately $T = -130$ °C.

However, any further elaboration on the actual implantation procedure will be discussed later in the analysis chapters. This is due to the fact, that the target production in case of the ${}^3He(\alpha,\gamma){}^7Be$ campaigns is based on a thorough optimization of the corresponding parameters. These include the optimization of the implantation depth of the helium into the backing (cf. section 6.1.1), the optimization of the areal density ρ_a (cf. section 6.1.2), and the calculation of the necessary implantation fluences F (cf. section 6.1.3), respectively.

3.3 The 3 MV Tandetron at the Ion Beam Center of HZDR

The two experimental campaigns IBC-I and IBC-II (cf. table 3.1) were conducted using the 3 MV Tandetron accelerator of the Ion Beam Center (IBC) at the Helmholtz-Zentrum Dresden-Rossendorf [106]. On the one hand, during these campaigns, the accelerator (cf. figure 3.8) provided a hydrogen beam ($^1\text{H}^+$ with $I_{\text{target}} \sim 3 - 4 \mu\text{A}$ and $^2\text{H}^+$ with $I_{\text{target}} \sim 0.1 \mu\text{A}$) extracted from a Cs sputter ion source ‘Model IONEX 860C’. On the other hand, it also provided a helium beam ($^3\text{He}^{2+}$ with $I_{\text{target}} \sim 10 \text{nA}$ or $^4\text{He}^{2+}$ with $I_{\text{target}} \sim 3 - 4 \mu\text{A}$)¹⁴ extracted from a TORVIS He-ion source with a rubidium charge exchange cell from NEC (see also chapter 2.6.1 for their subsequent calibrations).

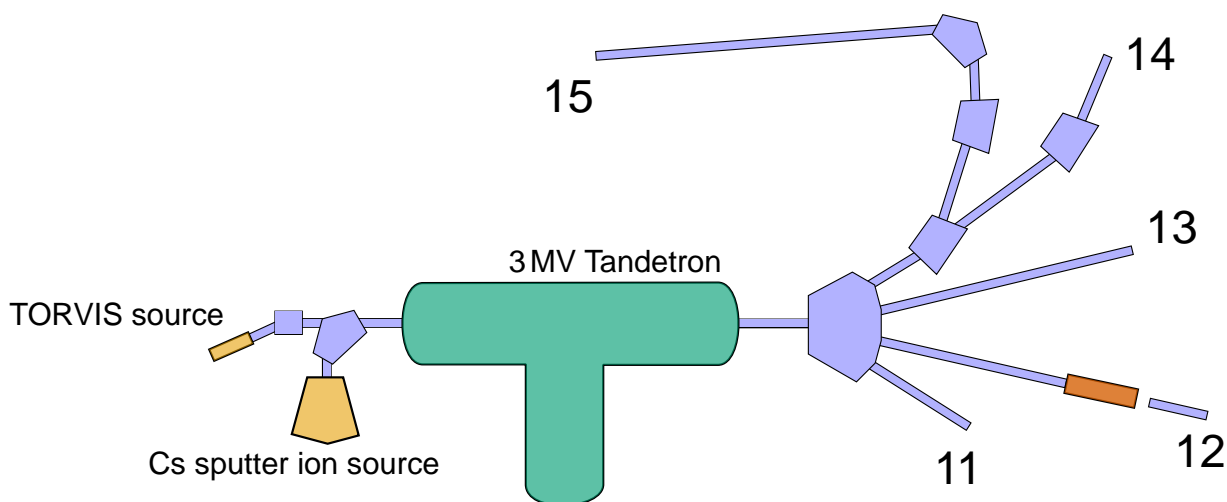


Figure 3.8: Schematic view of the 3 MV Tandetron accelerator (green) at the Ion Beam Center of the Helmholtz-Zentrum Dresden-Rossendorf. The applied ion sources are shown (yellow), as well as the different outgoing beam lines (blue). During the two subsequent campaigns at IBC, beam line 12 was utilized for the experimental setup (orange).

In both campaigns, the beam line towards end station 12 (30° deflection angle) was partially dismantled behind the analyzing magnet and equipped with an own setup and target chamber (orange element in figure 3.8), which will be discussed in the following sections for the IBC-I campaign, and the IBC-II campaign, respectively.

3.3.1 Setup for the $^2\text{H}(p,\gamma)^3\text{He}$ campaign (IBC-I) at the 3 MV Tandetron

The setup for the IBC-I campaign is shown in figure 3.9. The shutter, which still belongs to the IBC beamline (coming from the analyzing magnet) is visible on the left border of the upper left photo. The subsequently following four beam line elements will be discussed in the following section in the correct order of appearance behind the shutter.

¹⁴In case of non-single charged ions, the current is given as electrical current, and i.e. not particle current.

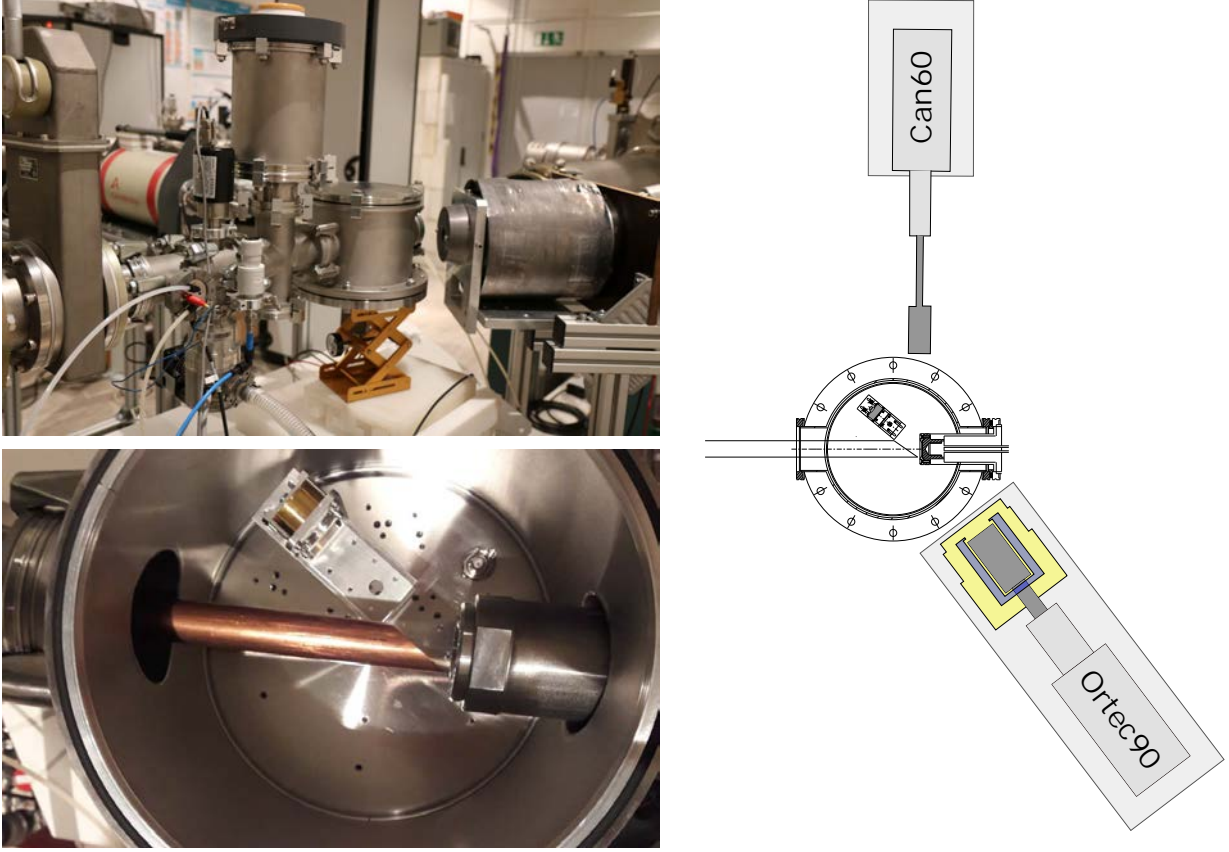


Figure 3.9: Setup of the ${}^2\text{H}(p,\gamma){}^3\text{He}$ campaign (IBC-I) at the IBC. Upper left: The target chamber in the middle is flanged onto beam line 12 (cf. figure 3.8). The two utilized HPGe detectors are visible to the left and the right of the target chamber. Lower left: Top view into the target chamber. The beam enters from the left through the copper pipe. A silicon detector is also mounted within the chamber. Right: Schematic top view of the target chamber, as well as the three detectors.

First element - the collimator: The first element is a centrally positioned circular collimator with a diameter of 5 mm. It is water-cooled, and electrically insulated with the exception of one outgoing cable to process the accumulated charge. The resulting current is read by an Ortec 439 current integrator, which subsequently feeds a CAEN N1145 quad scaler. The current integrator (digital output signal) is also supposed to feed the digitizer of the DAQ (CAEN V1725), which only accepts analog input signals. Both were therefore coupled via an BNC PB-5 Pulse generator. Typical current values on the collimator were $I = 5 - 8 \mu\text{A}$ (not secondary electron suppressed, and therefore actually smaller). Dedicated tests showed, that the collimator took 30-50% of the total intensity while shaping the beam.

Second element - the pumping station: The beam line element behind the collimator is a short ISO K63 pipe with three side flanges. The bottom flange is connected to a 80l/s turbomolecular pump (Turbo-V 81M) and a subsequently attached diaphragm pump (Vacuubrand MD 4 NT) leading to pressures of $[6 \text{ E-}8, 6 \text{ E-}7]$ mbar. These pressures are read out at the top flange with a Varian EYESYS MINI-IMG gauge controller. The side flange is connected to a needle valve, which provides dry nitrogen for venting the target chamber.

Third element - the cold trap: The third beam line element after the shutter is a ISO K63 ‘Cross Equal 4-Way’ with a blind flange at the bottom and the dewar for the cold trap mounted at the top. The structural and functional description of the cold trap, which simultaneously acts as secondary electron suppression, is described in section 3.1.6. The attached copper pipe in the center of the beam line is 12 cm long with an outer diameter of 2.2 cm and an inner diameter of 1.8 cm. The applied voltage on this copper pipe was optimized accordingly prior to the experimental campaign. A suitable voltage of $U = -400$ V was determined and chosen.

Fourth element - the target chamber: A top view into the target chamber is shown in the lower left picture of figure 3.9. The utilized target holder design I is water-cooled and thoroughly discussed in section 3.1.5. The target chamber itself is made of stainless steel and has a cylindrical shape with an inner diameter of 213 mm, a total height of 172.2 mm, and a side-wall thickness of 3 mm. Within the target chamber, there is also a particle detector mounted on a holder (cf. section 3.1.6), which is located under 144.5° with respect to the beam direction.

Positioning of the detectors The list of utilized detectors for this campaign is shown in table 3.6 and their properties are listed in table 3.5. Their respective angles and distances to the target are shown in table 3.7. The angles are given with respect to the beam direction and the distance is stated between the midpoint of the target and the midpoint of the respective end cap of the HPGe.

Table 3.7: List of distances and angles for the utilized HPGe detectors during the IBC-I campaign. The distances, as well as the angles are corresponding to the midpoint on the end cap of each HPGe detector, respectively. The angle is given with respect to the beam direction. The angular uncertainties, i.e. effective opening angles, will be discussed in section 6.2.3.

Name	Distance [cm]	Angle [$^\circ$]
Can60 (HPGe)	12.2	90.0
Ortec90 (HPGe + BGO)	12.6	55.0

Data acquisition The individual processing of six signals is necessary in order to conduct this experiment, namely the current at the target I_{Ta} , the current at the collimator I_{Co} , and the signals of the two HPGe detectors, the BGO detector and the particle detector, respectively.

In order to acquire, process and prepare the data for storage on a hard drive, there are two redundant data acquisition systems. The first one uses an ORTEC 919 multichannel buffer with the MAESTRO software (version 7.01). The second DAQ is a CAEN V1725 digitizer (and V1718 bridge), which is controlled with the software ‘MC2 Analyzer’ (Version 1.0.23.0).

In case of the ORTEC DAQ, the signals of the two HPGe detectors are amplified and shaped using an ORTEC 671 amplifier each. In case of the CAEN DAQ, they are directly fed into the digitizer. Both the signals of the BGO and the particle detector are amplified using a ORTEC 142 preamplifier and subsequently fed into the DAQs (with an additional ORTEC 671 amplifier in case of the particle detector).

3.3.2 Setup for ${}^3\text{He}(\alpha, \gamma){}^7\text{Be}$ campaign (IBC-II) at the 3 MV Tandetron

The setup for the IBC-II campaign is shown in figure 3.10. The entire setup between the shutter of the IBC beam line (cf. upper left photo in figure 3.9) and the target chamber is an exact reproduction with respect to the IBC-I campaign (cf. section 3.3.1). This includes all beam line elements, both pumps, the collimator, the cold trap and the target chamber itself.

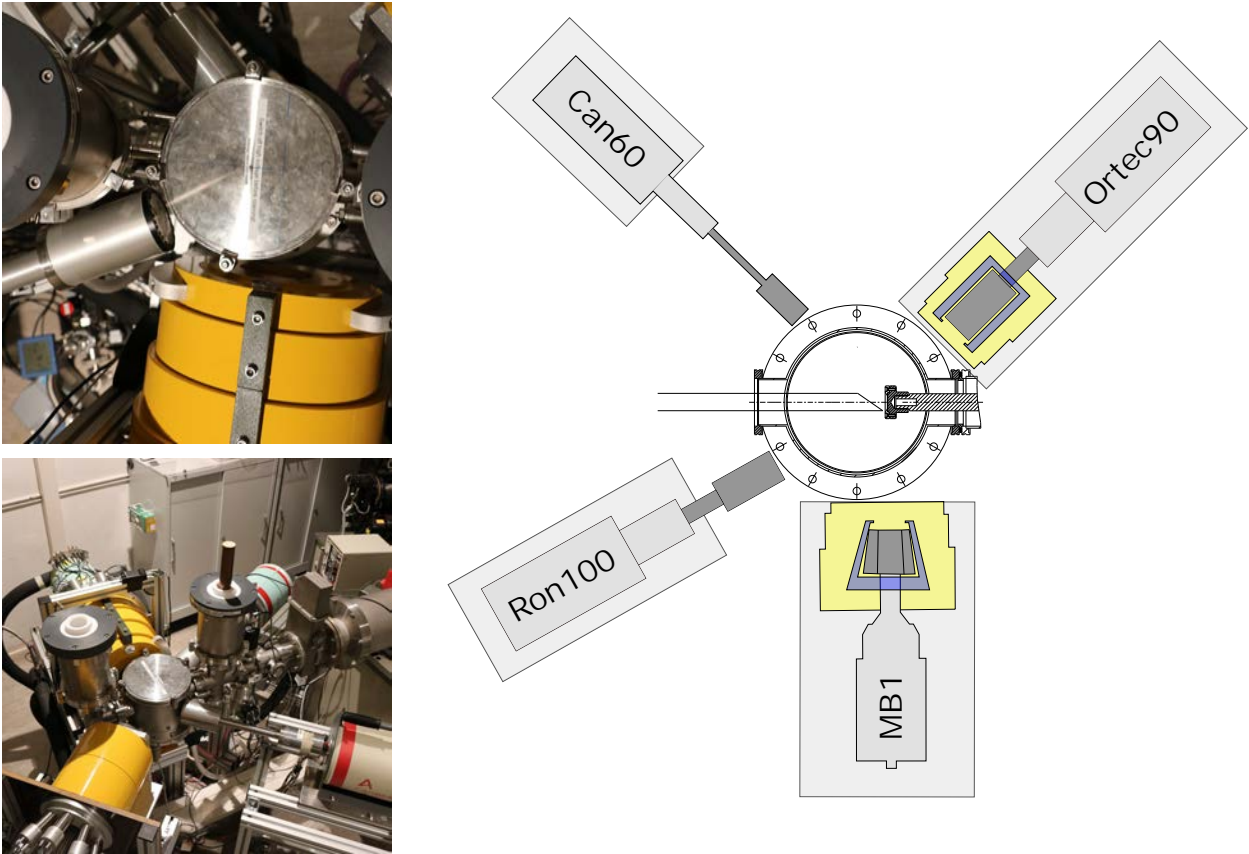


Figure 3.10: Setup of the ${}^3\text{He}(\alpha, \gamma){}^7\text{Be}$ campaign (IBC-II) at the IBC. Top left: Photo (top view) of the target chamber. Bottom left: Photo of the target area. Right: Schematic top view of the target chamber and the positioning of all HPGe detectors. The corresponding angles for Can60, Ortec90, MB1, and Ron100 are $\vartheta = 135^\circ$, $\vartheta = 45^\circ$, $\vartheta = 90^\circ$, and $\vartheta = 153^\circ$, respectively. The HPGes, the BGOs and the surrounding lead are shown in grey, blue and yellow, respectively. See table 3.5 and table 3.6 for details.

The main difference in the setup however concerns the target holder and the detectors. While the IBC-I campaign used a water cooled target (target holder design I, cf. section 3.1.5), the target holder for the IBC-II campaign was redesigned in order to gain the possibility of a LN2 cooling for the target (target holder design II, cf. section 3.1.5).

General information For all irradiations, the vacuum pressures within the beam line are ranging between $[9.1 \text{ E-}8, 1.1 \text{ E-}6]$ mbar. The current on the target is ranging between $[1.5, 4.6] \mu\text{A}$ and the current on the collimator (which is not secondary electron suppressed) is ranging between $[0.9, 3.0] \mu\text{A}$.

Data acquisition A total of eleven individual signals are processed during the IBC-II campaign in order to conduct this experiment. Six of them are related to the HPGe signals (Can60, Ortec90, Ron100, MB1/1, MB1/2, and MB1/3), two are related to the current at the target I_{Ta} , and the current at the collimator I_{Co} , and the remaining three signals are stemming from the two BGO detectors and the particle detector, respectively.

In order to acquire, process and prepare the data for storage on a hard drive, there are again two redundant data acquisition systems. The first one uses an ORTEC 919E multichannel buffer with the MAESTRO software (version 7.01) for Can60, Ortec90, MB1/1 and MB1/2 and an ORTEC 919 multichannel buffer with the MAESTRO software (version 7.01) for MB1/3 and Ron100. The second DAQ is a CAEN V1725 digitizer (and V1718 bridge), which is controlled with the software ‘MC2 Analyzer’ (Version 1.0.23.0). For the CAEN DAQ, all eleven signals are processed.

In case of the ORTEC DAQ, the signals of the six HPGe crystals are amplified and shaped using an ORTEC 671 amplifier each. In case of the CAEN DAQ, they are directly fed into the digitizer. The two signals of the BGOs are amplified using two ORTEC 113 preamplifiers and are subsequently fed into the DAQ. The signal of the particle detector is amplified by a Canberra AFT Research amplifier (Model 2025) before being fed into the CAEN DAQ.

3.4 The Felsenkeller shallow-underground laboratory

The Felsenkeller shallow-underground facility is a new laboratory in close proximity to Dresden (Germany) and consists of both overground and underground structural units. The overground unit is mainly used as office building including the operator desk for the accelerator, server infrastructure and working spaces. The underground unit consists of a system of two tunnels (tunnel VIII and tunnel IX), which are connected both in between, and at their rear (cf. figure 3.11).

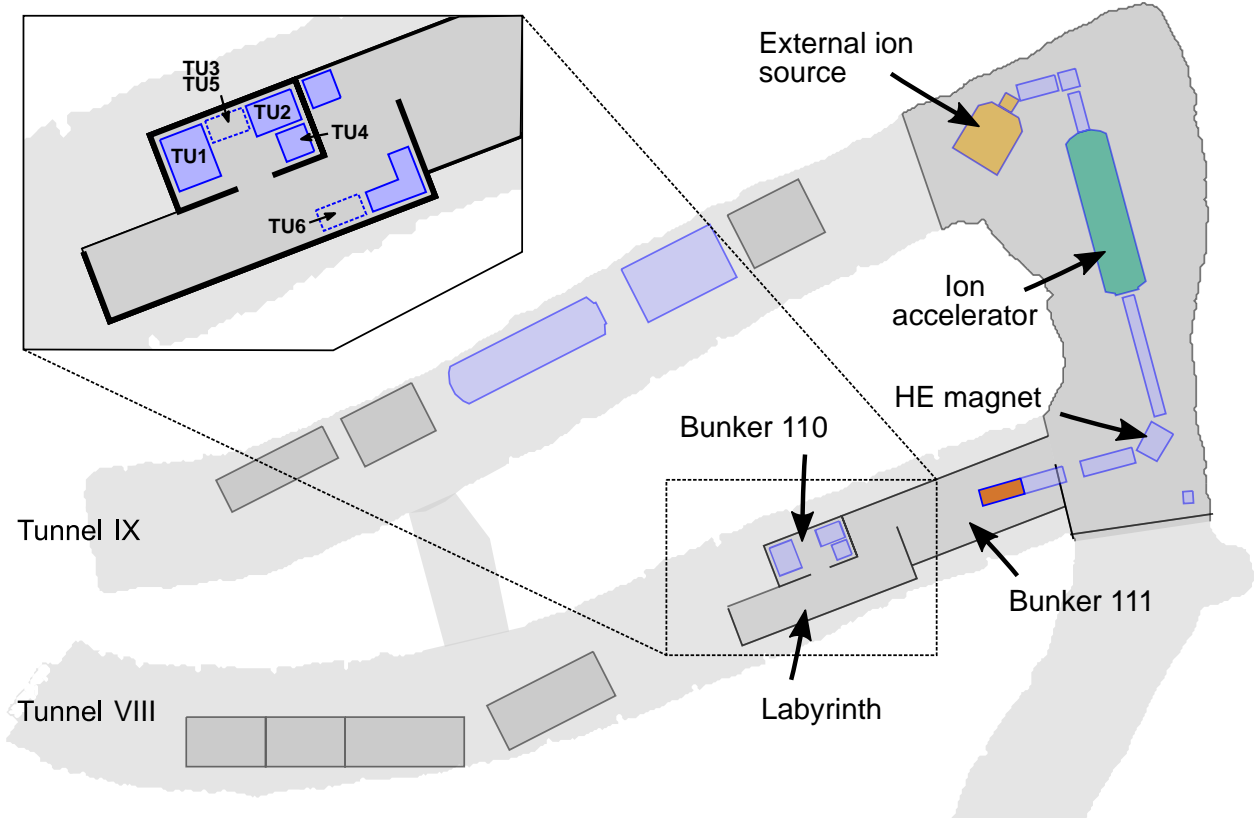


Figure 3.11: Scheme of the tunnel system at the shallow-underground facility Felsenkeller. The rear area is hosting an external ion source (beige), a 5 MV Pelletron accelerator (green), further beam line elements and two counting bunkers (110 and 111). These bunkers are used for offline-counting experiments (e.g. ‘TU1’, see inlet) and in-beam experiments (orange), respectively.

There are three distinct sections within the radiation safety area (dark grey in figure 3.11) at the end of the tunnels. The main area hosts an external cesium sputter ion source of type 134 MC-SNICS (further called ‘external source’) [4, 107] and a 5 MV Pelletron accelerator (15SDH-2) [4], which are both manufactured by NEC. Within the accelerator tank, an additional internal radio frequency ion source (further called ‘internal source’) is mounted on the high-voltage terminal.

The second section concerns bunker 111, which hosts the end of the beam line including the target and the in-beam detectors (cf. figure 3.13). The last section is bunker 110, which is dedicated for low-background detectors. This room will be described separately in section 3.5 with a special focus on the so-called TU1-detector (cf. inlet in figure 3.11).

The in-beam area of the Felsenkeller site is organized as follows: After passing the 90° high energy magnet, the ion beam passes a beam profile monitor (BPM5), a shutter (shutter 4), the LE and HE slits, another beam profile monitor (BPM6), a faraday cup (Cup4), a quadrupole magnet, and another shutter (shutter 5). This last shutter divides the beam line area from the further called ‘target area’. The respective target areas for different campaigns will be later described in the corresponding sections 3.4.2 to 3.4.5.

3.4.1 Development and construction of an extended solid target setup

There are almost 2.5 years of time between the IBC-II campaign and the FK-I campaign (cf. table 3.1). While this time was needed in order to construct, install, and test the entirety of the ion accelerator at Felsenkeller, as well as its beam line, its target area and the utilized detectors, the large time span is also partly affected by the COVID-19 pandemic.

The first successful beam on the target was accomplished on the 3rd July 2019 using the external ion source, which was used throughout in order to investigate its performance, as well as the $^{12}\text{C}(\alpha, \gamma)^{16}\text{O}$ reaction [4, 108]. The first stable successful beam tests on the target using the internal ion source were performed within October 2020. Subsequently, the FK-I campaign was conducted in November 2020.

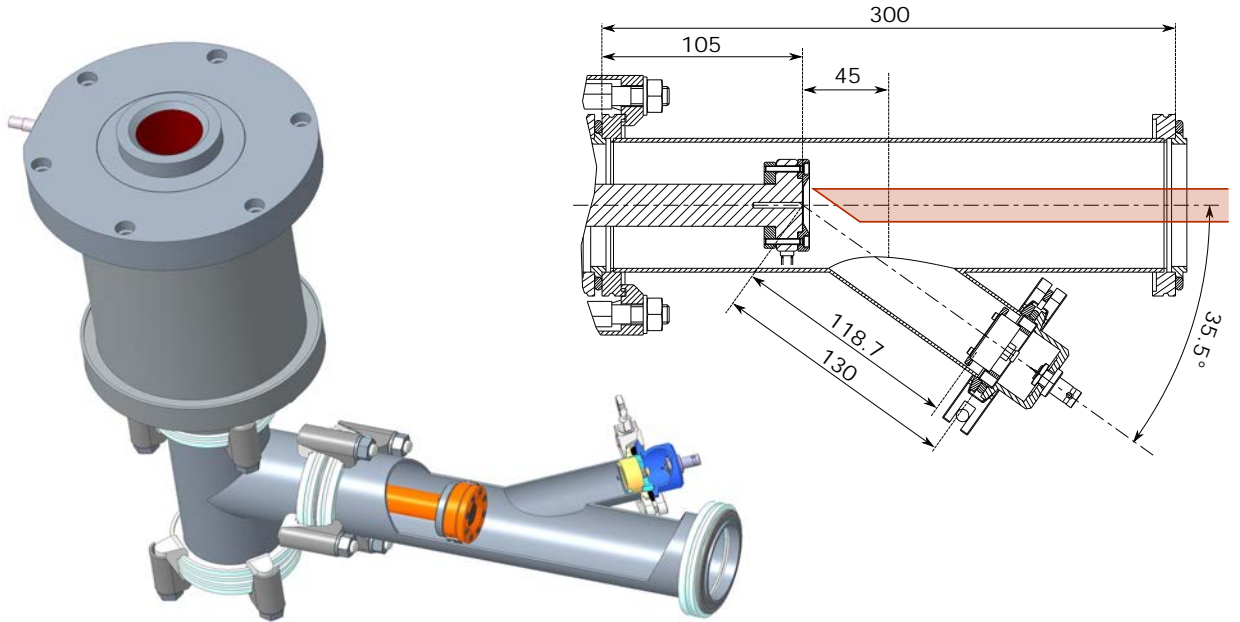


Figure 3.12: Schematic drawings of the new Y-shaped target chamber for the in-beam campaigns at Felsenkeller. Left: 3D view of the Y-shaped target chamber and its attached target holder design II (cf. section 3.1.5). Right: Schematic drawing of the target chamber, the secondary electron suppression entering from the right (orange) and the particle detector installed in the bottom at an angle of 144.5° . Its space was however mainly occupied by the target camera.

As it will be shown in the analyses chapters, the two already discussed setups at the Ion Beam Center of HZDR in general fulfilled their purpose. Nevertheless, the knowledge from these campaigns, as well as the available time until FK-I also gave rise for investigations on possible upgrades based on identified weak spots. Two of the main upgrades prior the campaigns at the Felsenkeller underground laboratory are related to the number of available HPGe detectors (cf. table 3.6) and the design of the target chamber. The maximum amount of utilized crystals at the IBC was six (Can60, Ortec90, Ron100 and three crystals for MB1, respectively). On the other side, the minimal amount of HPGe crystals for the experimental campaigns at Felsenkeller was 21 (Can60, 3x MB1, 3x MB2, 7x EB17 and 7x EB18).

In addition to the significant increase in detection capabilities (and also possibilities of covering different angles), the new target chamber allowed a potentially smaller distance between target and detector. The new target chamber was designed as compact as possible with the simultaneous possibility of mounting a silicon detector within the target chamber. These demands are both met by constructing a target chamber in a Y-shaped design (cf. figure 3.12). Despite the left schematic drawing of figure 3.12 is indicating otherwise, the small K25 pipe was usually pointing downwards, as shown in the right schematic drawing of figure 3.12. In this way, neither the target camera (or the particle detector), nor the KF25 pipe were in line of sight for the HPGe detectors.

The length of this target chamber however is a compromise. On the one hand, the chamber should be long enough in order to enable the HPGe detectors to be positioned without neighboring ISO-K 63 double claw clamps influencing their efficiency. On the other hand, the chamber should be as short as possible in order to minimize the distance between target and cold trap. Considering a given amount of beam induced power on the target, the effective temperature of the target will be lower, the closer its cooling reservoir is. Tests regarding an additional improvement on the heat conductivity (given a certain length of the target holder) will also be elaborated later in section D.3.

3.4.2 Setup for the ${}^3\text{He}(\alpha, \gamma){}^7\text{Be}$ campaigns FK-I and FK-II at Felsenkeller

A large fraction of the entire equipment at the target area remained more or less similar during the subsequent campaigns of FK-I, FK-II, FK-III, and FK-IV. In general, the setup during all these four campaigns consists of the target holder design II (cf. section 3.1.5), which is surrounded by the five HPGe detectors/clusters Can60, MB1, MB2, EB17 and EB18 (cf. section 3.1.4) with each of the five detectors/clusters standing on their own Bosch profile frame. However, there are certainly also differences in these setups due to subsequent upgrades, which were installed over time. The following sections will elaborate the important differences between these setups.

The distance between target and detector, as well as the angles of the detectors with respect to the beam direction are listed in table 3.8. A schematic drawing of the entire setup is shown in figure 3.13, and a more detailed photo is also shown in the appendix D.1.

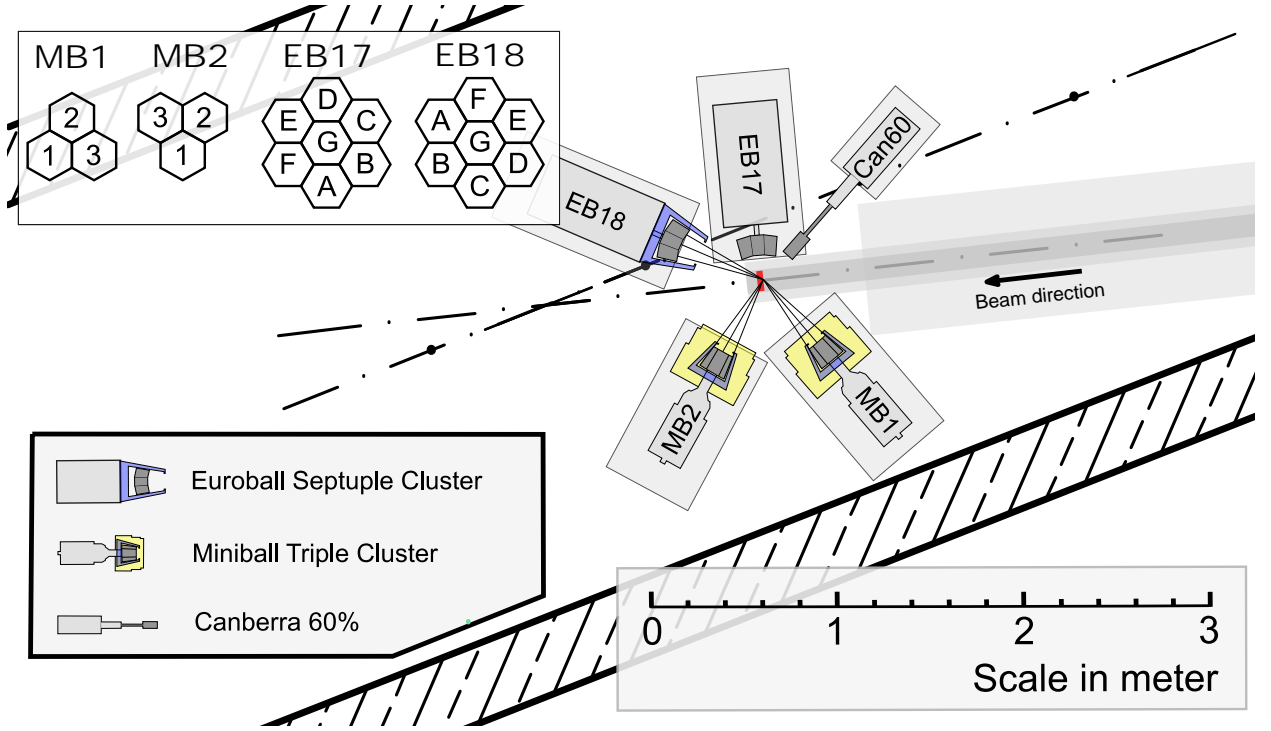


Figure 3.13: Scheme of the target area (bunker 111) at the shallow-underground facility Felsenkeller (cf. figure 3.11) during the first campaigns at Felsenkeller. The ion beam is propagating from right to left and is irradiated onto the target (red). The surrounding HPGe detectors are arranged horizontally around the target. The ordering of the crystals is shown in the upper left panel (view from target to the respective detector). A photo of this setup is shown in the appendix D.1.

Setup of the beam line elements After passing shutter 5, the ion beam enters the so-called target area. This target area consists of a T-shaped Bosch profile pipe (DN 63 ISO-K) with the flange rotated to the top. This flange is attached to the same pumping station (including turbo pump and backing pump), as for the IBC-I and the IBC-II campaign (cf section 3.3.1 and section 3.3.2). The next two parts of the beam line contain the collimator (and the ventilation system), as well as the secondary electron suppression. All of them were also used during the IBC-II campaign, and subsequently introduced in section 3.3.2. A significant difference to the IBC-II campaign concerns the target chamber, which was introduced in section 3.4.1 and was tilted upwards. This Y-shaped target chamber is the center of the target setup and is only followed by the target holder and target cold trap, as also described in section 3.4.1.

Table 3.8: List of distances and angles for the utilized HPGe detectors during the FK-I, FK-II, and FK-III campaign. The distances, as well as the angles are corresponding to the midpoint on the end cap of each detector, respectively. The angle is given with respect to the beam direction.

	Can60	MB1	MB2	EB17	EB18
Distance	19.2 cm	43.6 cm	43.6 cm	11.9 cm	43.6 cm
Angle	139.1°	117.3°	55.1°	90.0°	25.0°

Data acquisition In order to acquire, process and prepare the data for storage on a hard drive a CAEN V1725 digitizer and a V1718 bridge is used. A total of 26 individual signals are necessary in order to conduct this experiment. 21 of them are related to the HPGe signals (1x Can60, 7x EB17, 7xEB18, 3xMB1, and 3x MB2), two are related to the current at the target I_{Ta} , and the current at the collimator I_{Co} , and the remaining three signals are stemming from the three BGO detectors, respectively.

3.4.3 Setup for the ${}^3\text{He}(\alpha, \gamma){}^7\text{Be}$ campaign FK-III at Felsenkeller

The majority of the setup during the FK-III campaign is identical to the one of FK-I and FK-II. However, the turbo pump, as well as the backing pump were both replaced and upgraded. The new turbo pump is a Pfeiffer HiPace 700 with a pumping speed of up to 6851/s (for N_2). The new backing pump is now a diaphragm pump Vacuubrand MV 10 NT.

Holder for the collimator One of the most important upgrades prior to the FK-III campaign concerns the holder for the collimator, which will also be discussed in more detail later in section 6.2.4. As a short summary: During FK-I and FK-II, the collimator was installed, as shown in the left photo of figure 3.14 with the aluminum holder of the copper collimator facing the ion beam. This was done on purpose due to the fact, that this holder is water cooled, while the collimator itself is only sporadically attached to the holder via two screws. The holder was installed this way in order to dissipate the heat more efficiently and prevent the collimator from heating up. This turned out to be suboptimal due to in-beam contaminations during the irradiation of the aluminum. The new upgrade prior to FK-III (cf. right photo of figure 3.14) was replacing this aluminium holder with an identical holder made of copper.

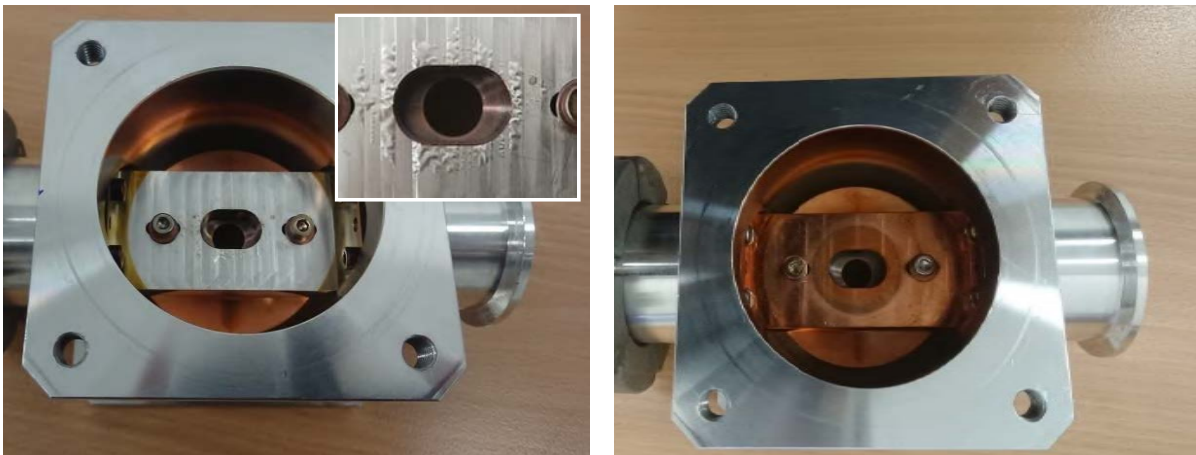


Figure 3.14: Photo of the in-beam collimator (circular element made of copper mounted behind the holder) and its water-cooled holder. Left: The aluminum holder (inner grey module) was irradiated by the beam (see blisters in the inlet), which led to significant problems (cf. section 6.2.4). Right: Upgraded version of the collimator holder, which is made of copper. See text for details regarding directions of installation.

In addition, the new upgrade was installed the other way around, so that mainly the collimator gets irradiated. This is also due to the fact, that the collimator is fixed to its holder using two screws, which are mounted from the side of the holder (cf. figure 3.14). Due to the fact, that it is preferable to use aluminum screws, they were faced away from any direct irradiation of the beam.

Data acquisition In order to acquire, process and prepare the data for storage on a hard drive, in March 2021 a second redundant data acquisition systems was taken into operation. Both systems are based on one CAEN V1725 digitizer and one V1718 bridge each (so-called DAQ1 and DAQ2), with the only difference being their energy calibrations. While DAQ1 has a comparatively good energy resolution (Coarse gain for this digitizer is ‘4x’) and an energy calibration of approximately 1:3.4, DAQ2 has a slightly worse energy resolution (Coarse gain for this digitizer is ‘1x’) and an energy calibration of 1:1. Hence, DAQ1 is used for the main analysis and DAQ2 is used both as backup, and for the investigation of the high energetic part of the spectrum (i.e. above ~ 4.5 MeV).

3.4.4 Setup for the ${}^3\text{He}(\alpha, \gamma){}^7\text{Be}$ campaign FK-IV at Felsenkeller

The majority of the target setup, the detectors, the hardware and the software during the FK-IV campaign is again very similar to the previous campaigns. However, there were two major changes, which are both concerning the detectors.

Detector setup One the one hand, the MB1 detector (along with its BGO) was moved closer to the target. While it was located at the focal point of the three HPGe crystals for the first campaigns at Felsenkeller, it was subsequently moved to a new distance of 40.9 cm in order to increase the absolute full energy peak efficiency. On the other hand, an additional lead castle was implemented around Can60, EB17 and partly EB18 in order to further attenuate the impact of the natural background component. Several photos of this partial lead castle are shown in [109].

3.4.5 Setup for the ${}^3\text{He}(\alpha, \gamma){}^7\text{Be}$ campaign FK-V at Felsenkeller

While most of the beam line elements, the hardware and the software remained similar, the main difference between FK-V and its predecessors concerns the entire setup around the target chamber. One the one hand, a large horizontal platform (approximately 2 m x 2 m) was installed, which substituted all of the Bosch profile frames from the HPGe detectors. This PVC platform is indicated in figure 3.15 as a grey rectangle below the schematic drawings of the utilized detectors. As also shown in this figure, all detectors were rearranged (i.e. also moved closer to the target) with respect to previous campaigns. An additional detector was added (detector Ron100), and one detector was also mounted vertically above the target (detector EB18).

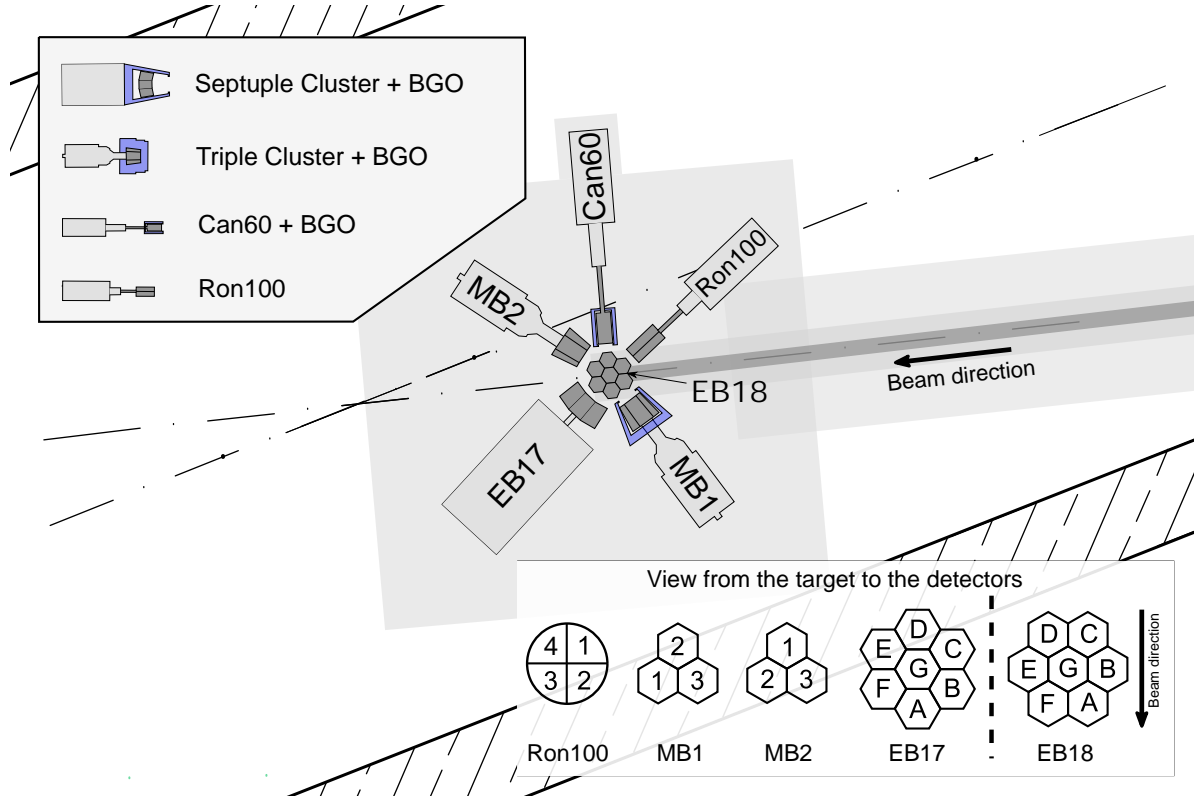


Figure 3.15: Scheme of the target area (bunker 111) at the shallow-underground facility Felsenkeller (cf. figure 3.11) during the FK-V campaign. The ion beam is propagating from right to left and is irradiated onto the target below EB18. While EB18 is mounted vertically, the other surrounding HPGe detectors are arranged horizontally around the target. The ordering of the crystals is shown in the lower right panel (view from target to the respective detector).

In addition, another large PVC platform (approximately 2 m x 2 m) was installed on top of all horizontally positioned HPGe detectors. A photo, as well as a schematic drawing of this ‘sandwich’ setup is shown in figure D.4 within the appendix. The lower platform was installed to arrange all detectors more freely around the target and both platforms were also used to wrap up the entire target area into one large lead castle. The new distances between target and detector, as well as the angles of the detectors with respect to the beam direction are listed in table 3.9.

Another major upgrade concerns the target holder. As shown in table 3.3 and introduced in section 3.1.5, the new target holder was exclusively used in the FK-V campaign and benefits from the reduction of material around the target, which subsequently reduces the attenuation of emitted γ -rays and therefore enhances the absolute full-energy peak efficiencies.

Table 3.9: List of distances and angles for the utilized HPGe detectors during the FK-V campaign. The distances, as well as the angles are corresponding to the midpoint on the end cap of each detector, respectively. The angle is given with respect to the beam direction.

	Can60	MB1	MB2	EB17	EB18	Ron100
Distance	19.0 cm	19.8 cm	18.4 cm	20.1 cm	5.0 cm	15.4 cm
Angle	90°	120°	36°	40°	90°	145°

3.5 The TU bunker at Felsenkeller

The TU bunker (bunker 110) is a 2 m x 4 m large room, which is designed for low-background experiments and rare event physics. It is shielded against cosmic radiation by 45 m of rock overburden (140 m.w.e) and against natural radiation by 40 cm of low-activity concrete. Furthermore, it has fully been characterized regarding its remaining muon, neutron and γ -ray flux components.

The γ -ray flux in the TU bunker is the main reason for the installation of the passive shielding and will be discussed in more detail in section 4.3. However, the surrounding rock is mostly hornblende monzonite [110] and shows contaminations of ^{238}U and ^{232}Th . Their specific activities are determined to be 130(30) Bq/kg and 170(30) Bq/kg, respectively [111]. The concrete shows contaminations of ^{238}U , ^{232}Th , and ^{40}K with specific activities of 17(3) Bq/kg, 18(2) Bq/kg (assuming secular equilibrium), and 280(30) Bq/kg, respectively [2]. The resulting ambient radon concentration will be discussed in chapter 4.2.

The muon flux was studied by Dr. Felix Ludwig regarding its flux density and its angular distribution [108, 112]. The study is based on experimental measurements, their comparison to range-energy calculations, and additional Geant4 simulations. The rock overburden of the laboratory is comparatively flat and ends abruptly with a vertical cliff, which results in a quasi-rectangular profile. By penetrating this particular geometry with a muon flux (which has an angular distribution of a squared cosine function), the resulting muon distribution within bunker 110 has two dedicated maxima. The first one points to the zenith ($\theta = 0^\circ$), and the other one is further tilted towards the cliff (and therefore towards the tunnel entries) with $\theta \approx 55^\circ$ and $\phi \approx 280^\circ$, as zenith and azimuth angles, respectively. These two maxima are confirmed by simulation, calculation, and measurement, which are also in agreement with each other regarding their resulting flux densities. The muon flux density in bunker 110 (angle integrated) is $\varphi = 5.4(4) \text{ m}^{-2}\text{s}^{-1}$, which is equivalent to an effective rock overburden of 140 m.w.e.

The neutron flux was investigated by Dr. Marcel Grieger regarding its flux density and its energy spectrum using ten moderated ^3He neutron counters [111, 113]. Within a broad energy interval of 10^{-9} MeV to 300 MeV, the flux density in bunker 110 was determined to be $0.61(3) \text{ m}^{-2}\text{s}^{-1}$.

3.5.1 The current status of detectors in the TU bunker

This bunker currently hosts three HPGe detectors for low-background γ -ray spectrometry (TU1, TU2 and TU4), as well as two silicon drift detectors (SDD) for low-background X-ray spectrometry (TU3 and TU5). An overview of these detectors is offered in table 3.10. All detectors (and their respective active veto detectors) are operated in list mode using CAEN digitizers (DT series). The data is processed with subsequent computers in the labyrinth (cf. figure 3.11) and is directly stored onto an external server for offline analyses.

Table 3.10: Specifications for the offline counting detectors at the Felsenkeller shallow-underground laboratory (cf. figure 3.11). The names, specifications, relative efficiencies (cf. section 2.4.2), physics purposes and optimal energy ranges (based on own experience) are stated.

Name	Detector	Type	Rel. eff. [%]	Physics purpose	Optimal E range [keV]
TU1	HPGe	Coax, p-type	163	γ -ray spectr.	100 - 2000
TU2	HPGe	Borehole, well-type	53.5	γ -ray spectr.	50 - 1000
TU3	SDD	109 mm ² active area		X-ray spectr.	5 - 30
TU4	HPGe	Coax, n-type	40.7	γ -ray spectr.	100 - 1500
TU5	SDD	170 mm ² active area		X-ray spectr.	5 - 30
TU6	HPGe	Coax, p-type	36.8	γ -ray spectr.	100 - 1500

TU1 detector Due to its importance for the thesis, this detector will be thoroughly described in chapter 3.5.2.

TU2 detector This is a small anode germanium well-type (SAGe Well) detector from Mirion/Canberra [114] in a specialty ultra low background (S-ULB) configuration. The active volume is 218 cm³, the cryostat well depth is 40 mm and the cryostat well diameter is 16 mm (crystal itself has 40 mm and 21 mm, respectively). The relative efficiency is 53.5% and the endcap is made of 1.5 mm very soft, pure aluminum.

TU3 detector This is a SDD from Ketek with the model number M10302 [115]. It is equipped with a silicon drift sensor of 109 mm² active area, and 450 μ m thickness. The collimator has a window of 80 mm² and contains of a multi-layer with different elements (graded down to lower atomic numbers for outer parts) to reduce fluorescence effects in the detector. The entrance window consists of 25 μ m DuraBeryllium and the resolution is stated with 139 eV FWHM at 5.9 keV. The detector itself is mounted at the end of a tube arm, which connects the SDD with its respective Peltier cooling element.

TU4 detector This is an coaxial n-type HPGe detector with vertical mounting on its dewar from Ortec [95]. The model number is GMX-35195-S, and the relative efficiency was determined to be 40.7%. The crystal diameter is 58.7 mm, its length is 71.1 mm and the endcap is made of 2 mm Kryal (aluminum alloy).

TU5 detector This is a SDD from RaySpec with the model number 881-1224A [116]. It is equipped with a silicon drift sensor of 170 mm² active area, and 450 μ m thickness. The collimator has a window of 150 mm² and also contains a multi-layer (see TU3). The entrance window consists of 25 μ m DuraBeryllium and the resolution is stated with 139 eV FWHM at 5.9 keV. The detector is mounted with a 90° angle on top of a 400 mm long tube.

TU6 detector This is a coaxial p-type HPGe from Ortec [95]. The model number is GEM-30195-S, and the relative efficiency was determined to be 36.8%. The crystal diameter is 57.5 mm, its length is 67.4 mm and the endcap is made of 1.27 mm magnesium.

3.5.2 The setup of the TU1 detector

The detector TU1 is a coaxial p-type HPGe detector from Mirion/Canberra (GX 150-250-R) with ultra low background (ULB) standards. The crystal mass is 3.06 kg, the active volume is 574 cm^3 and the resulting efficiency of TU1 is 163% (cf. section 2.4.2), which is on the upper end of commercially available coaxial p-type HPGe detectors regarding size and efficiency.

In order to enable a sensitivity for samples in the order of μBq , a great effort was undertaken in the production process of the detector itself. The cryostat materials fulfill the ultra-low background specifications of the company [114], the end cap of the detector is 1.5 mm of 99.999% pure aluminum (guaranteed uranium and thorium content of less than one part per billion), and the cold platine is additionally shielded from the crystal. During the construction of the detector, the working time above ground was minimized, as well as the transportation time. In order to even further minimize cosmic activation of the detector materials, transportation of the components via airplanes was also avoided.

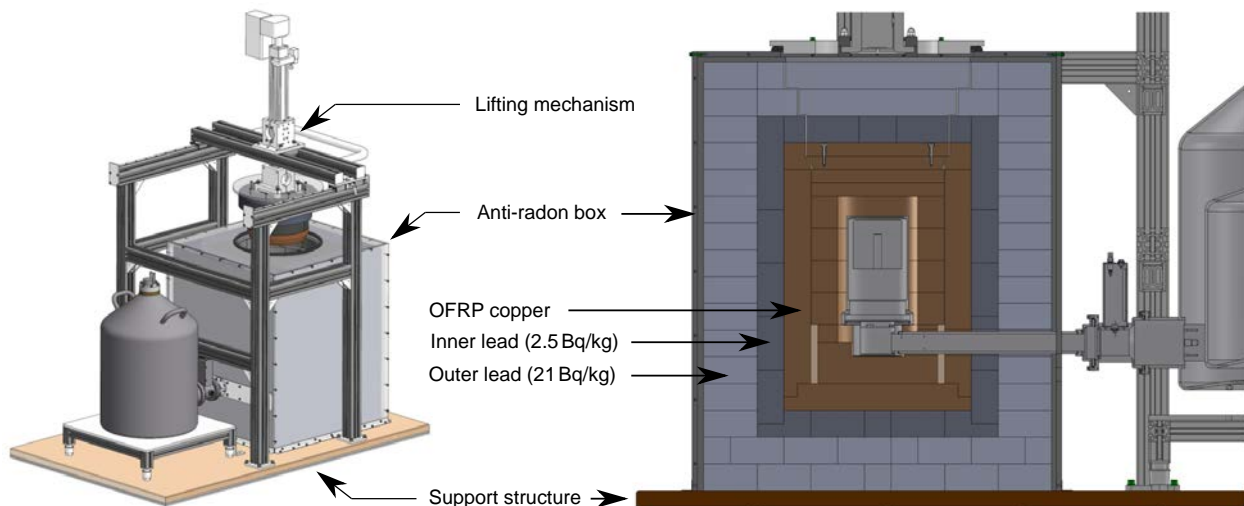


Figure 3.16: Left: Schematic drawing of the TU1 setup. The only missing elements are the five scintillation panels, which are located between the frame of the lifting mechanism, and the anti-radon box. Right: cross-sectional view of TU1, and its passive shielding. The detector elements, and lead bricks are shown in grey, and copper bricks are shown in brown.

3.5.2.1 Passive shielding

The main contribution to the counting rate of an unshielded HPGe detector is γ -radiation from the surrounding infrastructure, walls and other materials. Due to their comparatively long half-lives, the most common origins of natural occurring γ -radiation are radio nuclides of the natural decay chains (i.e. ^{235}U , ^{238}U and ^{232}Th), as well as ^{40}K , which emit photons in a broad energy region of a few keV up to 3 MeV.

Depending on the energy of the photon, and the atomic number of the material, these photons are attenuated, and absorbed via the photoelectric effect, incoherent scattering, and pair production. In general, their total attenuation coefficient is large for high atomic numbers, and for low photon energies (cf. section 2.1).

The most suitable candidate for the shielding of γ -radiation is lead. Every centimeter of lead

attenuates a photon field of 1 MeV to 44.7% of its initial intensity, so after 10 cm only 0.03% remain. Unfortunately, lead can not be provided without an own intrinsic radioactivity. Purification processes of lead are complex with the main problem being its isotope ^{210}Pb . This has a half-life of 22.2 y and has two comparatively short-living daughters, before reaching a stable isotope.

In order to shield the detector against these contaminations, as well as inevitable lead fluorescence X-rays, it is common to add an additional inner shielding of copper. Copper can be purified comparatively easy by separating it chemically from possible contaminations, and it also has no long-living isotopes itself. Nevertheless, regarding its attenuation, copper is not as effective as lead. Every centimeter of copper attenuates a photon field of 1 MeV to 58.9% of its initial intensity, so after 10 cm 0.5% remain.

The passive shielding of TU1 was designed according to the radiation conditions in bunker 110. It is important to notice that the dimensions of the shielding have to be estimated carefully. While the attenuation of photons always gets better for larger passive shieldings with high atomic numbers, an overestimation can also have negative implications. This is due to the fact, that muon cross sections also increase for large atomic numbers. The enlargement of the passive shielding against photons therefore also leads to an enhancement in muon-induced secondary particles (i.e. neutrons, electrons, and photons).

The design of the passive shielding for TU1 is as follows: The innermost layers of the shielding are made of oxygen-free radiopure (OFRP) copper (cf. figure 3.16). There are two subsequent layers of 5 cm each, whereby the inner one is of cylindrical shape, and the outer one is cuboid. This copper is provided by Aurubis and there is no published literature on its nominal contaminations, but only upper limits [117–119].

Surrounding the inner castle of OFRP copper, there is a 5 cm thick layer of ultra-low activity lead. The bricks are provided by ‘Von Gahlen’ with a specific ^{210}Pb activity of $A = 2.50(95)$ Bq/kg (Reference: 04.07.2010). The outermost layer of the passive shielding is made of low-activity lead. It has a thickness of 10 cm, and the bricks are provided by Röhr + Stolberg GmbH with a specific ^{210}Pb activity of $A = 21(2)$ Bq/kg (Reference: 01.01.2015).

The shortest possible way for a photon through the passive shielding is therefore a propagation through 15 cm of lead, and 10 cm of copper. This leads to an attenuation for 1 MeV, and 3 MeV photons of $3 \text{ E-}8$, and $3 \text{ E-}5$, respectively.

3.5.2.2 Anti-radon box

A common element in the passive shielding of underground HPGe setups is an anti-radon box. For standard ambient temperature and pressure (SATP), radon is the only gaseous element within the natural decay chains. While passive copper, and lead shieldings are effective in attenuating γ -radiation from the outside, it usually does not prevent radon gas from entering the shielding and subsequently decay within the inner setup. The radon concentration in

bunker 110 was also determined experimentally and will be discussed in chapter 4.2.

The anti-radon box of TU1 (cf. figure 3.16) is an air-tight casing of acrylic glass, which is installed between the lead castle and the scintillation panels. Its inner volume is continuously flushed with radon-free nitrogen gas, which is obtained from the LN2 dewar of TU1 via a silicon hose. The functionality of this flushing is indicated via a gas bubbler filled with silicon oil.

The nitrogen is guided via the hose into the innermost volume of the passive shielding, and driven by a slight overpressure in the LN2 dewar. The build-up of larger overpressures is prevented by attaching a teflon cap on top of the LN2 dewar, which seals the dewar using only its own weight.

3.5.2.3 Active shielding

The anti-radon box is encased by five individually designed plastic scintillation detectors from Scionix, which act as a veto system for cosmic muons (cf. figure 3.17). Their crystals have a thickness of 50 mm and they all range in height and width between 690 mm to 1000 mm. The active material consists of the scintillator type EJ200 from Eljen technology, which is based on a polyvinyltoluene (PVT) as its scintillating material and so-called fluors (fluorescence emitters) as wave length shifters. The proportion of the fluors is usually approximately 3% with respect to the PVT. When operating a scintillation panel as a veto detector, both a large light attenuation length and a fast timing is important. EJ200 fulfills these requirements, and is highly suitable for the needed purposes with an attenuation length of 380 cm, and a FWHM for their pulses of 2.5 ns [120].

Furthermore, the scintillation panels are coated with 0.2 mm aluminum, 0.5 mm Lexan, and 0.8 mm of vinyl tape. The aluminum acts as a reflector for the photons within the panel. Its reflection coefficient for the resulting emission spectrum is approximately 93%. Furthermore, the Lexan, and the vinyl are needed in order to shield the panels against ambient light, and also acts as an additional support structure.

Along their propagation paths, muons deposit energy within the panels via excitation and ionization (Bethe-Bloch). This process is accompanied by a subsequent de-excitation of the atomic shells, and the emission of photons. Muons, as well as photons and electrons, produce approximately 10000 photons per deposited MeV, and the amount of generated photons is proportional to the energy deposition of the propagating particle. However, it is worthwhile mentioning that neutrons are also able to indirectly produce a signal within a scintillation detector.

Due to the fluors, the emitted photons are shifted to larger wavelengths, which leads to a spectrum with a maximum at 425 nm within the panels. They subsequently propagate within the panel, are reflected and attenuated, and are collected with a photomultiplier (PMT). This photomultiplier tube (type ET9900) is embedded within each panel, is 30 mm in diameter, and 2π sensitive with partial side-wall sensitivity. They are operated with

low-power high-voltage supplies, which are also installed within the panels (cf. figure 3.17).

Due to its comparatively low atomic number, the main interaction process of photons (stemming from natural background sources) with PVT is incoherent scattering. If the main focus of the scintillation detector would be to maximize the peak-to-Compton ratio, scintillation materials with higher atomic number are preferable, e.g. BGO (cf. chapter 2.2.2), where photons are more dominantly interacting via the photo effect. In both cases, the secondary electrons produce the subsequent light signal in the panels, and propagate the energy information of the primary photon.

The interaction of neutrons with the panels strongly depends on their energy. Fast neutrons mainly interact with the panels via elastic scattering. The cross section of this process strongly varies with the atomic number of the material, so i.e. hydrogen nuclei in the panels are highly effective in order to moderate these neutrons. The corresponding recoil (e.g. the hydrogen nucleus) subsequently produces scintillation light. The panels therefore can be used to moderate, but potentially also to detect fast neutrons.

The dominant neutron contributions in the bunker 110 are from thermal neutrons. The total cross section of hydrogen and carbon for thermal neutrons is comparatively low. Regarding the detection and absorption of thermal neutrons, boron (using the $^{10}\text{B}(n,\alpha)^7\text{Li}^*$ reaction which can lead to doppler-broadened peak at 478 keV), as well as lithium (using the $^6\text{Li}(n,t)^4\text{He}$ reaction) can be used as additional components in scintillation detectors [78].

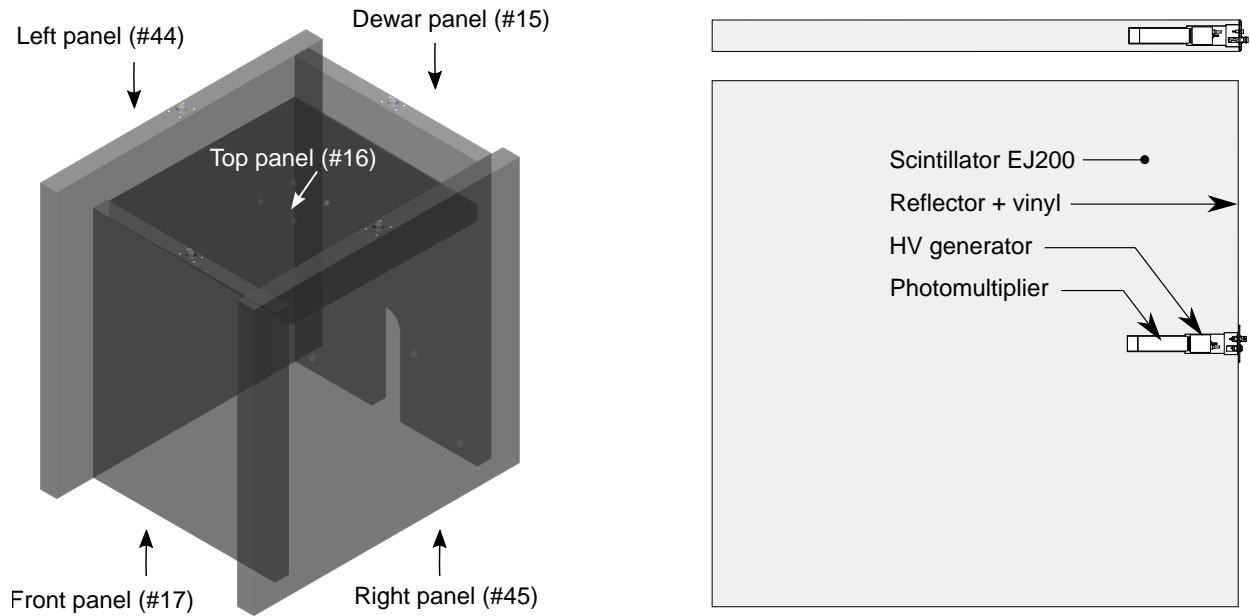


Figure 3.17: Left: Schematic drawing of the five scintillation panels, which surround the passive shielding of TU1. Right: Top view and side view of one panel, respectively. The scintillation material is shown in grey, and the non-active volumes are shown in white.

3.5.2.4 Hardware and data acquisition

While part of the optimization process for the data acquisition will be described in section 4.1, this section is dedicated to discuss the final setup of TU1 with both its supply components and its data acquisition components.

HV supply and bias shutdown The necessary high voltage for the HPGe crystal of $U = +3500\text{ V}$ is provided by an ‘Ortec 660 Dual 5 kV Bias Supply’. This module has the advantage of being able to provide a (when activated) permanent HV shutdown for both possible emergency cases for HPGe detectors, which are a power outage, and a non-sufficient temperature of the crystal. In both cases, the HV should remain turned off until further manual investigation, even if the temperature is sufficient again or the power recurs again. As a Canberra detector, TU1 uses TTL logic. While TTL is actually based on changes in the corresponding impedances, it is proven to be convenient to interpret the logic as ‘low’ in case of $U = 0 - 0.8\text{ V}$ and ‘high’ in case of $U > 2\text{ V}$. It therefore also turned out to be convenient to solely rely on changes in the voltage, instead of changes in the impedance. Usually, the signal in the bias shutdown (BSD) works properly with $U_{\text{low}} = 0\text{ V}$ and $U_{\text{high}} = 5\text{ V}$.

The untypical characteristic of TU1 is, that in its cold status, the BSD signal is at $U = 20\text{ mV}$, which is either the result of a previous manipulation, or a defect on the preamplifier platine. This only could have been investigated by warming the detector up to have a look at the BSD signal in a warm condition. Either it would jump to $U = 0\text{ V}$ (which would indicate a problem with the hardware) or it would jump to another (currently unpredictable) discrete value (e.g. $+5\text{ V}$ or -12 V), which then could be used as an indicator for sufficient temperature. Nevertheless, this test was not an option within the scope of this work, and remains an important task during a possible maintenance of TU1¹⁵.

Due to the fact, that the BSD is not properly set for TTL standards, and therefore can’t be used in case of temperature problems with TU1, the BSD cable is not connected at all (also in order to minimize cross-talk and noise, cf. section 4.1). Since in case of power outages, the Ortec 660 turns off anyway until manual reactivation, this BSD cable would currently not fulfill any purpose.

The current safety situation is therefore the following: The TU1 detector is automatically protected against automatic HV ramp up after power failure due to the Ortec 660. It is currently not automatically protected against an applied high voltage in case of a not sufficient cooling, which can e.g. lead to hazardous leaking currents, and a subsequent destruction of the hardware. This needs to be avoided. The cooling of the detector can become insufficient due to two scenarios: Either the dewar is not filled properly (usually done once a week), or the vacuum becomes insufficient over time. This would lead to an increased consumption of

¹⁵Even if the BSD of TU1 would be either repaired or understood under warm conditions, it is not possible with Canberra detectors to distinguish between an ‘open’ BSD cable and a ‘cold’ detector. Furthermore, the BSD error at the Ortec 660 can be canceled without further notice, even if the BSD signal would provide a faulty voltage. This is a big disadvantage with respect to e.g. Ortec detectors.

LN2, and remains the largest danger for the long term operation of TU1. This threat can be checked frequently by an inspection of any signs of possible condensation at the cooling finger, as well as by monitoring the weekly consumption of LN2.

Operating voltage supplies The operating voltage for the warm preamplifier of TU1 is provided by the rear port of a NIM-based D-Sub (DE-9) distribution module. The voltages for the five scintillation panels (which each have an intrinsic HV supply) is provided by the respective front outputs of the same module.

Data acquisition hardware Both energy outputs for the warm preamplifier of TU1, as well as the five signal outputs for the scintillation panels are connected to coaxial BNC cables, which forward the signal via additional BNC-to-MCX adapters to the digitizer. The digitizer is a stand-alone digitizer from CAEN (module DT5725S), which provides eight input channels with 14 bit at 250 MS/s (cf. table 3.11 for channel assignment). Furthermore, it is used with its PHA-firmware (DPP-PHA 4.22_139.130).

Table 3.11: Channel assignment between the signals and the digitizer channels for the TU1 setup. In channel 0, the TU1 signals of negative polarity are analyzed, and in channel 7, the signals of positive polarity are analyzed (cf. section 4.1).

Chan. 0	Chan. 1	Chan. 2	Chan. 3	Chan. 4	Chan. 5	Chan. 6	Chan. 7
TU1(-)	–	Sz15	Sz16	Sz17	Sz44	Sz45	TU1(+)

Data acquisition software While the data acquisition of the raw signals is done by the CAEN digitizer, the entire analysis (coincidences, veto, noise canceling etc.) is performed offline. Therefore the data is stored in list mode on a hard drive, which also saves the corresponding time stamp, and possible flags for each single event. The processing of this data was already discussed in section 2.3 and the resulting pulse height spectra, as well as the general treatment and specifications of the ingoing analog signals will be elaborated in separate sections within the analysis chapter of the TU1 detector (cf. chapter 4).

4 Development of an ultra-low background γ -ray spectrometer at Felsenkeller

The Felsenkeller shallow-underground laboratory is a rather new facility mainly for the investigation of nuclear astrophysics and the physics of rare events. A new ultra-low background γ -ray spectrometer, further called TU1 (cf. section 3.4), covers both of these goals and therefore acts as a crucial element of the Felsenkeller laboratory. While the infrastructure for bunker 110 and the detector TU1 were already introduced in section 3.5 and section 3.5.2, the following sections are focusing on several peculiarities of the detection setup, as well as the implementation and the impact of the passive and active shieldings.

This chapter is therefore structured as follows: Before discussing first pulse height spectra, the signal of the TU1 detector will be elaborated in section 4.1 along with its characteristics and anomalies. Section 4.2 will then focus on the radon concentration at Felsenkeller with an emphasize on the radon concentration in the hosting bunker of the TU1 detector. After this general introduction, the resulting spectra and the passively shielded detector will be discussed in section 4.3. However, one of the main features of the TU1 detector concerns the five scintillation panels, which act as an additional active veto. Dedicated measurements with these panels will be described in section 4.4 and the veto will be optimized in section 4.5. While the benefits of this veto are vastly dominating, its impact on full energy peaks nevertheless needs to be discussed thoroughly, which will be done in section 4.6 in addition to the deadtime of TU1. After discussing all these implications of the passive and active shielding, the last four sections will deal with the design of an appropriate target holder, the comparison to other underground HPGe setups, the sensitivity of the TU1 detector and possible further improvements in section 4.7 to 4.10, respectively.

Introductory remark: A paper on this detection setup has been peer-reviewed and published in *Astroparticle Physics* in 2023 [2]. This publication is mainly providing an introducing regarding the setup and the main results of the passive and active shieldings, respectively. However, some results will unavoidably be restated throughout this chapter. Nevertheless, the following section is aimed to limit duplications and it is also dedicated to a much more profound and more detailed summary on the diversity of this setup.

The design of the passive shielding for TU1 is also partly based on the work of Dr. Alexander Domula. Previous, yet entirely independent work on this setup can therefore also be found in a dedicated Staatsexamensarbeit by Benjamin Ullrich [121].

4.1 Characteristics and anomalies in the signal of TU1

Before discussing the resulting pulse height spectra of TU1 in more detail, this section will give an introduction into the preamplified signals themselves. This introduction spans a wide range from the signal optimization and its processing up to uncommon characteristics of the TU1 setup. Their phenomenology, the approaches of treatment, and their impact on the data acquisition will be described in the following section.

4.1.1 Noise level in the preamplified signal

The material and the thickness of the endcap for TU1 are chosen specifically to enable measurements down to comparatively low energies. The transmission probability T for 20 keV photons through the end cap of TU1 is $T \approx 25\%$. Despite its physical possibility of detecting 20 keV photons, these signals however also need to be propagated to the digitizer without being attenuated or superimposed by the noise of the baseline.

While an analog DAQ usually properly filters noise signals, they may nonetheless influence the measurement and have to be treated with caution. The most important handling of noise and oscillations effects is therefore to eliminate and attenuate them before they even enter the data acquisition, in order to not disturb later measurements.

In addition to the introduction of electronic noise in HPGe detectors (cf. section 2.4.4), other possible origins of noise include e.g. ground loops due to the connection of hardware to the same power supply. Furthermore, noise can also be generated by the HV, which will then be amplified by the preamplifier. In addition, the utilized electronic crates and modules, the length and the shielding of the signal cables, as well as the quality of all cabling adapters are additional important factors to consider. However, the origins of noise and oscillations have been located carefully in order to attenuate them below the threshold of possible physical signals. A full-energy deposition of a photon with $E = 22$ keV in TU1 leads to a preamplified pulse height of approximately 6 mV. The remaining background noise of the preamplified signal is 0.6 mV (root mean square), and 2.4 mVpp (95 % CL).

The resulting pulse height spectrum in the low-energetic region after eliminating noise and oscillations is shown in figure 4.1. In order to demonstrate the sensitivity of TU1 at low energies, a ^{133}Ba source was placed on the end cap of TU1. This source emits X-rays at $E \approx 31$ keV and $E \approx 35$ keV as its $K_{\alpha_{1,2}}$ - and K_{β_1} -lines, respectively, which are clearly visible in the spectrum.

4.1.2 Remaining noise of unknown origin

One of the remaining noise signals of the TU1 detector are temporary oscillations, which occur approximately in the order of once every 1000 s with $N = \mathcal{O}(100)$ subsequent triggered events. Most of these oscillations are flagged as pile-up events due to their short wave length in the order of microseconds. The total time of these disturbances is therefore less than

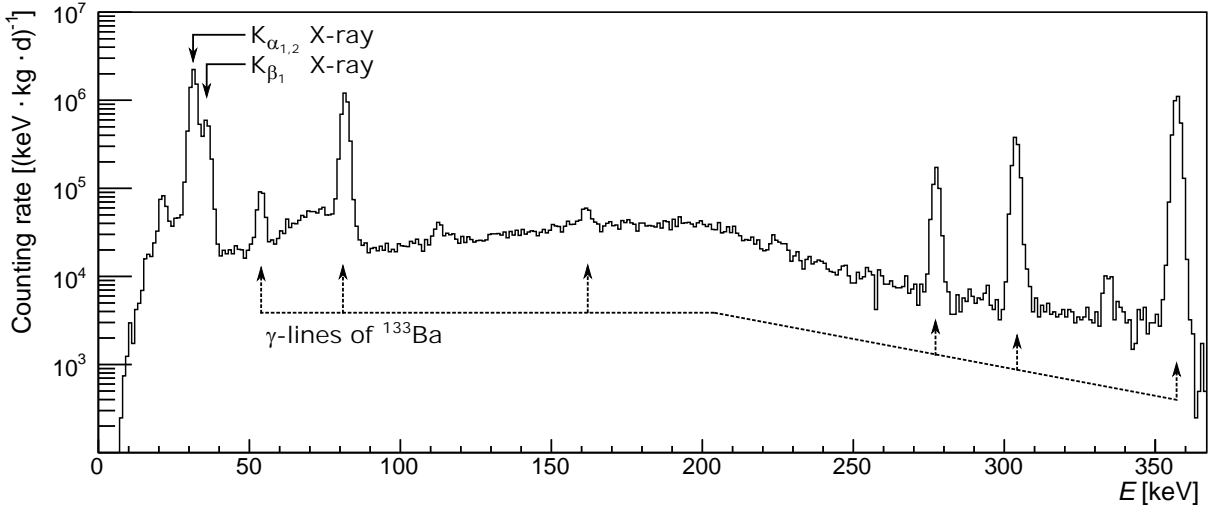


Figure 4.1: Rebinned pulse height spectrum of a ^{133}Ba source, which is positioned on the end cap of TU1. The result of the efficient noise reduction is emphasized by the evaluable X-rays of ^{133}Ba at $E = 31$ keV and $E = 35$ keV, respectively.

$t = 1$ ms. When treated properly, their impact on the actual dead time is comparatively negligible (cf. section 4.6).

Approximately once every hour, an oscillation occurs (also $N = \mathcal{O}(100)$ subsequent triggered events), which is not flagged as pileup due to the fact that its wavelength is in the order of $10\ \mu\text{s}$. The total time of this disturbance is approximately $t = 1$ ms, so their impact on the dead time is also comparatively negligible when treated correctly. By solely excluding events flagged as pile-up, these oscillations would be included in the pulse height spectrum. Nevertheless, the vast majority of these events deposit ‘energies’ with $E \leq 20$ keV¹⁶.

Oscillation events, which are neither flagged as pile-up, nor below $E \leq 20$ keV only occur approximately twice every week. As well as the previously discussed oscillations, they also lead to roughly $N = \mathcal{O}(100)$ subsequent events within the spectrum. These rare noise signals and oscillation events are also treated accordingly, which will be discussed in section 4.5.3.

4.1.3 Remaining noise due to LN2 filling of the dewar

The second reason for potentially remaining noise is dedicated to the filling procedure of liquid nitrogen into the dewar of TU1. This needs to be done once a week and has been found to result in strong disturbances on the baseline and hence in the signal processing. While typical noise and oscillation events slightly increase the rate and can be treated accordingly, the filling of the dewar leads to a temporary dead time of 100% and a subsequent drop in the count rate to $0\ \text{s}^{-1}$. In order to circumvent these effects, the DAQ is stopped once a week during the filling procedure (≈ 10 min), and only started again one hour after filling.

¹⁶The ‘energy’ of a triggered oscillation event is certainly not related to a physical energy deposition, but only an association based on their effective signal height.

4.1.4 Non-linearity in the energy calibration

The whole signal processing chain in HPGe detectors from energy deposition in the crystal to the signal input into the respective digitizer is optimized to result in an energy calibration, which is highly linear. Nevertheless, the energy calibration of TU1 shows a noteworthy non-linearity at comparatively high energies, which is independent of the geometry of the source and its distance to the detector (and hence independent of the count rate and possible related artifacts).

As shown in the upper panel of figure 4.2, the energy calibration of TU1 seems to result in a typical correlation between channel position of a peak and its theoretical energy, which should be properly described by a first order polynomial fit (cf. section 2.4.1). These data points (blue) were acquired by measuring a comparatively large rock sample containing the natural decay chains. While the γ -ray line at $E = 2615$ keV of ^{208}Tl is typically the highest energetic point available in a rock sample, its proximity to the detector led to well-pronounced summation lines, which enable an energy calibration to almost 3400 keV.

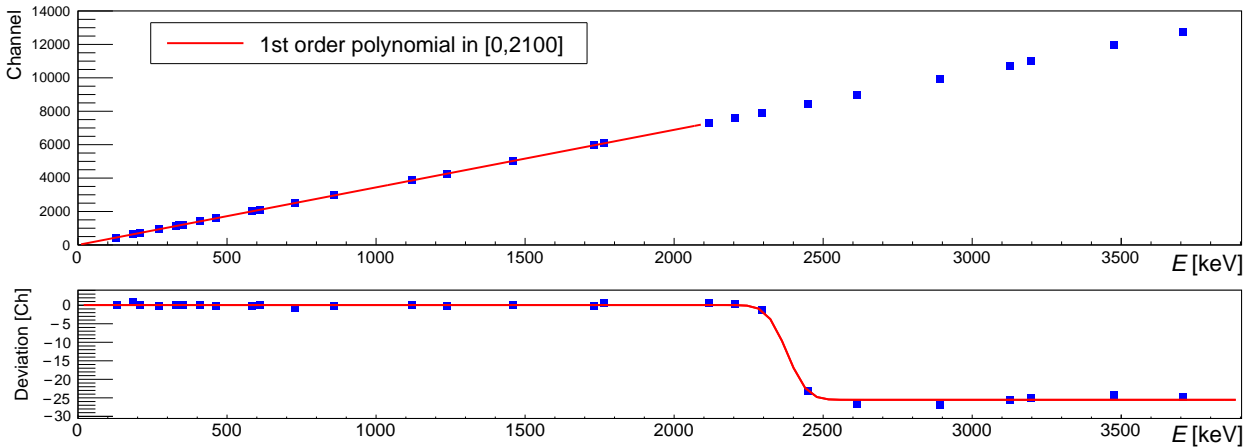


Figure 4.2: Non-linearity in the energy calibration of TU1. Top: Relation between channel position for the peaks in a measurement of an environmental rock sample on TU1, and their correlating energy. The first order polynomial fit (red) only considers the data points in the interval [0 keV, 2100 keV], where a proportionality is fulfilled. Bottom: Deviation between the channel positions for all peaks, and their residual position with respect to the upper fit. The correlation is fitted with a complementary error function including an offset (red). Uncertainties from the determination of the peak positions are included, but not visible.

The lower panel of figure 4.2 shows the deviation between the fit, and the data points. While the linearity seems to be fulfilled between $E = 0$ keV and $E = 2200$ keV, there is an increasing deviation around $E = 2380$ keV, which results in an offset of approximately 25 channels (≈ 7 keV) between expected peak position and actual peak position.

As shown in figure 4.3, this deviation can be effectively corrected by adding a step function to the 1st order polynomial fit. The upper panel shows the fit function over the whole energy region, and the lower panel shows the analog result of the deviation between expected peak position and actual peak position for the adjusted fit function.

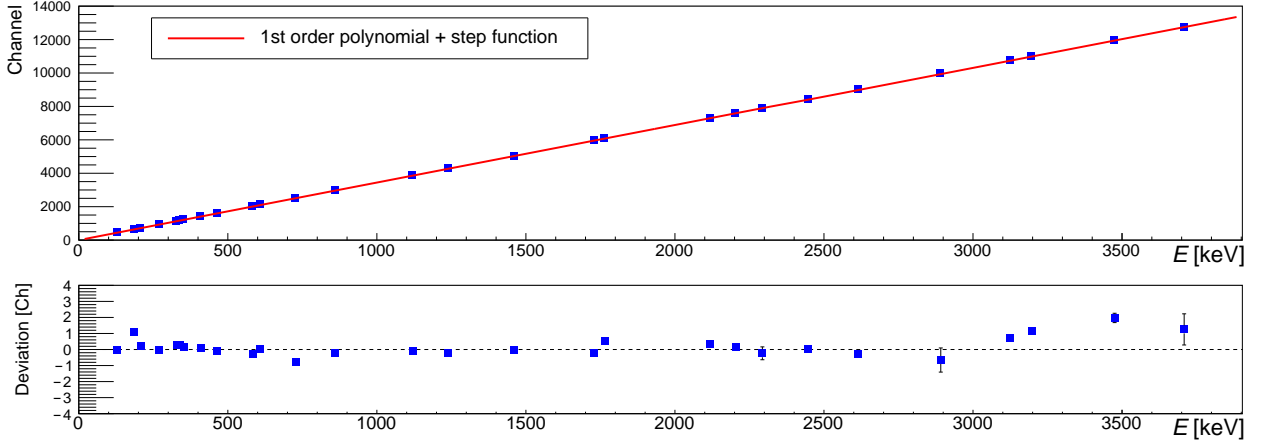


Figure 4.3: Top: Corrected energy calibration using a 1st order polynomial fit with an additional step function. Bottom: The deviation between the channel positions for all peaks, and their theoretical channel position with respect to the upper fit.

Despite a few outliers, most of the peak positions can be described within a deviation of ± 1 channel, which corresponds to 0.3 keV. The remaining four outliers can be well described within ± 2 channels, which corresponds to 0.6 keV.

It is worthwhile mentioning, that the partially large deviation in the residuum of up to 0.6 keV can also be enhanced due to imperfections in the peak energy determination, which are not accounted for in the uncertainty (e.g. asymmetric peaks due to charge carrier loss effects resulting in left tailings, summation with low-energy X-rays resulting in right tailings, field increment effects in the crystal etc.). Furthermore, the tendency of increased deviations for high energetic data points in the residuum can also be a result of poor statistics for these data points since most of them are comparatively small summation lines.

The resulting energy calibration for this specific sample in this specific geometry is shown in equation 34 with $\operatorname{erfc}(x)$ being a complementary error function.

$$E[\text{keV}] = -27.04 + 3.444 \cdot \text{Ch} + 13.31 \cdot \operatorname{erfc}\left(\frac{\text{Ch} - 2383.31}{7.86}\right) \quad (34)$$

The comparatively large offset of $p_0 = -27.04$ in equation 34 is due to the step function, which has a height of $p_2 = 26.62$ channels. Furthermore, it may be noticed, that this energy calibration also shows satisfactory results of similar deviations on a long term scale, and also by using sources of different geometry.

4.1.5 Occurrence of signals with the opposite (positive) polarity

The preamplified signals, which are used for later measurements, are all showing a negative polarity (cf. figure 4.4). A unique characteristic of the TU1 detector (i.e. with respect to the other ≈ 25 HPGe crystals, which are currently in operation within the Felsenkeller laboratory) are randomly appearing additional signals with opposite (positive) polarity. Two

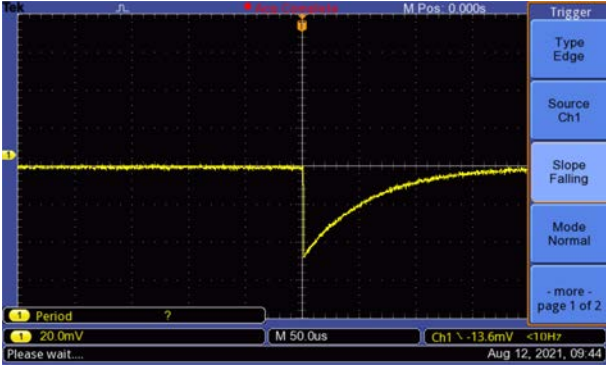


Figure 4.4: Snapshot of a typical signal behind the preamplifier of TU1. The pulse shows the expected polarity (negative) for physical events. The entire screen extends to $\Delta U = 160$ mV and $\Delta t = 450$ μ s.

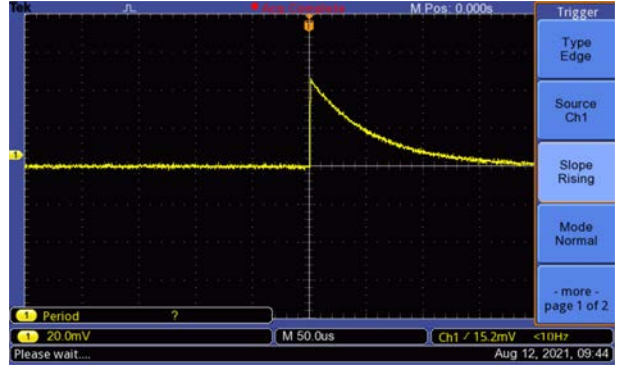


Figure 4.5: Snapshot of a typical signal behind the preamplifier of TU1. The pulse shows the opposite polarity (positive) with respect to the expected physical events. The entire screen extends to $\Delta U = 160$ mV and $\Delta t = 450$ μ s.

exemplary analog pulses for both the signals of the common polarity (negative), as well as signals of the unexpected polarity (positive) are shown in the figures 4.4 and 4.5, respectively. The shapes of these signals for both polarities are comparable regarding all important characteristics (rise time, amplitude and decay time).

The rate of these positive signals is approximately 10 s^{-1} and independent of the total rate of signals in TU1. Due to the fact that this effect is rather untypical and more importantly the origin for the majority of baseline distortions during background measurements of TU1, this effect also needs to be discussed in detail.

The distribution of resulting pulse heights seems continuous and the resulting spectral shape is comparable to a Landau distribution ($\text{MPV} = 56.25(2)$, $\sigma = 16.08(1)$ - using an ‘energy’ calibration, which is applied from the physical spectrum with the ordinary polarity). In order to investigate both polarities simultaneously, both signal outputs at the preamplifier of TU1 are used. One signal is fed into channel 0 of the digitizer and focuses on the analysis of the negative pulses, and the other signal is fed into channel 6 of the digitizer and focuses on the analysis of positive pulses (cf. chapter 3.5.2.4). Therefore, the correlation of pulses with different polarities can be investigated, which will be discussed in the following section.

Correlation between signals of positive polarity The rate of these untypical, positive signals is approximately 10 s^{-1} and their occurrence does not follow a specific pattern in time. This is supported by the time difference between two subsequent signals of positive polarity, which follows an exponential function, as expected from randomly distributed signals.

Correlation between signals of opposite polarity (both above a threshold energy)

The investigation of correlations between signals of opposite polarities is significantly more complex. This is due to the fact, that there is also an additional artificial correlation, which is certainly not the root of the problem, but subsequently generated during the processing

in the DAQ. This pseudo-correlation will be discussed separately in the next paragraph.

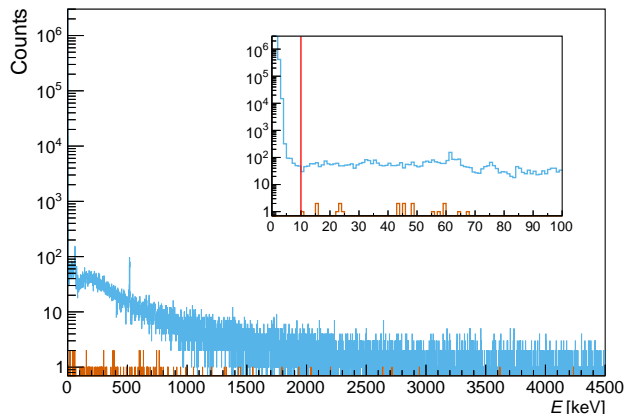


Figure 4.6: Pulse height spectrum of all signals with negative polarity in TU1 (blue). The orange histogram shows all events above $E \geq 10$ keV, which are coincident to any signal of positive polarity (cf. figure 4.7) with a corresponding pulse height also being above $\text{Ch} \geq 10$ (red vertical line in the inlay, which highlights again the low energetic part).

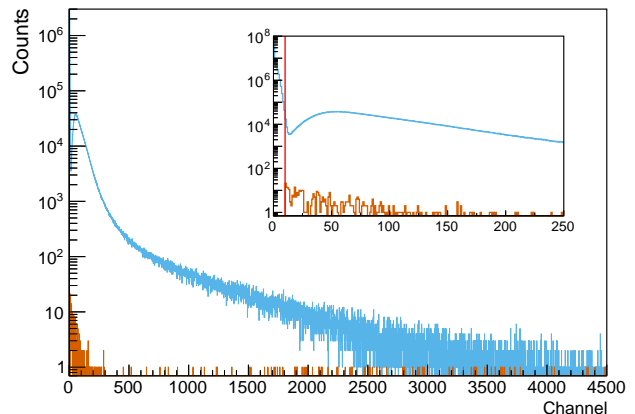


Figure 4.7: Pulse height spectrum of signals with positive polarity in TU1 (blue). The orange histogram shows all events above $\text{Ch} \geq 10$, which are coincident to any signal with negative polarity (cf. figure 4.6) with $E \geq 10$ keV (red vertical line in the inlays). The ‘channels’ are calibrated with the same calibration than its counterpart¹⁷.

However, this paragraph is solely dedicated to the investigation of real coincidences, where both events could potentially share the same origin and deposit at least a threshold energy above $E = 10$ keV within both polarity directions. The coincidence spectra for this investigation are shown in figure 4.6 and figure 4.7 for the negative and the positive polarity, respectively. In both figures, the blue histogram shows the respective raw data, which is plotted as a comparison for the subsequent ratio of coincident signals. Each orange event in both spectra indicates a coincidence between the signal with its respective polarity (left for negative and right for positive) and another signal of opposite polarity within an applied coincidence timing window of $\Delta t = \pm 1000 \mu\text{s}$, respectively. This coincidence condition is however only fulfilled, if both pulses are above a threshold of $E = 10$ keV.

Within both spectra there are no obvious structures of coincidences, but they are entirely comparable to the expected outcome of random coincidences. The corresponding timing plots further support this hypothesis. It is worthwhile mentioning, that the timing window was deliberately chosen to be so large in order to investigate also possible strongly delayed coincidences between pulses of opposite polarity. In addition, any typical coincidence timing window ($\Delta t \approx \pm 2 \mu\text{s}$) would have resulted in entirely empty coincidence pulse height spectra. In summary, there are no systematic physical correlations between events of opposite polarities within typical (and even extended) timing windows of usual coincidences.

¹⁷The term ‘energy’ in case of signals with positive polarity is avoided on purpose due to their unknown origin and their resulting random calibration.

Correlation between signals of opposite polarity (one above, one below threshold)

There are no apparent correlations between pulses of opposite polarity, but there is indeed a strong correlation between their respective pulse height spectra, when including events below the respective thresholds (cf. red lines in figure 4.6 and figure 4.7). This is due to the pulse processing in the digitizer, which uses a trapezoid algorithm for its pulse height analysis. In order to determine an energy-independent time stamp, the second derivative of the input pulse is used, as described in section 2.3.

This second derivative is comparable to one single sine wave, which first has an overshoot and then an equally large undershoot. The signal is subsequently triggered, whenever the overshoot exceeds a manually chosen value. However, this means that the DAQ does also trigger an event in case of the wrong polarity: In these cases, the second derivative is inverted beginning with an undershoot and subsequently an overshoot. However, whenever this overshoot exceeds the criterion value for a trigger, the event is ‘falsely’ triggered and a negative trapezoid will be reconstructed. Negative trapezoids are also evaluated by the DAQ, and the subsequent determination of the pulse height leads to values within the first bins of a histogram (further called ‘noise region’), since negative pulse heights are not defined.

As a direct consequence, every single pulse with a certain pulse height should be detected in both channels independent of its own polarity: If the pulse has a negative polarity, it will be recorded according to its energy and time stamp in channel 0 of the DAQ (which is set to measure negative polarities), but in addition it also deposits a signal (with according time stamp) in the noise region of channel 6 of the DAQ. If the pulse has a positive polarity, it will be recorded according to its energy and time stamp in channel 6 (which is set to measure positive polarities), but additionally also deposit a signal (with according time stamp) in the noise region of channel 0.

A confirmation of this relationship is offered in figure 4.8 and 4.9 for the spectra of negative and positive polarity, respectively. In both figures, the blue histogram shows the raw data, which is again plotted as a comparison. In the last paragraph, the orange histogram showed the coincidence between events of different polarity (both with $E \geq 10$ keV). This is however different in these figures: In order to confirm the hypothesis above, only the correlation between events within one channel and a possible coincident event in the noise region of the second channel will be investigated. If the statement is true, than every single event the noise region in each of the channels should subsequently be accompanied by a coincident event within the noise region in the other channel. Hence it would be straight forward to now investigate the coincidence histograms for events above the threshold in one channel and events below the threshold in the other channel. However, these coincidence histograms are expected to perfectly match the raw histograms.

This is why not the coincidence histograms are shown in orange (which would fulfill the criterion), but it is significantly more conclusive to show only these events, which are not coincident with signals within the noise region of the other channel. If these spectra are

empty, it would prove the statement that each signal above the threshold is accompanied by an event in the other channel, which is below the threshold.

The results are largely as expected: Almost all of the events above 10 keV (or $\text{Ch} = 10$) in each channel are accompanied by an event below the threshold in the other channel. However, a comparatively small amount of events with $E \geq 10$ keV (and negative polarity) and a larger amount of events with $\text{Ch} \geq 10$ (and positive polarity) are not detected by the other channel, and are therefore lost when only using one channel.

Nevertheless, this loss of events is counter-intuitive, due to the fact that if the second derivative is triggering in the channel with one polarity, its inverse signal should also always trigger the other polarity. It is therefore important to notice, that in both cases, these lost events are comparatively low in energy. The reason, why especially these events are lost in the other channel is, that the second derivative is not perfectly symmetric. Especially low-energetic noise, which is accidentally triggered (orange entries above $E = 10$ keV in figure 4.8) tends to lead to second derivatives, which are asymmetrical in height regarding the overshoot and the undershoot. These are triggered within only one of the two channels and therefore are not coincident with any counterpart. This is more likely in case of low-energetic signals. In case of high energetic events, even asymmetric second derivatives are likely to be triggered in both channels due to the fact, that (despite being asymmetric) both the overshoot and the undershoot are comparatively large.

In conclusion, it is crucial to reemphasize, that the untypical pulses of positive polarity are also triggered in channel 0 of the DAQ, and appear in the noise region of its histogram. This is true vice versa for negative pulses in channel 6. However, this statement is not bidirectional, i.e. it does not mean that all events in the first bins of the pulse height spectra are generated by correlated signals of the respective counter-polarity.

Possible origins and further treatment In summary, the signals of positive polarity are randomly distributed in time, and neither correlated to other signals of positive polarity, nor correlated to signals of negative polarity.

The origin of these signals could be related to a faulty HV module, which potentially could cause a temporary collapse or peak in the baseline, which would subsequently lead to a detector specific restoration with a decay time $\mathcal{O}(50\mu\text{s})$. While this would explain most of the properties, it has been excluded explicitly by testing different HV modules and supply cables. Furthermore, it is noticed that problems in the HV supply are expected to lead to more dilatory behaviors of the baseline, since the crystal acts as a capacitor. The rise time of these signals is however in the order of $\lesssim 1\mu\text{s}$, and therefore highly similar to events due to produced charge carriers in the active volume.

Except for the crystal, the cold and the warm preamplifier, all hardware components were checked, and exchanged, but the positive signals have remained.

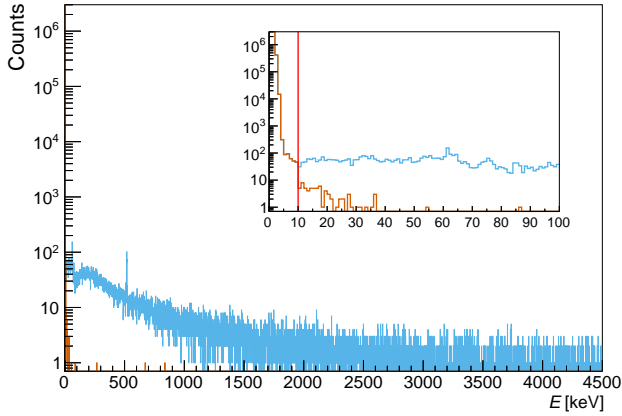


Figure 4.8: Pulse height spectrum of all signals with negative polarity in TU1 (blue). The orange histogram shows the remaining events, which are not coincident with signals of positive polarity (cf. figure 4.9), which fulfill $Ch \leq 10$ (red vertical line in the inlay).

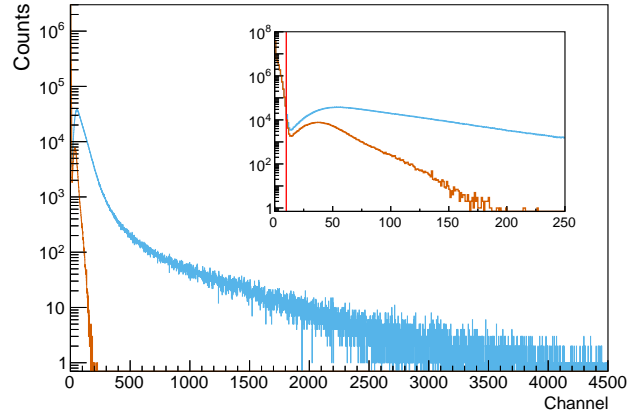


Figure 4.9: Pulse height spectrum of all signals with positive polarity in TU1 (blue). The orange histogram shows the remaining events, which are not coincident with signals of negative polarity (cf. figure 4.8), which fulfill $E \leq 10$ keV (red vertical line in the inlay). The channels are calibrated with the same calibration than its counterpart.

Assuming the stability of the high voltage on the crystal, a negative signal is induced by a cloud of charge carriers, which are absorbed by the anode and cathode, respectively. From an electronic perspective, one reason for signals with the opposite polarity could therefore be, if charge carriers of the opposite charge would induce a signal on anode and cathode, respectively. Due to the fact that the amplitude of a signal is proportional to the amount of charge carriers applied on the electrodes, this argument would however not be sufficient for possible candidates (i.e. single particles as e.g. cosmic muons μ^+/μ^-) to induce signals of comparable amplitude as entire charge carrier clouds.

One remaining reason for the occurrence of these signals is motivated by studying the behavior of other HPGe detectors, whose vacuum was broken due to maintenance prior to the application of a high voltage. In these specific environments, it has been shown ($N \geq 5$), that these detectors also tend to show additional signals of counter-intuitive polarity during the ramping of the HV. This has been attributed to the fact, that there might be minor sparks between the crystal and any grounds (e.g. its outer aluminum capsule), which lead to the short collapses of the HV with a subsequent restoration. This behavior is also known from accelerator physics, where it is a common effect during application of a HV after maintenance procedures. The HV terminal therefore needs to be conditioned slowly in order to prevent more intense sparks. While this effect is known from other HPGe detectors solely during their first ramping of the HV and always vanished after a maximum of some days, a probable reason for this continuous effect in TU1 could be a slightly insufficient vacuum, which would act in favor of more sustained sparks between crystal and aluminum capsule. This explanation is also supported by the fact, that these sparks would as well occur ran-

domly distributed. However, the only way to confirm this theory is to dismantle the entire shielding in order to reach the valve for reevacuation. This was not feasible in the current stage of the laboratory.

Independent of their origin, the time stamp for all relevant pulses of the positive polarity are recorded in channel 0 of the DAQ and can be treated accordingly with respect to their influence on the dead time (cf. section 4.6). Regarding more extended analyses and developments over a longer time period, the time stamp, as well as the pulse height remain being recorded simultaneously in channel 6 (cf. section 3.5.2.4).

In case the positive and negative signals are indeed entirely uncorrelated, the probability for a negative event to be distorted by a simultaneously occurring positive pulse is $10^{-3}\%$. Therefore, it is part of the good scientific practice to further monitor and account for these signals, but if their impact remains similar, it will not influence future measurements significantly. Nevertheless, this anomaly is by far the main contribution of background pulses. Regarding an estimation of the adjusted dead time, this has to be accounted for (cf. section 4.6).

4.2 Investigation of the radon concentration

The purpose of the anti-radon box for TU1 is to prevent radon (which is gaseous) from entering the passive shielding. Its relevance, as well as the construction was already introduced in section 3.5.2.

The radon concentration within underground laboratories strongly depends on the composition of the rock overburden, the design and permeability of the laboratory walls, and the air ventilation system within the laboratory.

The dominant contribution of radon-induced activity and dose rate within underground laboratories is due to ^{222}Rn , which has a half-life of $T_{1/2} = 3.8\text{ d}$ and stems from the natural decay chain of ^{238}U . Due to their comparatively shorter half-lives of $T_{1/2} = 56\text{ s}$ and $T_{1/2} = 4\text{ s}$, the radon nuclides ^{220}Rn and ^{219}Rn from the other two decay chains only play a subordinate role. Their probability to enter sensitive areas within their short gaseous phase is too small before they decay and subsequently condensate (i.e. becoming attached) to surrounding solid materials.

The air ventilation system within the bunkers of the Felsenkeller laboratory is designed to exchange the entire air volume within the laboratory four times per hour. Approximately 75% of the air gets dried and recirculated, and 25% is fresh air brought in from the outside. For common underground laboratories without clean rooms or further purification techniques, the radon-induced activity concentration is roughly in the order of $1\text{-}100\text{ Bq/m}^3$ [122, 123]. For the Felsenkeller laboratory, this has been determined experimentally at four different locations in the underground site and in the overground facility (cf. figure 4.10).

The radon concentration in these locations was measured in a campaign of 14 d using four

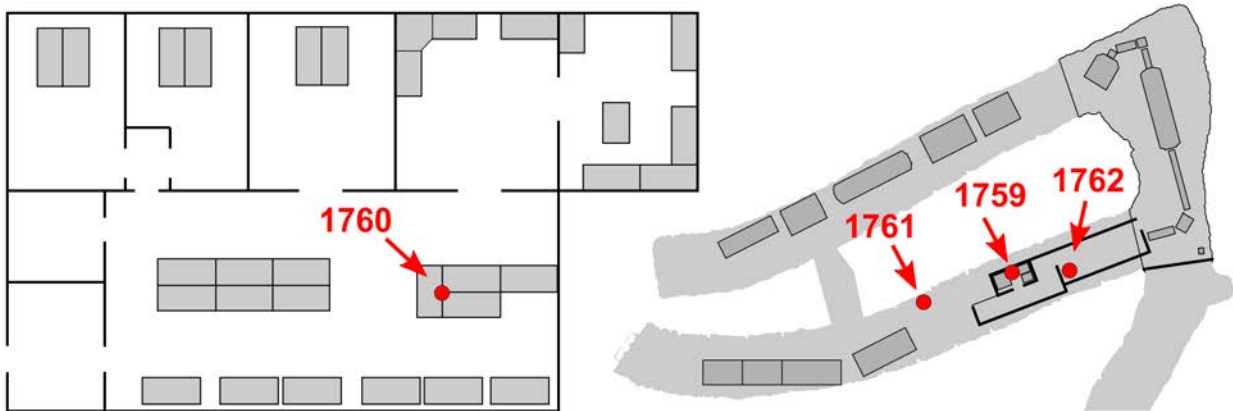


Figure 4.10: Scheme of the overground (left) and underground (right) sites at the shallow-underground facility Felsenkeller. The red circles indicate the position of the RadonScouts during the measurement of the radon concentration. The red numbers represent the serial number of each device.

RadonScouts from Sarad GmbH [124]. These devices are suited for measurements of low radon concentrations ($<100 \text{ Bq/m}^3$) and are calibrated according to DIN EN ISO/IEC 17025:2018. The devices were all positioned in approximately 1 m height on a flat surface. The campaign was conducted during winter and seasonal effects were not investigated.

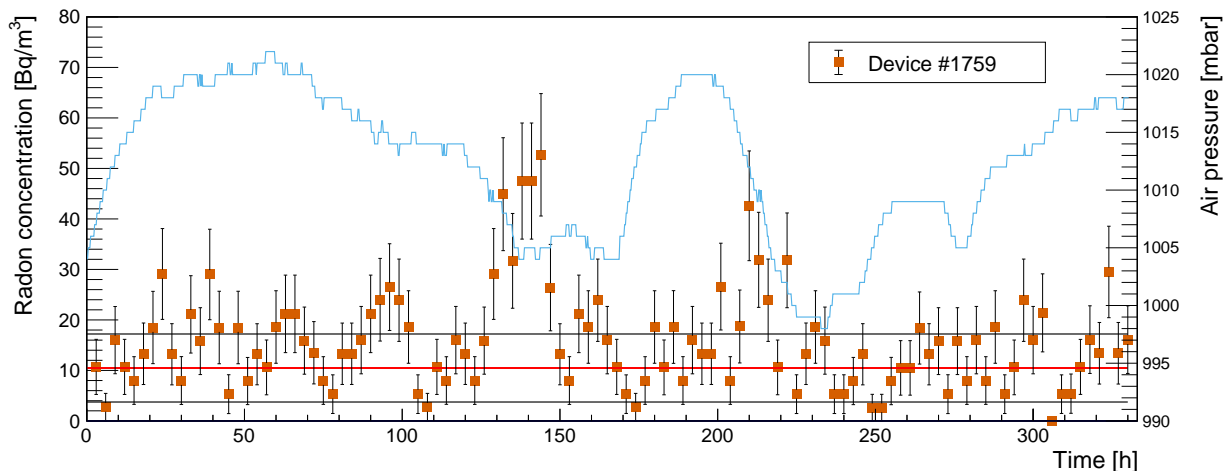


Figure 4.11: The measurement of the time-dependent radon concentration is shown in orange and was obtained with the device #1759, which was located in bunker 110 (cf. figure 4.10). The average radon concentration is shown in red. Due to systematic influences, the fluctuation is non-Gaussian. However, the effective interval for 68% of the data points is indicated with the black lines. The blue histogram represents the air pressure within the tunnel system during the same time period. See text for details.

The result of the radon concentration measurement of device #1759 is shown in figure 4.11. This device was located between TU1 and TU2 in bunker 110 (cf. figure 4.10), and was measuring from 01/10/2022 to the 01/24/2022. The other devices were measuring accordingly, and their results are attached to the appendix A.2.

Table 4.1: Radon concentration at various positions of the Felsenkeller laboratory. The exact positions of the devices during the measurements are shown in figure 4.10. The minimal and maximal values within the 14 d campaign are stated, as well as the average values. The uncertainties for a fit (polynomial of 0th grade), as well as the 1σ environment (corresponding to the average values) are shown. The precision of all values is according to the precision of the fit uncertainty.

#	Location	Minimum [Bq/m ³]	Maximum [Bq/m ³]	Average [Bq/m ³]	Fit unc. [Bq/m ³]	1σ env. [Bq/m ³]
1759	Undergr. (bunker 110)	0.0	52.7	10.5	0.5	6.7
1760	Overgr. (office room)	27.1	209.8	77.5	1.4	33.3
1761	Undergr. (tunnel VIII)	0.0	71.5	15.1	0.6	8.7
1762	Undergr. (bunker 111)	2.5	75.3	11.4	0.5	10.4

The average concentration in bunker 110 was determined by a constant fit to be 10.5(5) Bq/m³, but the variation of the experimental data points can not be explained by statistical fluctuations.

Its underlying systematic influences are dominated by the change on the prevailing air pressure, which is also shown in figure 4.11 as a blue curve. Whenever the air pressure is rapidly decreasing due to the weather changes, there is a pressure difference between the ambient air, and the air, which is located within the surrounding rock. This radon-rich air within the rock reacts to this pressure gradient by diffusing out into the tunnel system, which leads to a subsequent increase of the radon concentration. This effect influenced the measurement significantly after approximately 130 h, and 210 h of measuring time, respectively.

The variation of the radon concentration over time is therefore a convolution of statistical fluctuation and systematical change of the radon concentration, and is subsequently larger than suggested by the stated uncertainty from the fit. The minimal radon concentration in bunker 110 during this measurement of 14 days with an integration time of 3 h was 0 Bq/m³ and the maximum was 52.7 Bq/m³. An effective uncertainty, which includes 68 % of the data points can be stated as 10.5(67) Bq/m³, which is plotted as horizontal, black lines in figure 4.11.

The corresponding results for the other locations are listed in table 4.1. By comparing these measurements, it is apparent, that the radon concentration underground is significantly lower than overground, despite the massive rock surrounding of the underground laboratory. This difference is due to the fact, that the air circulation system within the tunnels efficiently exchanges the radon-rich air with radon-poor air from the outside. Comparing different locations within the underground site, the radon concentration in the open tunnel was measured to be higher than within the bunker areas. While the difference is not significant (depending on the analysis technique), the higher concentration in the open tunnel could also be a direct consequence of the proximity of the device to the surrounding rock.

The radon concentration in the overground site was accumulating over the weekend and was systematically the highest between 3 am and 6 am in the morning. Both trends indicate, that

the radon concentration is dependent on the manual air circulation by opening windows and doors.

While the relative fluctuations are comparable between overground and underground sites, the absolute change of the radon concentration is significantly larger in the overground site due to the missing air circulation system, which compensates systematic fluctuations.

The effectiveness of the air circulation system is also supported by the fact, that the radon concentration within the tunnels VIII and IX was ranging between 0 – 300 Bq/m³ before its installation, which is a factor of 20 more for the maximum concentration.

It may also be noticed here, that both the average, as well as the maximum value of the radon concentration during this measuring campaign is the lowest in bunker 110. This is a long-term benefit for all the low-level counting setups, which potentially suffer from long-living daughters of radon (namely ²¹⁰Pb). Due to the comparatively long half-life of ²¹⁰Pb, it is not in an activity equilibrium with ²²²Rn, but its feeding is nevertheless proportional to the concentration of ²²²Rn. Assuming 10 Bq/m³ of ²²²Rn, this already leads to an accumulation in activity of approximately 1 mBq/m³/d of ²¹⁰Pb, and additionally the same activity of its daughters, which are in secular equilibrium to ²¹⁰Pb.

Conservatively assuming the inner volume of a copper castle to be 1 dm³ (equivalent to an accumulation in activity of 1 μ Bq/d), this already leads to an additional decay rate of 0.1 d⁻¹ for each day of exposure within the proximity of the detector. Despite being only a very rough estimation, these activities are potentially non-negligible when accumulating on the inner copper shielding or detector crystal during longer maintenance or sample change.

4.3 The passively shielded TU1 detector

The construction of the passive shielding was discussed in section 3.5.2, and mainly consists of 140 m.w.e. of rock overburden, 40 cm of low-activity concrete, an anti-radon box and a lead and copper castle. The benefits of the different stages are discussed hereafter based on the histograms in figure 4.12.

The pulse height spectrum in black was obtained by operating TU1 in the bunker 110 (140 m.w.e. of rock overburden, and 40 cm of low-activity concrete) without any additional shielding. A variety of γ -ray lines is apparent, with the most dominant contributions stemming from the natural decay chains, and the decay of ⁴⁰K.

These contributions are already significantly attenuated, when adding a layer of 5 cm OFRP copper around the crystal (orange). Especially low energetic γ -ray lines are effectively shielded and become covered by incoherently scattered contributions from higher energetic particles, which are less effectively attenuated.

In order to significantly suppress these contributions from high energetic photons, an additional layer with 5 cm of low-activity lead (cf. section 3.5.2) was added (light blue). This drastically reduces the counting rate in all energy regions. Low-energetic photons from out-

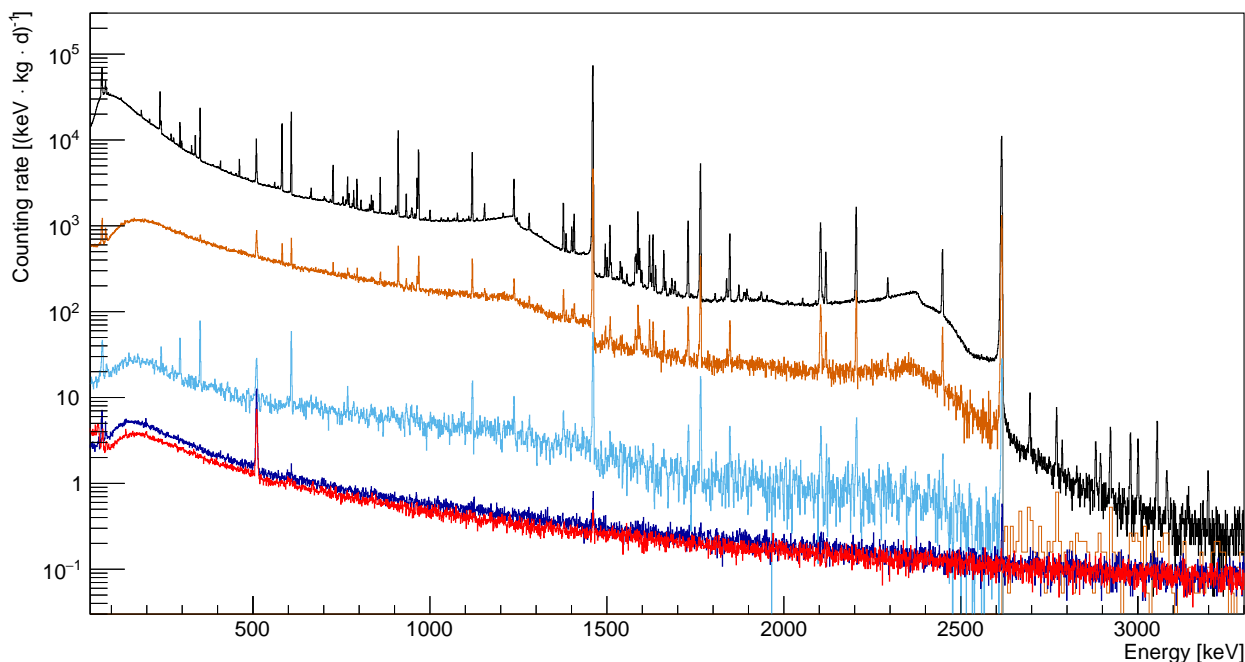


Figure 4.12: Counting rates for different stages of passive shielding for TU1. The black histogram was obtained in bunker 110 without additional shielding, and the orange and the light blue histogram was measured with 5 cm of copper and both 5 cm of copper and 5 cm of lead, respectively. The dark blue histogram shows the result for a preliminary shielding, and the red histogram shows the final passive background rate after adding additional 5 cm of copper. Due to a lack of statistics, the light blue spectrum was artificially improved in statistics by Monte-Carlo techniques, and the orange histogram is rebinned by a factor of eight above $E = 2620$ keV. For sake of comparability, the light blue spectrum is not shown above $E = 2620$ keV due to its accordance to both better and worse shieldings, respectively.

side the shielding become negligible, and high energetic photons are strongly attenuated. At first, it is unintuitive, that low energetic lines (which were covered in the orange histogram) become distinguishable from the background again. The origin of these re-appearing lines is the gaseous radio nuclide ^{222}Rn , which diffuses into the inner volume of the shielding, and subsequently decays. These low energetic part is dominated by its daughters ^{214}Pb (242 keV, 295 keV, and 352 keV), and ^{214}Bi (609 keV, 768 keV and 1120 keV). Besides ^{40}K and ^{208}Tl , these daughters also become dominant in the high-energetic region (mainly due to ^{214}Bi). A preliminary final stage of the passive shielding was achieved by adding additional 10 cm of lead, and covering the passive shielding in plastic foil against radon (dark blue). The remaining γ -ray induced background is already negligible with respect to muon-induced continuum, and the 511 keV γ -ray line. The remaining peaks are at 609 keV, 1120 keV, 1461 keV and 2615 keV, respectively.

This stage was present for a comparatively long time until a proper anti-radon box around the passive shielding was finally constructed and added. During this period, it was also decided to further add an additional inner layer of 5 cm OFRP copper. This was done due

to the fact, that contributions from ^{40}K , and ^{208}Tl might be negligible for the count rate in the passively shielded spectrum, but they were determined to be significant after applying an active veto. In the meantime, the entire hard- and software was also adjusted in order to fulfill ultra-low background conditions (cf. section 3.5.2.4 and section 4.1). The resulting final stage of the passive shielding for TU1 is shown in red.

It is worthwhile mentioning, that all pulse height spectra (besides the red one for the final configuration) were obtained with a different multi channel analyzer, than the typical CAEN digitizers, which are used within the scope of this thesis. These four histograms were measured using a FAST ComTec MCA4A (four channels, each at 125MHz). A systematic difference between both digitizers becomes apparent by comparing the dark blue, and the red histogram in the very low energy region.

Despite the red histogram benefiting from a better shielding, it seems to have a higher counting rate at energies below $E = 70$ keV. This is due to the fact, that the raw spectrum (red) was recorded with a CAEN digitizer. As mentioned in chapter 4.1 and later discussed in chapter 4.5.3 and chapter 4.6, noise and oscillation events can distort the low energetic part of the spectrum, and need to be accounted for. In case of the FAST ComTec MCA4A, these signals are already suppressed and filtered by the hardware. However, this can become problematic, when operating the detector for longer time with no supervision on these signals, and no opportunity to check their impact on the baseline. This hardware smoothing is also seen with other data acquisitions, e.g. Ortec 671 and Ortec 919 used in combination.

However, this improvement in data processing is solely done for the actively vetoed spectrum, since the shown passively vetoed spectrum won't be used further out.

4.4 Measurements and analysis of the scintillation panels

The passively shielded spectrum of TU1, as well as its values for the counting rate are comparable to the results of similar sophisticated HPGe setups in shallow-underground laboratories, which will be discussed in more detail in section (cf. section 4.8).

In order to improve the sensitivity of the TU1 detector even further, its dominating contribution to the remaining events in the pulse height spectrum has to be investigated in order to counteracted against them, which are muon-induced events.

Given a certain depth of the laboratory, an additional passive shielding against muons is not effective, due to their penetrability. Therefore, the TU1 detector and its passive shielding is surrounded by active veto detectors, which are supposed to identify and filter out the muonic events in the remaining spectrum of TU1, as introduced earlier in section 3.4.

This section is divided into two major sections. The first aim it to provide an introduction on the general working principle regarding the correlation between the deposited energy in the panel and the resulting position in the pulse height spectrum. This conversion depends on both an ordinary energy calibration, as well as an additional position-dependent light

collection efficiency of the panels. The second part of this section is dedicated to the discussion on coincident events between the panels and the TU1 detector, as well as the influence of active veto detectors on the passively shielded spectrum of the TU1 detector.

4.4.1 Energy calibration of the panels

The energy calibration for plastic scintillation detectors is not as straight-forward, as for HPGe detectors. Due to the fact, that these scintillation detectors have a comparatively low ordering number, photons mainly interact with the detection material via incoherent scattering. It is therefore more likely, that the energy of the initial photon is only partially deposited. This leads to a spectrum, which is dominated by Compton-continua, and Compton edges.

Nevertheless, the use of γ -ray calibration sources is considered to be without alternative, because typical beta sources emit a continuous spectrum and their corresponding electrons furthermore lose a significant fraction of their energy before entering the active detection material. One appropriate alternative is the use of conversion electron sources (e.g. ^{207}Bi , ^{109}Cd and ^{137}Cs , with 976 keV, 63 keV and 624 keV, respectively). These sources emit monoenergetic electrons, but also suffer from the effect, that the electrons lose energy on their path to the active detection volume. Furthermore, conversion electron sources are more appropriate for small detectors (e.g. Silicon detectors), where their photonic contributions are not likely to cover the electron-induced peak.

It is also worthwhile to mention, that the energy calibration is not needed for the subsequent analysis of the active veto. Cuts regarding a minimum deposited energy within the panels will be determined experimentally for every panel, which does not require an energy calibration. Nevertheless, the determination of the muon peak energy, as well as its comparison to theoretical expectations indeed requires an energy calibration. Furthermore, an investigation on the linearity of the energy calibration is also crucial in order to discuss possible quenching effects.

The energy calibration of the veto panels was studied on panel #45 (cf. figure 3.17), representatively for the other four panels. This was done using several calibration sources (namely ^{22}Na , ^{60}Co , ^{88}Y , and ^{137}Cs), which were positioned on the center point of the large outer surface of panel #45.

The pulse height spectrum in case of the ^{60}Co source is shown in figure 4.13 as black histogram, normalized on its live time. By comparing it to the corresponding background rate in panel #45 (light blue), it is apparent, that the count rate is dominated by the calibration source.

After subtracting both histograms from each other, the resulting histogram shows the exclusive contributions from the ^{60}Co source (orange). Both the Compton edge (actually two Compton edges close to each other), as well as a smaller back scatter peak is visible. Comparing the shape for the background (blue), as well as its threshold, it can be assumed, that

the height of the back scatter peak is not significantly affected by a drop in efficiency, but that its shape is reliable. Furthermore, the smaller height of the back scatter peak is also consistent with theoretical considerations, due to the fact, that essential amounts of material behind the calibration source would be required for the back scatter peak to become pronounced.

The Compton edges of all calibration sources were fitted with an error function $\text{erf}(x)$, and their resulting mean values were compared to their theoretical position. In case of ^{60}Co , and ^{137}Cs , only one Compton edge was fitted, respectively. While ^{137}Cs mainly emits γ -rays at one significant energy, the two Compton edges from ^{60}Co could not be separated from each other, due to their proximity. As a consequence, the intensity-weighted mean position of both Compton edges was determined and used throughout this analysis.

In the case of ^{22}Na , and ^{88}Y , two Compton edges were fitted per histogram. For the ^{22}Na source the lines at 511 keV and 1275 keV were investigated, and in case of ^{88}Y the lines at 898 keV, and 1836 keV were used.

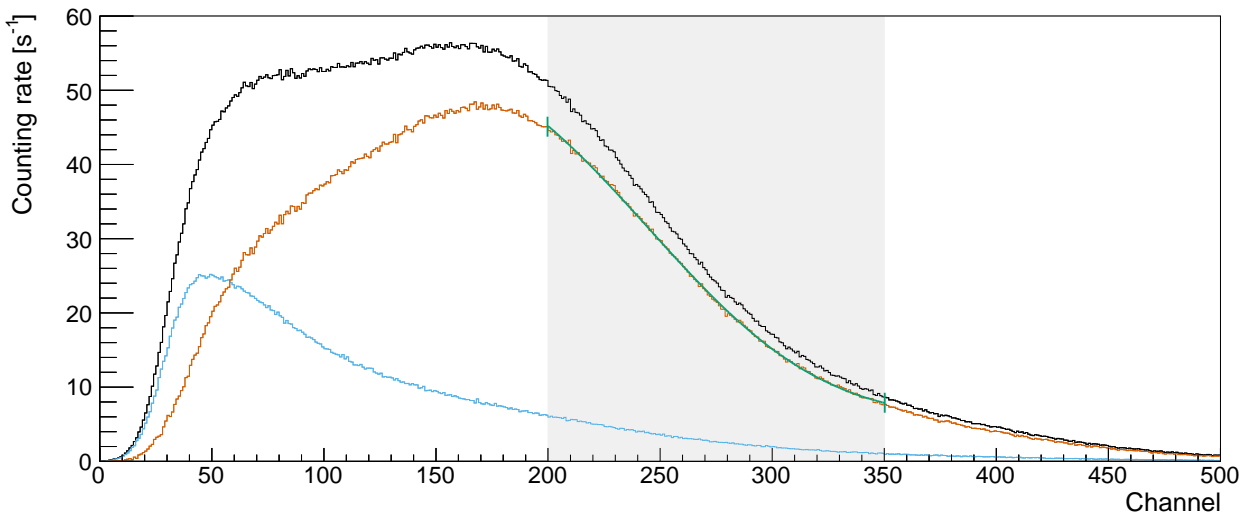


Figure 4.13: Counting rates of scintillation panel #45 (cf. figure 3.17). The black spectrum shows the counting rate in case of a ^{60}Co source, which was placed on the center point of the large outer surface, and the blue spectrum shows the counting rate of the background. Their difference (orange) is used to determine the position of the Compton edges. The data is fitted (green line) within its fit boundaries (grey box).

The result of this energy calibration is shown in figure 4.14. The uncertainties from the fit are included, but too small to be visible. Taking into account the broadness of the Compton edges, the data points on the energy calibration are in comparatively precise accordance. Nevertheless, there is a systematic deviation that can not be explained by the statistical uncertainty of the fit procedure. This deviation can partially be explained by random coincidences in the panel, which correlate with the activity of the calibration source. ^{137}Cs has the lowest activity, and therefore undergoes less random coincidences. ^{22}Na , and ^{60}Co have comparatively large activities, which leads to a larger effect of random coincidences,

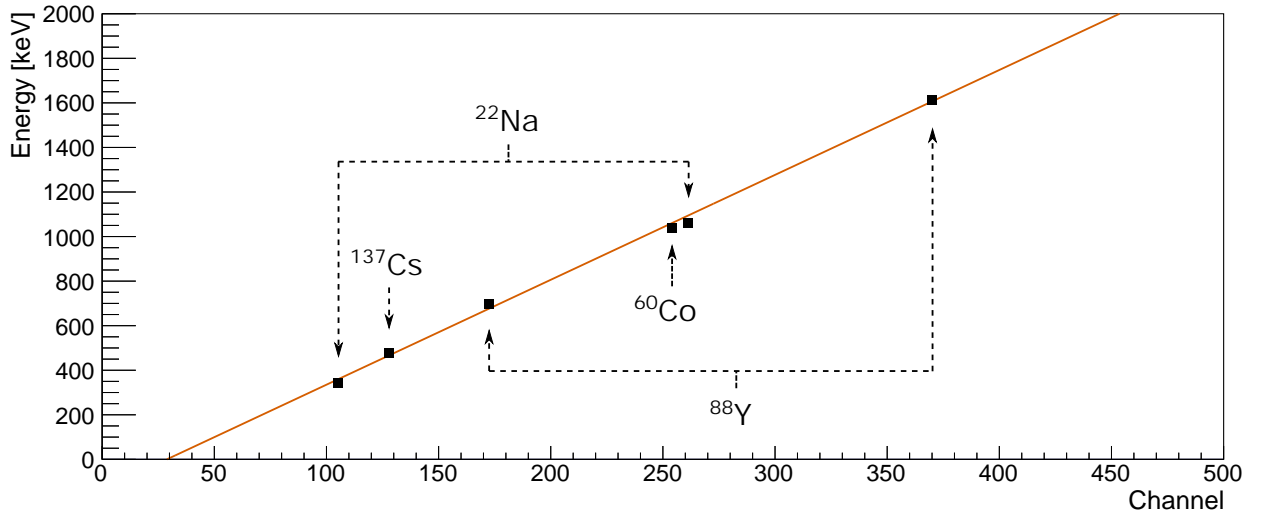


Figure 4.14: Energy calibration of scintillation panel #45 (cf. figure 3.17). The data points were acquired by fitting the Compton edges of ^{22}Na , ^{60}Co , ^{88}Y , and ^{137}Cs (cf. figure 4.13).

which subsequently moves the potential turning point of the error function further to higher channel numbers.

Despite some minor deviations, the trend of the energy calibration is unequivocally, and sufficient for its general purpose, which is mainly the determination of the energy position of the muon-induced events.

However, in order to understand the experimentally determined energy deposition of muons in the panels, another effect has to be discussed, which is the light collection efficiency of the panels for different positions.

4.4.2 Light collection efficiency of the panels

Within the last chapter, an energy calibration was performed for panel #45, which shows the correlation between the energy of the incident particle, and the amount of secondary photons, which are detected at the PMT. While the yield of produced secondary photons solely depends on the energy deposition of the primary particle, the total amount of photons which subsequently reach the PMT additionally depends on the position of the interaction on the panel.

The performed energy calibration within the last section is therefore only valid for particles, which interact at the former position of the calibration sources, namely the center of the panel. Considering interaction points, which take place further away from the PMT, the slope of the energy calibration is supposed to be smaller. This is due to fact, that larger distances (in average) lead to effectively smaller amounts of collected photons at the PMT, hence smaller induced signal heights.

The gravity of this effect will be investigated within this chapter by introducing the concept of so-called light collection efficiencies (LCE). The LCE is defined as the amount of photons

which reach the PMT for a certain primary particle energy, and is normalized to the LCE at the central position of the respective panel (position [5,5] in figure 4.16).

The entire range of LCE values for one panel is therefore a measure for the impact of the energy calibration smearing due to different interaction points on the panel.

The position dependent LCE was determined experimentally by using a collimated ^{90}Sr source, which is a pure beta emitter with an endpoint energy of 546 keV. Its daughter nucleus (^{90}Y) is in secular equilibrium to its mother and is mainly also a pure beta emitter with an endpoint energy of 2279 keV. A collimated beta source was chosen due to the fact, that γ -ray sources emit isotropically, and their proper collimation is more difficult, which subsequently adds an additional uncertainty on the initial interaction point. Furthermore, these difficulties regarding the collimation would also lead to comparability issues between measurements at the center of the panel (2π geometrical acceptance), at the edge (1π geometrical acceptance), and the corners ($\pi/2$ geometrical acceptance).

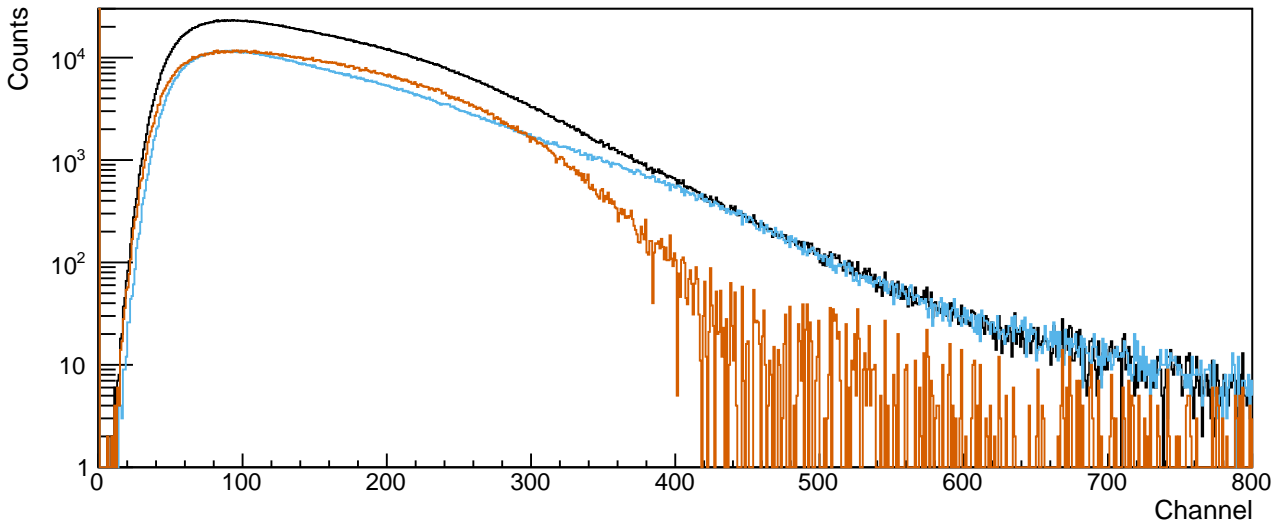


Figure 4.15: Pulse height spectra of scintillation panel #45 (cf. figure 3.17). The black spectrum shows the spectrum in case of a ^{90}Sr source, which was placed on the center point of the large outer surface, and the blue spectrum shows the background spectrum. Their difference (orange) shows the impact solely due to the calibration source.

The resulting spectrum of the collimated ^{90}Sr source at the panel position of [5,5] (cf. figure 4.16) is shown in black in figure 4.15. The resulting spectrum from the impact of the source itself (orange) is obtained by correcting the black spectrum using the natural background (blue).

While the end point of the spectrum might seem to be a suitable candidate for the subsequent comparison of different light yields at different panel positions, it also suffers from summation effects and from the complexity to properly fit one exact end point. Instead, the utilization of step functions and their turning points (as elaborated during the energy calibration, cf. section 4.4.1) resulted in reliable results. This technique was therefore also adopted for this

analysis.

Hence, the turning points for each spectrum at each source position are determined and normalized to the result of the measurement at the source position [5,5] (cf. figure 4.16).

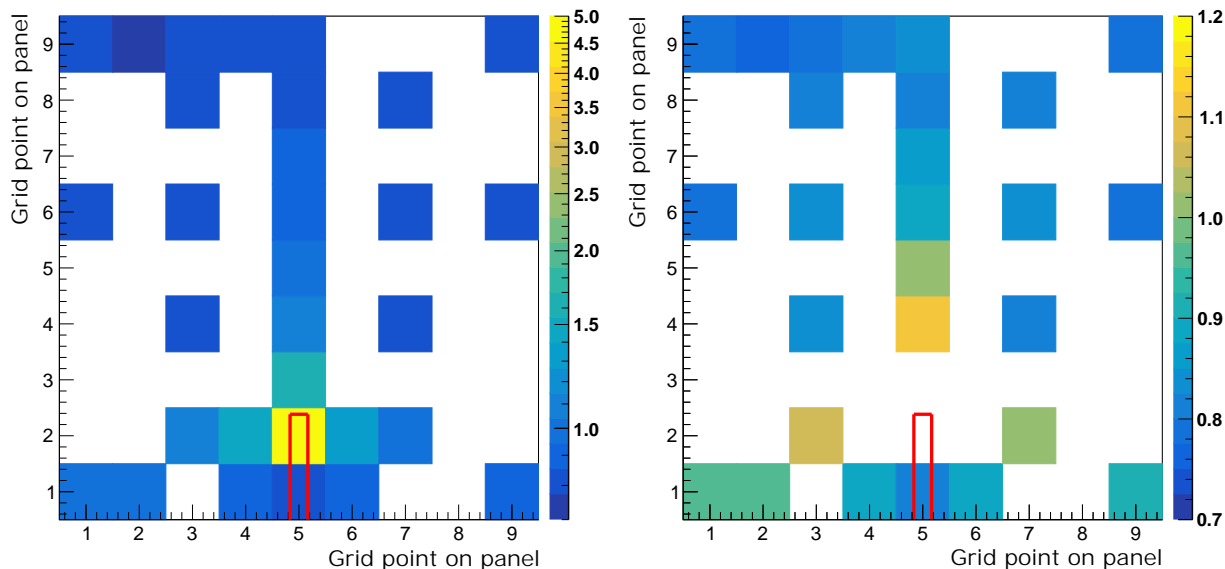


Figure 4.16: Light collection efficiency for panel #45, which is divided into 9x9 rectangulars. The position of the HV module and the PMT indicated as red line (cf. figure 3.17). Left: The color coding is on a logarithmic scale ranging from 0.7 to 5.0. Right: The color coding is on a linear scale ranging from 0.7 to 1.2, but the four values exceeding this interval are excluded.

The resulting light collection efficiencies of panel #45 are shown in figure 4.16 and confirm qualitative expectations: The LCE becomes significantly larger for small distances between sample and the position of the PMT. However, more than 90% of the panel show resulting light yields between 70% and 120% of the reference position. Only the positions very close to the PMT are resulting in light yields of up to 5 times the yield at the reference point.

It is also worthwhile mentioning, that the light yield of scintillation crystals strongly depends on their temperature. It is therefore important to operate them at a constant temperature. At Felsenkeller, this is ensured by the air ventilation system within the underground laboratory (cf. section 4.2).

4.4.3 Interpretation of energy calibrated spectra

As shown in the previous section, the light collection efficiency of a scintillation panel has a direct impact on its energy calibration. If two particles deposit the same amount of energy at different positions on the panel, their resulting pulse height in the spectrum varies with respect to their corresponding LCE values, which effectively leads to an artificial and inevitable smearing of the spectrum.

A scientifically reliable energy calibration, as performed in section 4.4.1, is therefore only valid for particles, which also deposit their energy at the central position of the panel, where the calibration sources was positioned.

The energy calibration of the long-term spectrum of panel #45 in figure 4.17 therefore has to be treated carefully. This is due to the fact, that a muon or photon being attributed with a certain energy in this histogram could potentially have deposited significantly more or less energy, respectively. It would therefore be more appropriate to avoid the term ‘energy’ on the x-axis. However, with recognition to those limitations this phrase is kept for the sake of a general interpretation of the muon spectrum.

The accurate interpretation however would be, that the x-axis shows the product of the deposited energy and the corresponding light collection efficiency at the position of the interaction on the panel. For particles interacting at the center of the panel, this LCE-induced correction factor is 1, and for larger distances to the PMT, the effective energy is quenched to lower value according to its LCE.

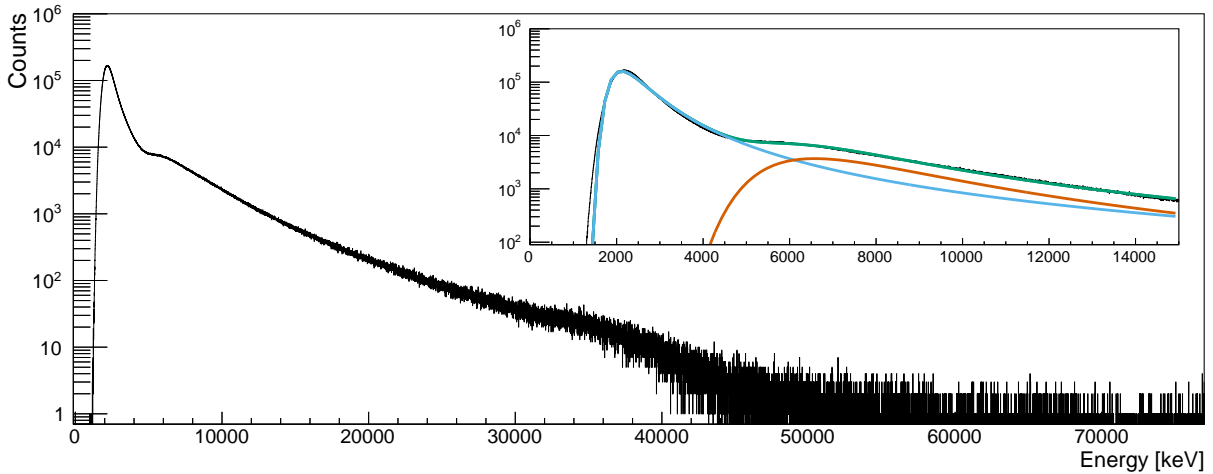


Figure 4.17: Background spectrum of scintillation panel #45 (cf. figure 3.17), which has been measured for 29.5 d. The low-energetic part is dominated by photon-induced events, and the high energetic part is dominated by muon-induced events. The inset shows a fit of both components with two Landau functions (green), as well as their disentangled contributions in light blue and orange for the photon-induced, and the muon-induced part, respectively. More accurately, the counts in the histogram are plotted with respect to the product of energy times LCE¹⁸.

The effect of photons was already discussed in chapter 4.4.1. Therefore, it will be focused on the muonic contribution hereafter, which will also be the contribution of interest for the further purpose of the panels in their function as veto detectors.

Cosmic muons are produced in the atmosphere (≈ 15 km altitude) with a mean energy of 6 GeV. While radiative effects are comparatively small at these energy regimes, their dom-

¹⁸The reason for the histogram starting at $E \approx 1500$ keV (equivalent to approximately a channel of 400) is a hard coded increase of the threshold in the DAQ during all subsequent measurements. If the threshold would be as low, as indicated by the blue histogram in figure 4.13, the data size would be 40 GB per month only for panel #45, instead of ≤ 10 GB per month. Furthermore, the low-energetic part is irrelevant for the subsequent coincidence analysis since only muon-induced events are needed (cf. section 4.4.4).

inant interaction channel is ionization according to the Bethe-Block formula. This formula has a minimum due to its strong $1/v^2$ dependency at low energies, and a slowly emerging logarithmic dependency towards higher energies. In case of muons, this minimum is at an energy of $E \sim 260 \text{ MeV}$ and $\beta\gamma \approx 3$. Muons at these energies are so-called minimum ionizing particles (MIP) [125].

Considering each single muon, they all lose energy during propagation through the atmosphere and the rock overburden until they are MIPs. For even lower energies, the $1/v^2$ -dependency subsequently begin to dominate their energy loss and they are more rapidly stopped. However, by considering the entire muon spectrum itself, this spectrum actually hardens up for larger rock overburdens. In case of the Felsenkeller underground laboratory, the peak maximum in the muon energy spectrum is around 30 GeV.

At 30 GeV, the mean energy loss of muons in the scintillation material is approximately $2 \text{ MeV}_{ee}/\text{cm}$ [125]. A muon, which propagates perpendicular to the large panel surface (thickness 5 cm), therefore deposits approximately 10 MeV_{ee} .

This theoretical estimation can now be compared to the inlet in figure 4.17, which shows the experimental result. The ‘energy’-calibrated spectrum was fitted with two Landau functions in order to qualitatively disentangle photon-induced, and muon-induced contributions¹⁹. The maximum of the experimentally determined muon-induced contribution is approximately at $E = 7 \text{ MeV}$. Considering the aforementioned limitations of this approach, this value is already comparable to the estimation of $E = 10 \text{ MeV}$. However, two additional effects are important to consider, when interpreting the experimental result.

The first effect is based on the aforementioned light collection efficiency, which systematically shifts the mean pulse height at the PMT to lower values due to the mean LCE being between 70% and 90% (cf. figure 4.16), but also allows significantly larger ‘energies’, i.e. when interacting very close to the PMT. The second effect is based on the geometrical consideration, that most muons don’t propagate perpendicular to the large panel surface of panel #45, but with a tilted angle. This leads to a larger mean path length than 5 cm, which subsequently also allows significantly larger energy depositions of muons (as confirmed by figure 4.17).

The impact of both effects will be further discussed in the following section during the investigation of coincidence spectra between different detectors. In this way, the second effect can be attenuated by analyzing the geometric dependency more precisely, which gives a possibility to disentangle both effects.

¹⁹Due to the convolution of the position-dependent LCE values, the panel thresholds, an energy dependent resolution of the panel, as well as the spectral complexity regarding the photon-induced spectral shape, these Landau fit functions are not physically motivated. They only serve as a phenomenological function to discuss the impacts of the muon-induced, and photon-induced part of the spectrum.

4.4.4 Coincidence spectra between panels and TU1

After introducing the physics of operating one single scintillation panel, this knowledge will now be used to combine different panels to search for coincident signals. The intuitive procedure for using the panels as veto detectors would be to build an equivalent analysis to the anti-Compton suppression in case of HPGe and BGO detectors, which was introduced in section A.1.1.

However, there is a crucial difference between both scenarios: In case of surrounding BGOs, any signal might be a potential candidate for a coincident event with the HPGe detector. This is due to the nature of inelastic scattering of photons and the main aim of the BGO is to reduce the Compton continuum in the HPGe. Hence, it is crucial to include both low-energetic, as well as high-energetic events. However, in case of muon vetos, there is a clear division between necessary and unnecessary signals in the panels: The aim of the muon veto is not to include low-energetic photon-induced events, but only high-energetic muon-induced events. Or to put it in other words: Due to the fact that photon-induced signals are responsible for the majority of the counting rate in the scintillation panels, excluding them from the veto conditions as much as reasonable is pivotal in order to optimize the entire veto performance.

As a result, one of the cuts, which will be introduced now, is an energy-cut for events in the scintillation panels. This exclusion of low-energetic signals can be performed in two different ways: Either the threshold in the panels can be increased in the software in order to avoid triggering them in the first place, or they are stored and rejected from the data during the offline analysis via a threshold energy in the cut condition.

Both approaches have the benefit of reducing random coincidences. However, the benefit of the hard coded software solution (by increasing the digitizers threshold) is a drastic reduction of saved data, and also allows a significant time reduction for running a script over the raw data²⁰. While the hard coded software solution is preferable, it has to be treated with utmost caution. This is due to the fact, that also low-energetic muon-induced events (or even neutron-induced events) in the panel might turn out to be important for an even more sophisticated stage of the analysis. This issue will also be discussed in more detail during the subsequent sections. However, within the scope of this thesis a compromise of both approaches is chosen by increasing the thresholds in the digitizer only to a certain degree.

In addition, also the offline-analysis was improved with respect to the previously used HPGe-BGO vetos by introducing a threshold energy for the panels within the offline scripts, which is further called E_{thresh} . In addition to all the important flags, the following information are stored in the ROOT tree for each event in TU1 (with PH, and TS being the pulse height and the time stamp, respectively):

²⁰Due to the lack of passive shields around the scintillation panels and their resulting comparatively large counting rate ($R > 100 \text{ s}^{-1}$), a hard coded increase of the threshold also reduces the amount of lost muon-induced events due to a busy trigger in the DAQ.

- PH and TS of the event in TU1
- PH and TS of the previous event in TU1
- PH and TS of the next event in TU1
- PH and TS of the previous event in each single panel
- PH and TS of the next event in each single panel
- PH and TS of the prev. event in each single panel with $E \geq E_{\text{tresh}}$ in this panel
- PH and TS of the next event in each single panel with $E \geq E_{\text{tresh}}$ in this panel

It is worthwhile mentioning, that the implementation of E_{tresh} would not be necessary in order to improve the veto efficiency: Imagine a muon inducing a signal in one of the panels, as well as in the TU detector. Even if there would be an uncorrelated photon-induced signal in the panel in between both of them (due to the non existing E_{tresh} and the subsequently high counting rate in the panels), the muon-induced signal in TU1 would still be vetoed by the ‘previous’ event in the panel despite being vetoed due to the uncorrelated photon-induced event. Nevertheless, the omission of implementing E_{tresh} would lead to a misinterpretation of coincidence spectra due to the case, that the script would indicate, that the photon in the panel (with its low energy) was actually responsible for triggering the veto, which is not true. Furthermore, it would also result in an unnecessary increase of random coincidences. In order to build up an understanding of both the raw data and the coincidences between different detectors, a very naive approach of coincidence plots is shown in figure 4.18. The foundation for these plots in order to fulfill a coincidence condition is a time coincidence window of $t_{\text{coinc}} = 5\mu\text{s}$. Whenever two signals of arbitrary energy occur in two detectors within this coincidence window, the respective energies are plotted into the histogram. Before discussing these figures separately, it is worthwhile to make some general comments: First of all, despite an existing ‘energy’ calibration, the spectra of all panels will be shown with respect to the channel throughout the following analysis. This is due to the fact, that the subsequent analysis is entirely independent of the energy calibration, and also because of the inaccuracy of the phrase ‘energy’ (since the LCE is position-dependent, cf. section 4.4.2). A comparison to figure 4.14 is nevertheless possible, and will be discussed subsequently. Another important remark concerns the entries at the first bins. These entries are artifacts from the DAQ (cf. section 4.1), and their coincidences are entirely occurring due to random coincidences.

The upper two histograms in figure 4.18 are showing the coincidence plots in case of TU1 (x-axis), and panel #45 (y-axis). The left histogram is filled, when the panel triggered first, and the right histogram is filled, when TU1 triggered first. A comparison of the number of total events between both cases reveals, that almost all coincident events have been triggered first in panel #45. This is entirely in agreement with geometrical considerations. Due to the lower position of the TU1 detector, it is significantly more likely, that the panel is triggered first by a cosmic muon. The remaining events in the upper right panel could be due to

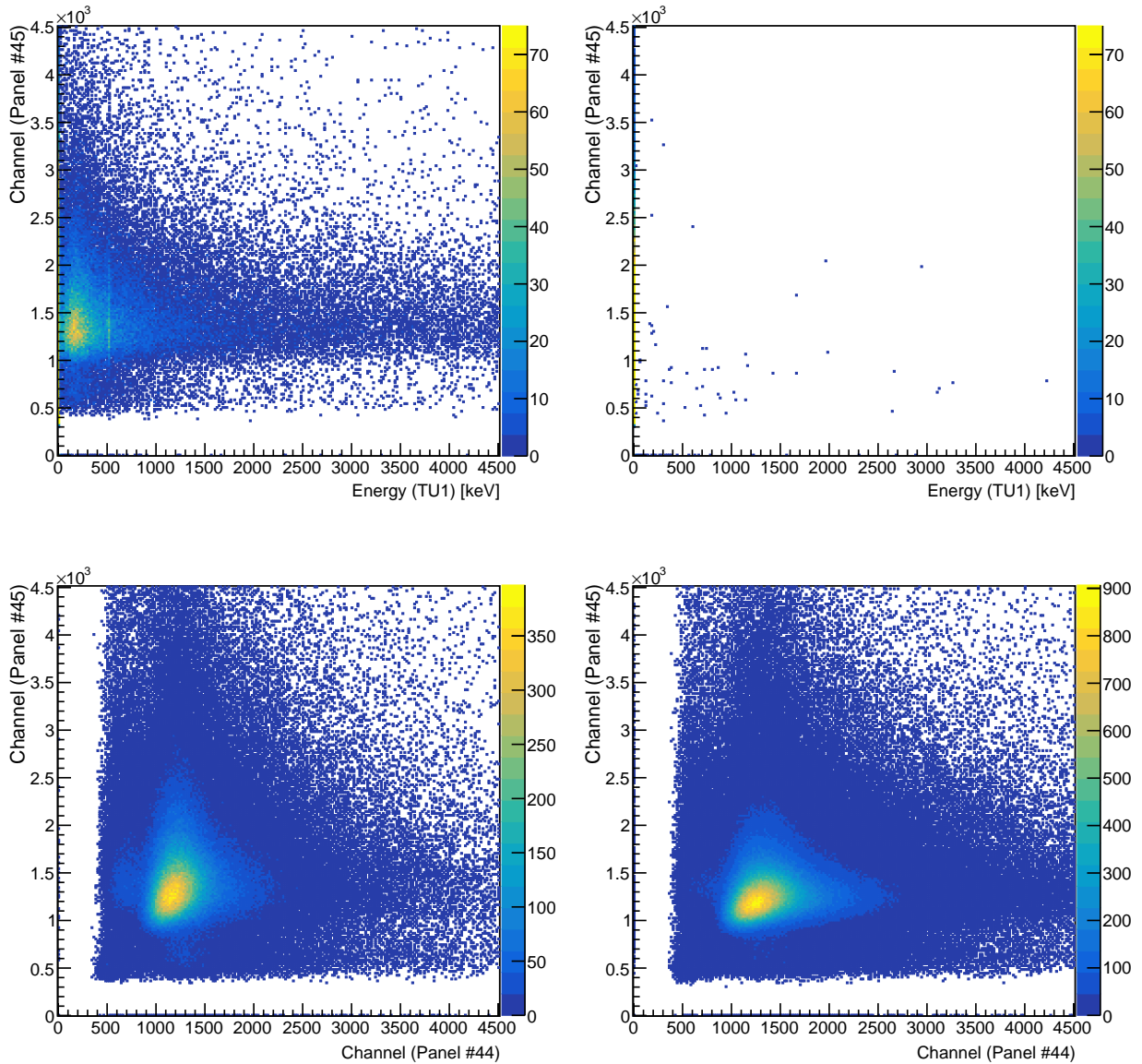


Figure 4.18: Coincidence plots between two detectors of the setup with a window of $t_{\text{coinc}} = 5\mu\text{s}$ and the statistics of 29.5 d. Upper left: Coincidence plot between panel #45 and TU1 for coincident events, which first took place in #45. Upper right: Coincidence plot between panel #45 and TU1 for subsequent events, which first took place in TU1. Lower left: Coincidence plot between panel #45 and panel #44 for subsequent events, which first took place in #45. Lower right: Coincidence plot between panel #45 and panel #44 for subsequent events, which first took place in panel #44.

random coincidences or due to the geometrical possibility of some muons, which are first triggered in TU1, and subsequently at the bottom part of panel #45. However, the same study with coincidences between TU1 and panel #16 (located directly above TU1) revealed, that these events are more likely to occur due to random coincidences.

The upper left figure further shows the result of the hard coded increase of the threshold for the scintillation panels, which is also seen for the lower two figures. Furthermore, it is more likely for muons to deposit energies below $E = 500\text{ keV}$ in TU1, than higher energies.

This is consistent with the result of the passively shielded spectrum (cf. figure 4.12), and the knowledge, that most of these remaining events should be muon-induced. Ultimately, the annihilation peak at $E = 511$ keV is also coincident with muonic-induced events in panel #45. While this could potentially also be due to random coincidences, the probability for events in TU1 being faced with a random coincidence within $5 \mu\text{s}$ due to panel #45 is below 0.01% (assuming a constant, and uncorrelated rate in the panel). Hence, the annihilation peak at $E = 511$ keV is by far dominated by true coincidences (cf. section 4.5.2 for more details).

Regarding the position of the muon peak maximum in the panel #45, the energy calibration of figure 4.14 can be used to compare it with the muon-induced maximum in figure 4.17 (Channel 1400 corresponds to an energy deposition of approximately 6500 keV). Considering, that the energy calibration is only valid for muons, which propagate through the center of panel #45 (cf. section 4.4.2), these figures are consistent with each other.

The lower two histograms in figure 4.18 are showing the coincidence plots in case of panel #44 (x-axis), and panel #45 (y-axis), which are two parallel panels facing each other in the setup (cf. figure 3.17). The coincidence condition for the left histogram is fulfilled, only when panel #45 triggered first, and the condition for the right histogram is fulfilled, only when the detector panel #44 triggered first.

Two major effects regarding these figures will be discussed in the following paragraphs with the first one being the differences in the scale of their z-axes. The binning of both figures is identical. The total number of coincidences, which first occur in panel #44 is approximately twice the number of coincidences, which first occur in panel #45. This discrepancy is consistent with the anisotropic muon flux in bunker 110 of the Felsenkeller laboratory [108, 112]. The angular distribution has an expected maximum on the zenith, but also a second maximum pointing to the tunnel entry, which leads to an increased likelihood for coincidences to be triggered first in panel #44.

The second effect in the lower two figures is dedicated to the asymmetry of both histograms. Due to the very similar fine gain of both panels, both histograms are expected to show symmetric entries in their x-axis and their y-axis. Nevertheless, in case panel #45 is triggered first, it seems that also more energy is deposited there than in panel #44. And in case panel #44 is triggered first, it seems that more energy is deposited there, than in panel #45.

This effect is most likely due to the position-dependent LCE values (cf. section 4.4.2). Both panels are orientated with the PMT being installed on the top side. If a muon deposits energy in both panels, it is more likely, that it propagates through the upper part of the first panel, and through the lower part of the second panel, which leads to this asymmetry. This is another indicator, that it is more convenient to further work with channels instead of energies. Due to these geometrical considerations, the energy deposition of one muon in two parallel panels should be exactly the same (assuming a negligible energy loss between the panel), but it certainly isn't.

After this introduction into the general understanding of coincidences in the raw data, it is now more convenient to concentrate on projections onto one of these axes instead of further working with 2D histograms. In this way, coincidence spectra can be compared to their corresponding raw spectrum or can be compared to spectra with different coincidence conditions, respectively.

4.4.5 Definition of the cut criteria for the active veto

During the last section, it became apparent, that there are two important cut criteria, which need to be optimized in order to process the raw data in a way, which efficiently reduces muon-induced events in TU1. These two criteria are the following:

- **Cut 1: A coincidence timing window t_{coinc}**

This cut describes the accepted timing interval, which two subsequent events in different detectors may have in order to be treated as ‘coincident’. During the last section, this interval was fixed to $t_{\text{coinc}} = [-5 \mu\text{s}, +5 \mu\text{s}]$ and discussed separately for its negative (the considered detector has been hit second), and positive (the considered detector has been hit first) time differences, respectively.

- **Cut 2: A threshold energy in the panels E_{thresh}**

The second cut introduces a threshold energy E_{thresh} in the scintillation panels. Events in the panels are only considered as possible candidate for a coincidence, when their energy deposition is larger than E_{thresh} .

It is crucial in the following to not only investigate the optimal combination of both cuts for each panel, but also to study their impact on the resulting spectrum. Every implementation of a cut on the raw data in the offline analysis invokes a potential risk for also cutting full-energy events from the raw data, which will then influence the reconstructed activity (cf. section 4.4.6).

In order to determine an appropriate approach on how to optimize these cut conditions, it is useful to also take the working principle of the panels into account: The utilized hardware, and software, as well as cable lengths, and the signal processing is identical for all five scintillation panels. Therefore, it will be presumed in the following, that the coincidence timing window t_{coinc} can be determined collectively for all panels. This assumption will be found later to be reasonable. However, the five scintillation panels are not matched in their fine gain, which leads to the conclusion, that E_{thresh} will be different for each panel.

This is challenging due to the fact, that the cut condition within the next section has to be optimized simultaneously for all panels in order to understand their global impact on the remaining events in the TU1 spectrum after applying these cuts. Hence, these threshold energies E_{thresh} within the panel spectra also have to be adjusted simultaneously.

As a result, a reference point was established within all coincidence spectra, which is subsequently used as starting point for the optimization procedure. The determination of these

reference points is shown in figure 4.19. The black curve shows the raw spectrum of panel #45, and the orange histogram is the result of a coincidence cut with a coincidence timing window t_{coinc} . Basically, the orange histogram is the projection of the upper left panel in figure 4.18 onto its y-axis.

The reference point for all panels was determined by searching for the minimum in the coincidence spectra of all panels by fitting a second order polynomial (blue curve in the inlet) to the region between the muon-induced, and the photon-induced part. This minimum is indicated by a red vertical line and is further called E_{min} . Due to the different fine gains, it had to be determined separately for each panel. The corresponding coincidence spectra of the other panels are shown in the appendix B.1.

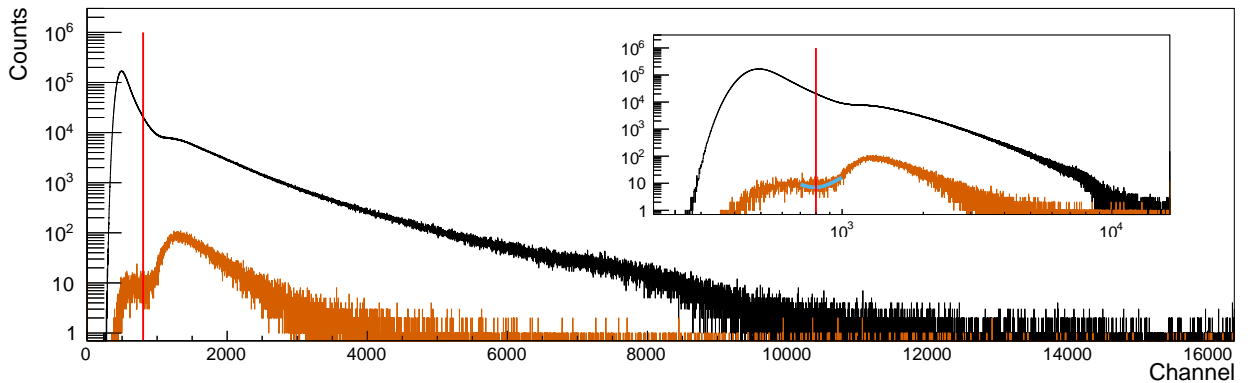


Figure 4.19: Pulse height spectra of panel #45 (cf. figure 3.17). The histogram of the raw data is shown in black, and the events surviving the final cut conditions regarding t_{coinc} are shown in orange. The inlet shows the identical data with a logarithmic x-axis. The blue line in the inlet is a second order polynomial fit in order to determine the minimum, which will be used as reference energy E_{min} . This channel is further marked with a red vertical line in both figures.

After determining E_{min} as a reference point in all panels, the optimization in the next chapter will elaborate on different threshold energies E_{thresh} with respect to this reference point (e.g. tests with 80 % of E_{min} in each panel or 120 % of E_{min} in each panels).

4.4.6 Optimization of the cut criteria for the active veto

During the last section, two cut conditions were established, which will be elaborated more thoroughly regarding their exact implementation in the following. This needs to be done by balancing out the efficiency of the muon-veto and the probability for a full-energy event to survive the cut conditions.

As shown in section 4.4.4, it is not beneficial to test symmetrical intervals for the coincidence timing window t_{coinc} . This is due to the fact that it is almost negligible to take coincidences into account, which were first triggered by TU1, and subsequently triggered by a panel. Nevertheless, it is geometrically possible for a muon to create such a coincidence, which leads to a fixed timing window for positive time differences of $5 \mu\text{s}$. This ‘right’ window is

optimized for a prompt energy deposition of a muon in both TU1 and the panel.

Hence, the cut for the timing window only needs to be optimized regarding different possible values only for the ‘left’ timing window, which allows events to first take place in the panel, and subsequently in TU1 ($t_{\text{coinc}} = [-t_{\text{left}}, +5 \mu\text{s}]$).

The second cut condition concerns the threshold energy E_{thresh} in the panels. As shown in the last section, it is convenient to adjust these thresholds simultaneously for all panels, not by shifting them by the same value to the left or to the right, but by decreasing or increasing them by the same factor with respect to the representative value of E_{min} . This second cut is therefore checking different ratios of $E_{\text{thresh}}/E_{\text{min}}$.

After establishing the two cut conditions for the active veto, their impact on two important measures will be investigated within this chapter. These two measures are the following:

- **First measure: Remaining events in a BG spectrum in [40 keV, 2700 keV]**

The first measure is the amount of remaining events in a background spectrum of TU1 after applying different combinations of $t_{\text{coinc}} = [-t_{\text{left}}, +5 \mu\text{s}]$ and $E_{\text{thresh}}/E_{\text{min}}$. The focus for the impact of the cuts on the TU1 spectrum is set to be the energy interval of [40 keV, 2700 keV]. This interval is a well established region for comparing HPGe detectors within the community of underground laboratories (cf. section 4.8). In general, the amount of remaining events are expected to become smaller for larger coincidence timing windows t_{coinc} , as well as for lower threshold energies E_{thresh} .

- **Second measure: Loss in full energy peaks during measurement of a sample**

The second measure is dedicated to the investigation of the loss of full energy events in a peak during the application of different combinations for $t_{\text{coinc}} = [-t_{\text{left}}, +5 \mu\text{s}]$ and $E_{\text{thresh}}/E_{\text{min}}$. This measure is as important as the first measure due to the fact, that e.g. an infinite large timing window would reduce the remaining events in the spectrum to $N = 0$. In general, a preferable low loss of full energy events is expected for small coincidence timing windows $t_{\text{coinc}} = [-t_{\text{left}}, +5 \mu\text{s}]$, as well as for high threshold energies $E_{\text{thresh}}/E_{\text{min}}$. This is in complete contrast to the first measure of preferring large values for $t_{\text{coinc}} = [-t_{\text{left}}, +5 \mu\text{s}]$, and small values for $E_{\text{thresh}}/E_{\text{min}}$.

The application of different combinations for $t_{\text{coinc}} = [-t_{\text{left}}, +5 \mu\text{s}]$ and $E_{\text{thresh}}/E_{\text{min}}$ is shown in figure 4.20, and figure 4.21, for the remaining events in a background run within [40 keV, 2700 keV] and the loss of events in the full energy peak of a spectrum taken with a ${}^7\text{Be}$ calibration source, respectively.

Both figures show their result in a logarithmic color coding, which is red in case of non preferable combinations of cuts, and green for preferable combinations.

As discussed previously, it is preferable for the remaining events in the BG spectrum (left figure) to choose large timing windows (e.g. 300 μs) and small threshold energies in the panel

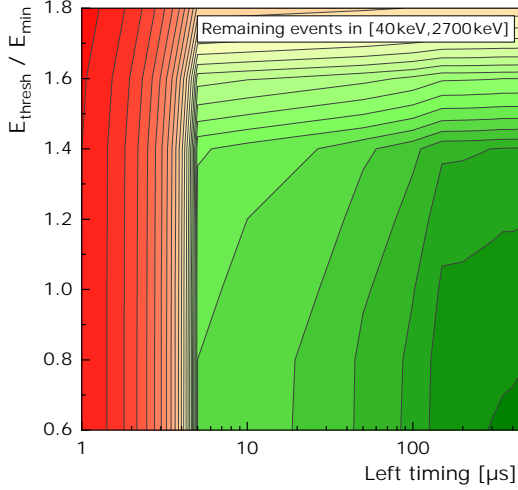


Figure 4.20: Remaining events within [40 keV, 2700 keV] of the TU1 spectrum after applying both a cut for the energy in all panels, as well as a cut on their timing windows. The color coding is shown in a logarithmic scale, and areas in green are by far more recommendable, than areas in red.

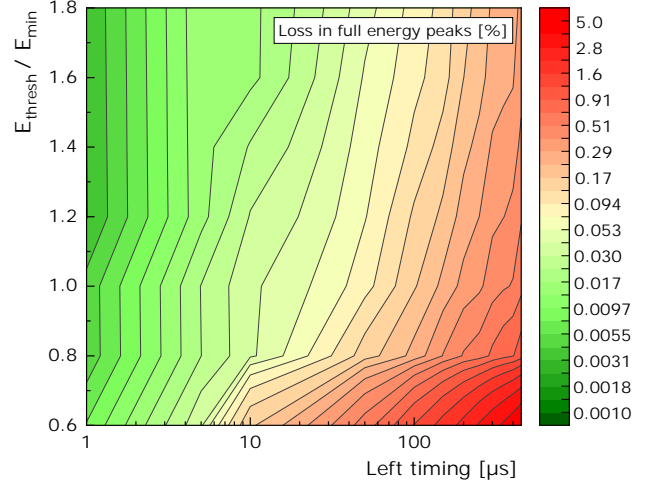


Figure 4.21: Loss of full energy events in the TU1 spectrum after applying both a cut for the energy in all panels, as well as a cut on their timing windows. The color coding is shown in a logarithmic scale, and areas in green are by far more recommendable, than areas in red.

(e.g. 60% of the minimum energy E_{\min}): Nevertheless, this region is highly disfavored by its significant loss of events in the full energy peak, which would be in the order of 5%.

Furthermore, the left figure reveals, that it is certainly not recommendable to use smaller left timing windows, than $5 \mu\text{s}$, due to the fact that this also prevents direct muon-induced events from being included in the cut. In addition, there is also a further significant benefit by taking e.g. $100 \mu\text{s}$, instead of e.g. $10 \mu\text{s}$. As an example, for $E_{\text{thresh}}/E_{\min}=1$, the additional loss of remaining events in the BG spectrum is 23%, but the loss of full energy events in a spectrum only increases from 0.02% to 0.16%. The benefit of significantly reducing the amount of remaining events therefore still outweighs the disadvantage of losing full energy events due to included random coincidences by far.

Instead of further describing the subsequent optimization process more extensively, the following paragraphs will use the final combination of cuts and further elaborate on the reason, why this combination is chosen. The effect of these finally used cut criteria is shown in the figures 4.22 and 4.23 for the raw spectrum of panel #45, as well as its corresponding timing histogram, respectively. Both figures show the raw data in black, and the coincident data (based on the final cut configuration) in orange, respectively. The data, which is excluded from the coincidence condition, is shown as grey areas in the respective figure. Due to the fact, that the shapes of the spectra in figure 4.22 were already discussed in figure 4.19, the main focus will lie on 4.23 in the following.

Before going into detail regarding this timing plot, there is one important additional remark: In order to resolve the coincidences as much as possible from the random coincidences, a

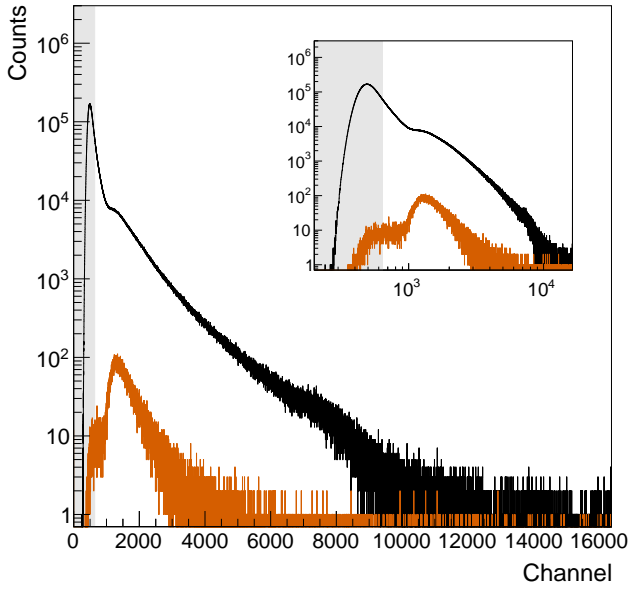


Figure 4.22: Pulse height spectra of panel #45 (cf. figure 3.17). The histogram of the raw data is shown in black, and the events surviving the final cut conditions regarding t_{coinc} are shown in orange. The grey area is excluded by the cut for E_{thresh} . The inset shows the identical data with a logarithmic x-axis.

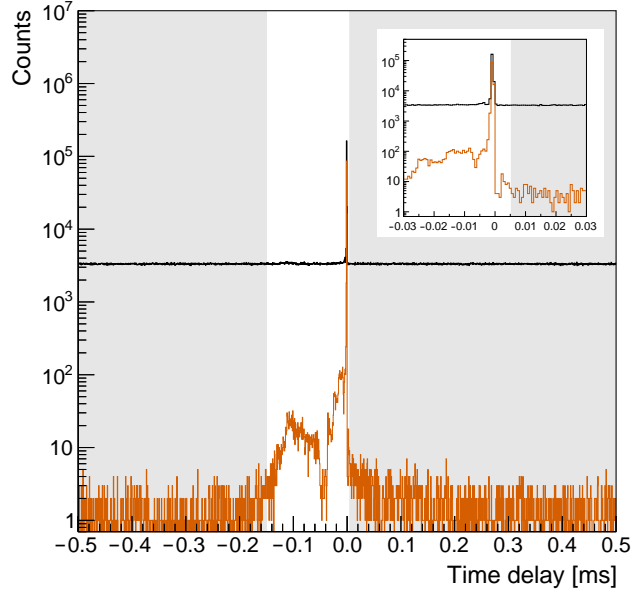


Figure 4.23: Time difference between events of TU1 and panel #45 (cf. figure 3.17). If the event triggered panel #45 first, the time difference is negative. The histogram of the raw data is shown in black, and the events surviving the final cut conditions regarding E_{thresh} are shown in orange. The grey area is excluded by the cut for t_{coinc} . The inset shows a closeup of the peak area.

third cut condition was established, which is a threshold energy of 20 keV for events in the TU1 detector. Due to both the very low hard coded threshold of TU1 in the digitizer, as well as the ultra-low counting rate, the ratio between noise (i.e. $E \leq 20$ keV) and physical events (i.e. $E > 20$ keV) is comparatively large. Due to the fact, that noise events in TU1 are certainly not triggered by muons (cf. figure 4.18), they are excluded from the coincidence in order to reveal even more rare coincidence events, like so-called ‘delayed coincidences’.

The vast majority of coincident events take place within $t_{\text{coinc}} = [-5 \mu\text{s}, 0 \mu\text{s}]$. These coincidences are already apparent in the raw data (black), and subsequently lead to the dark red area of unpreferable values in figure 4.20. By theoretically excluding this peak within $t_{\text{coinc}} = [-5 \mu\text{s}, 0 \mu\text{s}]$ from the coincidence condition, almost the entire amount of muon-induced events in TU1 would not be triggered at all. But in addition, also the previous statement becomes more comprehensible, where it was stated, that even larger time differences for the negative values seem to be very beneficial. As shown in figure 4.23, there is a significant amount of coincidences, which is not in the prompt peak within $t_{\text{coinc}} = [-5 \mu\text{s}, 0 \mu\text{s}]$, but delayed with values up to $t_{\text{left}} = -150 \mu\text{s}$. The origin of these events will be discussed in the upcoming section, but it already becomes apparent, that it is beneficial to include these delayed coincidences, as far as the increasing of the timing interval does not lead to large

losses of full energy events in subsequent measurements.

This loss can now be investigated with the results from figure 4.21. By fixing the timing window to $t_{\text{coinc}} = [-150 \mu\text{s}, 5 \mu\text{s}]$, an appropriate value for $E_{\text{thresh}}/E_{\text{min}}$ has to be chosen in order to limit these losses in subsequent full energy peaks.

In order to discuss the entire complexity of this decision, one fact is important to notice: From the perspective of sensitivity, one could argue, that it is always beneficial to choose smaller values for $E_{\text{thresh}}/E_{\text{min}}$, as long as the percentual decrease in remaining events is steeper, than the percentual increase the loss of full energy events. And in fact, this loss in the full energy peak still increases slightly slower than the subsequent decrease of remaining events within the TU1 spectrum. This is a convincing indicator, that there are still some muon-induced coincidences even below $E_{\text{thresh}}/E_{\text{min}} = 0.6$, which are worthwhile taking into account.

Nevertheless, it has been decided, that the loss of full energy events should not exceed 0.5 %, due to the fact, that it is not appropriate to cut significant amounts of the signal during the search for rare event physics. Due to limited measurement times for each sample, it gets apparent, that at a certain point, it is more important to measure as much signal as possible instead of reducing the background as much as possible.

To elucidate this important problem, a rough calculation shall be noted here, which is based on realistic measurement conditions for upcoming measurements on TU1. Lets assume a sample of 200 μBq , which emits a 800 keV γ -ray line in 10 % of its decays. When further assuming roughly a full energy peak efficiency of 10 %, then a measurement time of approximately one week is needed in order to measure one single event in the full energy peak.

Due to the fact that these numbers reflect more or less possible scenarios for the desired sensitivity, it is therefore much more convenient to determine a cut condition, which does influence the full energy peak as little as possible, instead of reducing the remaining events even further in order to maximize the sensitivity as much as possible. In summary, by performing realistic measurements with TU1, the usual limitation will not be the sensitivity of the detector, but the available measuring time, which is worth putting in to the measurement.

In summary, this leads to the final combination of cut conditions between signals in the TU1 detector and signals within the scintillation panels:

- Coincidence timing window: $t_{\text{coinc}} = [-150 \mu\text{s}, +5 \mu\text{s}]$
- Threshold energy in each panel: $E_{\text{thresh}} = 0.8 \cdot E_{\text{min}}$
- Threshold energy in the TU1: $E_{\text{thresh}} = 20 \text{ keV}$

It is crucial to emphasize, that the loss of full energy events due to the veto, as shown in figure 4.21, neither depends on the activity of the sample, nor on the energy of the emitted γ -rays. This is due to the fact, that the loss of full energy events can solely be thought of as fraction in time, where the panels are intervening the data acquisition on the TU1

detector. This loss in events due to the active veto therefore solely depends on the counting rate in the panels, their trigger hold-off (cf. section 2.3), the threshold energy E_{thresh} and the coincidence timing interval t_{coinc} .

Hence, as long as the muon panels further work properly, and its pulse processing remains unchanged, the loss in full energy events, and subsequently the veto efficiency, are therefore fixed values for future measurements.

The most interesting next step is undoubtedly the investigation of these cut conditions on the passively shielded spectrum of TU1 in order to reveal the impact of excluding all coincidences from the raw data. Nevertheless, there are two major sections, which will be discussed beforehand, with the next one investigating the origin of delayed coincidences, which were introduced in figure 4.23.

4.4.7 Origin of prompt and delayed coincidences in TU1

The timing histograms (as shown in figure 4.23 in case of the coincident events between panel #45 and TU1) are highly similar regarding their structures for all panels. They all show the prompt signal around $0 \mu\text{s}$, as well as some delayed signals between $-150 \mu\text{s}$, and $-5 \mu\text{s}$, respectively. In order to compare the coincidence spectrum of TU1 with the corresponding coincidence spectrum of the panel, this chapter will keep focusing only on coincidences between TU1 and panel #45. The corresponding spectra, which show the coincidences between TU1, and any other detectors are shown in the appendix B.2.

The time difference between two subsequent events in panel #45, and TU1 (cf. figure 4.23), generally shows an expected result. Nevertheless, there are some rare additional events, which seem to be more retarded in time, than expected by two purely muon-induced, subsequent interactions in both detectors. The entire region of coincident events seems to span a timing interval of $[-150 \mu\text{s}, 0 \mu\text{s}]$ with the peak region being at $[-5 \mu\text{s}, 0 \mu\text{s}]$.

For the subsequent analysis within this section, this timing interval of $[-150 \mu\text{s}, 0 \mu\text{s}]$ is shown again in figure 4.24 with a finer binning. Furthermore, the timing shows three coincidence areas, which seem to be independent of each other. The plot is therefore divided into three sections (separated by two red vertical lines), which will be further investigated independently from each other.

4.4.7.1 Prompt coincidences: The timing interval of $[-5 \mu\text{s}, 0 \mu\text{s}]$

This so-called prompt area in figure 4.24 around $[-5 \mu\text{s}, 0 \mu\text{s}]$ shows the most intuitive result. The prompt coincidence peak is most likely due to muons, which propagate through both the panel, and the TU1 and subsequently deposit energy in both detectors.

The corresponding coincidence spectra of TU1 and panel #45 are shown in figure 4.25, and figure 4.26, respectively. The raw spectra are shown in black, and the events, which fulfill the timing interval of $[-5 \mu\text{s}, 0 \mu\text{s}]$ are filled into the orange histograms. Despite only

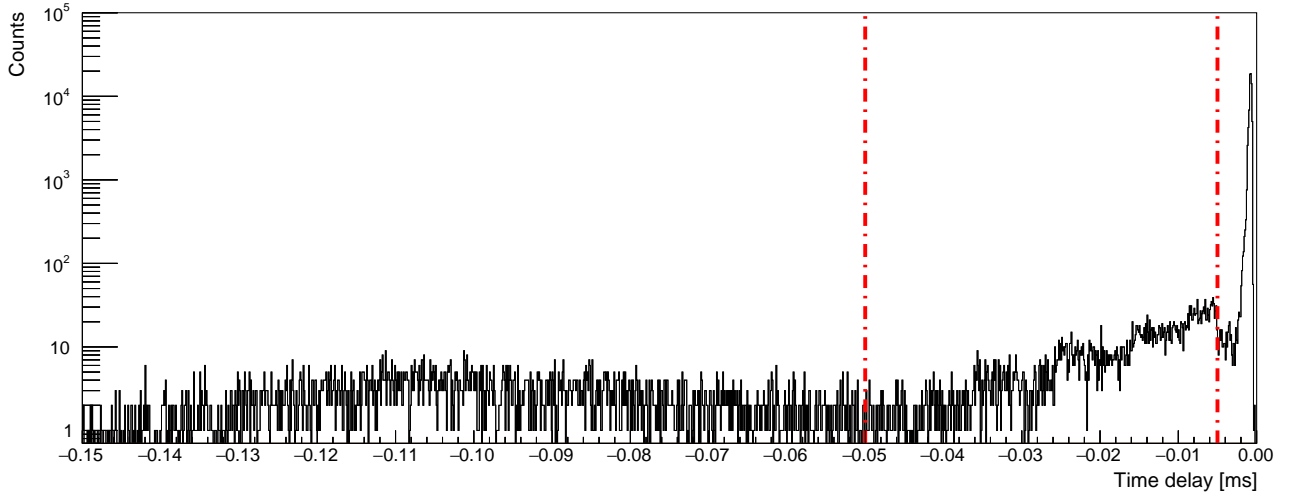


Figure 4.24: Time difference between events of TU1 and panel #45 (cf. figure 3.17). Only negative values are shown, which is equivalent to a coincidence, which first occurred in the panel, and subsequently in TU1. The figure is the result of figure 4.23 by solely displaying the negative part of the final coincidence timing interval of $[-150 \mu\text{s}, +5 \mu\text{s}]$. The red vertical lines indicate the division of the three areas $[-150 \mu\text{s}, -50 \mu\text{s}]$, $[-50 \mu\text{s}, -5 \mu\text{s}]$, and $[-5 \mu\text{s}, 0 \mu\text{s}]$.

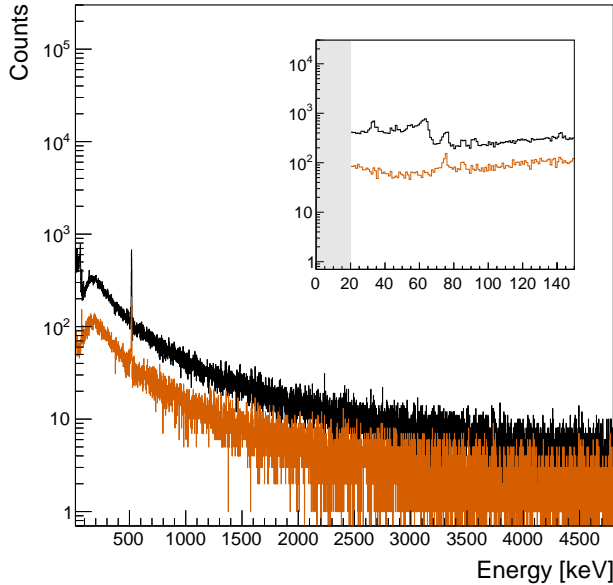


Figure 4.25: Pulse height spectra of the raw TU1 data (black), and for a coincidence timing window of $[-5 \mu\text{s}, 0 \mu\text{s}]$ regarding events in panel #45. The grey area is excluded by the cut for E_{thresh} .

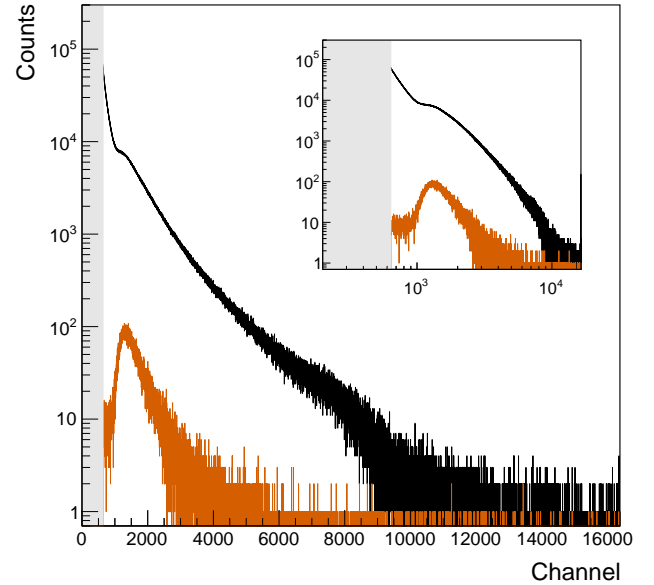


Figure 4.26: Pulse height spectra of the raw data of panel #45 (black), and for a coincidence timing window of $[-5 \mu\text{s}, 0 \mu\text{s}]$ regarding events in TU1. The grey area is excluded by the cut for E_{thresh} .

showing the coincidences between TU1, and one of the five scintillation panels, the amount of coincident events (orange) is already comparable to the total amount of events (black) in the raw spectrum of TU1. This supports the earlier statement, that most of the events in

the passively shielded spectrum of TU1 are muon-induced²¹.

While the high energetic part of the coincident TU1 spectrum (orange histogram in figure 4.25) follows the trend of the passively shielded spectrum, there seems to be a discrepancy in their shape for low energies when comparing the orange and the black histogram in the inlet of figure 4.25). As shown in the following paragraphs, this discrepancy is due to the delayed coincidences, which are not triggered yet with $t_{\text{coinc}} = [-5 \mu\text{s}, 0 \mu\text{s}]$.

4.4.7.2 Delayed coincidences: The timing interval of $[-50 \mu\text{s}, -5 \mu\text{s}]$

The area of delayed coincidences in figure 4.24 around $[-50 \mu\text{s}, -5 \mu\text{s}]$ approximately follows an exponential drop towards larger time delays. The corresponding coincidence spectra of TU1 and panel #45 for this timing interval are shown in figure 4.27, and figure 4.28, respectively. The corresponding raw spectra are again shown in black, and the events, which fulfill the timing interval of $[-50 \mu\text{s}, -5 \mu\text{s}]$ are filled into the orange histograms.

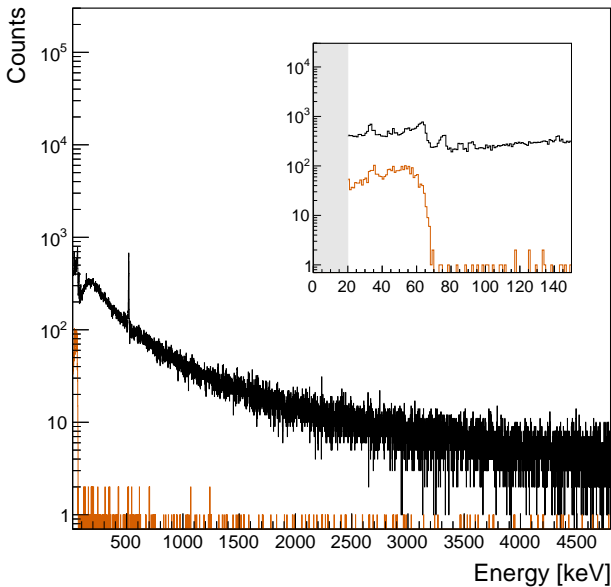


Figure 4.27: Pulse height spectra of the raw TU1 data (black), and for a coincidence timing window of $[-50 \mu\text{s}, -5 \mu\text{s}]$ regarding events in panel #45. The grey area is excluded by the cut for E_{thresh} .

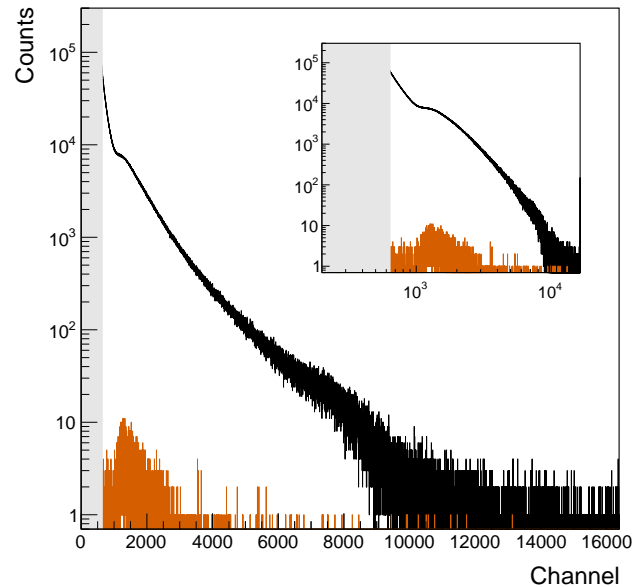


Figure 4.28: Pulse height spectra of the raw data of panel #45 (black), and for a coincidence timing window of $[-50 \mu\text{s}, -5 \mu\text{s}]$ regarding events in TU1. The grey area is excluded by the cut for E_{thresh} .

Comparing the raw spectrum of the panel (black histogram in figure 4.28), and its coincidence spectrum (orange histogram in figure 4.28), it already can be excluded, that the delayed coincidences are due to uncorrelated photon-induced events. If this effect would be due to random coincidences or time-delayed overshoots in the analog signals, the coincidence

²¹The corresponding coincidence plots, which compare the passively shielded spectrum to coincident events in **any** of the five panels, are shown in the appendix B.2 in figure B.5. Despite being highly important for the analysis, these figures would be counter-intuitive in this section. This is due to the fact, that their corresponding panel spectra can not be shown since the histograms have different fine gains.

spectrum would be similar in shape to the raw spectrum. Nevertheless, below the muon-induced peak, the black curve rises for lower energies due to photon-induced events, while the coincidence spectrum remains at a low level. This is already a strong indicator, that the delayed effects in TU1 are definitely muon-induced, which is further supported by its similarity to the corresponding coincidence spectrum of the prompt signals (orange histogram in figure 4.26).

Having a look at the corresponding spectra from TU1, it is apparent, that these delayed signals mainly result in a low energetic continuum, which rapidly breaks off at approximately 70 keV. Higher energies are appearing only rarely in the coincidence plot (orange histogram in figure 4.27), which could e.g. be due to random coincidences or due to other rare delayed effects, which can not be further investigated due to their low statistics.

The corresponding coincidence plots, which compare the raw spectrum to coincident events in any of the five panels are again shown in the appendix B.2 in figure B.6.

4.4.7.3 Delayed coincidences: The timing interval of $[-150 \mu\text{s}, -50 \mu\text{s}]$

The area of delayed coincidences in figure 4.24 around $[-150 \mu\text{s}, -50 \mu\text{s}]$ approximately follows a Gaussian shape with a mean value around $-100 \mu\text{s}$. The corresponding coincidence spectra of TU1 and panel #45 for this timing interval are shown in figure 4.29, and figure 4.30, respectively. The raw spectra are again shown in black, and the events, which fulfill the timing interval of $[-150 \mu\text{s}, -50 \mu\text{s}]$ are filled into the orange histograms.

The coincidence histogram of the panel spectrum (orange histogram in panel 4.30) is comparable to the previous two equivalents. It is therefore also here taken as a reason to assume, that the delayed coincidences in TU1 within $[-150 \mu\text{s}, -50 \mu\text{s}]$ are most likely muon-induced signals.

Comparing the corresponding coincidence spectrum from TU1 (orange histogram in the inlet figure 4.29) to the previous case, it is apparent, that these delayed signals result in low energetic peak structures around 33 keV and 60 keV, respectively. Higher energies again occur only rarely in the coincidence plot (orange histogram in figure 4.29).

The corresponding coincidence plots, which compare the raw spectrum to coincident events in any of the five panels are again shown in the appendix B.2 in figure B.7.

4.4.7.4 Time delay dependency of energy depositions in TU1

While it was shown in the previous three paragraphs, that the delayed coincidences in fact do not lead to comparable energy depositions in TU1, their actual origin is still not resolved yet.

In order to extend the information content regarding the coincident events, the time difference between coincident events with respect to the energy deposition in TU1 is plotted in figure 4.31. While during the previous sections, the focus was only on coincidences between

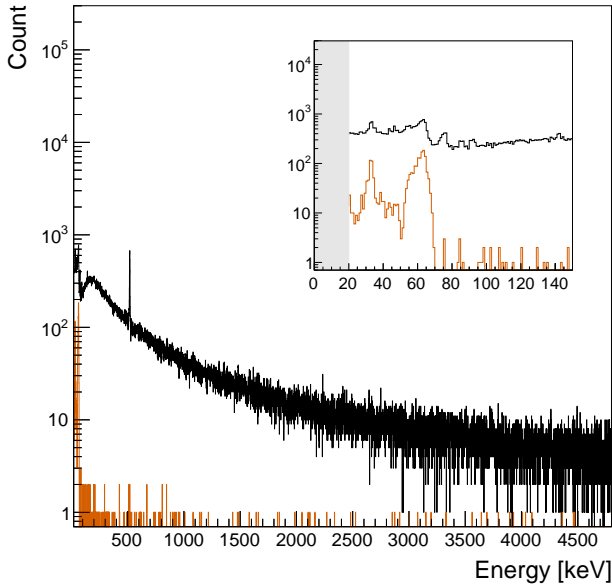


Figure 4.29: Pulse height spectra of the raw TU1 data (black), and for a coincidence timing window of $[-150 \mu\text{s}, -50 \mu\text{s}]$ regarding events in panel #45. The grey area is excluded by the cut for E_{thresh} .

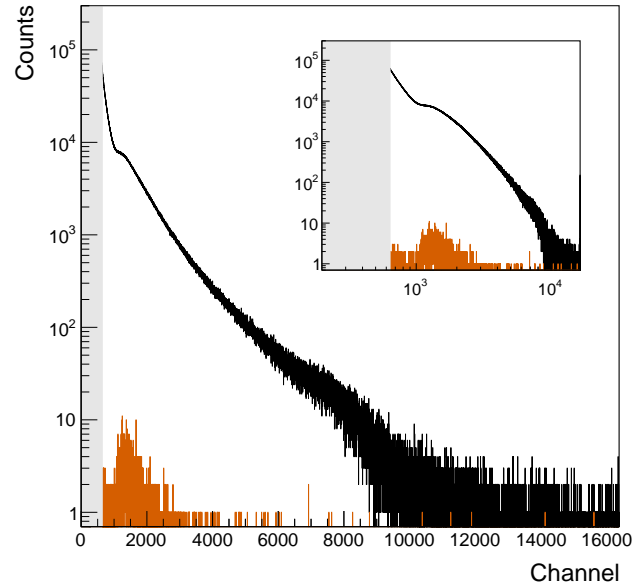


Figure 4.30: Pulse height spectra of the raw data of panel #45 (black), and for a coincidence timing window of $[-150 \mu\text{s}, -50 \mu\text{s}]$ regarding events in TU1. The grey area is excluded by the cut for E_{thresh} .

TU1 and panel #45, it may be noticed here, that figure 4.31 shows the coincidences between TU1 and **any** other panel. This is due to the fact, that the panel spectra themselves are not relevant, but only the spectra of TU1.

This figure is shown for the case that the energy deposition first occurred in one of the panels (left figure) and the case that the energy deposition first occurred in TU1 (right figure). The projection of these two plots onto the x-axis therefore results in coincidence spectra of the respective timing interval (cf. e.g. figure 4.25), while the projection onto the y-axis results in the corresponding timing spectra (cf. figure 4.23).

Both figures are plotted with a logarithmic x-axis in order to reveal their low-energetic features. The three timing intervals from the previous sections are separated by horizontal dashed, red lines. Furthermore, the z-axis is zoomed into the interval of $[0, 160]$ events per bin, despite exceeding 500 events per bin in the region of the prompt coincident events in $[-5 \mu\text{s}, 0 \mu\text{s}]$ of the left figure.

By investigating the left figure, it again becomes apparent, that the vast majority of muon-induced coincidence events in TU1 occur within $[-5 \mu\text{s}, 0 \mu\text{s}]$, which was already discussed in section 4.4.7.1. While its narrow timing window does not allow any further interpretations on the corresponding events, there are undoubtedly multiple interesting features for both delayed timing intervals $[-50 \mu\text{s}, -5 \mu\text{s}]$, and $[-150 \mu\text{s}, -50 \mu\text{s}]$.

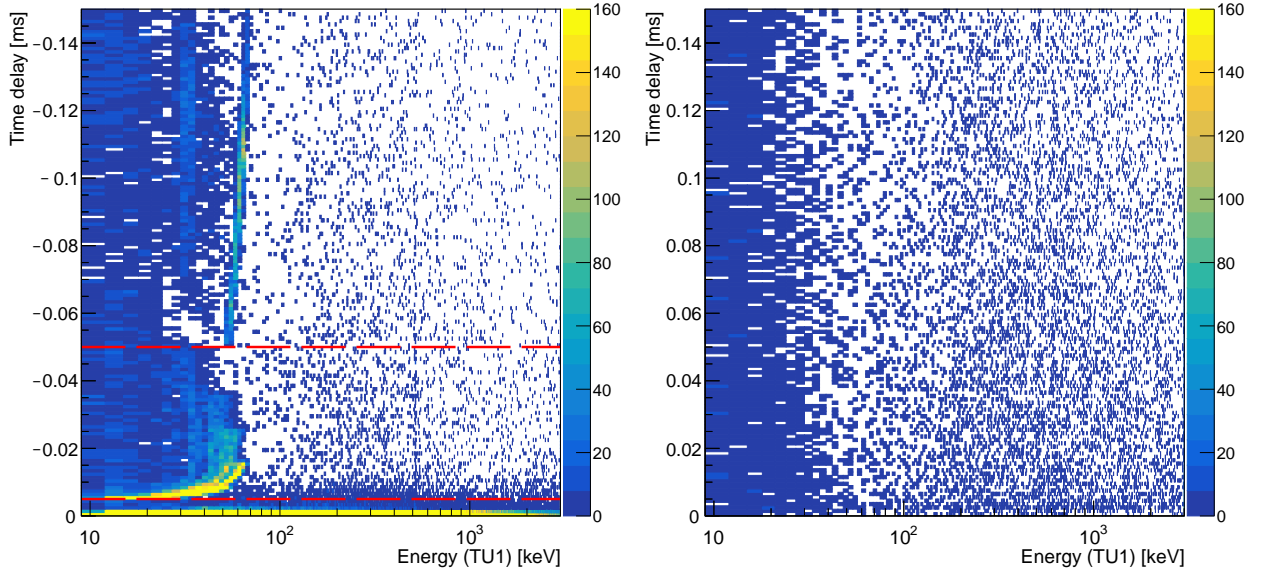


Figure 4.31: Left: Time delay between two subsequent events, which first occur in one of the panels, and then in TU1 with respect to the energy deposition in TU1. It shows the actual timing interval of $t_{\text{coinc}} = [-150 \mu\text{s}, 0 \mu\text{s}]$, which is also used for the final cut. Right: Time delay between two subsequent events, which first occur in TU1, and then in one of the panels with respect to the energy deposition in TU1. For the sake of comparability, the right figure also shows $t_{\text{coinc}} = [0 \mu\text{s}, +150 \mu\text{s}]$, despite only using $t_{\text{coinc}} = [0 \mu\text{s}, +5 \mu\text{s}]$ for the final cut²².

The features in the left panel of figure 4.31 can be summarized as follows:

- The energy deposition at 511 keV occurs in all three coincidence timing windows
- The comparatively small peaks at 75 keV and 85 keV in the pulse height spectrum of TU1 for a coincidence timing window of $[-5 \mu\text{s}, 0 \mu\text{s}]$ (cf. figure 4.25) are not related to effects at larger coincidence timing windows. This is an independent feature, which solely occurs in the prompt timing region.
- Both delayed timing intervals reveal an energy independent effect, which deposits approximately 33 keV in TU1.
- Within a timing interval of $[-30 \mu\text{s}, -5 \mu\text{s}]$ and an energy deposition in TU1 of $[10 \text{ keV}, 70 \text{ keV}]$, there is a correlation between the time delay and the energy deposition in TU1.
- Within a timing interval of $[-150 \mu\text{s}, -50 \mu\text{s}]$ there is a similar feature ranging from 50 keV to 70 keV where the energy deposition in TU1 seem to correlate with the time delay between panel and TU1. In this case, there is a local maximum at $-110 \mu\text{s}$ and 60 keV.

It is worthwhile mentioning, that all of these described effects are also apparent, when plotting the respective figures for each panel separately. These plots can be found in the appendix (cf. section B.3) and further support a systematical physical origin. In order to

²²Due to the comparatively low total amount of coincidences after optimization of the panel thresholds, also the coincident events below $E = 20 \text{ keV}$ can be shown.

complete the picture, the corresponding plots with respect to the energy deposition in the respective scintillation panel are shown in the appendix B.4.

Peak at 511 keV for all timing intervals During the decay of positively charged muons, positrons are emitted, which can subsequently lead to an energy deposition of their 511 keV annihilation photons in TU1. However, it is unlikely that there are delayed energy deposition of 511 keV in the order of 100 μs in TU1 stemming from muon decay due to three reasons: The direct muon-induced events in TU1 are only delayed by $< 5 \mu\text{s}$ (also including cable length etc.), the positron annihilation life-time is far below the order of microseconds and the half-life of muons is $T_{1/2} = 2.2 \mu\text{s}$.

Due to the fact that there are only approximately 100 coincident events at 511 keV within 90 days within the timing window of $[-150 \mu\text{s}, -20 \mu\text{s}]$, it is also possible, that these entries are based on random coincidences. The spectrum of random coincidences should mimic the shape of the raw spectrum, which further supports this statement (cf. also section 4.10).

Peaks at 75 keV and 85 keV in the prompt coincidence spectrum Within the coincidence spectrum for prompt coincidences (cf. figure B.5 for better statistic than in figure 4.25), there is a broader peak at 75 keV with a left tail and a narrow peak at 85 keV. These prompt signals in TU1 are a strong indicator for lead X-rays. The X-ray energies for $K_{\alpha,1}$, $K_{\alpha,2}$, and $K_{\beta,1}$ are at $E = 74.97 \text{ keV}$, $E = 72.80 \text{ keV}$, and $E = 84.94 \text{ keV}$ with relative intensities of $I = 100\%$, $I = 60\%$, and $I = 23\%$, respectively. The relative intensities, as well as the peak positions therefore match precisely the expectations of lead X-rays.

While it is intuitive to assume, that these lead X-rays are due to the surrounding lead castle, this can be excluded by calculating the attenuation within the copper between lead castle and TU1. Within 10 cm of copper, a photon beam of $E = 85 \text{ keV}$ gets attenuated down to a remaining intensity of $2 \cdot 10^{-26}$. It is therefore highly plausible to assume, that there are remaining lead contaminations in the inner volume - most likely within TU1 itself.

However, muon-induced X-rays stemming from other materials within the inner volume (copper, aluminum, germanium etc.) are well below 20 keV and therefore not measurable.

Correlation between time delay and energy deposition There is an agglomeration of coincident events, where a muon deposits a usual amount of energy in one of the scintillation panels (cf. figure B.9), and within 5 μs to 30 μs , there is an energy deposition in TU1 of 10 keV to 70 keV. Furthermore, there is a correlation between time delay and deposited energy, and it seems that there are multiple paths of correlation, with some of them ending at lower energies, than others (cf. figure 4.31 for the sum of all panels and section B.3 for each panel separately).

Any correlation between time delay and deposited energy is an indicator for neutrons or heavy charged particles being involved in this process. While fast neutrons (with larger

energies) need to be thermalized first (resulting in time delay) in order to enhance scattering processes with energy transfer, charged particles can also be faced with this correlation due to ionization via Bethe-Bloch, which delays the final energy deposition also in correlation to their energy.

At these energies, elastic scattering is the dominant interaction channel for neutrons, which can easily be tested as a possible origin of these features: During one elastic scattering process, the maximal energy transfer of a neutron onto the nucleus is given as elaborated in equation 35.

$$X = \frac{4Mm_n}{(M + m_n)^2} \cdot \cos(\beta)^2 \quad (35)$$

This ratio of energy transfer X only depends on the mass of the neutron m_n , the mass of the target nucleus M and the recoil angle β . In case of the germanium crystal, fast neutrons can interact with a variety of isotopes ranging from ^{70}Ge to ^{76}Ge . According to equation 35, the maximum energy transfer in germanium ranges between 5.7 % and 5.2 % of the initial neutron energy, respectively.

The muon-induced neutron flux at Felsenkeller is known from simulations and measurements and has a maximum around 1 MeV [111]. Regarding a 1 MeV neutron, the recoil nucleus after elastic scattering would receive 52 keV to 57 keV in case of a recoil scattering angle of 0° depending on the isotope. Due to the fact, that the muon-induced neutron flux around 1 MeV is also not monoenergetic, there is an additional straggling of the final deposited energy.

Independent of the isotope, the recoil nucleus can then have angles between 0° and 90° , which are equally probable in first order. For each isotope, this results in energy transfers between 0 keV ($\beta = 90^\circ$) and the maximum energy transfer with a time delay, which correlates with the final energy deposition.

4.5 The actively shielded TU1 detector

The passive shielding of the TU1 detector, as well as the resulting background spectrum was introduced in section 4.3. After optimizing the active muon veto in section 4.4, the following section will now reveal the impact of the active muon veto on the data of the passively shielded TU1 detector.

4.5.1 The pulse-height spectrum of a long-term background measurement

The impact of different components of the passive shielding onto the counting rate of TU1 was introduced in figure 4.12 with the final configuration being represented by the red histogram. This histogram is shown again in figure 4.32 in black.

The orange histogram is the result of applying the final cut criteria (coincidence timing

window $t_{\text{coinc}}=[-150\ \mu\text{s},+5\ \mu\text{s}]$, the threshold energy in the panels $E_{\text{thresh}}=0.8\cdot E_{\text{min}}$, and threshold energy in TU1 of $E=20\ \text{keV}$) on the passively shielded spectrum. There are two important issues, when comparing these two spectra. The first one is the similarity of the respective slopes of their continua. Due to the counting rate in the passively shielded spectrum being dominated by muon-induced events, as well as the non perfect coverage of active scintillation material around TU1, it is reasonable to assume, that the actively vetoed spectrum also still contains muon-induced events. This is also supported by the partly remaining annihilation peak at 511 keV. The second issue addresses the exposed peaks in the vetoed spectrum. These peaks, as well as their Compton continua were covered in the passively shielded spectrum by the continuous muon-induced background, and are now contributing to the remaining counting rate in a relevant amount.

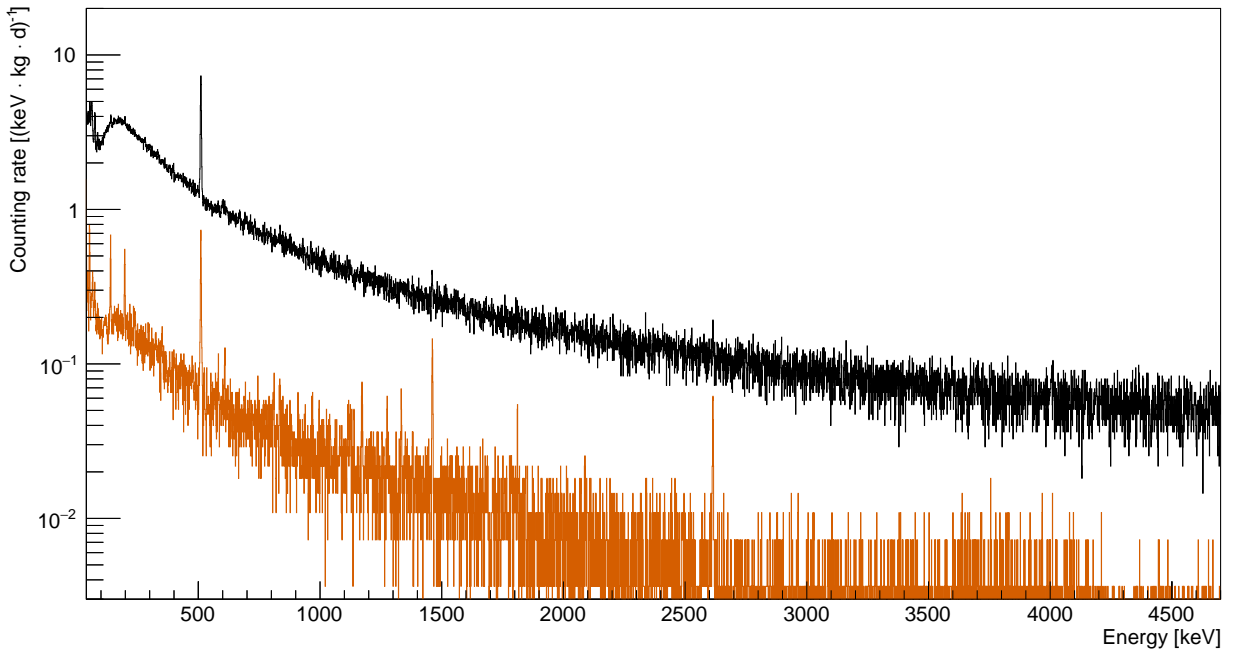


Figure 4.32: Comparison of the counting rates for the passively shielded spectrum (black) and the actively vetoed spectrum (orange) of the TU1 detector. For the active veto the cut conditions elaborated in section 4.4 are used. The data is shown for a total measuring time of 90 d.

Table 4.2: Comparison of the counting rate for the unshielded, the passively shielded and the (additionally) actively shielded stages of TU1 in the interval of [40 keV, 2700 keV]. The measurement time t_{meas} , as well as the improvement factors are also given.

Detector stage	t_{meas} [d]	Counting rate [$\text{kg}^{-1}\text{d}^{-1}$]	Improvement factor to previous stage
TU1 in bunker 110 without shielding	6.8	8603400 ± 600	
Passive shielding without active veto	90.0	1982 ± 3	≈ 4300
Passive shielding with active veto	90.0	116 ± 1 ²³	≈ 17

In order to compare different low-level HPGe detectors, as well as different stages of shielding

²³This value is from the corresponding publication [2]. For more recent values, see equation 36 to 38.

of a HPGe detector, it is an established procedure, to integrate the counting rate within [40 keV, 2700 keV] and normalize it to the mass of the active detector volume.

The comparison for TU1 regarding its unshielded state, its passively shielded stage, and the actively vetoed stage is shown in table 4.2. In total, the passive shielding and the active veto are attenuating the counting rate by a factor of approximately 74000.

4.5.2 Analysis on the remaining background components

Within the actively vetoed background spectrum, a total of 16 γ -ray lines were identified, and have been studied subsequently regarding their origin and their counting rate. An expanded view on the background spectrum is presented in figure 4.33 which shows the histogram in approximately 500 keV intervals per panel. Most of the identified γ -ray lines are located within the lower half of the spectrum (40 keV-1500 keV), and only one γ -ray line was identified in the upper half (1500 keV-3000 keV).

A list of the identified γ -ray lines, as well as their origin, and their counting rate is shown in table 4.3. The origin of these remaining γ -ray lines can be divided into four different subgroups, namely γ -rays from primordial nuclei, γ -rays from neutron activation, γ -rays from lab-specific nuclei and the remaining annihilation peak at 511 keV.

Table 4.3: Remaining γ -ray lines in the actively vetoed background spectrum of TU1. Their energy, the corresponding nuclide, their origin, and their counting rate is shown. This table is similar to the table published in [2]. The number of the peak structure is related to the enumeration in figure 4.33.

#	Energy [keV]	Nuclide	Subgroup	Origin	Count rate [kg ⁻¹ d ⁻¹]
1	52.0 - 55.6	^{73m} Ge	Neutron activation	⁷² Ge(n, γ) & ⁷⁴ Ge(n,2n)	1.28(19)
2	63.9 - 66.7	^{73m} Ge	Neutron activation	⁷² Ge(n, γ) & ⁷⁴ Ge(n,2n)	0.38(17)
3	72.8 - 75.0	Pb K _{α} , K _{β}	Primordial nuclide		0.33(12)
4	139.7	^{75m} Ge	Neutron activation	⁷⁴ Ge(n, γ) & ⁷⁶ Ge(n,2n)	1.34(16)
5	198.4	^{71m} Ge	Neutron activation	⁷⁰ Ge(n, γ) & ⁷² Ge(n,2n)	1.00(15)
6	295.2	²¹⁴ Pb	Primordial nuclide	²³⁸ U decay chain	0.19(12)
7	351.9	²¹⁴ Pb	Primordial nuclide	²³⁸ U decay chain	0.29(11)
8	511		Annihilation	e^+e^-	2.64(13)
9	583.2	²⁰⁸ Tl	Primordial nuclide	²³² Th decay chain	0.14(8)
10	609.3	²¹⁴ Bi	Primordial nuclide	²³⁸ U decay chain	0.21(8)
11	834.8	⁵⁴ Mn	Neutron activation	⁵⁴ Fe(n,p) ⁵⁴ Mn	0.17(7)
12	1173.2	⁶⁰ Co	Neutron activation	⁶³ Cu(n, α) ⁶⁰ Co	0.18(5)
13	1274.5	²² Na	Lab-specific nuclide		0.20(5)
14	1332.5	⁶⁰ Co	Neutron activation	⁶³ Cu(n, α) ⁶⁰ Co	0.16(5)
15	1460.8	⁴⁰ K	Primordial nuclide		0.49(6)
16	2614.5	²⁰⁸ Tl	Primordial nuclide	²³² Th decay chain	0.22(4)

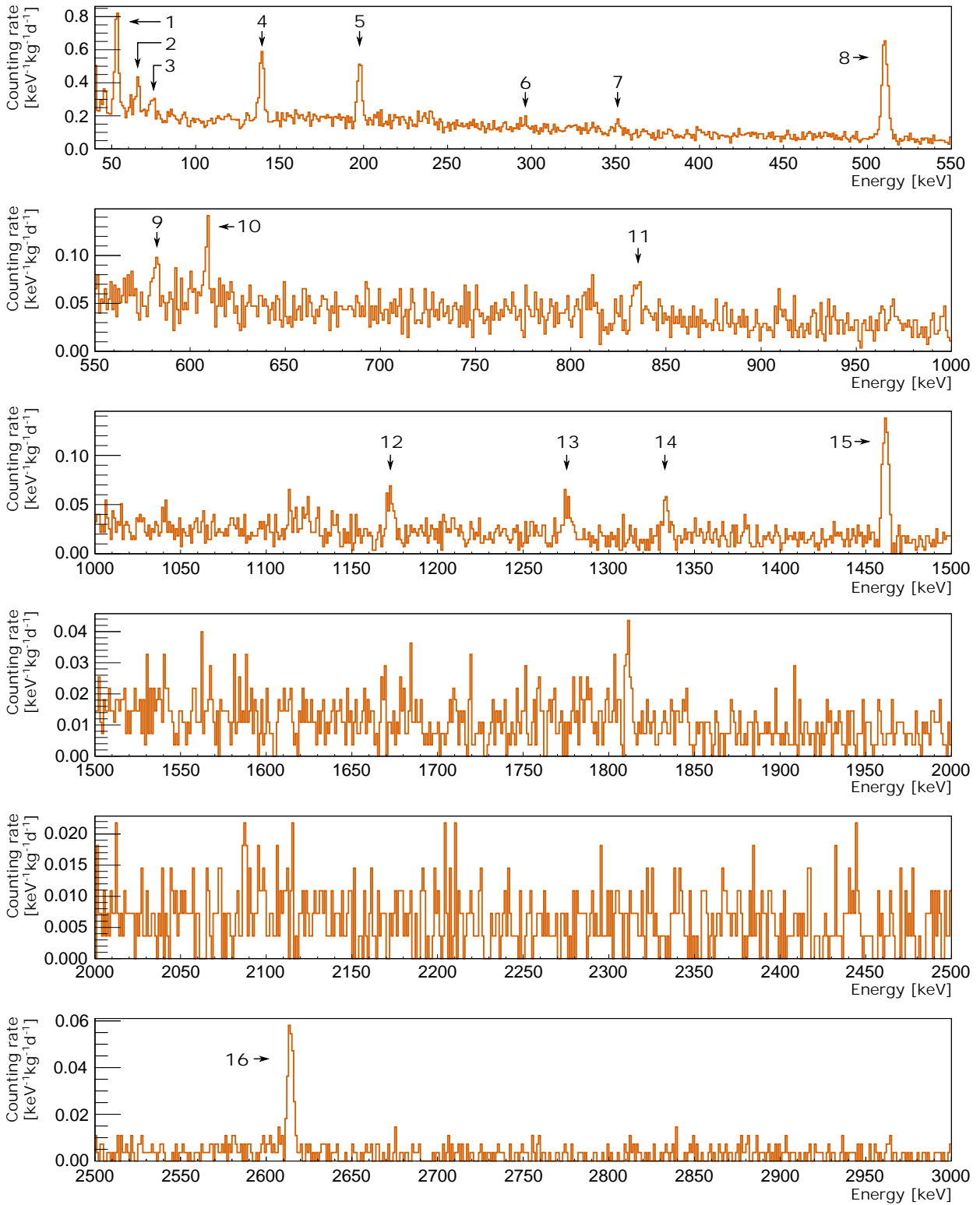


Figure 4.33: Background counting rate in the actively vetoed TU1 detector within the ROI of [40 keV,3000 keV]. The different panels show different energy intervals of 500 keV width. The first two panels are deviating from this rule in order to bring the annihilation peak into the first panel, which enables the second panel to make smaller peaks visible. The data was acquired with a total measuring time of 90 d. The identified peak structures are numbered and their origin is listed in table 4.3.

4.5.3 Treatment of remaining oscillation events within TU1

As discussed in section 4.1.2, there are some rarely occurring oscillations remaining on the baseline of the TU1 signal (approximately twice to five times a week). These oscillations have an impact on the final spectrum due to their non-negligible pulse height (resulting energy $E > 40$ keV), as well as an impact on the dead time provided by the DAQ software. This is due to the fact, that the dead time becomes untrustworthy when facing a considerable amount of non-Poisson events above the trigger threshold (cf. section 2.5).

The counting rate of a usual run of TU1 is shown in the upper panel of figure 4.34 in red over approximately one week of background measurement. There are four obvious and one minor distinct events, where the counting rate exceeds drastically. The prevention and/or careful treatment of these events is crucial. As shown in this figure, each oscillation event can trigger around 100 events, which subsequently leads to approximately 400 additional events per week. Without correcting for them, the integrated counting rate would be approximately 15% larger, but even more importantly: The sensitivity in the low-energy regime would collapse due to the overlaying oscillation events. This fact is emphasized by the upper panel of figure 4.35, which shows the corresponding raw pulse height spectrum of TU1 for the same run as figure 4.34 in red. It is apparent, that these oscillations seem to result in monoenergetic energy depositions in the low energetic part of the spectrum.

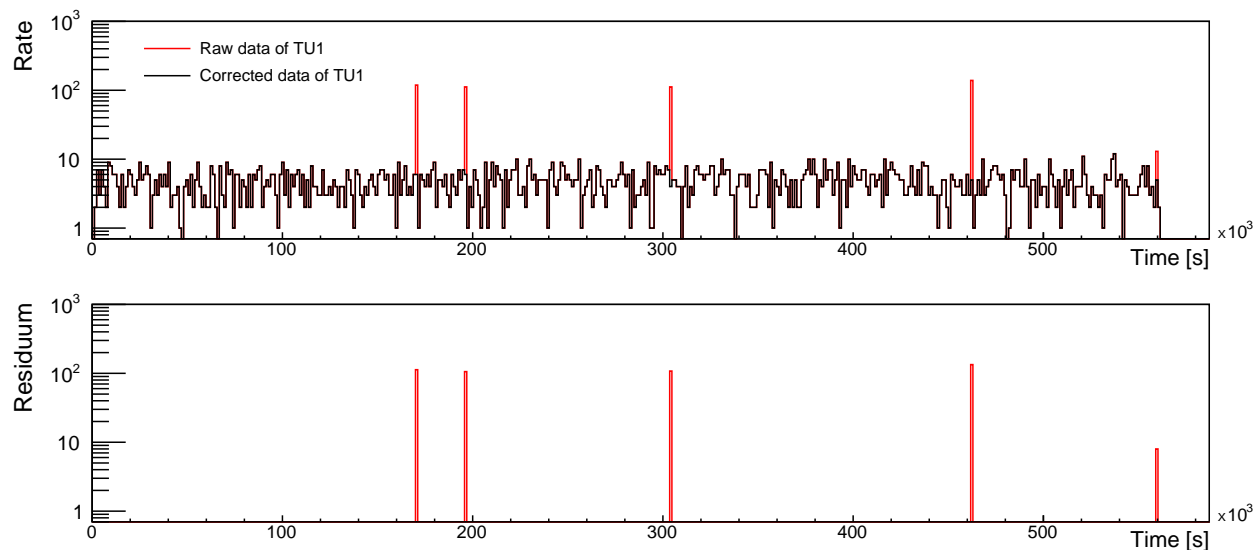


Figure 4.34: Top: Rate of events in $[40 \text{ keV}, 2700 \text{ keV}]$ in TU1 after applying the active veto for the same run, as shown in figure 4.35. The red curve shows the raw data without correcting for the rarely occurring oscillations. The black histogram shows the remaining events after applying an appropriate cut. Bottom: This residuum emphasizes the quality of the cut. No single other event has been rejected.

In order to investigate an offline cut criterion for the rejection of these events, multiple oscillation patterns were analyzed by their frequencies and their effective energy depositions. Two extremely different cases are shown in figure 4.36 and figure 4.37. Both of them show

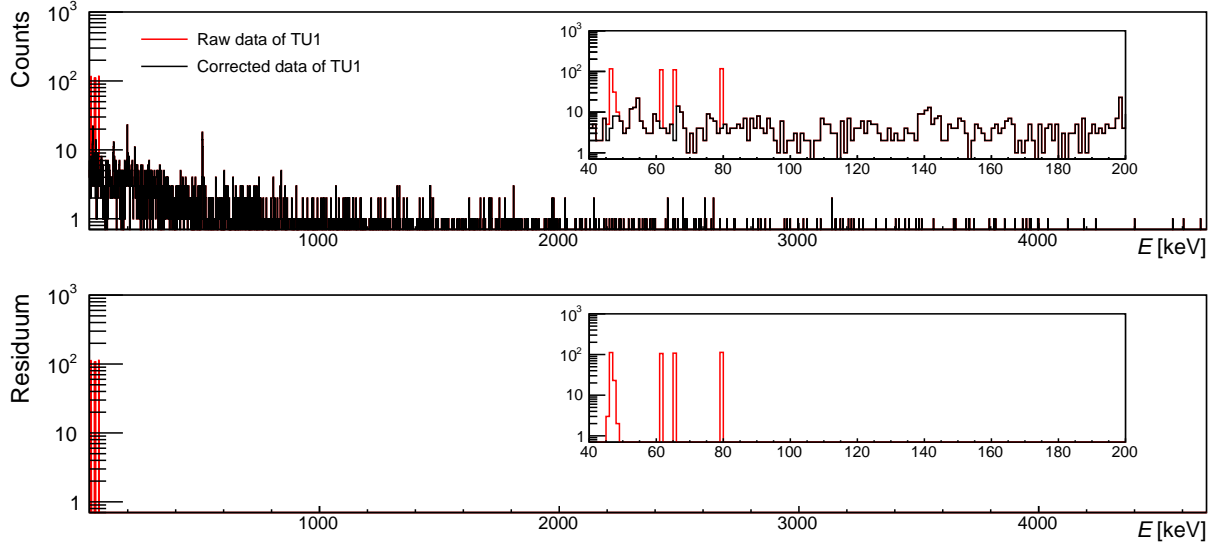


Figure 4.35: Top: Pulse height spectrum of TU1 after applying the active veto for the same run, as shown in figure 4.34. The respective inlets only show the low energetic part of the spectrum. The red curve shows the raw data without correcting for the rarely occurring oscillations. The black curve shows the remaining events after applying an appropriate cut. Bottom: This residuum emphasizes the quality of the cut. No single other event has been rejected.

one single oscillation each, which happens only within the fraction of a second (15 ms and $250\mu\text{s}$, respectively). Each dot represents the energy deposition due to one triggered event within this oscillation along with its triggered time stamp. Both events occurred during the same run, which was also used for figure 4.34 and figure 4.35 (cf. e.g. the time stamps in figure 4.34).

To emphasize the severity of these oscillations it is worthwhile mentioning, that such events contain approximately the same number of triggered events, which usually would be triggered during one whole day in TU1.

The first exemplary oscillation in figure 4.36 strongly varies regarding its energy deposition over the total length of 15 ms and only eight of them deposited an effective energy of more than 40 keV. In figure 4.36, most of them are plotted on top of each other, this is why it looks like less than eight events. This varying energy deposition is also the reason for the small height of the last peak in figure 4.34 in comparison to the other oscillations: Most of its events are below the applied threshold of 40 keV.

The second exemplary oscillation in figure 4.37 shows a very stable energy deposition over time with all events depositing between $E = 78.3\text{ keV}$ and $E = 78.6\text{ keV}$ within the $250\mu\text{s}$. Both events are barely comparable in their phenomenology, but they both have one thing in common, what makes them unique with respect to physical events in TU1: Their extremely high trigger rate of events with rather similar energy deposition.

Hence, the following cut criterion was added to the offline analysis:

- For each event, which survives the active veto it is checked, whether there was (or will be) an energy deposition within the previous (or upcoming) $10\ \mu\text{s}$, which in addition deposits an energy with more than 80% and less than 120% of its energy. If so: Both events are rejected.

The effect of the cut criterion onto the exemplary BG run of TU1 is shown as a black curve in the upper panels of figure 4.34 and figure 4.35. In addition, the respective lower panels show the resulting residuum between raw and corrected data.

It is crucial to highlight the negligible impact of this cut for the veto efficiency. Even by placing a sample with 1 kBq and an emission probability of 100% right in top of the end cap of the crystal, the ratio of affected full energy events will be below 0.1%. In case of realistic sample scenarios with count rates of about 1000 events per day, the probability to have two events within the same $10\ \mu\text{s}$ window (even without the additional cut on their energy) is $1\ \text{E-}7$. However, for certain measurements with calibration nuclides, where this cut might actually influence the full energy peaks (i.e. when dealing with activities $\mathcal{O}(100)$ kBq), this cut can be turned off due to the negligible effect of these remaining oscillation events onto the respective measurement.

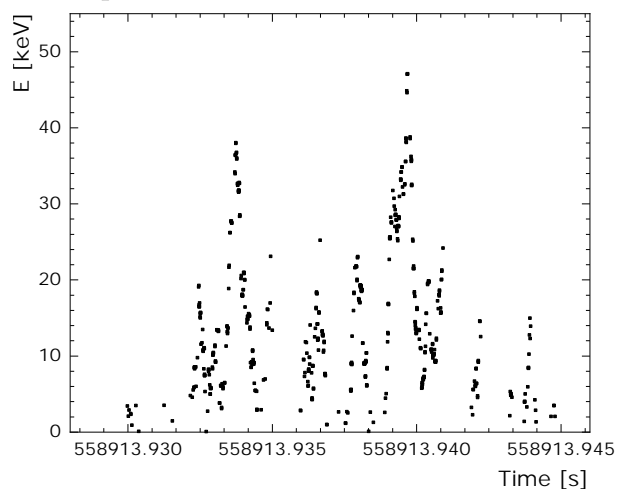


Figure 4.36: Example of an oscillation event in TU1 with the energy of each triggered event over time. The time span of the entire event is approximately 15 ms. This event corresponds to the last event in figure 4.34 and to some of the events in the lowest peak of figure 4.35.

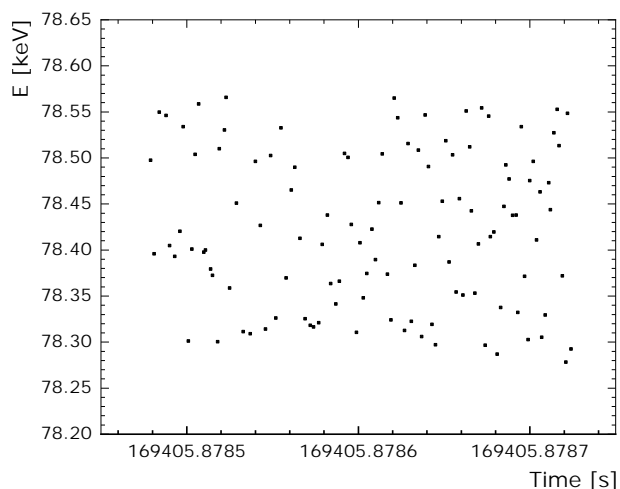


Figure 4.37: Example of an oscillation event in TU1 with the energy of each triggered event over time. The time span of the entire event is approximately $250\ \mu\text{s}$. This event corresponds to the first event in figure 4.34 and to the highest peak in figure 4.35.

Due to the broad variety of different oscillations, it is certainly possible, that there might appear an oscillations within TU1 at some point, which does survive this procedure. However, regarding the background study of 90 days, this cut criterion managed to eliminate all of the occurring vibrations. Nevertheless, the rate of low-background experiments should be checked for each run in order to identify oscillations, which might survive this procedure.

4.5.4 Effective half-life of the radon-induced rate

During each opening of the anti-radon box, the radon concentration within the interior of the passive shielding becomes enriched again. After closing the box, the amount of radon isotopes within the setup mainly depends on the time span of the opening, which usually takes ~ 5 min.

The subsequent decrease in the counting rate of TU1 is a convolution of two processes: On the one hand, radon isotopes are flushed out of the box due to the inflowing nitrogen gas. On the other hand, some of the remaining radon nuclides, as well as their daughters, decay within the box.

Due to the low counting rate ($N \approx 600$ events in total between 40 keV and 2700 keV within the first 100000 s after closing the box), it is not possible to analyze the decrease of this counting rate for a single radon-induced γ -ray line. The most intense radon-induced γ -ray line at $E = 609$ keV from ^{214}Bi (fed by ^{222}Rn) only shows approximately $N \approx 5$ full-energy events within the first 100000 s after closing the box, which is less than 1% of the total count rate. A decrease of the counting rate in TU1 after closing the box is therefore dominated by incoherently scattered events and statistically not significant peaks in the spectrum. Hence, neither a distinction between ^{220}Rn and ^{222}Rn (cf. section 4.2), nor a peak-assigned decay analysis after closing the anti-radon box is feasible.

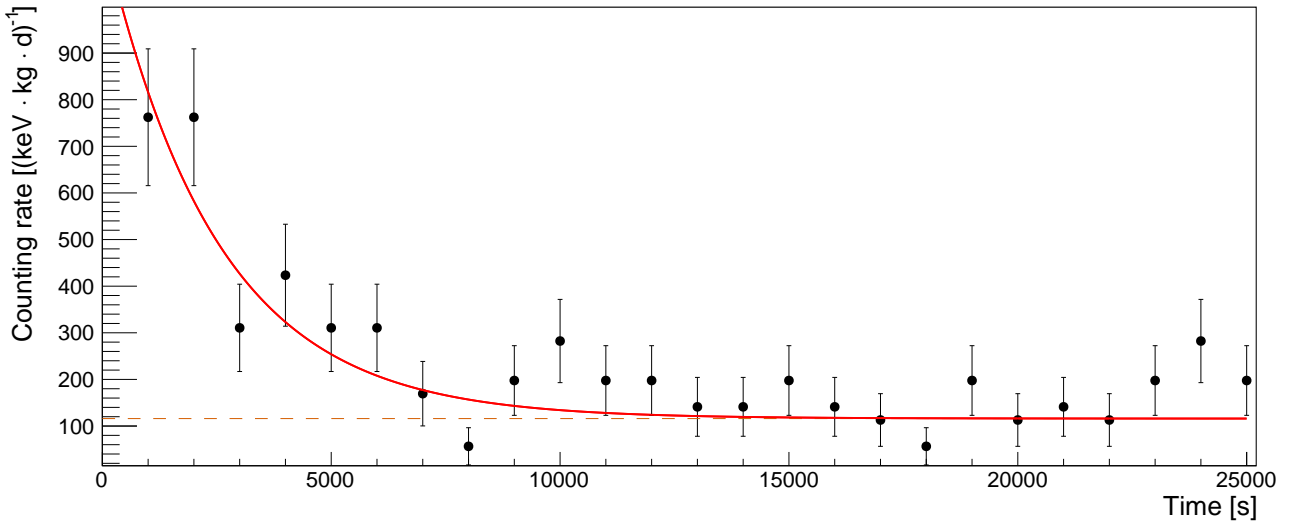


Figure 4.38: Decreasing counting rate of the vetoed TU1 spectrum in [40 keV, 2700 keV] after closing the anti-radon box. The data is shown for the first 25000 s, and each data point represents the integrated counting rate for the previous 1000 s, respectively. This time regime is dominated by the flushing of large amounts of radon. The red line shows an exponential fit, which approaches the fixed final value of the counting rate (orange dotted line). The effective half-life is $T_{1/2,\text{short}} = (1700 \pm 300)$ s with $\chi^2/\text{NDF} = 28/23$.

Nevertheless, the decrease of the total counting rate between 40 keV and 2700 keV after closing the box can be investigated. It is worthwhile mentioning, that this analysis is only

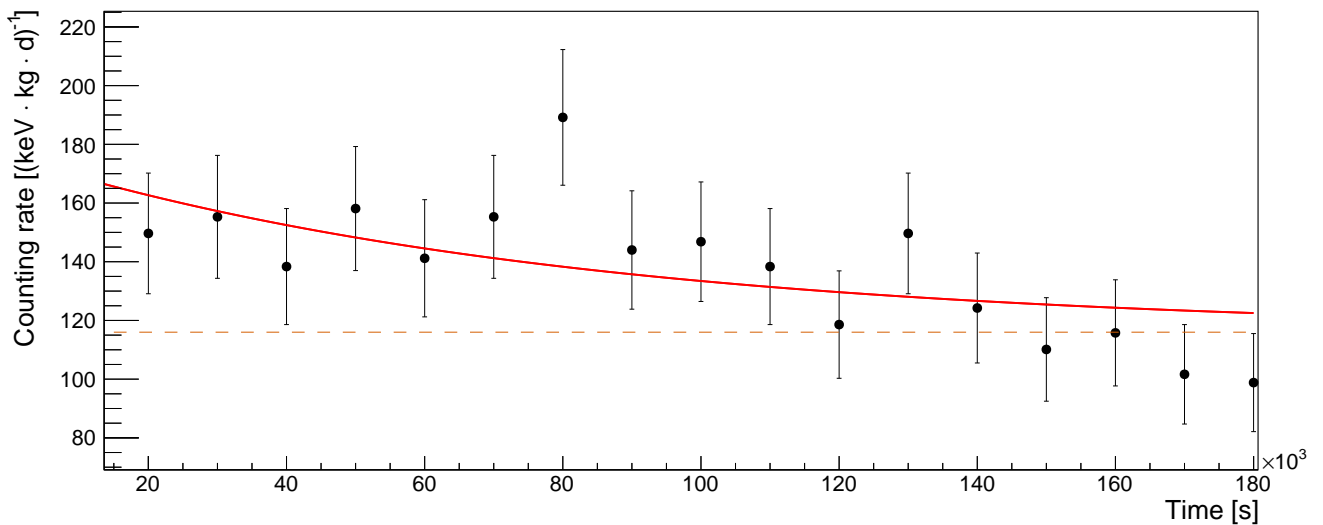


Figure 4.39: Decreasing counting rate of the vetoed TU1 spectrum in [40 keV, 2700 keV] after closing the anti-radon box. The data is shown for the first 180000 s, and each data point represents the integrated counting rate for the previous 10000 s, respectively. This time regime is characterized by both the flushing, and the decay of the remaining radon. The first 10000 s are excluded due to the strong effect of the flushing in the beginning (cf. figure 4.38). The red line shows an exponential fit, which approaches the fixed final value of the counting rate (orange dotted line). The effective half-life is $T_{1/2,\text{long}} = (60 \pm 20) \cdot 10^3 \text{s}$ with $\chi^2/\text{NDF} = 13.3/15$.

possible with the actively vetoed data of TU1. The counting rate within the passively shielded spectrum is increased by a factor of ≈ 17 (cf. table 4.2), and dominated by muon-induced events, which prevent radon-induced events from being properly distinguishable.

The counting rate of the actively vetoed data of TU1 within [40 keV, 2700 keV] is shown in figure 4.38 for the first 25000 s after closing the anti-radon box. Each data point represents the integrated counting rate for the previous 1000 s normalized to the usual units of $[\text{keV}^{-1}\text{kg}^{-1}\text{d}^{-1}]$.

4.5.5 Annual modulation and long-term development of the counting rate

There are two main reasons for questioning the long-term stability of the determined background counting rate of 116(1) events per kilogram and per day in TU1. On the one hand, medium long-living radio nuclides with half-lives in the order of hundreds of days or a few years, stemming from prior activations (i.e. due to cosmic radiation) will decay over time. If they are in the close proximity of TU1, this will further reduce the background counting rate. On the other hand, the impact of non-vetoed muons seems to be an essential contribution to the remaining actively vetoed TU1 spectrum, which will also be discussed in section 4.10. However, it is well known for decades, that the cosmic muon flux can be subject to annual modulations [126]. It is therefore an intuitive assumption, that there could be an annual modulation also in the background rate of the TU1 detector.

In a nutshell, although being counterintuitive, the annual muon flux at sea level is at its

maximum during winter [127], while in deep underground laboratories, the maximal flux is measured during summer [128]. The underlying physics of these modulations in their entirety are too complex for the scope of this section. Nevertheless, the key statement remains the same, when focusing only the atmospheric density profiles without discussing geomagnetical, meteorological or tidal influences: Both counterintuitive phenomena rely on the fact, that during summer the higher air temperatures lead to subsequently lower average air densities. In winter, the cold temperatures are accompanied by higher densities, respectively²⁴.

The overall production of secondary particles in the earths atmosphere in general is positively correlated to the atmospheric density (i.e. its projected total areal density). The annual modulation of the muon flux at sea level (with a maximum in winter) is therefore also a direct consequence of the annual density profile of the atmosphere.

However, deep underground laboratories are only sensitive to muons, which initially were produced with comparatively high energies stemming from mesonic decays. Due to the lower air pressure in summer, the interaction mean free path of mesons is increased, while the decay mean free path is independent of temperature and pressure. Their ratio therefore enhances in favor of decays with less prior interactions and therefore less energy loss. This means that during summer, mesons tend to decay with higher energies, which subsequently leads to the production of muons with higher energies that are able to reaching deep underground laboratories.

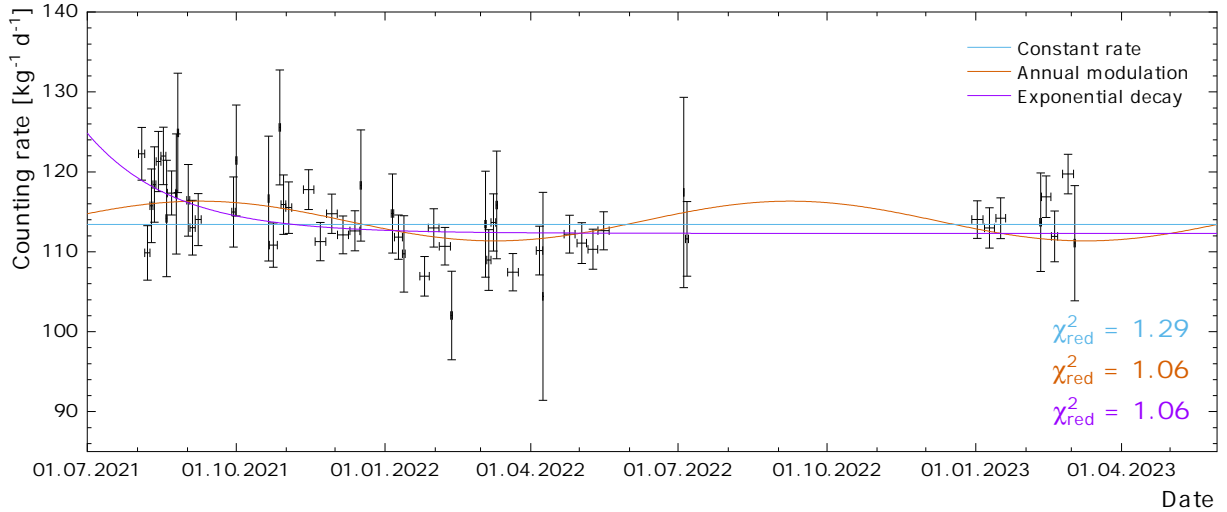


Figure 4.40: Long-term counting rate of the background in the TU1 detector from August 2021 to March 2023. The uncertainty on the x-axis is showing the duration of the respective measurement. Three subsequent fit procedures are shown: A constant rate (blue), an annual modulation with a fixed frequency (orange) and an exponential decay (purple). The respective χ^2_{red} -values are shown with the according colors in the lower right of the figure²⁵.

²⁴Even the phraseology ‘temperature’ is dangerously simplified. In fact, an effective temperature is needed based on altitude-dependent distributions for both the temperature and the pressure.

²⁵There are some data points, which seem to result in counting rates that are systematically too high (e.g. in March 2023). It can not be entirely ruled out, that these runs might be affected by remaining radon gas (e.g. due to an open anti-radon box prior to the run without any note in the logbook).

Without going into further detail regarding the energy dependency, at sea level, these changes in the annual modulations (with maximum in winter) can be in the order of 10% [127], while in deep underground laboratories, these annual modulations (with maximum in summer) can be in the order of 3% [128].

The long-term background rate in the TU1 detector is shown in figure 4.40. Especially during the later stages of these 19 months of operation, the TU1 detector was also used several times for scientific measurements and thus excluded from the background study. However, during the first months, the detector was mainly used for collecting information on the actively vetoed spectrum (90 days of statistics).

In total, three different approaches are executed in order to check the long-term development of the counting rate: A constant fit (blue), an annual modulation with a fixed oscillation length of 365 d (orange) and an exponential decay (purple) using the following function: $y = A + B \cdot \exp(-(x - C)/D)$.

Regarding the minimization of the residuum (and hence the χ^2_{red} -values), the approach with a constant rate seems to be slightly disfavored by the data. The approaches using an annual modulation and an exponential decay are equally likely. However, it is worth mentioning, that the current statistics is low, which also enhances over-fitting during the latter two approaches.

For the corresponding publication in Astroparticle Physics, only 90 d of statistics were used. Due to the fact, that the first data points in figure 4.40 are systematically higher, the resulting total counting rate in the paper was stated with $116(1)\text{kg}^{-1}\text{d}^{-1}$ [2].

However, by including the entire available statistics of figure 4.40, the most updated values for the background counting of TU1 in [40 keV, 2700 keV] are the following:

$$\text{Assuming a constant rate: } R = 113.4(5) \text{ kg}^{-1}\text{d}^{-1} \quad (36)$$

$$\text{Assuming an annual modulation: } R = 113.8(5) \text{ kg}^{-1}\text{d}^{-1} \quad (37)$$

$$\text{Assuming an exponential trend: } R = 112.3(7) \text{ kg}^{-1}\text{d}^{-1} \quad (38)$$

In case of an annual modulation, the maximum counting rate would be during the beginning of September of each year. Furthermore, the most likely peak-to-peak deviation would be $5.0(13)\text{kg}^{-1}\text{d}^{-1}$, which is approximately a relative peak-to-peak deviation of 4.4%. The influence of medium long-living nuclides however can only be properly elaborated based on significantly longer operation times of TU1.

4.6 Determination of losses in the full energy peaks

For the vast majority of experiments in γ -ray spectrometry, it is unavoidable to have a discrepancy between the original number of full energy events, which were actually deposited

in a HPGe detector during the measurement, and the subsequent amount of full energy events, which are evaluated in the spectrum. In case of TU1, this discrepancy is based on two effects, which both deteriorate the amount of full energy events and will be discussed in the following.

The first effect is the dead time during the data acquisition, which was already discussed in section 2.5, but which needs to be adjusted in case of ultra-low background measurements. The second effect are losses in the full energy peaks due to the cuts of the active muon veto. Its impact was introduced in section 4.4.6, and the determination of its final value will be part of this section.

4.6.1 Determination of the dead time

The basic procedure for estimating dead times during a typical measurement was elaborated in section 2.5. Within this section it was also emphasized, that the presented procedure is only valid in case of events in the detector, which follow a Poisson distribution and are therefore entirely independent of each other. In case of the TU1 setup (as discussed in section 4.5.3), there are remaining, rarely occurring oscillations, which certainly do not follow any Poisson distribution. While these oscillations also exist in other detection systems, they are usually negligible with respect to the amount of events with ‘physical origin’. Their contribution to the estimation of the dead time can therefore usually be neglected²⁶.

However, in case of ultra-low background setups with count rates in the order of $\dot{N} = 100 \text{ d}^{-1}$, one single oscillation event per day with 100 subsequently signals above the threshold would already account for 50% of the total amount of signals. Now it strongly depends on frequency of this oscillation, whether all 100 events are properly evaluated, all being flagged as pile-up, all being reconstructed as one single summation event or a mixture of all of them. Hence, depending on the frequency of this oscillation, the software would state any random dead time between 0% and 50%, which is certainly incorrect. While the real dead time of this example is negligibly small, in the worst case (dead time of 50%) of this basic example the determination of any activity within this measurement would systematically be too large by a factor of two after dead time correction.

Based on this small example, the necessary procedure seems to be straight forward:

- Identify as many non-Poisson events as possible and discard them from the subsequent estimation of the dead time in order to get back into a regime, where the number of non-Poisson events becomes again insignificant for the iterative procedure.

However, it is important to add some comments to this procedure. Firstly, due to the non-existent information about the origin of any single event in a detector, it is not possible

²⁶In a typical experiment, there are also other effects (besides oscillations), which lead to non-Poisson distributions. Depending on the half-life of the involved excited states, photons stemming from the same cascade may also cause troubles. However, as long as non-Poisson events are negligible in their occurrence with respect to Poisson events, the estimation procedure presented in section 2.5 remains a valid method.

to categorize each event as ‘Poisson’ or ‘non-Poisson’. Only suspicious groups of subsequent events (e.g. due to an oscillating signal) can be identified and treated properly. Secondly, the mere omission of every oscillating signal is also certainly not flawless. During the occurrence of an oscillation (depending on the frequency), it might very likely be the case, that physical events could not have been analyzed during this period due to a saturated input stage or a busy trigger. Nevertheless, the proposed procedure only eliminates the oscillation without taking into account an actual dead-time generating effect based on it.

However, in case of TU1, the total fraction of time, where there are oscillations on the signal, is always entirely negligible with respect to the total measurement time (approximately 5 oscillations per week with a length of ~ 1 ms each). This is however not the case for the ratio of oscillation events with respect to the total amount of events. Depending on the measurement, this ratio might very much be significant. Therefore, (in case of TU1) this procedure is well justified in order to receive a significantly more trustworthy dead time estimation.

In summary, it is crucial to emphasize, that there is no flawless way to determine dead times. The goal can only be to find a procedure, which minimizes systematic flaws of the estimation as much as possible. The treatment of the dead time in case of TU1 is therefore a combination of identifying suspicious non-Poisson events (cf. section 4.5.3), and discard them from the normal iterative process (cf. section 2.5).

One alternative could be to omit dead times completely for low-background setups. In case of TU1 and in case of comparatively low counting rates, this would actually also result in a significantly more accurate result than not treating non-Poisson events at all. As an example, the utilized software for TU1 usually shows a dead time of 1-2% in case of a background measurement. Due to the fact that the actual dead time is far below 0.1%, by entirely omitting this dead time, the results of the measurement would already be significantly less erroneous. However without any further proof it is claimed, that the proposed procedure estimates the dead time more precisely. It also turned out to be entirely suitable in case of calibration measurements with higher non-negligible dead time.

4.6.2 Determination of the veto efficiency

In addition to the effects of an unavoidable dead time, the applied cut conditions on the raw data also have to be taken into account regarding potential loss of full energy events.

The result of this veto efficiency $\varepsilon_{\text{veto}}$ was already discussed in section 4.4.6, and the final value for this efficiency can already be estimated by using figure 4.21 with the final coincidence timing window $t_{\text{coinc}} = [-150 \mu\text{s}, +5 \mu\text{s}]$, and the final threshold energy in the panels $E_{\text{thresh}} = 0.8 \cdot E_{\text{min}}$. The underlying analysis behind this plot, as well as the determination of the final veto efficiency will be discussed in this section.

As already discussed in section 4.4.6, this veto efficiency neither depends on the activity of the sample, nor on the energy of the emitted γ -rays, but solely on the properties, and

the settings of the panels. Therefore, four independent measurements were conducted using a ${}^7\text{Be}$ source. A raw spectrum of an activated sample on TU1 is shown in black in figure 4.41. The γ -ray line of interest at $E = 478$ keV is the most prominent line in the spectrum, followed by the annihilation line at $E = 511$ keV.

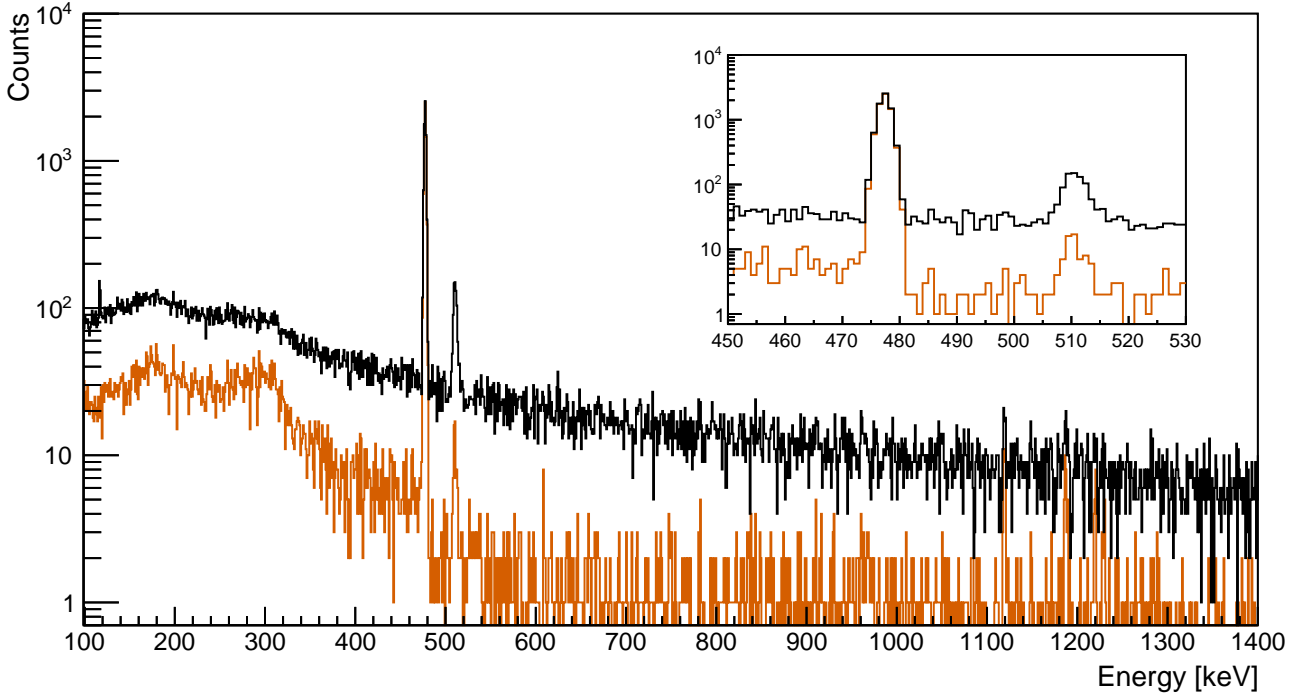


Figure 4.41: Pulse height spectrum of a ${}^7\text{Be}$ sample on TU1, which was measured for 6.9 d. The raw data is shown in black, and the resulting histogram after applying the final cut conditions is shown in orange. The inset shows a zoom into the region of interest with the evaluated γ -ray line at 478 keV, and the annihilation peak at 511 keV, respectively.

After applying the active veto, the full energy peaks should remain as unaffected as possible, while the rest of the spectrum is supposed to be attenuated as much as possible. The result of this active veto is shown in orange, which shows exactly this intended outcome. Due to ${}^7\text{Be}$ converting to ${}^7\text{Li}$ purely via electron capture (i.e. with no proportion of β^+ -decays), the annihilation peak is also solely due to external background (mainly muons), and therefore also experiences a certain attenuation from the veto.

These two spectra were subsequently analyzed regarding their peak content at $E = 478$ keV in order to investigate the inevitable loss of full energy events due to the applied cut. In order to improve the statistics on the veto efficiency, four distinct runs were analyzed in this way, and their results are shown in figure 4.42.

The uncertainties of these measurements are purely due to Poisson statistics during the peak evaluation. They vary between 0.2 – 0.3 % for each spectrum resulting in uncertainties of 0.3 – 0.4 % for each data point shown in figure 4.42 after determining the ratio of the peak contents.

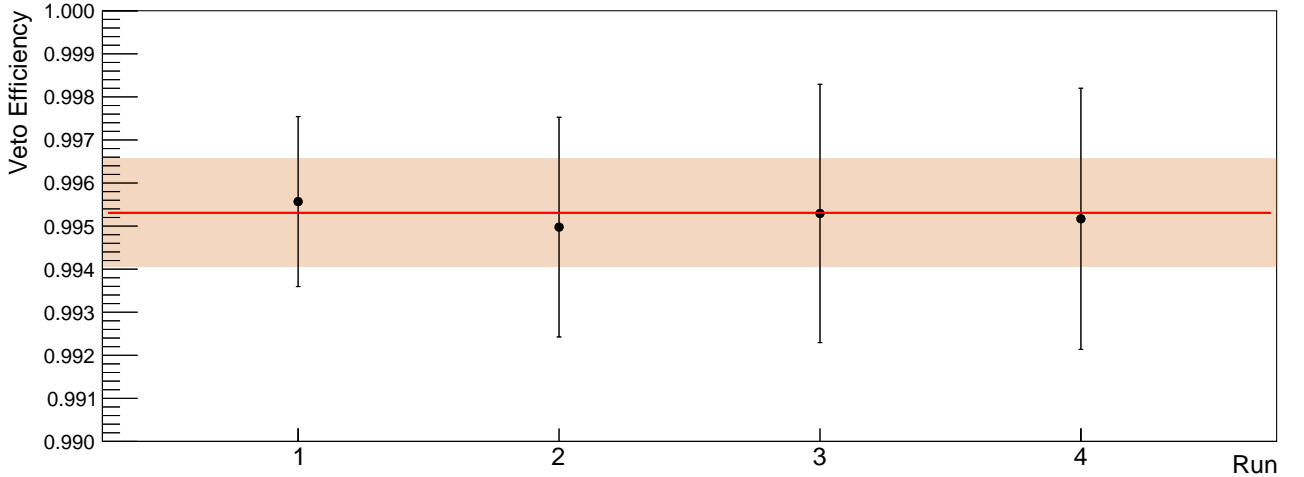


Figure 4.42: Resulting veto efficiency $\varepsilon_{\text{veto}}$ for TU1 using all five scintillation panels and the final cut conditions (coincidence timing window $t_{\text{coinc}} = [-150 \mu\text{s}, +5 \mu\text{s}]$, the threshold energy in the panels $E_{\text{thresh}} = 0.8 \cdot E_{\text{min}}$ and the threshold energy in TU1 is $E = 20 \text{ keV}$). The four independent measurements are fitted with a constant fit (red), and its 1σ -uncertainty is plotted as shaded area. The result of the fit is $\varepsilon_{\text{veto}} = 0.9953 \pm 0.0013$.

Due to the fact, that the actual muon veto cut is unaware of a subsequently applied peak analysis, this analysis adds an uncertainty, which is larger than the variation of the data points, and furthermore dominates the total uncertainty. It is also worthwhile mentioning, that the true value of the veto efficiency does not have an uncertainty, as long as the properties of the panels remain constant. Only the determination of it is afflicted with an uncertainty due to limited statistics.

Furthermore, the data of the raw and the vetoed spectra are indeed correlated, which is important to mention, but neglected due to the anyhow conservative approximation.

The result of a constant fit is a veto efficiency of $\varepsilon_{\text{veto}} = 0.9953 \pm 0.0013$, which has a relative uncertainty of approximately 0.1%. This could be potentially improved by including more data into the analysis, but is already an order of magnitude smaller, than typical uncertainties on γ -ray spectrometry measurements.

In summary, the uncertainty was determined conservatively by using Poisson analysis of the γ -spectra and the ‘cut-and-count method’ (cf. section 2.4.3), but is nevertheless negligible with respect to usual future measurements with TU1.

Due to the analysis in figure 4.21 being also based on this analysis, their values need to match. This is also confirmed by reading off the approximate value in case of a coincidence timing window $t_{\text{coinc}} = [-150 \mu\text{s}, +5 \mu\text{s}]$, and a threshold energy in the panels $E_{\text{thresh}} = 0.8 \cdot E_{\text{min}}$. As discussed in the end of section 4.4.6, the full energy peaks should not be attenuated by more than 0.5%, which was aimed for and is also fulfilled.

It is worthwhile mentioning, that the validity of this veto efficiency can also be verified for each upcoming measurement separately. This is due to the fact, that the raw peak entries

always can be compared to the peak entries in the vetoed spectrum during the offline analysis.

4.7 Design of an appropriate sample holder

In order to ensure reproducibility of measurements, as well as guaranteeing a defined geometry for conducting simulations, target holders are inevitable for sophisticated γ -ray spectrometry setups. Within this chapter, two subsequent generations of sample holders will be discussed, with the first one being too contaminated for TU1 and the second one being the final approach.

4.7.1 First attempt: Sample holders from aluminum

Due to its robustness, its well established material processing techniques and its price, sample holders for HPGe detectors are commonly designed out of aluminum, which was also the first attempt for a sample holder of TU1.

A picture of this holder is shown in figure 4.44. The holder consists of three stages in order to enable different distances between sample and detector. While the uppermost stage can be directly placed on the end cap of TU1, there are also two additional stages, which subsequently increase the distance between sample and TU1, respectively.

After its production, the sample holder underwent an additional cleaning procedure (supersonic bath and isopropanol). For a test measurement, only the uppermost stage of the holder was put directly on the end cap of TU1. The result of this measurement (with active veto) is shown in figure 4.43 as blue histogram.

The comparison to the passively shielded (black) and the actively shielded spectrum (orange) of TU1 without sample holder (rebinned version of figure 4.32) is also shown.

Neither the threshold of the run with the aluminum target holder was correctly set (cut-off already at approximately 100 keV), nor enough statistics was available for a detailed comparison. Nevertheless, a rough comparison of the overall counting rate with respect to the actively vetoed spectrum without holder is already sufficient to claim, that this sample holder is too contaminated for a use in the TU1 setup.

By adding the uppermost stage of the aluminum sample holder to the end cap of TU1, the overall counting rate within [100 keV, 2700 keV] increased by more than a factor of 5. While this might be acceptable for the passively shielded TU1 detector, it is definitely not applicable for the actively shielded case.

4.7.2 Final attempt: Sample holder from OFRP copper

A proper sample holder for ultra-low background experiments needs to be as radiopure (i.e. as low in activity) as possible. This can be achieved by minimizing the mass of the sample holder, and by optimizing its material. One of the radiopurest materials, which is

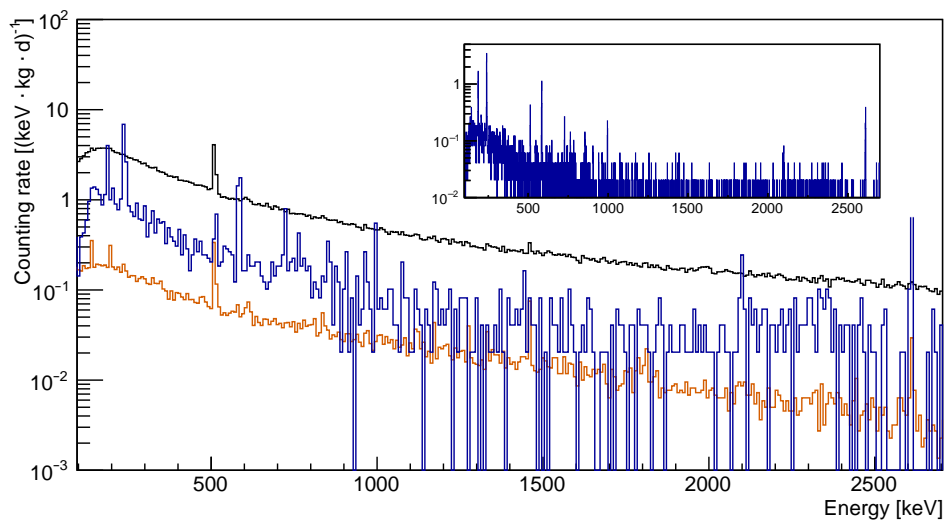


Figure 4.43: Actively vetoed counting rate with the aluminum sample holder on TU1 (blue) in comparison to the passively shielded spectrum (black) and the actively vetoed spectrum (orange) without sample holder. Due to the poor statistics of the blue spectrum, all three spectra are rebinned by a factor of 8. The inset shows the spectrum with target holder without rebinning.



Figure 4.44: Aluminum sample holder for TU1. It consists of three distinct parts for different heights.

occasionally commercially available is OFRP copper, that is also used in the passive shielding of TU1 (cf. section 3.5.2).

Despite the fact, that a sample holder made of OFRP copper would most certainly not increase the background rate at all, there are two additional reasons to also redesign the holder with respect to the first attempt: On the one hand, the first design is able to physically trap radon contaminated air within its inner volume. The nitrogen flushing would therefore be less effective for a certain amount of air in close proximity to TU1. The second reason concerns the rarity and the price of OFRP copper: The shape of the first holder is not optimized for an efficient usage of material, because of its high amount of milling residuals. The resulting set of elements, which further can be used as a multi-purpose target holder for TU1 is shown in figure 4.45. There are three different distances, which can be realized with this approach. Either ‘main frame 1’ is put directly on the endcap, which results in a distance of 2.5 mm between source and detector, or ‘main frame 2’ is used in combination with ‘distance rods - set 1’ or ‘distance rods - set 2’, which results in a distance of 30 mm, and 70 mm, respectively.

Regarding smaller samples (especially calibration sources) ‘sample holder 1’ can be stocked into one of the main frames. This can then be stocked with ‘sample holder 2-5’. A list of possible source diameters is shown in table 4.4.

It is worthwhile mentioning, that sample holder 3, 4 and 5 have a smaller inlay height of 1 mm instead of the typical inlay height of 2.5 mm (as in case of sample holder 1, 2 and 3). In case these inlets are used, the effective distances between sample and detector are also

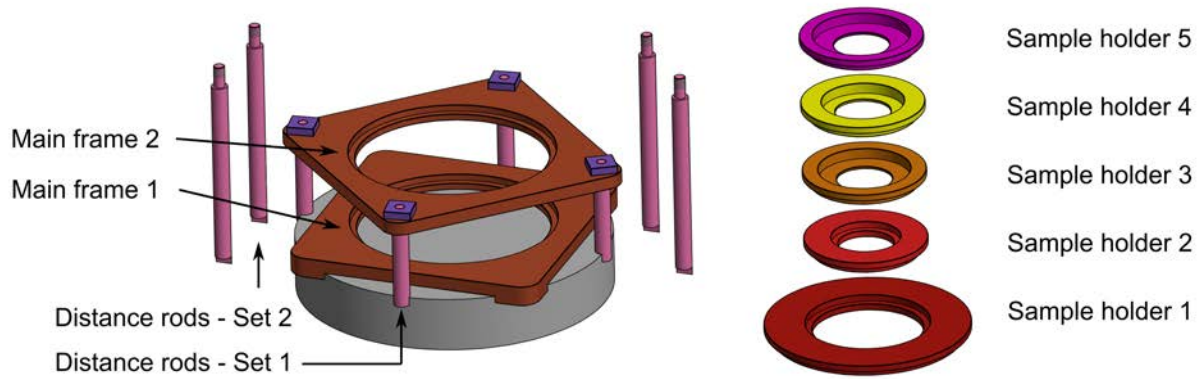


Figure 4.45: Final set of elements, which can be used in various combinations as a sample holder for TU1. The set consists of two main frames, five sample holders, two sets of distance rods (four each), and four screws. All of these elements are made of OFRP copper. The corresponding technical drawings are shown in appendix B.5.

1.5 mm smaller than stated before. The smaller inlay height is implemented for these three holders in order to enable the use of typical samples along with their own sample frames (e.g. the frame of a calibration source). This frame height compensates the 1.5 mm, which effectively leads to an emission point of these samples, which is identical to the 2.5 mm, 30 mm and 70 mm, respectively.

So-called ‘HZDR targets’ are small disks with 27 mm diameter and 220 μm thickness. They are designed for the in-beam campaigns at Felsenkeller and are a common standard, which is frequently used.

Table 4.4: Hole diameters, inlay diameters, and inlay heights of all sample holder components for TU1. The inlay diameters are 0.2 mm larger than needed in order to fit properly. The inlay heights are smaller for sample holder 3-5, because the sources have a height of 3 mm with the radioactive material located at 1.5 mm. The sources therefore emit at the same position as the exact bottom position of usual samples. The technical drawings are shown in the appendix B.5.

Name	Purpose	Hole diameter [mm]	Inlay diameter [mm]	Inlay height [mm]
Main frame 1/2	Samples with $d=75$ mm	70.2	75.2	2.5
Sample holder 1	Samples with $d=45$ mm	40.2	45.2	2.5
Sample holder 2	Samples with $d=25$ mm	20.2	25.2	2.5
Sample holder 3	HZDR targets	20.2	33.5	1.0
Sample holder 4	PTB sources	20.2	30.0	1.0
Sample holder 5	^{88}Y source	20.2	35.3	1.0

All elements, which are not needed for the current measurement, are stored within an desiccator, which is flushed with nitrogen and subsequently evacuated after each removal or storage in order to prevent radio contamination. The corresponding technical drawings are shown in appendix B.5.

4.8 Comparison to other underground γ -ray counting setups

By combining passive and active shieldings for the TU1 setup, the background counting rate reaches a value of $116 \pm 1 \text{ kg}^{-1} \text{ d}^{-1}$, as discussed in table 4.2. This is close to the results of the worlds most sensitive HPGe setups in deep underground laboratories and also unprecedented for non-deep underground laboratories.

A thorough comparison to a selection of other underground HPGe is carried out in the corresponding publication on this setup [2]. However, a brief summary regarding its results shall also be presented in the following for sake of completeness.

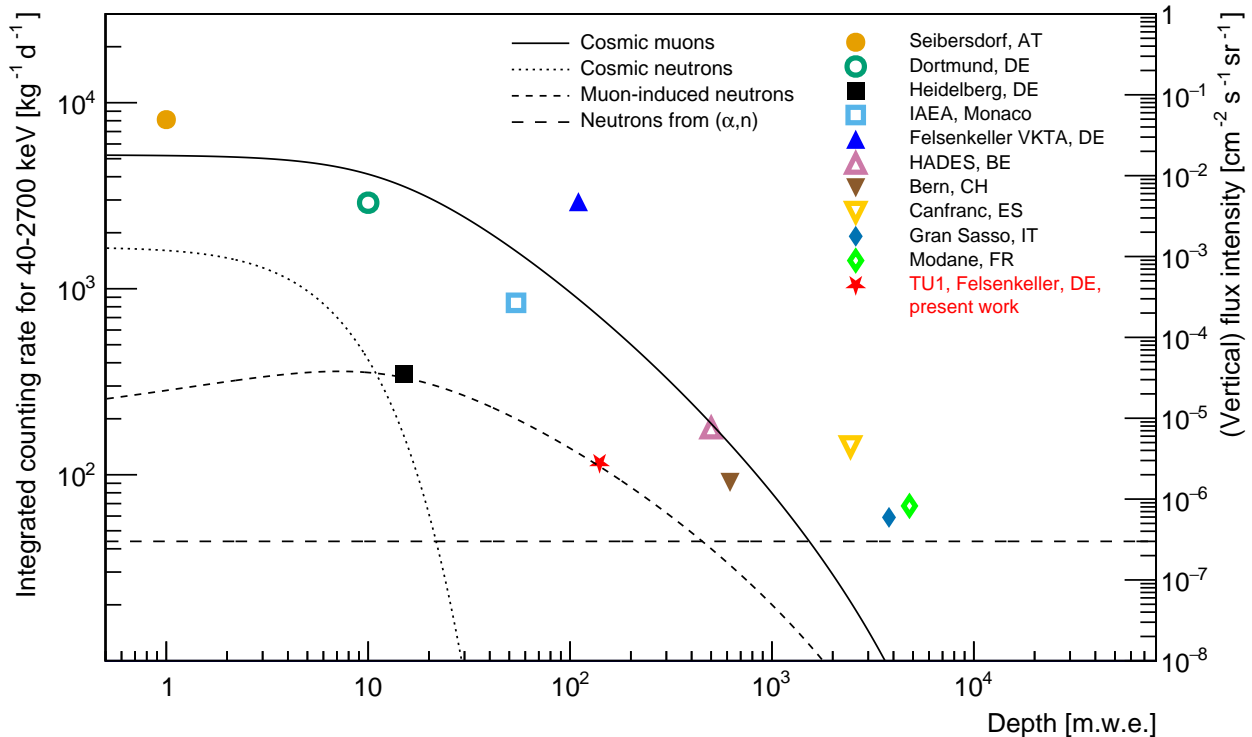


Figure 4.46: Integrated counting rate within [40 keV, 2700 keV] with respect to the rock overburden of several underground HPGe. Estimations of the vertical flux intensity for the muonic and neutron components are shown as a line, and dashed line, respectively [111, 129]. The first knee in the neutron component is related to cosmic neutrons, the second knee is due to muon-induced neutrons and the plateau at higher depths is related to neutrons from spallation and (α, n)-reactions. The corresponding references can be found in table 4.5.

Figure 4.46 shows the resulting background counting rates of different underground HPGe setups with respect to their respective rock overburden. Additionally, estimations for the flux intensity of both muons and neutrons are plotted as solid line and dotted/dashed lines, respectively. It is important to notice, that these curves are only of qualitative nature and do not claim to precisely predict the fluxes in underground labs [111, 129]. Especially the value of muon-induced neutrons e.g. strongly depends on the composition of the given rock surroundings. However, the qualitative statement is still valid: The cosmic muon flux intensity (solid line) drops significantly with increasing rock overburden. The overall neutron intensity also disfavors larger amounts of rock overburden, but is more complex

in detail. The dominant source of neutrons for laboratories with a low rock overburden ($\lesssim 10$ m.w.e.) are cosmic neutrons (dotted line). While this component can be attenuated by operating a shallow-underground lab, a second bulge of neutron intensity is usually apparent at shallow depths (≈ 100 m.w.e.) due to muon-induced neutrons (narrow dashed line). This component shows a similar behavior as the muon component, and only varies from it due to the subsequent hardening of the muon spectrum at larger depths. Within deep underground labs (≈ 1000 m.w.e.), any neutron source stemming from cosmic radiation slowly becomes insignificant with respect to neutrons from the surrounding rock due to e.g. (α, n) reactions (wide dashed line).

The negligibility of muons in case of deep underground laboratories is also emphasized by the omission of active muon vetos in any deep underground HPGe setup, as also shown in the corresponding table 4.5.

Table 4.5: Background count rates in [40 keV, 2700 keV] for selected underground HPGe detectors. The rates are given as $[\text{kg}^{-1}\text{d}^{-1}]$ with the mass referring to the active detection volume. When the data was not available, it is marked with ‘N/A’. If there is no active veto used, it is noted with ‘—’. ‘UC’ indicates, that it is currently under construction. See [2] for details.

Detector/ Facility	Location	Depth [m.w.e]	Count rate without veto [$\text{kg}^{-1} \text{d}^{-1}$]	Count rate with veto [$\text{kg}^{-1} \text{d}^{-1}$]	Ref.
D4	Seibersdorf Laboratory, AT	≈ 1	85100(400)	8110(40)	[130, 131]
DLB	TU Dortmund, DE	10	34400 (60)	2900 (6)	[132]
GIOVE	MPIK Heidelberg, DE	15	31027 (48)	348 (3)	[133, 134]
CAVE	IAEA, MC	54 ²⁷	N/A	840(50)	[135]
D6	Felsenkeller (VKTA), GE	140	2938 (5)	UC	[123]
TU1 ²⁸	Felsenkeller (TUD/HZDR), GE	140	1982 (3)	116 (1)	
Ge-14	HADES, BE	500	208 (4)	178 (8)	[136, 137]
GeMSE	La Vue-des-Alpes lab., CH	620	N/A	91 (1)	[138, 139]
GeOroel	LSC, Canfranc, ES	2450	142	—	[140]
GeCRIS	LNGS, Gran Sasso, IT	3800	111 (1)	—	[141]
GeMPI	LNGS, Gran Sasso, IT	3800	59 (1)	—	[141]
Gator ²⁹	LNGS, Gran Sasso, IT	3800	89.0 (7)	—	[141]
OBELIX	LSM, Modane, FR	4800	68 (1)	—	[142]

4.9 Sensitivity for future measurements

The main aim of this setup is to measure samples of ultra-low activities. This can be either due to their comparatively long half-lives, their small mass, their low natural abundances or their low amount of activated nuclei stemming from experiments e.g. related to nuclear

²⁷Due to the geometric complexity of the rock overburden, the effective depth of this laboratory was calculated based on the integrated muon intensity. [108, 129].

²⁸These values are from the corresponding publication [2]. For more recent values, see equation 36 to 38.

²⁹Count rate is given within an energy interval of 60-2700 keV.

astrophysics (i.e. by using the 5 MV Pelletron accelerator at the Felsenkeller underground laboratory). In order to quantify the limitations of the TU1 setup, this section is dedicated to discuss the achievable sensitivity under different circumstances.

Detection sensitivities in general are neither trivial to specify, nor to compare for different detectors. This is due to the fact, that the sensitivity of a certain measurement depends on the size and mass of the sample, its distance to the detector, on the available measuring time, on the energy of the expected signal, the full-energy peak efficiency and the subsequent background rate in the respective detector.

In order to state a comparable sensitivity for TU1, and to enable possibilities to quickly perform feasibility tests, it is therefore assumed, that all samples are point-like, and positioned with the appropriate sample holder (cf. section 4.7) directly on the end cap of TU1. The actual sensitivity for the measurement of a volumetric sample then only has to be corrected for its energy-dependent self-absorption, and its subsequently lower effective full-energy peak efficiency.

Due to the fact, that both the background rate and the full-energy peak efficiency are energy dependent, the sensitivity is calculated for three different energies, namely $E = 122$ keV, $E = 478$ keV, and $E = 1836$ keV, which can be used to also roughly interpolate the required sensitivity at another energy of interest.

A crucial value for estimating the success of a future measurement is the detection limit L_D . It is a measure for the necessary activity of a sample in a measurement in order to claim a signal detection within a certain confidence limit [77]. This value can be determined by knowing the background rate \dot{N}_{BG} of the detector³⁰, fixing a requested degree of confidence k_α , knowing the absolute full-energy peak efficiency ε , the branching ratio β , the decay correction C_{decay} , and the counting time t , as shown in equation 39.

$$L_D = \frac{k_\alpha^2 + 2k_\alpha \sqrt{2\dot{N}_{BG}t}}{\varepsilon \cdot \beta \cdot C_{\text{decay}} \cdot t} \quad (39)$$

In the following, the degree of confidence is assumed to be $k_\alpha = 1.282$ (1-tailed confidence for 90% confidence level). The decay correction C_{decay} is a term, which becomes necessary, whenever the half-life $T_{1/2}$ of the radio nuclide is not significantly longer than the measurement time t . Hence, this term takes into account the subsequent decay during the measurement, as shown in equation 40. In other words: For comparatively short half-lives, the initial activity needs to be subsequently larger to counteract its decay at later stages during the necessary measurement time. In case of measuring a sample for the duration of its own half-life (e.g. measuring ${}^7\text{Be}$ for $t \approx 53$ d), this factor is e.g. $C_{\text{decay}} \approx 0.72$.

³⁰Within this section, all calculations are based on the background rate of a conservatively chosen region of interest of 10 keV around the γ -ray energy. Furthermore, it is worthwhile mentioning, that the background rate in TU1 might certainly increase during a measurement due to any intrinsic activity of the sample.

$$C_{\text{decay}} = \frac{1 - e^{-\frac{\ln(2) \cdot t}{T_{1/2}}}}{\frac{\ln(2) \cdot t}{T_{1/2}}} \quad (40)$$

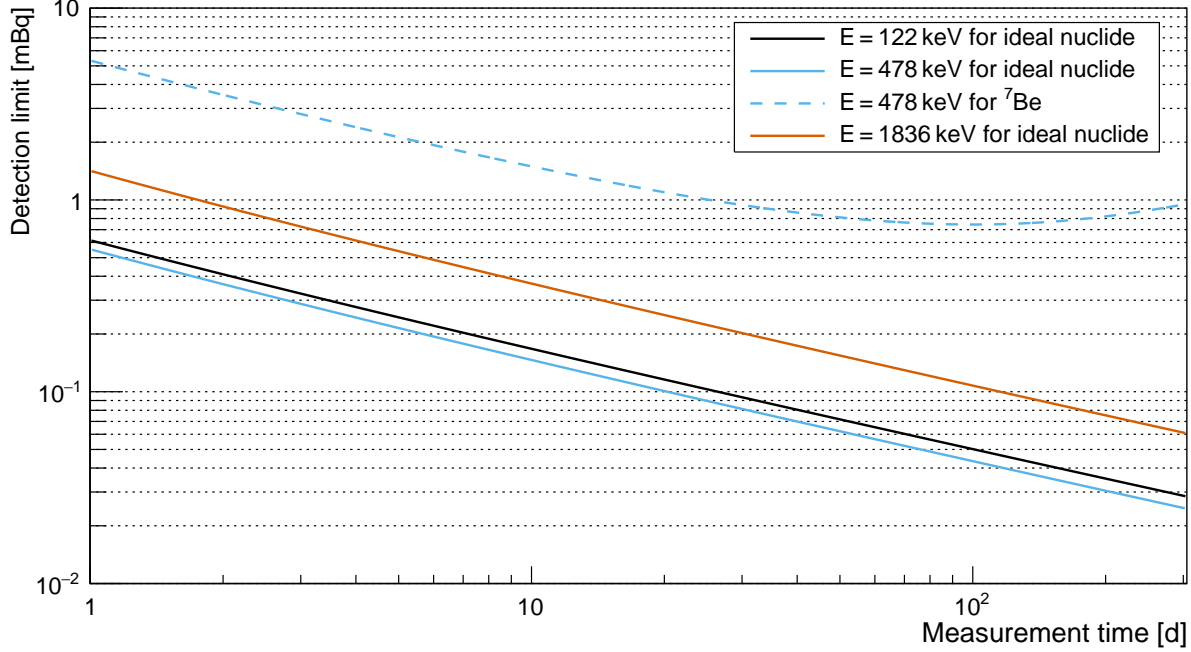


Figure 4.47: Detection limit in case of a point source on top of the end cap of TU1 for three different γ -ray energies. The ROI is conservatively assumed to be 10 keV wide. An ‘ideal nuclide’, as labeled in the legend, has a comparatively long half-life (no correction term C_{decay} needed, and a branching ratio of $\beta = 100\%$). However, in case of ${}^7\text{Be}$ (dashed line), the detection limit is suffering from a lower branching ratio, as well as a comparatively short half-life.

The resulting detection limit L_D is shown in figure 4.47 for the three different energies 122 keV, 478 keV, and 1836 keV. All three cases are plotted for an ‘ideal nuclide’, which has a comparatively long half-life ($T_{1/2} \gg t_{\text{meas}}$, i.e. no correction term C_{decay} needed), and a branching ratio of $\beta = 100\%$. For all considered γ -ray energies, the resulting detection limit is rather comparable. This is due to the fact, that the background rate and the full-energy peak efficiency both have a similar trend in energy and cancel out each other to a certain extend. However, regarding the three considered energies, the highest sensitivity can be achieved with the medium energy of $E = 478$ keV. The reason is, that lower energies are facing a larger background rate, and higher energies are facing a significant drop in efficiency. When considering a realistic nuclide (e.g. ${}^7\text{Be}$, shown as a dashed blue line in figure 4.47), the detection limit becomes worse for two reasons. The first reason is the low γ -ray branching ratio of $\beta = 10.44\%$, which leads to a decrease in the detection limit in form of a constant factor, independent of the measurement time. The second reason is its comparatively short half-life, which generates an optimal measurement time of approximately 100 d. Afterwards, any additional measurement time is counterproductive due to the worsened peak-to-background ratio based on the decayed sample activity.

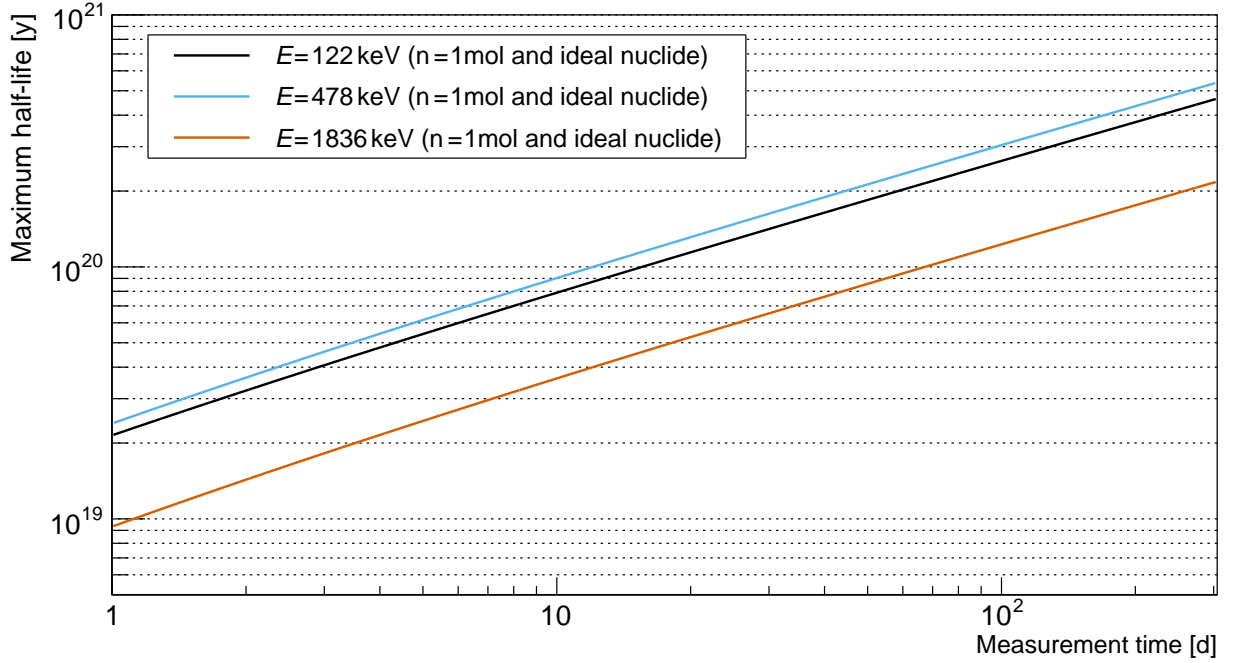


Figure 4.48: Sensitivity for obtainable half-lives in case of a point source with $n = 1$ mol on top of the end cap of TU1 for three different γ -ray energies. The ROI is assumed to be 10 keV. An ‘ideal nuclide’, as labeled in the legend, has a branching ratio of $\beta = 100\%$. The special case of ${}^7\text{Be}$ is not propagated from figure 4.47 due to its short half-life. In case of negligible self-absorption, the mass and emission probabilities of a sample of interest are scaling the end result in a proportional way, and quickly can be derived from this figure.

The resulting detection limit can also be transferred into an achievable half-life. The minimal activity, which is needed in order to claim a signal detection within a certain confidence limit therefore results in a maximal achievable half-life $T_{1/2}$ given a certain number of sample nuclei N or an amount of substance n .

$$T_{1/2,\text{max}} = \frac{\ln(2) \cdot N}{L_D} = \frac{\ln(2) \cdot n \cdot N_A}{L_D} \quad (41)$$

The resulting maximal achievable half-life $T_{1/2}$ for nuclei emitting different γ -ray energies is shown in figure 4.48. The decay correction C_{decay} can be neglected in this case, due to the fact, that the order of magnitude in achievable half-lives will always be much larger than the measurement time (i.e. the activity can be assumed to remain constant during the measurement). While it is expected, that the chosen γ -ray energy is again not a significant game changer, the overall achievable half-lives are of particular interest: Even with an amount of substance of only $n = 1$ mol, nuclides with half-lives in the order of $T_{1/2} = 10^{20}$ y can be properly analyzed within one month of measurement time. By simply scaling the sample mass, this means, that with an amount of substance of $n = 100$ mol, radio nuclei with half-lives in the order of $T_{1/2} = 10^{22}$ y can also be analyzed within one month³¹.

³¹It is worthwhile noticing, that this scaling will certainly not be perfectly proportional due to the fact, that larger amount of substances will subsequently lead to larger self-absorptions. Furthermore, intrinsic contaminations within the samples were not considered at all.

4.10 Comments on further improvements

Despite reaching unprecedented background counting rates with respect to the amount of rock overburden, there are reasonable conclusions on how to further improve the sensitivity of TU1 after taking into account the analysis of the previous sections.

Expansion of the passive shielding The entire amount of counting rate stemming from full-energy peaks is $9.2 \text{ kg}^{-1} \text{ d}^{-1}$, which is approximately 8% of the entire counting rate and does not even account for incoherently scattered events. Hence, the actual influence will be even larger, when compared to the impact of remaining prompt muonic events. While an expansion of the passive shielding might be intuitive (cf. table 4.3), this idea has to be treated with caution, as already mentioned in previous sections. On the one hand, the ratio between photon-induced events coming from outside the lead castle and photon-induced events due to internal contaminations is not yet investigated, but is expected to be comparatively small. On the other hand, a further expansion of the passive shielding could be also counterproductive in terms of additional counting rate due to an increased amount of muon-induced neutrons.

Vetoing remaining muons As shown in section 4.5, the shape of the actively vetoed continuum, as well as the prominence of the remaining peak at 511 keV, indicates a non-negligible amount of muons, which are not detected by the veto system. As discussed in section 4.4.2, the light collection efficiency, as well as the physical overlap of neighboring muon panels does suggest, that muons propagating through the active scintillation material should also be detected, if their signal does not get lost due to dead time effects. Nevertheless, there are less sensitive areas (position of HV module and PMT inside the scintillation panels), and also non-sensitive areas (bore holes of the lifting mechanism), which lead to an inevitable amount of muons passing the veto panels without a sufficient energy deposition for the veto condition.

The boreholes could be circumvented by disentangling the upper veto panel from the lifting mechanism. By mounting the upper panel on an independent horizontal rail system, it could be moved away easily during a sample change. After closing the lead castle, the lifting mechanism could be released from the upper lead plug to make room again for the muon panel. A similar mechanism has been successfully installed by the VKTA Dresden under supervision of Dr. Detlev Degering.

Reducing the background counting rate in the veto panels Furthermore, the non-trivial separation between muon-induced and photon-induced signals in the scintillation panels, as well as all of its consequences in the analysis (cf. section 4.4.5 and section 4.6.2) could be circumvented by shielding the panels against natural background radiation and therefore reducing their photon-induced counting rate. A lead plate of 2 cm thickness would already

reduce the photon intensity down to below 3 % in case of 500 keV and below 20 % for 1 MeV. Another approach in order to decrease the background counting rate could be a possible reduction in size. It is reasonable to assume, that the lower parts of the muon panels do not significantly contribute to the veto efficiency of the setup. Nevertheless, it is worthwhile mentioning, that this low-positioned active material is also beneficial regarding the issue of the last paragraph: Even if a muon is not detected by the upper part of the veto system, it might deposit a signal in the lower half after passing through TU1. So, while removing the lower half of scintillation material only reduces the photon-induced rate by a factor of approximately 2 (which does not solve the issue of an entangled muon-induced and photon-induced part of the spectrum), this ‘upgrade’ may indeed be counterproductive.

Thick veto panels A more promising upgrade would be the installation of thicker muon panels. While the total energy deposition of muons in the panel is (in first order) proportional to the thickness of the scintillation panel, an according gain shift of the photon-induced part of the spectrum should be non-existent (if possibly elevated summation effects are neglected). It is therefore reasonable to assume, that the separation of muon-induced and photon-induced signals is easier, the thicker the scintillation panels are.

Active and passive neutron shielding While it is inevitable at a certain level of sensitivity to consider some kind of neutron shielding, there is neither an optimal solution for passive, nor for active neutron shieldings in case of HPGe detectors. Both suffer from the fact, that they are neither appropriate to use outside of the lead castle (due to non-absorbed and non-detected muon-induced neutrons within the lead), nor appropriate to install them inside the lead castle (due to a lacking radio purity of such installations and counterproductive γ -emission during the moderation and absorption of neutrons). The least invasive and technically complex solution for this already existing setup in a shallow-underground laboratory could therefore be a passive neutron absorber (borated polyethylen, water etc.) outside of the passive shielding. In this way, at least neutrons stemming from (α, n) -reactions within the surrounding rock and muon-induced neutrons stemming from outside the lead castle could be attenuated. For further information and recent attempts, see also [133, 143].

Nevertheless, it is worthwhile reemphasizing the main message of section 4.9, which deals with the balancing act between reachable sensitivities and needed measurement time. A sample with an activity of $A = 10 \mu\text{Bq}$, an emission probability of $\eta = 100 \%$ and a full energy peak efficiency of $\varepsilon = 10 \%$ deposits one single full-energy event every 12 days, or 32 full energy events per year, respectively. Even if TU1 would be sensitive enough to measure this, it is necessary to weigh the benefit of this particular measurement versus the blocked time interval for multiple other short-term measurements.

5 Experimental campaign on the ${}^2\text{H}(p, \gamma){}^3\text{He}$ reaction

The experimental campaign on the ${}^2\text{H}(p, \gamma){}^3\text{He}$ reaction took place from 15.01.18 to 27.01.18 at the Ion Beam Center of HZDR, as shown in table 3.1. It was investigated in direct kinematics by irradiating deuterated targets (titanium evaporation on tantalum) using a proton beam (cf. table 3.2). The solid targets were water cooled (cf. figure 3.1) and the emitted prompt γ -rays were analyzed using two surrounding HPGe detectors (cf. figure 3.9.) This chapter is therefore structured as follows: Section 5.1 will summarize the results of previous work in order to ensure transparency of the own data. Section 5.2 and section 5.3 will discuss the analysis of the in-beam HPGe spectra, as well as elaborate the impact of the γ -ray angular distribution. Within section 5.4 the number of target atoms, i.e. the areal density will be determined. The last section is dedicated to the evaluation of the astrophysical S -factor, and will also give a summary on the obtained data.

Introductory remarks: The analysis of the presented data is also the foundation for the Master theses from Sebastian Hammer [10] and Eliana Masha [144], who preliminarily analyzed part of the data in the energy region of $E_p=400\text{ keV}-800\text{ keV}$. While Sebastian Hammer was co-supervised by the author of this thesis (cf. page 12), Eliana Masha participated in the experimental campaign as part of a cooperation with the LUNA collaboration. She subsequently analyzed the data within the working group of Prof. Dr. Alessandra Guglielmetti at the University of Milan (Italy). Furthermore, a paper on the analysis of this data was peer-reviewed and published in 2021 with the author of this thesis being also the first author of the publication. In the publication, the analysis of the master students was extended by reanalyzing the entire available data set in the energy region of $E_p=400\text{ keV}-1650\text{ keV}$ [1]. Especially the analysis procedure by Sebastian Hammer is in parts unavoidably similar to the analysis within this section, despite an independent subsequent reanalysis within the scope of this thesis. Nevertheless, in order to ensure a transparent classification on what has been used from the Master's thesis for this dissertation, as well as for the publication, the following section is dedicated to the results of Sebastian Hammer, which were used throughout the further analysis. If not stated differently, the other sections are the result of an independent analysis, which was necessary in order to circumvent flaws in the Master theses, as well as extend the data set to higher energies, and perform additional analyses.

5.1 Results of previous work on the data of this campaign

After carefully retracing the analysis of the two predecessors, it turned out to be adequate to use some results from the Master's thesis of Sebastian Hammer as a foundation of the further evaluation of this experimental campaign. In order to separate the work of Sebastian Hammer from the own analysis, this section will briefly summarize the results, which will be used throughout the further analysis.

5.1.1 Statements on the stability of the targets

The areal density of the targets was investigated using two different techniques, namely NRA and ERDA (cf. section 2.7). However, both techniques will not permanently monitor the areal density of the targets (i.e. their stability over time), but only enable distinct measurements of the areal density at certain points in time. A study on the stability of the targets is therefore crucial in order to make reliable statements on the determined cross sections.

A dedicated analysis on sputtering effects, as well as the thermal decomposition of the targets during irradiation is found in [10].

Sputtering effects Within the aforementioned master thesis, the effect of sputtered ^2H atoms in proximity to the target surface is elaborated. However, in case of the given target characteristics it is summarized, that the relative change of the amount of deuterated ions during the subsequent irradiation with protons due to sputtering is negligible. I.e. the effect was estimated to be $\Delta\rho(^2\text{H})/\rho(^2\text{H}) \leq 0.3\%$, even by assuming conservative parameters [10].

Thermal degrading It is known from literature, that target temperatures of more than 150°C can potentially lead to diffusion processes of deuterium within the target, which subsequently can lead to a degradation of the deuterium areal density [145, 146]. Based on calculations, as e.g. found in [94], thermal degradation during the irradiation can not completely be ruled out based on these conservative assumptions. However, visual changes in the appearance of the target, which should occur after temperature exposures of $\theta \geq 100^\circ\text{C}$ due to vaporization of water on the backside of the target, are not at all apparent. In addition, a dedicated paragraph in section 5.4.2 will further address these concerns.

5.1.2 Absolute full-energy peak efficiency of the HPGe detectors

An introduction into the concept of the absolute full-energy peak efficiency of HPGe detectors is given in section 2.4.2. The utilized γ -ray calibration sources for the determination in this case are ^{60}Co (ID: 3394), ^{88}Y (ID: 4433), and ^{137}Cs (ID: 3396), respectively. A dedicated list of their characteristics can be found in table 3.4. However, the resulting energy interval covered by these sources ($E_\gamma=[662,1836]$ keV) is highly insufficient, when compared to the

expected ROI for the prompt γ -rays, as approximated in equation 42 and shown in figure 5.2 in its inlet with an additional 200 keV margin.

$$E \approx Q + E_{\text{cm}} \approx 5500 \text{ keV} + (300\dots1100) \text{ keV} \approx (5800\dots6600) \text{ keV} \quad (42)$$

Hence, a well known reaction is used, which emits several γ -rays over a broad energy interval. The resulting efficiency shape stemming from the evaluation of this reaction, namely ${}^{27}\text{Al}(p,\gamma){}^{28}\text{Si}$, can subsequently be used to determine efficiencies at higher energies [147].

The measurement was done in-situ using the resonance at $E_p = 992 \text{ keV}$, resulting in well known γ -rays with $E = 1778.9 \text{ keV}$ and γ -rays with $E \approx 2800\dots10800 \text{ keV}$ [148]. While the first energy can be used to align its shape to the result of the efficiency from the calibration sources (see dashed arrow in figure 5.1), the latter ones can be used to extrapolate the available energy range, as also indicated with the according arrows in figure 5.1.

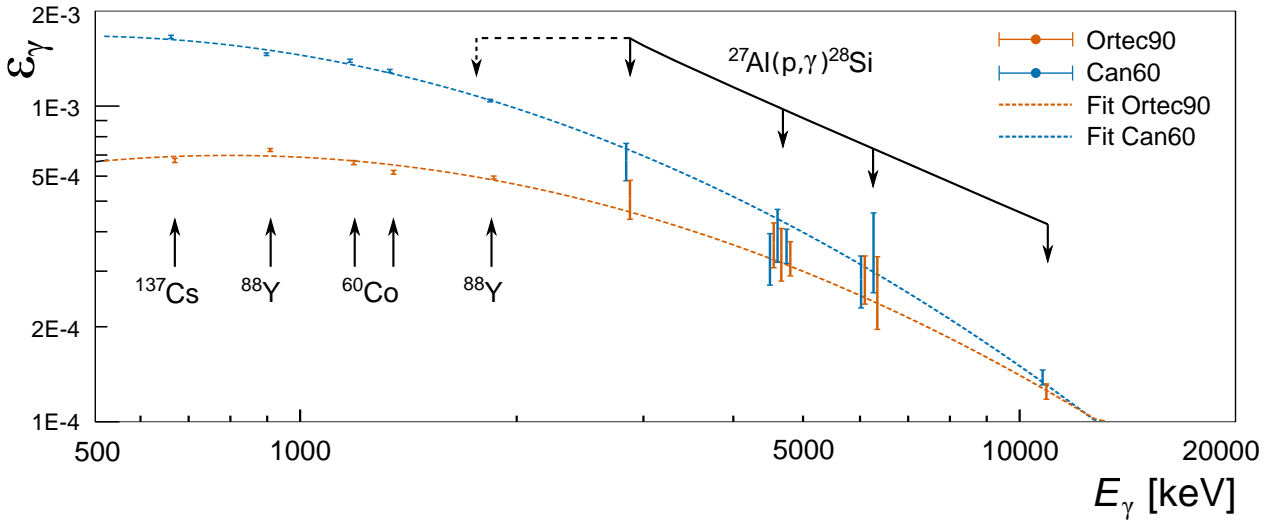


Figure 5.1: Absolute full-energy peak efficiency for the Ortec90 detector (orange), and the Can60 detector (blue). The fit takes into account the data from calibration sources, as well as the result of the ${}^{27}\text{Al}(p,\gamma){}^{28}\text{Si}$ reaction. Its normalization data point at $E = 1778.9 \text{ keV}$ is not plotted, but indicated by a dashed arrow. Data points of identical energies are slightly misaligned for the sake of clarity.

5.1.3 Laboratory and beam-induced background

The laboratory background, as well as the beam-induced background during the ${}^2\text{H}(p,\gamma){}^3\text{He}$ reaction in the IBC at HZDR was also extensively investigated by Sebastian Hammer. The assignment of the γ -ray lines in the background spectrum to the typical radio nuclei is fully adopted within the scope of this thesis. Main contributions from the natural background are ${}^{40}\text{K}$ at $E = 1461 \text{ keV}$, ${}^{214}\text{Bi}$ at $E = 609 \text{ keV}$, $E = 1764 \text{ keV}$ etc., ${}^{208}\text{Tl}$ at $E = 2615 \text{ keV}$, and the annihilation line at 511 keV .

However, due to the large Q -value of the reaction, this laboratory background (which typically becomes negligible above $E = 2615 \text{ keV}$) is only of minor interest, as shown in an

exemplary in-beam spectrum in figure 5.2. Instead, muon-induced background and the by far dominating beam-induced background play a significant and also limiting role in the analysis of the ROI, especially at larger irradiation energies. Main contributors are γ -rays from the $^{19}\text{F}(p,\alpha\gamma)^{16}\text{O}$ reaction, the $^{13}\text{C}(p,\gamma)^{14}\text{N}$ and the $^{15}\text{N}(p,\alpha\gamma)^{12}\text{C}$ reactions, respectively. While fluorine is a well-known contamination within tantalum, ^{13}C and ^{15}N are most likely due to condensation on the surface layer of the target, as further elaborated in chapter 5.4.2. For more detailed information on the origin, the energies and the impact of the in-beam background, see also [1, 10].

5.2 Evaluation of the in-beam spectra

In order to calculate a cross section and an astrophysical S -factor, the number of projectiles need to be known, as well as the number of target atoms and the number of emitted prompt γ -rays. This section is devoted to the latter one, i.e. the evaluation of acquired in-beam spectra.

Table 5.1: Characteristic energies for the irradiation runs on the targets TiD2-2-3 and TiD2-2-4, respectively. In addition to the run number and the accumulated charge, the terminal voltage TV is given, which determines the proton energy E_p , the effective energy E_{eff} , the center of mass energy E_{cm} , and the resulting expected γ -ray energies E_γ under $\vartheta = 55^\circ$ (Ortec90), and $\vartheta = 90^\circ$ (Can60), respectively. The red values correspond to pulse height spectra, which are lacking of statistics and not further evaluated. See text for details and section 2.6 for calculation.

Target	Run	Charge [mC]	TV [kV]	E_p [keV]	E_{eff} [keV]	E_{cm} [keV]	$E_\gamma(55^\circ)$ [keV]	$E_\gamma(90^\circ)$ [keV]
TiD2-2-3	164	17.2	197.5	423.7	418.1	278.7	5799.1	5766.1
	160	27.9	287.5	605.2	600.7	400.4	5927.9	5887.5
	161	58.3	332.6	696.1	692.0	461.3	5992.1	5948.2
	152	83.7	387.5	806.9	803.1	535.3	6069.9	6022.1
	150	10.0	487.5	1008.6	1005.3	670.1	6211.3	6156.6
	162	30.1	505.1	1044.1	1040.8	693.8	6236.1	6180.3
	163	38.6	628.4	1292.8	1289.4	859.8	6409.8	6345.9
	159	51.9	757.3	1552.9	1550.3	1033.4	6591.0	6519.1
	154	18.0	802.5	1644.0	1641.5	1094.2	6654.4	6579.8
TiD2-2-4	179-181	40.3	187.5	403.4	397.7	265.1	5784.6	5752.5
	167-169	83.2	237.5	504.3	499.3	332.8	5856.4	5820.0
	170-173	94.1	287.1	604.3	599.8	399.8	5927.2	5886.9
	174	48.4	337.5	705.9	701.8	467.8	5998.9	5954.8
	175+178	85.9	387.5	806.9	803.1	535.3	6069.9	6022.1

The underlying kinematics of this reaction, as well as the corresponding reaction scheme were introduced in chapter 1.3 and in figure 1.4, respectively. According to equation 24, the expected energy of the prompt γ -ray mainly depends on the Q -value of the reaction, as well as the center-of-mass energy E_{cm} . In addition, the positioning of the detector, i.e. its angle

with respect to the beam direction ϑ leads to a (comparatively small) Doppler shift, which also needs to be accounted for, as well as the recoil energy. A list of all evaluated runs, as well as their applied E_{cm} and resulting E_γ for both utilized detectors is shown in table 5.1. Due to the comparatively large Q -value of the reaction, the emitted prompt γ -rays are expected within the high-energetic energy interval of $E \approx 5800 - 6600$ keV.

A representative pulse height spectrum stemming from the irradiation with $E_{\text{cm}} = 535.3$ keV on TiD2-2-3 is shown in figure 5.2 for both detectors. Both spectra are plotted within their broad energy range of $E = 0 - 7500$ keV. Furthermore, the respective inlets show the region of $E \approx 5600 - 6800$ keV (also indicated by black, dashed, vertical lines in the main figures). The theoretically predicted regions of interest for the emitted prompt γ -rays are additionally plotted as a shaded orange area.

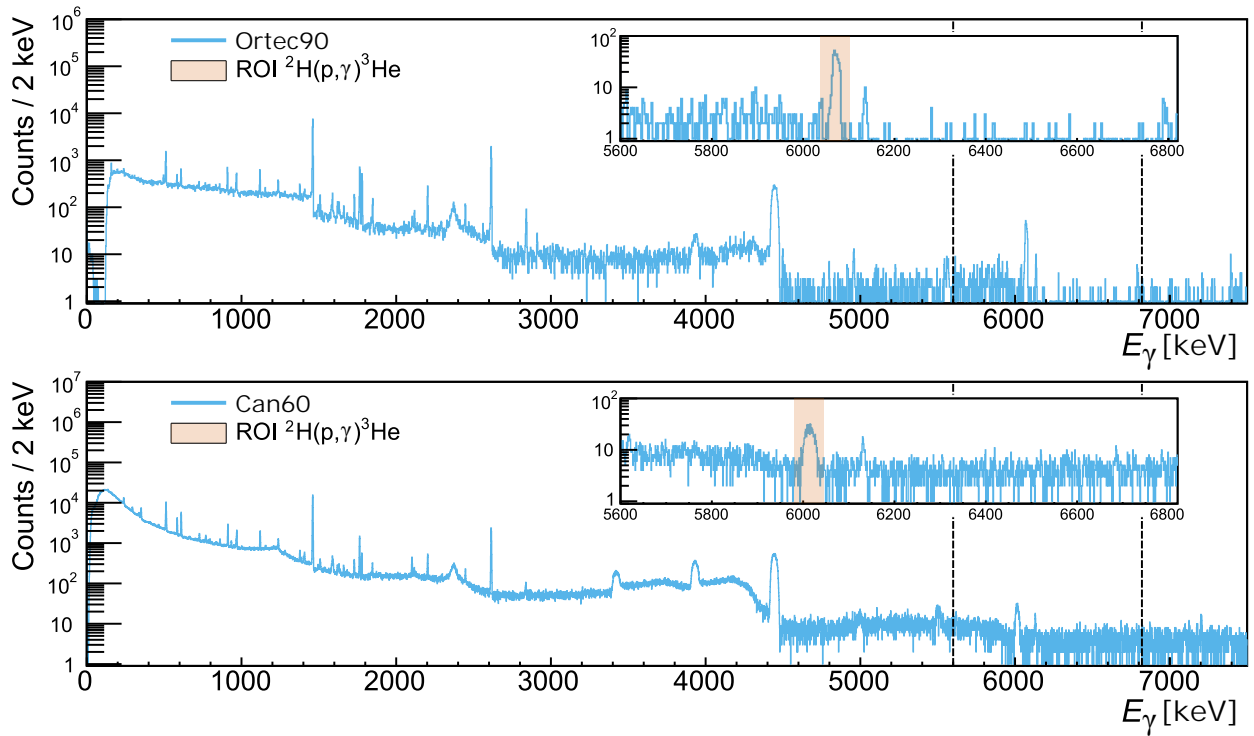


Figure 5.2: Resulting pulse height spectra using $E_{\text{cm}} = 535.3$ keV during the irradiation of target TiD2-2-3. The respective inlet of both figures show the region of $E = 56000 - 6800$ keV, which is also indicated by the vertical black lines, respectively. Top: Result for the actively vetoed spectrum of the Ortec90 detector. Bottom: Resulting spectrum of the Can60 detector.

Analog figures for all relevant evaluated pulse height spectra can also be found in the appendix C.2. They also show the entire energy range, as well as an inlet containing the ROI. The x-axis, as well as the y-axis of these inlets are fixed for all figures, i.e. within the figures of the appendix, in order to enable direct comparability of different runs.

These pulse height spectra are analyzed based on the technique presented in section 2.4.3 and the number of counts within the peaks, as well as their uncertainties are determined subsequently. However, there are four cases, where only one of the two detectors (namely ‘Ortec90’) acquired data with statistically significant net counts. While both detectors are

similar in distance to the target, the Ortec90 detector is equipped with a BGO and an additional lead shield. Hence, the improved peak-to-Compton ratio enables the analysis of net counts even if the overall accumulated charge for these runs is comparatively low. These four cases, where the analysis of the spectra from Can60 did not result in statistically relevant net counts are labeled with red values in table 5.1 and are not further considered. The resulting net counts $N \pm \Delta N$ for each irradiation energy and each detector can subsequently be normalized to the accumulated charge and their corresponding absolute full-energy peak efficiency ε . Considering this experimental campaign, this quantity will further be called the yield Y within each detector. Due to the normalization on ε , any systematic differences in the yield between the two detectors are related to the γ -ray angular distribution.

5.3 Theoretical ab initio γ -ray angular distribution

In common γ -ray spectrometry, the association between the number of emitted photons from a source, and the detected amount of events in the full-energy peak of a detector solely depends on the full-energy peak efficiency ε_{abs} (in case of negligible dead time issues and summation effects). However, in case of in-beam γ -ray spectrometry, the physics can be more complex. This is due to the fact, that the ion beam induces an environment with a directional dependency, which might reveal underlying angular distributions of the emitted γ -rays.

Precise experimental information about γ -ray angular distributions are only rarely available. Hence, theoretical input is crucial in order to correct in-beam data for the position of the utilized detectors. It was already elaborated in section 1.4.2, that the γ -ray angular distribution for the ${}^3\text{He}(\alpha, \gamma){}^7\text{Be}$ reaction shows a rather complex behavior in the energy region around the BBN Gamow window (cf. figure 1.8) with multiple non-negligible Legendre polynomials. However, this is not expected in case of the ${}^2\text{H}(\text{p}, \gamma){}^3\text{He}$ reaction.

State-of-the-art theoretical calculations on the γ -ray angular distribution show significantly less energy dependency in the region around the BBN Gamow window. This also makes it less susceptible for major misprognosis and thus more robust to use it as an input for the correction of experimental data. In detail, this distribution is assumed to be widely dominated by a negative a_2 component³² leading to a higher yield at $\vartheta = 90^\circ$, and subsequently lower yields towards $\vartheta = 0^\circ$ and $\vartheta = 180^\circ$, as also shown in figure 5.3.

These ab initio calculations for the ground-state transition of the ${}^2\text{H}(\text{p}, \gamma){}^3\text{He}$ reaction were kindly provided by Laura E. Marcucci et al. [44, 149, 150], as also discussed in more detail in section 1.3. While the following section is purely devoted to its introduction and the utilization for the further analysis, dedicated crosschecks of the experimental data and the ab initio calculation can also be found in [1, 10].

³²The physics of γ -ray angular distributions is introduced in section 1.4.2 and utilized in section 6.3.6. The a_2 component refers to one the coefficients in the sum of $a_i \cdot \cos(\theta)^i$ functions, as shown in equation 59.

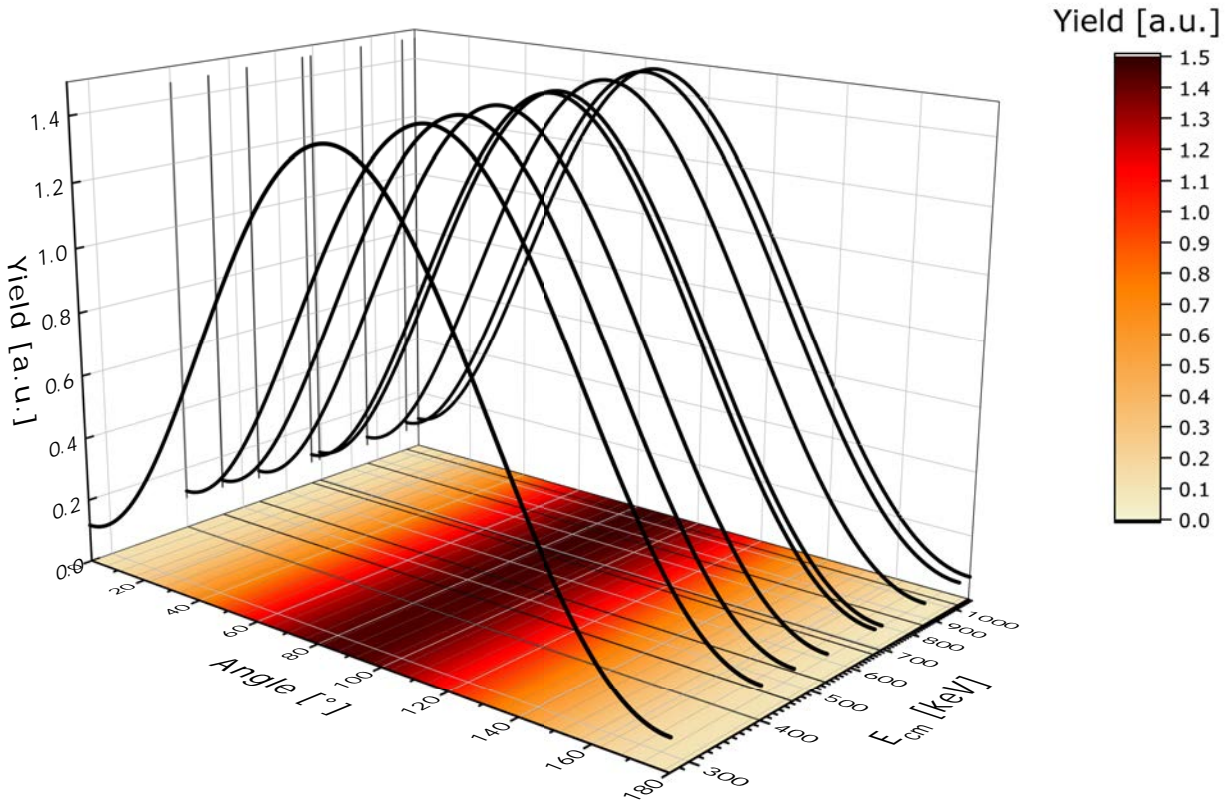


Figure 5.3: Theoretical γ -ray angular distribution of the ${}^2\text{H}(p,\gamma){}^3\text{He}$ reaction. The yield is shown with respect to E_{cm} and the emission angle of the prompt γ -rays. The bottom layer shows a projection of an interpolation between the distinct energies of interest (black curves). The plotted values are chosen according to the irradiation energies of TiD2-3 (cf. table 5.1). Compared to the distribution of ${}^3\text{He}(\alpha,\gamma){}^7\text{Be}$, its shape is almost energy independent within the investigated ROI. Based on data from [44, 149].

The resulting theoretical prediction of the γ -ray angular distribution is shown in figure 5.3. The expected yield is plotted with respect to the γ -ray emission angle and the center-of-mass energy E_{cm} . The predictions by Marcucci et al. were kindly calculated and provided for the exact energies, which were used during this campaign (cf. table 5.1). For sake of clarity, only the respective energies for target TiD2-2-3 are displayed. This is due to the fact, that the energies for target TiD2-2-4 are covered in the same energy range and are partly highly similar to the energies for target TiD2-2-3. This would lead to an unnecessary overlap in figure 5.3 without providing any additional information.

As previously discussed, the angular distribution only barely depends on the energy in the investigated energy range. However, small deviations can be seen by focusing on the projection on the bottom panel, which shows a very slight trend towards smaller angles for larger values of E_{cm} . When discussing about a change of ratio between the yield of Can60 ($\vartheta = 90^\circ$) and Ortec90 ($\vartheta = 55^\circ$) at all, then the only trend would be a very small predicted enhancement in the yield of Ortec90 for larger irradiation energies.

5.3.1 Yield correction using the theoretical γ -ray angular distribution

The theoretical γ -ray angular distribution can subsequently be used to correct the yield in both detectors (Ortec90 and Can60). However, there is a discrepancy for both detectors between their positioning angle in the laboratory frame and the center-of-mass frame, as elaborated in section 2.6.5. The effective angle of a detector with respect to the beam direction becomes subsequently greater for larger irradiation energies. The two angles of $\vartheta = 0^\circ$, and $\vartheta = 180^\circ$ are not distorted and the largest effect can be seen in case of a detector at $\vartheta = 90^\circ$ (cf. also figure 2.6 in case of the ${}^3\text{He}(\alpha, \gamma){}^7\text{Be}$ reaction).

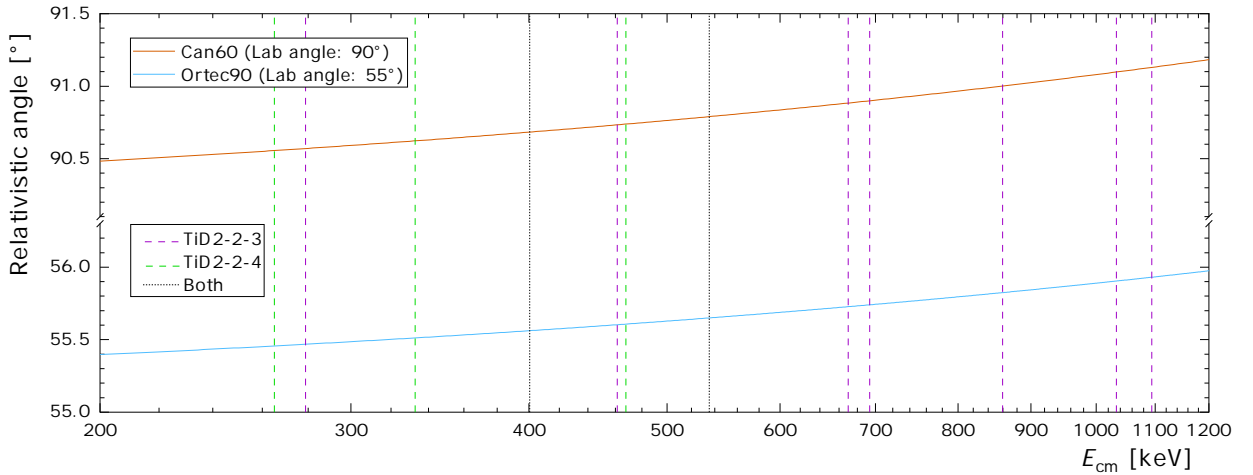


Figure 5.4: Relativistic angle for the ${}^2\text{H}(p, \gamma){}^3\text{He}$ reaction with respect to the center-of-mass energy E_{cm} . This relation is shown for both the Can60 detector at a laboratory angle of $\vartheta = 90^\circ$ (orange), as well as for the Ortec90 detector at a laboratory angle of $\vartheta = 55^\circ$ (blue). The investigated energies for both targets are shown as vertical lines (cf. table 5.1). In case of an energy difference of < 1 keV, there is only one line for sake of clarity, which is labeled with ‘Both’.

In case of the ${}^2\text{H}(p, \gamma){}^3\text{He}$ reaction, the relativistic angle correction is shown in figure 5.4. The relativistic angle is plotted with respect to E_{cm} for both detectors and the relevant irradiation energies (cf. table 5.1) are indicated by vertical black lines. Hence, the relativistic angles for both detectors are approximately $0.5^\circ - 1^\circ$ larger than the laboratory angles.

However, the γ -ray angular distribution can now be used to correct the obtained yield within both detectors according to their effective angle for each irradiation energy. It is therefore possible to calculate the number of occurred reaction based on the number of detected prompt γ -rays, as well as the full-energy peak efficiency ε , the theoretical γ -ray angular distribution and a dead-time correction. This is performed entirely independent for both detectors and will be used in section 5.5 in order to calculate the cross section.

However, the calculation of the cross section also depends on the determination of the areal density for each target. This analysis will be elaborated within the next chapter.

5.4 Determination of the target areal density

Among references to a variety of different techniques, there are two approaches for the determination of the areal densities of a sample, which were thoroughly introduced in section 2.7, namely the nuclear reaction analysis NRA and the elastic recoil detection analysis ERDA. Both of them were performed within the scope of this experiment and their analysis will be topic of the subsequent chapters.

5.4.1 Nuclear reaction analysis

The general technique of the nuclear reaction analysis (NRA) was described in section 2.7.1. In case of the ${}^2\text{H}(\text{p}, \gamma){}^3\text{He}$ campaign, the areal density of the implanted ${}^2\text{H}$ is determined by irradiation of ${}^3\text{He}$ and a subsequent investigation via the ${}^2\text{H}({}^3\text{He}, \text{p}){}^4\text{He}$ reaction. This reaction is commonly used to determine areal densities of solid target experiments containing implanted deuterium [151, 152].

In the particular case of the IBC-I campaign (cf. section 3.1), the ${}^2\text{H}$ in the target is irradiated by ${}^3\text{He}^{2+}$. The advantage of the utilized 3 MV tandetron accelerator in the IBC of HZDR is the possibility to perform the NRA in-situ due to its ability to provide both a proton beam for the reaction of interest via a cesium (Cs) sputter ion source, as well as a helium beam for the NRA reaction via a TORVIS ion source (cf. section 3.3).

Due to the high costs of ${}^3\text{He}$, the low amount of necessary beam intensity on the target (due to the high cross section), and the subsequent comparatively high losses during beam optimization, it is not reasonable to extract a pure beam of ${}^3\text{He}$. In order to prevent unnecessary losses of ${}^3\text{He}$, the provided gas bottle (0.40 l @12.5 bar, 5 l STP) contained 95% of ${}^4\text{He}$ and only 5% of ${}^3\text{He}$.

The differential cross section of the ${}^2\text{H}({}^3\text{He}, \text{p}){}^4\text{He}$ reaction is well known regarding proton emission angles at $\vartheta = 135^\circ$, $\vartheta = 144.5^\circ$, and $\vartheta = 175^\circ$ over a wide energy range from 250 keV up to 6 MeV [153]. The utilized target chamber was therefore specifically designed in a way, which enables the positioning of a silicon surface barrier detector under $\vartheta = 144.5^\circ$ with respect to the beam axis (cf. section 3.1.6 for more information on the detector, and section 3.3.1 for its use in the setup).

The energy calibration of this detector, as well as the determination of its solid angle will be discussed in the following two sections. The third section will then discuss the subsequent determination of the areal density.

It is worthwhile mentioning, that the nickel foil in front of the silicon detector (cf. section 3.1.6) was removed before conducting the measurements of both the energy calibration, and the solid angle. This is due to the fact, that α particles in the order of $E = 5 - 6$ MeV experience an energy loss of approximately $dE/dx = 400$ keV/ μm while propagating through nickel. The thickness of the nickel foil is 50 μm , which would lead to a complete absorption

of the alpha particles. The energy calibration, as well as the determination of the solid angle are therefore determined without nickel foil in a pressurized environment of approximately 1 mbar.

5.4.1.1 Energy calibration of the silicon detector

A precise energy calibration of the silicon detector is crucial for the later analysis of the NRA spectra. This is due to a beam induced contamination in the corresponding spectra, which is overlapping with the ROI of the ${}^2\text{H}({}^3\text{He,p}){}^4\text{He}$ reaction (cf. figure 5.7), and though has to be treated carefully. Furthermore, the energy calibration will hereafter be needed at energies above $E = 10$ MeV, while the calibration sources only provide α -lines in the order of $E = 5 - 6$ MeV. This potentially leads to a subsequent magnification of uncertainty due to a comparatively large extrapolation by almost a factor of two.

During this experimental campaign, two different α sources were used. While an available ${}^{241}\text{Am}$ calibration source (ID: AJ-5470, cf. table 3.4) provides the lowest relative uncertainty on its emission rate, and therefore will be used for the determination of the areal density, the energy calibration is done using a so called triple alpha source (ID: EC221). This source contains the three radio nuclides ${}^{239}\text{Pu}$, ${}^{241}\text{Am}$, and ${}^{244}\text{Cm}$, which emit α particles in the order of $E = 5 - 6$ MeV. The utilized α -lines, as well as their emission probabilities are listed in table 3.4. In summary, the triple alpha source provides a wider span for the energy calibration, than the single alpha source.

The energy calibration of the silicon detector was performed in-situ during the experimental campaign in the IBC at HZDR. The setup, which was used for the calibration was introduced in figure 3.9 with the main difference being the prior removal of the nickel foil, which was already discussed in the beginning of this chapter. The resulting pulse height spectrum from the measurement with the triple alpha source is shown in blue in the uppermost panel of figure 5.5. The ROI of the same pulse height spectrum is shown in the second panel of the respective figure. Furthermore, the data in the ROI is fitted with an appropriate fit function for α spectrometry. This function is an adapted version of a recently proposed fit algorithm [154], which also was discussed and validated in the PhD thesis of Dr. Heinrich Wilsenach [155].

The originally proposed fit function uses a Gaussian distribution with three scientifically motivated exponential tails for each peak (two sharp tails, and one flat tail). This approach for high-resolution and high-statistics spectra is adjusted within the subsequent analysis to a two-tail approach (one sharp tail, and one flat tail). However, the inclusion of tailings in general is important, due to their subsequent shift of the correct mean value, when implementing them. The fit function $F(E, \mu, \tau, \sigma)$, which is used for each peak in the second panel in figure 5.5 is shown in equation 43.

The resulting residuum (cf. third panel in figure 5.5) shows some minor systematic flaws of the fit approach (small oscillations around peak regions) which might be related to the

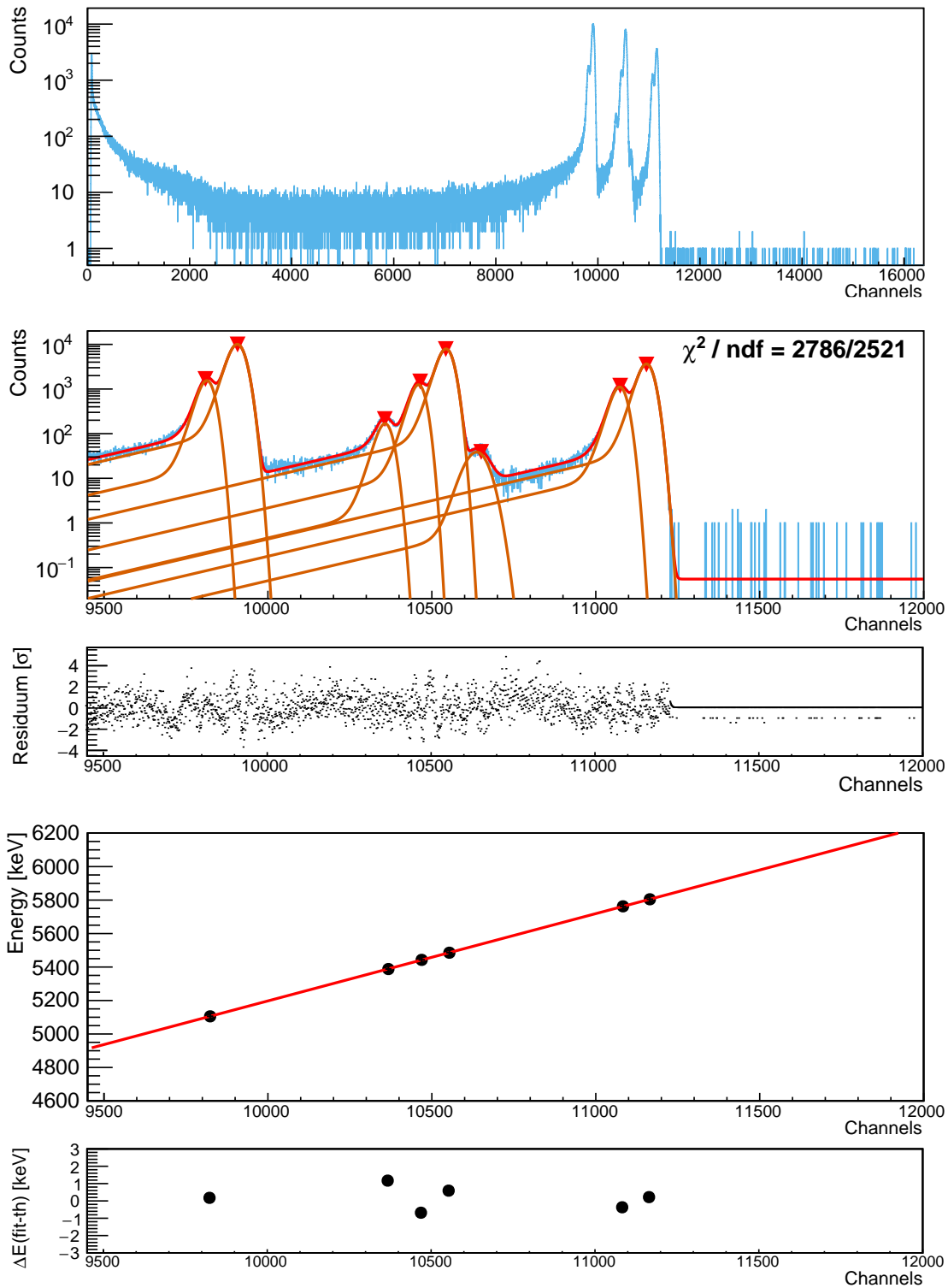


Figure 5.5: Top panel: Pulse height spectrum of a silicon detector using the triple alpha source EC221 (cf. table 3.4) for the energy calibration. Second panel: ROI of the same pulse height spectrum (blue) with a global fit of the ROI (red) and the contribution of each peak (orange). Third panel: Residuum for the second panel in terms of standard deviations. Fourth panel: Corresponding energy calibration with a first order polynomial. Two peaks were excluded to their double peak structure (see text for details). Fifth panel: Residuum of the fourth panel in terms of keV.

missing third exponential term or due to non-ideal Gaussian peak shapes. While these fluctuations also results in a rather unreasonable Chi-squared value ($\chi^2/\text{ndf} = 2786/2521$), most of them are within a comparatively small band of $\pm 2\sigma$.

$$F(E, \mu, \tau, \sigma) = A_0/\sigma \cdot \exp\left(-\frac{(x - \mu)^2}{\sigma^2}\right) + \sum_{i=1}^2 \frac{A_i \cdot A_0}{\tau_i} \cdot \exp\left(\frac{x - \mu}{\tau_i} + \frac{\sigma^2}{2\tau_i^2}\right) \cdot \text{erfc}\left(\frac{x - \mu}{\sqrt{2}\sigma} + \frac{\sigma}{\sqrt{2}\tau_i}\right) \quad (43)$$

The adjustment with respect to formulas found in literature additionally takes into account, that the ratio between both tail intensities A_i and their respective peak intensity A_0 always needs to be constant throughout each peak in the ROI.

The total fit function (red) in the second panel of figure 5.5 is obtained by using the ‘Search()’ function of TSppectrum, which resulted in eight fittable peaks. The ROI is subsequently fitted with a first order polynomial, and eight peak shapes according to equation 43. As already mentioned, the relative ratio between peak and tailings is a shared parameter between all peaks, which leads to the following amount of totally needed parameters: Two parameters for the first order polynomial, the four globally shared parameters A_1 , A_2 , τ_1 and τ_2 , as well as three parameters for each of the eight peaks corresponding to their subsequent amplitude A_0 , their position μ , and their width σ .

It is worthwhile mentioning, that the peak width σ was kept as a free parameter for each peak. This is due to the fact, that the triple alpha source has two cases, where two peaks are in close proximity to each other. This is on the one hand the inseparable double peak of ^{241}Am at $E = 5511.5 \text{ keV}$ ($\eta = 0.225(5)\%$) and $E = 5544.5 \text{ keV}$ ($\eta = 0.37(3)\%$), which is represented by the sixth peak from the left (and also smallest one) in the second panel of figure 5.5. On the other hand there is a inseparable double peak of ^{239}Pu at $E = 5144.3 \text{ keV}$ ($\eta = 17.11(14)\%$) and $E = 5156.59 \text{ keV}$ ($\eta = 70.77(14)\%$), which is represented by the second peak from the left (and also the most intense one) in the second panel of figure 5.5. These double peaks lead to a sigma of 18.8 keV and 27.5 keV, respectively, while all other peaks vary regarding their σ between 15.4 keV and 17.2 keV.

The residuum in terms of standard deviations is shown in the third panel of figure 5.5. While there are some small remaining systematical deviations between fit and data, the overall accordance is sufficient, which is also reflected by the χ_{red}^2 .

It is evident, that the most intense peak, and the smallest peak should nevertheless be excluded from the energy calibration due to their double peak structure. While their contribution to the global fit can be properly estimated with one peak each to receive a proper residuum, they are certainly no suitable candidates for the energy calibration.

The subsequent energy calibration, and its residuum in terms of ‘Deviation from literature in keV’ is shown in the fourth and fifth panel of figure 5.5, and shows a notable maximum deviation of 1 keV at energies around 5-6 MeV.

5.4.1.2 Solid angle of the silicon detector

While the energy calibration for the silicon detector was conducted by using a triple alpha source with a larger span of energies, the determination of its solid angle is performed with the single alpha source AJ-5470 containing the α emitter ${}^{241}\text{Am}$ (cf. table 3.4), mainly due to its lower relative uncertainty on its activity.

As discussed in chapter 2.4.2, in case of γ -spectrometry, the full-energy peak efficiency ε depends on a self-absorption term of the source ε_s , the geometric probability of hitting the detector ε_g (which also includes absorption/scattering in the propagation medium), and the probability of depositing its full energy in the active volume ε_d , when entering it.

Within this chapter of determining a corresponding efficiency in particle spectrometry, the first and the last term (ε_s and ε_d) are not needed. While the first term is usually crucial for particle spectrometry, the data sheet of the calibration source is providing the surface emission rate R_S , which already takes care of absorption within the source itself.

The last term, which is the intrinsic detection efficiency, is set to be $\varepsilon_d=1$ within the scope of this thesis. The range of the utilized protons ($\approx 800\ \mu\text{m}$), and α particles ($\approx 30\ \mu\text{m}$) is comparatively small with respect to both the thickness of the active area ($2000\ \mu\text{m}$) and the surface of the detector ($300\ \text{mm}^2$). While the thickness is sufficient enough to stop all particles, the comparatively large total area makes it redundant to elaborate possible edge effects, where the particles enter the outermost coat of the cylindrical active volume and potentially leaves it without full-energy deposition.

The 4π surface emission rate of AJ-5470 at the date of calibration was $R_{S,0}=5380(110)\ \text{s}^{-1}$ (cf. table 3.4), which results in a 4π surface emission rate at the date of the measurement (12.11.2018) of $R_S=5374(110)\ \text{s}^{-1}$.

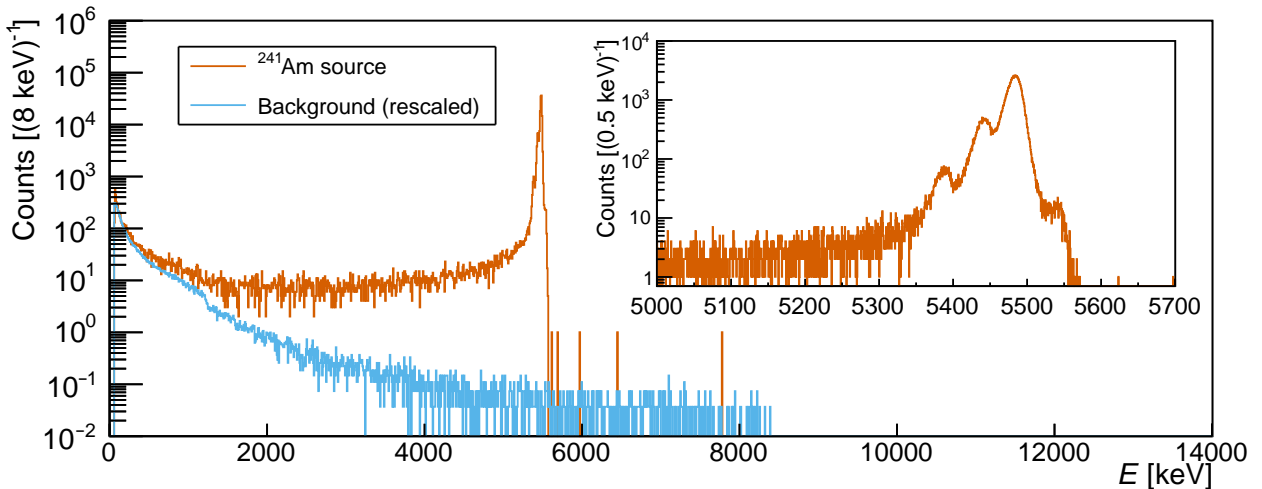


Figure 5.6: Pulse height spectrum during the calibration of the Si-detector with an ${}^{241}\text{Am}$ source (orange). The corresponding background (blue) is rescaled to the live time of the orange spectrum. The inlet shows a zoom into the ROI of the four α -lines from ${}^{241}\text{Am}$.

The pulse height spectrum for the determination of the solid angle Ω is shown in figure 5.6. During the measurement, the chamber was also evacuated ($p \approx 3 \text{ E-6 mbar}$) in order to neglect the attenuation correction factors of possible remaining air and create an environment, which is as similar to the in-beam conditions as possible. The solid angle Ω can therefore subsequently be calculated via equation 44 with \dot{N} being the counting rate in the silicon detector.

$$\Omega = \frac{\dot{N}}{R_S} = 2.22 \cdot 10^{-3} \quad (44)$$

$$\Delta\Omega_{\text{sys}} = 0.04 \cdot 10^{-3} \quad (45)$$

$$\Delta\Omega_{\text{stat}} = 0.006 \cdot 10^{-3} \quad (46)$$

The systematic uncertainties are due to the uncertainty on the surface emission rate R_S , while the statistical uncertainties are due to the counting statistics.

5.4.1.3 Determination of the areal density

As mentioned earlier, the areal density of the implanted ^2H is determined via the $^2\text{H}(^3\text{He,p})^4\text{He}$ reaction by irradiating the deuterized targets with a beam of ^3He . Unfortunately, the actual nuclear reaction analysis was only performed on the last target TiD2-2-4 (cf. table 3.2). This is due to delays in the delivery of the earlier mentioned ^3He - ^4He gas mixture, which arrived with a delay, and was not available over a wide span of the experimental campaign. Regarding target TiD2-2-4, there are three conducted NRA runs. The first run (Run166) took place prior to the actual proton irradiation of the target. The second and the third run (Run176 and Run177, respectively) took place after an approximate total accumulated charge of 70 % for this target, namely after investigating the energies of $E = 333 \text{ keV}$, $E = 400 \text{ keV}$, and $E = 468 \text{ keV}$.

The result of all three NRA runs is shown in figure 5.8. While the first two runs (Run166 and Run176) are performed at $E_{\text{lab}}=1987 \text{ keV}$, the last run (Run177) was performed at $E_{\text{lab}}=2188 \text{ keV}$. These energies are chosen (as well as the angle of the silicon detector) due to their well-known differential cross section [153]. Their subsequent differential cross sections at 144.5° are $\sigma = 12.7(5) \text{ mb/sr}$ for $E_{\text{lab}}=1987 \text{ keV}$ and $\sigma = 10.7(5) \text{ mb/sr}$ for $E_{\text{lab}}=2188 \text{ keV}$, respectively. Furthermore, these specific energies were chosen due to a broad resonance at $E_{\text{lab}} \approx 600 \text{ keV}$, which was avoided for reasons of reliability (cf. section 2.7.1).

As shown in figure 5.8, all three resulting spectra show a double peak structure around $E = 11 \text{ MeV}$, which needs to be investigated properly. This structure was also the reason for the detailed energy calibration of the silicon detector in chapter 5.4.1.1. The theoretically expected energies for protons from the $^2\text{H}(^3\text{He,p})^4\text{He}$ reaction, which are emitted under $\theta = 144.5^\circ$ for both irradiation energies, are $E_{\text{p,lab}} = 12.262 \text{ MeV}$, and $E_{\text{p,lab}} = 12.175 \text{ MeV}$, respectively.

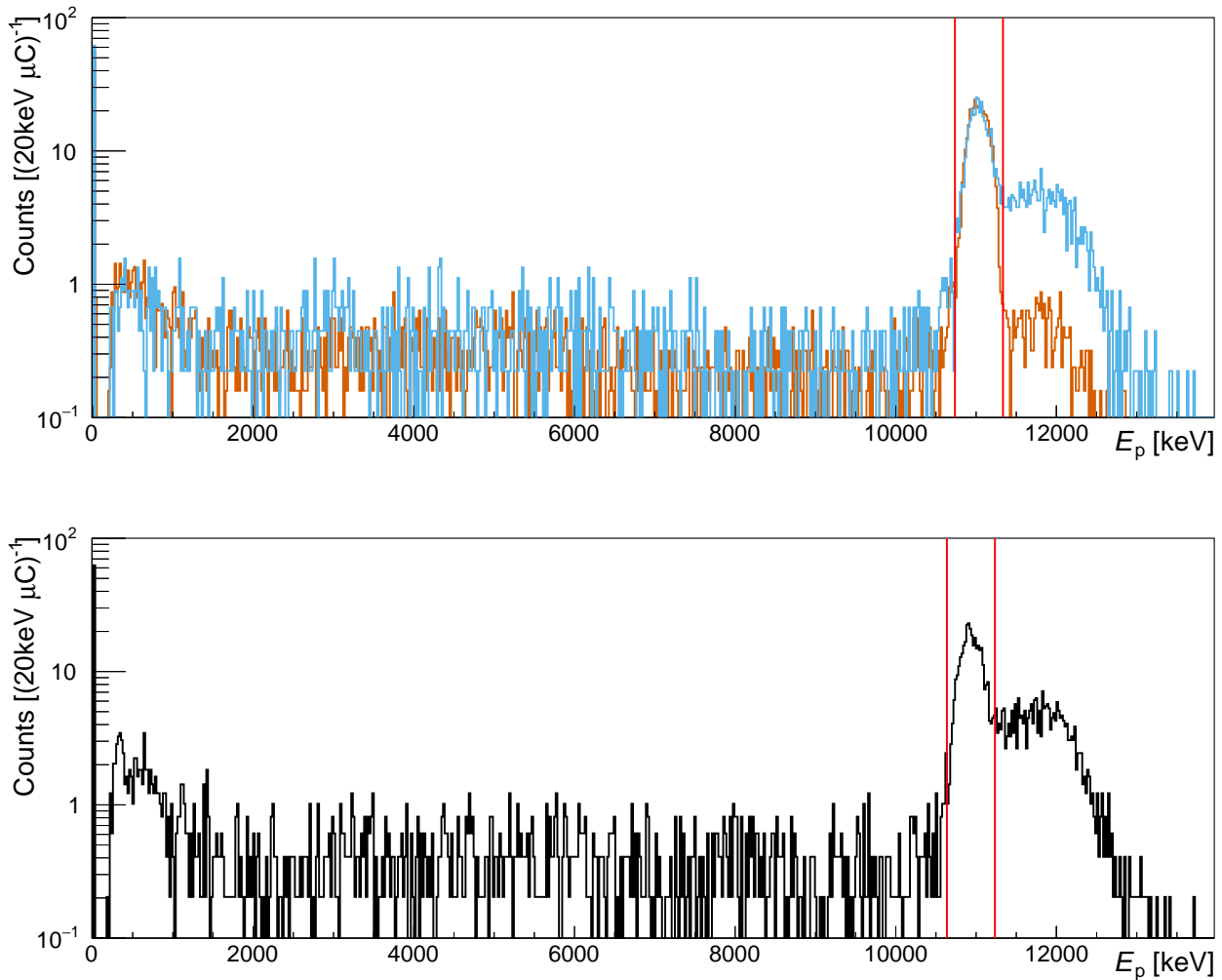


Figure 5.7: Pulse height spectra of all three NRA runs, which are normalized to their accumulated charge, respectively. The theoretically predicted energy interval (see text for details) is indicated with red vertical lines. Top: The results for Run166 (orange) and Run176 (blue), which have been performed at $E_{\text{lab}} = 1987$ keV. Bottom: The result for Run177 (black), which has been performed at $E_{\text{lab}} = 2188$ keV.

Due to the opening angle of the silicon detector (distance $d = 85.4$ mm, area $A = 300$ mm², $\vartheta = 144.5^\circ \pm 6.5^\circ$, $\vartheta_{\text{min}} = 138.0^\circ$ and $\vartheta_{\text{max}} = 151.0^\circ$), as well as the energy loss ($\Delta E \approx 1$ MeV), and the straggling ($\sigma \approx 60$ keV) in the $50 \mu\text{m}$ nickel foil, the protons in the silicon detector are neither at the expected energy, nor are they mono energetic, but have a peak width in the order of 100 keV. In addition, the resolution of the silicon detector leads to an additional smearing during the reconstruction of the proton energy. The prediction of the minimal, and the maximal energies after taking all energy related effects into account are shown as red vertical lines in figure 5.8.

The main peak in the double peak structures of figure 5.8 is therefore determined to be the expected signal from the ${}^2\text{H}({}^3\text{He}, p){}^4\text{He}$. The satellite peak on the right side is most likely stemming from the ${}^{14}\text{N}({}^3\text{He}, p){}^{16}\text{O}$ reaction ($Q = 15.243$ MeV) due to nitrogen impurities in

the target. Due to the fact that the yield is increasing for subsequent runs, it is likely, that there is an accumulation of nitrogen on the target over time.

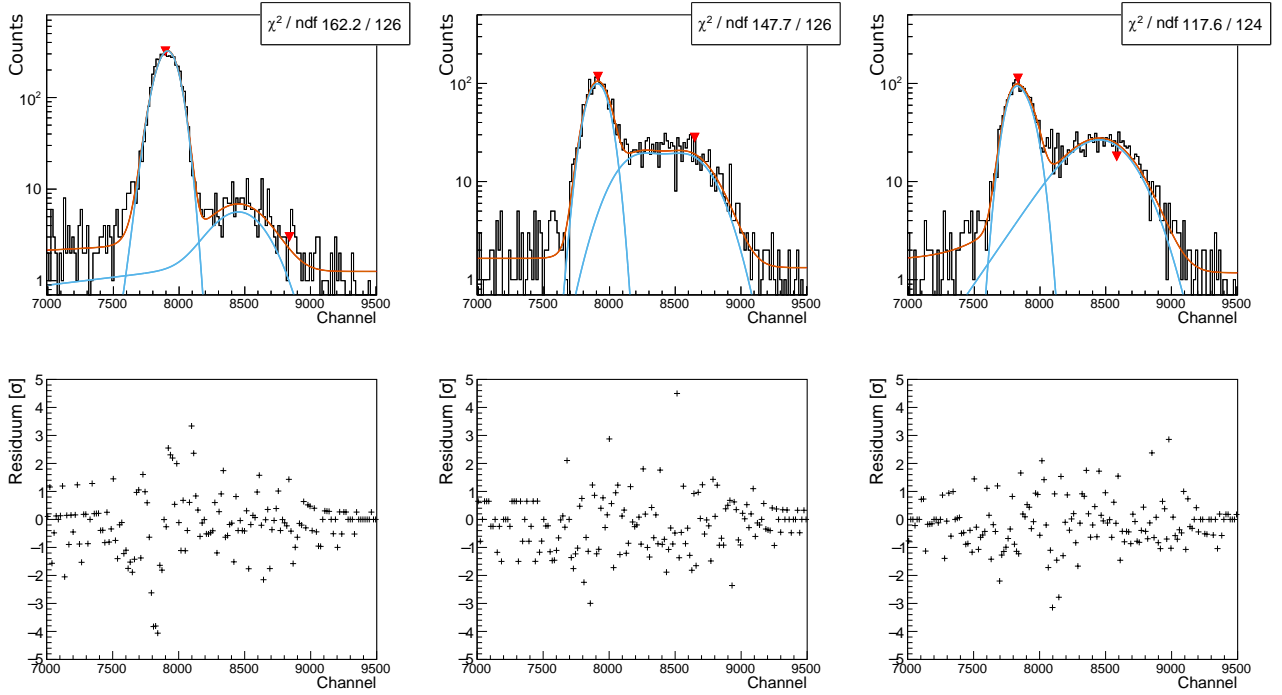


Figure 5.8: Investigation of the ROI regarding the pulse height spectra of all three NRA runs (cf. figure 5.7). Top figures: ROI with three fits each: A Gaussian, and a Gaussian with a left tail are shown in blue, and the sum of them is shown in orange. Bottom: The respective residuum of the upper figure is shown in units of standard deviations.

In order to determine the counts in the main peaks, it is unfortunately not reliable to integrate the counts within the vertical red lines in figure 5.7 due to the contributions from the satellite peak. In order to get an idea regarding the contribution of the satellite peak to the main peak, a double peak fit is performed for all three runs and plotted in figure 5.8. Due to the fact, that the correct peak shape of the satellite peak is unknown and a pure Gaussian led to significantly unsatisfying χ_{red}^2 -values, a Gaussian with an additional left tail and no further boundaries is chosen to fit the data.

It is worthwhile mentioning, that the presented double peak fit is only conducted to get an estimate for the impact of the satellite peak. Due to the fact, that there is no empirical equation to fit the physical complexity of both peak shapes, it is avoided to take the integral of the fit into the further analysis.

While the values for the χ_{red}^2 -analysis, as well as the residua are reasonably acceptable in all three cases, the peak shapes of the fitted satellite peaks are drastically different from run to run. It is therefore even more unreliable to take one ‘phenomenologically appropriate’ fit function to analyze the data. Nevertheless, it is possible to compare the ratios between the satellite peak and main peak for both the entire energy interval shown in figure 5.8, as well as the ratio solely in the ROI (red vertical lines in figure 5.7), which is shown in table 5.2.

Table 5.2: For all three NRA runs, the ratio between the satellite peak and the main peak is listed. This is shown for both the entire range shown in figure 5.7, as well as for the ratio in the ROI (red vertical lines in figure 5.7).

	Run166	Run176	Run177
Ratio of satellite peak vs. main peak in full range [%]	6.2 (4)	76 (3)	85 (3)
Ratio of satellite peak vs. main peak in ROI [%]	1.24 (8)	17.4 (6)	16.5 (5)

The ratio of the entire satellite peak to the entire main peak varies between 6% in case of Run166, and 85% in case of Run177. When investigating only the ROI (red vertical lines in figure 5.7), this still leads to a ratio of 1% in case of Run166, and 17% in case of Run176.

In case of Run176 and Run177, both the unreliable describability of the peak shape, as well as the significance of net counts from the satellite peak in the ROI lead to the inevitable exclusion of these two runs within the further analysis.

$$\rho_{2\text{H}} = \frac{N_{\text{p}}}{N_{3\text{He}} \cdot \sigma} = \frac{N_{\text{peak}}}{N_{3\text{He}} \cdot \sigma \cdot \Omega \cdot t_{\text{live}}/t_{\text{real}}} = \frac{N_{\text{peak}}}{Q_{3\text{He}}/2e \cdot \sigma \cdot \Omega \cdot t_{\text{live}}/t_{\text{real}}} \quad (47)$$

In order to determine the areal density $\rho_{2\text{H}}$ via the NRA technique, equation 47 is utilized with N_{p} being the number of emitted protons, $N_{3\text{He}}$ being the number of accumulated ${}^3\text{He}$ projectiles on the target, and σ being the cross section, which is obtained by the differential cross section for $\theta = 144.5^\circ$ ³³.

The number of emitted protons is measured via N_{peak} (which is the number of peak entries in the NRA run), the solid angle Ω , and a live time correction $t_{\text{live}}/t_{\text{real}}$. The number of ${}^3\text{He}$ projectiles on the target depends on the accumulated charge Q during the run, and the charge state of the nuclei, which was ${}^3\text{He}^{2+}$.

The resulting areal density due to the NRA technique on target TiD2-2-4 (cf. table 3.2) is $\rho_{2\text{H}} = 2.85(13)(9) \cdot 10^{17} \text{at/cm}^2$ with the first uncertainty being the systematical, and the second one being the statistical uncertainty. The systematical uncertainty covers the uncertainty on the target charge integration ΔQ_{sys} , the uncertainty on the cross section $\Delta \sigma_{\text{sys}}$ [153], and the uncertainty on the solid angle $\Delta \Omega_{\text{sys}}$ due to the uncertainty on the surface emission rate $\Delta R_{\text{S,sys}}$ of the calibration source. The statistical uncertainty stems from the uncertainty on the peak entries ΔN_{peak} , as well as on the uncertainty on the solid angle $\Delta \Omega_{\text{stat}}$ due to the uncertainty on the surface emission rate $\Delta R_{\text{S,stat}}$ of the calibration source.

5.4.2 Elastic recoil detection analysis

The basic principle of the elastic recoil detection analysis (ERDA) was described in section 2.7.2. The ERDA analysis for the IBC-I campaign (cf. table 3.1) was performed at the 6 MV Tandetron accelerator at HZDR after the experimental campaign using a ${}^{35}\text{Cl}^{7+}$ -beam

³³A similar formula was already introduced in equation 29. The underlying physics is the same, but it was formulated in a way, which is applicable in a more general manner.

($E = 43 \text{ MeV}$, $I = 200 \text{ pA} - 350 \text{ pA}$). The targets were positioned under an angle of $\theta = 75^\circ$ between beam axis and sample normal. Furthermore, two different detectors were used, namely a Bragg Ionization Chamber ($\theta = 31^\circ$ with respect to the sample normal), and a silicon detector ($\theta = 41^\circ$ with respect to the sample normal). The silicon detector also was equipped with a $18 \mu\text{m}$ thick Al foil to stop heavy recoils, as well as the scattered beam. The analyzed area for each measurement was approximately $1.5 \text{ mm} \times 1.5 \text{ mm}$.

As discussed in chapter 2.7.2, a Bragg Ionization Chamber can be used in order to measure both the energy loss, and the total energy of recoils, which are sputtered by the chlorine atoms. The resulting 2D-histogram of the energy loss with respect to the total energy is shown on the left in figure 5.9. The most intense contribution stems directly from the elastically scattered chlorine nuclei, which have to be subtracted from the result in order to investigate the actual elemental abundance within the targets. Furthermore, there are clear signals of titanium, oxygen and carbon, as well as a possible contribution of nitrogen. While titanium and oxygen are identified with a continuous energy distribution (which implies a continuous depth distribution), carbon has a maximum at high energies, corresponding to a surface contamination of the target and only smaller contributions at larger depths.

The limitation of this technique is reached when trying to distinguish both low ordering numbers, and different isotopes from each other. Due to the fact, that the aimed determination of the deuterium content requires both of them, a silicon detector was added to the setup, which measured the respective light recoil nuclei. The resulting pulse height spectra for both a measurement in the beam spot area (light blue), as well as in a non-irradiated area (dark blue) is shown on the right in figure 5.9. In addition to the expected deuterium content, both spectra also show significant amounts of hydrogen.

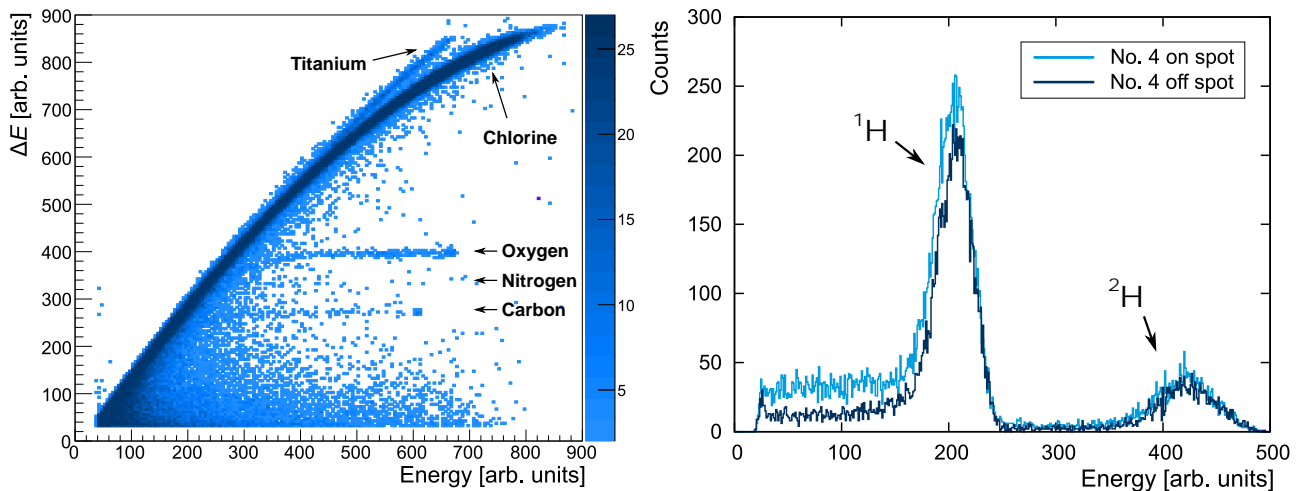


Figure 5.9: Histograms of the ERDA analysis during the IBC-I campaign at HZDR. Left: $\Delta E(E)$ -plot from a Bragg Ionization Chamber for the investigation of the beam spot of target TiD2-2-4. Right: Pulse height spectra from a silicon detector for the investigation of both the beam spot (light blue), and the non-irradiated area (dark blue) of target TiD2-2-4.

The results of both measurements are corrected for peak broadening effects, e.g. the resolution of the detection system and straggling in the target, and are subsequently evaluated using the software NDF v9.3g [156]. The resulting depth distribution in case of target TiD2-2-4 is shown in figure 5.10.

The resolution on the deuterium depth profile is affected by systematic uncertainties, pronounced e.g. in negative values for the resulting depth. These normalization issues are among others due to the fact, that the tails of the hydrogen and deuterium peak in the right plot of figure 5.9 are partially overlapping. Also the depth distribution of the Bragg Ionization Chamber suffers from significant fluctuations, but results in more distinct overlaps between surface of the target and non-physical values in ‘negative’ depths.

It is worthwhile mentioning, that this depth distribution is only used to provide a qualitative statement. The crucial quantity, which is the integrated areal density of deuterium, is independent of these tailing effect due to the fact, that the areal density is calculated by a Gaussian fit on the peaks in the right plot of figure 5.9 and a subsequent comparison with simulated spectra using a dedicated software (NDF v9.3g [156]).

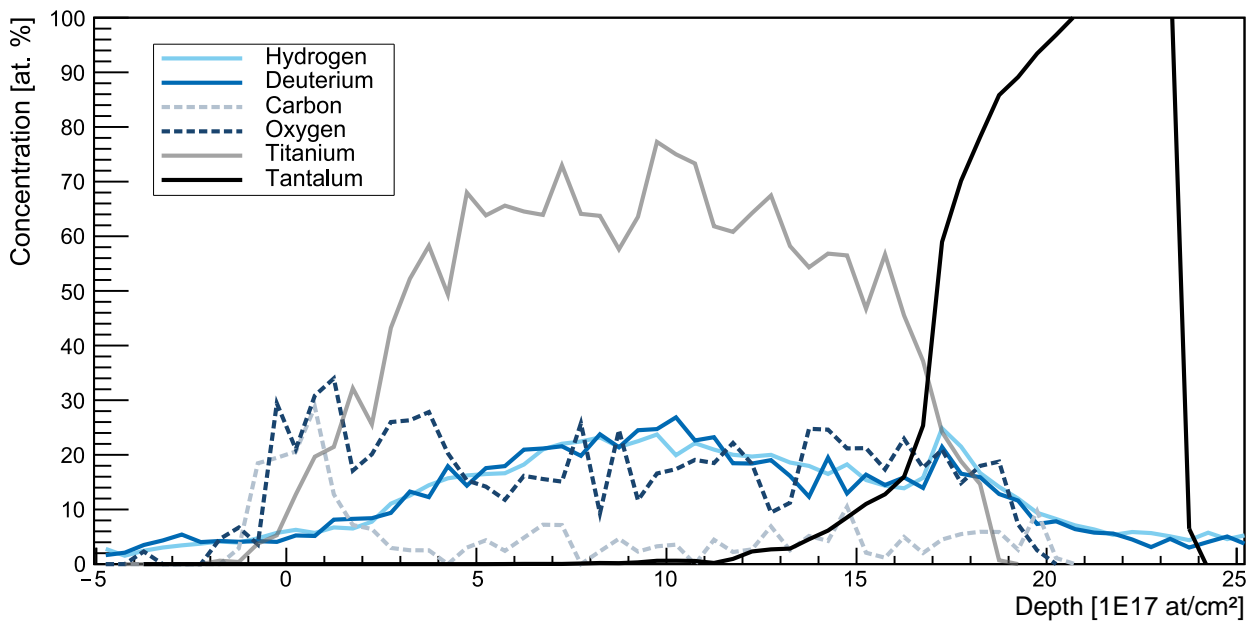


Figure 5.10: Depth distribution of TiD2-2-4 from the ERDA analysis. While the data for carbon, oxygen, titanium, and tantalum are from the Bragg Ionization Chamber (left histogram in figure 5.9), the data for hydrogen and deuterium are from the silicon detector (right spectrum in figure 5.9).

The initial determination of the deuterium areal density was performed in the center of the beam spot, as well as at a non-irradiated spot on the target. The reason was to investigate possible degradation effects due to beam-induced heat in the beam spot. As shown in the right panel of figure 5.9, this deterioration does not seem to be of significance. In fact, the areal density of both beam spots (TiD2-2-3 and TiD2-2-4) are by coincidence actually larger within their statistical boundaries, than their non-irradiated analogon.

Table 5.3: Areal densities of hydrogen and deuterium from the ERDA analysis for both targets TiD2-2-3, and TiD2-2-4. The analyses were performed both in the irradiation spot, as well as outside of it.

Target	Measurement	Hydrogen ^1H		Deuterium ^2H	
		ρ^1_{H} [at/cm 2]	$\Delta\rho$ [at/cm 2]	ρ^2_{H} [at/cm 2]	$\Delta\rho$ [at/cm 2]
TiD2-2-3	On the irradiation spot	2.98	0.30	3.16	0.32
TiD2-2-3	Non-irradiated spot	2.66	0.27	2.70	0.27
TiD2-2-4	On the irradiation spot	3.31	0.33	2.84	0.28
TiD2-2-4	Non-irradiated spot	2.90	0.29	2.50	0.25

Table 5.4: Averaged areal densities of hydrogen and deuterium from the ERDA analysis for both targets TiD2-2-3, and TiD2-2-4.

Target	Hydrogen ^1H			Deuterium ^2H		
	ρ^1_{H} [at/cm 2]	$\Delta\rho_{\text{sys}}$ [at/cm 2]	$\Delta\rho_{\text{stat}}$ [at/cm 2]	ρ^2_{H} [at/cm 2]	$\Delta\rho_{\text{sys}}$ [at/cm 2]	$\Delta\rho_{\text{stat}}$ [at/cm 2]
TiD2-2-3	2.82 E17	0.28 E17	0.16 E17	2.93 E17	0.29 E17	0.23 E17
TiD2-2-4	3.11 E17	0.31 E17	0.21 E17	2.67 E17	0.27 E17	0.17 E17

In order to treat this case conservatively, the unweighted average of both values (on the beam spot, and at a non-irradiated point) was used for the targets. The statistical uncertainty was subsequently increased in order to cover both values. The resulting areal densities of hydrogen and deuterium for the targets TiD2-2-3, and TiD2-2-4 are shown in table 5.3 and table 5.4, respectively.

Heat transfer and target stability

Due to the applied beam power of several watts on the target during the experimental campaign (voltage equivalent: $U \approx 0.4 - 1.6$ kV, beam current: $I \approx 6 - 10$ μA), it is crucial to investigate possible temperature related outgassing effects of the deuterium.

While the ERDA measurements in the beam spot of the target were supposed to analyze the actual areal density, the measurements at the non-irradiated areas were supposed to act as a reference in order to investigate the target stability throughout the irradiation. This argument, however, is only valid, when the outer areas were not heated up substantially as well. If the entire target would heat up homogeneously during the irradiation, the subsequent ERDA measurement could only be used as an upper limit on the areal density, due to possible outgassing along the entire surface.

A thorough investigation regarding the thermal evolution of the target temperature at the beam spot was performed in the master thesis based on calculations [10]. Furthermore, rough estimation are given regarding the temperature gradient towards the backside of the target, where the water cooling is mounted.

Nevertheless, an investigation regarding the lateral temperature gradient is inevitable to

use the ERDA measurements throughout the further analysis. This investigation was done by using the Energy2D Interactive Heat Transfer Simulation software [157]. This software simulates heat transfer for convection, conduction and radiation by also coupling it to particle dynamics. Furthermore, it enables the use of heat sources (e.g. the utilized water cooling) and power sources (e.g. for the particle beam).

A simplified model of the target setup based on Energy2D is shown in figure 5.11. It consists of a tantalum blank connected to a water reservoir ($T = 20^\circ\text{C}$) and an evacuated surrounding. Parameters for thermal conductivity, specific heat, and density are chosen accordingly and a constant heat source is placed on the surface of the tantalum blank. It is worthwhile to mention, that the simulation is not shown true to scale, but highly zoomed in regarding the x-axis, as shown on the grey dimensions in the figures.

While the temperature of the target without beam follows the temperature of the water reservoir as expected, the beam induced constant temperature of conservatively estimated 160°C leads to a temperature gradient throughout the target. Due to the comparatively small thickness of the targets, the lateral conduction of the generated heat at the beam spot is strongly suppressed by the water cooling and can be neglected at the non-irradiated spots of the ERDA measurements.

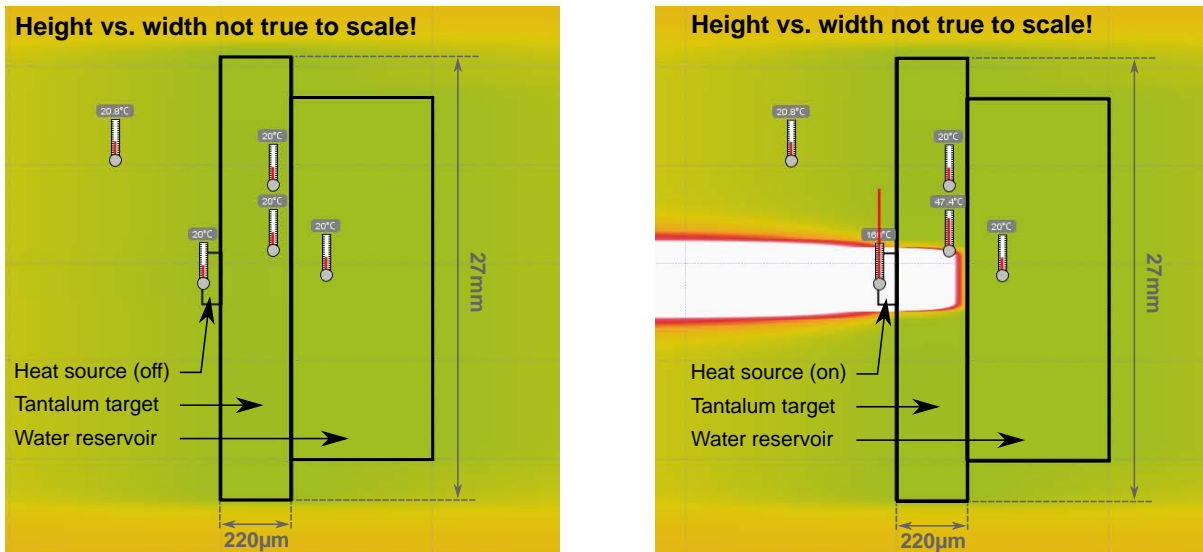


Figure 5.11: Simulation of the heat transfer in the target using the Energy2D Interactive Heat Transfer Simulation software [157]. The aspect ratio is strongly distorted in order to make temperature gradients in the target visible. Left: No beam, and running water cooling of 20°C . Right: Beam on target and running water cooling of 20°C .

5.4.3 Summary

The areal density from the NRA of target TiD2-2-4 is $\rho_{2\text{H}} = 2.85(13)(9) \text{ E17 at/cm}^2$ with the first uncertainty being the systematical, and the second one being the statistical uncertainty.

Table 5.5: Summary of the deuterium areal densities from both the ERDA measurement, and the NRA measurement for both targets TiD2-2-3, and TiD2-2-4. Furthermore, the adopted value is given for further calculations.

Target	ERDA			NRA			Adopted	
	ρ^2_{H} [at/cm ²]	$\Delta\rho_{\text{sys}}$ [at/cm ²]	$\Delta\rho_{\text{stat}}$ [at/cm ²]	ρ^2_{H} [at/cm ²]	$\Delta\rho_{\text{sys}}$ [at/cm ²]	$\Delta\rho_{\text{stat}}$ [at/cm ²]	ρ^2_{H} [at/cm ²]	$\Delta\rho$ [at/cm ²]
TiD2-2-3	2.93 E17	0.29 E17	0.23 E17				2.93 E17	0.23 E17
TiD2-2-4	2.67 E17	0.27 E17	0.17 E17	2.85 E17	0.13 E17	0.09 E17	2.82 E17	0.14 E17

The areal density from the ERDA measurements on the targets TiD2-2-3 and TiD2-2-4 are shown in table 5.4. For the target TiD2-2-3, the ERDA result is adopted to be the final value, and for the target TiD2-2-4, the weighted average of the NRA and the ERDA result is taken. The corresponding final results of the areal density are shown in table 5.5.

5.5 Evaluation of the cross section and the S -factor

The underlying relation between measured prompt γ -rays in an accelerator-based experiment and the resulting cross section was already elaborated in equation 29 and further developed in equation 47. However, the formulas from NRA need some adjustments due to e.g. the effect of γ -ray angular distributions (which are already included in NRA due to the use of differential cross sections). Based on these equations, the determination of the cross section for the ${}^2\text{H}(p,\gamma){}^3\text{He}$ reaction can be elaborated as shown in equation 48.

$$\sigma(E_{\text{cm}}) = \frac{R}{Q/e \cdot \rho^2_{\text{H}}} = \frac{N_{\gamma,\text{det}}}{\varepsilon(E_{\text{cm}}) \cdot W(\vartheta) \cdot t_{\text{live}}/t_{\text{real}} \cdot Q/e \cdot \rho^2_{\text{H}}} \quad (48)$$

Hence, the cross section σ can be calculated based on the number of occurred reactions R , the accumulated charge Q (the projectile is ${}^1\text{H}^+$, i.e. it is single charged) and the areal density ρ^2_{H} . As discussed in section 5.3, the number of occurred reactions R can be independently determined for both detectors by measuring their number of detected prompt γ -rays $N_{\gamma,\text{det}}$, determining their respective absolute full-energy peak efficiency ε , as well as accounting for corrections regarding both the anisotropic γ -ray angular distribution $W(\vartheta)$, and the live time correction $t_{\text{live}}/t_{\text{real}}$.

These independently determined cross sections are shown in table 5.6 for all relevant irradiation energies (cf. table 5.1). As mentioned in the corresponding chapter, there are four irradiation energies, where only the data of Ortec90 revealed sufficient statistics. Hence, the cross section for these cases is also not determined in table 5.6 in case of Can60.

As elaborated in chapter 2.8, the astrophysical S -factor and the cross section are connected via the center-of-mass energy E_{cm} and the masses of both the projectile and the target. Hence, table 5.6 also shows the corresponding S -factor for each determined cross section.

Table 5.6: Resulting cross sections and S -factors from the irradiations of the targets TiD2-2-3 and TiD2-2-4, respectively. In addition to the effective energy E_{eff} and the center of mass energy E_{cm} , the resulting cross sections and S -factors are also shown for both detectors separately.

Target	E_{eff} [keV]	E_{cm} [keV]	Ortec90 (55°)			Can60 (90°)			S [eV b]	$\frac{\Delta S_{\text{stat}}}{S}$ [%]	$\frac{\Delta S_{\text{sys}}}{S}$ [%]
			σ [μb]	S [eV b]	$\frac{\Delta S_{\text{stat}}}{S}$ [%]	σ [μb]	S [eV b]	$\frac{\Delta S_{\text{stat}}}{S}$ [%]			
TiD2-2-3	418.1	278.7	3.6	4.7	24	2.1	2.7	21	3.1	21	8
	600.7	400.4	3.4	4.9	24	2.5	3.6	21	4.0	16	8
	692.0	461.3	3.5	5.3	15	3.6	5.5	10	5.4	8	8
	803.1	535.3	4.4	7.2	9	4.7	7.6	7	7.4	6	8
	1005.3	670.1	6.3	11.3	25	—	—	—	11.3	25	8
	1040.8	693.8	4.8	8.8	21	—	—	—	8.8	21	8
	1289.4	859.8	6.3	12.9	19	—	—	—	12.9	29	8
	1550.3	1033.4	6.2	14.3	18	—	—	—	14.3	18	8
1641.5	1094.2	6.1	14.4	35	7.1	16.9	27	15.8	21	8	
TiD2-2-4	397.7	265.1	2.6	3.3	23	2.2	2.8	16	2.9	13	5
	499.3	332.8	3.2	4.4	13	3.4	4.7	9	4.6	8	5
	599.8	399.8	3.2	4.6	13	3.5	5.1	9	4.9	8	5
	701.8	467.8	3.7	5.6	14	3.8	5.8	11	5.7	8	5
	803.1	535.3	2.9	4.7	15	3.4	5.5	10	5.2	8	5

5.5.1 Discussion on the resulting S -factor

The state-of-the-art until mid 2020 for the ${}^2\text{H}(p, \gamma){}^3\text{He}$ reaction, as well as its astrophysical S -factor was elaborated in section 1.3. The subsequent discussion including the new data sets (namely the data set by the LUNA collaboration [48], and this data set) will be divided into two parts. The first part will concentrate on the impact of the data set originating from this work and place it into the current understanding of the reaction. The second part (cf. section 5.5.2) will then concentrate on the entire scope after also including the LUNA data set.

The updated astrophysical S -factor from figure 1.5, which now also includes the current data set, is shown in figure 5.12. While the data sets used for the Solar Fusion fit (triangles) are anticipating a rather low trend at high energies, the data by Tišma et al., as well as the data set from this thesis seem to predict a comparatively larger S -factor, especially within the BBN Gamow window. This becomes even more obvious, when plotting a residuum of this figure with respect to the fit from the Solar Fusion II workshop, as shown in figure 5.13. While all data sets for the Solar Fusion II fit (triangles) are scattering around zero (as expected), the data sets from Tišma et al. and the data set from the presented experiment seem to be consistent with each other and systematically show a deviation to larger S -factors. As a result, these two new data sets are indicating a larger cross section for this deuterium-destructing reaction, hence pointing towards a significantly smaller amount of deuterium after the BBN. A new S -factor fit including all plotted data sets is also shown in figure 5.12 and figure 5.13 as a red line along with its uncertainty band.

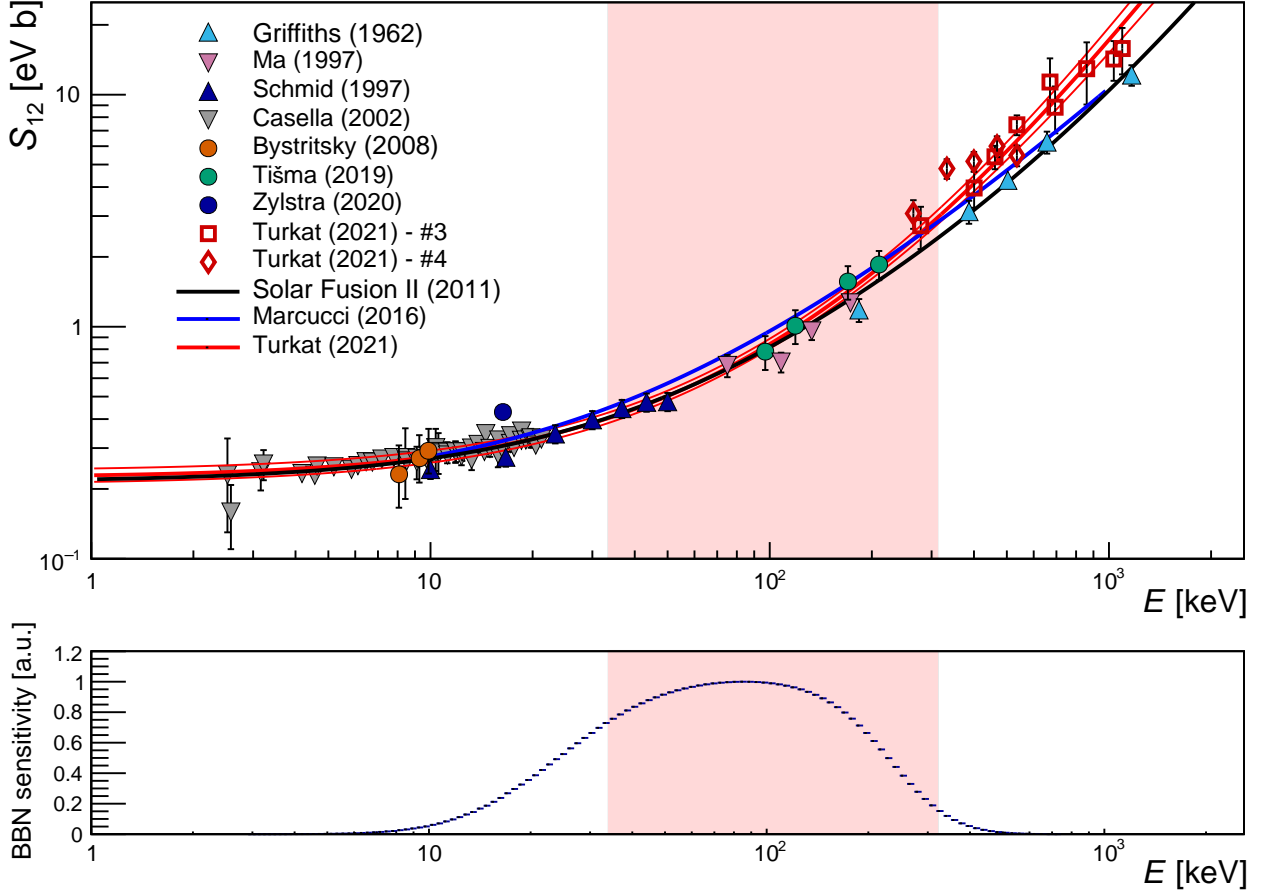


Figure 5.12: Top: Experimental campaigns on the astrophysical S -factor of the ${}^2\text{H}(p,\gamma){}^3\text{He}$ reaction, which were performed past 1990, are shown with respect to the energy [1, 37–42]. In addition, the result of the solar fusion II fit [43] and an ab initio theory [44] is shown as black line, and blue line, respectively. The triangles represent the data sets, which were used for the solar fusion II fit. The new fit including all data sets (except Mossa et al. [48]) is shown as red line along with its standard deviation (1σ). Bottom: Sensitivity of this reaction for Big Bang Nucleosynthesis in arbitrary units. The red shaded area marks the central 90% of the sensitivity (note the phenomenologically linear binning on the otherwise logarithmic x-scale). The same plot including the dominating data set of Mossa et al. is shown for completeness in appendix C.1.

However, there is also another crucial data set, which needs to be discussed, namely the new data set by the LUNA collaboration [48].

$$S_{12}(E) = S_{12}^0 + S'_{12} \left(\frac{E}{\text{keV}} \right) + S''_{12} \left(\frac{E}{\text{keV}} \right)^2 \quad (49)$$

In accordance to the proposed fit function by the Solar Fusion II workshop (cf. equation 49), the adjusted parameters after taking into account all data sets shown in figure C.1 are shown in equation 50.

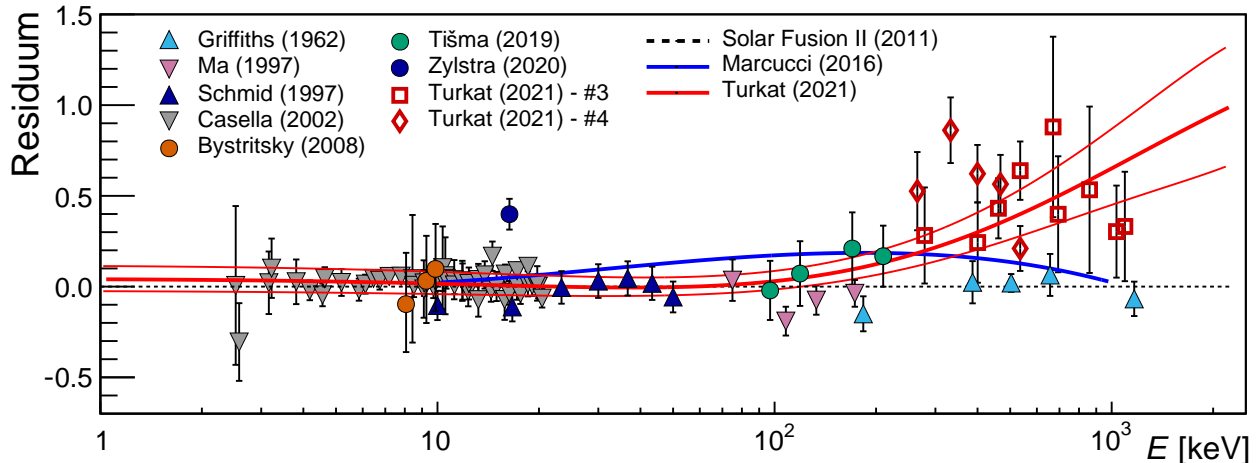


Figure 5.13: Residuum for all data sets (except Mossa et al. [48]) and fit curves of the astrophysical S -factor for the ${}^2\text{H}(p,\gamma){}^3\text{He}$ reaction with respect to the solar fusion II fit (black dotted line) [43]. The residuum is plotted in units of standard deviations. The same plot with the dominating data set of Mossa et al. is shown for completeness in appendix C.1.

$$\begin{aligned}
 S_{12}^0 &= (0.219 \pm 0.004) \text{ eV b} \\
 S_{12}' &= (5.4 \pm 0.2) \cdot 10^{-3} \text{ eV b} \\
 S_{12}'' &= (8.1 \pm 0.9) \cdot 10^{-6} \text{ eV b}
 \end{aligned}
 \tag{50}$$

5.5.2 Discrepancy with the new data set from LUNA

The previous section was focused on the sole implementation of the current data set, without adding the most important recently published data set for this reaction, namely the data set by the LUNA collaboration [48]. The corresponding S -factor curve, as well as the residuum, are shown in the appendix C.1.

As shown in these figures, the new data set by Mossa et al. remarkably covers the entire BBN range and furthermore shows particularly low uncertainties [48]. However, these low uncertainties are also the reason, why the previous section first elaborated all data sets excluding this particular data set from the LUNA collaboration. In fact, by adding the new LUNA data set, their low uncertainties are dominating any fit and do not allow any other data sets to play a role for the shape of the S -factor curve.

From a scientific perspective, it is crucial to emphasize, that (due to their low uncertainties) the resulting S -factor should undoubtedly follow the LUNA data set. Nevertheless, in the chosen way of subsequently describing both results after each other, the focus can be turned more onto the following statement: While the residuum in the appendix might encourage the reader to interpret the presented data (measured at HZDR) as faulty and being in disagreement with the entire literature, the situation should actually be handled more carefully. As emphasized with the residuum plot in figure 5.13, this discrepancy is solely between both

data sets from LUNA and from the presented experiments. All other modern data sets (i.e. by Tišma et al. and Ma et al.) are in a general agreement with either the LUNA data set or presented data set.

In summary, it was avoided to show all data sets simultaneously in order to avoid the impression, that the presented data set is in general disagreement with the entire literature which is certainly not the case. The current situation can actually be interpreted as a discrepancy solely between the LUNA data set and the presented data set.

However, both data sets point towards an astrophysical S -factor for the ${}^2\text{H}(p,\gamma){}^3\text{He}$ reaction at BBN energies, which is subsequently larger than assumed by the Solar Fusion II workshop. Its implications will be elaborated once again more thoroughly in the discussion 7.

5.5.3 Treatment of uncertainties

The treatment of systematic and statistical uncertainties widely matches the procedure discussed in [10] and is also more thoroughly elaborated in [1]. Hence, this section is kept considerably concised. While the statistical uncertainties can be treated straight forward, the systematic uncertainties are divided into two different contributions. The first contribution (further called ‘individual systematic uncertainties’) affects each target separately and is also stated in table 5.6. The second part (further called ‘scaling systematic uncertainties’) concerns an overall systematic uncertainty, which is identical for both targets.

Individual systematic uncertainties The individual systematic uncertainties are 8% in case of target TiD2-2-3 and 5% in case of target TiD2-2-4. They are based on the individual analyses of each areal density, as discussed in section 5.4.

Scaling systematic uncertainties Overall systematic uncertainties, which are independent of the target, are introduced via the absolute full-energy peak efficiency (3%), the current integration (1%), and the correction for the γ -ray angular distribution (6%). However, the main contribution stems from the ERDA analysis (10%), which leads to a total systematic uncertainty of additional 12%.

Statistical uncertainties The main contribution for final statistical uncertainties (6-29%) is stemming from the counting statistics of the HPGe detectors. Only a small contribution is due to the counting statistics in the ERDA and the NRA analysis (cf. table 5.5), which is subsequently leading to a statistical uncertainty of the areal density $\rho_{2\text{H}}$.

6 Experimental campaigns on the ${}^3\text{He}(\alpha, \gamma){}^7\text{Be}$ reaction

The chronological order of corresponding campaigns for the investigation of the ${}^3\text{He}(\alpha, \gamma){}^7\text{Be}$ reaction is shown in table 3.3, with IBC-II being the first one, followed by FK-I, FK-II, FK-III, FK-IV and FK-V. Despite mixing up the chronological order, the FK-campaigns will be discussed prior to the IBC-II campaign. This is due to the fact, that the FK-V campaign was by far the most successful one in terms of a scientifically robust data analysis and comparatively low resulting statistic uncertainties. Its analysis will therefore act as a role model for the more vulnerable IBC-II campaign.

The subsequent sections are therefore organized as follows: Before shedding light on the analysis of the in-beam data, there are several considerations in advance, which will be discussed in section 6.1 (An additional issue will also be elaborated in the appendix D.3). The FK-I to FK-IV campaigns were all using partly unsuccessful targets, inoperable detectors, major problems with the accelerator, as well as unresolved in-beam background issues and multiple subsequent upgrades. While all these irradiations were in fact inevitable for the success of the FK-V campaign, and therefore will be described thoroughly in section 6.2, they were themselves not suitable for a reliable analysis of γ -ray angular distribution. The subsequent analysis of the FK-V campaign will be elaborated in section 6.3, which will also introduce an adequate analysis technique for the investigation of the γ -ray angular distribution. It is worthwhile mentioning, that more than 80% of the totally accumulated charge on targets during the Felsenkeller campaigns was acquired during the FK-V campaign. This already gives an insight into the relevance of this campaign with respect to FK-I, FK-II, FK-III, and FK-IV. Despite being chronologically the first campaign, the IBC-II campaign will be discussed afterwards in section 6.4, which will also take advantage of the previously introduced analysis techniques. The last section, which is section 6.5, will be devoted to the activation analyses of all targets, which were irradiated with only one single energy in order to independently elaborate the corresponding activities at the end of each irradiation, respectively.

Introductory remarks: Due to the fact, that the presented campaigns were conducted over the time span of several years, a variety of Bachelor and Master theses are also addressing the presented setup and the data. These theses are e.g. focusing on full-energy peak efficiencies of detectors, characterizations of the setup in general, on activation analyses or in case of the Master thesis even on a preliminary γ -ray angular distribution. In addition, the main causes for the inability to properly extract γ -ray angular distributions from the campaigns FK-I to FK-IV are also thoroughly elaborated there [9, 12, 14, 16, 20, 109, 158]. While the conclusions within these theses are congruent with this thesis, the presented analysis within this section will be entirely independent from previous analyses. However, in order to keep this section as condensed and focused as possible, in some cases, it will be emphasized to consult these theses for a more thorough argumentation, respectively.

6.1 General considerations in advance

The investigation of the ${}^3\text{He}(\alpha,\gamma){}^7\text{Be}$ reaction was conducted within several experimental campaigns between May of 2018 and October of 2022 in both the IBC of HZDR, and the Felsenkeller shallow-underground laboratory (cf. table 3.1). It was investigated in indirect kinematics by irradiating implanted targets (mainly ${}^3\text{He}$ in tantalum) with a ${}^4\text{He}$ beam (cf. table 3.2). The solid targets were cooled with LN2 (cf. figure 3.2 and figure 3.3) and the emitted prompt γ -rays were analyzed using surrounding HPGe detectors (cf. section 3.3.2 and section 3.4.2-3.4.5).

However, prior to the main analyses of both the resulting in-beam data (cf. section 6.2 to section 6.4), as well as the elaboration of the offline analysis (cf. section 6.5), the following section will address multiple other considerations in advance. These subsections are relevant in order to also illuminate related surrounding issues with the attention they deserve, due to their contribution to the success of the subsequent analysis.

6.1.1 Optimization of the implantation depth

As discussed in section 3.2, the implantation depth of ${}^3\text{He}$ into the backing has to be chosen as an optimum between two competitive issues: It should be chosen as thick as necessary due to the resulting increase in reaction rate, but also as thin possible in order to minimize both the energy loss of the subsequent projectile, as well as the width of the resulting ROI for the prompt γ -rays. Both these limiting factors for choosing an overly large implantation depth are shown in figure 6.1 and figure 6.2, respectively. They both are based on SRIM simulations [90].

The left figure shows the expected relative loss of laboratory energy in case of ${}^4\text{He}$ for different implantation depths (100 nm, 200 nm and 300 nm) with respect to the initial laboratory energy. However, the region for the investigated laboratory energies is approximately $E_{\text{lab}} = [1000, 3000]$ keV (cf. table 3.3). Throughout all of these investigated energies, the final uncertainty on the irradiation energy should be kept reasonably small, i.e. it should not exceed the expected uncertainty from any subsequent counting statistics. This is why implantation depths of 300 nm, and thicker, turn out to be unsuitable for the investigation of the ${}^3\text{He}(\alpha,\gamma){}^7\text{Be}$ reaction. Considering an aimed relative energy loss of less than 10% for the entire range of investigated energies, the focus should be an aimed implantation depth below 200 nm.

In addition to the energy loss in the target (and its resulting problem on a precise statement of one specific investigated energy), the energy loss in the target will also lead to a broader peak of the prompt γ -rays in the resulting pulse height spectra. This is due to the fact, that the investigated reaction is a direct capture reaction. However, the total width of the final peak in the ROI is a convolution of mainly three factors listed in descending order of

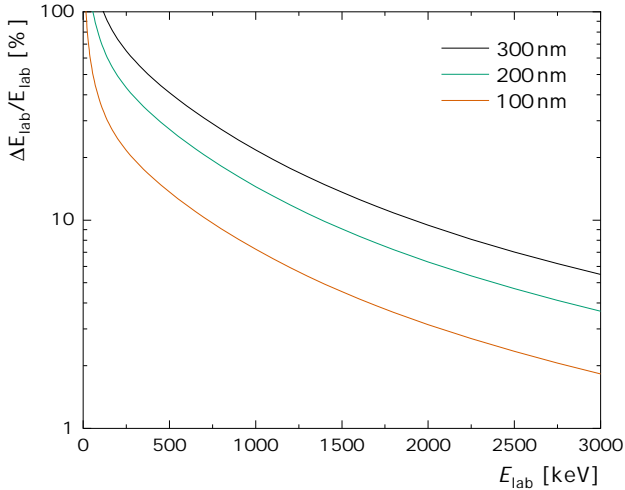


Figure 6.1: Relative loss in laboratory energy during the propagation of ${}^4\text{He}$ through different implantation depths with respect to its initial laboratory energy. The target is assumed to be a compound of ${}^3\text{He}$ and ${}^{181}\text{Ta}$ with an assumed stoichiometric ratio of 1:1. Based on SRIM [90].

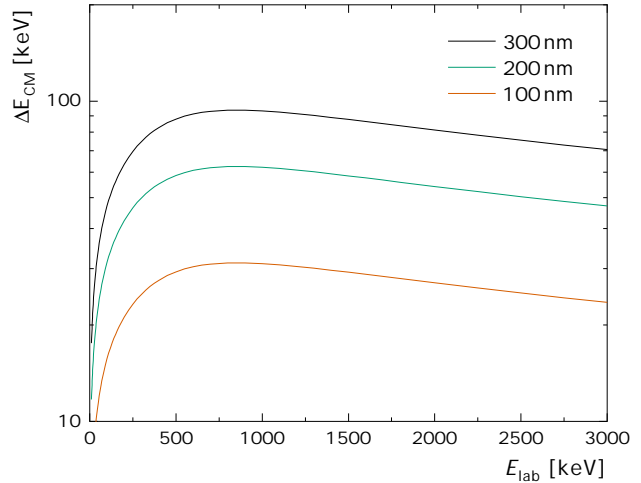


Figure 6.2: Loss of E_{cm} during the propagation of ${}^4\text{He}$ through different implantation depths with respect to its initial laboratory energy. The target is assumed to be a compound of ${}^3\text{He}$ and ${}^{181}\text{Ta}$ with an assumed stoichiometric ratio of 1:1. Based on SRIM [90].

importance: The energy loss of the projectile in the target, the finite opening angle of the HPGe detectors (resulting in the increase of peak width due to Doppler-broadening), as well as the intrinsic FWHM of the peaks due to the detectors and their software.

Figure 6.2 shows the expected loss of E_{CM} during the propagation of the ${}^4\text{He}$ projectiles through different thicknesses of target material, which is an appropriate indicator for the expected width of the peak in the ROI due to the target thickness (cf. section 2.6). Within the expected region of investigated laboratory energies of $E_{\text{lab}} = [1000, 3000]$ keV, a target thickness of 100 nm will therefore lead to a contribution to the total peak width of 20–30 keV, a target thickness of 200 nm will lead to 50–60 keV, and a target thickness of 300 nm will subsequently lead to 70–100 keV. While peak widths of 50 keV are still manageable if both the statistics and the analysis method is appropriate, peaks broader than 100 keV should be avoided if possible (cf. section 3.3). Therefore, the limit on the peak width leads to a weaker, but very similar constraint on target thicknesses of approximately 200 nm.

In order to also account for longitudinal straggling, temperature induced diffusion processes into larger depths, as well as an additional contribution to the width of the ROI due to the opening angles of the detectors, the following calculations are aimed to achieve a target thickness of ~ 180 nm.

In case of an irradiation with ${}^4\text{He}$, a target thickness of 180 nm would result in a relative energy loss of 13% in case of $E_{\text{lab}} = 1000$ keV, and 3% in case of $E_{\text{lab}} = 3000$ keV. The resulting change of E_{CM} between surface and the back area of the implantation depth would be $\Delta E = 56$ keV in case of $E_{\text{lab}} = 1000$ keV, and $\Delta E = 42$ keV in case of $E_{\text{lab}} = 3000$ keV.

6.1.2 Optimization of the areal density

After determining an appropriate thickness for the implantation process, this layer has to be implanted with as much ^3He ions, as possible in order to maximize the reaction rate. The implanted fluence of ^3He ions is hereby a compromise between a desired high amount of areal density and the high costs of ^3He . Furthermore, there is also a natural limit for its uptake into a solid target during the implantation process.

In typical solid target experiments, where there is the need of implanting noble gases, a stoichiometric ratio³⁴ of 1:2 or 2:3 is reasonable. A stoichiometric ratio of 1:1 is of course highly favorable, but only rarely achievable [26]. Especially in case of helium as the implanted ion, effects like blistering will be a strong limit for a larger stoichiometric ratio [159–161].

Due to the fact, that a high areal density is crucial in order to investigate nuclear reactions with low-cross sections, the following calculations is aimed for an optimistic 1:1 ratio. This aspired ratio is optimistic enough in order to certainly reach the scientifically possible receptivity of ^3He into the backing material, but is not unreasonably large, which would result in a unreasonable loss of valuable ^3He .

However, the number density n_a of a material depends on its density ρ , its molar mass M_{mol} , and the Avogadro constant N_A . In case of tantalum and gold, this results in a number density, as shown in equation 51.

$$n_a = \frac{\rho}{M_{\text{mol}}} \cdot N_A \stackrel{\text{Ta}}{=} \frac{16.6 \text{ g/cm}^3}{180.95 \text{ g/mol}} \cdot N_A = 0.55\text{E}23 \text{ at/cm}^3 \quad (51)$$

$$\stackrel{\text{Au}}{=} \frac{19.3 \text{ g/cm}^3}{196.97 \text{ g/mol}} \cdot N_A = 0.59\text{E}23 \text{ at/cm}^3 \quad (52)$$

In case of an aimed implantation ratio of 1:1, these values of equation 51 and equation 52 will be identical to the necessary number densities n_a for the implanted ^3He ions. Taking into account the aimed implantation depth of 180 nm (cf. section 6.1.1), the resulting necessary areal densities are shown in equation 53.

$$\rho_A = n_a \cdot 180 \text{ nm} \stackrel{\text{Ta}}{=} 1.00\text{E}18 \text{ at/cm}^2 \quad (53)$$

$$\stackrel{\text{Au}}{=} 1.06\text{E}18 \text{ at/cm}^2 \quad (54)$$

In both cases, the aimed areal density ρ_A after implantation is therefore $\rho_A \approx 1.00 \text{ E}18 \text{ at/cm}^2$. However, there is a discrepancy between the amount of implanted ions, and the initial implantation fluence, which will be discussed in the following section.

³⁴The stoichiometric ratio is defined as the ratio between ^3He nuclei and tantalum nuclei within the respective implantation volume.

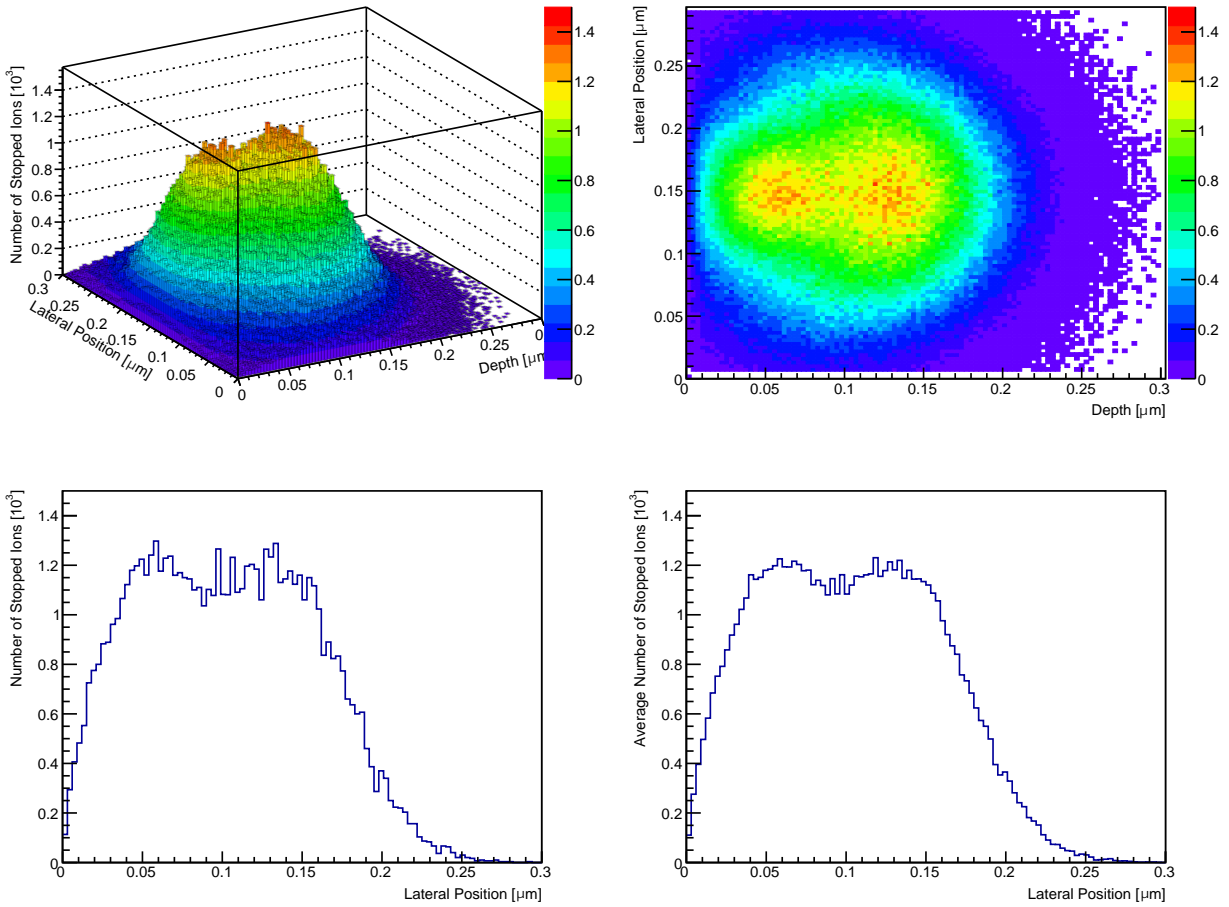


Figure 6.3: Depth distribution based on the implantation of ${}^3\text{He}$ ions with 15 keV and 45 keV into a tantalum blank, which entered perpendicular to the target surface at a lateral position of $0.15\ \mu\text{m}$. The results are obtained using the SRIM software [90]. Upper left: Number of stopped ions as a 3D depth distribution. Upper right: Projection of the ion distribution onto the spatial axes. Lower left: Depth distribution for the central bin of the lateral position at $0.15\ \mu\text{m}$. Lower right: Mean depth distribution for a $0.05\ \mu\text{m}$ broad section around the central lateral position.

6.1.3 Calculation of the implantation fluence

The determined areal density of the last section needs to be implanted homogeneously in depth throughout the aimed layer of 180 nm thickness. However, there are two major remaining obstacles in doing so.

The first one is the resulting depth profile of the ${}^3\text{He}$ ions with only one single implantation energy. Such an exemplary depth profile in case of an implantation energy of $E = 45\ \text{keV}$ is shown in the appendix (cf. figure D.8). One single implantation energy certainly does not lead to a homogeneously resulting depth distribution, but to a energy-dependent maximum within a certain depth. Furthermore, the proposed procedure of implanting the ions into a maximum certain depth is not compatible with reality, since the ion distribution only fades out slowly with larger depths, instead of abruptly dropping at 180 nm. This effect is called straggling, and will be briefly discussed at the end of this section.

While this fading-out can not be avoided, a quasi-homogeneous depth distribution can in fact be obtained by using several implantation energies in order to fill up vacancies closer to the surface. While it is unrealistic, as well as unnecessary, to obtain a perfectly homogeneous depth profile, a comparatively flat depth distribution is shown in the appendix in figure D.9) using three implantation energies (45 keV, 15 keV, and 5 keV). By comparing figure D.8 and figure D.9 it becomes apparent, that the highest energy also needs the highest fluence, while lower energies subsequently need lower fluences.

Due to time constraints and technical feasibilities, the actual implantations were based on only two different irradiation energies instead of three (cf. table 3.2). Furthermore, in theory the highest appropriate implantation energy was determined to be 45 keV. With this energy, the implantation profile dropped to approximately half of its maximal value at the aimed 180 nm (cf. figure 6.3). This was however reduced during the campaigns to 40 keV or 35 keV in order to prevent a straggling of ^3He into too large depths. While the first obstacle is therefore compensated to a satisfying degree, the second obstacle will be described hereafter. While the different energy dependent implantation doses D_i can be determined based on the procedure elaborated in the last paragraph, there is however a discrepancy to the actually necessary implantation fluences F_i , which need to be applied onto the backing. The main reason for this discrepancy is due to backscattering of ions during the implantation, which prevents ions from being deposited within the backing. The ratio of backscattered ions is energy dependent, non negligible, and shown in figure 6.4 in case of tantalum and gold.

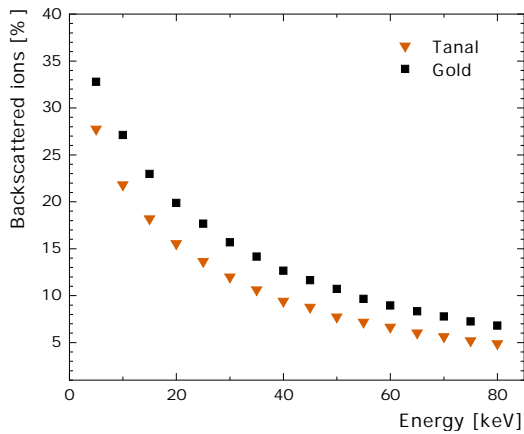


Figure 6.4: Ratio of backscattered ^3He ions during ion implantation with respect to their implantation energy. The relation is shown for the two materials of tantalum (orange) and gold (black), which are perpendicularly irradiated. The data is based on SRIM simulations [90].

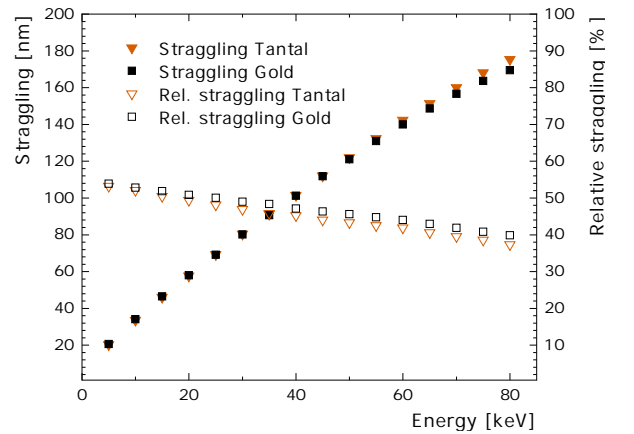


Figure 6.5: Straggling of ^3He ions within tantalum (orange) and gold (black) with respect to their implantation energy. The right axis shows the relative straggling with respect to the ions mean range and uses the unfilled symbols. The data is based on SRIM simulations [90].

Lower implantation energies lead to a significant rise in the ratio of backscattered ions. This can lead up to values above 25% in case of 5 keV implantation energy and an implantation angle, which is perpendicular to the surface of the backing ($\vartheta = 0^\circ$). In case of larger implantation angles, this ratio increases even further. At an implantation angle of e.g.

$\vartheta = 55^\circ$, this ratio exceeds 50%. Due to the high costs of ${}^3\text{He}$, an angle of $\vartheta = 0^\circ$ is chosen. The effect of energy dependent backscattering is taken into account for the calculation of the implantation fluences F_i . Based on figure 6.3, the ratio factors α_i for different implantation energies E_i can be calculated. These factors are defined as the respective ratio with respect to the total areal density ρ_A within the backing, which is needed in order to result in a quasi-homogeneous depth distribution. The sum of all ratio factors α_i is equal to one.

$$\rho_A = D_1(E_1) + D_2(E_2) = \alpha_1 \cdot \rho_A + \alpha_2 \cdot \rho_A \quad (55)$$

Each resulting implantation dose D_i for each respective energy E_i needs to be corrected separately for its backscattering ratio R_i . As shown in figure 6.4, this ratio is defined as the amount of backscattered ions with respect to the total amount of utilized ions. The total implantation fluence F_i for each energy E_i , which needs to be applied onto the backing, can therefore be calculated using equation 56.

$$F_i(E_i) = \frac{D_i}{1 - R_i} = \frac{\alpha_i}{1 - R_i} \cdot \rho_A \quad (56)$$

After discussing the determination of the necessary implantation fluences $F_i(E_i)$ for different implantation energies, the effect of straggling will be discussed briefly in order to reveal its significance during the implantation process. For a given setup, each implantation energy results in an expectation value on the mean lateral range (depth) of an ion in matter. Due to scattering processes, there is a statistically varying discrepancy between the actual path length and the final lateral range of an ion in matter. The expectation value is therefore distorted by a variance both in the lateral and the longitudinal axes. While the lateral spread is canceled out due to the fact, that the ion beam is homogeneously scanned along the surface during the implantation process, the longitudinal spread can not be avoided. The square root of this variance is called straggling and is a measure for the susceptibility of an ion to be scattered along its path. As shown in figure 6.5, the absolute straggling increases with increasing ion energy, but the relative straggling in fact decreases reasonably. This is an important relation, which at higher energies leads to the proper development of Bragg-peaks and the ability to use them for instance in tumor therapy, where the relative straggling is only in the order of 1% [162]. At comparatively low energies, which are used throughout this thesis, the straggling can still be in the order of 50% of the expected depth, which leads to the depth profile shown in figure D.8.

In conclusion, the planing of ion implantations at low irradiation energies is not a high precision tool with expected results on the sub-percentage level. This is even enhanced by the fact, that neither thermal diffusion processes during implantation are considered, nor even more complex effects as changes in density or reflectivity during implantation because of already implanted ions. The resulting depth distribution will nevertheless follow the aimed intentions elaborated in this chapter, which is supported by experiences gained in prior solid target experiments in the field of nuclear astrophysics (cf. section 3.2).

6.1.4 Reliability of the quoted effective energies

The effective energies E_{eff} (and therefore center-of-mass energies E_{cm}) are stated in table 3.3 and are based on the equations elaborated in section 2.6. However, the reliability of these energies also depends on the actual implantation ratio between ^3He and its backing material ^{181}Ta . According to the applied fluence of ^3He during the prior implantation process (cf. table 3.2), an implantation ratio of 1:1 has been aimed for (cf. also chapter 3.2.4). Effectively, this would result in an areal density of approximately $\rho = 1 \text{ E18 at/cm}^2$ for both ^3He and ^{181}Ta within the first 180 nm (cf. section 6.1.2).

However, this ratio might change due to any loss of ^3He during storage or irradiation of the samples (e.g. due to diffusion processes or sputtering). While it is not possible to precisely monitor the time dependent areal density for the entire storage and irradiation period, it is indeed possible to investigate the impact of different implantation ratios on the energy loss of ^4He in the target.

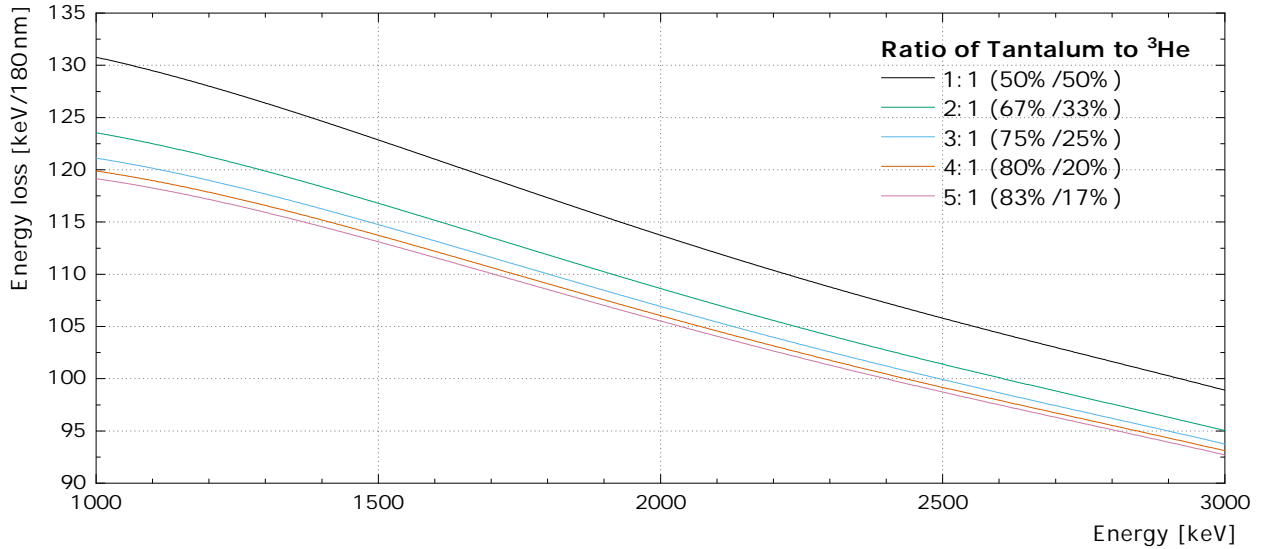


Figure 6.6: Energy loss of ^4He ions in 180 nm of target material with respect to the laboratory ion energy. This correlation is shown for different composition ratios between tantalum and the implanted amount of ^3He .

This energy loss of ^4He ions within the tantalum targets is shown with respect to their irradiation energy (in terms of E_{lab}) for different implantation ratios. It shows, that the energy loss becomes larger for low irradiation energies (due to the Bethe-Bloch formula), as well as for larger implantation ratios (due to the increased overall areal density of atoms in general). As it will be discussed in section 6.5.5, realistic implantation ratios widely vary between 1:2 and 1:10. Considering all relevant irradiation energies, this results in differences of expected energy losses of less than 5 keV within 180 nm. According to equation 23, this leads to an upper estimation of $\Delta E \lesssim 1 \text{ keV}$ for the uncertainty on the stated center-of-mass energy E_{cm} . However, the calculations in section 6.5 only act as a lower boundary on the ^3He areal density at the end of the irradiations.

6.1.5 Suitable irradiation energies

The astrophysical S -factor for the ${}^3\text{He}(\alpha, \gamma){}^7\text{Be}$ reaction is shown in figure 1.6 with various experimental data points at various energies. However, in case of an in-beam investigation, not all irradiation energies might be equally suitable. As elaborated in equation 24-26, the energy of the resulting γ -ray depends on the irradiation energy, and subsequently on the center-of-mass energy E_{cm} . Hence, any resulting region of interest for the prompt γ -rays can and should be chosen in a way, which minimizes contamination peaks in its vicinity and paves the way for a proper analysis of the net counts.

In general, it can be stated, that lower center-of-mass energies will also decrease the amount of contamination peaks (as well as Compton background) in the resulting spectrum, which subsequently enhances the possibility of locating a suitable flat region of interest. However, due to resonant reactions, this is only a general trend, which can have exceptions. The resulting in-beam spectra after irradiation of pure tantalum blanks at four different center-of-mass energies is shown in figure 6.7.

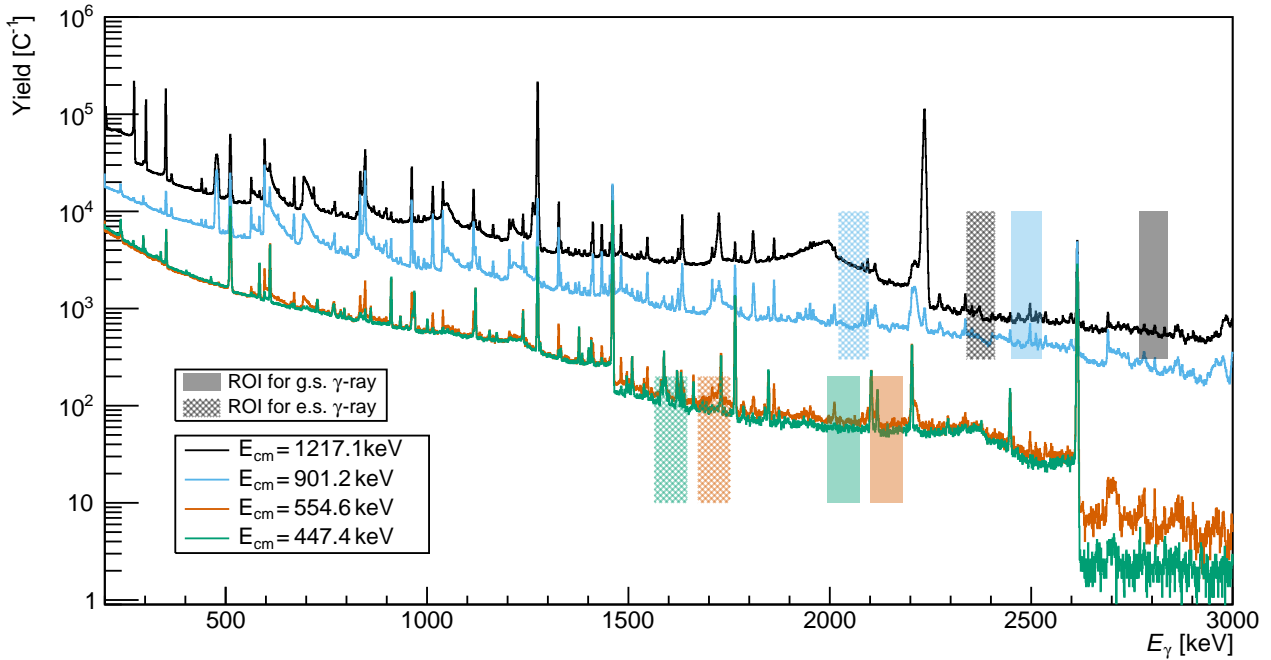


Figure 6.7: Verification of suitable irradiation energies based on the resulting pulse height spectra from the irradiation of tantalum blanks Ta51 in black, Ta52 in blue, Ta53 in orange, and Ta54 in green (cf. table 3.3). The expected ROI for the prompt γ -rays is shown for each irradiation energy as filled, and hatched box with the same color, respectively and also takes Doppler shifts into account. The main aim was to find a comparatively flat ROI (at least) for the ground state transition within a scientifically relevant and also feasible beam energy range.

These four energies correspond to the four final energies from the FK-V campaign (cf. table 3.3). It is worthwhile mentioning, that these spectra are normalized only to the accumulated charge on the target Q_{tar} . Hence, a genuine comparison of these spectra is only valid in case

of comparatively small contributions stemming from other sources (e.g. beam on collimator or natural background), which are not expected to be proportional to the current on the target. However, the overall stable beam parameters during FK-V (i.e. current on target and current on collimator) softens this concern. Due to the focus on a stable beam over the long-term measurements, the overall picture would not vastly change when e.g. normalizing these graphs to the live time instead of the applied current on the target.

Each color in figure 6.7 subsequently deals with one irradiation energy and the aforementioned trend of lower overall counting rates for lower irradiation energies is clearly apparent. The expected ROI for the prompt γ -rays stemming from the ground state transition and the transition into the first excited state are shown for each irradiation energy as a filled and a hatched box, respectively. Comparing each spectrum with the corresponding ROI for the ground state transition, it is visible, that there is no major peak contribution in the ROI, but that these regions are (comparatively) flat. Hence, this careful choice of irradiation energies prior to the long-term investigations will subsequently lead to a great improvement in the ability to properly evaluate the ROI.

Simultaneously, the beam energies were also optimized with respect to a comparatively flat ROI for the transition into the first excited state. Whenever there was a certain freedom of choice in the irradiation energy in order to get a comparatively flat ROI for the ground state transition, the final energy was also chosen to optimize the ROI for the transition into the first excited state, as also shown in figure 6.7. Only in case of $E_{\text{cm}} = 447.4 \text{ keV}$ (green histogram) the ROI for the transition into the first excited state is facing a variety of non-avoidable contamination peaks.

6.2 In-beam analysis of FK-I to FK-IV

Almost 2.5 years passed after the IBC-II campaign in June 2018 at the Ion Beam Center of HZDR until the first ${}^3\text{He}(\alpha, \gamma){}^7\text{Be}$ reaction took place at the new underground laboratory Felsenkeller in Dresden. This is mainly due to the fact, that the construction work on the accelerator, the beam line and the target area was not completed until July 2019. The first ever beam on the target at Felsenkeller was achieved on the 3rd of July 2019 at 17:32, which was only one day prior to the large opening ceremony with the Nobel laureate Prof. Dr. Takaaki Kajita.

However, this ${}^{12}\text{C}$ beam was extracted by the external ion source, and it took until 22nd of October 2020 to realize the very first ${}^4\text{He}$ beam on the target from the internal ion source.

6.2.1 Results for the in-beam analysis during the FK-I campaign

The corresponding targets ST3 and ST4 for the FK-I campaign (cf. table 3.3) were produced back in June 2019 and irradiated in November 2020. This so-called FK-I campaign was therefore conducted directly after the successful installation of the internal ion source at

the Felsenkeller site (including the first successful extraction of the beam and the first test irradiations on a target).

The very first test targets however, which were irradiated based on a beam from the internal ion source, were pure tantalum disks, as shown in figure 6.8. These photos show all the test targets after irradiation along with their time line. These pure tantalum blanks were mainly irradiated in order to understand the beam optics on a long term scale, as well as to gain knowledge on the process of blistering in the target.

As shown in the very last photo in figure 6.8, the resulting appearance of this target after irradiation, as well as the obtained knowledge up to this point were sufficient for a first campaign using the very first ${}^3\text{He}$ implanted targets at Felsenkeller (target ST3 and ST4). Due to their significant age (irradiation was 16 months after implantation), these targets were thought to be already low in areal density. Furthermore, at this point also a new set of targets was already in production at the IBC at HZDR (ST5 to ST8). It was therefore decided to use the remaining time until the arrival of new targets to consume these old targets (ST3 and ST4) in order to gain experience with possible in-beam contaminations, and with a first activation analysis on the new TU1 detector.

The mean currents on target ST3 and ST4 were $13\ \mu\text{A}$, and $17\ \mu\text{A}$, respectively. Their accumulated charges are $Q = 2.4\ \text{C}$, and $Q = 0.8\ \text{C}$ and the irradiation times are approximately 50 h and 12 h, respectively.

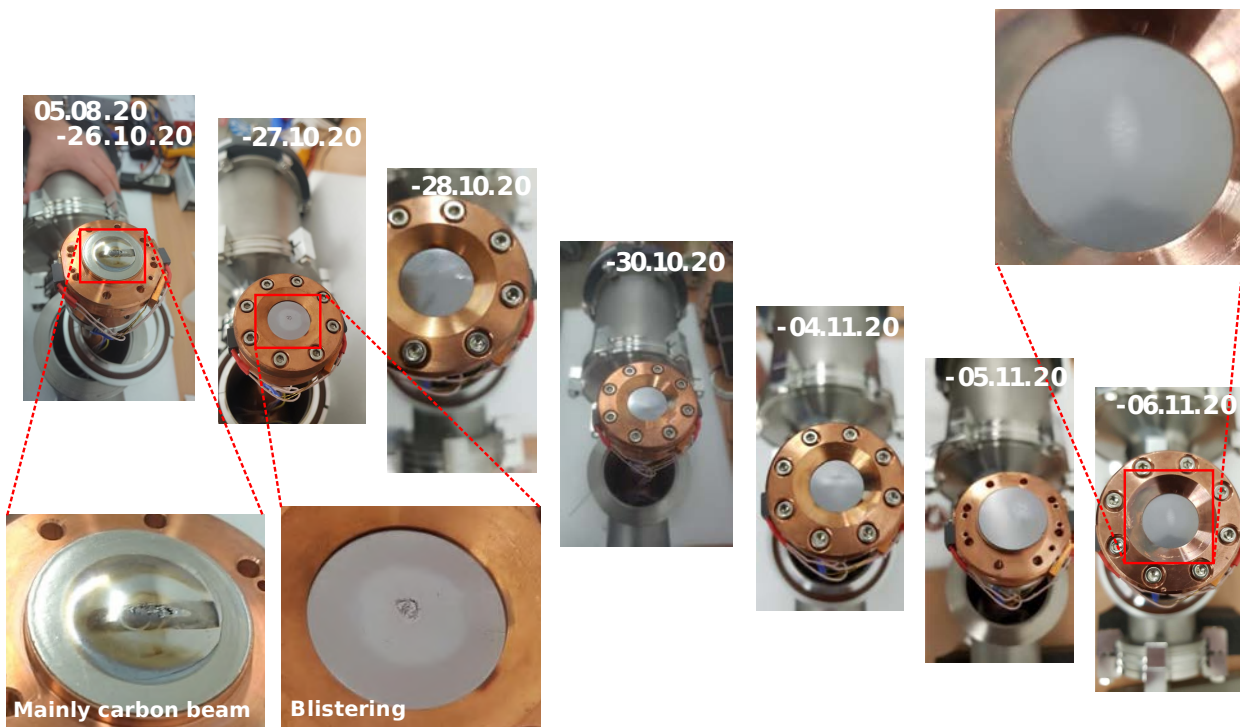


Figure 6.8: Photos of tantalum targets after their ${}^4\text{He}$ irradiation along with their date of removal from the target holder. These tantalum blanks were the first test targets during the installation of the internal ion source at the Felsenkeller site and amid the first beam extraction tests. The first target was mainly irradiated by a ${}^{12}\text{C}$ beam and only irradiated by ${}^4\text{He}$ since 22.10.2020.

The resulting pulse height spectra in case of ST3 are shown in figure 6.9. As also later confirmed by the activation analysis (cf. table 6.11), there was barely any ^3He left in the targets (e.g. way less than 10% from the initial implantation in case of ST3). However, the main achievements during this campaign are nonetheless worthwhile mentioning:

Achievements during the FK-I campaign

- First test of a nuclear fusion reaction at Felsenkeller using the internal ion source.
- Successful tests of the secondary electron suppression (SES), the target cooling, and the control of the target pressure.
- Tests on the long-term beam stability, as well as investigation of blistering effects.
- Investigation of the beam-induced background and a first activation analysis on the TU1 detector.

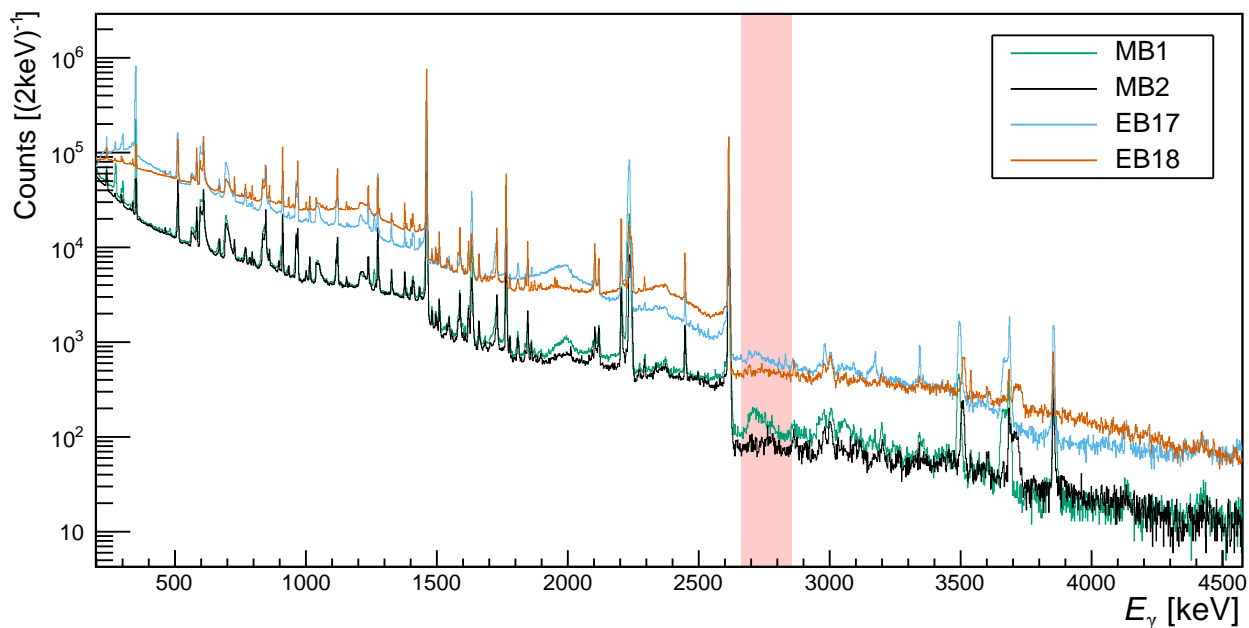


Figure 6.9: Pulse height spectra from the irradiation of ST3 during the FK-I campaign. The ROI for the prompt γ -ray from the ground state transition of the $^3\text{He}(\alpha,\gamma)^7\text{Be}$ reaction is indicated by a transparent red area.

This campaign was mainly thought to be a test run with 2-3 days of irradiation each for ST3 and ST4. The resulting low accumulated charge, the low areal density, as well as the anticipation of the new targets (ST5-ST8) made it unfeasible to also run subsequent irradiations on tantalum blanks in order to correct these spectra for their corresponding in-beam background. However, the emerged experiences from the FK-I campaign also gave insights into several reasonable and necessary upgrades. A list of limiting conditions during the FK-I campaign is offered below:

Limiting conditions during the FK-I campaign

- The areal density degraded significantly over time during the storage process and was too low during irradiation due to the significant age of the targets.
- The energy calibration of the accelerator was not yet accomplished, which hampered a correct estimation of the ROI for prompt γ -rays in the spectra.
- The necessary extrapolation of the efficiency, which was only known up to 1332 keV (cf. also the Bachelor thesis of Max Osswald [14]) further limited the precision significantly.
- While the low areal density limited the investigation of the γ -ray angular distribution, the bursting of blisters in the targets limited the investigation during the activation analysis.

An extensive analysis and discussion on more detailed in-beam results of the FK-I campaign and also the FK-II campaign can be found in the Bachelor thesis of Jannis Michaelis [16].

6.2.2 Results for the in-beam analysis during the FK-II campaign

The FK-I campaign with its irradiation of ST3 and ST4 was mainly seen as a first attempt in gaining experience on the internal ion source, on the target setup, on the detectors and on the subsequent analysis by using comparatively old targets. However, by end of 2020 (between FK-I and FK-II) also a lot of issues were still under investigation.

Upgrades prior to the FK-II campaign

- The avoidance of blistering on ST3 and ST4 was unsuccessful. Reasons were mainly a very small beam spot and no wobbling. For FK-II it was planned to use a significantly larger beam spot.
- There were major problems with the target pressure especially during the irradiation of ST4. These issues were finally resolved by realizing, that these peaks in target pressure are correlated with the cooling of the target cold trap. Apparently, there was a temperature dependent vacuum leak due to partly malfunctioning welds in the bottom cylinder of the target cold trap. This cold trap shares its vacuum with the beam line and subsequently led to problems of the target pressure during each filling. This was ultimately solved prior to FK-II.
- Tests with different heat conducting materials between target holder and target in order to dissipate the heat more efficiently were unsuccessful (cf. section 3.4.1).
- Tests with an upgraded shape for the end of the copper pipe (secondary electron suppression) resulted in no meaningful improvements.

The FK-II campaign took place in end of February 2021 and was able to use comparatively new targets (ST5-ST8), which were produced within the range of October to December 2020. The positioning of the detectors, as well as the setup of the target remained the same, as

also discussed in section 3.4.2. As also elaborated in section 6.5, the new targets are indeed showing a larger areal density, which subsequently enables more reactions of interest to occur per time. However, the accelerator at this time was only able to provide $\sim 5\text{-}6\ \mu\text{A}$ on target ST5, which again reduced the actual reaction rate.

In addition, the signal-to-background ratio significantly suffered from a unresolved in-beam contamination, as shown in figure 6.10. While the dominant peaks were subsequently identified to be due to an aluminum contamination, the actual position of any aluminum within the beam line could not be identified within this one week of irradiation.

The contamination reactions were ultimately identified to be stemming from the irradiation of the holder for the collimator. This holder was made of pure aluminum and was barely irradiated during the FK-I campaign due to the significantly smaller beam size. However, the decision to use a large beam spot in order to increase the uptake of ^4He without blistering subsequently led to significant new problems.

During the investigation of this contamination reaction, the two cluster detectors MB2 and EB18 malfunctioned and ended this campaign, which therefore also just lasted for one week. During the maintenance of these detectors, the accelerator was planned to be conditioned to 3.1 MV for the upcoming irradiation of the ST6 target. However, this conditioning unfortunately led to major sparks on the terminal of the internal ion source, which destroyed several of the mounted HV modules. The subsequent maintenance took several months and prevented any beam extraction from the internal ion source. Hence, no irradiation was possible during the summer of 2021.

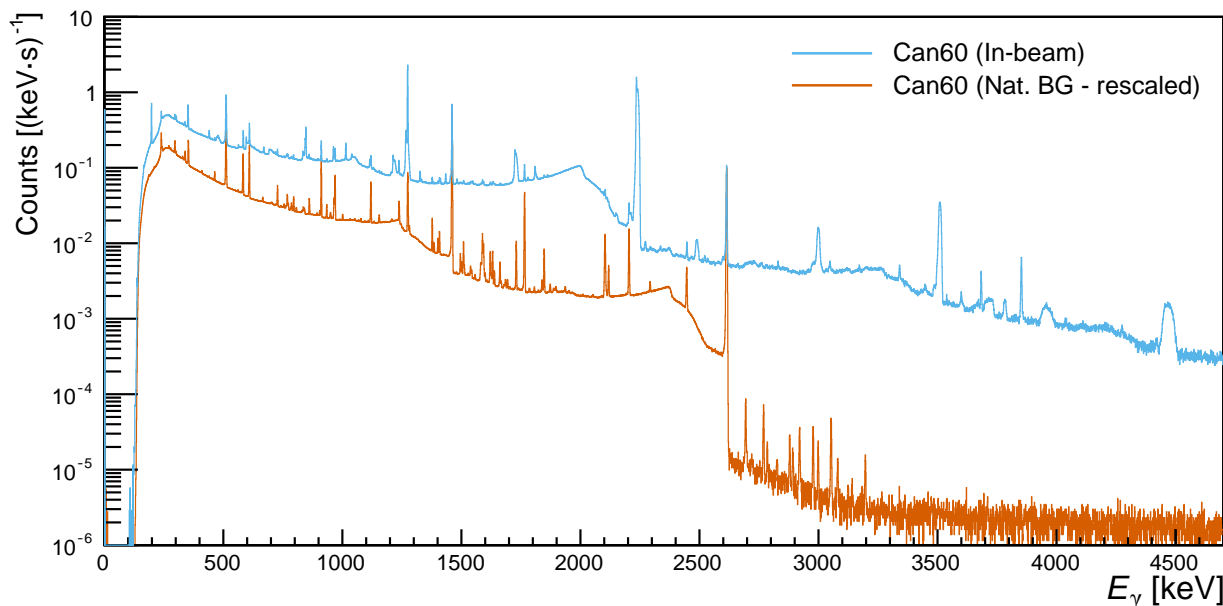


Figure 6.10: Pulse height spectrum of the Can60 detector from the irradiation of ST5 during the FK-I campaign (blue). The normalized pulse height spectrum from the natural background is shown in orange. The ratio of in-beam BG and natural BG in the ROI ($E \sim 2800\ \text{keV}$) is 50000:1.

Achievements during the FK-II campaign

- Small beam spot of FK-I successfully increased to a homogeneous beam spot of ~ 10 mm (cf. photos in the appendix D.1).
- Successful avoidance of bursted blisters in the target ST5.
- Improvements in the activation analysis, which also benefited from the intact target, as well as new calibration sources of ${}^7\text{Be}$ from ATOMKI.
- Successful irradiation of ST5 also during the night with sufficient beam stability.

Limiting conditions during the FK-II campaign

- The ratio of in-beam background to natural background in the ROI was as large as 50000:1, which limited any proper analysis. The main contamination was identified to be stemming from aluminum in the collimator. However, this collimator suffers from a non-reliable current integration due to missing electron suppression and missing insulation due to a water cooling. This fact, as well as the contaminations stemming from different sources (with significant changes in their applied current ratio over time) also disabled any proper subtraction of beam-induced background in the ROI. However, their intense contribution to the pulse height spectrum called for a subsequent identification and elimination.

An extensive analysis and discussion on more detailed in-beam results of the FK-II campaign can be found in the Bachelor thesis of Jannis Michaelis [16].

6.2.3 Angular uncertainty for full-energy events deposition in the HPGe

The major downtime of the accelerator between the FK-II campaign and the FK-III campaign was used for several upgrades on the in-beam setup. While the majority of them will be elaborated in section 6.2.4, one crucial element will be described in the following section: The determination of the effective opening angles for detectors based on Geant4 simulations. One of the main goals of these campaigns is the γ -ray angular distribution from the prompt γ -rays emitted during the ${}^3\text{He}(\alpha, \gamma){}^7\text{Be}$ reaction. However, all detectors do have a finite size, which inevitably lead to a geometrical limit on the angular precision of each measurement. In order to quantify this uncertainty, Geant4 simulations were performed. These simulations isotropically emitted monoenergetic photons with the energy of interest from the center of the target position. The resulting events, which deposited their full energy in a certain detector, were then analyzed regarding their initial emission angle. In this way, an angular distribution is obtained, which reflects the effective opening angle in case of full-energy peak events for each detector. The corresponding distributions are subsequently fitted with a two-sided step function (cf. appendix D.5), and their inflection points are evaluated, respectively. The resulting angular uncertainties due to the spread of acceptable detection angles for full-energy events are shown in figure 6.11.

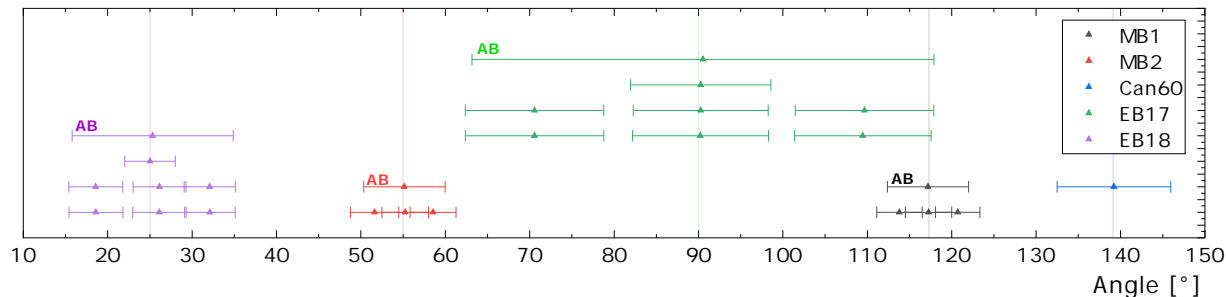


Figure 6.11: Intervals for the effective detector angles in case of full-energy event depositions. The actual angle of each detector is marked with a vertical line. Each color represents the results of one of the detectors/clusters with one data point for each crystal, respectively. In case of cluster detectors, the result for the add-back mode is also given and marked with ‘AB’. The general overlap of single crystals in case of Miniball clusters is slightly larger than for Euroball clusters due to their geometric arrangement (cf. figure 3.13). The corresponding distributions are shown in appendix D.5.

While each cluster in figure 6.11 shows the result of each single crystal, it also shows the result of the detectors used in add-back mode (cf. section A.1.2). Both the add-back mode, as well as detectors in close geometries reveal one significant disadvantage: The resulting uncertainty on the opening angle of the detectors is significantly increased. Hence, the distance of a detector should always be a compromise between being close enough to the target for sufficient statistics (limiting uncertainty on the y-axis in the resulting γ -ray angular distribution) and being away far enough (limiting uncertainty on the x-axis in the resulting γ -ray angular distribution).

6.2.4 Results for the in-beam analysis during the FK-III campaign

As discussed in the last two sections, during summer 2021 there was a period of major maintenance and upgrades regarding the internal components of the accelerator tank. In the meantime (and therefore prior to the FK-III campaign), this time was also used to perform several additional upgrades for the in-beam detection setup at Felsenkeller.

Upgrades prior to the FK-III campaign

- Installation of a new holder for the collimator, which is made of pure copper in order to significantly attenuate contamination reactions.
- Upgrade of both the turbo pump (new: Pfeiffer HiPace 700) and the bake pump (new: Vacuubrand MV 10 NT) for the target setup (cf. section 3.4.3)
- Installation of a redundant DAQ2 for also measuring the high energetic part of the pulse height spectra. DAQ2 has a 1:1 calibration between channel and energy.
- Installation and optimization of an active muon veto for the TU1 detector, which significantly increased its sensitivity for subsequent activation analyses.

The FK-III campaign itself took place in the week from 21.09.2021 to the 29.09.2021 and was using target ST6, which was also produced within the range of October to December 2020. The positioning of the detectors, as well as the setup of the target remained the same, as also discussed in section 3.4.2. The main goal of this campaign was the verification of the severe reduction in in-beam background, which hindered any useful analysis of the ROI during FK-II. As shown in figure 6.12, this contamination was indeed removed.

Achievements during the FK-III campaign

- First reliable in-data for both the ground state transition and the first excited state transition.

At the evening of the 29.09.2021, all in-beam detectors went into bias-shutdown, which abruptly ended the FK-III campaign. The full recovery from this event took until end of October, since detectors also had to be repaired, pumped, heated and turned back on, respectively. Also the elimination of noise on the majority of signals took a significant amount of time. One of the main improvements was to eliminate any possible ground loops, e.g. by separating NIM HV modules from all NIM modules, which provide the power supply for the preamplifiers.

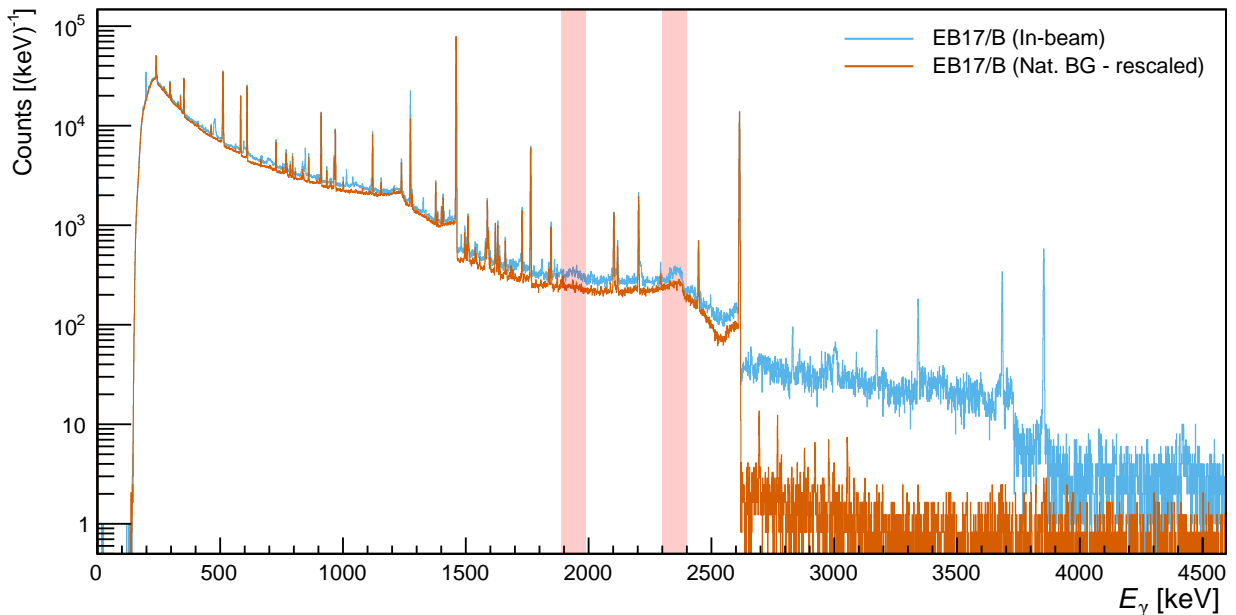


Figure 6.12: Pulse height spectrum of the EB17/B detector from the irradiation of ST6 during the FK-III campaign (blue). The normalized pulse height spectrum from the natural background is shown in orange. The ROIs for the ground state transition and the first excited state transition are shown as vertical red bands. The main background contribution to the ROI is stemming from the Compton continuum of the ${}^{208}\text{Tl}$ γ -ray line at $E = 2615$ keV.

Limiting conditions during the FK-III campaign

- During the irradiation of ST6 in the FK-III campaign, the natural radiation finally became the dominant source of background for the first time. This is on the one hand due to the fact, that the in-beam background was successfully attenuated (mainly due to the new copper holder for the collimator). But on the other hand, the irradiation energy was also significantly lower. Hence, some important contamination reaction channels were energetically disfavored or not possible.
- Bias Shutdown of all HPGe detectors (and subsequent maintenance phase) prohibited a proper acquisition of data from a pure tantalum blank.

The outcome of analyzing a γ -ray angular distribution without proper acquisition of data from a pure tantalum blank is shown in the Master thesis of Armin Freimann [158]. The data point from ST6 deviates significantly from all other data points due to the disregard of in-beam contributions.

An extensive analysis and discussion on more detailed in-beam results of the FK-III campaign can also be found in the Bachelor thesis of Fabia Dietrich [109].

6.2.5 Results for the in-beam analysis during the FK-IV campaign

During the necessary maintenance of the in-beam detectors during October and November 2021, there was sufficient time to implement further upgrades based on the knowledge of the FK-III campaign.

Upgrades prior to the FK-IV campaign

- Installation of a lead castle around Can60, EB17 and partly EB18 in order to further attenuate the impact of the natural background component
- Repositioning of MB1 away from the focal point of the crystals and 2.7 cm closer to the target
- Installation of a beam wobbling unit during mid of October 2021, which effectively distributes the accumulated charge on a broader area of the target.

The FK-IV campaign itself took place from 29.11.2021 to the 05.12.2021 and was using the two targets ST7 and ST8, which were produced within the range of October to December 2020. The positioning of the detectors, as well as the setup of the target remained mainly the same, as also discussed in section 3.4.2.

While the first in-beam campaigns at Felsenkeller were always struggling with the dominating in-beam background, after FK-III it was finally suppressed so efficiently, that the natural background became dominant for the first time. This is why it was decided to build a lead castle around Can60, and EB17, and partly around EB18 during the downtime of the detectors.

During the irradiation of ST7 and ST8 in the FK-IV campaign, the natural background was successfully attenuated by a factor of 2-3 (cf. Bachelor thesis of Fabia Dietrich [109]). However, the beam energy was increased again back to significantly larger values, and the obtained spectra during FK-IV have a clear indication of neutron-producing processes, i.e. (α, n) -processes, as shown in figure 6.13. Free neutrons are able to propagate into the HPGe detectors and generate so-called neutron triangles in the pulse height spectra (e.g. at $E = 596$ keV in figure 6.13) via inelastic scattering on the germanium [163].

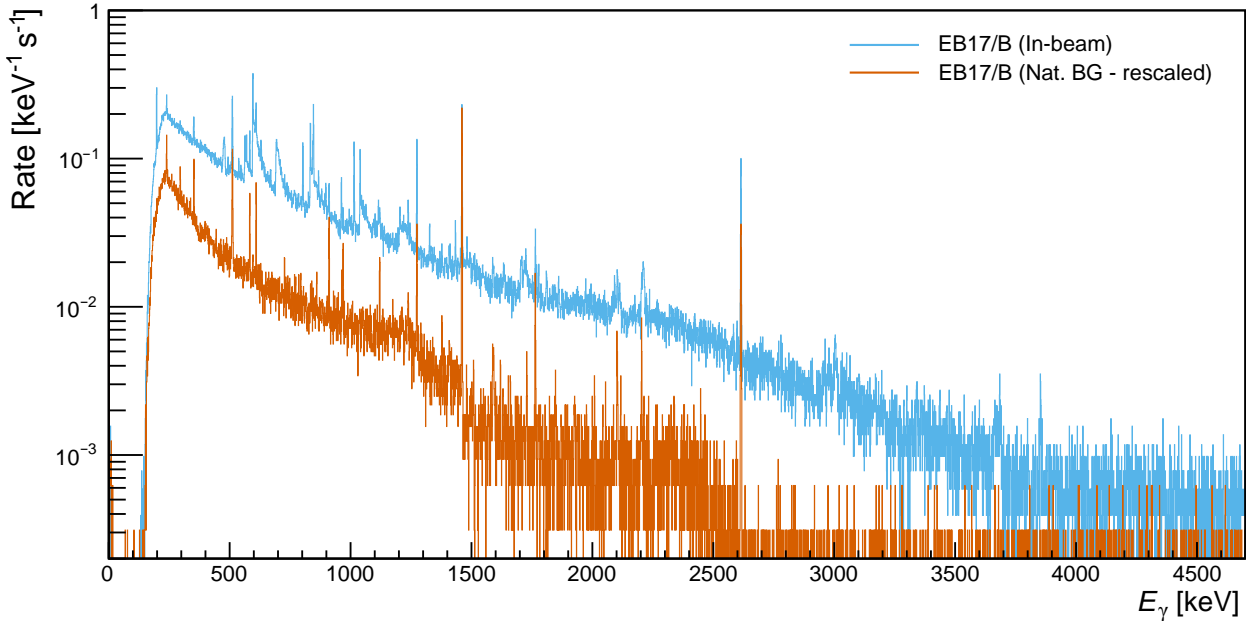


Figure 6.13: Pulse height spectrum of the EB17/B detector from the irradiation of ST7 during the FK-IV campaign (blue). The normalized pulse height spectrum from the natural background is shown in orange.

Hence, ST7 and ST8 were subsequently used to investigate these neutron triangles. This was done by performing separate runs with either more beam on the target, more beam on the collimator or more beam on the copper pipe, respectively. This was done using also different beam spot sizes and with and without wobbling, respectively. Furthermore, the yield for these neutron triangles was investigated by performing a wide beam energy scan, as well as smaller scans along expected resonances [109].

Limiting conditions during the FK-IV campaign

- The dominant beam-induced background is stemming most likely from (α, n) reactions on carbon or oxygen contaminations on the target surface. The subsequently present neutron field is scattering inelastically on the germanium in the HPGe crystals. The results are so-called neutron-triangles in the HPGe detectors. This contribution was suppressed during FK-III due to its low irradiation energy and also strongly suppressed during FK-II due to the by far dominating aluminum-induced background (cf. Bachelor thesis of Fabia Dietrich [109]).

The level of background contaminations during FK-IV was mainly at a satisfactory level. Due to the fact, that new targets were planned for the upcoming main campaign (FK-V), an improved target cleaning technique was investigated (Cleaning procedure II, cf. section 3.2.1) in order to prevent carbon and oxygen contaminations on the surface of the targets as efficiently as possible. In addition to the upgrades prior to FK-I to FK-IV, the subsequent success of the FK-V campaign relied on three major final upgrades:

Final upgrades for the FK-V campaign

- The reduction of the natural background by shielding the entire setup with one surrounding large lead castle (cf. section 3.4.5).
- The improvement of the target holder (cf. section 3.1.5) in order to avoid the attenuation of γ -rays in case of detectors at forward angles as much as possible.
- Improvement of the cleaning procedure in order to reach for larger areal densities (cf. section 3.2.1).

An extensive analysis and discussion on more detailed in-beam results of the FK-IV campaign can be found in the Bachelor thesis of Fabia Dietrich [109].

6.3 In-beam analysis of FK-V

The campaign FK-V was conducted between July and October 2022, and four implanted targets (ST9, ST10, ST11 and ST15), as well as four pure tantalum targets (Ta51, Ta52, Ta53 and Ta54) were irradiated, respectively. Each target was only irradiated at one specific energy in order to strengthen the physics case of the subsequent activation analyses. The assignment of targets and irradiation energies is listed in table 3.3. The order and duration of the irradiations with respect to the time are shown in figure 6.14, in addition to the corresponding target currents for all ‘ST’-runs (orange). During the second irradiation of target ST9 (further called ST9B), the secondary electron suppression malfunctioned, and therefore there is no reliable data available for the target current. The mean target current for all other ‘ST’-runs is $I = 13.4 \mu\text{A}$.

The crucial difference between campaign FK-V and its predecessors is the availability of high-statistics in-beam background runs with long-term stability on pure tantalum targets, which were not properly conducted for FK-I to FK-IV. As discussed during the last sections, this was either due to a prompt malfunction of the accelerator/detectors, or due to the insight, that the remaining in-beam background had to be properly suppressed prior to the main campaign. While preceded campaigns therefore relied on both a ROI with no contaminating in-beam γ -ray lines, as well as a peak-to-Compton ratio in the ROI of at least 1:1, more sophisticated analyses can be performed in case of campaign FK-V.

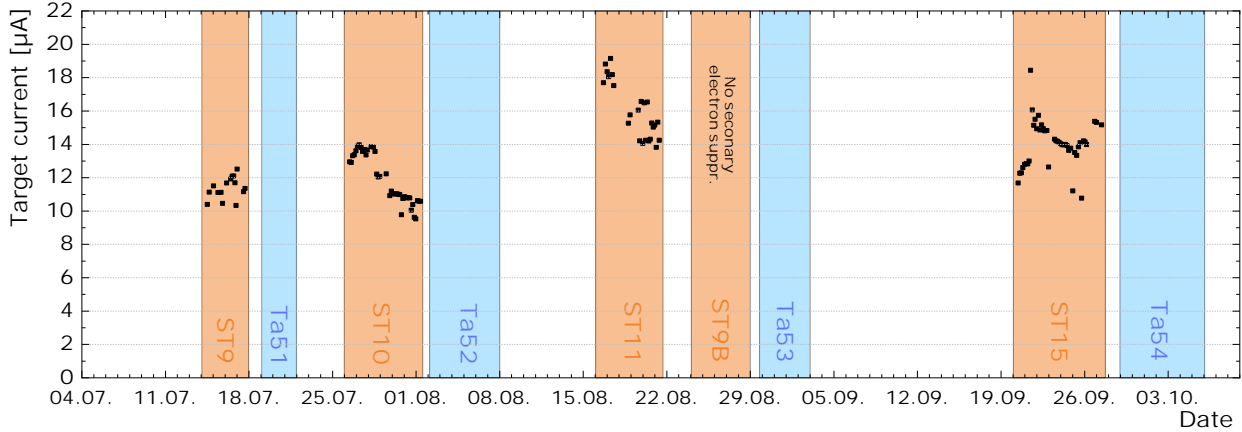


Figure 6.14: Order and duration of all irradiations during the FK-V campaign. Irradiations of the implanted targets and pure tantalum blanks are shown in orange and blue, respectively. In addition, the target current is shown for the ‘ST’-runs, when available. See text for details.

6.3.1 Target stability

During the subsequent irradiations of all implanted targets, the preliminary yield was monitored closely in order to balance out the gain of additional statistics versus the necessary beam time. As discussed in section 3.1.6, it is well known, that a high accumulation of ${}^4\text{He}$ can lead to blistering effects on the target, which have an impact on the areal density. So both a constant degradation, as well as sudden drops in yield are possible. However, they are delayed by continuously scanning the beam along the target in order to distribute the implanted ions per area (wobbling technique). As soon as the target degraded too much, and the yield dropped significantly without sufficiently acquired statistics, the beam was tried to be focused onto another point on the target. If this was also unsuccessful, either the statistics was accepted or the target was exchanged.

The net yield per run is shown for all targets in figure 6.15. It is apparent, that most of these targets degrade more or less continuously over the first 24 h, and remain stable at approximately 50-70% of the initial yield within the next days of irradiation. While this was not investigated in great detail, one reasonable explanation could be related to heat-induced diffusion processes out of the most upper layers near to the target surface despite using the wobbler and the LN2 cooling. However, this is supported by the fact, that during ST15 (lowest irradiation energy and hence lowest application of power on the target), this degradation of yield seems to be less significant (cf. bottom panel in figure 6.15).

Small temporary increases in yield, as e.g. during the evening of 28th of July in ST10, are directly related to attempts by the operators to steer the beam onto a different point on the target in order to increase the yield. In case of ST11, the yield suddenly dropped far below the usual degree at the evening of the 19th of August and was not recoverable. Due to a lack of statistics for this energy, the target was exchanged and ST9 was re-installed (further called ‘ST9B’ during this second irradiation). It is worthwhile mentioning, that it was re-installed after completion of its subsequent activation analysis for $E_{\text{cm}} = 1217.1$ keV.

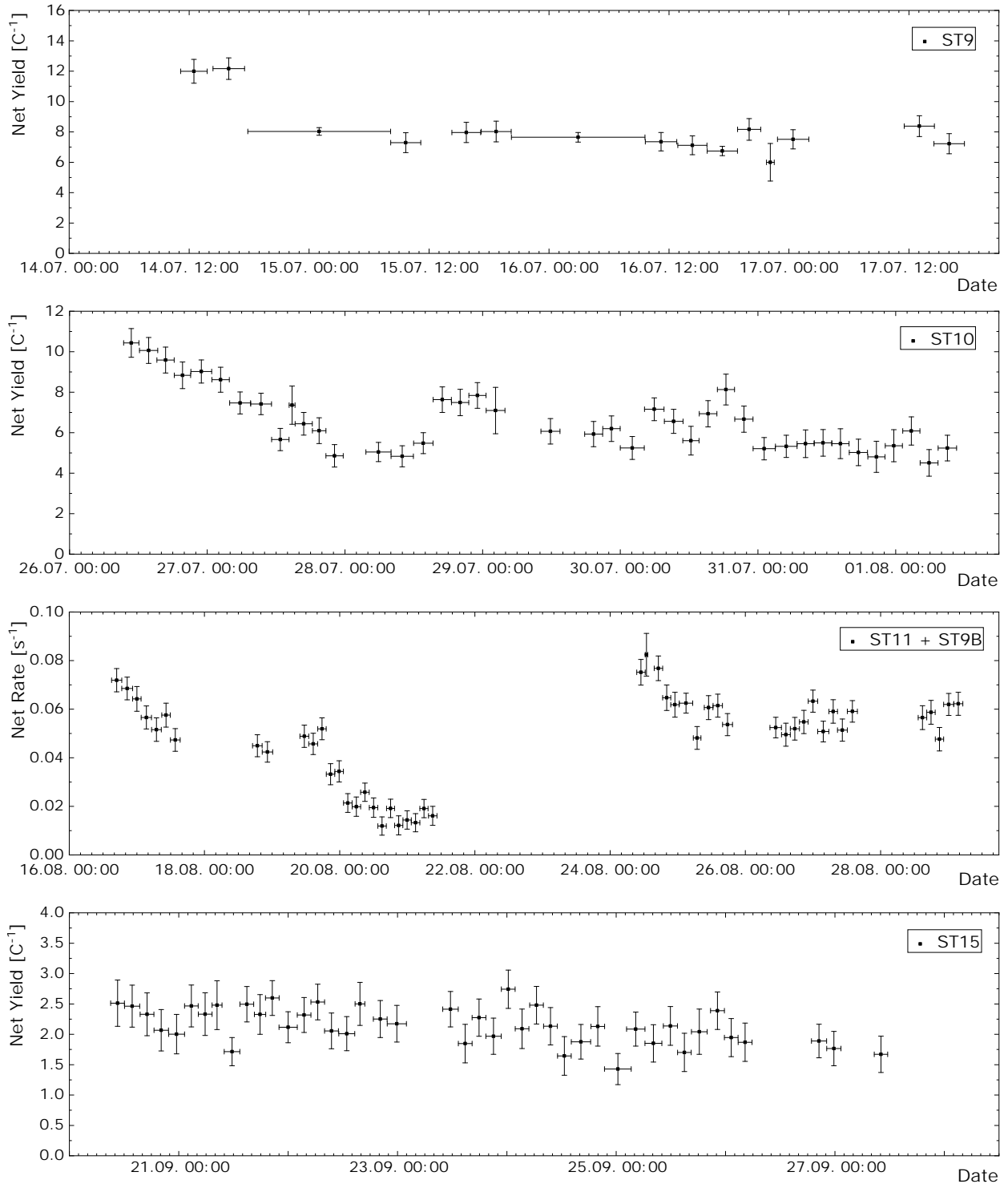


Figure 6.15: Net yield for each run based on the irradiation of all four target during the FK-V campaign. The horizontal uncertainty indicated the duration of each run. Due to the short duration of each run, this yield is based on a simple cut-and-count method on each spectrum (cf. section 6.3.2 for proper analysis). Top panel: Yield from the irradiation of ST9. Second panel: Yield from the irradiation of ST10. Third panel: Net rate from the irradiation of ST11 (until 22th of August) and ST9B (starting at 24th of August). For the irradiation of ST9B, the SES did not work properly. Therefore, the rate is plotted instead, and the data can only be interpreted properly in case of a stable beam current. Fourth panel: Yield from the irradiation of ST15.

6.3.2 Prompt γ -ray analysis

In total there are three available categories of data sets for each irradiation energy during the FK-V campaign, which are listed below:

- **Main runs ('ST' runs):** Long-term, high-statistic in-beam investigations using implanted targets. The background contributions within these runs depend on both the in-beam background, as well as natural background sources. These runs are further called 'ST' runs due to the use of the targets ST9-ST15 (cf. table 3.3).
- **In-beam BG ('Ta' runs):** Long-term, high-statistic in-beam investigations using pure tantalum targets. These runs are supposed to result in identical pulse height spectra, as the main runs, but are lacking of prompt γ -rays from the ${}^3\text{He}(\alpha, \gamma){}^7\text{Be}$ reaction. The background contributions within these runs also depend on both in-beam background, as well as natural background sources. However, their ratios might vary with respect to the respective ratio in the main runs. These runs are further called 'Ta' runs due to the use of the targets Ta51-Ta54 (cf. table 3.3).
- **Natural BG ('BG' runs):** Long-term, high-statistic investigations without any irradiation. The background contributions therefore solely relies on natural background sources. These runs are further called 'BG' runs.

As mentioned in the items above, both the ST runs as well as the Ta runs suffer from natural BG and in-beam BG. While the natural BG mainly depends on the measurement time, the amount of in-beam BG additionally depends on the accumulated charge on the target³⁵. Hence, as soon as the accumulated charge per time is not identical for the respective ST and Ta run, the BG-correction for the ST runs can not be done solely by using the Ta runs.

In summary: While the ST runs contain all the valuable information about the prompt γ -ray angular distribution, they also suffer from both in-beam BG, as well as natural BG. In order to account for these contributions, the Ta runs **and** the BG runs have to be taken into account. This is done in a way, that both the ST runs, as well as the Ta runs are first of all each corrected for their natural BG contributions. Afterwards the (natural BG corrected) Ta runs can be used to correct the in-beam BG for the (natural BG corrected) ST runs. In this way, the entanglement between natural BG and in-beam BG (which face different ratios for the ST and the Ta runs) can be properly dissolved.

³⁵This statement is only true, if the in-beam BG in the spectra is mainly stemming from reactions in the target (when e.g. compared to reactions taking place in the collimator). But even if this is not the case, due to the high beam stability at Felsenkeller, the ratio of accumulated charge on target and on the collimator is always highly similar, which significantly softens this matter of concern. Furthermore, this statement is only true in case of negligible contributions stemming from long-living contaminations.

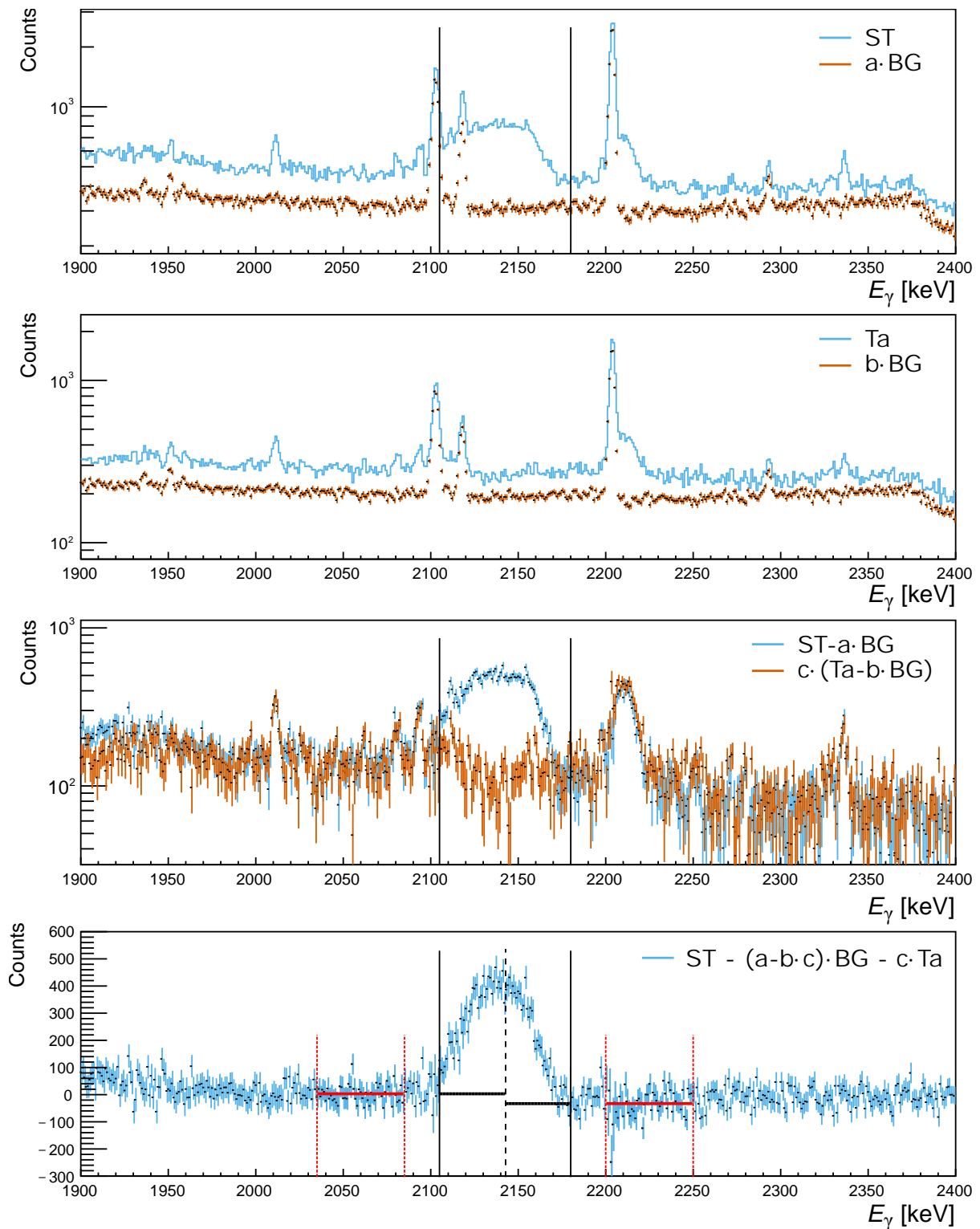


Figure 6.16: Pulse height spectra for detector EB17BGE from the in-beam analysis of the FK-V campaign based on the irradiations of the targets ST11, and ST9B (same irradiation energy) and Ta53 (cf. table 3.3). The binning in all panels is 1 keV. In case of prompt γ -rays in the spectrum, the theoretically predicted ROI is indicated by black vertical lines. Top panel: Result of the ‘raw’ ST runs (blue) and the normalized BG runs (orange). Second panel: Result of the ‘raw’ Ta runs (blue) and the normalized BG runs (orange). Third panel: Result of the BG-corrected ST runs (blue) and the BG-corrected Ta runs (orange). Furthermore, the Ta runs are normalized with respect to the in-beam BG. Bottom panel: Resulting residuum after properly correcting natural BG and in-beam BG according to equation 58. This exemplary spectrum is chosen due to the fact, that the inevitable correction of both natural and in-beam BG is apparent.

Correction of the natural background for Ta and ST runs

As mentioned in the last paragraph, the first step is to correct both the ST runs, as well as the Ta runs for their natural background using the BG runs. On the one hand this could be done by adjusting the available BG runs based on the corresponding live time ratio to the ST (and Ta) runs. However, there is a clear flaw in this approach: In between all of the ST, Ta and BG runs, the ST targets and Ta targets had to be replaced by another target. Hence, the lead castle was partly removed in order to reach the target holder. During the subsequent reconstruction of the lead castle, the individual lead bricks were tried to be arranged as similar as possible to their position in the predecessor castle. However, this campaign took several months and the lead castle was subsequently rebuilt multiple times. It was shown, that this fact inevitably led to slightly different counting rates during the BG runs in all detectors (dominantly the ones with low angle due to their proximity to the point of target changes) subsequently causing major flaws when conducting this approach.

On the other hand, the BG runs could be adjusted to the ST (and Ta) runs by comparing the full-energy peak entries of a high-statistics peak stemming from the natural background. It is worthwhile mentioning, that the rebuilding of the lead castle leads to a unique energy-dependent attenuation of the natural BG for each run. Hence, this approach strongly relies on the use of a peak, which has a high statistics **and** is close in energy to the ROI of the expected prompt γ -rays. In the best case, this peak should in addition be located above the ROI, so that the high statistics in the peak also makes this peak the dominating cause of background (due to the incoherent scattering) in the ROI.

An exemplary analysis procedure is shown in figure 6.16. The corresponding ST and the Ta runs for $E_{\text{cm}} = 554.6 \text{ keV}$ are shown in the first and the second panel in blue, respectively. The corresponding BG runs, which are adjusted via this technique, are shown in orange. As indicated by the corresponding legend for these four spectra in the first two panels of figure 6.16, they represent the corresponding terms in formula equation 57 for the final residuum. It is worthwhile mentioning, that these spectra are not solely subtracted from each other, due to the loss of information on bin uncertainties. This will be further discussed in section 6.3.5. However, after correcting both the ST and the Ta runs for their natural background, the in-beam background still needs to be corrected for the ST runs.

Correction of the in-beam background for the ST runs

After correcting both the ST and the Ta runs for their natural BG within the ROI, the Ta runs can be used to correct the ST runs regarding their in-beam BG within the ROI. By using the same arguments as in the case of the natural BG, this procedure also could be done by either aligning these runs based on their accumulated charge or by taking an in-beam peak (or a natural BG-corrected in-beam region) with high statistics close to the ROI, which is solely stemming from reactions within the target (and not e.g. the collimator). However, an in-beam peak with high statistics is not always available close to the ROIs (especially in

case of low irradiation energies). While most tested methods were not flawless for all four irradiation energies, the most robust approach turned out to be the following: Due to the fact, that both spectra were corrected for their natural background, the correction factor c was chosen in a way, that the sum of both the left and the right BG regions (cf. red vertical lines in figure 6.16) within the resulting residuum vanishes. The resulting factor c is subsequently used to align the background-corrected ST and the Ta runs, as shown in the third panel of figure 6.16, where the correction factor c is already applied to the Ta runs.

$$(\mathbf{ST} - a \cdot \mathbf{BG}) - c \cdot (\mathbf{Ta} - b \cdot \mathbf{BG}) \quad (57)$$

In summary, the peak-to-BG ratio within the ROI of the ST runs can be significantly enhanced, by first correcting both the ST runs and the Ta runs by their natural BG, as shown in equation 57. As discussed before, this will lead to the two weighting factors a and b . Subsequently, the in-beam contaminations can be accounted for by comparing the resulting Ta runs and ST runs, as expressed by the weighting factor c in equation 57.

Improvement of this approach and resulting residua

As shown in equation 57, the ST runs and the Ta runs can be accounted for their natural BG using the weighting factor a and b , respectively. In addition, the weighting factor c can be used to correct the (natural BG corrected) ST runs with help of the (natural BG corrected) Ta runs in order to account for the in-beam BG. However, in case of substantial amounts of natural BG in the ROI, this approach leads to unnecessarily large uncertainties in the ROI. This is due to the fact, that the natural BG is used twice. Hence, its uncertainty is also propagated twice into the resulting residuum.

The more appropriate approach (which is also used throughout this thesis) first of all needs to calculate these weighting factors a , b and c . However, the equation 57 can be reformulated, as shown in equation 58, which only uses the BG spectra once. Therefore, its uncertainty will also just be propagated once, which leads to a more accurate result.

$$\mathbf{ST} - (a - b \cdot c) \cdot \mathbf{BG} - c \cdot \mathbf{Ta} \quad (58)$$

Hence, a , b and c are determined based on the first three panels and the raw ST, Ta and BG runs are then treated according to equation 58 by using the BG spectra only once.

While an exemplary analysis for generating the resulting residuum is shown in figure 6.16, the resulting residua for the ground state transition in case of ST9 ($E_{\text{cm}} = 1217.1 \text{ keV}$) is shown in figure 6.17. The background color of each residuum indicates, whether it was used in the final analysis (green = accepted, red = rejected). A more thorough elaboration on the acceptance and rejection of residua will be given in chapter 6.3.4.

The corresponding plots for the residua from the first excited state transitions, as well as other irradiation energies during the FK-V campaign are shown in the appendix D.7.

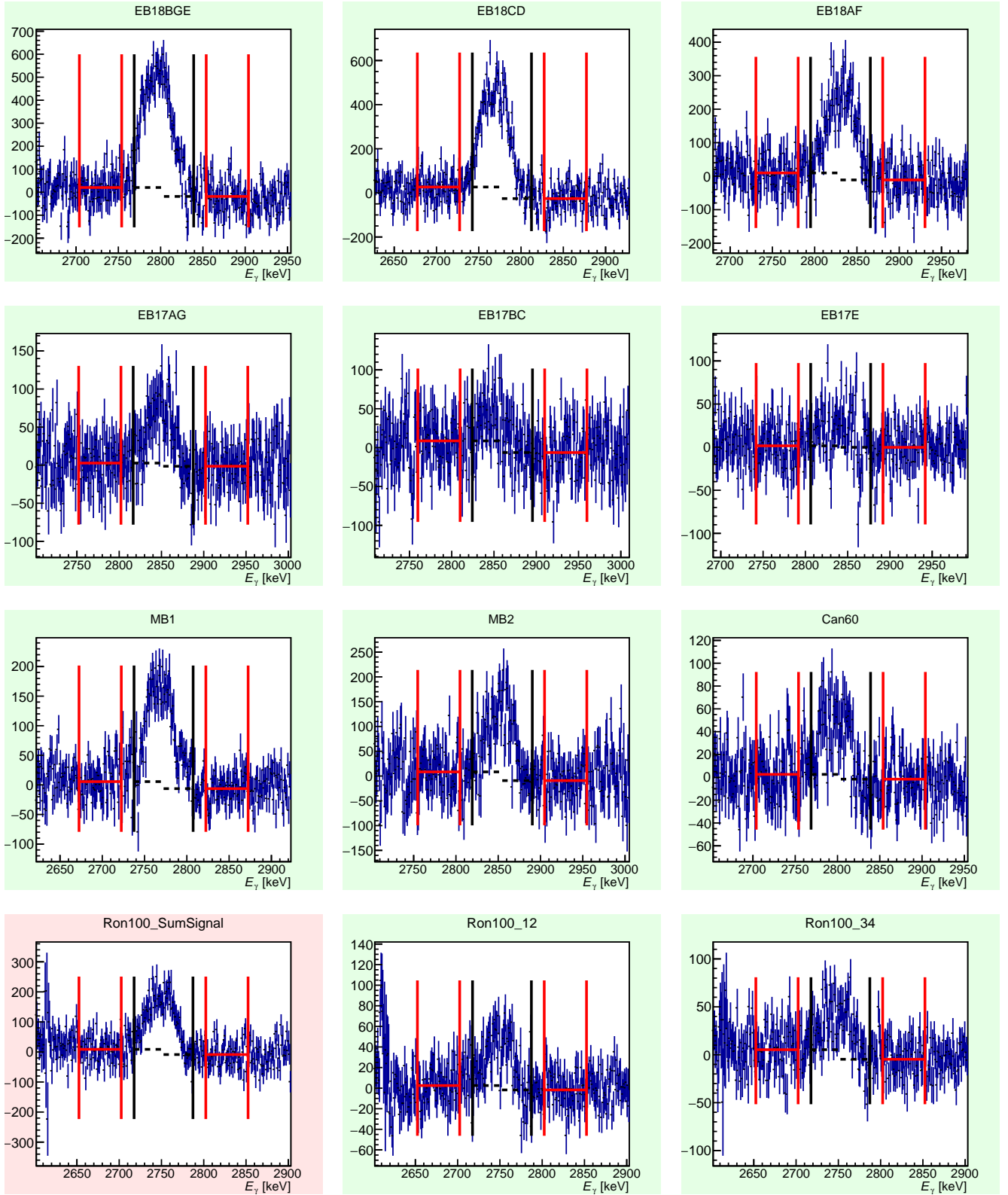


Figure 6.17: Residua resulting from the analysis of prompt γ -rays in the FK-V campaign based on the example of ground state transitions in case of target ST9 ($E_{\text{cm}} = 1217.1$ keV). From top to bottom, and from left to right, the panels show the residua from EB18BGE, EB18CD, EB18AF, EB17AG, EB17BC, EB17E, MB1, MB2, Can60, Ron100, Ron100 (segment 1&2), and Ron100 (segment 3&4). The residua are obtained by using the procedure introduced in figure 6.16. The background color of each panel indicates, whether it was (green), or wasn't (red) used for further analysis (cf. section 6.3.4). For additional residua from the FK-V campaign, see appendix D.7.

The determination of the ROI (black vertical lines in figure 6.17) is based on theoretical expectations including the Q -value, the center-of-mass energy (at the surface for the right border and at 180 nm depth for the left border), and the angle of the detector. Furthermore, both borders are artificially expanded by additional 10 keV in order to account for the detectors FWHM, for angular uncertainties and uncertainties stemming from the depth distribution. When comparing the theoretically predicted ROI with the actual peak shape (e.g. in case of EB18BGE), the peak shape seems to match the lower ROI border, but not the higher ROI border. This would be in agreement with the assumption in section 6.3.1, that the decrease in yield over time could be correlated to heat-induced diffusion processes out of the surface of the target. This ‘outgassing’ would subsequently lead to less prompt γ -rays from the layer close to the surface and could therefore explain the asymmetric peak shape within the ROI.

Limiting conditions during the FK-V campaign

- Beam-induced background stemming most likely from carbon contaminations on the target. The subsequently occurring $^{13}\text{C}(\alpha, n)^{16}\text{O}$ reactions lead to a neutron field, which inelastically scatters on the germanium in the HPGe crystals. The results are so-called neutron-triangles in the HPGe detectors (cf. Bachelor thesis of Simon Vincent [20]).
- Additional beam-induced background is mainly due to inelastic α -scattering (especially on ^{13}C , ^{19}F , ^{27}Al , ^{63}Cu , ^{65}Cu and ^{181}Ta , as well as in-beam reactions from e.g. $^{10}\text{B}(\alpha, p)^{13}\text{C}$, $^{19}\text{F}(\alpha, p)^{22}\text{Ne}$, $^{19}\text{F}(\alpha, n)^{22}\text{Na}$, $^{27}\text{Al}(\alpha, \gamma)^{31}\text{P}$ and $^{27}\text{Al}(\alpha, p)^{30}\text{Si}$ (cf. Bachelor thesis of Simon Vincent [20]).

6.3.3 Absolute full-energy peak efficiency

The experimentally determined γ -ray angular distribution mainly depends on both the amount of prompt γ -rays depositing their full energy in the respective detectors, as well as on the corresponding absolute full-energy peak efficiency ε (cf. section 2.4.2). Taking both into account, the amount of prompt γ -rays being emitted into a certain direction can be deduced.

The determination of absolute full-energy peak efficiencies was introduced in section 2.4.2 and was already discussed during the investigation of the $^2\text{H}(p, \gamma)^3\text{He}$ reaction (cf. section 5.1.2), as well as during the investigation of the $^3\text{He}(\alpha, \gamma)^7\text{Be}$ reaction (cf. section 6.4.4). Hence, the result will only be briefly discussed within this section.

In case of the FK-V campaign, the fit function for the efficiency is based on a second order polynomial within its exponential term (cf. section 2.4.2). This necessity becomes apparent by comparing detectors in forward direction (EB18AF, MB2 and EB17) and detectors in backwards direction (Ron100, MB1, EB18CD). There is a clear trend, that the detectors in forward direction are more affected by the γ -ray attenuation due to the target holder.

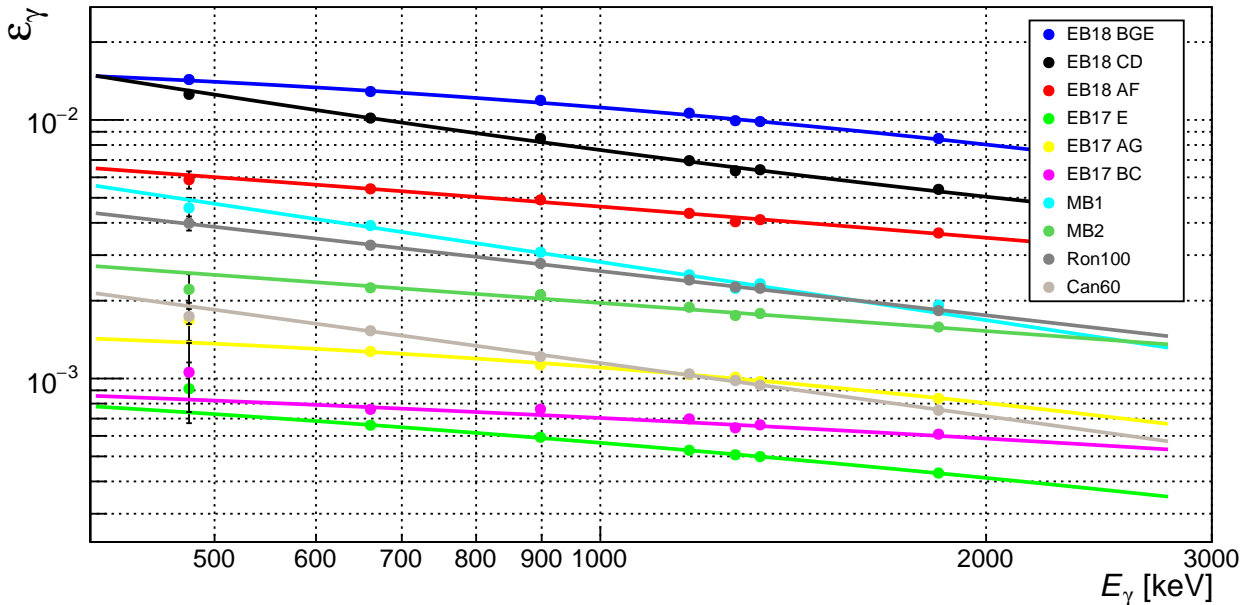


Figure 6.18: Absolute full-energy peak efficiency for all detectors in use during the FK-V campaign (cf. table 3.6). Calibration sources containing the radio nuclides of ${}^7\text{Be}$ (ID: 4697), ${}^{22}\text{Na}$ (ID: 4659), ${}^{60}\text{Co}$ (ID: 3393), ${}^{88}\text{Y}$ (ID: 4753), and ${}^{137}\text{Cs}$ (ID: 3396) are used (cf. table 3.4). Detectors in close geometry are corrected for true coincidence summing (see also [158] for details). According to section 6.3.5, these fits only include the statistical uncertainty. An increased χ^2 is therefore expected and inevitable.

This subsequently leads to a clear non-linear behavior of ε in a double-log plot and moves the knee to comparatively large energies. A more thorough discussion on this effect can be found in [14], where the ‘old’ target holder design II led to even more drastic non-linearities (cf. section 3.1.5).

While the detectors in close geometry (i.e. all EB18 crystals) are benefiting from the large efficiency, which especially for EB18BGE results in more precise results for the important angle of $\vartheta = 90^\circ$, it also leads to the disadvantage of non-negligible true coincidence summing, which has to be corrected accordingly. The ratio of γ -rays undergoing true coincidence summing (with respect to properly reconstructed energy depositions) mainly depends on the distance between source and detector, the total efficiency of the detector, as well as possible γ -ray angular correlations. However, in contrast to random coincidences, this ratio does not depend on the activity of the sample. For more details see [158].

6.3.4 Resulting γ -ray angular distribution

The resulting in-beam residua from all irradiations during the FK-V campaign are shown in figure 6.17 and appendix D.7. For each target, these residua include the analysis for the ROI of the ground state transition and the first excited state transition for 12 different combinations of detector crystals: EB18BGE, EB18CD, EB18AF, EB17E, AB17AG, EB17BC, MB1, MB2, Can60, Ron100, Ron100(12), and Ron100(34). In case of the Ron100 detector there are multiple analysis techniques: When there is sufficient statistics in the single seg-

ments, the segment 1 and 2 are added up accordingly, which is further called Ron100(12). In case of the sum of segment 3 and segment 4, this residua is called Ron100(34). If the corresponding statistics is not sufficient, the entire Ron100 signal is used. This reduces the angular precision, but enables the inclusion of a rather extreme angle.

However, this means, that only **either** Ron100(12) and Ron100(34) **or** Ron100 is utilized for the determination of the respective γ -ray angular distribution. The information, which of them is used is encoded within the background color of the respective residuum: If the background color is red, it is not used further and if the color is green, it is used.

As addressed earlier, this background color also indicates for all of the other residua in general, whether they are used for the further analysis. The procedure on how to objectively decide this in an unbiased manner is elaborated below:

- Whenever the net area in the ROI is statistically significant (2σ C.L.) and there is no obvious remaining structure (neither in the BG region, nor in the ROI), then the residuum is accepted for further analysis.
- In case of obvious remaining structures within the BG region, the BG interval is shifted to a structure-free region. If this is also not possible, the residuum is excluded from further analysis.

The remaining visible structures in the residuum are mainly due to time-dependent changes in the FWHM of a crystal. Shifting energy calibrations can mostly be circumvented by performing an own calibration for each run, respectively. However, if the FWHM changes significantly between the ST, Ta and BG runs, the residuum will inevitably show remaining structures. This subsequently leads to over- and under-compensations in the residuum, which are non-physical. They also do not cancel out each other, since they also affect the weighting factors a, b and c . These residua are therefore excluded from further analysis. Furthermore, obvious remaining structures might also occur in case of varying in-beam background with non-target origins, e.g. due to the irradiation of the collimator. If there is a major contribution in the ROI stemming from in-beam reactions within the collimator and the ratio between collimator current and target current changes significantly between ST and Ta runs, the compensation will not be done appropriately.

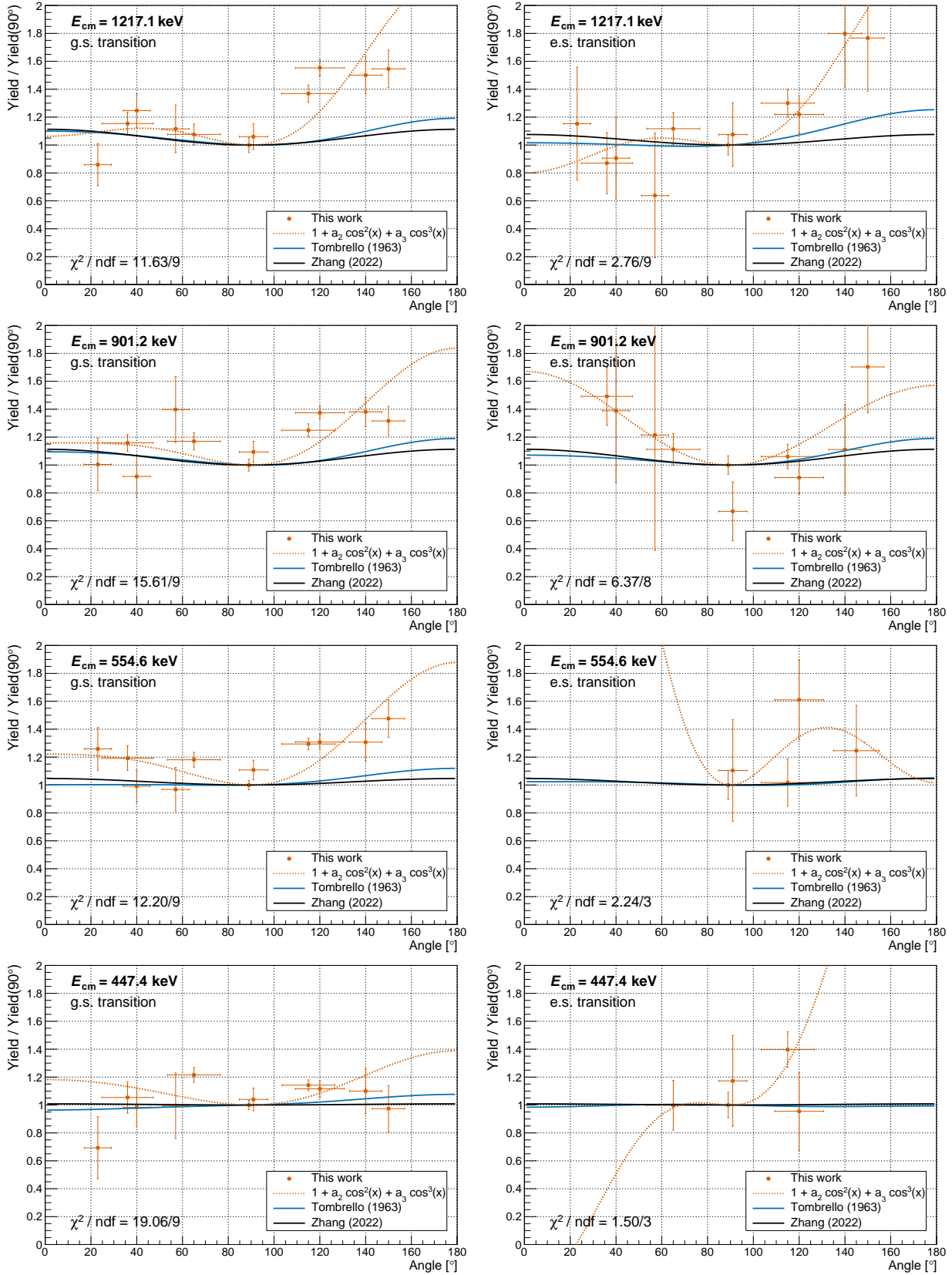


Figure 6.19: Resulting γ -ray angular distributions for all irradiations during the FK-V campaign. The corresponding fit function uses only the second and third Legendre polynomial, respectively. For different approaches, see appendix D.8. From top to bottom: Results for ST9, ST10, ST11+ST9B, and ST15 (cf. tables 3.3) with the result of the ground state transition (left) and the excited state transition (right). Regarding the fit function (orange), see chapter 6.3.6 for details.

6.3.5 Treatment of uncertainties

The following section will discuss the resulting uncertainties in figure 6.19. It is divided into two paragraphs elaborating separately the resulting uncertainty for the x-axis, which shows the angle, and the y-axis, which shows the yield (normalized to 90°), respectively.

Uncertainty on the angle

The uncertainty on the x-axis has to be interpreted as the effective interval of angles, in which the prompt γ -rays were emitted, which subsequently contributed to the net area in the ROI of the residuum for a certain detector. It should not be misinterpreted as an angle based on the geometric size of the crystal or end cap, respectively. This would be significantly larger and unnecessarily inflate this uncertainty.

As discussed in section 6.2.3, this value mainly depends on the distance and geometry of the respective crystal and only negligibly on the energy of the photons. Unfortunately, this extensive investigation on the effective angle for the prompt γ -rays was not done exclusively for the FK-V campaign, but only for FK-I and FK-II. However, the corresponding results were interpolated from the data of these earlier campaign by plotting the resulting uncertainty with respect to the distance of the crystal to the target, as shown in figure 6.20. The fit function used an $A \cdot \tan^{-1}(B/x)$ approach, as suggested by geometric considerations. This interpolation was separately done for single crystals and crystals, which were used in add-back mode.

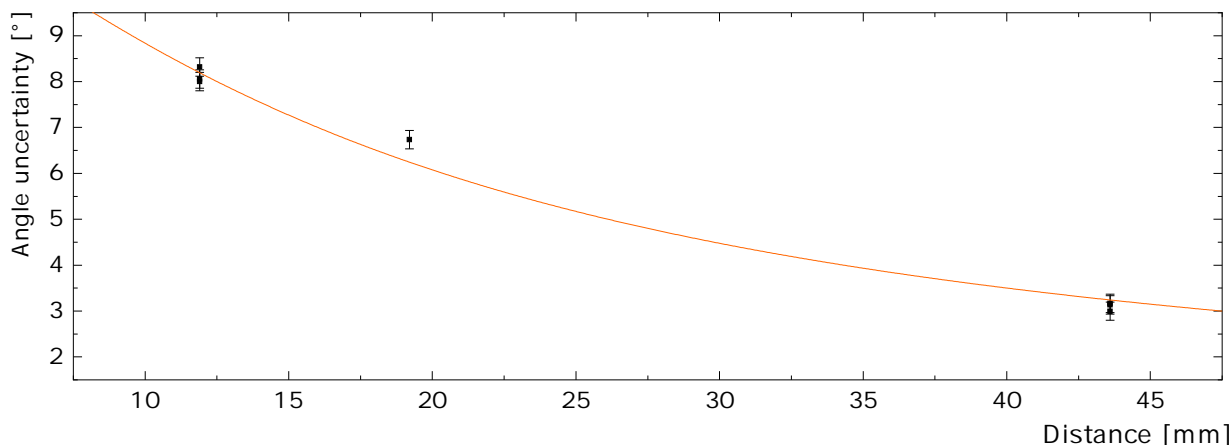


Figure 6.20: Interpolation of angular uncertainties for FK-V with respect to the distance between target and the end cap of the detector. The fit function used an $A \cdot \tan^{-1}(B/x)$ approach, as suggested by geometric considerations. The plotted data stems from the simulations with single crystals based on earlier simulations from FK-I and FK-II.

Uncertainty on the yield

The yield in each detector is determined based on the net counts in the respective ROI and the full-energy peak efficiency of the detector. The statistical uncertainty on the net count

is properly propagated based on the utilized ST, Ta, and BG runs, respectively. The error propagation of single histograms is not done by simply adding or subtracting the entries in the channels, but by using the ROOT functions `Sumw2()`, `Add()`, and `IntegralAndError()`. Hence, regions where e.g. two peaks were subtracted from each other, suffer from a larger uncertainty in the residuum, as e.g. neighboring flat regions, which were subtracted from each other. This inevitable, and necessary treatment of error propagation can e.g. nicely be seen in the EB17 spectra of figure D.14, where the region around the ${}^{208}\text{Tl}$ peak at 2614 keV is also shown within the figure.

The systematic uncertainty on the net counts solely depends on the contribution stemming from the determination of the dead time, which is conservatively set to 1%. A typical systematic contribution stemming from the charge integration is not needed for the γ -ray angular distribution, since the accumulated charge is not needed in the respective formula and is always exactly identical for all detectors.

The statistical uncertainty on the absolute full-energy peak efficiency ε is determined based on the approach elaborated in chapter 2.4.2. It is worthwhile mentioning, that in addition to the Q -value, and the irradiation energy, also the Doppler shift was taken into account for each detector, when determining ε and $\Delta\varepsilon$. This is crucial in order to prevent systematic underestimations of the yield at low detection angles and overestimations at large angles. It is determined via the fit in figure 6.18, which only shows the statistical uncertainties on the determination of net areas. Due to the fact, that only calibration sources between 478 keV and 1836 keV are used, this uncertainty is the largest for the ground state transition at the highest irradiation energy ($E_{\text{cm}} = 1217.1$ keV resulting in a ROI around $E_{\gamma} \sim 2800$ keV). In summary, high irradiation energies suffer from large statistical uncertainties due to the extrapolation of ε , while low irradiation energies are suffering from large statistical uncertainties due to low cross sections.

A proper error propagation on the systematic uncertainty on ε is non-trivial. In principle it consists of two contributions, namely the uncertainty on the activity of the calibration nuclides and the uncertainty stemming from the correction of the true coincidence summing (which only affects ${}^{22}\text{Na}$, ${}^{60}\text{Co}$, and ${}^{88}\text{Y}$). Regarding the activity, usually a conservative approach can be used (when affordable for the resulting error budget) by propagating the systematic uncertainty of the radio nuclide with the largest relative uncertainty regarding its activity. However, the relative uncertainties of the utilized calibration sources are not similar, but there is one source (${}^7\text{Be}$) which has by far the largest relative uncertainty. Solely propagating this uncertainty would significantly undermine the precision of the other sources and artificially inflate the uncertainty to an unacceptable degree. Hence, both contributions were quadratically summed up and an approach based on chapter 2.4.2 was used in order to propagate the systematic uncertainty. It is worthwhile mentioning, that no relative systematic uncertainty is smaller than the largest relative uncertainties on the activities of the calibration nuclides (except from ${}^7\text{Be}$, as intended).

All systematic and statistical uncertainties are separately propagated into a total systematic and statistical uncertainty of the yield ($Y \pm \Delta Y_{\text{sys}} \pm \Delta Y_{\text{stat}}$). However, for the subsequent fit of the Legendre polynomials (as shown in figure 6.23), the combination of systematic and statistical uncertainties by taking their quadratic sum is inevitable for a simultaneous consideration of both contributions.

Comparison of systematic and statistical uncertainties

A comparison of systematic and statistical uncertainties is shown in figure 6.21 with filled markers for the statistical uncertainties and unfilled markers for the systematic uncertainties. Comparing both, it becomes obvious that in most cases, the statistical uncertainty limits the overall uncertainty.

Regarding the systematic uncertainties, there is also a clear trend, which is supported by the arguments of the last section: The detectors in close geometry (EB18BGE, EB18AF, EB18CD) are suffering from comparatively larger systematic uncertainties due to the correction of true coincidence summing. In case if EB18BGE and EB18CD, the benefit of low statistical uncertainties due to the proximity to the target is even undermined by the comparatively larger systematic uncertainties.

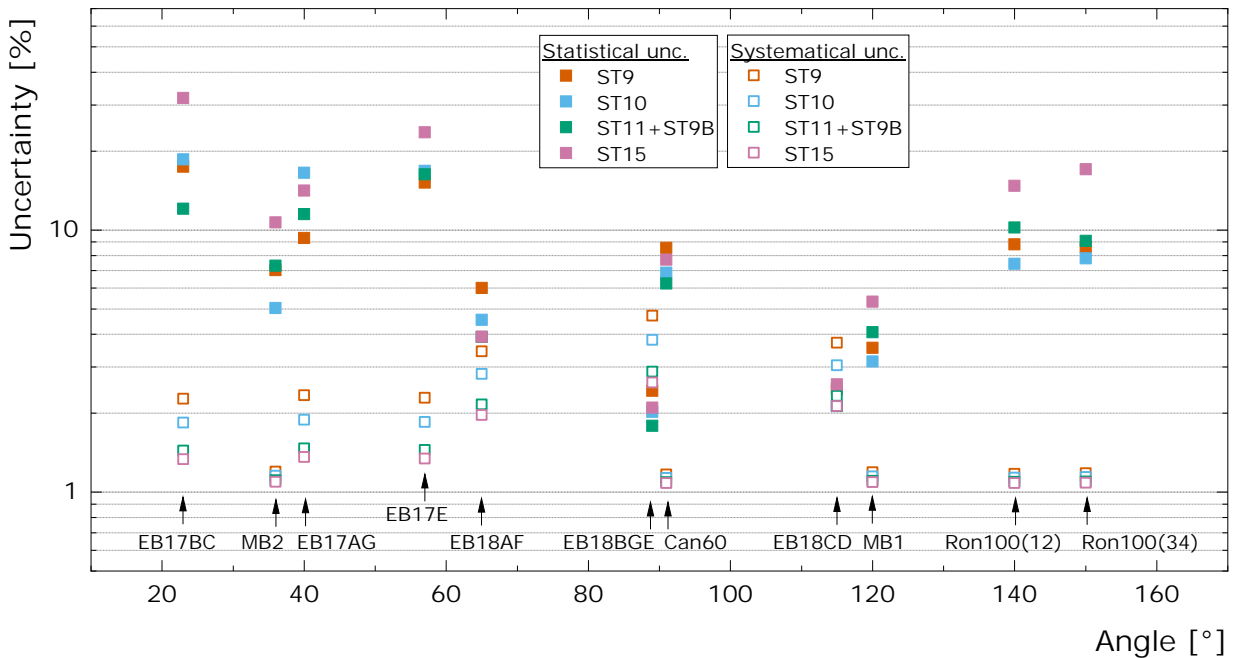


Figure 6.21: Systematic and statistical uncertainties for the yield in all detectors during FK-V. The statistical uncertainties are plotted using filled markers, and the systematic uncertainties are shown using unfilled markers.

In case of statistical uncertainties the overall goal was to achieve a similar accuracy for different irradiation energies. This goal is certainly fulfilled with the slight exception of ST15. But also for this lowest energy data point, the resulting statistical uncertainty is only worst in $\sim 50\%$ of the detectors. It is also apparent (with the exception of detectors in very close geometry), that the statistical uncertainty seems to be in a direct relationship to the distance of the detector to the target (and hence in a direct relationship to the efficiency).

6.3.6 Deduction of Legendre polynomials

The experimental result of the γ -ray angular distributions for both the ground state transition and the first excited state transition is shown in figure 6.19 for the four different irradiation energies of the FK-V campaign³⁶. However, due to the lack of knowledge about the γ -ray angular distribution of this reaction, it is not straightforward how to fit the corresponding data sets. A scientifically motivated approach is based on the use of multiple terms of Legendre polynomials, i.e. $P_0(x) = 1$, $P_1(x) = x$, $P_2(x) = 0.5 \cdot (3x^2 - 1)$ etc. (cf. section 1.4.2).

However, as elaborated in chapter 1.4.2, the theoretical predictions by Tombrello et al. and Zhang et al. are not stated in terms of actual Legendre polynomials, but given as a sum of ‘ $\cos^i(\vartheta)$ ’ terms with increasing integers of i (starting with $i=0$). Therefore, the notation by Tombrello and Zhang is also used throughout this thesis [60, 61]. It is worthwhile mentioning, that the terms $a_i \cdot \cos^i(\vartheta)$ are further also called ‘Legendre polynomials’ (despite not being entirely correct).

$$Y(\vartheta) \propto 1 + a_1 \cos(\vartheta) + a_2 \cos^2(\vartheta) + a_3 \cos^3(\vartheta) + a_4 \cos^4(\vartheta) \quad (59)$$

An intuitive way of further proceeding would be a fit for figure 6.19, which is based on equation 59 and would follow the results from Tombrello [60]. However, the available statistics from the analysis does not enable such a complex fit function. Combining the theoretically predicted significance of the single factors a_1 , a_2 , a_3 and a_4 and the limitations stemming from the statistics of the experimental data set, there are three different reasonable approaches for implementing a fit:

- **Approach 1:** $Y(\vartheta) \propto 1 + a_2 \cos^2(\vartheta) + a_3 \cos^3(\vartheta)$

From a theoretical perspective and according to Tombrello, this approach seems to be the most reasonable one [60]. Independent of the investigated irradiation energy ($E_{\text{cm, min}} = 447.4 \text{ keV}$, $E_{\text{cm, max}} = 1217.1 \text{ keV}$), the values for a_2 and a_3 are expected to be more significant, than a_1 and a_4 (cf. figure 1.7).

³⁶It is crucial to emphasize, that the plotted yield for all detectors is normalized to the yield of EB18BGE at 90° . However, the uncertainty of the yield from EB18BGE is **not** taken into account during the error propagation of the other yields. The normalized yield at all angles is therefore to be understood as their original yield normalized by a certain ‘constant factor’ in order to scale them down to the order of one.

- **Approach 2:** $Y(\vartheta) \propto 1 + \mathbf{a}_2 \cos^2(\vartheta)$

Due to this experimentally challenging reaction, the resulting overall statistics of this experimental campaign is limited. A reduction of parameters can therefore be appropriate, especially due to the fact, that e.g. Zhang are also only considering the a_2 component [61]. However, it is worthwhile mentioning, that especially the results from the highest irradiation energy are strongly in favor of a non-symmetrical component.

- **Approach 3:** $Y(\vartheta) \propto 1 + \mathbf{a}_1 \cos(\vartheta) + \mathbf{a}_2 \cos^2(\vartheta)$

From a theoretical point of view, this approach is disfavored by theory with respect to the first approach. However, during a corresponding master thesis, this approach was chosen [158]. So for the sake of comparability, it is also used here.

In summary, approach 1 seems to be the most reasonable one when accounting for theoretical predictions, as well as the experimentally indicated anisotropy with respect to 90° . Its implementation is therefore shown in figure 6.22 for the ground state transition and figure 6.23 for the first excited state transition, while the other two approaches can be found in the appendix D.8.

Ground state transition

The graphical implementation of approach 1 regarding the ground state transition is shown in figure 6.22, and the resulting Legendre polynomials for all approaches are listed in table 6.2. Comparing the results with the theoretical predictions in table 6.1, it is apparent, that the experiment leads to significantly larger anisotropies, than predicted by theory. It is also worthwhile mentioning, that the resulting a_2 component (which is present in all three approaches) seems to be in agreement within their statistical uncertainties along all irradiation energies. So independent of the approach, a_2 results in an inherently similar value, which results in a comparatively robust discrepancy between experiment and theory.

Table 6.1: Theoretical predictions for the Legendre polynomials of γ -ray angular distribution for the ground state transition of the ${}^3\text{He}(\alpha, \gamma){}^7\text{Be}$ reaction [60, 61]. Three significant digits are shown in all cases. See also figure 1.7 and figure 1.9.

Ground state - Theoretical predictions							
	Tombrello et al.				Zhang et al.		
E_{cm} [keV]	a_1	a_2	a_3	a_4	a_2	$a_{2,\text{min}}$	$a_{2,\text{max}}$
447.4	-0.0252	0.00647	-0.0300	0.00205	0.00824	0.00554	0.0112
554.6	-0.0197	0.0499	-0.0403	0.00317	0.0467	0.0447	0.0492
901.2	0.0205	0.133	-0.0716	0.00700	0.117	0.109	0.125
1217.1	0.0174	0.136	-0.0680	0.0118	0.113	0.0974	0.131

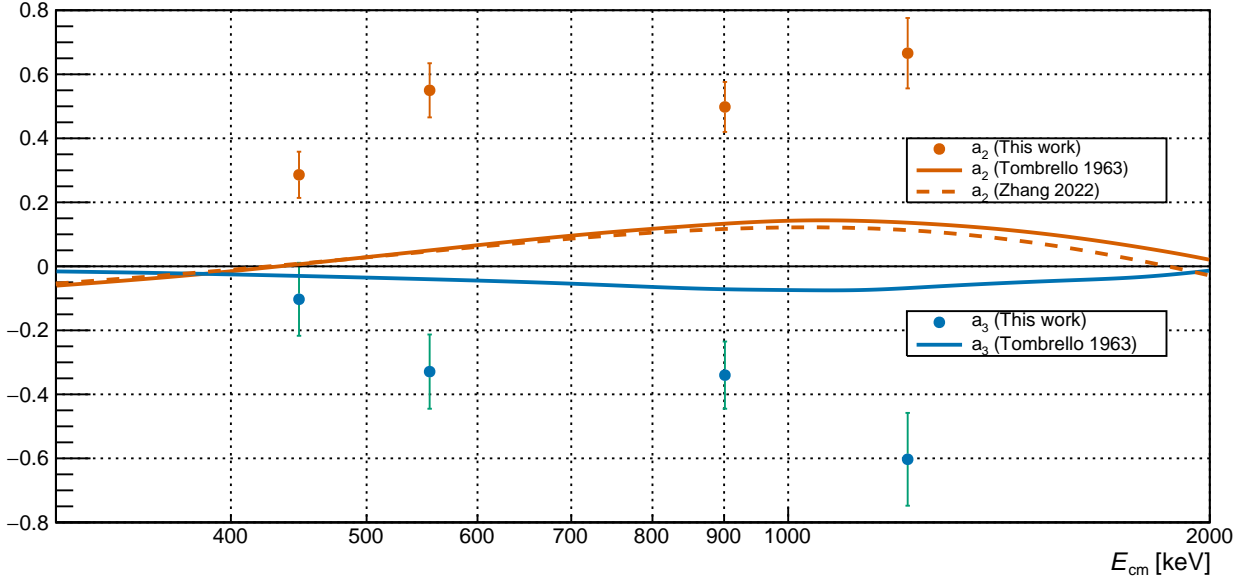


Figure 6.22: Energy dependent Legendre polynomials for the ground state transition during FK-V using approach 1, which takes into account the a_2 component (orange) and the a_3 component (blue). The corresponding experimental results are compared to the theoretical expectation by Tombrello et al. and Zhang et al. For different approaches, see appendix D.8.

Table 6.2: Experimental results for the Legendre polynomials of the γ -ray angular distribution for the ground state transition of the ${}^3\text{He}(\alpha, \gamma){}^7\text{Be}$ reaction.

Ground state - Experimental results					
E_{cm} [keV]	Approach 1		Approach 2	Approach 3	
	a_2	a_3	a_2	a_1	a_2
447.4	0.29(7)	-0.10(11)	0.28(7)	-0.02(4)	0.28(7)
554.6	0.55(8)	-0.33(12)	0.55(7)	-0.16(6)	0.54(8)
901.2	0.50(8)	-0.34(11)	0.54(7)	-0.16(5)	0.47(7)
1217.1	0.67(11)	-0.60(15)	0.67(8)	-0.30(6)	0.58(8)

First excited state transition

The graphical implementation of approach 1 regarding the first excited state transition is shown in figure 6.23, and the resulting Legendre polynomials for all approaches are listed in table 6.4. Comparing the results with the theoretical predictions in table 6.3, it is apparent again, that the experiment also in case of the first excited state leads to larger anisotropies, than predicted by theory. However, especially the two lower irradiation energies are facing major uncertainties. This is due to the fact, that only a few detectors at comparatively central angles (around 90°) showed sufficient statistics. Hence, the extreme angles are missing in the determination of the γ -ray angular distribution.

This fact could also have been anticipated during the determination of suitable irradiation energies (cf. figure 6.7). While irradiation energies are chosen in way, that most of the resulting ROIs are in a comparatively flat region of the histograms, the ROIs for the first excited states of the lowest two irradiation energies (green and orange hatched in figure

6.7) are within an inevitable region of background γ -ray lines. However, also comparatively lower or higher energies would have resulted in this fact, and furthermore the ROIs for the respective ground state transitions would not have been located in empty regions anymore, respectively.

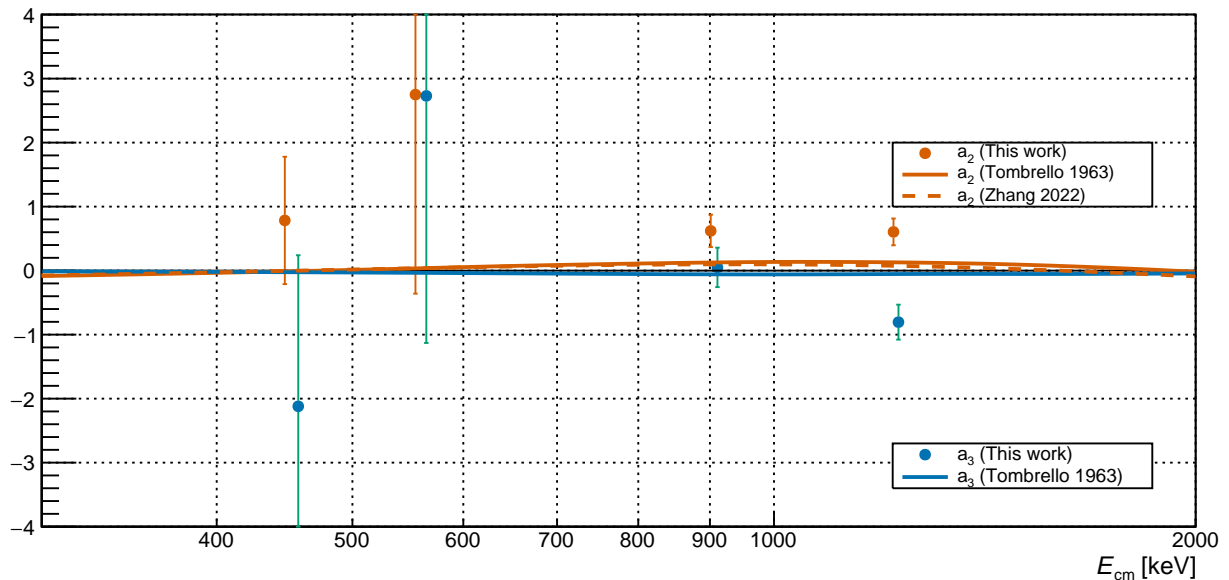


Figure 6.23: Energy dependent Legendre polynomials for the excited state transition during FK-V using approach 1, which takes into account the a_2 component (orange) and the a_3 component (blue). The corresponding experimental results are compared to the theoretical expectation by Tombrello et al. and Zhang et al. For different approaches, see appendix D.8.

Table 6.3: Theoretical predictions for the Legendre polynomials of γ -ray angular distribution for the first excited state transition of the ${}^3\text{He}(\alpha, \gamma){}^7\text{Be}$ reaction [60, 61]. Three significant digits are shown in all cases. See also figure 1.7 and figure 1.9.

First excited state - Theoretical predictions							
E_{cm} [keV]	Tombrello et al.				Zhang et al.		
	a_1	a_2	a_3	a_4	a_2	$a_{2,\text{min}}$	$a_{2,\text{max}}$
447.4	0.0200	-0.0123	-0.0244	0.00122	-0.00460	-0.0111	0.00250
554.6	0.0211	0.0350	-0.0345	0.00205	0.0368	0.0294	0.0436
901.2	-0.00229	0.127	-0.0576	0.00401	0.0982	0.0802	0.114
1217.1	-0.0652	0.130	-0.0534	0.00527	0.0756	0.0423	0.107

6.4 In-beam analysis of IBC-II

The general properties of the utilized targets, as well as an overview of the setup, and the list of irradiation energies for the IBC-II campaign was already introduced within chapter 3.1. The following section is dedicated to the analysis of the obtained in-beam data, and is divided into four topics: The characterization of the target areal densities using a ${}^2\text{H}$ beam (cf. section 6.4.1), the evaluation of the in-beam γ -ray spectra during ${}^4\text{He}$ irradiation (cf. section 6.4.2), the HPGe efficiency calibrations (cf. section 6.4.3), and the analysis of the

Table 6.4: Experimental results for the Legendre polynomials of the γ -ray angular distribution for the first excited state transition of the ${}^3\text{He}(\alpha, \gamma){}^7\text{Be}$ reaction.

First excited state - Experimental results					
	Approach 1		Approach 2	Approach 3	
E_{cm} [keV]	a_2	a_3	a_2	a_1	a_2
447.4	0.8(10)	-2.1(24)	1.4(9)	-0.31(30)	0.8(7)
554.6	2.8(31)	2.7(39)	0.7(5)	-0.3(10)	0.3(16)
901.2	0.62(25)	0.05(31)	0.63(24)	0.14(15)	0.61(24)
1217.1	0.61(21)	-0.81(27)	0.54(18)	-0.36(14)	0.54(22)

resulting γ -ray angular distribution (cf. section 6.4.4). The comparison of areal density (based on the NRA) and the resulting activity (based on an activation analysis) in order to make a statement on the reaction cross section will be provided in section 6.5.

6.4.1 Nuclear reaction analysis - NRA

The technique of using well known nuclear reactions in order to calibrate the target areal density during in-beam measurements was introduced in section 2.7.1 and already thoroughly elaborated based on the data from the IBC-I campaign in section 5.4.1.

The underlying analysis within this section is highly similar to the intensively discussed NRA in case of the analysis for the ${}^2\text{H}(p, \gamma){}^3\text{He}$ reaction. Both NRAs are based on the use of the ${}^3\text{He}(d, p){}^4\text{He}$ reaction [153]. However, there is one main difference between both campaigns: While section 5.4.1 used this reaction in inverse kinematics (irradiation of a deuterated target with a ${}^3\text{He}$ beam), the following section will discuss the NRA based on normal kinematics (irradiation of ${}^3\text{He}$ -implanted target with a deuteron beam).

However, the study by Wielunska also investigated the reaction in inverse kinematics [153]. In order to use the same center-of-mass energies for both investigations, the laboratory energy E_{lab} of the further utilized ${}^2\text{H}$ projectiles needs to be converted accordingly, as shown in equation 60.

$$\begin{aligned}
 E_{\text{lab}, {}^2\text{H}} &= \frac{m_{{}^3\text{He}} + m_{{}^2\text{H}}}{m_{{}^3\text{He}}} \cdot E_{\text{cm}} = \frac{m_{{}^3\text{He}} + m_{{}^2\text{H}}}{m_{{}^3\text{He}}} \cdot \frac{m_{{}^2\text{H}}}{m_{{}^3\text{He}} + m_{{}^2\text{H}}} \cdot E_{\text{lab}, {}^3\text{He}} \\
 &= \frac{m_{{}^2\text{H}}}{m_{{}^3\text{He}}} \cdot E_{\text{lab}, {}^3\text{He}}
 \end{aligned} \tag{60}$$

In case of one of the two previously investigated energies of $E_{\text{lab}, {}^3\text{He}} = 1987.4$ keV, the same corresponding center-of-mass energy of $E_{\text{cm}} = 795.8$ keV can therefore be achieved by irradiating the target with a deuteron beam of $E_{\text{lab}, {}^2\text{H}} = 1327.1$ keV.

It is worthwhile mentioning, that this procedure/argument was used prior to the NRA for the IBC-II campaign in order to calculate an appropriate irradiation energy. However, this calculation in fact only results in similar E_{cm} , and subsequently only similar cross sections.

This is due the fact, that the energy loss within the target needs to be accounted for as well, which results in different effective energies E_{eff} (cf. section 2.6.3). This was taken into account during the offline analysis, and results in slightly different cross sections for both campaigns. However, this has no impact for the subsequent analysis.

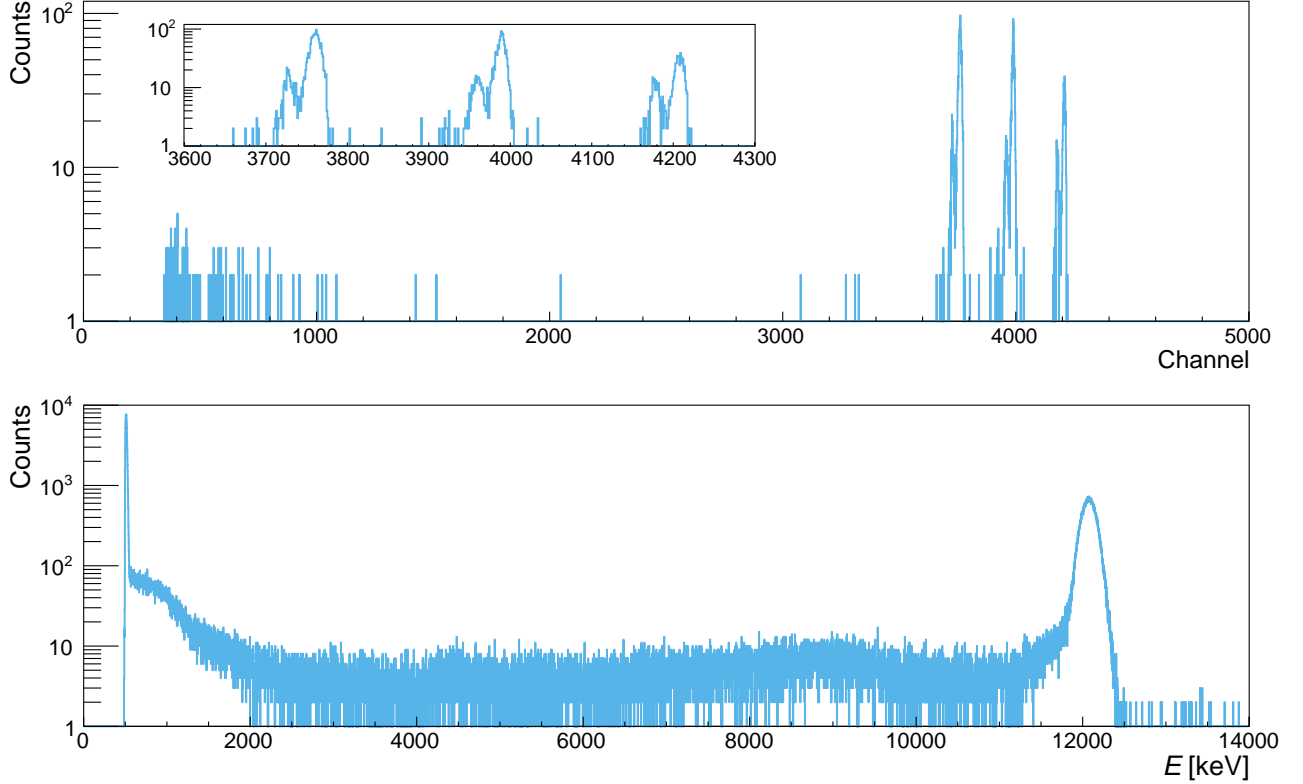


Figure 6.24: Pulse height spectra from the Si detector during IBC-II campaign. Top: Pulse height spectrum of the silicon detector during the energy calibration with the triple alpha source EC221 (cf. table 3.4). Bottom: Resulting pulse height spectrum of the NRA measurement for target Ta502 based on the emitted protons stemming from the ${}^3\text{He}(\text{d},\text{p}){}^4\text{He}$ reaction.

Two exemplary resulting pulse height spectra for the NRA in case of target Ta502 (cf. table 3.3) are shown in figure 6.24. The upper figure shows the resulting spectrum of the triple alpha source EC221 (cf. table 3.4), which is the analogue to figure 5.5 in case of the IBC-I campaign. The resulting energy calibration was subsequently used to calibrate the particle spectrum during the deuteron irradiation, which is shown in the lower panel of figure 6.24. The expected energy deposition of the emitted protons is again ~ 12 MeV (cf. figure 5.7). The shift of the ROI between both campaigns is mainly due to a missing $50\ \mu\text{m}$ nickle foil in front of the Si detector for the corresponding run of the IBC-II campaign (12 MeV protons lose approximately 1 MeV in $50\ \mu\text{m}$ of nickle) and only barely due to the effectively not identical E_{cm} .

The resulting areal densities for all four irradiated targets (cf. table 3.3) are shown in table 6.5. It is worthwhile mentioning, that the table indicates a worse suitability for gold evaporated targets with respect to pure tantalum targets, as expressed by the lower ratio

between implanted and measured areal density. This general trend is also strongly supported by the (non-)analyzeability of the corresponding in-beam spectra. However, the result has to be treated carefully due to the fact, that both NRAs with the gold targets were performed after irradiation, while both NRAs on the tantalum targets were performed prior to their actual irradiation. However, the analyzed yield in the ROI over time suggests only very minor outgassing during irradiation, which is most likely due to the low target current and the low amount of totally accumulated charge. Nevertheless, as shown in section 6.3.1, there are cases with subsequently higher beam currents, where the loss of areal density during irradiation is proven experimentally.

Table 6.5: Areal densities ρ_{He} from the NRA during the IBC-II campaign (cf. table 3.3) along with their uncertainties and their comparison to the initially implanted areal density ρ_{impl} . The fact, that most of the relative statistical uncertainties are similar is due to the fact, that they stem from the dominating statistical uncertainty from the underlying efficiency calibration.

Name	ρ_{He} [at/cm ²]	$\Delta\rho_{\text{He,sys}}$ [at/cm ²]	$\Delta\rho/\rho _{\text{sys}}$ [%]	$\Delta\rho_{\text{He,stat}}$ [at/cm ²]	$\Delta\rho/\rho _{\text{stat}}$ [%]	ρ_{impl} [at/cm ²]	$\rho_{\text{impl}}/\rho_{\text{meas}}$
Au50	1.77 E17	0.08 E17	4.3	0.08 E17	4.3	5 E17	35%
Au100	2.24 E17	0.10 E17	2.5	0.06 E17	4.3	10 E17	22%
Ta100	6.38 E17	0.27 E17	2.5	0.16 E17	4.3	10 E17	64%
Ta502	4.65 E17	0.20 E17	2.5	0.12 E17	4.3	5 E17	93%

This areal density could subsequently be used in order to make a careful statement on the reactions cross section after also performing an activation analysis. This will however be elaborated later in section 6.5.

6.4.2 Prompt γ -ray analysis

Regarding the four utilized targets during the IBC-II campaign, only the two tantalum targets (Ta100 and Ta502) revealed sufficient statistics for a proper in-beam analysis of the ground state transition. Both the low areal density of the gold evaporated targets (cf. table 6.5), as well as the low amount of applied charge (cf. table 3.3) resulted in less than 100 net counts for $E_{\text{lab}} = 2880$ keV, even in the detector with the highest efficiency.

Unfortunately, even regarding the Ta100 target and the Ta502 target, the subsequent in-beam analysis is not as straight forward, as discussed for the analysis of the FK-V campaign (cf. section 6.3.2). This is due to the fact, that no adequate long-term irradiations of pure tantalum disks were performed, which significantly limits the resulting statistics.

The sum of all in-beam runs with target Ta100 is shown in figure 6.25. As mentioned earlier, four detectors were used in order to investigate the γ -ray angular distribution, namely Ron100 (orange), Can60 (green), MB1 (blue) and Ortec90 (red). In addition, the figure also shows the rescaled background spectrum in case of the Can60 detector as a black line. Due to the missing in-beam irradiation of a tantalum blank, the analysis elaborated in section

6.3.2 had to be adjusted accordingly. Instead of applying the procedure of equation 58, the in-beam runs could solely be adjusted by the natural background component.

As shown in figure 6.25, there are two prominent γ -ray lines emerging from the natural background of ^{214}Bi , namely the γ -ray line at $E = 2694.66(13)$ keV with an emission probability of $\eta = 0.0300(14)\%$ and the γ -ray line at $E = 2769.92(15)$ keV with an emission probability of $\eta = 0.0245(14)\%$. The first one is clearly visible in case of Ron100, Can60 and MB1, and the right one is covered directly in the ROI in most cases. The proper treatment of these two lines is inevitable in order to obtain a trustworthy residuum. However, the lack of information on additional peak structures within the ROI stemming from other in-beam reactions significantly diminishes the validity of the further analysis. In addition, the in-beam background is responsible for approximately 2/3 of the entire background contribution in the ROI (cf. green and black spectra in figure 6.25), which further underlines the significance of the in-beam background. This fact is also emphasized on all relevant upcoming captions within this section in order to highlight its importance.

The resulting residua after applying the corresponding procedure regarding the compensation for the natural background (cf. section 6.3.2) are shown in figure 6.26. Both of them show the result of the 60Can detector with the left one showing the result of target Ta100 and the right one showing the result of target Ta502.

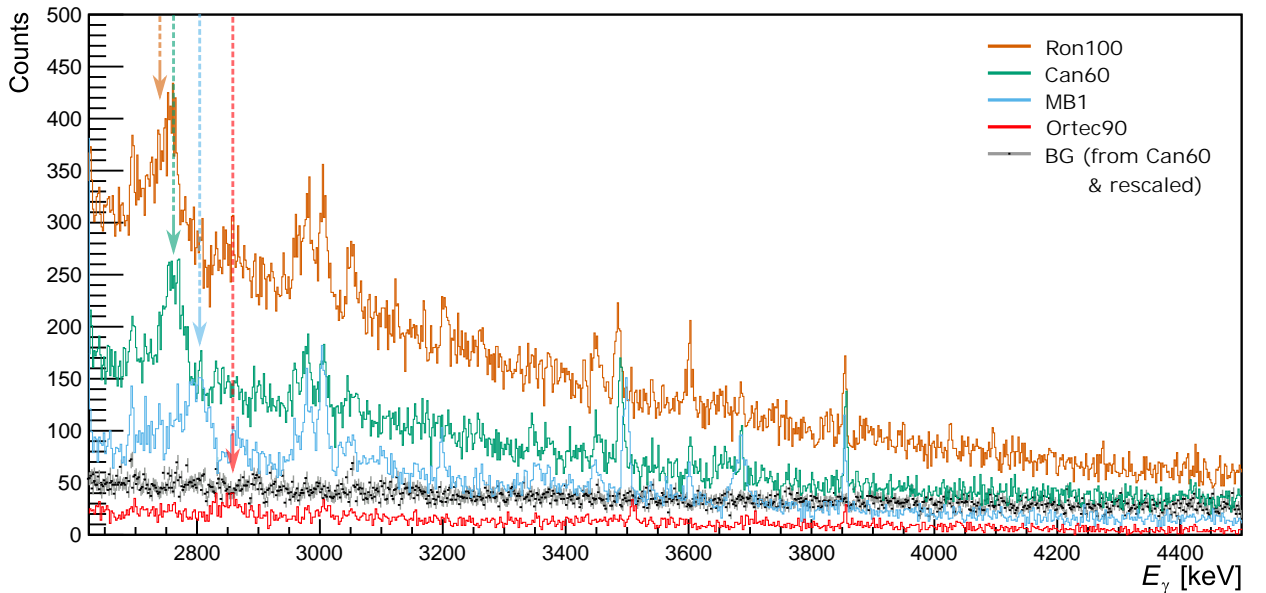


Figure 6.25: Pulse height spectra from the irradiation of Ta100 during the IBC-II campaign. The spectra of Ron100, Can60, MB1 and Ortec90 are shown in orange, green, blue and red, respectively. In addition, the rescaled background spectrum from Can60 is also shown (black). The respective ROI for different detectors is indicated by vertical color-matching arrows around $E = 2800$ keV.

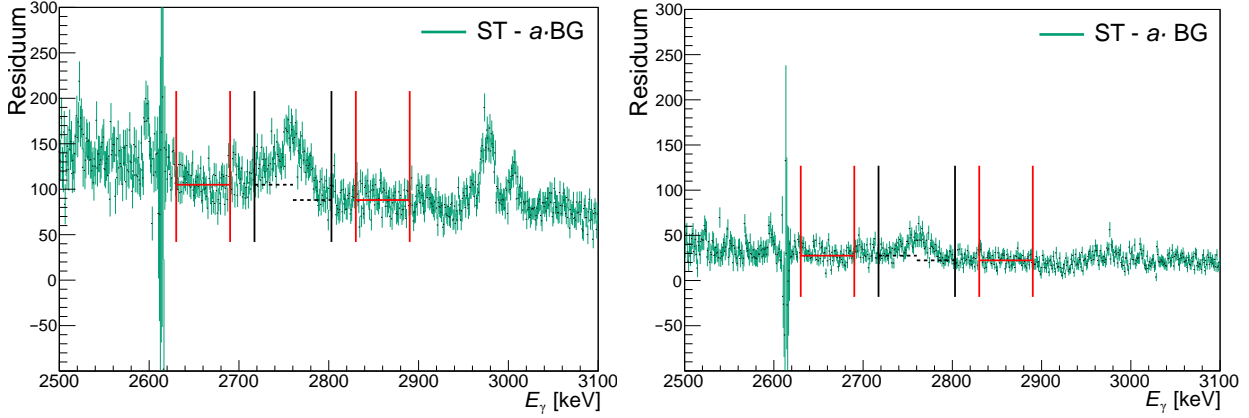


Figure 6.26: Residua of the Can60 detector during the irradiation of Ta100 (left) and Ta502 (right). According to equation 57, the residuum is only based on a correction for the natural background (ST- $a \cdot \text{BG}$). Hence, additional structures stemming from other in-beam reactions can not be excluded. The scalings of the left and right figure are identical. The resulting discrepancy in statistics is due to the difference in applied charge.

6.4.3 Absolute full-energy peak efficiency

The absolute full-energy peak efficiency during the IBC-II campaign was obtained using calibration nuclides ${}^{137}\text{Cs}$ (ID: 4199), ${}^{60}\text{Co}$ (ID: 3393) and ${}^{88}\text{Y}$ (ID: 4433), as well as the ${}^{27}\text{Al}(p, \gamma){}^{28}\text{Si}$ reaction (cf. table 3.4, and section 5.1.2, respectively). The resulting efficiency, along with its statistical uncertainties is shown in figure 6.27.

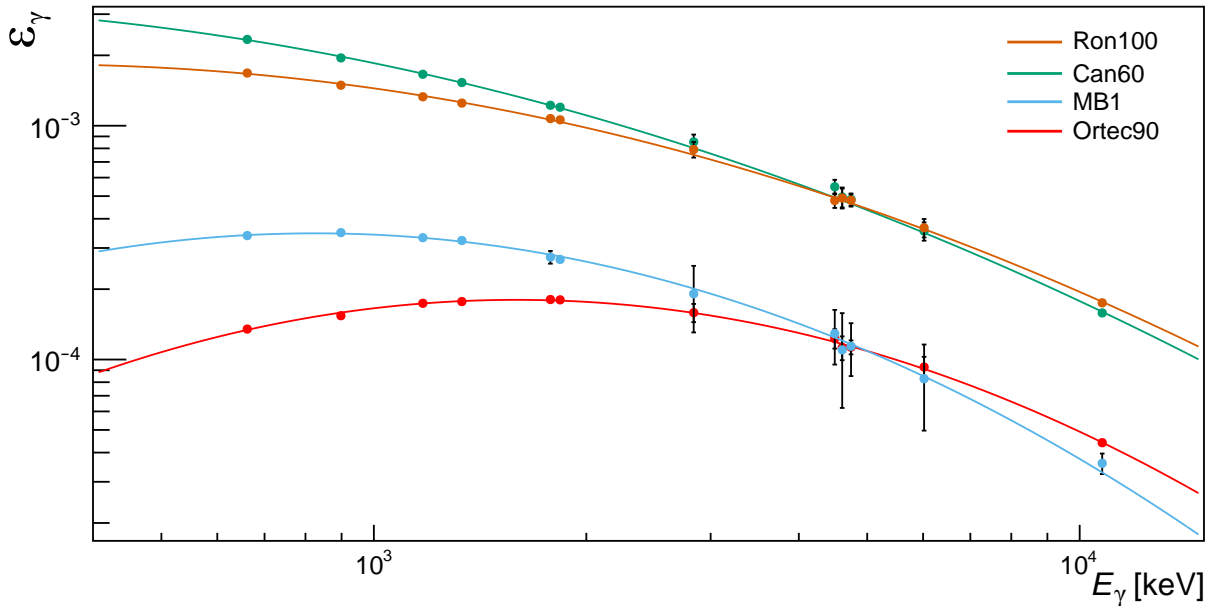


Figure 6.27: Absolute full-energy peak efficiency for the utilized HPGe detectors during the IBC-II campaign. Standard calibration sources were used, as well as the ${}^{27}\text{Al}(p, \gamma){}^{28}\text{Si}$ reaction (see text for details). The data points only include their respective statistical uncertainty (cf. section 6.3.5).

Otherwise, the general procedure is identical to the approach elaborated earlier in section 6.3. The subsequent full-energy peak efficiencies are listed in table 6.6 along with the systematical and statistical uncertainties.

Table 6.6: Absolute full-energy peak efficiencies during the IBC-II campaign. The efficiencies are given in terms of the respective ROIs of the ground state transition of the ${}^3\text{He}(\alpha,\gamma){}^7\text{Be}$ reaction. All values are stated with three digits according to the lowest uncertainty in the table.

Name	Angle [$^\circ$]	ε_{abs} [10^{-4}]	$\Delta\varepsilon_{\text{abs,sys}}$ [10^{-4}]	$\Delta\varepsilon_{\text{abs,stat}}$ [10^{-4}]
Can60	135	8.258	0.099	0.056
Ortec90	45	1.581	0.019	0.018
MB1	90	7.200	0.087	0.059
Ron100	153	7.725	0.093	0.054

Treatment of uncertainties

The resulting fit uncertainty of the data points is propagated into a total statistical uncertainty according to the procedure elaborated in chapter 2.4.2. The systematic uncertainty is propagated separately based on the uncertainty of the emission probability, the half-life, and the activity of the calibration sources, as well as the uncertainty on the dead time. In addition, it also includes the uncertainty stemming from the normalization peak at $E = 1778.9$ keV, which is used to align both the data from calibration sources and the data from the ${}^{27}\text{Al}(\text{p},\gamma){}^{28}\text{Si}$ reaction. Regarding the systematic uncertainty on the activity, the largest relative systematic uncertainty resulting from any calibration source is propagated as total systematic uncertainty on the activity.

6.4.4 Resulting γ -ray angular distribution

In accordance to the procedure elaborated in section 6.3.4, the net counts for the prompt γ -rays and the absolute full-energy peak efficiency at the energy of interest can be used to determine the yield at different angles, as shown in figure 6.28.

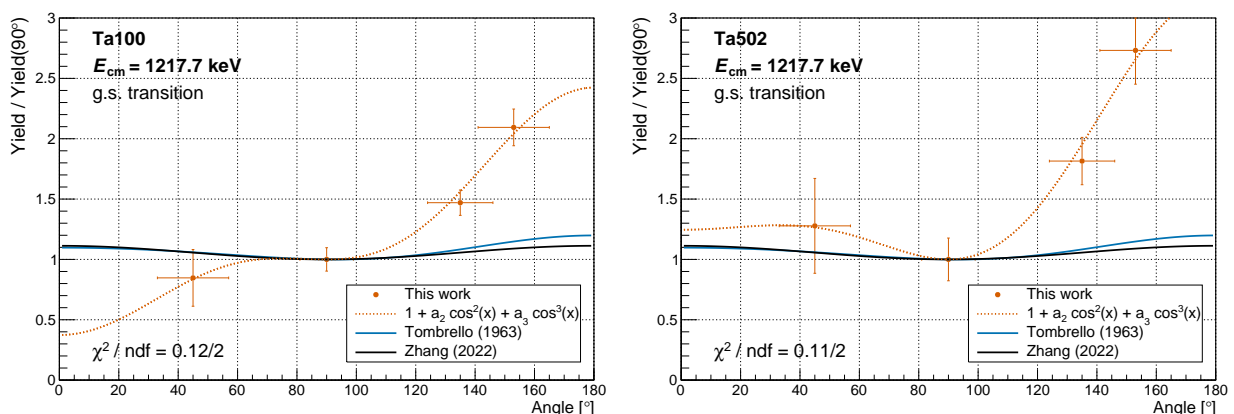


Figure 6.28: Resulting γ -ray angular distributions from the ground state transitions for both irradiations during the IBC-II campaign with the results from target Ta100 and target Ta502 in the left and right panel, respectively. The corresponding fit function uses only the second and third Legendre polynomial, respectively (cf. section 6.3.6). Regarding the fit function (orange), see chapter 6.3.6 for details. These results have to be treated with utmost caution, see text for details.

The two figures show the resulting γ -ray angular distribution for the ground state transition of the ${}^3\text{He}(\alpha, \gamma){}^7\text{Be}$ reaction as a result of the irradiation on target Ta100 (left) and target Ta502 (right), respectively.

As emphasized earlier, these distributions stemming from the IBC-II campaign have to be treated with utmost caution due to the lack of knowledge regarding other possible structures in the ROI stemming from contaminant in-beam reactions. However, these results can be interpreted as an independent and systematic trend towards the results from the FK-V campaign: The experimental results from the IBC-II campaign also seem to indicate a noticeable preference of γ -rays being emitted in backwards direction, which clearly deviates from theoretical expectations.

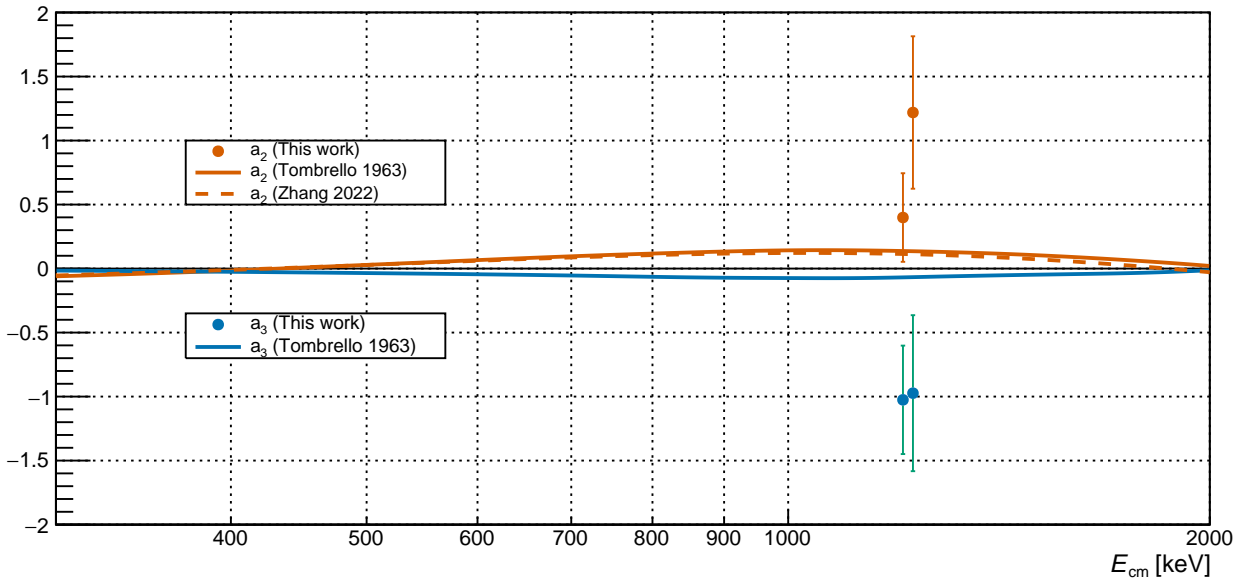


Figure 6.29: Energy dependent Legendre polynomials for the ground state transition during IBC-II using an a_2 component (orange) and an a_3 component (blue), cf. also section 6.3.6. Both targets were irradiated with identical energies, but for sake of clarity, the results of Ta100 are shifted 10 keV to the left and results from Ta502 are shifted 10 keV to the right. For the a_2 component both the prediction by Tombrello and Zhang are given as straight and dashed line, respectively (cf. section 1.4.2). Regarding the a_3 component, only a prediction by Tombrello is available (cf. section 1.4.2). These results have to be treated with utmost caution, see text for details.

During the analysis of the FK-V campaign, three different approaches were offered regarding the subsequent fit of Legendre polynomials (cf section 6.3.6). In addition to the (theory-preferred) analysis using the a_2 and a_3 component, also the result of two different approaches were given, namely the use of only the a_2 component, as well as the use of the a_1 and the a_2 component. However, in case of the IBC-II campaign, only the preferred analysis using the a_2 and a_3 component was conducted in order to avoid an overemphasis on the meaningfulness of these results. In detail, these results are scientifically vulnerable and should also be treated as such. The resulting Legendre polynomials in case of the analysis using an a_2 and a_3

component are however given in figure 6.29 and table 6.7 in order to act as a supporting argument for the results from the FK-V campaign.

Table 6.7: Experimental results for the Legendre polynomials of the γ -ray angular distribution regarding the ground state transition of the ${}^3\text{He}(\alpha, \gamma){}^7\text{Be}$ reaction during the IBC-II campaign. These results have to be treated with caution, see text for details.

Ground state - Experimental results during IBC-II				
	Target Ta100		Target Ta502	
E_{cm} [keV]	a_2	a_3	a_2	a_3
1217.7	0.40(35)	-1.03(42)	1.22(60)	-0.97(61)

6.5 Activation analyses

Within the following section, the activation analyses of multiple samples, which were irradiated during the investigation of the ${}^3\text{He}(\alpha, \gamma){}^7\text{Be}$ reaction, will be discussed. As elaborated in section 1.4, this analysis provides an entirely independent approach to investigate the resulting activity of the accumulated ${}^7\text{Be}$ nuclei within the samples and subsequently enables statements on the cross section or on the areal density.

The general procedure will be introduced in section 6.5.1 with the resulting analyses for different campaigns thereafter. In general, an activation analysis will only be discussed in case of a sample being irradiated with a single energy. In case of multiple irradiation energies on one target (cf. ‘mult.’ in table 3.3), the resulting activity is a convolution of different cross sections at multiple energies and therefore not further considered within the scope of this thesis.

6.5.1 General procedure

During all subsequent activation analyses, the radio nuclide of interest will be ${}^7\text{Be}$, which decays via electron capture with a half-life of $T_{1/2} = 53.22(6)$ d (cf. figure 1.4). This half-life can not be assumed to be infinitely large with respect to the duration of the subsequent investigation of the sample, but it will decay during irradiation, as well as during dismantling, probable storage, and the subsequent measurement on an offline HPGe detector. The utilized procedure for analyzing the ${}^7\text{Be}$ activity at the end of the irradiation (‘eoi’) is shown in figure 6.30.

In this figure, the activity of a fictitious sample is shown as black curve with respect to the time. During the subsequent measurement time t_m of the sample (with t_0 being the start time and t_1 being the stop time), the activation analysis will reveal a mean activity \bar{A} . This procedure of activation analyses was introduced in section 2.4.2 and is expressed by equation 9. However, in order to extract the activity at the begin of the measurement A_0 ,

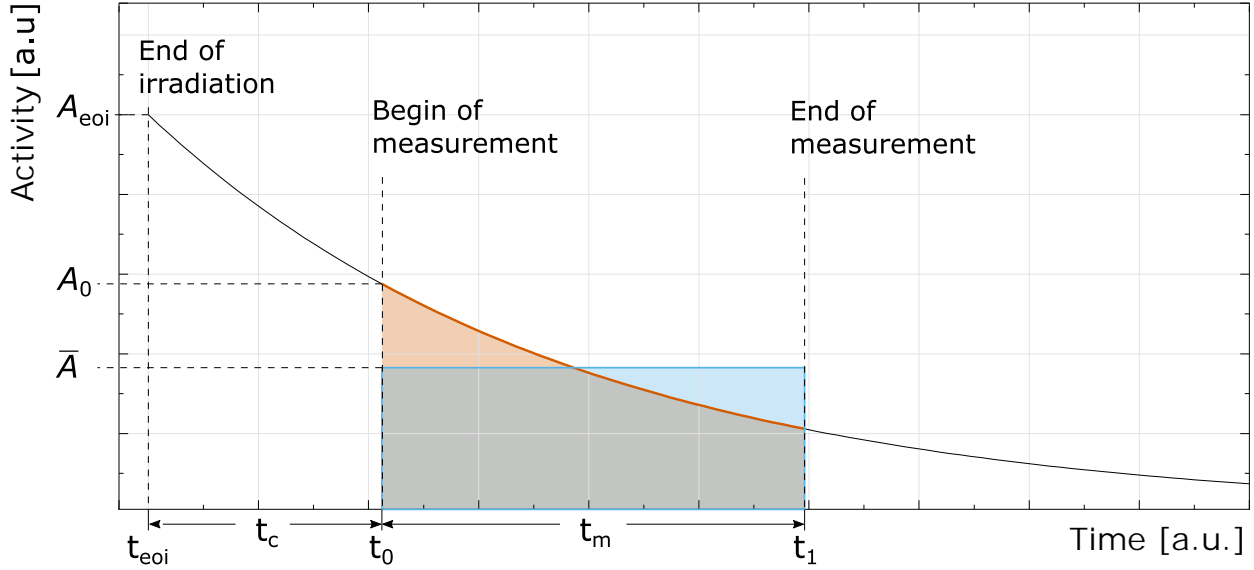


Figure 6.30: Procedure for the determination of an activity at the end of irradiation A_{eoi} using an activation analysis. The exponential curve (black) represents the activity of a random sample over a random period of time. The elaborated mean activity \bar{A} during the measurement time t_m is used to reconstruct the initial activity A_0 at begin of the measurement. This activity is used to reconstruct A_{eoi} using the cool down time t_c .

the resulting blue and orange shapes in figure 6.30 need to have the same integral size, as indicated in equation 61.

$$\bar{A} \cdot t_m = \int_{t_0}^{t_1} A_0 \cdot \exp(-\lambda t) dt \quad (61)$$

$$\Rightarrow A_0 = \frac{\bar{A} \cdot t_m \cdot \lambda}{1 - \exp(-\lambda t_m)} \quad (62)$$

In order to reconstruct the activity A_{eoi} at the end of the corresponding irradiation, the cool down time t_c (between end of irradiation and start of the measurement) can be used to extrapolate A_0 back to the end of the irradiation, as shown in equation 63.

$$A_{\text{eoi}} = A_0 \cdot \exp(\lambda t_c) = \frac{\bar{A} \cdot t_m \cdot \lambda}{1 - \exp(-\lambda t_m)} \cdot \exp(\lambda t_c) \quad (63)$$

Regarding the systematic uncertainties, the uncertainty on the absolute full-energy peak efficiency $\Delta\varepsilon_{\text{abs}}$ is propagated, as well as the uncertainties on the emission probability $\Delta\nu$, and the half-life $\Delta T_{1/2}$ (all three stemming from \bar{A} , cf. equation 9). In addition, the veto efficiency of the detector $\Delta\varepsilon_{\text{veto}}$ is propagated in case of an active veto (cf. section 4.6.2). Regarding the statistical uncertainties, mainly the counting statistics from the net counts ΔN is taken into account and propagated accordingly, as well as a potential statistical uncertainty on the full-energy peak efficiency $\Delta\varepsilon_{\text{abs}}$.

6.5.2 Activation analyses for IBC-II

During the IBC-II campaign, only one sample was irradiated with a single beam energy, which is target Ta502 (cf. table 3.3). The irradiation took place at a time, where the TU1 detector was not available yet. Hence, the first three activation analyses were conducted by the VKTA (HPGe detector ‘D10’ in tunnel IV of the Felsenkeller site) and completed within the first 30 d after the end of irradiation. A fourth run was conducted after successful installation of the TU1 detector, which was approximately 145 d after end of irradiation (so almost three half-lives of ${}^7\text{Be}$ and considerably lower activity than for the first measurements). Even though this lower activity is partially compensated by a considerably longer measurement time of the fourth run (three times longer than the other runs), it is still remarkable that the resulting relative statistical uncertainty is significantly lower than the ones of the first three measurements. This is mainly due to the larger efficiency of TU1, as well as its very low background counting rate (cf. table 6.8). However, the relative systematic uncertainty is comparatively large with $\Delta A/A \approx 1.6\%$ in case of TU1, instead of $\Delta A/A \approx 0.5\%$ in case of D10. This is mainly due to the fact, that the efficiency in case of TU1 was not determined as precisely, but also the error propagation of $T_{1/2}$ during the calculation of A_{eoi} leads to an inevitable increase in uncertainty due to long storage time. Comparing the results of both detectors, as shown in table 6.8, the resulting activities are however in good agreement with each other (cf. also figure 6.31).

Table 6.8: Resulting activities from the activation analyses during the IBC-II campaign. The mean activities \bar{A} during the measurement are given as well as the resulting activities at the end of the irradiations A_{eoi} . Systematic and statistic uncertainties are stated as well and all values are stated with four digits according to the lowest uncertainty in the table. See text for details.

Activation analysis of the IBC-II campaign							
Target	Run	\bar{A} [Bq]	$\Delta\bar{A}_{\text{sys}}$ [Bq]	$\Delta\bar{A}_{\text{stat}}$ [Bq]	A_{eoi} [Bq]	$\Delta A_{\text{eoi,sys}}$ [Bq]	$\Delta A_{\text{eoi,stat}}$ [Bq]
Ta502	1	0.1088	0.0005	0.0195	0.1256	0.0005	0.0225
Ta502	2	0.0754	0.0003	0.0169	0.0941	0.0004	0.0211
Ta502	3	0.0783	0.0003	0.0199	0.1072	0.0004	0.0272
Ta502	4	0.0189	0.0003	0.0021	0.1317	0.0020	0.0147

6.5.3 Activation analyses for FK-I to FK-IV

There are four targets during the campaigns FK-I to FK-IV, which contained ${}^3\text{He}$ (and therefore also ${}^7\text{Be}$ after irradiation) and additionally were solely irradiated with one beam energy, namely ST3, ST4, ST5, and ST6. The activation analyses of the other samples, which did not contain ${}^3\text{He}$ also showed no statistically significant amount of ${}^7\text{Be}$. Hence, they will not be discussed further. Any calculations of upper limits on the activity within these samples are scientifically not of interest for the scope of this thesis, as also discussed later.

Table 6.9: Resulting activities from the activation analyses during the FK-I to FK-IV campaigns. The mean activities \bar{A} are given as well as the resulting activities at the end of the irradiations A_{eoi} . Systematic and statistic uncertainties are stated as well. See text for details.

Activation analysis for the FK-I to FK-IV campaigns							
Target	Run	\bar{A} [Bq]	$\Delta\bar{A}_{\text{sys}}$ [Bq]	$\Delta\bar{A}_{\text{stat}}$ [Bq]	A_{eoi} [Bq]	$\Delta A_{\text{eoi,sys}}$ [Bq]	$\Delta A_{\text{eoi,stat}}$ [Bq]
ST3	002	0.257	0.004	0.009	0.267	0.004	0.009
ST3	003	0.279	0.002	0.057	0.301	0.002	0.062
ST3	004	0.325	0.002	0.075	0.358	0.002	0.083
ST3	005	0.197	0.003	0.006	0.263	0.004	0.008
ST3	006	0.176	0.003	0.007	0.254	0.004	0.011
ST4	001	0.209	0.001	0.055	0.229	0.001	0.061
ST4	002	0.166	0.003	0.018	0.185	0.003	0.020
ST4	003	0.160	0.003	0.005	0.184	0.003	0.006
ST4	004	0.097	0.002	0.002	0.171	0.003	0.004
ST4	005	0.067	0.001	0.003	0.175	0.003	0.007
ST4	006	0.050	0.001	0.003	0.178	0.003	0.010
ST5	001	1.552	0.021	0.014	1.674	0.023	0.015
ST5	004	1.361	0.019	0.068	1.658	0.023	0.083
ST5	005	1.438	0.020	0.229	1.755	0.024	0.280
ST5	006	1.175	0.016	0.007	1.637	0.022	0.010
ST5	007	0.919	0.013	0.010	1.668	0.023	0.018
ST5	008	0.768	0.011	0.006	1.648	0.023	0.013
ST5	009	0.579	0.008	0.058	1.448	0.020	0.146
ST6	053	0.378	0.005	0.007	0.402	0.006	0.008

ST5 and ST6 were irradiated in 2021, when TU1 was already in operation, even though without active veto. However, ST3 and ST4 suffer from a lack of appropriate ${}^7\text{Be}$ calibration sources, as well as appropriate target holders to ensure proper geometric reproducibility. Furthermore, all four targets are still lacking the benefit of TU1's active veto, which further limits the statistical uncertainty of these runs. However, comparing the different runs of each target, the resulting values for A_{eoi} are also in good agreement, as shown in table 6.9 and figure 6.31.

6.5.4 Activation analyses for FK-V

The FK-V campaign took place, when TU1 (as well as its active veto) was in full operation. An appropriate target holder was available (cf. section 4.7), the absolute full-energy peak efficiency at $E = 478\text{ keV}$ was well determined using dedicated ${}^7\text{Be}$ calibration sources and the active veto was also available and deployed accordingly.

While the resulting values for A_{eoi} in case of ST9, ST10 and ST15 are in the expected order of $\sim 1\text{ Bq}$, the value for ST11 seemed unreasonably low, especially when considering the accumulated charge (cf. table 3.3). Both measurements of ST11 (Run206 and Run207) are however in agreement with each other and were both directly performed within the

subsequent days after the end of irradiation.

It is not plausible, that the sample ST11 was put upside down on top of TU1, since only $\sim 5\%$ of its $E = 478 \text{ keV}$ photons would be absorbed within the tantalum backing. After considering also other possible explanations, only one remains plausible: The predecessor run (Run205) prior to the investigation of ST11 on the TU1 detector used a target holder with distance rods which increased the distance between sample and detector to 70 mm (cf. section 4.7). It is very likely, that this target holder remained on top of the TU1 detector during the investigation of the ST11 sample. Hence, the utilized efficiency was too large, which subsequently underestimated A_{eoi} .

Table 6.10: Resulting activities from the activation analyses during the FK-V campaign. The mean activities \bar{A} are given as well as the resulting activities at the end of the irradiations A_{eoi} . Systematic and statistic uncertainties are stated as well. The activities in case of ST11(2) are based on an alternative approach which tries to explain the low activity of ST11. See text for details.

Activation analysis of the FK-V campaign							
Target	Run	\bar{A} [Bq]	$\Delta\bar{A}_{\text{sys}}$ [Bq]	$\Delta\bar{A}_{\text{stat}}$ [Bq]	A_{eoi} [Bq]	$\Delta A_{\text{eoi,sys}}$ [Bq]	$\Delta A_{\text{eoi,stat}}$ [Bq]
ST9	160	1.133	0.016	0.019	1.158	0.016	0.019
ST9	161	1.152	0.016	0.031	1.210	0.017	0.033
ST10	170	1.123	0.015	0.018	1.146	0.016	0.018
ST10	183	1.035	0.014	0.013	1.189	0.016	0.015
ST11	206	0.0482	0.0007	0.0041	0.0499	0.0007	0.0042
ST11	207	0.0475	0.0007	0.0032	0.0515	0.0007	0.0035
ST15	218	0.356	0.005	0.007	0.381	0.005	0.007
ST11(2)	206	0.328	0.005	0.028	0.343	0.005	0.029
ST11(2)	207	0.322	0.005	0.022	0.341	0.005	0.023

Fortunately, Run205 investigated also a ^7Be calibration source and can therefore be used to independently determine the activity of ST11 after irradiation. However, this explanation of a misused target holder on distance rods is only ‘highly likely’, but not entirely certain (especially due to the fact, that this error also should have been noticed during the dismantling of ST11). Hence, the subsequently resulting activities are only listed in table 6.10 as an alternative suggestion, which is further labeled as ST11(2), but they are not propagated to table 6.11 and figure 6.31, respectively.

6.5.5 Deductions from the activation analyses

The following section will summarize and elaborate on the results and implications of all activation analyses, and put them into context to each other, as well as in context to the in-beam analyses.

It is crucial to emphasize the limitation of these activation analyses for certain targets. Especially the irradiations during the FK-V campaign were mainly optimized regarding a

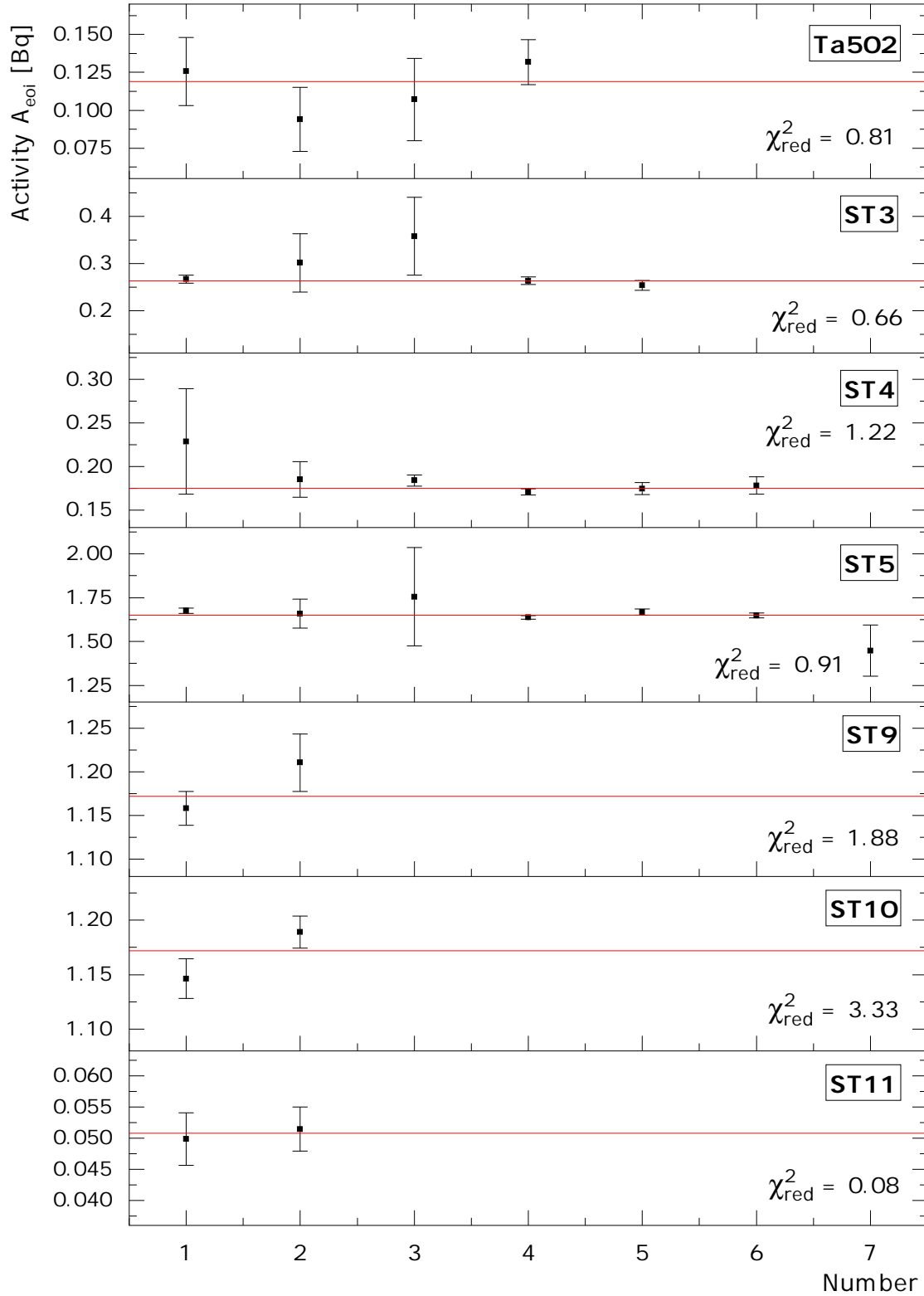


Figure 6.31: Activities at the end of irradiation for all relevant activation analyses during the ${}^3\text{He}(\alpha, \gamma){}^7\text{Be}$ campaigns. The data within this figure is based on table 6.8, table 6.9, and table 6.10. However, only the statistical uncertainties are plotted and utilized for the fit. The resulting mean activities for each target are shown in table 6.11.

Table 6.11: Mean activities at the end of each irradiation campaign obtained from figure 6.31. The statistical uncertainties are extracted from the fit and the systematic uncertainties are propagated by using the largest relative systematic uncertainty of each single A_{eoi} (cf. table 6.8, table 6.9, and table 6.10). Furthermore, the accumulated charge Q , the implanted dose D_{impl} and the resulting activity per accumulated Coulomb and implanted dose of 1 E17 at/cm² is shown.

Target	A_{eoi} [Bq]	$\Delta A_{\text{eoi,sys}}$ [Bq]	$\Delta A_{\text{eoi,stat}}$ [Bq]	Q [C]	D_{impl} [at/cm ²]	$A_{\text{eoi}}/Q/D_{\text{impl}}$ [Bq/C/(1 E17 at/cm ²)]
Ta502	0.119	0.009	0.002	0.2	5.0E17	0.119
ST3	0.263	0.004	0.004	2.4	1.0E18	0.011
ST4	0.175	0.003	0.003	0.8	1.0E18	0.022
ST5	1.650	0.007	0.023	0.9	1.0E18	0.183
ST6	0.402	0.006	0.008	0.7	1.0E18	0.057
ST9	1.172	0.023	0.016	2.7	8.9E17	0.049
ST10	1.172	0.021	0.016	5.5	8.9E17	0.024
ST11	0.0508	0.0008	0.0007	4.7	8.9E17	0.001
ST15	0.381	0.005	0.007	7.0	8.9E17	0.006

sufficient statistics for the γ -ray angular distribution. Hence, the premise was a high beam intensity in order to maximize the peak-to-background ratio for the in-beam detectors. On the one hand, the beam intensity is unfortunately proportional to the applied heating power on the target, which might enhance diffusion processes at the vicinity of the beam spot. This is especially true during the use of the target holder III, which in addition suffers from inferior heat dissipation due to the lower amount of copper. The associated yield drop was already addressed and confirmed in figure 6.15. On the other hand, the accumulated charges for all targets during the FK-V campaign are far beyond earlier determined limits for the avoidance of blisters. While these actions were inevitable for a proper investigation of the γ -ray angular distribution, they also caused that the determination of the respective values for A_{eoi} can only provide a lower limit for the areal densities, especially in case of blistered targets.

However, in order to properly investigate the resulting issues of reliability, it is worthwhile to further elaborate on figure 6.31 and table 6.11. In case of multiple measurements per target, figure 6.31 shows the deviation from their average value, as well as the corresponding χ_{red}^2 . The uncertainties were propagated as follows: Figure 6.31 only uses statistical uncertainties and the resulting fit provides the statistical uncertainty for the average value (cf. table 6.11). Regarding systematic uncertainties, the largest relative uncertainty of all runs (per target) is propagated further as the conservatively chosen value for the final systematic uncertainty. In case of only one run per target (ST6 and ST15), the value for A_{eoi} , as well as its uncertainties are used for the final result, as shown in table 6.11.

However, table 6.11 also provides the accumulated charges Q , as well as the initially implanted doses D_{impl} (not to be confused with the applied fluence - cf. section 3.2.4). These two values are tabulated due to the fact that the ratio between the accumulated activity

at the end of irradiation A_{eoi} and $Q \cdot D_{\text{impl}}$ are an excellent measure of reproducibility for the entire handling process of the target, i.e. the implantation, storage, irradiation, mounting/dismounting, and activation analysis. To be more precise, this value provides the information, how much activity of ${}^7\text{Be}$ will be accumulated (or better: ‘measured subsequently’) for one Coulomb of applied charge of ${}^4\text{He}^+$ and 1 E17 at/cm^2 of implanted ${}^3\text{He}$ ³⁷.

In case that targets with identical irradiation energies (but different storage times, target currents, etc.) always result in the same value of $A_{\text{eoi}}/Q/D_{\text{impl}}$, the following statements could be deduced:

- The implantation process leads to reproducible areal densities and there is no significant loss of areal density over time during the storage of the sample
- The irradiation process does not lead to significant loss of areal density due to heat-induced diffusion or due to broken blisters.
- The dismounting, possible storage after irradiation and subsequent analysis of the ${}^7\text{Be}$ content neither has an impact on the integrity of the sample, nor on its activity.
- Discrepancies for different irradiation energies are solely emerging from the difference in cross section.

This is however not the case, as shown in table 6.11. The targets Ta502, ST3, ST4, ST5 and ST9 were investigated using roughly the same irradiation energy and therefore experienced similar cross sections. However, ST5 and Ta502 show comparatively larger values of $A/Q/D$, than ST9, and significantly larger values than ST3 and ST4. In total they vary by a factor up to ~ 17 .

In order to investigate the main cause of this discrepancy, one can have a look for correlations of $A/Q/D$ with multiple potentially contributing factors. These factors include the storage time, as well as the storage conditions before irradiation (leading to possible diffusion out of the sample), the target current (leading to possible heat induced effects) and the total applied charge (being an indicator of possible blistering effects)³⁸.

These possible causes are shown in table 6.12, which lists the five samples with similar irradiation energy from top to bottom in order of favorable activity outcome. Neither the storage conditions, nor the applied charge Q seem to be the main reasons for the discrepancy, due to the fact that there is no obvious correlation between them and $A/Q/D$. However, there seems to be a correlated trend for the storage time before irradiation, as well as the target current (both mean current and maximum current) and the visual appearance of ruptured blisters: Whenever the targets were stored for a short time period before irradiation and

³⁷This is certainly only true in case of a comparatively long half-life of ${}^7\text{Be}$ with respect to the irradiation period due to the fact that only Q is considered, but not the accumulation of Q over time with a potential subsequent decay of ${}^7\text{Be}$. However, this is reasonably ensured, as elaborated later (cf. figure 6.32).

³⁸For the total applied charge as possible cause for problematic outcomes, the following fact has to be taken into account: The size of the beam spot, as well as wobbling might distort this correlation.

Table 6.12: List of probable causes which could influence the quality of a target, ordered from favorable targets (with high values for $A/Q/D$) to unfavorable targets. These causes include storage time and storage conditions before irradiation, mean target current \bar{I}_t , maximum target current $I_{t,\max}$, applied charge Q , and the information on visibly ruptured blisters ('Bl.'). In order to disentangle effects stemming from different cross sections, only targets with similar irradiation energy are shown.

Target	$A_{\text{eoi}}/Q/D_{\text{impl}}$ [Bq/(C 1 E17 at/cm ²) ⁻¹]	Storage time	Storage cond.	\bar{I}_t [μ A]	$I_{t,\max}$ [μ A]	Q [C]	Bl.
ST5	0.183	4 months	Freezer	5.7	6.3	0.9	
Ta502	0.119	1 month	Freezer	3.1	3.5	0.2	
ST9	0.049	1 month	Freezer	11.4	12.5	2.7	X
ST4	0.022	16 months	Freezer	16.8	17.4	0.8	X
ST3	0.011	16 months	Freezer	13.4	13.8	2.4	X

subsequently irradiated with lower currents, the resulting activity (and therefore the available mean areal density) was always significantly larger compared to long storage times, high target currents and ruptured blisters. It is however worth mentioning, that this approach only shows a trend and certainly does not exclude the other possible causes.

The fact that ST3 is still significantly worse than ST4 regarding the resulting activity (despite otherwise very similar conditions and even lower target currents) could be related to the larger amount of applied charge Q .

Under perfect conditions, the activity A_{eoi} could now be used to determine an areal density, and therefore the cross section of the ${}^3\text{He}(\alpha,\gamma){}^7\text{Be}$ reaction independently of the in-beam results. However, as thoroughly discussed during this section, the effective mean areal density (which would be proportional to $A/D/Q$ in case of reproducible values), is varying by a factor of 17, which underlines the instability of the areal density, especially during the irradiation of the FK-V targets.

Hence, for the vast majority of irradiations, there is no precise information on the areal density prior and after the irradiation, let alone precise information for the time dependent development of the areal density during irradiation. This is again especially true for the FK-V campaign, where the irradiation conditions were chosen in favor of an analyzable γ -ray angular distribution, instead of a scientifically robust activation analysis (and hence scientifically robust result for the areal density).

Nevertheless, the astrophysical S -factor for the investigated irradiation energies around $E_{\text{cm}} = 1$ MeV is actually known to a satisfying degree. Therefore, it is worth testing a reverse approach by using the S -factor and the activity A_{eoi} in order to make more statements on the mean areal density during the irradiation itself (instead of a lower limit based on A_{eoi}).

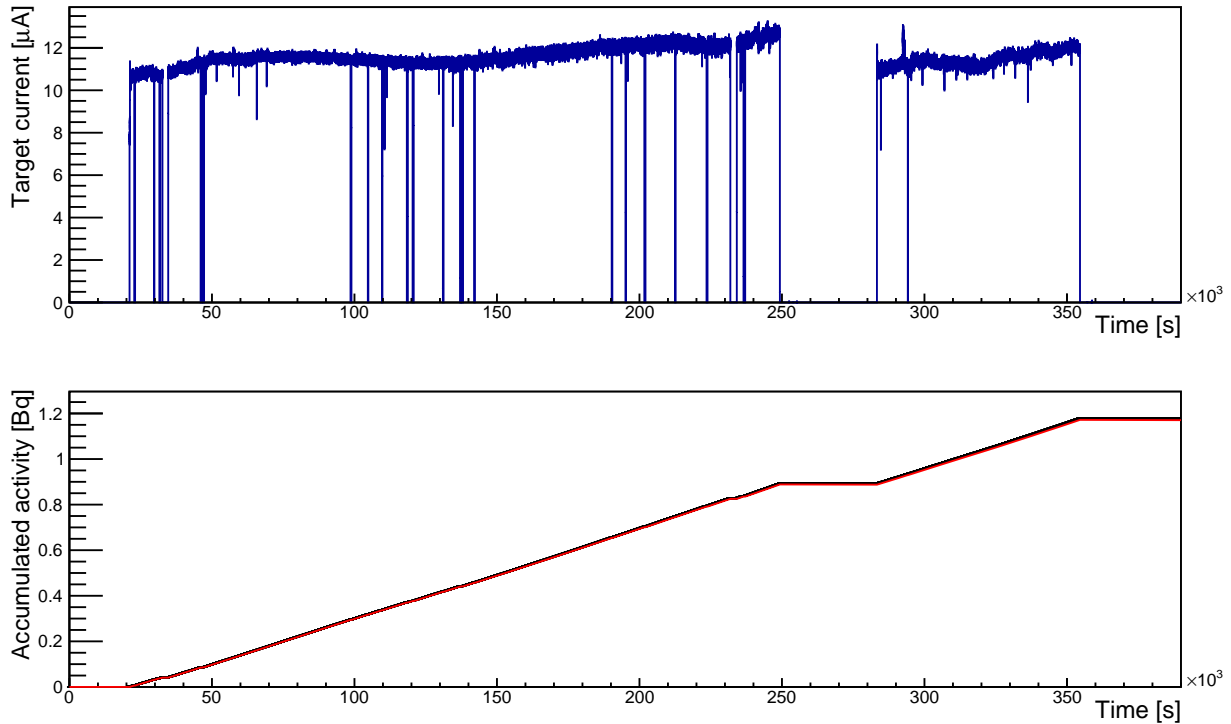


Figure 6.32: Top: Target current during the irradiation of ST9 with respect to the time (~ 4.5 d). Bottom: Corresponding accumulated activity of ${}^7\text{Be}$ within ST9. The black and the red curve represent the accumulation of activity without and with inclusion of the subsequent decay of ${}^7\text{Be}$. This figure is only valid in case of negligible changes in areal density during irradiation.

However, even this is only valid under the following conditions:

- **Available information about the target current over time**

The subsequent investigation of A_{eoi} via activation analysis does neither account for the duration of the irradiation (where early produced ${}^7\text{Be}$ nuclei could potentially already be decayed), nor inhomogenities in the time dependent target current. In case of strong variations in target current, the ${}^7\text{Be}$ nuclei are also produced non-uniformly in time.

- **Negligible loss of ${}^7\text{Be}$ during dismantling, storage and activation analysis**

This loss does not refer to the loss in activity due to radioactive decay since this is taken into account by the analysis. Instead, it refers to physical loss of nuclei, e.g. due to open blisters, where activated matter could subsequently flake off partly from the target and distort the resulting value of A_{eoi} .

While there is no indication to assume that the second point is of major concern for this thesis, the first point does provide some additional possibilities. The information of the target current over time is indeed available and subsequently enables an investigation on the impact of the decay of ${}^7\text{Be}$ while the irradiation is still ongoing. Furthermore, the target current over time can subsequently be used to vaguely estimate the mean areal density,

which would be necessary throughout the entire irradiation process in order to bring the cross section, the applied charge and the resulting activity into agreement with each other. The top panel in figure 6.32 shows the target current over time in case of the irradiation of ST9. In order to understand its activity at the end of irradiation ($A_{\text{eoi}} = 1.172 \text{ Bq}$, cf. table 6.11), the necessary areal density can now be tuned in a way which matches the time dependent current and the resulting activity, while the cross section remains at a fixed value. The bottom panel in figure 6.32 shows the resulting accumulation of activity in case of no subsequent decay of ${}^7\text{Be}$ (black curve) and in case ${}^7\text{Be}$ is decaying during irradiation (red curve). While the areal density was tuned to $\rho = 1.57 \text{ E17 at/cm}^2$ in order to match the red curve with the known activity at the end of irradiation ($A_{\text{eoi}} = 1.172 \text{ Bq}$), the black curve would result in $A_{\text{eoi}} = 1.178 \text{ Bq}$, which is a discrepancy of 0.5% building up over 4 d of irradiation.

However, it is important to keep in mind, that even this way of approach is also not entirely convincing due to the fact that it does matter, when and how target degradation takes place during irradiation. The real accumulated activity over time is very likely much more complicated. In case of heat-induced diffusion processes, the subsequent slope of accumulation should become more flat (i.e. for still constant target currents). And in case of blisterings it strongly depends, whether ${}^3\text{He}$ is removed from the target (which also flattens the slope) or whether ${}^7\text{Be}$ is removed from the target (which would result in a sudden drop in activity).

When employing the analysis presented in figure 6.32 on all irradiated targets, a wide variety of areal densities is obtained. While their result has to be treated with caution (as elaborated thoroughly), most of the resulting areal densities are in the range of 1 E17 at/cm^2 and 5 E17 at/cm^2 , which corresponds to implantation ratios of 1:10, and 1:2, respectively (cf. section 6.1.4). A mean ratio, which can be expected with the utilized approaches is approximately 1:3.

6.5.6 Cross section analysis for target Ta502

Within the previous section, the resulting activities from the offline measurements were used to investigate the areal density. This was mainly due to the fact that there was no reliable information available on the areal density. However, in case of target Ta502, the areal density was determined in-situ with an NRA analysis (cf. section 6.4.1). Furthermore, the yield during irradiation showed no visible degradation, and the target current as well as the totally accumulated charge were reasonably low (cf. table 6.12). Hence, in this single case it is possible to reverse the analysis and use both the activity at the end of irradiation as well as the areal density in order to determine a cross section for the ${}^3\text{He}(\alpha, \gamma){}^7\text{Be}$ reaction. Based on equation 48, the cross section σ solely depends on the number of occurred reactions R , the accumulated charge Q , and the areal density ρ . Therefore, only the transition from A_{eoi} (cf. table 6.11) to the number of occurred reactions R is still needed in order to obtain

a cross section, and hence an astrophysical S -factor.

The activity at the end of irradiation A_{eoi} can simply be converted to the number of available ${}^7\text{Be}$ nuclei at the end of irradiation. However, there is a discrepancy between this number and the amount of occurred reactions, which is due to the fact that ${}^7\text{Be}$ is unstable and already partly decaying during irradiation. In addition, the production rate of ${}^7\text{Be}$ is not constant, but depends on the time-dependent target current. Based on the considerations done for figure 6.32 (plotted for ST9, see [9] for similar analysis on Ta502), a correction factor C_{act} can be calculated. This correction factor ($C_{\text{act}} = 1.011$ in case of Ta502) takes into account the estimated number of decayed nuclei using the time-dependent target current³⁹. Hence, it acts as the link between A_{eoi} (or the number of available ${}^7\text{Be}$ nuclei at the end of irradiation, respectively) and the amount of occurred reactions, as also shown in equation 64.

$$\sigma(E_{\text{cm}}) = \frac{R}{Q/e \cdot \rho_{2\text{H}}} = \frac{A_{\text{eoi}}/\lambda \cdot C_{\text{act}}}{Q/e \cdot \rho_{2\text{H}}} \quad (64)$$

In addition, this equation can be used together with equation 31 in order to determine the cross section and the astrophysical S -factor in case of the irradiation of Ta502, as shown in table 6.13.

The current state of the art of the astrophysical S -factor for the ${}^3\text{He}(\alpha, \gamma){}^7\text{Be}$ reaction was introduced in section 1.4 and is shown in figure 1.6. The subsequent figure 6.33 shows the same content, but highlights all these contributions, which were not plotted in figure 1.6, i.e. all data sets, which were not included in the fit from the Solar Fusion II workshop. In addition, the new data point from this analysis is displayed as a red star, respectively.

Table 6.13: Resulting values for the cross section (cf. equation 64) and the astrophysical S -factor (cf. equation 31) of the ${}^3\text{He}(\alpha, \gamma){}^7\text{Be}$ reaction based on the IBC-II campaign.

E_{cm}	σ [μb]	$\Delta\sigma_{\text{sys}}$ [μb]	$\Delta\sigma_{\text{stat}}$ [μb]	S [keV b]	ΔS_{sys} [keV b]	ΔS_{stat} [keV b]
1217.7	2.23	0.20	0.06	0.300	0.026	0.008

However, it is important to emphasize, that the foundation of this analysis is based on some assumptions, which can not entirely be neglected and will be highlighted again in the discussion thoroughly, namely thermally induced diffusion processes and ruptured blisters.

³⁹This correction factor C_{act} is similar to C_{decay} in section 4.9. However, in the current case, a numerical integration is needed in order to obtain it. In addition, it is crucial to emphasize, that the cross section itself is an input parameter for figure 6.32. However, a change in C_{act} is mainly driven by the half-life of ${}^7\text{Be}$ and highly uncorrelated to the cross section. This is due to the fact, that the cross section influences both curves in figure 6.32 simultaneously.

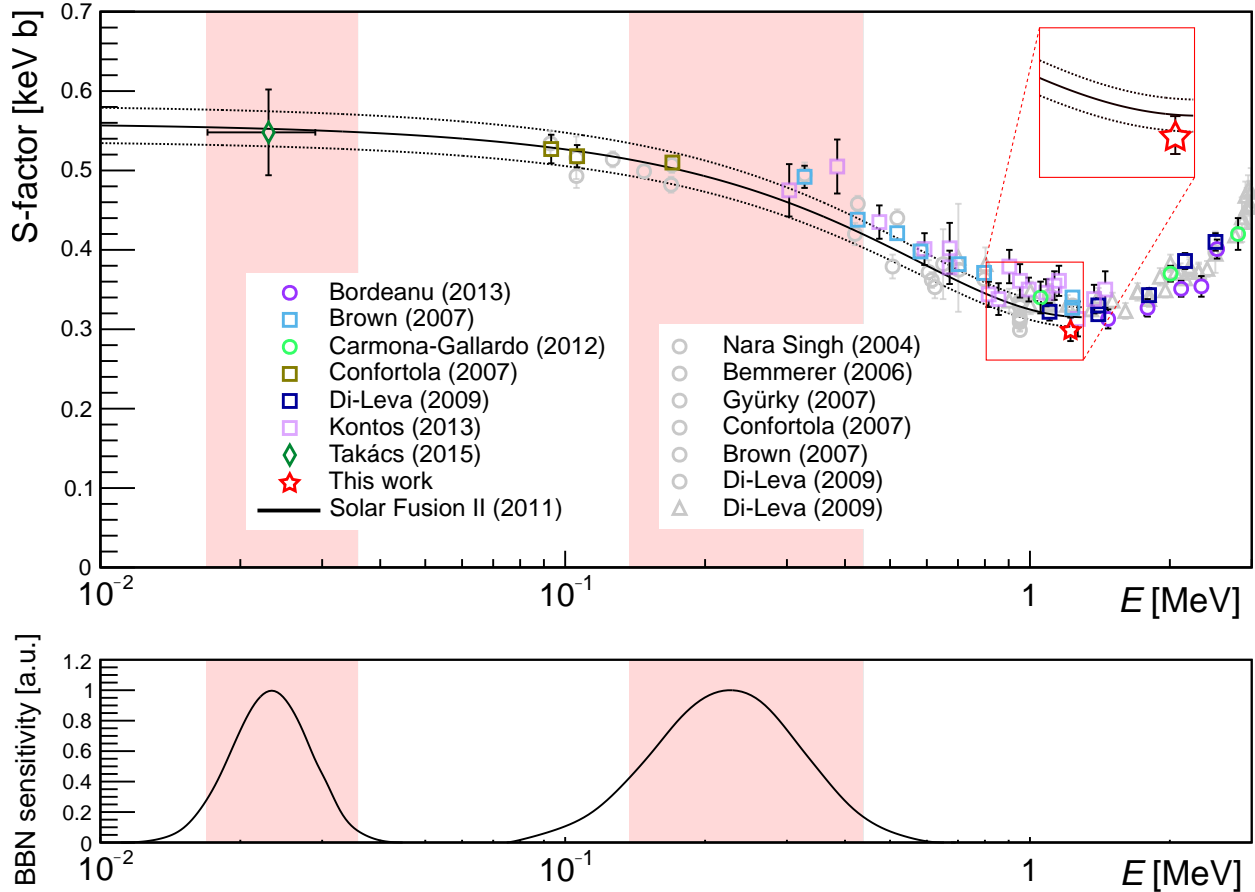


Figure 6.33: Top: Experimental campaigns on the astrophysical S -factor for the ${}^3\text{He}(\alpha,\gamma){}^7\text{Be}$ reaction. While figure 1.6 only shows the data sets from the Solar Fusion II fit [52–57], these particular experiments are greyed-out here for sake of clarity (cf. right legend). The other data sets, which were either not used for the Solar Fusion II fit, or did not exist yet, are shown here with colored markers (cf. left legend). These data sets are taken from [55–58, 164–166]. The data point originating from this thesis is shown as red star. In addition, the result of the solar fusion II fit [43] and its uncertainty band is shown as a black line and dotted lines up to $E = 1.3$ MeV, respectively. The circles represent the data sets based on offline measurements. The triangles show the data set based on ERDA, the squares represent data sets from in-beam measurements and the rhombus is a reversely derived data point stemming from the solar neutrino flux measurements. In small inlet without axes (upper right) is only plotted in order to highlight the relation between the data point of this thesis, and the S -factor fit. Bottom: Sensitivity of this reaction for nucleosynthesis within our sun, and during the Big Bang Nucleosynthesis, respectively [58, 59]. The red shaded areas mark the central 90% of these sensitivities.

7 Discussion

This thesis is dedicated to provide an improved nuclear physics input for our understanding of the universe, as well as its chemical evolution. This was done by investigating both the ${}^2\text{H}(p,\gamma){}^3\text{He}$ reaction and the ${}^3\text{He}(\alpha,\gamma){}^7\text{Be}$ reaction which both play a crucial role in the field of Big Bang nucleosynthesis and stellar nucleosynthesis. However, also the theoretically predicted solar neutrino fluxes of ${}^7\text{Be}$ and ${}^8\text{B}$, the cosmological lithium problem, the deuterium bottleneck, and the baryon-to-photon ratio are topics, which are related to this work.

The ${}^3\text{He}(\alpha,\gamma){}^7\text{Be}$ reaction was studied within the scope of this thesis mainly regarding its γ -ray angular distribution. During the main campaign at the Felsenkeller shallow-underground laboratory, this distribution was investigated at $E_{\text{cm}} = 0.45$ MeV, 0.55 MeV, 0.90 MeV, and 1.22 MeV, respectively. The resulting yield shows a minimum at emission angles around $\theta = 90^\circ$. In addition, the backward angles seem to be systematically preferred, i.e. for larger irradiation energies. Independent of the applied fit approach, the results indicate a positive a_2 component in the γ -ray angular distribution along all irradiation energies. However, the investigation of this reaction is still ongoing and another campaign was conducted in March 2023 at Felsenkeller. A conclusive analysis combining all experimental campaigns, as well as a coherent support by simulations is still pending. Additional simulations also need to shed light on the impact of the experimental beam spot, which is both finite in size and not centrally positioned on the targets: As shown in the appendix (cf. figure D.2), especially the photos from ST11 and ST15 indicate a beam spot which was located more towards the upper half of the target. This might have an impact on the underestimation of the detection efficiency of EB18BGE, which is used for the normalization of the other detectors' yields. However, the data of Can60 (also positioned at 90°), as well as another campaign at the Ion Beam Center of HZDR seem to support these results.

In case this anisotropy in the γ -ray angular distribution is confirmed, it would have an impact on an important issue: Due to the fact that typical detectors in an in-beam setup are usually not positioned at extremely large (or small) angles, other publications based on prompt γ -ray analyses might have underestimated the total cross section of this reaction. In general, this would be in agreement with the statement from the Solar Fusion II workshop, which stated that “the cross section determined from activity-based experiments was somewhat larger than that determined from prompt- γ experiments” [43]. However, this statement is most likely a typing mistake in this publication, because activity-based experiments currently result in smaller S -factors than those determined from prompt γ -ray experiments (cf. figure 6.33). In addition, a publication by Zhang et al. also predicts an anti-correlation between a_2 (at $E = 1.5$ MeV) and the astrophysical S -factor (expressed by $S(0)$). The experimentally determined a_2 component of this thesis would therefore result in an S -factor for the solar Gamow window, that is smaller than currently predicted [61]. However, it is crucial to reemphasize, that this work is still ongoing and that different theoretical publications are

widely in agreement regarding their predicted γ -ray angular distributions.

In addition, a coherent data set on the S -factor of this reaction is still needed which connects the low-energetic data points from the LUNA collaboration ($E_{\text{cm}} = 0.1 - 0.2 \text{ MeV}$) with higher-energetic data sets around $E_{\text{cm}} = 1 \text{ MeV}$. This can be achieved with the new gas jet target which will be assembled soon at Felsenkeller. Additionally, this laboratory is now well-equipped for highly sensitive activation analyses. These conditions can also be used in the future to provide a connection to the LUNA data set. However, the main campaign presented in this thesis was not designed for subsequent activation analyses, but optimized for the in-beam analysis. The reasons were thoroughly discussed and experimentally supported by the decreasing yield during irradiation.

The second topic of this thesis concerns the investigation of the ${}^2\text{H}(\text{p},\gamma){}^3\text{He}$ reaction. Within the scope of both this thesis and a dedicated publication, this reaction was mainly studied regarding its astrophysical S -factor at $E_{\text{cm}} = [265 \text{ keV}, 1094 \text{ keV}]$ which represents the high energetic end of the BBN Gamow window and the energies above [1]. Deuterium is an outstanding nucleus within the chart of nuclei. It has the lowest binding energy per nucleon of all bound nuclei, it was the first compound nucleus which has been formed in the universe, and the precision on its primordial abundance based on astronomical observations is unprecedented [31]. In addition, this primordial deuterium abundance is an excellent probe for the cosmological baryon density due to their intense correlation. The two new data sets from the LUNA collaboration [48] and the one presented within the scope of this thesis both point towards a larger astrophysical S -factor within the BBN Gamow window. While this in fact indicates a smaller primordial deuterium abundance than previously assumed, a discrepancy between both data sets remains and is currently under investigation at Felsenkeller.

However, there were two main limitations regarding the precision of the presented data set: The first one concerns the systematic uncertainty which arises from the determination of the areal density. While it was planned to use thorough nuclear reaction analyses during the entire campaign, delays in the delivery of the ${}^3\text{He}$ only enabled an analysis for the very last target. Hence, the ERDA measurements were needed in order to compensate for the lack of precision in areal density which was only partially successful. The second limitation dealt with the short amount of available beam time at the Ion Beam Center of HZDR. While 12 d were initially planned, the first charge of targets turned out to be deteriorated in their amount of implanted deuterium. Only the last four days of this beam time were used for a valid investigation. This however led to significant statistical uncertainties.

The third aim of this thesis concerns the installation of a new ultra-low background HPGe setup at the Felsenkeller shallow-underground laboratory. In order to efficiently attenuate the contributions from natural γ -ray sources, a sophisticated passive shielding was installed which consists of low-activity lead, OFRP copper, and a surrounding anti-radon box. This shielding reduces the background counting rate in the HPGe detector by more than three orders of magnitude within $[40 \text{ keV}, 2700 \text{ keV}]$ down to $1982(3) \text{ kg}^{-1}\text{d}^{-1}$. This is comparable,

and in fact already lower than similar HPGe setups in shallow-underground laboratories [123]. While remaining γ -ray contributions seem to be absent in this passively shielded spectrum, the majority of remaining events stem from muon-induced signals. Hence, an additional active muon shield was taken into operation and subsequently optimized which further reduces the background counting rate down to $116(1) \text{ kg}^{-1}\text{d}^{-1}$. This value was also claimed in a dedicated publication on this setup [2]. However, more recently, this background counting rate even further improved to $113(1) \text{ kg}^{-1}\text{d}^{-1}$. In summary, this detection setup is now the most sensitive device for measuring radioactivity in Germany, and among the most sensitive devices worldwide. While further improvements were already discussed thoroughly and might have their justifications, it is worthwhile to consider the balancing act between reachable sensitivities and required measurement time. Current available detection limits are however below $\mathcal{O}(100 \mu\text{Bq})$ and the resulting examinable half-lives surpass 10^{20} y even with only $n = 1 \text{ mol}$ of sample substance.

In conclusion, the presented work contributes to the urge of ramping up the capabilities of nuclear astrophysics and supports this field regarding a more precise understanding of the universe. Furthermore, the new detection setup at Felsenkeller also enables highly sensitive measurements in other fields, e.g. dark matter research, the physics of double beta decays, and other rare event searches.

References

- [1] S. Turkat, S. Hammer, E. Masha, et al. “Measurement of the ${}^2\text{H}(p,\gamma){}^3\text{He}$ S factor at 265–1094 keV.” In: *Physical Review C* 103.4 (2021). DOI: 10.1103/physrevc.103.045805.
- [2] S. Turkat, D. Bemmerer, A. Boeltzig, et al. “A new ultra low-level HPGe activity counting setup in the Felsenkeller shallow-underground laboratory.” In: *Astroparticle Physics* (2023), p. 102816. DOI: 10.1016/j.astropartphys.2023.102816.
- [3] S. Turkat, X. Mougeot, B. Singh, and K. Zuber. “Systematics of log ft values for β^- , and EC/ β^+ transitions.” In: *At. Data Nucl. Data Tables* (in review).
- [4] T. Szücs, D. Bemmerer, D. Degering, et al. “Background in γ -ray detectors and carbon beam tests in the Felsenkeller shallow-underground accelerator laboratory.” In: *The European Physical Journal A* 55.10 (2019). DOI: 10.1140/epja/i2019-12865-4.
- [5] J. Wilhelmy, M. Müscher, G. Rusev, et al. “Dipole response of ${}^{87}\text{Rb}$ and its impact on the ${}^{86}\text{Rb}(n,\gamma){}^{87}\text{Rb}$ cross section.” In: *Physical Review C* 102.4 (2020). DOI: 10.1103/physrevc.102.044327.
- [6] R. Schwengner, R. Massarczyk, M. Scheck, et al. “Electric and magnetic dipole strength in ${}^{66}\text{Zn}$.” In: *Physical Review C* 103.2 (2021). DOI: 10.1103/physrevc.103.024312.
- [7] R. Schwengner, R. Massarczyk, K. Schmidt, et al. “Photoexcitation of ${}^{76}\text{Ge}$.” In: *Physical Review C* 105.2 (2022). DOI: 10.1103/physrevc.105.024303.
- [8] T. Shizuma, S. Endo, A. Kimura, et al. “Low-lying dipole strength distribution in ${}^{204}\text{Pb}$.” In: *Physical Review C* 106.4 (2022). DOI: 10.1103/physrevc.106.044326.
- [9] L. Hübinger. “Investigation of the ${}^3\text{He}(\alpha,\gamma){}^7\text{Be}$ reaction at $E_{\text{com}} = 1.5$ MeV.” Bachelor Thesis. TU Dresden, 2018. URL: https://iktp.tu-dresden.de/IKTP/pub/18/Lisa_Huebinger_Bachelor.pdf.
- [10] S. Hammer. “Study of the ${}^2\text{H}(p,\gamma){}^3\text{He}$ cross section at $E_p = 400$ keV–800 keV.” Master Thesis. TU Dresden, 2019. URL: https://iktp.tu-dresden.de/IKTP/pub/19/Sebastian_Hammer_Master.pdf.
- [11] J. Koch. “Untergrund und Test der Offline Gammadektoren am Felsenkeller.” Bachelor Thesis. TU Dresden, 2020. URL: https://iktp.tu-dresden.de/IKTP/pub/20/Jonas_Koch_Bachelor.pdf.
- [12] M. Müller. “Monte-Carlo-Simulation des in-beam- γ -Spektroskopie-Aufbaus im Felsenkeller.” Bachelor Thesis. TU Dresden, 2020.
- [13] P. Hempel. “Studien zur Bestimmung der Halbwertszeiten von ${}^{139}\text{Ce}$, ${}^{143}\text{Pm}$, ${}^{144}\text{Pm}$, ${}^{146}\text{Pm}$.” Bachelor Thesis. TU Dresden, 2020.

- [14] M. Osswald. “Test und Kalibrierung der Reinstgermaniumdetektoren für die ${}^3\text{He}(\alpha, \gamma)$ - ${}^7\text{Be}$ -Messung am Felsenkeller.” Bachelor Thesis. TU Dresden, 2020. URL: https://iktp.tu-dresden.de/IKTP/pub/20/Max_Osswald_Bachelor.pdf.
- [15] M. Pichotta. “Investigating the background of the GERDA experiment by ${}^{76}\text{Ge}(\text{n,p})$ - ${}^{76}\text{Ga}$ reaction studies.” Master Thesis. TU Dresden, 2021.
- [16] J. Michaelis. “In-beam γ -spektroskopische Untersuchung der ${}^3\text{He}(\alpha, \gamma){}^7\text{Be}$ -Reaktion.” Bachelor Thesis. TU Dresden, 2021.
- [17] C. Seibt. “Operation of the X-Ray Detector at Felsenkeller Dresden and First Measurements.” Bachelor Thesis. TU Dresden, 2021.
- [18] B. Vergoosen. “X-ray Spectrometry: Attenuation of the background components in a silicon drift detector.” Bachelor Thesis. TU Dresden, 2022.
- [19] M. Wolf. “Study on the emission probability of gamma-rays from ${}^{74}\text{Ga}$ and ${}^{76}\text{Ga}$ in the ROI of GERDA/LEGEND.” Bachelor Thesis. TU Dresden, 2022.
- [20] S. Vincent. “In-Beam-Experimente am Felsenkeller zur komischen Lithium-7-Produktion.” Bachelor Thesis. TU Dresden, 2022.
- [21] C. E. Rolfs, W. S. Rodney, and D. D. Clayton. “Cauldrons in the Cosmos.” In: *American Journal of Physics* 57.2 (1989), pp. 188–189. DOI: 10.1119/1.16074.
- [22] E. W. Kolb and M. S. Turner. *The Early Universe*. Ed. by E. W. Kolb and M. S. Turner. CRC Press, 2018. DOI: 10.1201/9780429492860.
- [23] R. H. Cyburt, B. D. Fields, K. A. Olive, and T.-H. Yeh. “Big bang nucleosynthesis: Present status.” In: *Reviews of Modern Physics* 88.1 (2016). DOI: 10.1103/revmodphys.88.015004.
- [24] P. A. Zyla, R. M. Barnett, J. Beringer, et al. “Review of Particle Physics (Section: Astrophysics and Cosmology).” In: *Particle Data Group, Progress of Theoretical and Experimental Physics* 2020.8 (2020). DOI: 10.1093/ptep/ptaa104.
- [25] E. M. Burbidge, G. R. Burbidge, W. A. Fowler, and F. Hoyle. “Synthesis of the Elements in Stars.” In: *Reviews of Modern Physics* 29.4 (1957), pp. 547–650. DOI: 10.1103/revmodphys.29.547.
- [26] C. Iliadis. *Nuclear physics of stars*. John Wiley & Sons, 2015.
- [27] E. Grohs and G. M. Fuller. “The surprising influence of late charged current weak interactions on Big Bang Nucleosynthesis.” In: *Nuclear Physics B* 911 (2016), pp. 955–973. DOI: 10.1016/j.nuclphysb.2016.08.034.
- [28] M. Pospelov and J. Pradler. “Big Bang Nucleosynthesis as a Probe of New Physics.” In: *Annual Review of Nuclear and Particle Science* 60.1 (2010), pp. 539–568. DOI: 10.1146/annurev.nucl.012809.104521.

- [29] A. V. Gruzinov and J. N. Bahcall. “The ${}^7\text{Be}$ Electron Capture Rate in the Sun.” In: *The Astrophysical Journal* 490.1 (1997), pp. 437–441. DOI: 10.1086/304854.
- [30] E. Aver, K. A. Olive, and E. D. Skillman. “The effects of He I $\lambda 10830$ on helium abundance determinations.” In: *Journal of Cosmology and Astroparticle Physics* 2015.07 (2015), pp. 011–011. DOI: 10.1088/1475-7516/2015/07/011.
- [31] R. J. Cooke, M. Pettini, and C. C. Steidel. “One Percent Determination of the Primordial Deuterium Abundance.” In: *The Astrophysical Journal* 855.2 (2018), p. 102. DOI: 10.3847/1538-4357/aaab53.
- [32] M. Spite, F. Spite, E. Caffau, and P. Bonifacio. “Lithium abundance in a turnoff halo star on an extreme orbit.” In: *Astronomy and Astrophysics* 582 (2015), A74. DOI: 10.1051/0004-6361/201526878.
- [33] N. Aghanim, Y. Akrami, M. Ashdown, et al. “Planck 2018 results.” In: *Astronomy and Astrophysics* 641 (2020), A6. DOI: 10.1051/0004-6361/201833910.
- [34] S. W. Stahler and F. Palla. *The Formation of Stars*. Wiley, 2004. DOI: 10.1002/9783527618675.
- [35] P. D. Serpico, S. Esposito, F. Iocco, et al. “Nuclear reaction network for primordial nucleosynthesis: a detailed analysis of rates, uncertainties and light nuclei yields.” In: *Journal of Cosmology and Astroparticle Physics* 2004.12 (2004), pp. 010–010. DOI: 10.1088/1475-7516/2004/12/010.
- [36] G. M. Griffiths, E. A. Larson, and L. P. Robertson. “THE CAPTURE OF PROTONS BY DEUTERONS.” In: *Canadian Journal of Physics* 40.4 (1962), pp. 402–411. DOI: 10.1139/p62-045.
- [37] L. Ma, H. J. Karwowski, C. R. Brune, et al. “Measurements of ${}^1\text{H}(d,\gamma){}^3\text{He}$ and ${}^2\text{H}(p,\gamma){}^3\text{He}$ at very low energies.” In: *Physical Review C* 55.2 (1997), pp. 588–596. DOI: 10.1103/physrevc.55.588.
- [38] G. J. Schmid, B. J. Rice, R. M. Chasteler, et al. “The ${}^2\text{H}(p,\gamma){}^3\text{He}$ and ${}^1\text{H}(d,\gamma){}^3\text{He}$ reactions below 80 keV.” In: *Physical Review C* 56.5 (1997), pp. 2565–2581. DOI: 10.1103/physrevc.56.2565.
- [39] C. Casella, H. Costantini, A. Lemut, et al. “First measurement of the $d(p,\gamma){}^3\text{He}$ cross section down to the solar Gamow peak.” In: *Nuclear Physics A* 706.1-2 (2002), pp. 203–216. DOI: 10.1016/s0375-9474(02)00749-2.
- [40] V. Bystritsky, V. Gerasimov, A. Krylov, et al. “Study of the pd reaction in the astrophysical energy region using the Hall accelerator.” In: *Nuclear Instruments and Methods in Physics Research Section A: Accelerators, Spectrometers, Detectors and Associated Equipment* 595.3 (2008), pp. 543–548. DOI: 10.1016/j.nima.2008.07.152.

- [41] I. Tišma, M. Lipoglavšek, M. Mihovilovič, et al. “Experimental cross section and angular distribution of the ${}^2\text{H}(p,\gamma){}^3\text{He}$ reaction at Big-Bang nucleosynthesis energies.” In: *The European Physical Journal A* 55.8 (2019). DOI: 10.1140/epja/i2019-12816-1.
- [42] A. B. Zylstra, H. W. Herrmann, Y. H. Kim, et al. “ ${}^2\text{H}(p,\gamma){}^3\text{He}$ cross section measurement using high-energy-density plasmas.” In: *Physical Review C* 101.4 (2020). DOI: 10.1103/physrevc.101.042802.
- [43] E. G. Adelberger, A. García, R. G. H. Robertson, et al. “Solar fusion cross sections. II. The pp chain and CNO cycles.” In: *Reviews of Modern Physics* 83.1 (2011), pp. 195–245. DOI: 10.1103/revmodphys.83.195.
- [44] L. Marcucci, G. Mangano, A. Kievsky, and M. Viviani. “Implication of the Proton-Deuteron Radiative Capture for Big Bang Nucleosynthesis.” In: *Physical Review Letters* 116.10 (2016). DOI: 10.1103/physrevlett.116.102501.
- [45] G. M. Griffiths, M. Lal, and C. D. Scarfe. “THE REACTION $\text{D}(p,\gamma)\text{He}^3$ BELOW 50 KEV.” In: *Canadian Journal of Physics* 41.5 (1963), pp. 724–736. DOI: 10.1139/p63-077.
- [46] G. M. Bailey, G. M. Griffiths, M. A. Olivo, and R. L. Helmer. “Gamma-ray yields from the reaction $\text{D}(p,\gamma){}^3\text{He}$ at low energies.” In: *Canadian Journal of Physics* 48.24 (1970), pp. 3059–3061. DOI: 10.1139/p70-379.
- [47] G. J. Schmid, M. Viviani, B. J. Rice, et al. “Effects of Non-nucleonic Degrees of Freedom in the $\text{D}(p,\gamma){}^3\text{He}$ and $p(d,\gamma){}^3\text{He}$ Reactions.” In: *Physical Review Letters* 76.17 (1996), pp. 3088–3091. DOI: 10.1103/physrevlett.76.3088.
- [48] V. Mossa, K. Stöckel, F. Cavanna, et al. “The baryon density of the Universe from an improved rate of deuterium burning.” In: *Nature* 587.7833 (2020), pp. 210–213. DOI: 10.1038/s41586-020-2878-4.
- [49] G. Bellini, J. Benziger, D. Bick, et al. “Precision Measurement of the ${}^7\text{Be}$ Solar Neutrino Interaction Rate in Borexino.” In: *Physical Review Letters* 107.14 (2011). DOI: 10.1103/physrevlett.107.141302.
- [50] B. Aharmim, S. N. Ahmed, A. E. Anthony, et al. “Combined analysis of all three phases of solar neutrino data from the Sudbury Neutrino Observatory.” In: *Physical Review C* 88.2 (2013). DOI: 10.1103/physrevc.88.025501.
- [51] A. Serenelli, C. Peña-Garay, and W. C. Haxton. “Using the standard solar model to constrain solar composition and nuclear reaction S factors.” In: *Physical Review D* 87.4 (2013). DOI: 10.1103/physrevd.87.043001.

- [52] B. S. N. Singh, M. Hass, Y. Nir-El, and G. Haquin. “New Precision Measurement of the ${}^3\text{He}({}^4\text{He},\gamma){}^7\text{Be}$ Cross Section.” In: *Physical Review Letters* 93.26 (2004). DOI: 10.1103/physrevlett.93.262503.
- [53] D. Bemmerer, F. Confortola, H. Costantini, et al. “Activation Measurement of the ${}^3\text{He}(\alpha,\gamma){}^7\text{Be}$ Cross Section at Low Energy.” In: *Physical Review Letters* 97.12 (2006). DOI: 10.1103/physrevlett.97.122502.
- [54] G. Gyürky, F. Confortola, H. Costantini, et al. “ ${}^3\text{He}(\alpha,\gamma){}^7\text{Be}$ cross section at low energies.” In: *Physical Review C* 75.3 (2007). DOI: 10.1103/physrevc.75.035805.
- [55] F. Confortola, D. Bemmerer, H. Costantini, et al. “Astrophysical S factor of the ${}^3\text{He}(\alpha,\gamma){}^7\text{Be}$ reaction measured at low energy via detection of prompt and delayed γ rays.” In: *Physical Review C* 75.6 (2007). DOI: 10.1103/physrevc.75.065803.
- [56] T. A. D. Brown, C. Bordeanu, K. A. Snover, et al. “ ${}^3\text{He} + {}^4\text{He} \rightarrow {}^7\text{Be}$ astrophysical S factor.” In: *Physical Review C* 76.5 (2007). DOI: 10.1103/physrevc.76.055801.
- [57] A. D. Leva, L. Gialanella, R. Kunz, et al. “Stellar and Primordial Nucleosynthesis of ${}^7\text{Be}$: Measurement of ${}^3\text{He}(\alpha,\gamma){}^7\text{Be}$.” In: *Physical Review Letters* 102.23 (2009). DOI: 10.1103/physrevlett.102.232502.
- [58] M. P. Takács, D. Bemmerer, T. Szücs, and K. Zuber. “Constraining big bang lithium production with recent solar neutrino data.” In: *Physical Review D* 91.12 (2015). DOI: 10.1103/physrevd.91.123526.
- [59] K. M. Nollett and S. Burles. “Estimating reaction rates and uncertainties for primordial nucleosynthesis.” In: *Physical Review D* 61.12 (2000). DOI: 10.1103/physrevd.61.123505.
- [60] T. Tombrello and P. Parker. “Direct-capture model for the $\text{He}3(\alpha,\gamma)\text{Be}7$ and $\text{T}(\alpha,\gamma)\text{Li}7$ reactions.” In: *Physical Review* 131.6 (1963), p. 2582.
- [61] X. Zhang, K. M. Nollett, and D. R. Phillips. “ S -factor and scattering-parameter extractions from ${}^3\text{He} + {}^4\text{He} \rightarrow {}^7\text{Be} + \gamma$.” In: *Journal of Physics G: Nuclear and Particle Physics* 47.5 (2020), p. 054002. DOI: 10.1088/1361-6471/ab6a71.
- [62] B. T. Kim, T. Izumoto, and K. Nagatani. “Radiative capture reaction ${}^3\text{He}(\alpha,\gamma){}^7\text{Be}$ at low energies.” In: *Physical Review C* 23.1 (1981), pp. 33–41. DOI: 10.1103/physrevc.23.33.
- [63] T. Kajino. “The ${}^3\text{He}(\alpha,\gamma){}^7\text{Be}$ and ${}^3\text{He}(\alpha,\gamma){}^7\text{Li}$ reactions at astrophysical energies.” In: *Nuclear Physics A* 460.3 (1986), pp. 559–580. DOI: 10.1016/0375-9474(86)90428-8.
- [64] K. M. Nollett. “Radiative α -capture cross sections from realistic nucleon-nucleon interactions and variational Monte Carlo wave functions.” In: *Physical Review C* 63.5 (2001). DOI: 10.1103/physrevc.63.054002.

- [65] T. Neff. “Microscopic Calculation of the ${}^3\text{He}(\alpha, \gamma){}^7\text{Be}$ and ${}^3\text{H}(\alpha, \gamma){}^7\text{Li}$ Capture Cross Sections Using Realistic Interactions.” In: *Physical Review Letters* 106.4 (2011). DOI: 10.1103/physrevlett.106.042502.
- [66] J. Dohet-Eraly, P. Navrátil, S. Quaglioni, et al. “ ${}^3\text{He}(\alpha, \gamma){}^7\text{Be}$ and ${}^3\text{H}(\alpha, \gamma){}^7\text{Li}$ astrophysical S factors from the no-core shell model with continuum.” In: *Physics Letters B* 757 (2016), pp. 430–436. DOI: 10.1016/j.physletb.2016.04.021.
- [67] Y.-H. Kim, S.-J. Lee, and B. Yang. “Superconducting detectors for rare event searches in experimental astroparticle physics.” In: *Superconductor Science and Technology* 35.6 (2022), p. 063001. DOI: 10.1088/1361-6668/ac6a1c.
- [68] K. Zuber. *Neutrino Physics, Series in High Energy Physics, Cosmology and Gravitation*. CRC Press, 2021.
- [69] R. Agnese, A. Anderson, T. Aramaki, et al. “Projected sensitivity of the SuperCDMS SNOLAB experiment.” In: *Physical Review D* 95.8 (2017). DOI: 10.1103/physrevd.95.082002.
- [70] E. Armengaud, Q. Arnaud, C. Augier, et al. “Performance of the EDELWEISS-III experiment for direct dark matter searches.” In: *Journal of Instrumentation* 12.08 (2017), P08010–P08010. DOI: 10.1088/1748-0221/12/08/p08010.
- [71] G. Aad, T. Abajyan, B. Abbott, et al. “Observation of a new particle in the search for the Standard Model Higgs boson with the ATLAS detector at the LHC.” In: *Physics Letters B* 716.1 (2012), pp. 1–29. DOI: 10.1016/j.physletb.2012.08.020.
- [72] A. D. Leva, D. A. Scott, A. Caciolli, et al. “Underground study of the ${}^{17}\text{O}(\text{p}, \gamma){}^{18}\text{F}$ reaction relevant for explosive hydrogen burning.” In: *Physical Review C* 89.1 (2014). DOI: 10.1103/physrevc.89.015803.
- [73] K. Schmidt, S. Akhmadaliev, M. Anders, et al. “Resonance triplet at $E_\alpha=4.5$ MeV in the ${}^{40}\text{Ca}(\alpha, \gamma){}^{44}\text{Ti}$ reaction.” In: *Physical Review C* 88.2 (2013). DOI: 10.1103/physrevc.88.025803.
- [74] C. Brogini, D. Bemmerer, A. Caciolli, and D. Trezzi. “LUNA: Status and prospects.” In: *Progress in Particle and Nuclear Physics* 98 (2018), pp. 55–84. DOI: 10.1016/j.pnpnp.2017.09.002.
- [75] T. W. Burrows. “The evaluated nuclear structure data file: Philosophy, content, and uses.” In: *Nuclear Instruments and Methods in Physics Research Section A: Accelerators, Spectrometers, Detectors and Associated Equipment* 286.3 (1990), pp. 595–600. DOI: 10.1016/0168-9002(90)90922-s.
- [76] *IAEA Nuclear Data Section*. Accessed on 31.03.2023. URL: <https://www-nds.iaea.org/relnsd/vcharthtml/VChartHTML.html>.

- [77] G. R. Gilmore. *Practical Gamma-Ray Spectrometry*. John Wiley & Sons, Ltd, 2008. DOI: 10.1002/9780470861981.
- [78] G. F. Knoll. *Radiation detection and measurement*. John Wiley & Sons, 2010.
- [79] M. Berger, J. Hubbell, S. Seltzer, et al. “XCOM: Photon cross sections database.” In: (2010). URL: <http://www.nist.gov/pml/data/xcom>.
- [80] K. Debertin and R. G. Helmer. *Gamma-and X-ray spectrometry with semiconductor detectors*. 1988.
- [81] T. Papp, M.-C. Lépy, J. Plagnard, et al. “A new approach to the determination of the Fano factor for semiconductor detectors.” In: *X-Ray Spectrometry: An International Journal* 34.2 (2005), pp. 106–111.
- [82] P. R. T. Pengesan, S. Samat, and W. Priharti. “Determination of fano factor and pre-amplifier noise from the measurement of energy resolution of a HPGe detector.” In: *Sains Malaysiana* 44.5 (2015), pp. 761–764.
- [83] S. Croft and D. Bond. “A determination of the Fano factor for germanium at 77.4 K from measurements of the energy resolution of a 113 cm³ HPGe gamma-ray spectrometer taken over the energy range from 14 to 6129 keV.” In: *International journal of radiation applications and instrumentation. Part A. Applied radiation and isotopes* 42.11 (1991), pp. 1009–1014.
- [84] *Scionix Holland*. Accessed on 14.11.2022. URL: <https://eljentechnology.com/products/plastic-scintillators/>.
- [85] G. Choppin, J.-O. Liljenzin, J. Rydberg, and C. Ekberg. “Detection and Measurement Techniques.” In: *Radiochemistry and Nuclear Chemistry*. Elsevier, 2013. DOI: 10.1016/b978-0-12-405897-2.00009-4.
- [86] *CAEN, UM5960 CoMPASS User Manual (Rev. 20)*. Accessed on 18.11.2022. URL: <https://www.caen.it/?downloadfile=7161>.
- [87] S. Raman, C. Yonezawa, H. Matsue, et al. “Efficiency calibration of a Ge detector in the 0.1–11.0 MeV region.” In: *Nuclear Instruments and Methods in Physics Research Section A: Accelerators, Spectrometers, Detectors and Associated Equipment* 454.2-3 (2000), pp. 389–402.
- [88] G. W. Phillips and K. W. Marlow. “Automatic analysis of gamma-ray spectra from germanium detectors.” In: *Nuclear Instruments and Methods* 137.3 (1976), pp. 525–536.
- [89] W. R. Leo. *Techniques for nuclear and particle physics experiments: a how-to approach*. Springer Science & Business Media, 2012.

- [90] J. F. Ziegler, M. Ziegler, and J. Biersack. “SRIM – The stopping and range of ions in matter (2010).” In: *Nuclear Instruments and Methods in Physics Research Section B: Beam Interactions with Materials and Atoms* 268.11-12 (2010), pp. 1818–1823. DOI: 10.1016/j.nimb.2010.02.091.
- [91] S. W. C. Richard Brundle Charles A. Evans Jr. *Encyclopedia of Materials Characterization*. Elsevier, 1992. DOI: 10.1016/c2009-0-26077-6.
- [92] I. J. Thompson and F. M. Nunes. *Nuclear Reactions for Astrophysics*. Cambridge University Press, 2009. DOI: 10.1017/cbo9781139152150.
- [93] L. Wagner, S. Akhmadaliev, M. Anders, et al. “Astrophysical S factor of the $^{14}\text{N}(p,\gamma)^{15}\text{O}$ reaction at 0.4–1.3 MeV.” In: *Physical Review C* 97.1 (2018). DOI: 10.1103/physrevc.97.015801.
- [94] S. Reinicke. “Wasserstoffbrennen in der Sonne: Die $^{12}\text{C}(p,\gamma)^{13}\text{N}$ -Reaktion und die Radiofrequenz-Ionenquelle für den Felsenkeller-Beschleuniger.” Doctoral dissertation. TU Dresden, 2018.
- [95] *AMETEK ORTEC*. Accessed on 24.01.2023. URL: <https://www.ortec-online.com/>.
- [96] M. Marta, E. Trompler, D. Bemmerer, et al. “Resonance strengths in the $^{14}\text{N}(p,\gamma)^{15}\text{O}$ and $^{15}\text{N}(p,\alpha\gamma)^{12}\text{C}$ reactions.” In: *Physical Review C* 81.5 (2010). DOI: 10.1103/physrevc.81.055807.
- [97] K. Schmidt, S. Akhmadaliev, M. Anders, et al. “Strength of the $E_p=1.842$ MeV resonance in the $^{40}\text{Ca}(p,\gamma)^{41}\text{Sc}$ reaction reexamined.” In: *Physical Review C* 89.4 (2014). DOI: 10.1103/physrevc.89.045802.
- [98] R. Depalo, F. Cavanna, F. Ferraro, et al. “Strengths of the resonances at 436, 479, 639, 661, and 1279 keV in the $^{22}\text{Ne}(p,\gamma)^{23}\text{Na}$ reaction.” In: *Physical Review C* 92.4 (2015). DOI: 10.1103/physrevc.92.045807.
- [99] T. P. Reinhardt, S. Akhmadaliev, D. Bemmerer, et al. “Absolute hydrogen depth profiling using the resonant $^1\text{H}(^{15}\text{N},\alpha\gamma)^{12}\text{C}$ nuclear reaction.” In: *Nuclear Instruments and Methods in Physics Research Section B: Beam Interactions with Materials and Atoms* 381 (2016), pp. 58–66. DOI: 10.1016/j.nimb.2016.05.009.
- [100] K. Stöckel. “Experimente zur Untersuchung des Bethe-Weizsäcker-Zyklus in der Sonne.” Diploma thesis. TU Dresden, 2015.
- [101] C. Herlitzius. “The Doppler Shift Attenuation Method Facility: Its Design, Setup and Commissioning with the $^{32}\text{S}(^3\text{He},^4\text{He})^{31}\text{S}$ Reaction.” Doctoral dissertation. Technische Universität München, 2013.

- [102] V. Bystritsky, G. Dudkin, M. Filipowicz, et al. “Targets of deuterides TiD_2 , ZrD_2 , NbD , and CrD_2 with different structures used in experiments on the study of pd and dd reactions at astrophysical energies.” In: *Nuclear Instruments and Methods in Physics Research Section A: Accelerators, Spectrometers, Detectors and Associated Equipment* 810 (2016), pp. 80–85. DOI: 10.1016/j.nima.2015.12.006.
- [103] S. Seuthe, H. Becker, A. Krauss, et al. “Production and properties of implanted targets.” In: *Nuclear Instruments and Methods in Physics Research Section A: Accelerators, Spectrometers, Detectors and Associated Equipment* 260.1 (1987), pp. 33–42.
- [104] T. Alexander, G. Ball, W. Lennard, et al. “Measurement of the absolute cross section of the ${}^3\text{He}({}^4\text{He},\gamma){}^7\text{Be}$ reaction at $E_{\text{c.m.}} = 525$ keV.” In: *Nuclear Physics A* 427.3 (1984), pp. 526–544.
- [105] A. R. Totemeier. “Helium Ion Implantation in Zirconium: Bubble Formation & Growth.” Doctoral dissertation. 2015.
- [106] M. Friedrich, W. Bürger, D. Henke, and S. Turuc. “The Rossendorf 3 MV tandetron: a new generation of high-energy implanters.” In: *Nuclear Instruments and Methods in Physics Research Section A: Accelerators, Spectrometers, Detectors and Associated Equipment* 382.1-2 (1996), pp. 357–360. DOI: 10.1016/s0168-9002(96)00393-2.
- [107] R. L. Loger, J. E. Raatz, M. L. Sundquist, et al. “ ${}^{134}\text{MC-SNICS}$ sample multi-cathode source of negative ions by cesium sputtering (134 MC-SNICS).” In: *AIP Conference Proceedings*. AIP, 1999. DOI: 10.1063/1.59205.
- [108] F. Ludwig. “Underground measurements and simulations on the muon intensity and ${}^{12}\text{C}$ -induced nuclear reactions at low energies.” Doctoral dissertation. TU Dresden, 2021.
- [109] F. Dietrich. “ γ -Winkelverteilung der ${}^3\text{He}(\alpha, \gamma){}^7\text{Be}$ -Reaktion bei 0,8 MeV Schwerpunktsenergie.” Bachelor Thesis. TU Dresden, 2022.
- [110] W. Pälchen and H. Walte. *Geologie von Sachsen - Geologischer Bau und Entwicklungsgeschichte*. Schweizerbart Science Publishers, Stuttgart Germany, 2008.
- [111] M. Grieger. “Neutronenfluss in Untertagelaboren.” Doctoral dissertation. TU Dresden, 2021.
- [112] F. Ludwig, L. Wagner, T. Al-Abdullah, et al. “The muon intensity in the Felsenkeller shallow underground laboratory.” In: *Astroparticle Physics* 112 (2019), pp. 24–34. DOI: 10.1016/j.astropartphys.2019.04.006.
- [113] M. Grieger, T. Hensel, J. Agramunt, et al. “Neutron flux and spectrum in the Dresden Felsenkeller underground facility studied by moderated ${}^3\text{He}$ counters.” In: *Physical Review D* 101.12 (2020). DOI: 10.1103/physrevd.101.123027.

-
- [114] *Mirion Technologies, Application Note: Ultra Low-Background Detector Systems*. Accessed on 27.02.2022. URL: <https://www.mirion.com>.
- [115] *Ketek GmbH*. Accessed on 24.01.2023. URL: <https://www.ketek.net/>.
- [116] *RaySpec Ltd*. Accessed on 24.01.2023. URL: <https://www.rayspec.co.uk/>.
- [117] *Database for radiopure materials*. Accessed on 20.03.2022. URL: <https://radiopurity.org>.
- [118] J. Loach, J. Cooley, G. Cox, et al. “A database for storing the results of material radiopurity measurements.” In: *Nuclear Instruments and Methods in Physics Research Section A: Accelerators, Spectrometers, Detectors and Associated Equipment* 839 (2016), pp. 6–11.
- [119] D. Leonard, P. Grinberg, P. Weber, et al. “Systematic study of trace radioactive impurities in candidate construction materials for EXO-200.” In: *Nuclear Instruments and Methods in Physics Research Section A: Accelerators, Spectrometers, Detectors and Associated Equipment* 591.3 (2008), pp. 490–509.
- [120] *Eljen Technology*. Accessed on 12.06.2022. URL: <https://eljentechnology.com/products/plastic-scintillators/ej-200-ej-204-ej-208-ej-212>.
- [121] B. Ullrich. “Inbetriebnahme eines Plastik-Szintillations-Detektors für den Nachweis atmosphärischer Myonen und Analyse des Messspektrums.” Staatsexamensarbeit. TU Dresden, 2018.
- [122] I. Štekl, J. Hülka, F. Mamedov, et al. “Low Radon Cleanroom for Underground Laboratories.” In: *Frontiers in Public Health* 8 (2021), p. 1086.
- [123] M. Köhler, D. Degering, M. Laubenstein, et al. “A new low-level γ -ray spectrometry system for environmental radioactivity at the underground laboratory Felsenkeller.” In: *Applied Radiation and Isotopes* 67.5 (2009), pp. 736–740.
- [124] *SARAD GmbH*. Accessed on 30.03.2023. URL: <https://www.sarad.de/>.
- [125] D. E. Groom, N. V. Mokhov, and S. I. Striganov. “Muon stopping power and range tables 10 MeV–100 TeV.” In: *Atomic Data and Nuclear Data Tables* 78.2 (2001), pp. 183–356.
- [126] M. Forró. “Temperature Effect of Cosmic Radiation at 1000-M Water Equivalent Depth.” In: *Physical Review* 72.9 (1947), pp. 868–869. DOI: 10.1103/physrev.72.868.
- [127] H. Takai, C. Feldman, M. Minelli, et al. “Tidal frequencies in the time series measurements of atmospheric muon flux from cosmic rays.” In: *arXiv preprint arXiv:1610.05983* (2016).

- [128] G. Bellini, J. Benziger, D. Bick, et al. “Cosmic-muon flux and annual modulation in Borexino at 3800 m water-equivalent depth.” In: *Journal of Cosmology and Astroparticle Physics* 2012.05 (2012), pp. 015–015. DOI: 10.1088/1475-7516/2012/05/015.
- [129] A. I. Barbouti and B. C. Rastin. “A study of the absolute intensity of muons at sea level and under various thicknesses of absorber.” In: *Journal of Physics G: Nuclear Physics* 9.12 (1983), pp. 1577–1595. DOI: 10.1088/0305-4616/9/12/018.
- [130] Personal communication with T. Schröttner, Seibersdorf Labor GmbH, 2444 Seibersdorf, Austria. (2022).
- [131] M. Schwaiger, F. Steger, T. Schroettner, and C. Schmitzer. “A ultra low level laboratory for nuclear test ban measurements.” In: *Applied Radiation and Isotopes* 56.1-2 (2002), pp. 375–378. DOI: 10.1016/S0969-8043(01)00217-2.
- [132] C. Nitsch, M. Gerhardt, C. Gößling, and K. Kröninger. “Improvements to the muon veto of the Dortmund Low Background Facility.” In: *Applied Radiation and Isotopes* 126 (2017), pp. 201–203. DOI: 10.1016/j.apradiso.2017.02.041.
- [133] G. Heusser, M. Weber, J. Hakenmüller, et al. “GIOVE: a new detector setup for high sensitivity germanium spectroscopy at shallow depth.” In: *The European Physical Journal C* 75.11 (2015). DOI: 10.1140/epjc/s10052-015-3704-2.
- [134] J. Hakenmüller. “Simulation of the cosmic ray induced background in the GIOVE detector.” Master thesis. University of Heidelberg, 2015.
- [135] M. Laubenstein, M. Hult, J. Gasparro, et al. “Underground measurements of radioactivity.” In: *Applied Radiation and Isotopes* 61.2 (2004). Low Level Radionuclide Measurement Techniques - ICRM, pp. 167–172. DOI: <https://doi.org/10.1016/j.apradiso.2004.03.039>. URL: <https://www.sciencedirect.com/science/article/pii/S0969804304001009>.
- [136] Personal communication with M. Hult. (2022).
- [137] M. Hult, G. Marissens, H. Stroh, et al. “Characterisation of an ultra low-background point contact HPGe well-detector for an underground laboratory.” In: *Applied Radiation and Isotopes* 134 (2018), pp. 446–449. DOI: 10.1016/j.apradiso.2017.08.002.
- [138] D. R. García, D. Baur, J. Grigat, et al. “GeMSE: a low-background facility for gamma-spectrometry at moderate rock overburden.” In: *Journal of Instrumentation* 17.04 (2022), P04005. DOI: 10.1088/1748-0221/17/04/p04005.
- [139] Personal communication with M. Laubenstein. (2022).
- [140] J. Pérez-Pérez, J. C. Amare, I. C. Bandac, et al. “Radon Mitigation Applications at the Laboratorio Subterráneo de Canfranc (LSC).” In: *Universe* 8.2 (2022), p. 112. DOI: 10.3390/universe8020112.
- [141] Personal communication with D. R. García and M. Schumann. (2022).

- [142] V. Brudanin, V. Egorov, Hodak, et al. “The Low-Background HPGE Γ -Spectrometer OBELIX for the Investigation of the Double Beta Decay to Excited States.” In: *IOSR Journal of Applied Physics* (2017). DOI: 09.22-29.10.9790/4861-0901012229.
- [143] A. J. Khan, X. Li, D. K. Haines, et al. “Investigation of neutron shielding materials for low-background gamma spectrometry.” In: *Journal of Radioanalytical and Nuclear Chemistry* 328.3 (2021), pp. 941–950.
- [144] E. Masha. “Big Bang Nucleosynthesis and the deuterium abundance: Study of the ${}^2\text{H}(p,\gamma){}^3\text{He}$ reaction in the energy range 400-800 keV.” Master Thesis. University of Milan, 2018.
- [145] M. Malinowski. “The desorption of TiD_2 films formed during simulated tokamak gettering cycles.” In: *Journal of Nuclear Materials* 85-86 (1979), pp. 957–962. DOI: 10.1016/0022-3115(79)90384-2.
- [146] R. Checchetto, L. M. Gratton, A. Miotello, et al. “Structural evolution and thermal stability of deuterated titanium thin films.” In: *Physical Review B* 58.7 (1998), pp. 4130–4137. DOI: 10.1103/physrevb.58.4130.
- [147] F. Zijderhand, F. Jansen, C. Alderliesten, and C. van der Leun. “Detector-efficiency calibration for high-energy gamma-rays.” In: *Nuclear Instruments and Methods in Physics Research Section A: Accelerators, Spectrometers, Detectors and Associated Equipment* 286.3 (1990), pp. 490–496. DOI: 10.1016/0168-9002(90)90903-j.
- [148] A. Antilla, J. Keinonen, M. Hautala, and I. Forsblom. “Use of the ${}^{27}\text{Al}(p,\gamma){}^{28}\text{Si}$, $E_p = 992$ keV resonance as a gamma-ray intensity standard.” In: *Nuclear Instruments and Methods* 147.3 (1977), pp. 501–505. DOI: 10.1016/0029-554x(77)90393-7.
- [149] Personal communication with L. E. Marcucci (2017).
- [150] L. Girlanda, A. Kievsky, L. E. Marcucci, et al. “Thermal Neutron Captures on d and ${}^3\text{He}$.” In: *Physical Review Letters* 105.23 (2010). DOI: 10.1103/physrevlett.105.232502.
- [151] V. K. Alimov, M. Mayer, and J. Roth. “Differential cross-section of the $\text{D}(3\text{He},p){}^4\text{He}$ nuclear reaction and depth profiling of deuterium up to large depths.” In: vol. 234. 3. 2005, pp. 169–175.
- [152] M. Mayer, E. Gauthier, K. Sugiyama, and U. v. Toussaint. “Quantitative depth profiling of deuterium up to very large depths.” In: *U*. Vol. 267. 2009, pp. 506–512.
- [153] B. Wielunska, M. Mayer, T. Schwarz-Selinger, et al. “Cross section data for the $\text{D}({}^3\text{He},p){}^4\text{He}$ nuclear reaction from 0.25 to 6 MeV.” In: *Nuclear Instruments and Methods in Physics Research Section B: Beam Interactions with Materials and Atoms* 371 (2016), pp. 41–45. DOI: 10.1016/j.nimb.2015.09.049.

- [154] S. Pommé and B. C. Marroyo. “Improved peak shape fitting in alpha spectra.” In: *Applied Radiation and Isotopes* 96 (2015), pp. 148–153. DOI: 10.1016/j.apradiso.2014.11.023.
- [155] H. Wilsenach. “Long live alpha decay.” Doctoral dissertation. TU Dresden, 2021.
- [156] N. P. Barradas, C. Jeynes, and R. P. Webb. “Simulated annealing analysis of Rutherford backscattering data.” In: *Applied Physics Letters* 71.2 (1997), pp. 291–293. DOI: 10.1063/1.119524.
- [157] C. Xie. “Interactive Heat Transfer Simulations for Everyone.” In: *The Physics Teacher* 50.4 (2012), pp. 237–240. DOI: 10.1119/1.3694080.
- [158] A. Freimann. “In-beam gamma spectroscopy of the ${}^3\text{He}(\alpha,\gamma){}^7\text{Be}$ reaction at Felsenkeller.” Master Thesis. TU Dresden, 2023. URL: https://iktp.tu-dresden.de/IKTP/pub/19/Sebastian_Hammer_Master.pdf.
- [159] W. Cole and G. W. Grime. “Thick Noble Gas Targets Prepared by Ion Implantation.” In: *Preparation of Nuclear Targets for Particle Accelerators*. Springer US, 1981, pp. 109–115. DOI: 10.1007/978-1-4684-3956-4_15.
- [160] H. Trinkaus and B. Singh. “Helium accumulation in metals during irradiation – where do we stand?” In: *Journal of Nuclear Materials* 323.2-3 (2003), pp. 229–242. DOI: 10.1016/j.jnucmat.2003.09.001.
- [161] F. Pászti, E. Kótai, L. Pócs, T. Lohner, et al. “Investigations on blistering and exfoliation in gold by 3.52 MeV helium ions.” In: *Journal of Nuclear Materials* 98.1-2 (1981), pp. 11–17.
- [162] U. Linz. *Ion beam therapy: fundamentals, technology, clinical applications*. Springer Science & Business Media, 2011.
- [163] M. Anders. “S-factor measurement of the ${}^2\text{H}(\alpha,\gamma){}^6\text{Li}$ reaction at energies relevant for Big-Bang nucleosynthesis.” PhD thesis. TU Dresden, 2013.
- [164] C. Bordeanu, G. Gyürky, Z. Halász, et al. “Activation measurement of the ${}^3\text{He}(\alpha,\gamma){}^7\text{Be}$ reaction cross section at high energies.” In: *Nuclear Physics A* 908 (2013), pp. 1–11. DOI: 10.1016/j.nuclphysa.2013.03.012.
- [165] M. Carmona-Gallardo, B. S. N. Singh, M. J. G. Borge, et al. “New measurement of the ${}^3\text{He}(\alpha,\gamma){}^7\text{Be}$ cross section at medium energies.” In: *Physical Review C* 86.3 (2012). DOI: 10.1103/physrevc.86.032801.
- [166] A. Kontos, E. Uberseder, R. deBoer, et al. “Astrophysical S factor of ${}^3\text{He}(\alpha,\gamma){}^7\text{Be}$.” In: *Physical Review C* 87.6 (2013). DOI: 10.1103/physrevc.87.065804.

- [167] M. Schumaker and C. Svensson. “Compton-suppression and add-back techniques for the highly segmented TIGRESS HPGe clover detector array.” In: *Nuclear Instruments and Methods in Physics Research Section A: Accelerators, Spectrometers, Detectors and Associated Equipment* 575.3 (2007), pp. 421–432. DOI: 10.1016/j.nima.2007.02.084.
- [168] T. Szücs, D. Bemmerer, C. Broggini, et al. “An actively vetoed Clover γ -detector for nuclear astrophysics at LUNA.” In: *The European Physical Journal A* 44.3 (2010), pp. 513–519. DOI: 10.1140/epja/i2010-10967-1.
- [169] *IEEE Standard Test Procedures for Germanium Gamma-Ray Detectors*. DOI: 10.1109/ieeestd.1987.81600.

A General appendix

A.1 Coincidences between detectors

Coincident events in neighboring detection crystals are based on the fact, that one particle (i.e. a photon) is able to deposit energy in multiple crystals, e.g. due to incoherent scattering or pair production. The crystals in the utilized cluster detectors (cf. section 3.1.4) have an ideal size and composition for coincident events, i.e. due to an incoherent scattering in a first HPGe crystal and subsequently a photoelectric effect in a second, neighboring HPGe crystal.

By far the most likely interaction channel for photons with $E \approx 1$ MeV in germanium is incoherent scattering. However, independent of the position of this first interaction (via incoherent scattering) within the first HPGe crystal, the mean distance to any other point in the second, neighboring detector (cf. right panel of figure A.1) is very similar to the mean free path of photons with $E \approx 1$ MeV in germanium (cf. left panel of figure A.1). Hence, as long as the scattered photon propagates into an appropriate direction of a second crystal, both the mean free path and the geometry of the cluster lead to a reasonably likely second interaction in the second crystal. After two subsequent interactions, the photon is either already absorbed, or subsequently lost so much energy, that the remaining mean free path is too small to leave the second crystal (cf. left panel of figure A.1).

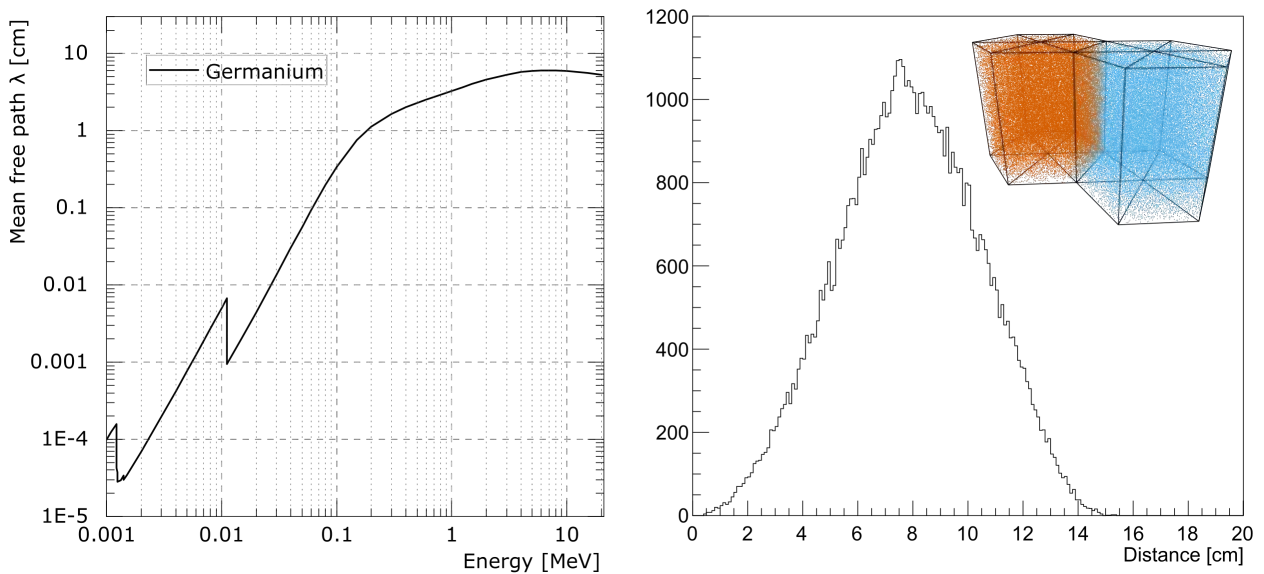


Figure A.1: Left: Mean free path of photons in germanium with respect to their energy. Right: Distribution of distances between two arbitrary points in two neighboring crystals. Inlet: Schematic (and simplified) view of two neighboring HPGe crystals of the Euroball and Miniball standard. Each dot represents an arbitrary point in the respective volume.

There are two techniques which are taking advantage of this and which will be introduced in the following: The so-called anti-Compton suppression and the so-called add-back technique. Whenever there are multiple HPGe crystals close to each other or there is a scintillation

detector involved, one of them will be applied. For a more thorough introduction, see e.g. also [167, 168].

A third approach, which differs from both of these techniques, is the use of the active veto for TU1 (cf. section 4.4.4). This veto solely fulfills the purpose of an active veto against muonic contributions and won't be discussed in the following due to its unique methodological approach in the use of the TU1 detector.

A.1.1 Anti-Compton suppression

Both the analysis chapters of the in-beam campaigns, as well as the chapter about the construction and optimization of the TU1 detector are dealing with experiments of comparatively low signal counting rates. Whenever the rate of the expected signal in a detector is particularly low, the underlying background in the pulse height spectra should be minimized as much as possible (cf. section 1.5).

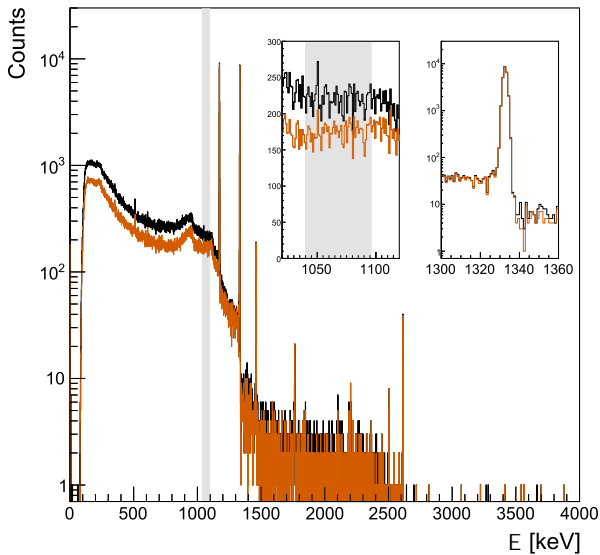


Figure A.2: Raw pulse height spectrum for ^{60}Co (black) and with applied anti-Compton suppression (orange). The two inlets show the ROI for $S_{\text{ACS}} = 1.26$ and the peak at $E = 1332$ keV, respectively. See text for details.

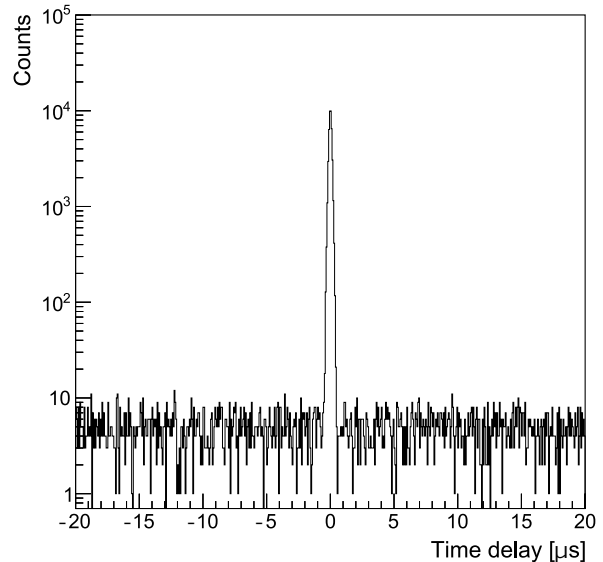


Figure A.3: Time delay histogram for events within two neighboring HPGe crystals in case of a ^{60}Co source in front of them. The peak in the center marks the coincident events between both detectors.

This can be realized by either using a passive shielding, which protects the detector by covering it with materials of high density and low intrinsic activity (e.g. lead, cf. chapter 4.3), or by using an active veto (cf. e.g. chapter 4.5). An active veto is typically realized by identifying coincident events within the detector of interest and surrounding detectors. Within this thesis, these coincidences can occur between HPGe and HPGe (in case of MB and EB detectors, cf. table 3.5), as well as between an HPGe detector and its designated scintillation detector (cf. e.g. table 3.6). The benefit of this technique is, that the events within the

full-energy peaks never deposited energy in another detector. This means, independent of its origin, coincident events between different detectors can be discarded in order to increase the peak-to-background ratio within a pulse height spectrum⁴⁰.

Coincident events can be identified by plotting the time difference between two subsequent events in two neighboring detectors, as shown in figure A.3. While there is a low-level background component of uncorrelated events, there is also a clear peak of coincident events, which are mainly due to incoherently scattered photons depositing energy in both detectors. By rejecting these events, the resulting improvement in the peak-to-Compton ratio can be seen as orange histogram in figure A.2.

However, whenever an active veto is used, utmost caution is needed regarding the survival probability of full-energy peaks. In case of experiments with a high rate in the detector, random coincidences are unavoidable. These coincidences depend on the rate in the veto detector, the rate in the detector of interest, and the coincidence timing window.

It is therefore necessary to introduce a correction factor, which determines the inevitable loss of full-energy events due to the active veto. In case of figure A.2, this factor can be calculated offline by comparing the peak entries in case of enabled and disabled veto (cf. right panel within this figure).

$$S_{\text{ACS}} = \frac{\sum_{i=1040}^{i=1096} N_{i,\text{free}}}{\sum_{i=1040}^{i=1096} N_{i,\text{ACS}}} \quad (65)$$

Furthermore, the quality of the anti-Compton suppression itself strongly depends on the energy of the photon of interest, as well as of the geometry of the two utilized detectors. In order to compare different setups, a suppression factor S_{ACS} is introduced, as shown in equation 65. This factor is defined by analyzing the spectrum of a ^{60}Co source with and without anti-Compton suppression and subsequently compare the energy region of $E = 1040$ keV to $E = 1096$ keV [78, 169], which is shown as a grey shaded area in figure A.2. In order to get a feeling for the energy dependency of one single system, the same procedure can also be done by using a ^{137}Cs source and the energy region of $E = 358$ keV to $E = 382$ keV [78].

A.1.2 Add-back techniques

The underlying technique in the previous chapter is based on the identification and elimination of coincident events between different detectors. By discarding these coincident events, the peak-to-background ratio can be improved.

⁴⁰This argument is not flawless. Within a prompt cascade of several emitted photons, it might happen, that there are coincidences with involved full-energy events in the detector of interest. Furthermore, random coincidences may also influence full-energy peaks, when discarded. However, a passive shielding in front of the veto detector, a comparatively low total counting rate, as well as the comparison of the raw and the suppressed spectrum minimizes these effects.

Another technique in the treatment of correlated events is to use coincidences in order to recover additional photopeak events instead of suppressing Compton continua. This technique is called ‘add-back’ and it is of particular interest for the Miniball and Euroball clusters, where there are multiple HPGe crystals (with good energy resolution) in close proximity to each other (cf. section 3.1.4). This technique becomes beneficial in case of negligible random coincidences (i.e. for low overall counting rates), as well as in the absence of γ -ray cascades. Basically it becomes interesting, whenever the coincident events are assumed to be dominated by incoherently scattered photons and high energy photons with reasonable probability of undergoing pair production.

However, it is worthwhile mentioning, that the add-back method is neither appropriate for comparatively low full-energy peaks (e.g. below 500 keV), nor for comparatively high full-energy peaks (e.g. above 2 MeV). At low energies, the mean free path rapidly falls below 2 cm, which deteriorates the probability to reach a second crystal at all (cf. left panel in figure A.1). At high energies, the differential cross section (according to the Klein-Nishina formula) shows a clear trend to forward scattering of the photon. Even at 2 MeV, already the vast majority of photons is scattered within less than 30° with respect to their initial path. The typical positioning of a cluster is therefore not ideal for a photon from the target, which needs to undergo a scattering angle of more or less 90° into the neighboring crystal. Nevertheless, due to the isotropic emission of annihilation photons at comparatively high energies, single escape peaks and double escape peaks can also be attenuated via the add-back mode with simultaneous recovering of additional full-energy events.

It is crucial to emphasize, that the effective full-energy peak efficiency in the add-back mode (similar to the efficiency with anti-Compton suppression) clearly differs from the usual full-energy peak efficiency. Whenever coincidences are used offline in order to manipulate full-energy events or Compton continua, utmost caution has to be exercised not to falsify the scientific result. This is especially true in case of γ -ray cascades (e.g. in case of calibration sources), where there are also additional effects like angular correlations. One important countermeasure however is to stick to the same analysis technique for each detector/cluster throughout one single campaign (both for calibration and analysis).

A.1.3 Approach for ACS and add-back

The general policy for both techniques within this thesis is, that the surrounding scintillation detectors (cf. table 3.6) are always used as anti-Compton suppression, and never in add-back mode. The bad energy resolution of scintillation detectors prohibits a proper reconstruction of full-energy events, but it has no influence on the efficiency of the anti-Compton suppression. Furthermore, in this way, the surrounding scintillation detectors also act as a veto against cosmic muons.

Despite not being discussed in section 3.1.4, especially the anti-Compton shield of the Eu-

robust clusters is actually even more complex and more powerful, than they are with the utilized way. These shields consists of 18 single scintillation crystals (six back catchers behind each of the outer HPGe crystals, and 12 side catchers with 6 in the edges and 6 in the side faces). An advanced anti-Compton suppression would therefore read out six separate HPGe signals and 18 separate scintillation signals in total. Hence, the single scintillation signals could be used as veto only for the neighboring HPGe detectors. In this way, random coincidences could be inhibited even more and more comfortable coincidence windows could be chosen.

However, the current status of the setup adds up all 18 signals in order to act as one single veto signal. This procedure is supported by the fact, that clusters are additionally shielded with lead as much as possible in order to reduce the counting rate from external events and therefore also suppress random coincidences.

The policy for coincidences within neighboring HPGe detectors in a cluster in general depends on the distance of the cluster to the target. If the cluster is reasonably far away, the crystals can be used in add-back mode. However, the add-back mode is always accompanied by an increasing of the effective opening angle of the detector, which can be disadvantageous when dealing with angular distributions. Whenever the clusters are used in close proximity to the target, the coincidences between neighboring HPGe are certainly not used in add-back mode, but used with an anti-Compton suppression, as discussed in the following.

Whenever the signal of a cluster is only referred to as e.g. ‘EB18’, the add-back mode is used. In case of labels as e.g. ‘EB18B’ (especially when used in proximity to the target), each single crystal underwent an anti-Compton analysis by both the surrounding BGO, as well as the three (in case of the central crystal six) neighboring HPGe crystals.

In case of e.g. ‘EB18BGE’, these single, anti-Compton suppressed spectra of ‘EB18B’, ‘EB18G’ and ‘EB18E’ are subsequently summed up, because they are positioned under the same azimuth angle.

It is worthwhile mentioning, that it is not feasible to use both techniques simultaneously. Both are relying on exactly the same physical principle of coincidences by (mostly) incoherent scattering. Either the coincidence information is used to attenuate the resulting continuum, or the information can be used to recover additional photopeak events. Using different coincidence timing windows would only be beneficial, if the underlying production mechanisms of these coincidences would significantly differ from each other with respect to their mean time difference between both events. Even if the additional life time of a positron in matter after pair production would enhance a systematical time difference between incoherent scattering and pair production: In these time regimes, different cable lengths and the limited ability of the DAQ to properly reconstruct the time stamp will limit the outcome of this endeavor.

A.2 Radon concentration at Felsenkeller

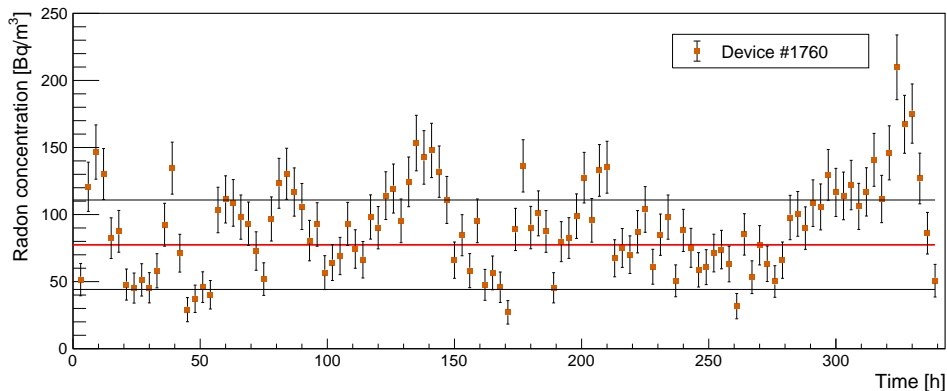


Figure A.4: Measurement of the time-dependent radon concentration (orange), obtained with the device #1760, which was located in the overground site (cf. figure 4.10). The average radon concentration is shown in red. Due to systematic influences, the distribution is non-Gaussian, but the effective environment for 68 % of the data points is indicated with the black lines.

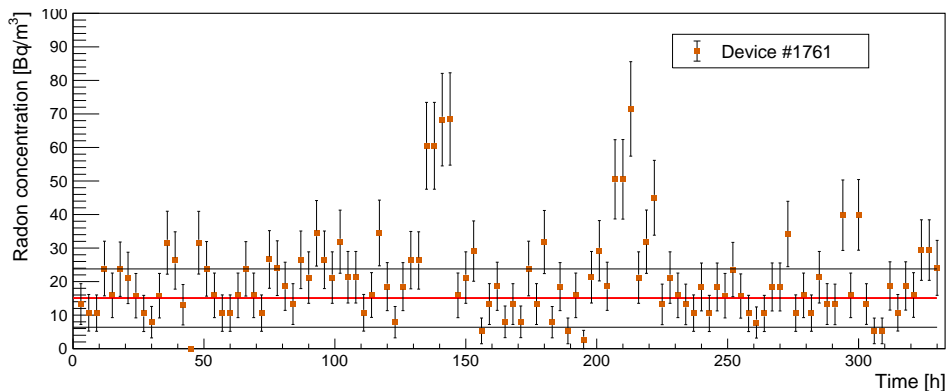


Figure A.5: Measurement of the time-dependent radon concentration (orange), obtained with the device #1761, which was located in the open tunnel system (cf. figure 4.10). The average radon concentration is shown in red. Due to systematic influences, the distribution is non-Gaussian, but the effective environment for 68 % of the data points is indicated with the black lines.

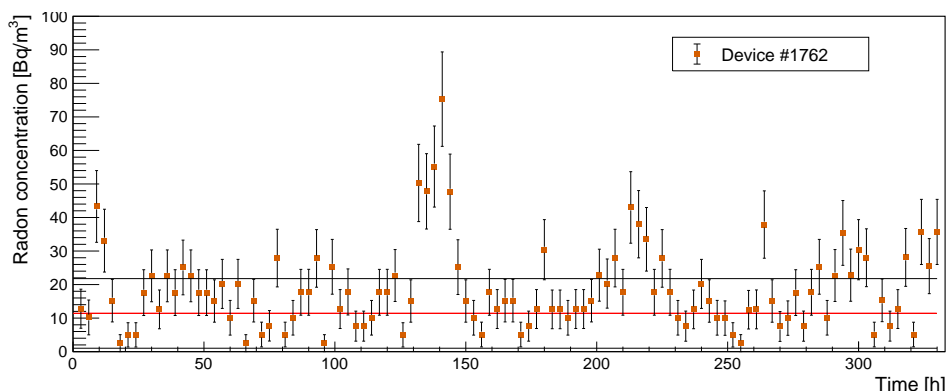


Figure A.6: Measurement of the time-dependent radon concentration (orange), obtained with the device #1762, which was located in bunker 111 (cf. figure 4.10). The average radon concentration is shown in red. Due to systematic influences, the distribution is non-Gaussian, but the effective environment for 68 % of the data points is indicated with the black lines.

B Appendix regarding the TU1 setup

B.1 Panel spectra and their coincidences with TU1

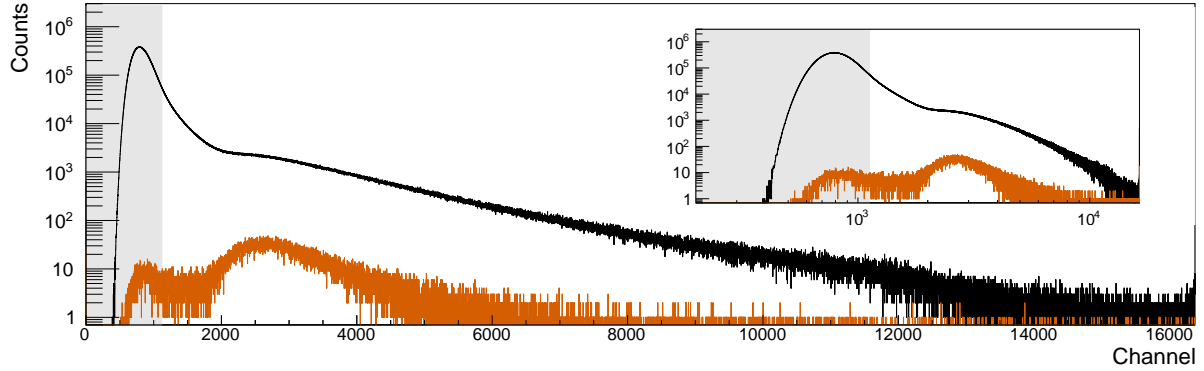


Figure B.1: Pulse height spectra of panel #15 (cf. figure 3.17). The histogram of the raw data is shown in black, and the events, which are coincident with events in TU1 are shown in orange. The area in grey is excluded by the cut concerning E_{thresh} . See section 4.4.6 for details.

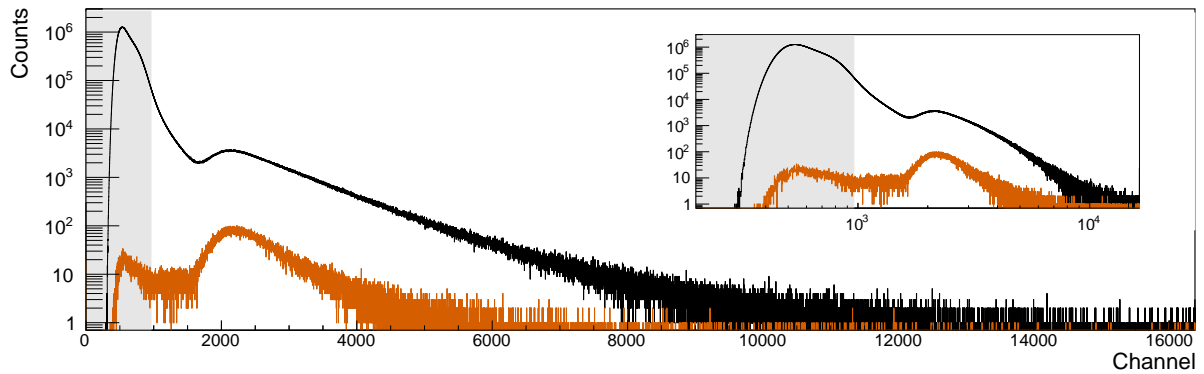


Figure B.2: Pulse height spectra of panel #16 (cf. figure 3.17). The histogram of the raw data is shown in black, and the events, which are coincident with events in TU1 are shown in orange. The area in grey is excluded by the cut concerning E_{thresh} . See section 4.4.6 for details.

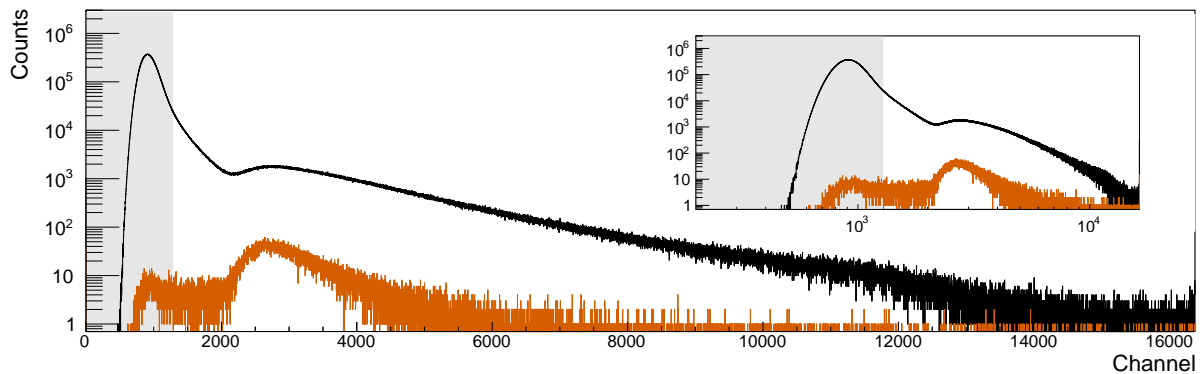


Figure B.3: Pulse height spectra of panel #17 (cf. figure 3.17). The histogram of the raw data is shown in black, and the events, which are coincident with events in TU1 are shown in orange. The area in grey is excluded by the cut concerning E_{thresh} . See section 4.4.6 for details.

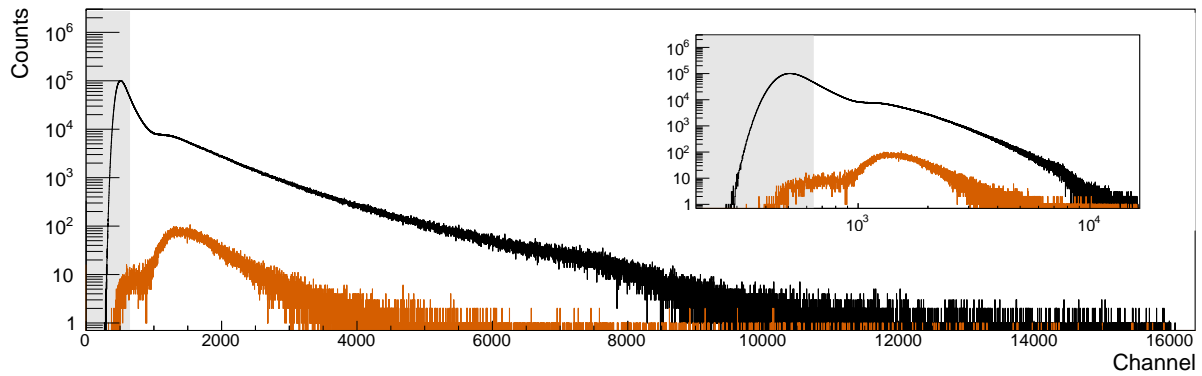


Figure B.4: Pulse height spectra of panel #44 (cf. figure 3.17). The histogram of the raw data is shown in black, and the events, which are coincident with events in TU1 are shown in orange. The area in grey is excluded by the cut concerning E_{thresh} . See section 4.4.6 for details.

B.2 Delayed coincidences in TU1

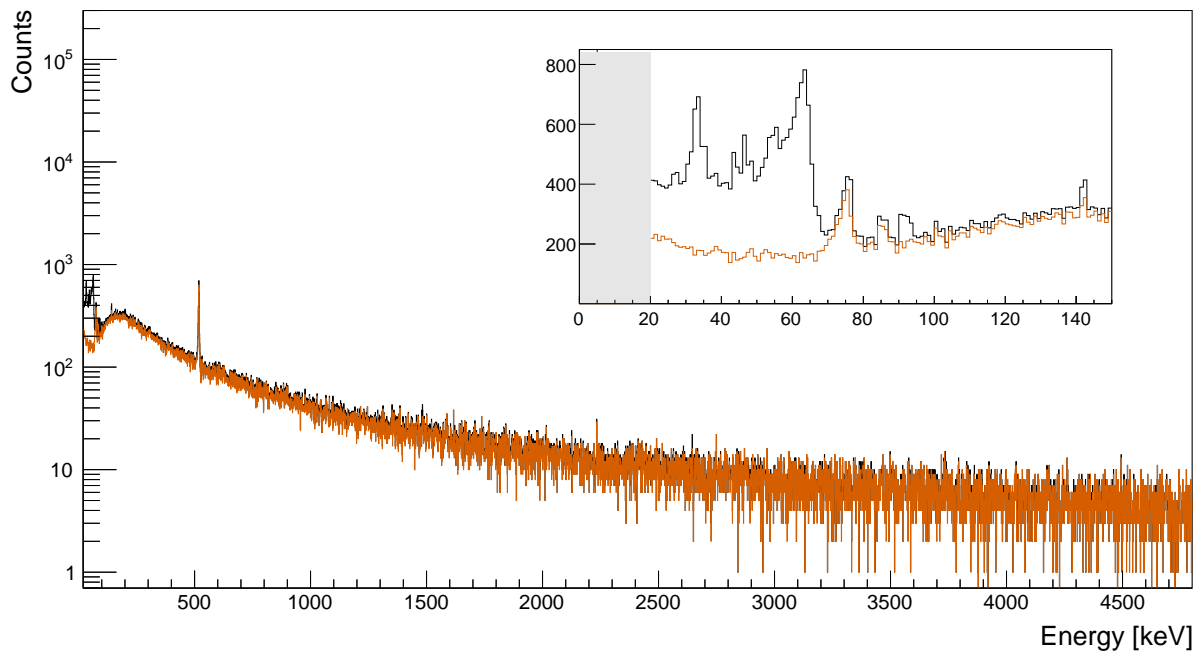


Figure B.5: Raw pulse height spectrum of the passively shielded TU1 (black), as well as the coincident events in orange. The corresponding coincidence timing window is $[-5 \mu\text{s}, 0 \mu\text{s}]$. The area in grey is excluded by the cut concerning E_{thresh} .

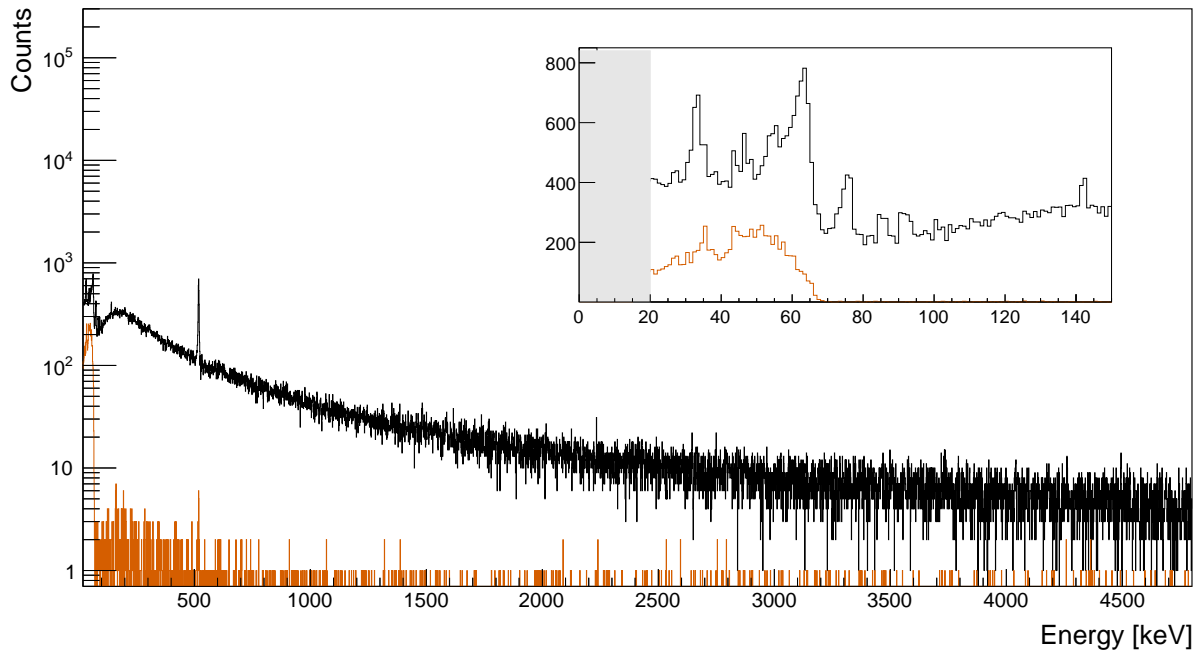


Figure B.6: Raw pulse height spectrum of the passively shielded TU1 (black), as well as the coincident events in orange. The corresponding coincidence timing window is $[-50 \mu\text{s}, -5 \mu\text{s}]$. The area in grey is excluded by the cut concerning E_{thresh} .

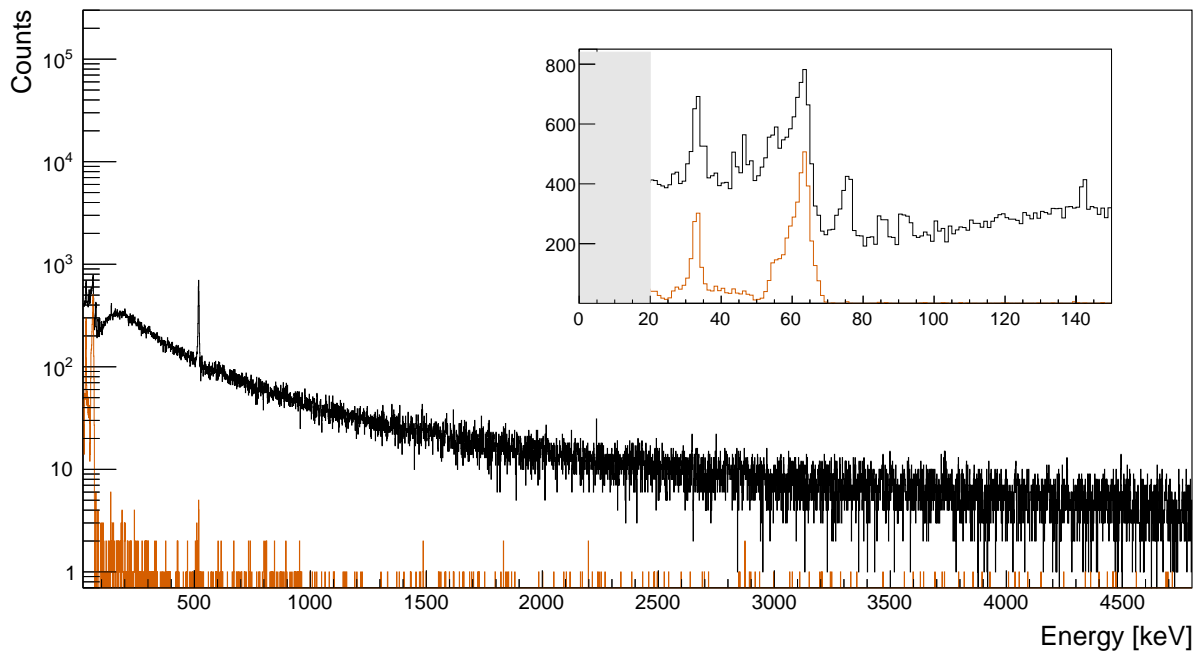


Figure B.7: Raw pulse height spectrum of the passively shielded TU1 (black), as well as the coincident events in orange. The corresponding coincidence timing window is $[-150 \mu\text{s}, -50 \mu\text{s}]$. The area in grey is excluded by the cut concerning E_{thresh} .

B.3 Time delay dependency for each panel

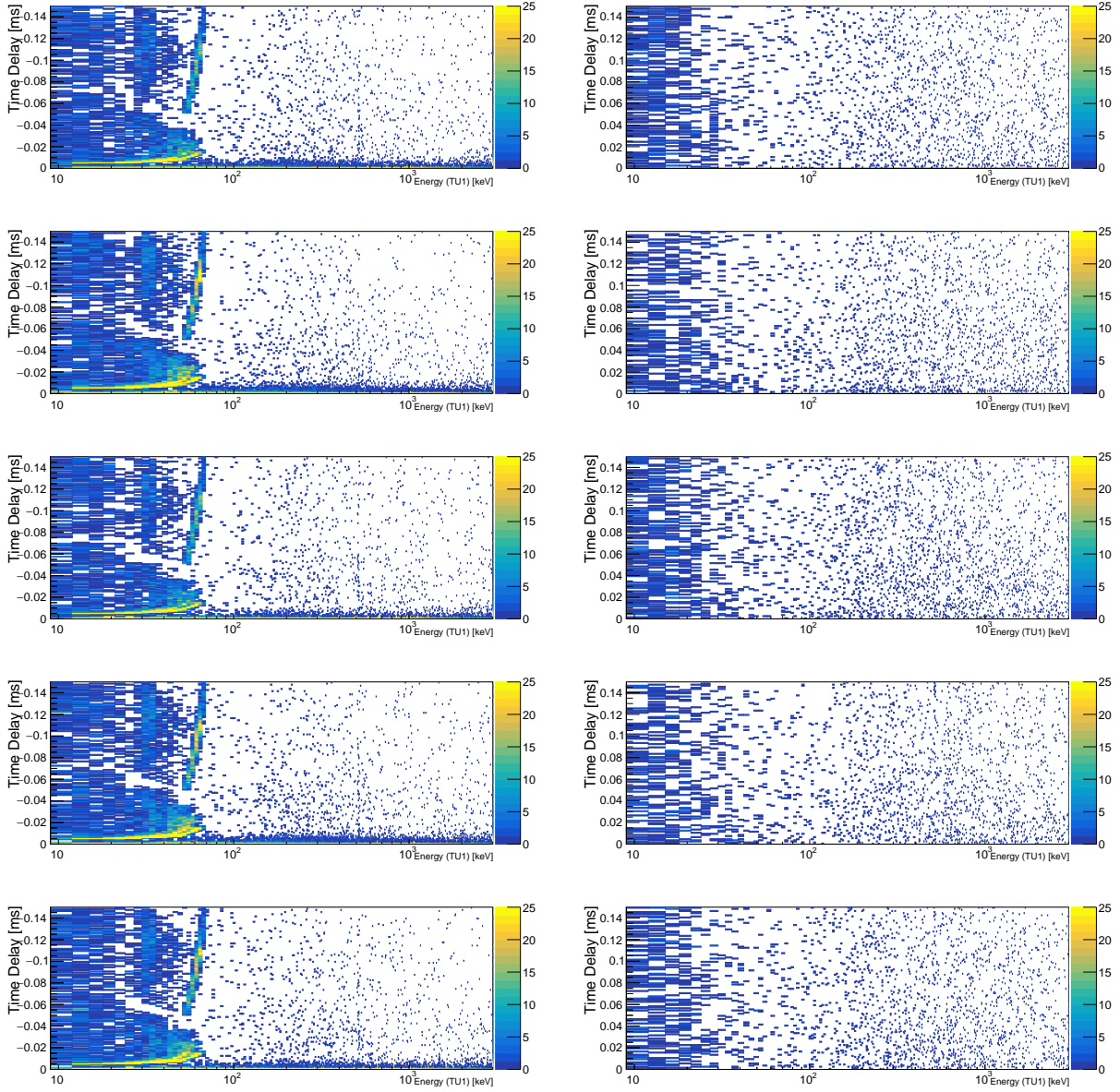


Figure B.8: Left figures: Time delay between two subsequent events, which first occur in one of the panels, and then in TU1 with respect to the energy deposition in TU1. Right figures: Time delay between two subsequent events, which first occur in TU1, and then in one of the panels with respect to the energy deposition in TU1. The left figures show the actual timing interval of $t_{\text{coinc}} = [-150 \mu\text{s}, 0 \mu\text{s}]$, which is also used for the final cut. For the sake of comparability, the right figures also show $t_{\text{coinc}} = [0 \mu\text{s}, +150 \mu\text{s}]$, despite only using $t_{\text{coinc}} = [0 \mu\text{s}, +5 \mu\text{s}]$ for the final cut. From top to bottom: Coincidences with panel #15, #16, #17, #44, and #45.

B.4 Time delay dependency for energy depositions in the panels

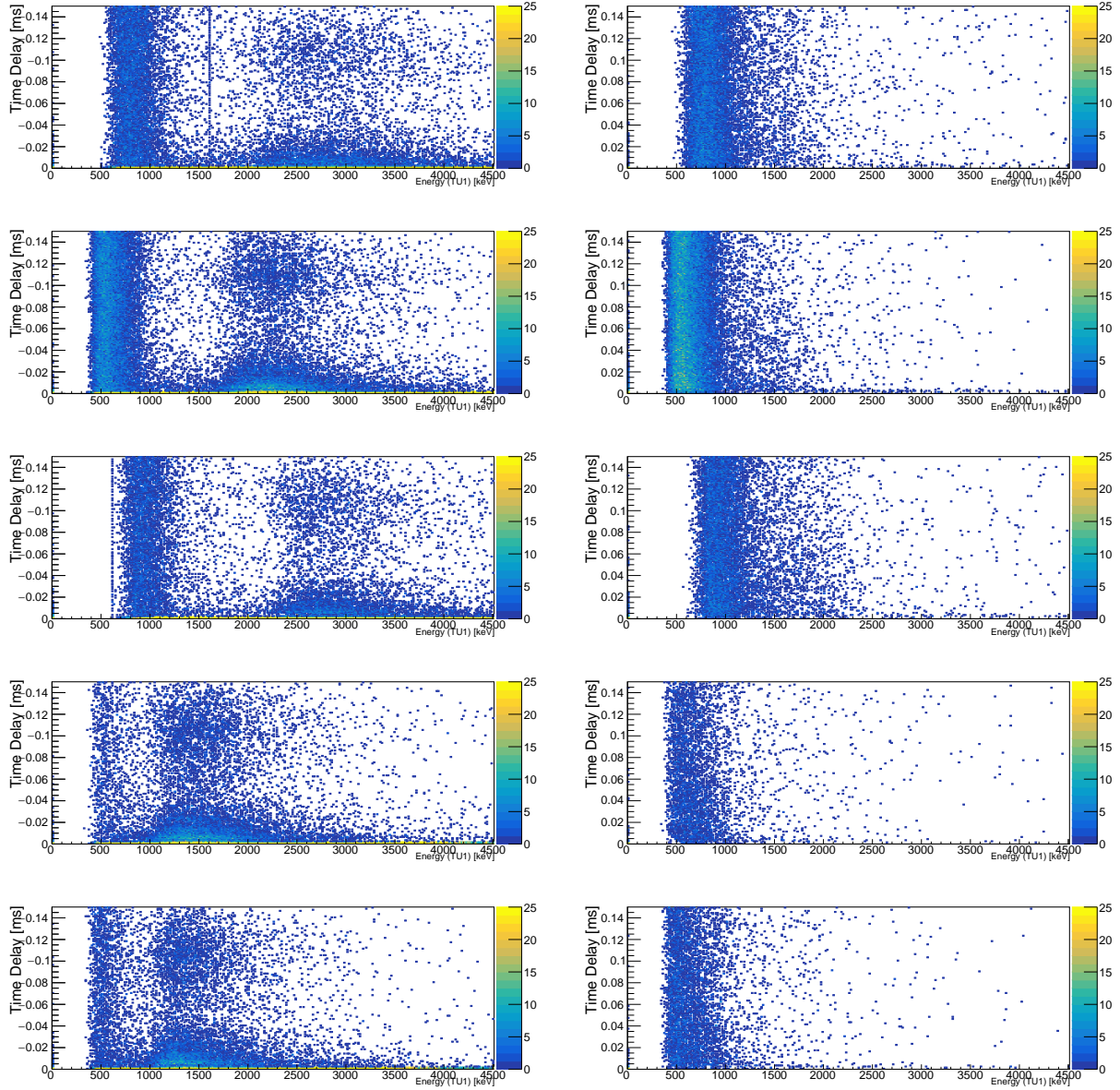
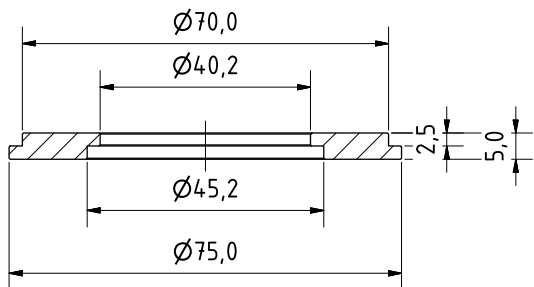


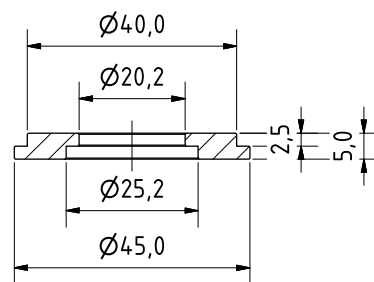
Figure B.9: Left figures: Time delay between two subsequent events, which first occur in one of the panels, and then in TU1 with respect to the energy deposition in the subsequent panel. Right figures: Time delay between two subsequent events, which first occur in TU1, and then in one of the panels with respect to the energy deposition in the subsequent panel. The left figures show the actual timing interval of $t_{\text{coinc}} = [-150 \mu\text{s}, 0 \mu\text{s}]$, which is also used for the final cut. For the sake of comparability, the right figures also show $t_{\text{coinc}} = [0 \mu\text{s}, +150 \mu\text{s}]$, despite only using $t_{\text{coinc}} = [0 \mu\text{s}, +5 \mu\text{s}]$ for the final cut. From top to bottom: Coincidences with panel #15, #16, #17, #44, and #45.

B.5 Technical drawings of the final target holder for TU1

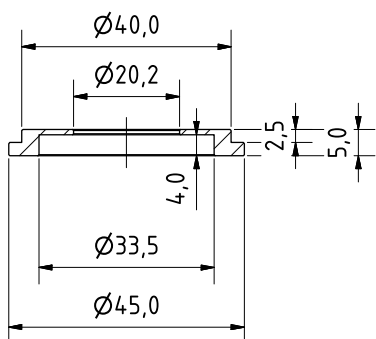
Sample holder 1



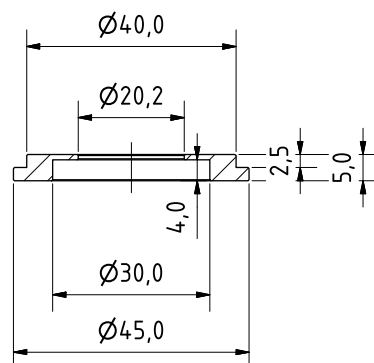
Sample holder 2



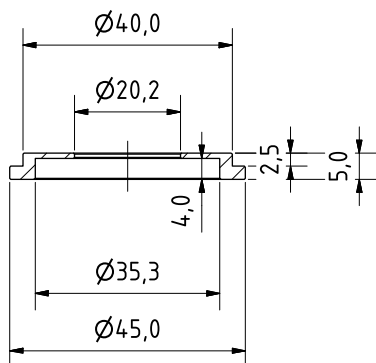
Sample holder 3



Sample holder 4



Sample holder 5



Distance rods 1/2

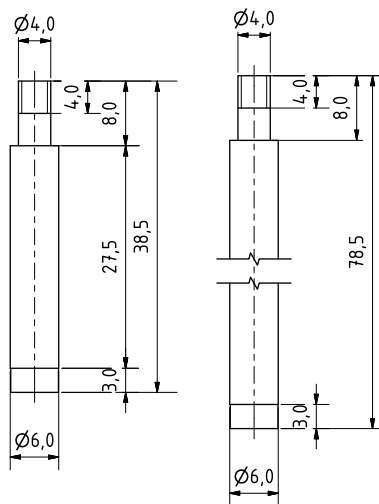


Figure B.10: Technical drawings of the new target holder for TU1. From top left to bottom right: Sample holder 1, Sample holder 2, Sample holder 3 (for HZDR samples), Sample holder 4 (for PTB calibration sources), Sample holder 5 (for the ^{88}Y source at FK, and the distance rods 1/2. More information can be found in section 4.7.

C Appendix regarding the ${}^2\text{H}(p,\gamma){}^3\text{He}$ reaction

C.1 The S -factor fit for ${}^2\text{H}(p,\gamma){}^3\text{He}$ with Mossa et al.

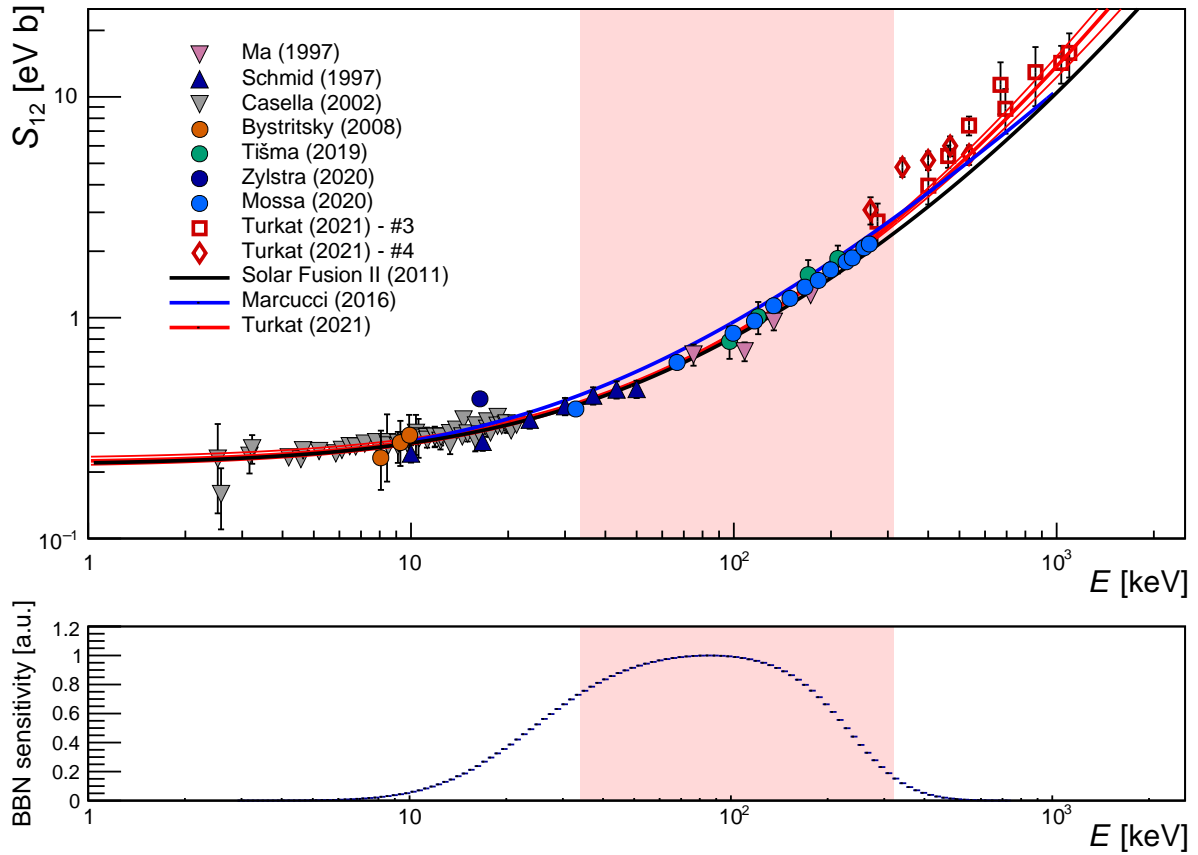


Figure C.1: This plot and its legend is identical to figure 5.12, but showing the dominating data set of Mossa et al. [48] as well. The new S -factor fit (red) here is therefore also including all data sets along with their standard deviation (1σ).

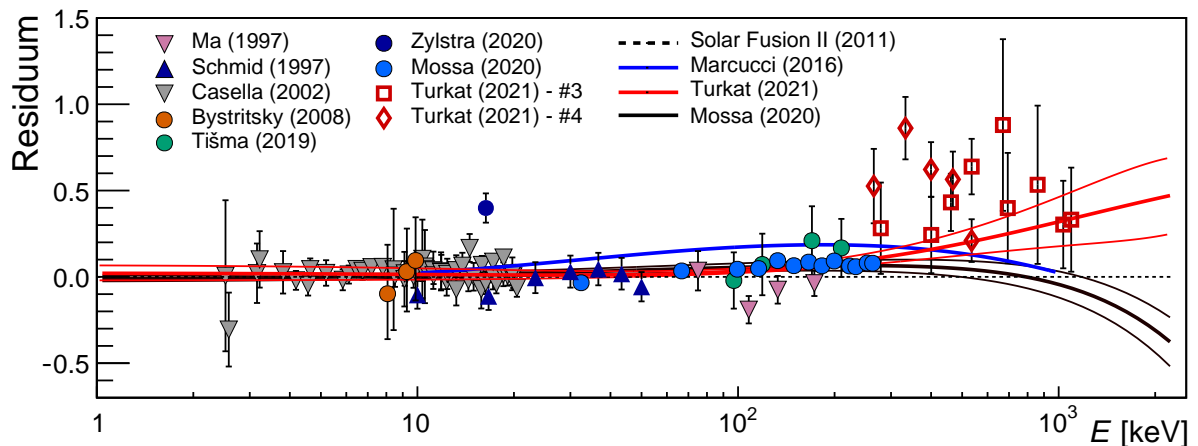


Figure C.2: This plot and its legend is identical to figure 5.13, but showing the dominating data set of Mossa et al. [48] as well. The residuum of the new S -factor fit with respect to the Solar Fusion II fit (red) is therefore also including all data sets including Mossa et al. While the resulting fit by Mossa et al. is not shown in figure C.1 for sake of clarity, it is plotted here as additional black line. The legend in this figure is identical to the items in figure C.1

C.2 Pulse height spectra for the ${}^2\text{H}(p,\gamma){}^3\text{He}$ campaign

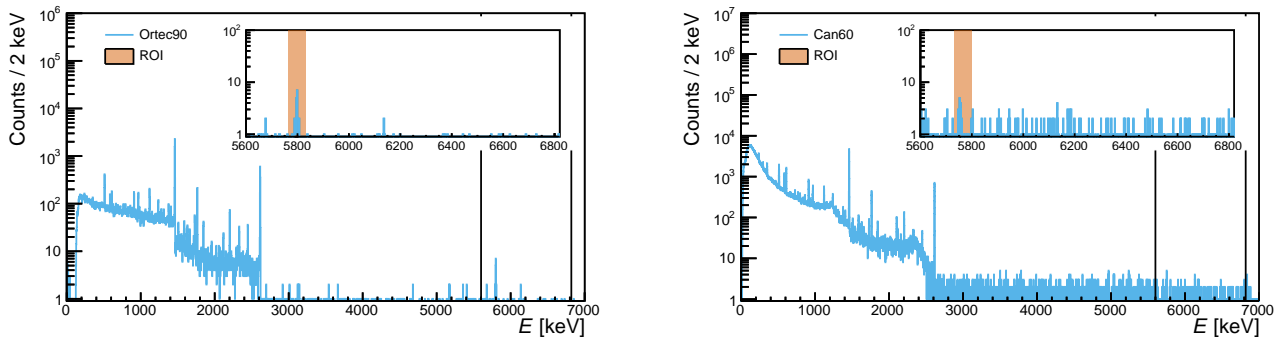


Figure C.3: $E_{\text{cm}} = 278.7$ keV (cf. table 5.1) & TiD2-2-3. The inlets with $E = (5600 - 6800)$ keV are indicated by two vertical black lines. Left: Result of Ortec90. Right: Result of Can60.

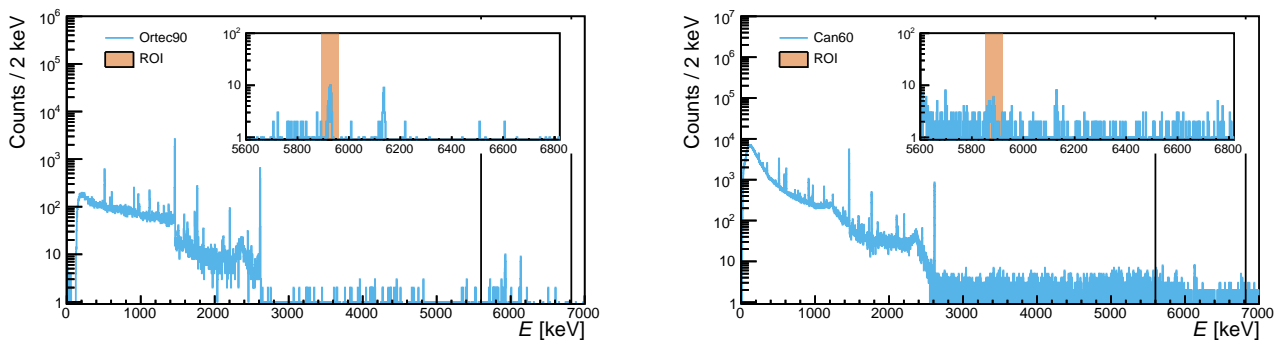


Figure C.4: $E_{\text{cm}} = 400.4$ keV (cf. table 5.1) & TiD2-2-3. The inlets with $E = (5600 - 6800)$ keV are indicated by two vertical black lines. Left: Result of Ortec90. Right: Result of Can60.

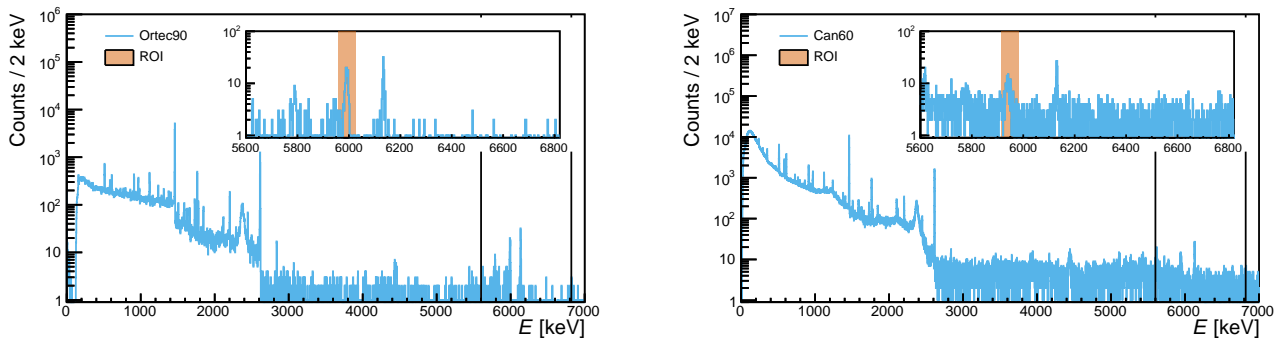


Figure C.5: $E_{\text{cm}} = 461.3$ keV (cf. table 5.1) & TiD2-2-3. The inlets with $E = (5600 - 6800)$ keV are indicated by two vertical black lines. Left: Result of Ortec90. Right: Result of Can60.

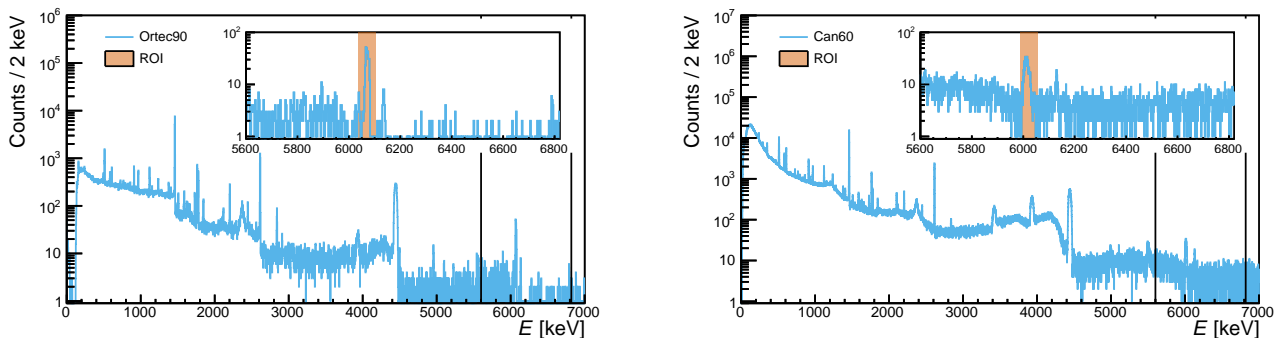


Figure C.6: $E_{\text{cm}} = 535.3$ keV (cf. table 5.1) & TiD2-2-3. The inlets with $E = (5600 - 6800)$ keV are indicated by two vertical black lines. Left: Result of Ortec90. Right: Result of Can60.

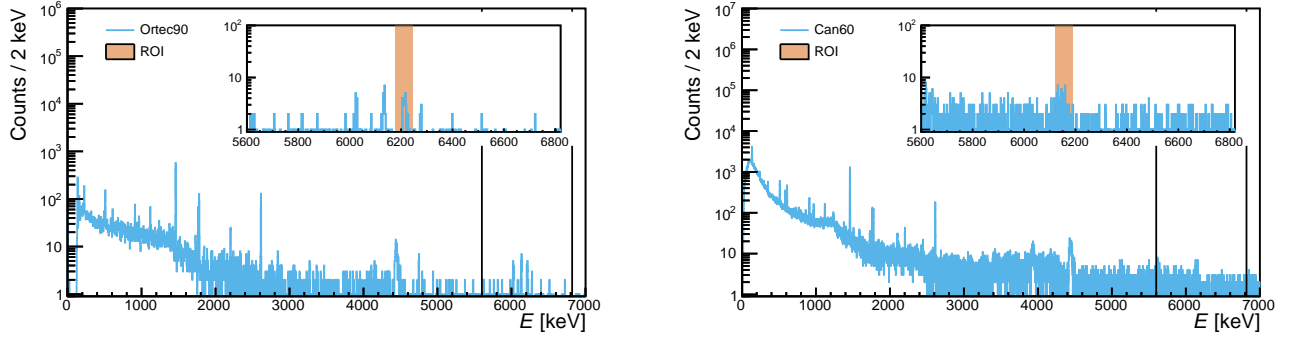


Figure C.7: $E_{\text{cm}} = 670.1$ keV (cf. table 5.1) & TiD2-2-3. The inlets with $E = (5600 - 6800)$ keV are indicated by two vertical black lines. Left: Result of Ortec90. Right: Result of Can60.

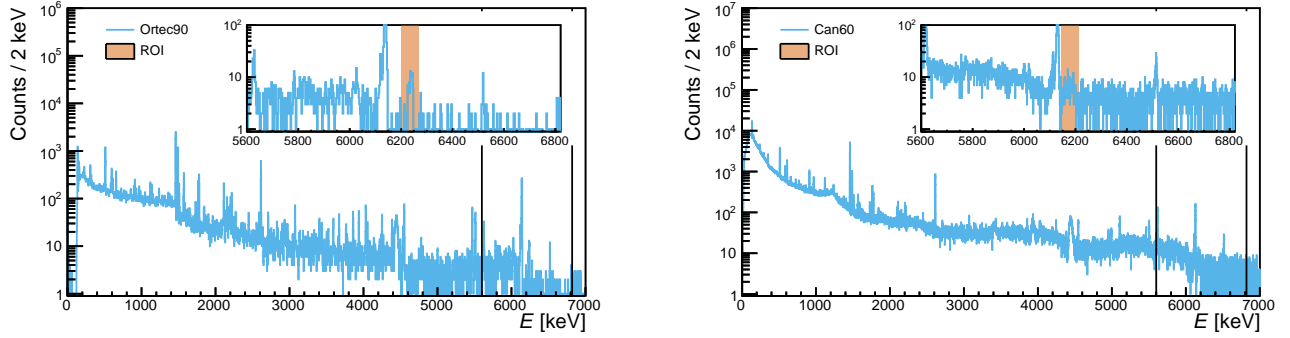


Figure C.8: $E_{\text{cm}} = 693.8$ keV (cf. table 5.1) & TiD2-2-3. The inlets with $E = (5600 - 6800)$ keV are indicated by two vertical black lines. Left: Result of Ortec90. Right: Result of Can60.

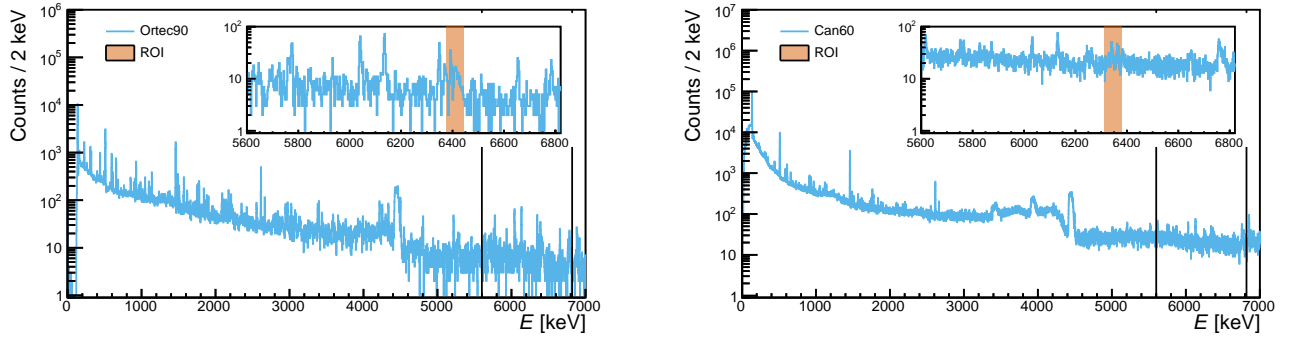


Figure C.9: $E_{\text{cm}} = 859.8$ keV (cf. table 5.1) & TiD2-2-3. The inlets with $E = (5600 - 6800)$ keV are indicated by two vertical black lines. Left: Result of Ortec90. Right: Result of Can60.

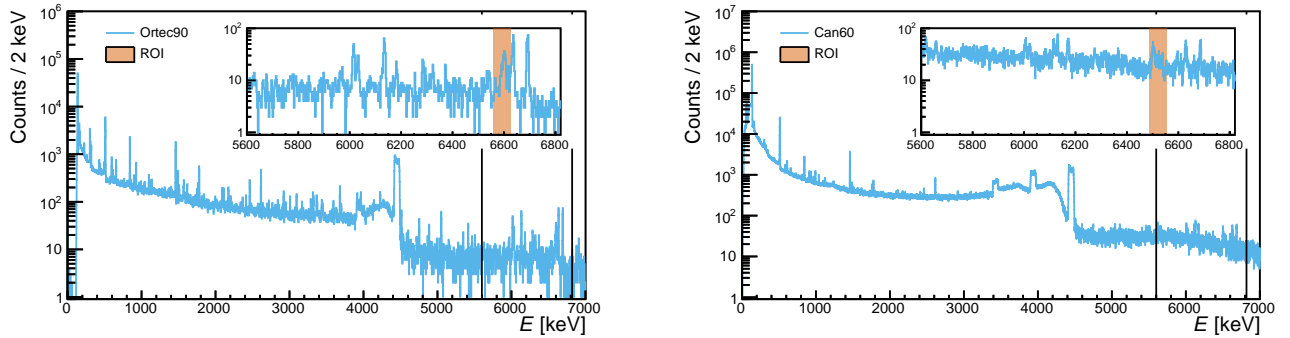


Figure C.10: $E_{\text{cm}} = 1033.4$ keV (cf. table 5.1) & TiD2-2-3. The inlets with $E = (5600 - 6800)$ keV are indicated by two vertical black lines. Left: Result of Ortec90. Right: Result of Can60.

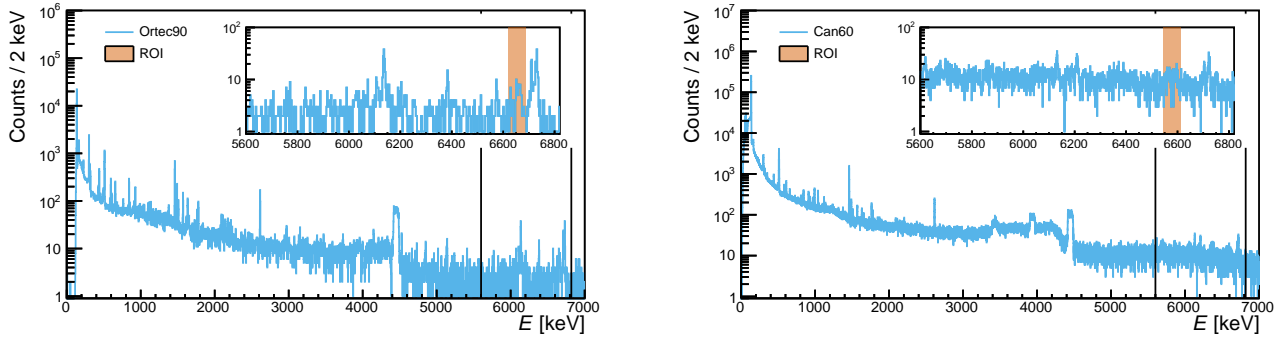


Figure C.11: $E_{\text{cm}} = 1094.2$ keV (cf. table 5.1) & TiD2-2-3. The inlets with $E = (5600 - 6800)$ keV are indicated by two vertical black lines. Left: Result of Ortec90. Right: Result of Can60.

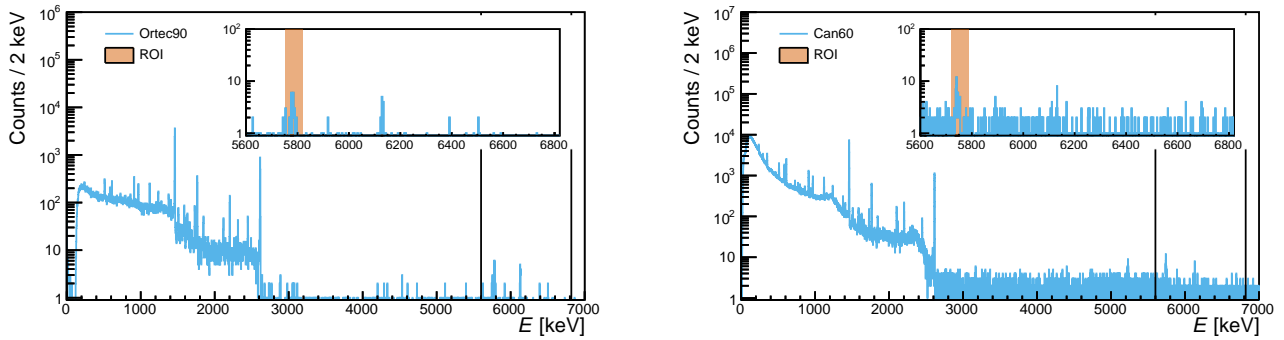


Figure C.12: $E_{\text{cm}} = 265.1$ keV (cf. table 5.1) & TiD2-2-4. The inlets with $E = (5600 - 6800)$ keV are indicated by two vertical black lines. Left: Result of Ortec90. Right: Result of Can60.

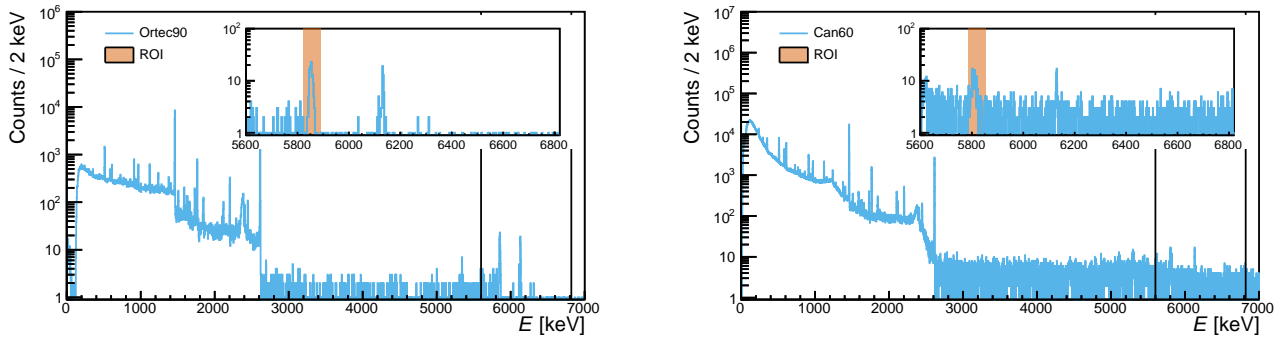


Figure C.13: $E_{\text{cm}} = 332.8$ keV (cf. table 5.1) & TiD2-2-4. The inlets with $E = (5600 - 6800)$ keV are indicated by two vertical black lines. Left: Result of Ortec90. Right: Result of Can60.

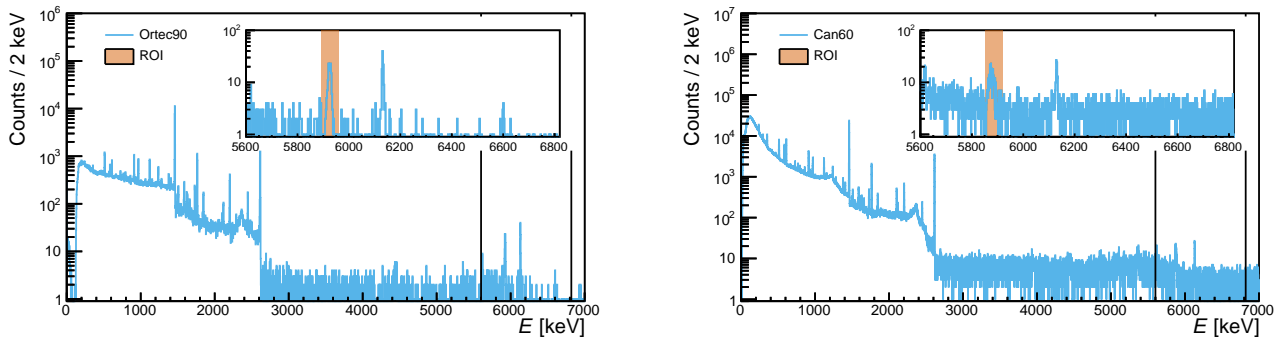


Figure C.14: $E_{\text{cm}} = 399.8$ keV (cf. table 5.1) & TiD2-2-4. The inlets with $E = (5600 - 6800)$ keV are indicated by two vertical black lines. Left: Result of Ortec90. Right: Result of Can60.

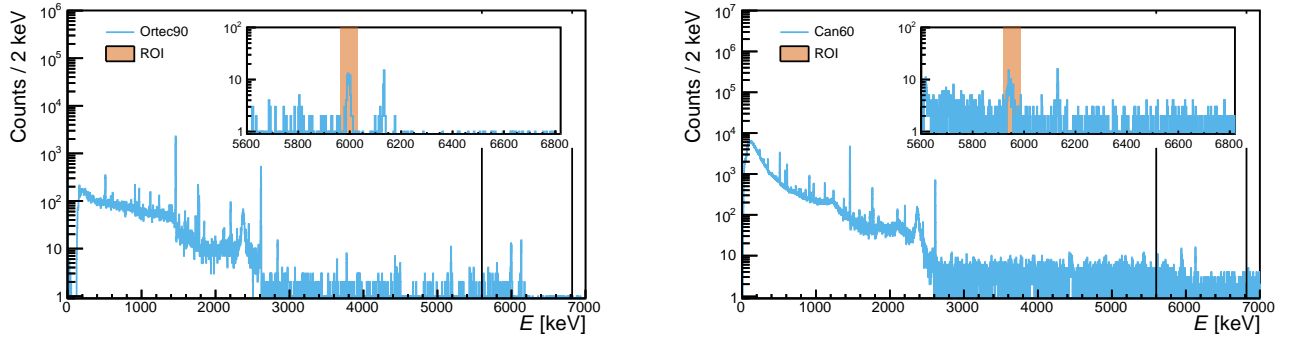


Figure C.15: $E_{\text{cm}} = 467.8$ keV (cf. table 5.1) & TiD2-2-4. The inlets with $E = (5600 - 6800)$ keV are indicated by two vertical black lines. Left: Result of Ortec90. Right: Result of Can60.

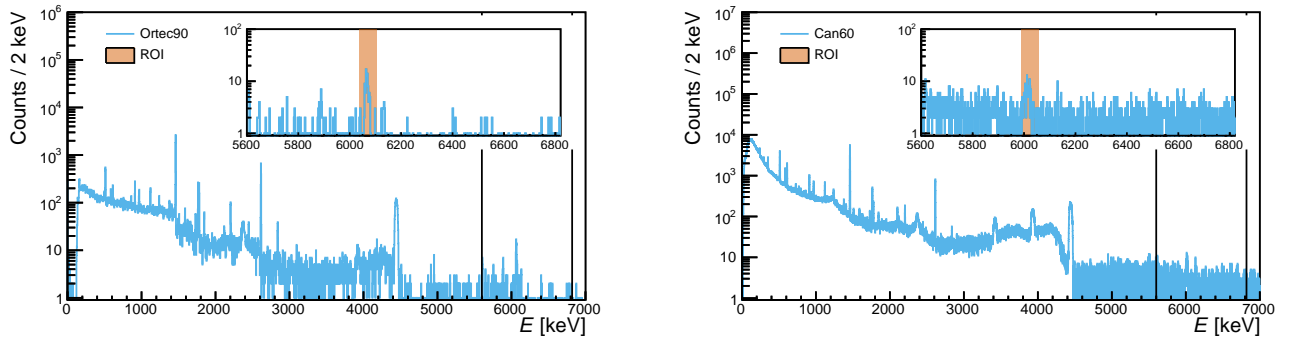


Figure C.16: $E_{\text{cm}} = 535.3$ keV (cf. table 5.1) & TiD2-2-4. The inlets with $E = (5600 - 6800)$ keV are indicated by two vertical black lines. Left: Result of Ortec90. Right: Result of Can60.

D Appendix regarding the ${}^3\text{He}(\alpha,\gamma){}^7\text{Be}$ reaction

D.1 Photos of irradiated targets and targets setups

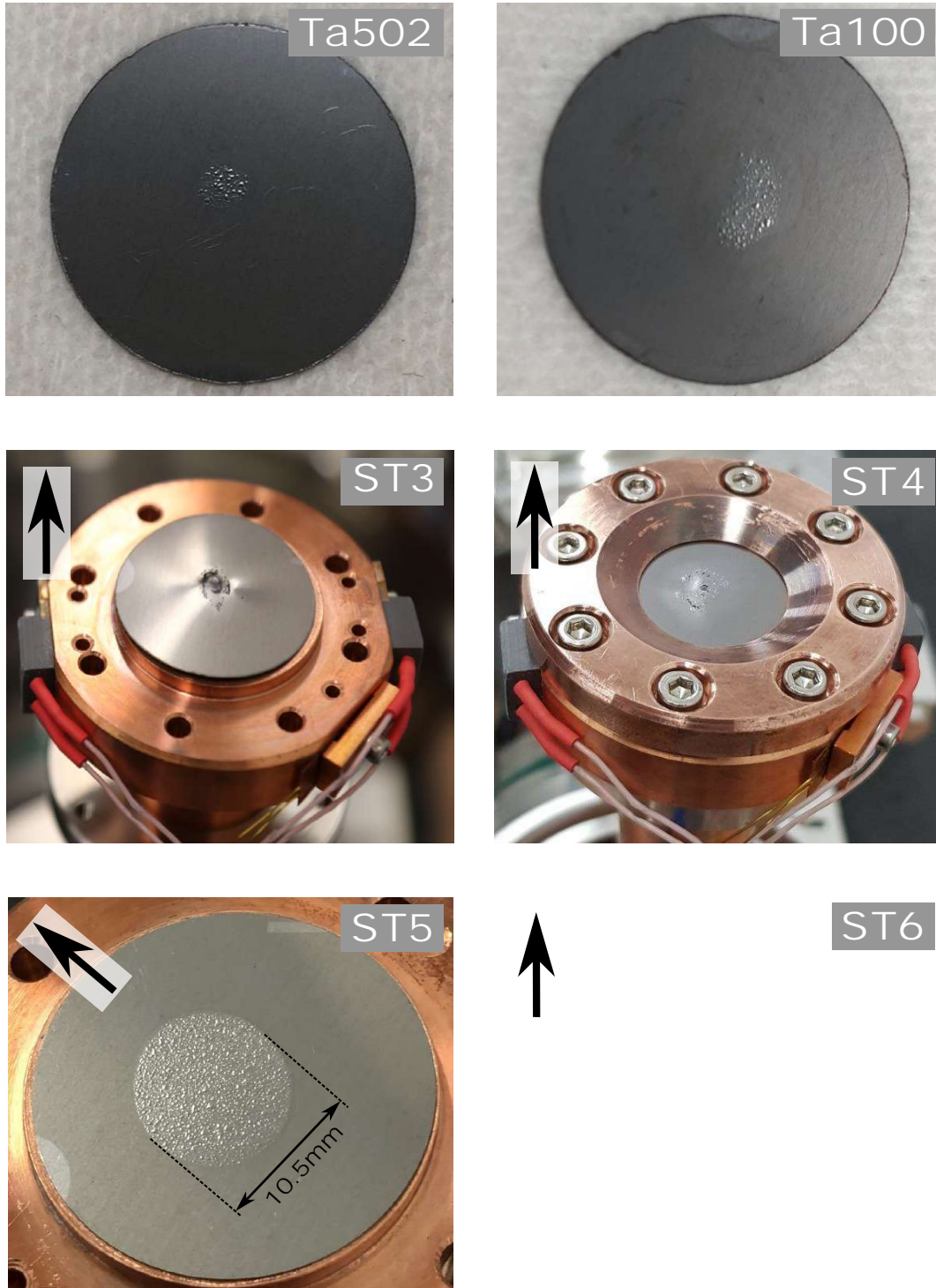


Figure D.1: Photos of several targets after irradiation. The name of the target is stated in the upper right edge of each photo (cf. table 3.3). The black arrow in the upper left edge of a photo indicates the top of the target, while it was vertically mounted on the target holder. The photos for the targets from IBC-I are shown in figure 3.7.

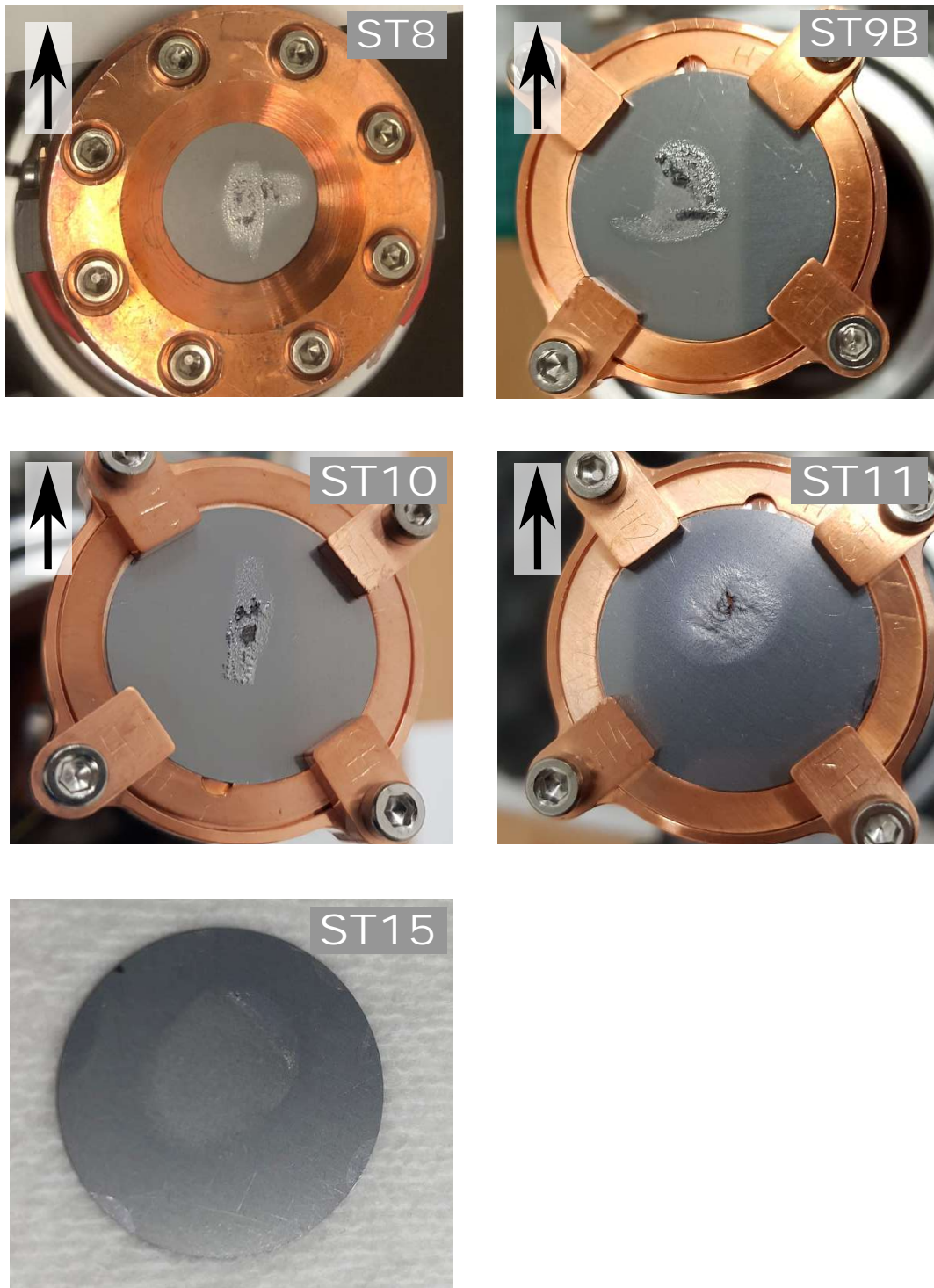


Figure D.2: Photos of several targets after irradiation. The name of the target is stated in the upper right edge of each photo (cf. table 3.3). The black arrow in the upper left edge of each photo indicates the top of the target, while it was vertically mounted on the target holder. The photos for the targets from IBC-I are shown in figure 3.7.

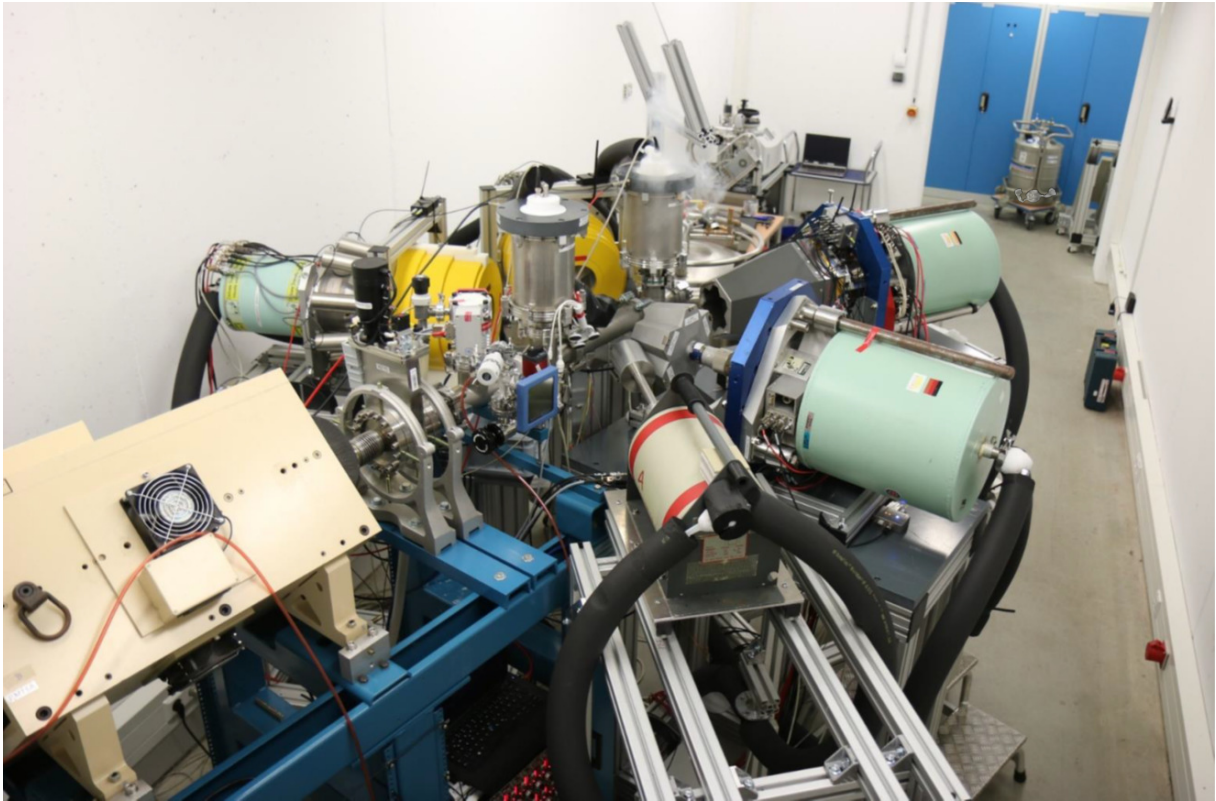


Figure D.3: Photo from the target area during first campaigns at FK. The beam propagates through the quadrupole magnet (beige in the lower left) towards the target (in the center of the photo). The surrounding detectors are all mounted horizontally and pointed towards the target.

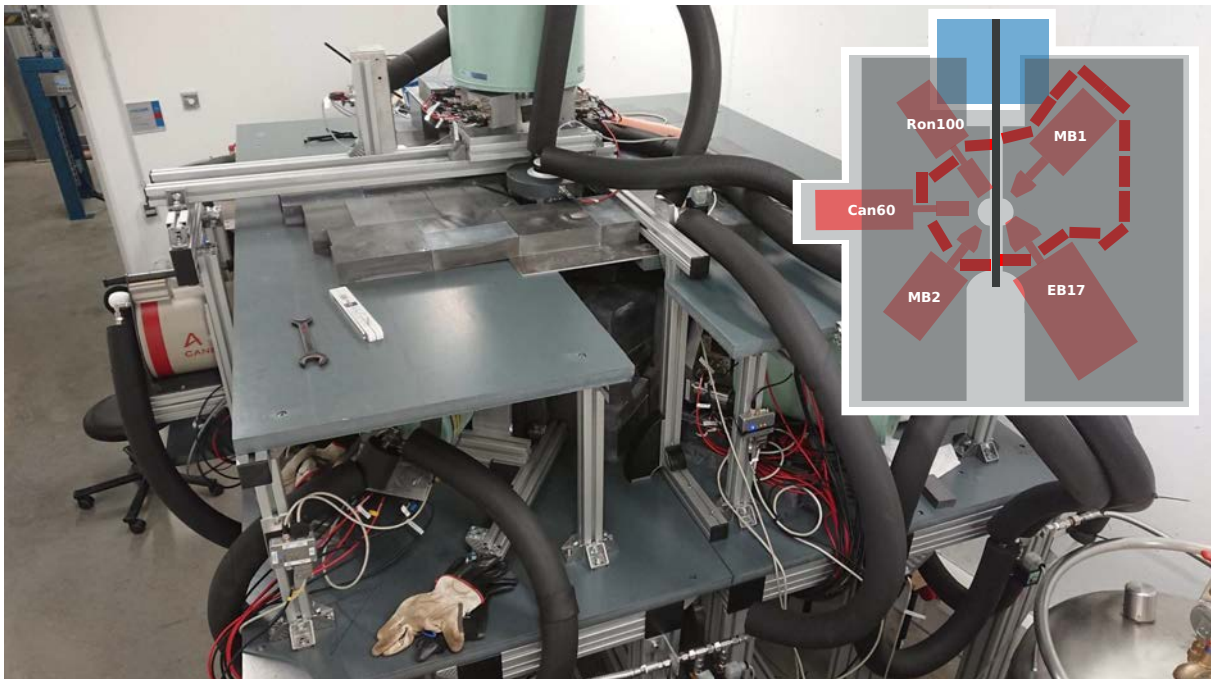


Figure D.4: Setup of the target area during FK-V and prior to the building of the surrounding lead castle. The lead is added on top of both platforms, as well as stapled around the HPGe crystals. The inlet gives an insight between the platforms and also shows an approximate position of the surrounding lead bricks (red).

D.2 New dewar design for in-beam experiments at FK

An upgraded design for the LN2 dewars of the target cooling and the copper pipe cold trap became necessary in order to circumvent several problems with the respective first design (cf. section 3.1.6).

The top part of the first design was made of both a teflon element and a PVC element (cf. figure 3.4). On top of these two elements, ice was frequently building up during the operation of the cold trap. When this ice was melting, the resulting water ended up in between the PVC and the teflon and created a very thin water film, which subsequently was able to create an electric connection between the inner and the outer part of the cold trap (cf. figure 3.4). The new design is compensating this problem by substituting both elements with one single PVC element.

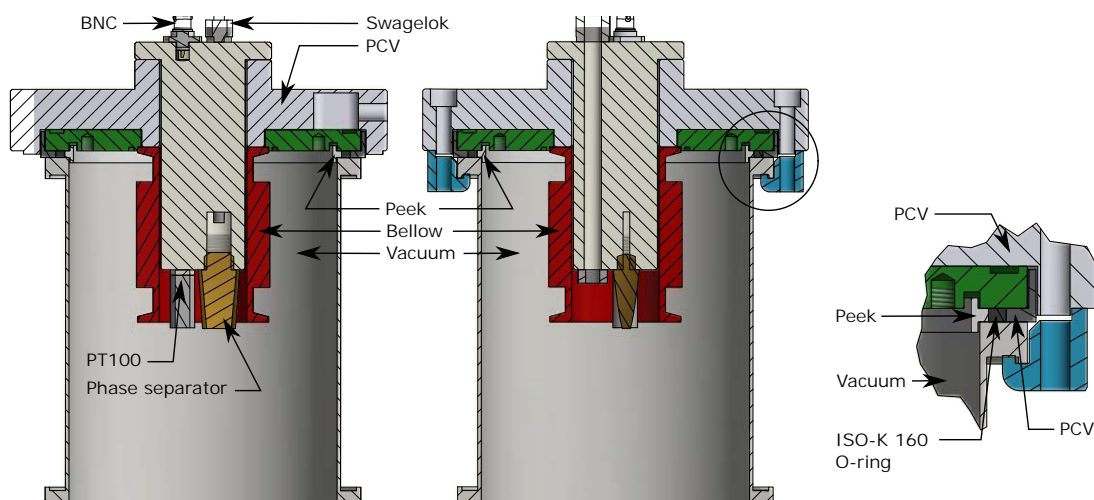


Figure D.5: Schematic drawing of the upgraded cold trap design for the target area at Felsenkeller. The inner LN2 dewar which is attached to the bellows is not shown, but is identical to the one in figure 3.4. Left: Cross section with focus on the PT100 and the corresponding BNC connector. Middle and right: Cross section with focus on the pipe for the LN2 dewar.

In order to further prevent any moisture from degrading the electrical insulation, the closest distance between any inner and outer metallic elements was increased by using the additional ‘L’-shaped PVC ring, which is shown in dark grey in the cutout of figure D.5. Prior to the upgrade, this was only a thin ring, which enhanced the electric insulation issues in case of any moisture.

Another unrelated problem was the build-up of icicles within the vertical exit channel for the gaseous nitrogen. As soon as water was building up on top, it dropped down into this exit channel and ultimately froze again due to the cold temperatures within the cold trap. These icicles acted as a plug, which prevented the nitrogen gas from exiting. Hence, also no new LN2 was able to enter due to the intrinsic over pressure. This problem was circumvented by implementing a solid pipe into the vertical exit channel (cf. middle drawing in figure D.5), which is connected to a swagelok adapter on top (cf. left drawing in figure D.5). By connecting this to another pipe, it successfully prevented water from entering the LN2 dewar.

D.3 Tests for improving the thermal conductivity

Prior to the in-beam campaigns at Felsenkeller, a new target setup was designed (cf. section 3.4.1). As discussed earlier, the length of the Y-shaped chamber is a compromise between the necessary ability to arrange the detectors around the chamber, and the demand to design it as short as possible in order to guarantee an acceptable heat conductivity between the LN2 dewar and the target.

The structural, as well as the thermal connection between the target and its holder is realized by the use of clamps and screws, which are pressing the target onto the holder. Considering an efficient thermal conductivity, this approach (despite being without suitable alternatives) is non-ideal due to the fact, that it certainly marks its ‘weakest’ point. While these clamps are responsible for the majority of heat transfer, the center of the target is only loosely touching its holder behind. The resulting labyrinth for the heat to be dissipated from the beam spot will therefore inevitably lead to subsequently higher temperatures in the beam spot and therefore to an increase in heat-induced diffusion processes. In order to further reduce the resulting temperature gradient, a thin film of heat conducting thermal paste between target and holder was tested (cf. figure D.6). This silicon-free paste has a thermal conductivity of only $\lambda = 0.9 \text{ W/mK}$, but its viscosity is suitable to physically connect the two metal surfaces. However, this paste is suitable only above $T = -50^\circ$, and became crumbly at lower temperatures. Furthermore, it completely lost its integrity during irradiation, as shown in figure D.6.

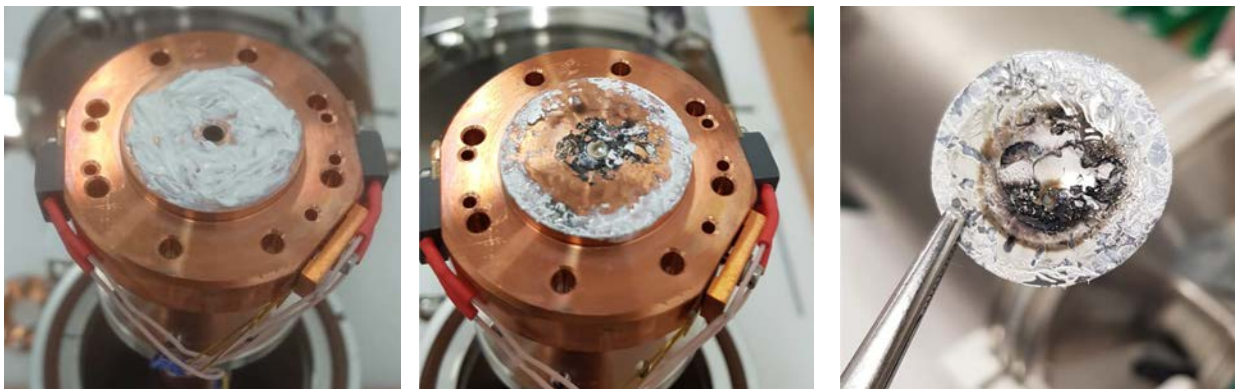


Figure D.6: Tests of increasing the heat conductivity between target and holder using thermal conductivity paste. Left: Picture of the target holder before irradiation on 02.11.2020. Middle and right: Picture of target holder and backside of the target after irradiation on 04.11.2020.

While thermal pastes do not seem to be suitable, also a thermal conductivity pad was tested. This solid, bendable pad is based on graphite and has a thickness of $100 \mu\text{m}$. Its thermal conductivity is $\lambda = 700 \text{ W/mK}$, which is even $\sim 4\text{x}$ larger compared to copper.

As shown in the lower left picture of figure D.7, the thermal pad does not lose its integrity during extreme cooling and subsequent irradiation of the target. In order to measure the effect of the thermal pad on the conductivity of the holder system, eight measurements with-

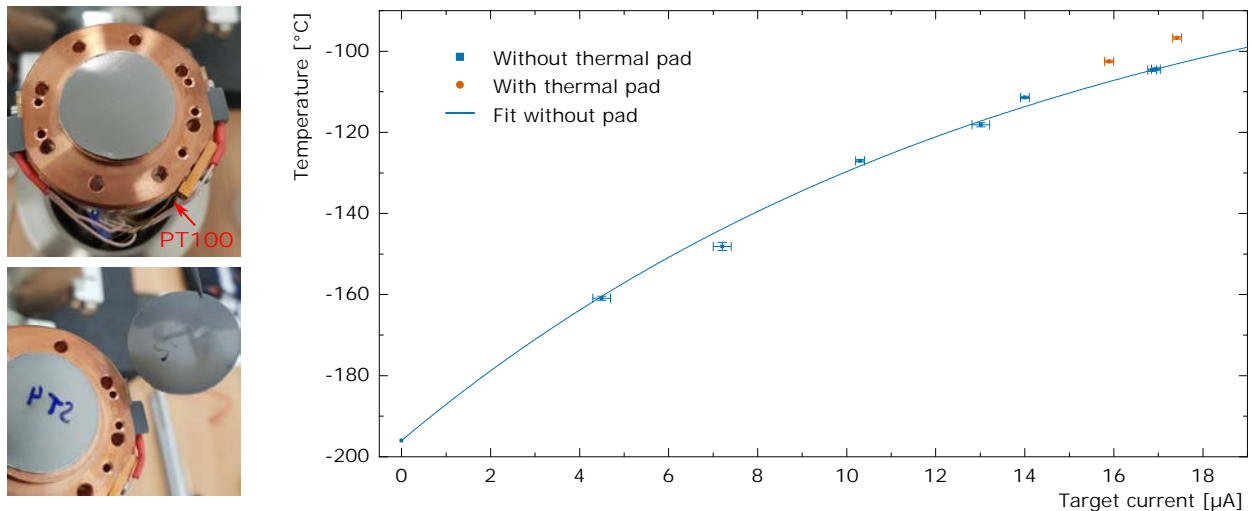


Figure D.7: Impact of a thermal pad on the conductivity of the target system. Top left: Photo of the thermal pad on the target holder before mounting the target ST4 on top. Bottom left: Photo during removal of the target after irradiation. The backside of the target is shown on the right. Right: Saturation temperature at the position of the PT100 (cf. upper left photo) with respect to the current on the target. The measurement was done with (red) and without (blue) thermal pad.

out thermal pad, and two measurements with the thermal pad are compared to each other. For each data point, the current on the target was kept stable until the target temperature saturated based on an equilibrium between LN2 cooling and simultaneous application of thermal power from the irradiation.

Due to the position of the PT100 being closer to the LN2 reservoir than the target, an increase of thermal conductivity (and therefore less steep temperature gradient) would result in a higher expected temperature readout. In other words: By increasing the conductivity due to the installation of the pad, the heat is dissipated more efficiently, which leads to a higher effective temperature at any given point between target and LN2 reservoir.

While the qualitative result in figure D.7 meets the expectation, the effect of $\Delta T = 6\text{ K}$ is only a comparatively small change in temperature. Despite the fact, that temperature difference in the beam spot will be comparatively larger, than the 6 K at the position of the PT100, the thermal pad is not assumed to be a worthwhile game changer.

It should be noted here, that these data points can only be used for comparison in case of a stable beam energy, stable beam optics and similar resulting beam spot position on the target. Any resulting effects on the saturation temperature due to small deviations in these parameters are not taken into account for the plotted uncertainties.

D.4 Resulting depth distributions during ion implantation

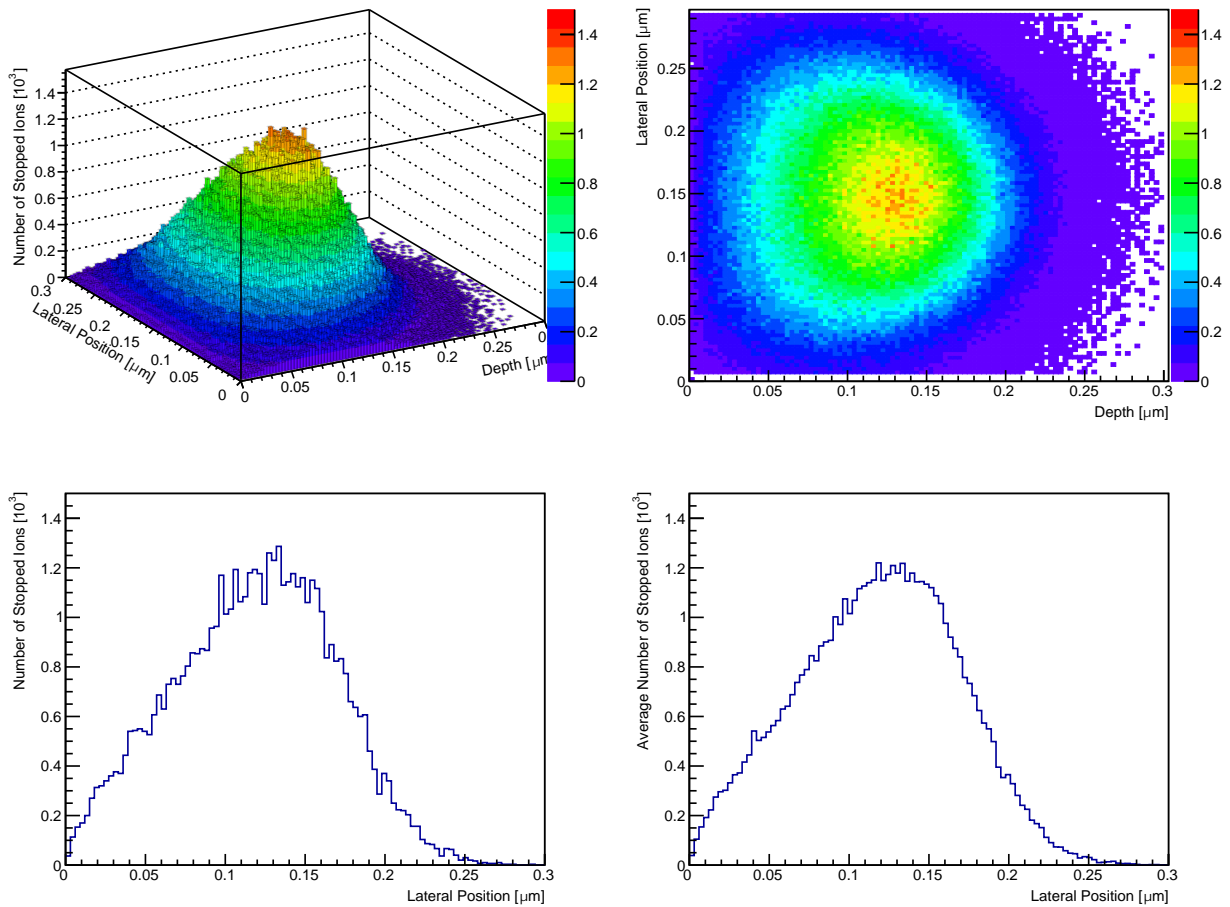


Figure D.8: Resulting ion depth distribution based on the implantation of ${}^3\text{He}$ ions with 45 keV into a tantalum blank, which entered perpendicular to the target surface at a lateral position of $0.15 \mu\text{m}$. The results are obtained using SRIM software. Upper left: Number of stopped ions as a 3D depth distribution. Upper right: Projection of the ion distribution onto the spatial axes. Lower left: 1D depth distribution for the central bin of the lateral position at $0.15 \mu\text{m}$. Lower right: 1D mean depth distribution for a $0.05 \mu\text{m}$ broad section around the central lateral position of $0.15 \mu\text{m}$.

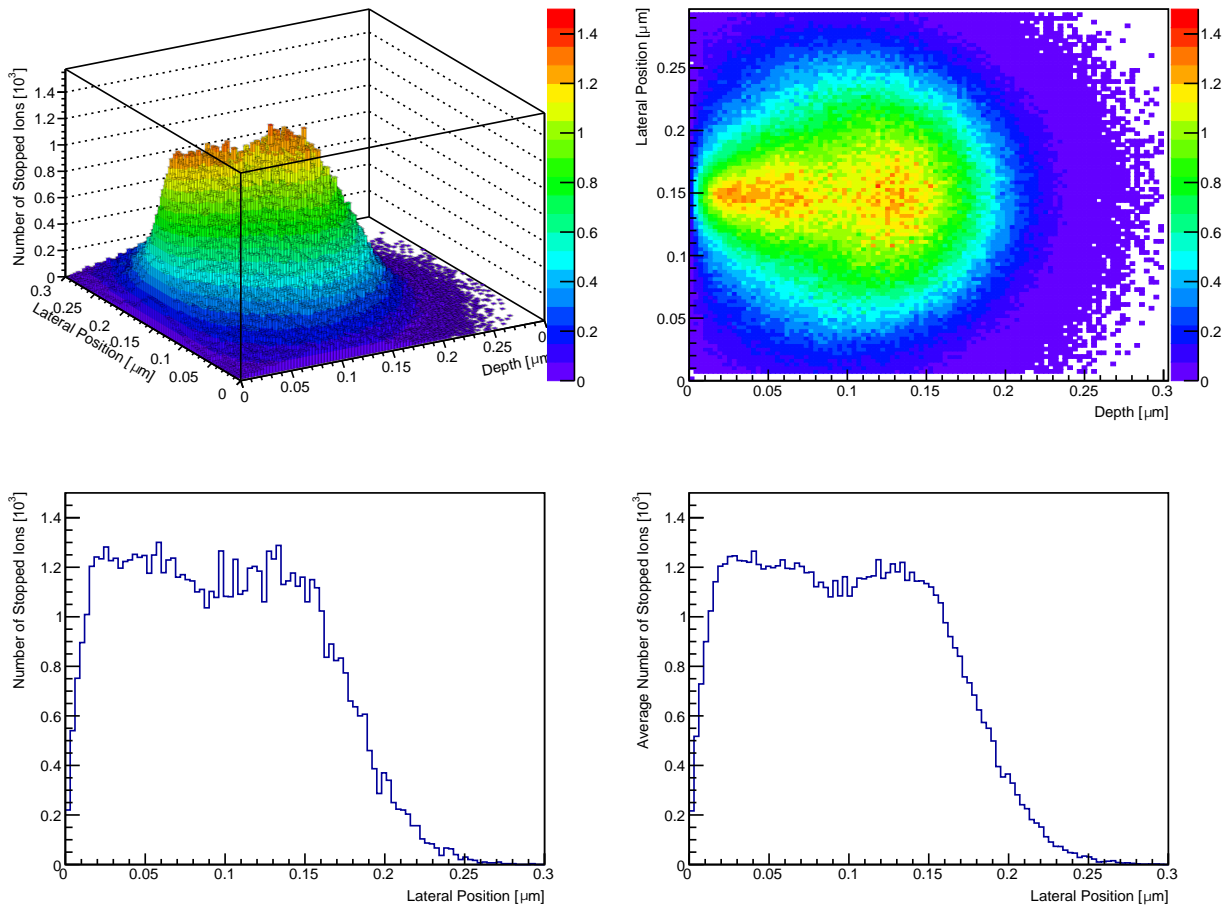


Figure D.9: Resulting ion depth distribution based on the implantation of ^3He ions with 45 keV, 15 keV and 5 keV into a tantalum blank, which entered perpendicular to the target surface at a lateral position of $0.15\ \mu\text{m}$. The results are obtained using SRIM software. Upper left: Number of stopped ions as a 3D depth distribution. Upper right: Projection of the ion distribution onto the spatial axes. Lower left: 1D depth distribution for the central bin of the lateral position at $0.15\ \mu\text{m}$. Lower right: 1D mean depth distribution for a $0.05\ \mu\text{m}$ broad section around the central lateral position of $0.15\ \mu\text{m}$.

D.5 The effective opening angle of HPGes

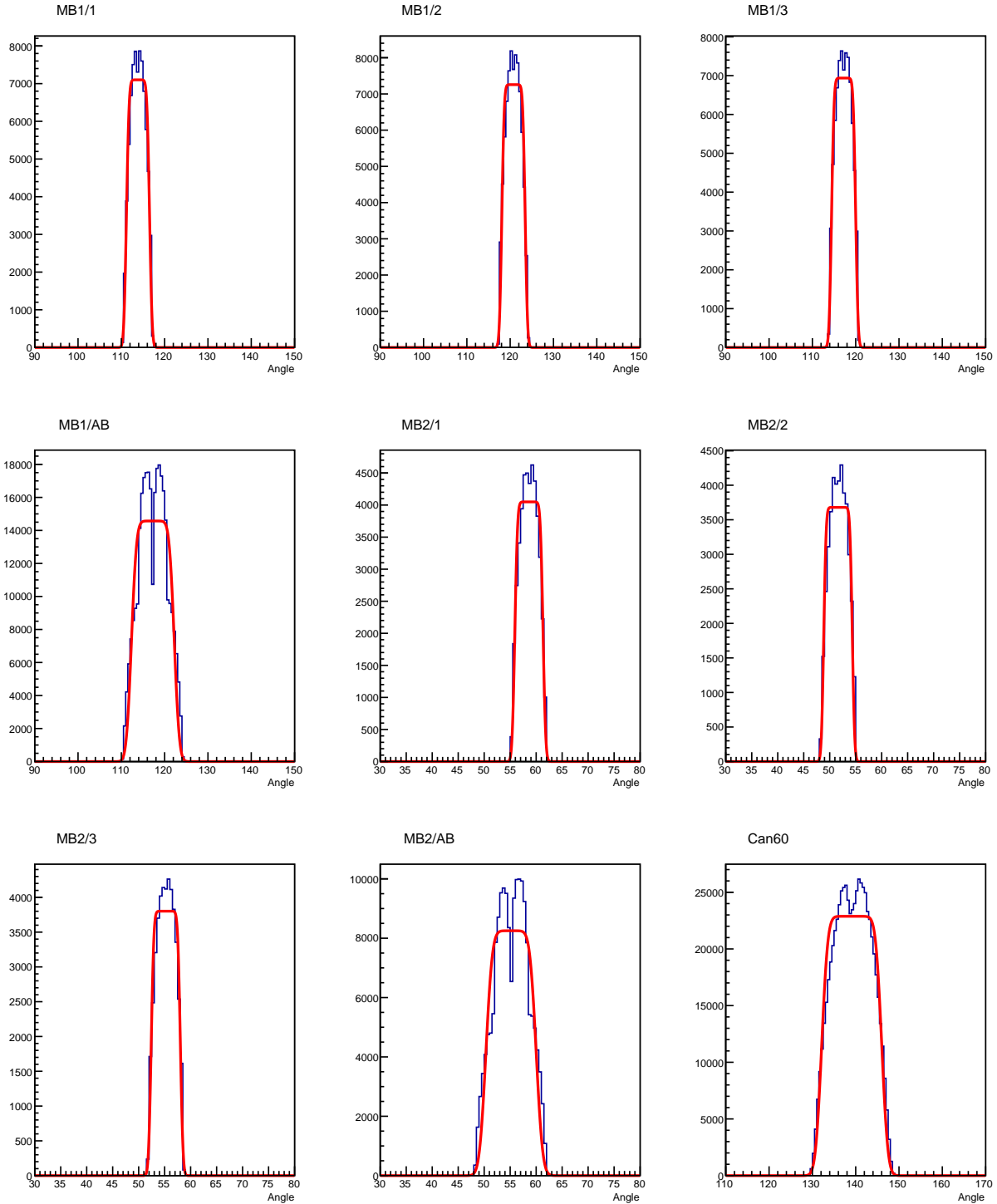


Figure D.10: Spectra from MB1, MB2 and Can60 for the determination of the effective opening angle. The data is based on simulations and shows the initial emission angle of full-energy peak events in a ceratin detector. The fit is based on a two-sided step function. The drop in certain detector centers is due to their bore hole, which decreases the change of a full-energy event and is more pronounced in case of close detector geometries. The notation “AB’ stands for the result of the addback mode.

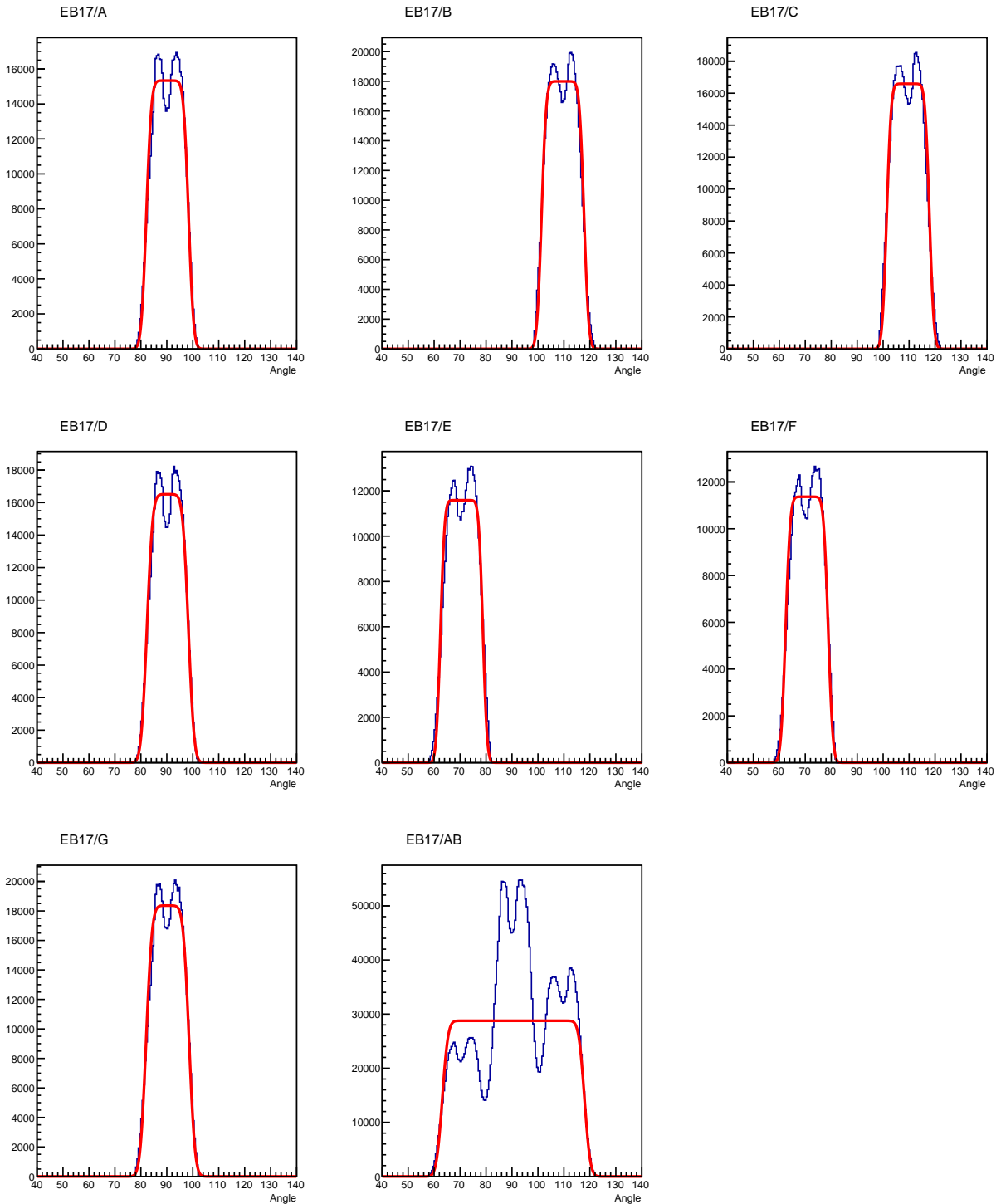


Figure D.11: Spectra from EB17 for the determination of the effective opening angle. The data is based on simulations and shows the initial emission angle of full-energy peak events in a ceratin detector. The fit is based on a two-sided step function. The drop in certain detector centers is due to their bore hole, which decreases the change of a full-energy event and is more pronounced in case of close detector geometries. The notation “AB” stands for the result of the addback mode.

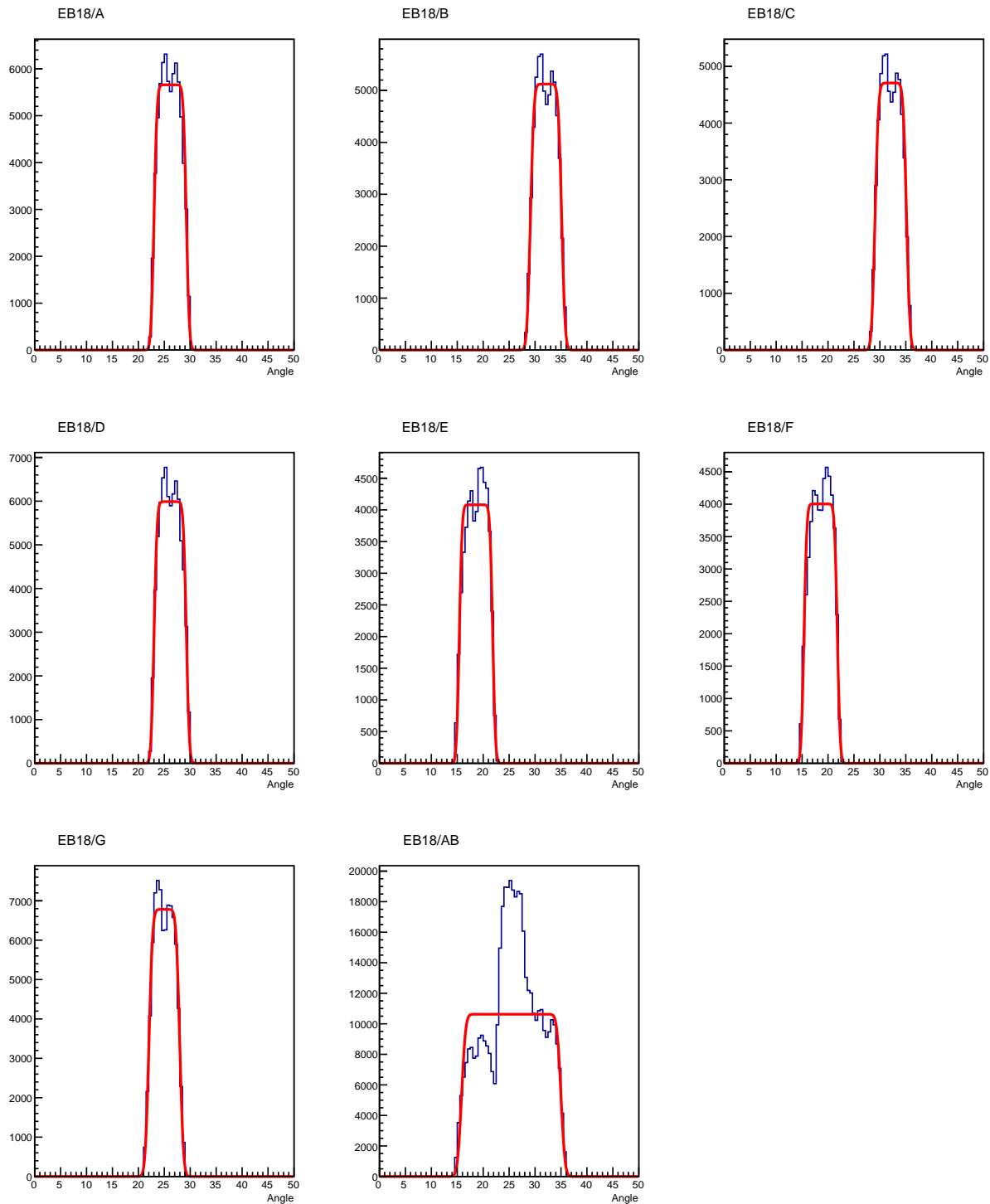


Figure D.12: Spectra from EB18 for the determination of the effective opening angle. The data is based on simulations and shows the initial emission angle of full-energy peak events in a ceratin detector. The fit is based on a two-sided step function. The drop in certain detector centers is due to their bore hole, which decreases the change of a full-energy event and is more pronounced in case of close detector geometries. The notation “AB” stands for the result of the addback mode.

D.6 Utilized runs for the analysis of FK-V

Table D.1: Utilized runs for the in-beam analysis of the FK-V campaign (cf. table 3.3). For each investigated irradiation energy, the run numbers are stated with respect to their use during the ‘ST’ campaigns, the ‘Ta’ campaigns or the ‘BG’ campaigns, respectively (cf. section 6.3.2).

E_{cm} [keV]	‘ST’ runs	‘Ta’ runs	‘BG’ runs
	Target ST9	Target Ta51	No Target
1217.1	0950, 0951, 0953, 0954, 0957, 0958, 0959, 0960, 0961, 0962, 0963, 0964, 0965, 0968, 0969, 0970, 0971	0976, 0977, 0978, 0979, 0980, 0981, 0982, 0983, 0984, 0985, 0986, 0987, 0989, 0991, 0995, 0996, 0997, 0998, 0999	1021, 1070, 1117, 1118 1186, 1215, 1216, 1217, 1218, 1219, 1220, 1221, 1222, 1223, 1224
	Target ST10	Target Ta52	No Target
901.2	1022, 1023, 1024, 1025, 1026, 1027, 1028, 1029, 1030, 1031, 1032, 1033, 1034, 1037, 1038, 1039, 1040, 1041, 1042, 1043, 1045, 1049, 1050, 1051, 1052, 1053, 1054, 1055, 1056, 1057, 1058, 1059, 1060, 1061, 1062, 1063, 1064, 1065, 1066, 1067, 1068	1072, 1073, 1074, 1075, 1076, 1077, 1078, 1080, 1081, 1082, 1083, 1084, 1085, 1086, 1087, 1088, 1089, 1090, 1091, 1092, 1093, 1094, 1095, 1096, 1097, 1098, 1099, 1100, 1101, 1102, 1103, 1104	1021, 1070, 1117, 1118 1186, 1215, 1216, 1217, 1218, 1219, 1220, 1221, 1222, 1223, 1224
	Target ST11+ST9B	Target Ta53	No Target
554.6	1120, 1121, 1122, 1123, 1124, 1125, 1126, 1127, 1131, 1132, 1135, 1136, 1137, 1154, 1155, 1156, 1157, 1158, 1159, 1160, 1162, 1163, 1164, 1167, 1168, 1169, 1170, 1171, 1172, 1173, 1174, 1175, 1176, 1179, 1180, 1181, 1182, 1183	1187, 1189, 1190, 1195, 1196, 1197, 1198, 1199, 1200, 1201, 1202, 1203, 1204, 1205, 1206, 1207, 1208, 1209, 1210, 1211	1021, 1070, 1117, 1118 1186, 1215, 1216, 1217, 1218, 1219, 1220, 1221, 1222, 1223, 1224
	Target ST15	Target Ta54	No Target
447.4	1232, 1233, 1234, 1235, 1236, 1237, 1238, 1239, 1241, 1242, 1243, 1244, 1245, 1246, 1247, 1248, 1249, 1250, 1251, 1252, 1255, 1256, 1257, 1258, 1259, 1260, 1261, 1262, 1263, 1264, 1265, 1266, 1267, 1268, 1269, 1270, 1271, 1272, 1273, 1274, 1279, 1280, 1282	1285, 1286, 1290, 1291, 1292, 1293, 1294, 1295, 1296, 1297, 1298, 1299, 1300, 1303, 1304, 1305, 1306, 1307, 1308, 1309, 1310, 1311, 1312, 1313, 1314, 1315, 1316, 1317, 1318, 1319, 1320, 1321, 1322, 1323, 1325, 1326, 1327, 1328, 1329, 1331	1021, 1070, 1117, 1118 1186, 1215, 1216, 1217, 1218, 1219, 1220, 1221, 1222, 1223, 1224

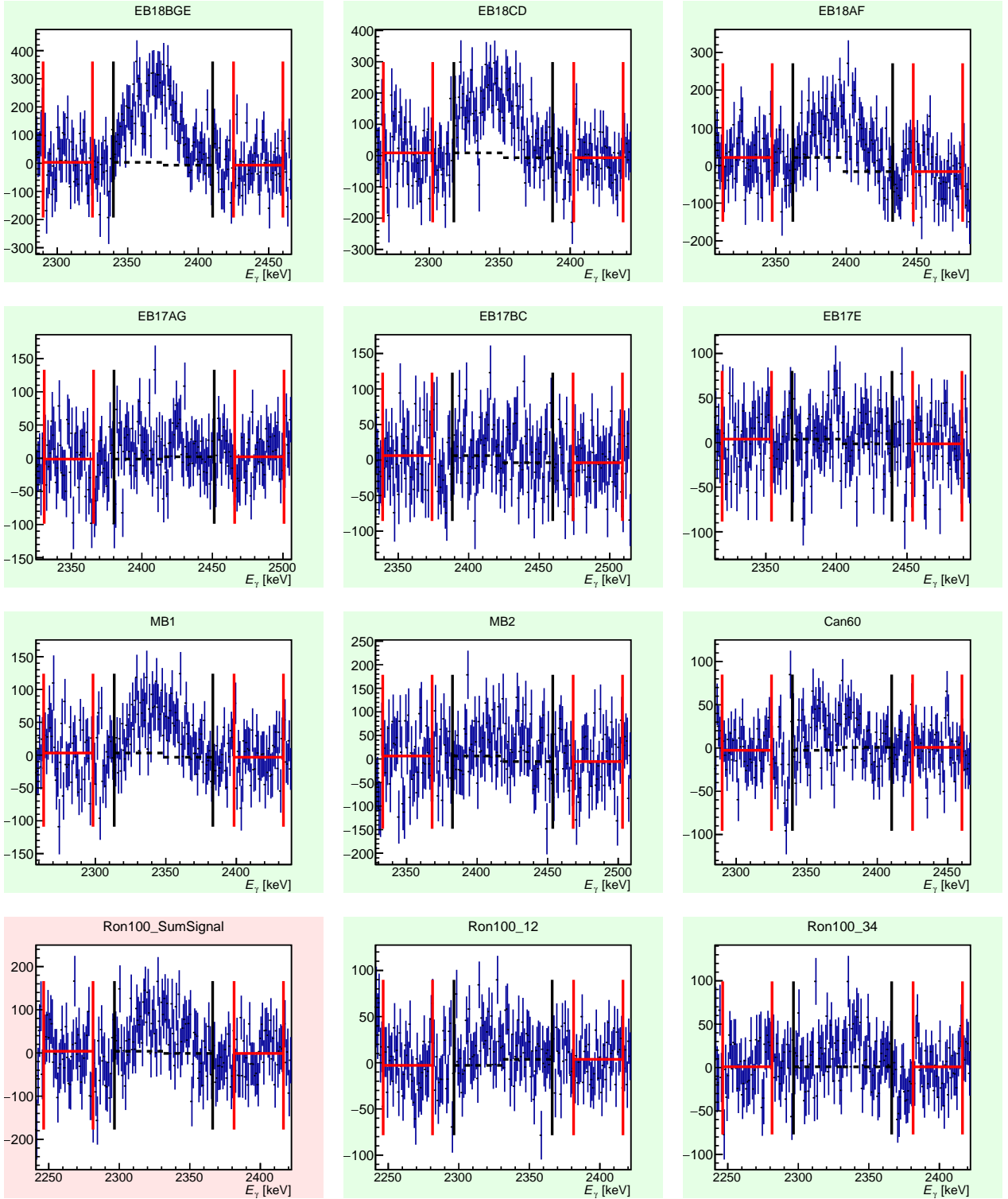
D.7 Residua for the analysis of prompt γ -rays in FK-V

Figure D.13: Residua for the analysis of prompt γ -rays into the first excited state with the ST9 target (cf. table 3.3). From top to bottom, and from left to right, the panels show the residua from EB18BGE, EB18CD, EB18AF, EB17AG, EB17BC, EB17E, MB1, MB2, Can60, Ron100, Ron100 (segment 1&2), and Ron100 (segment 3&4). The residua are obtained by using the analysis technique introduced in figure 6.16.

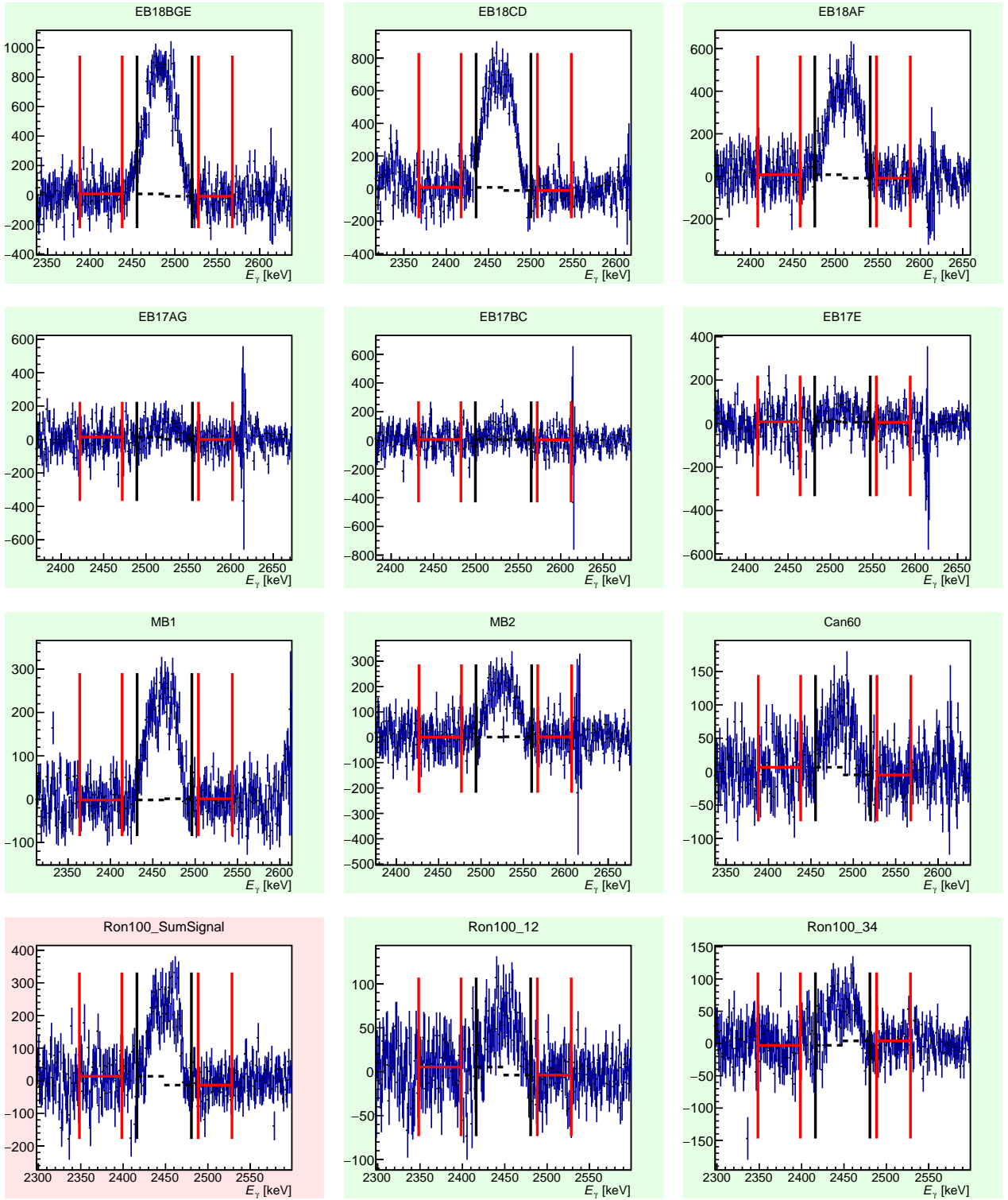


Figure D.14: Residua for the analysis of prompt γ -rays into the ground state with the ST10 target (cf. table 3.3). From top to bottom, and from left to right, the panels show the residua from EB18BGE, EB18CD, EB18AF, EB17AG, EB17BC, EB17E, MB1, MB2, Can60, Ron100, Ron100 (segment 1&2), and Ron100 (segment 3&4). The residua are obtained by using the analysis technique introduced in figure 6.16.

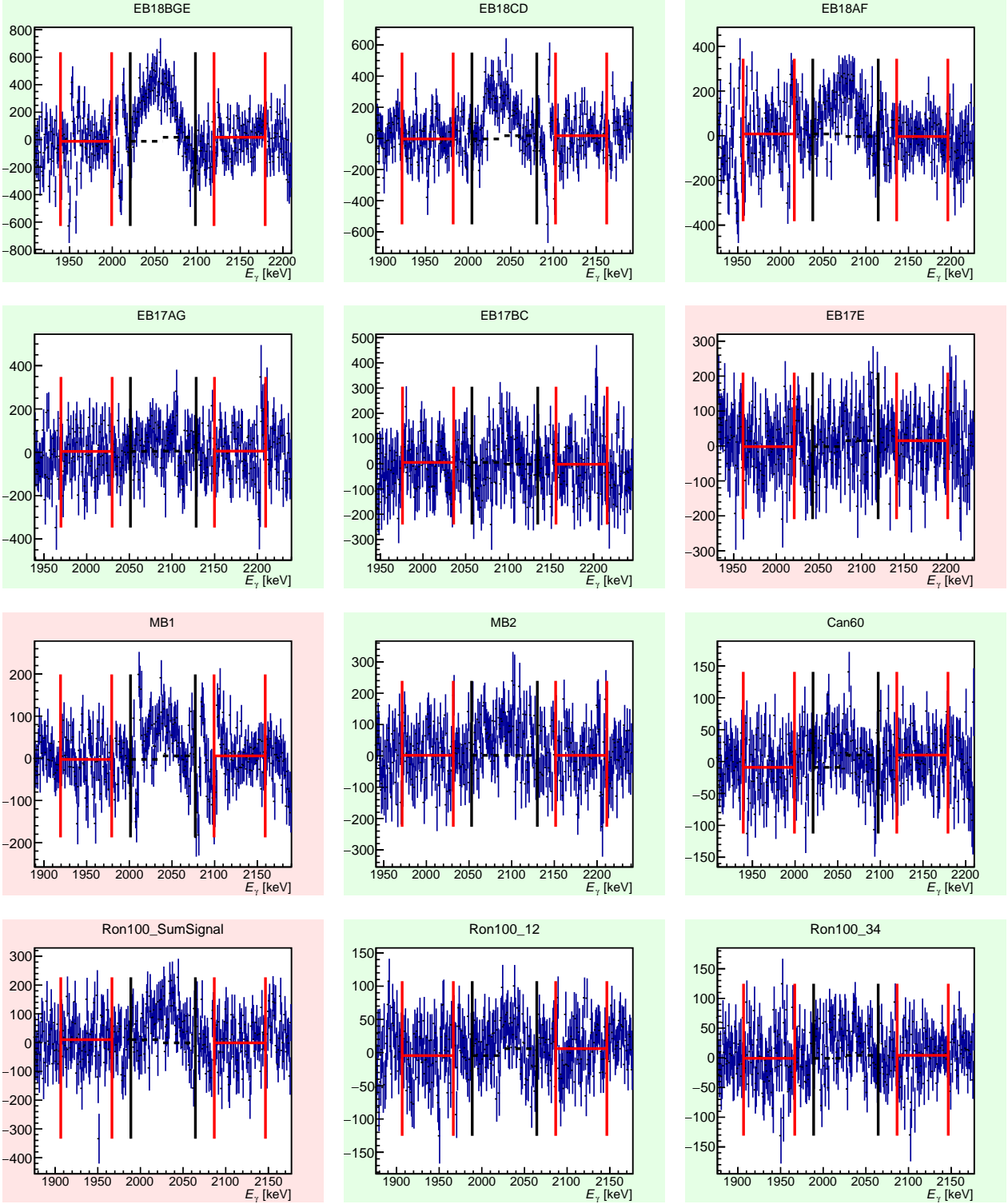


Figure D.15: Residua for the analysis of prompt γ -rays into the first excited state with the ST10 target (cf. table 3.3). From top to bottom, and from left to right, the panels show the residua from EB18BGE, EB18CD, EB18AF, EB17AG, EB17BC, EB17E, MB1, MB2, Can60, Ron100, Ron100 (segment 1&2), and Ron100 (segment 3&4). The residua are obtained by using the analysis technique introduced in figure 6.16.

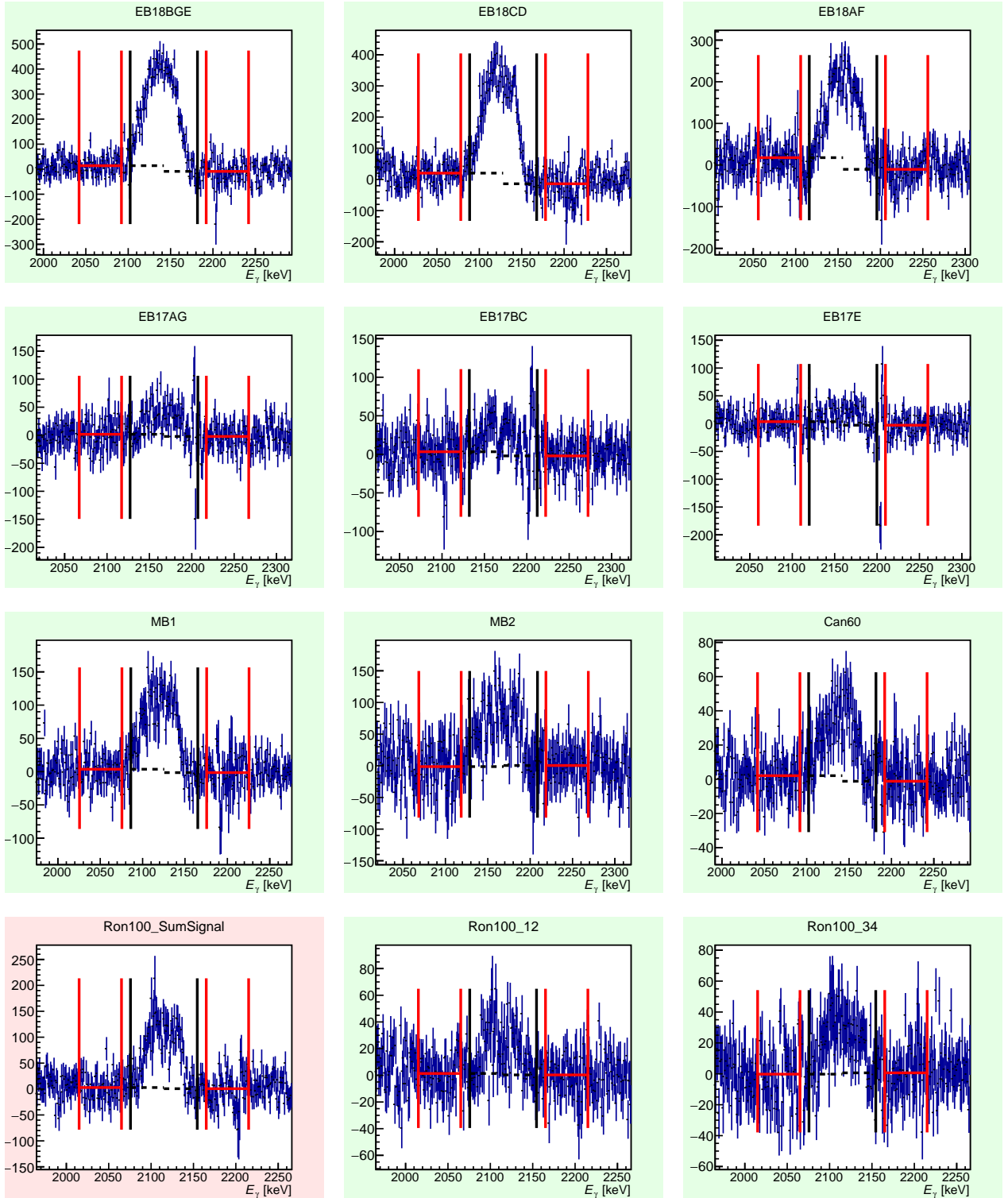


Figure D.16: Residua for the analysis of prompt γ -rays into the ground state with the ST11 and ST9B target (cf. table 3.3). From top to bottom, and from left to right, the panels show the residua from EB18BGE, EB18CD, EB18AF, EB17AG, EB17BC, EB17E, MB1, MB2, Can60, Ron100, Ron100 (segment 1&2), and Ron100 (segment 3&4). The residua are obtained by using the analysis technique introduced in figure 6.16.

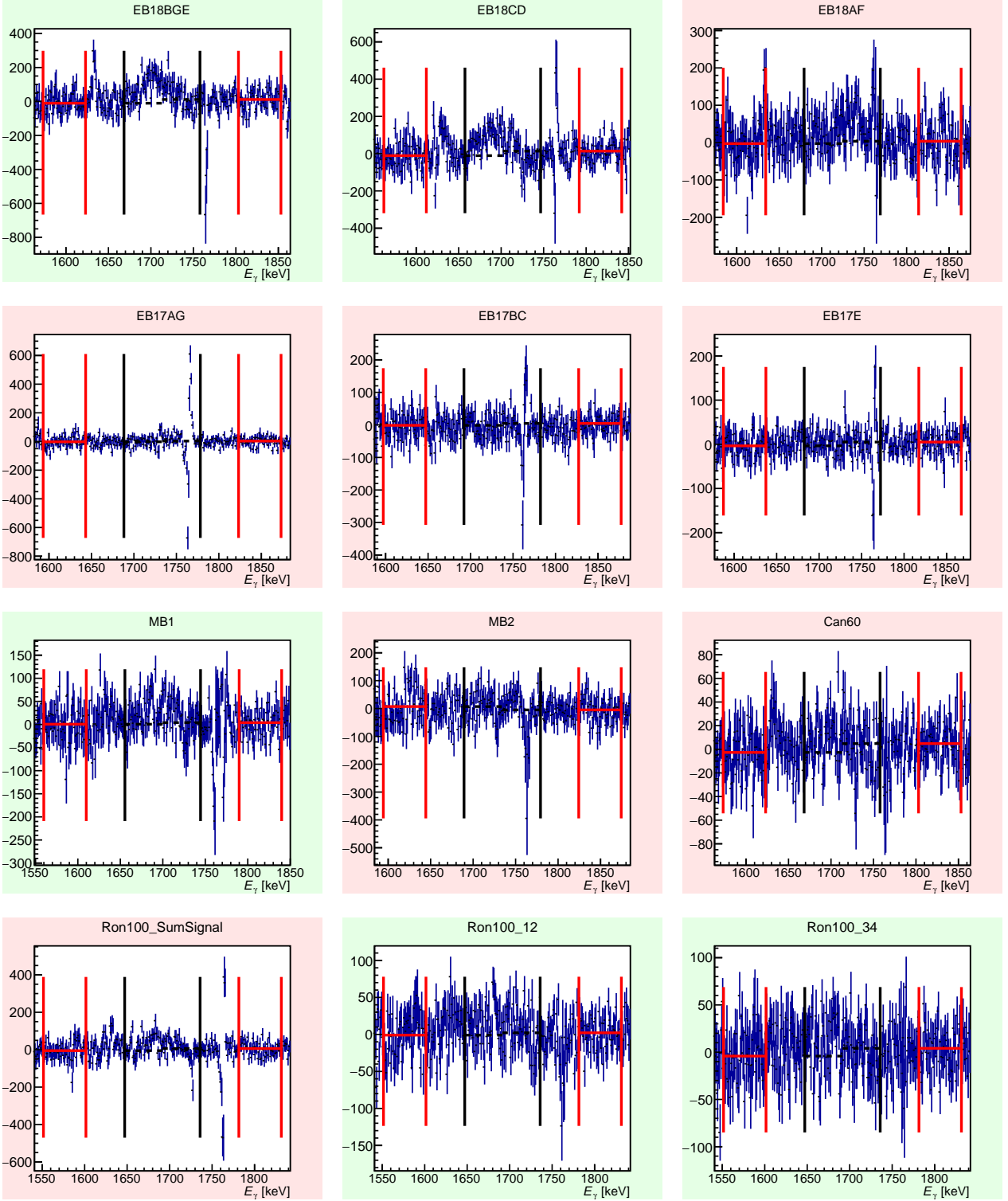


Figure D.17: Residua for the analysis of prompt γ -rays into the first excited state with the ST11 and ST9B targets (cf. table 3.3). From top to bottom, and from left to right, the panels show the residua from EB18BGE, EB18CD, EB18AF, EB17AG, EB17BC, EB17E, MB1, MB2, Can60, Ron100, Ron100 (segment 1&2), and Ron100 (segment 3&4). The residua are obtained by using the analysis technique introduced in figure 6.16.

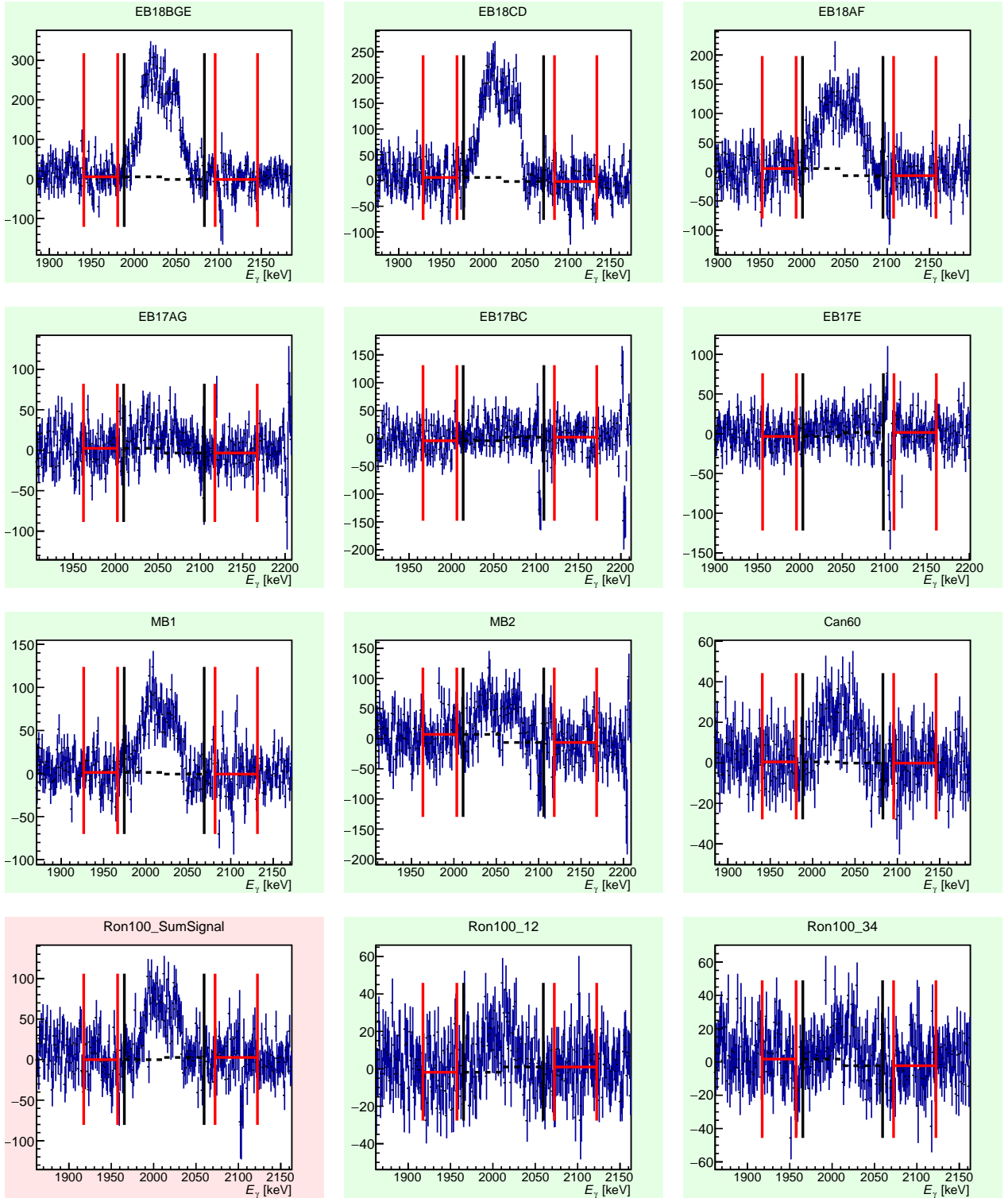


Figure D.18: Residua for the analysis of prompt γ -rays into the ground state with the ST15 target (cf. table 3.3). From top to bottom, and from left to right, the panels show the residua from EB18BGE, EB18CD, EB18AF, EB17AG, EB17BC, EB17E, MB1, MB2, Can60, Ron100, Ron100 (segment 1&2), and Ron100 (segment 3&4). The residua are obtained by using the analysis technique introduced in figure 6.16.

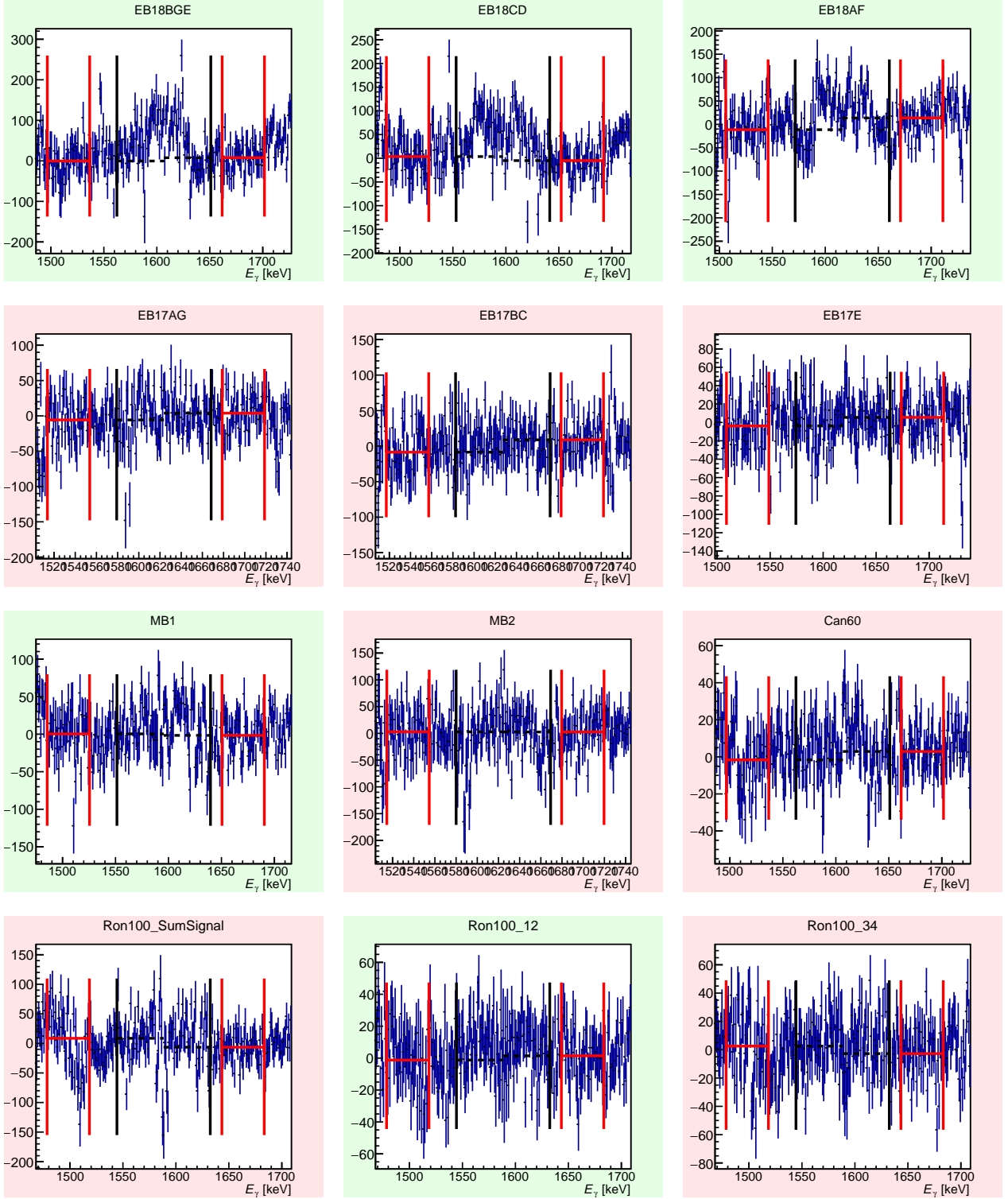


Figure D.19: Residua for the analysis of prompt γ -rays into the first excited state with the ST15 target (cf. table 3.3). From top to bottom, and from left to right, the panels show the residua from EB18BGE, EB18CD, EB18AF, EB17AG, EB17BC, EB17E, MB1, MB2, Can60, Ron100, Ron100 (segment 1&2), and Ron100 (segment 3&4). The residua are obtained by using the analysis technique introduced in figure 6.16.

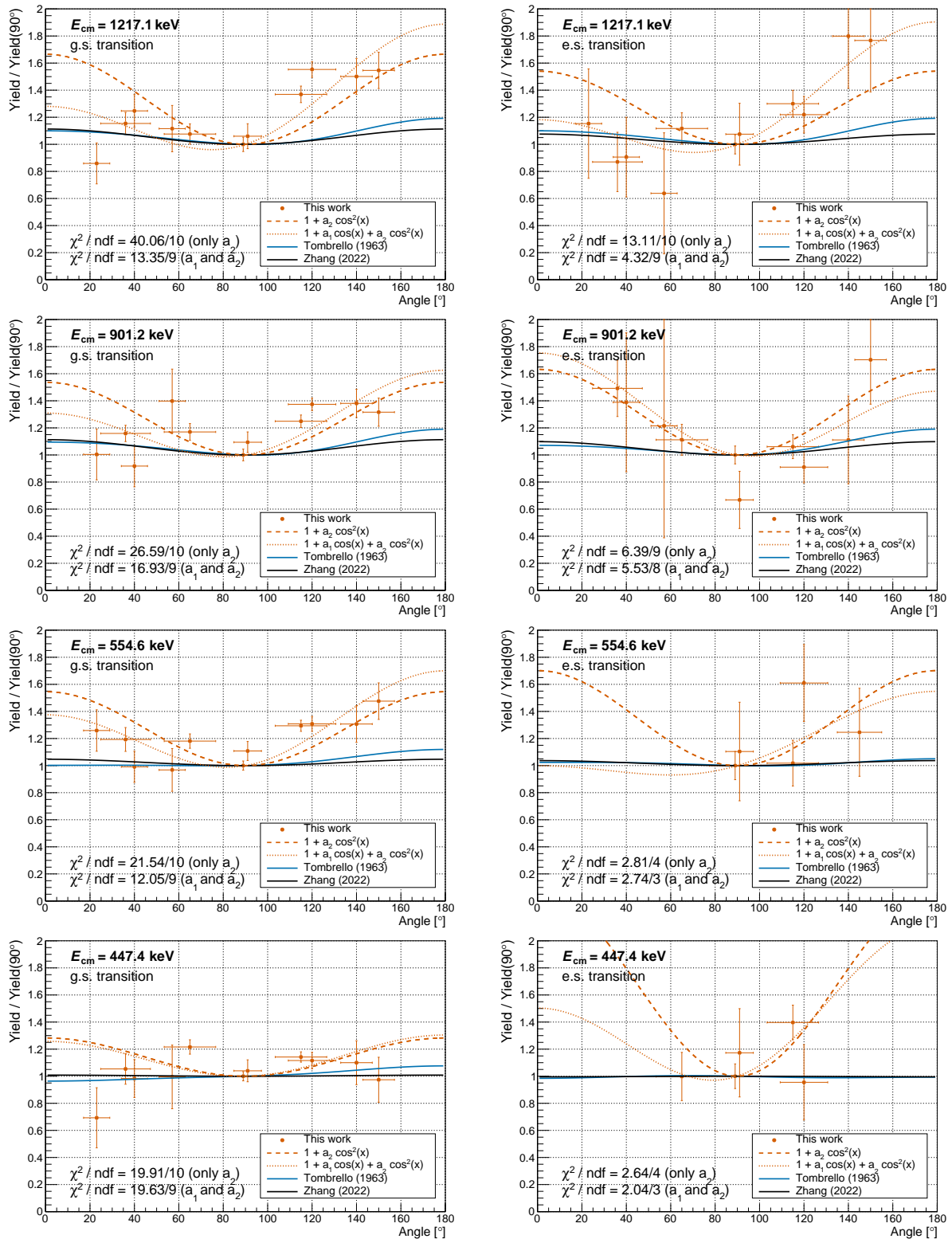
D.8 Fits for the ${}^3\text{He}(\alpha,\gamma){}^7\text{Be}$ γ -ray angular distribution


Figure D.20: Resulting γ -ray angular distributions for all irradiations during the FK-V campaign. The corresponding fit function uses either only the second (dotted) or the first and the second Legendre polynomial (dotted), respectively. From top to bottom: Results for ST9, ST10, ST11+ST9B, and ST15 (cf. tables 3.3) with the result of the g.s. transition (left) and the e.s. transition (right).

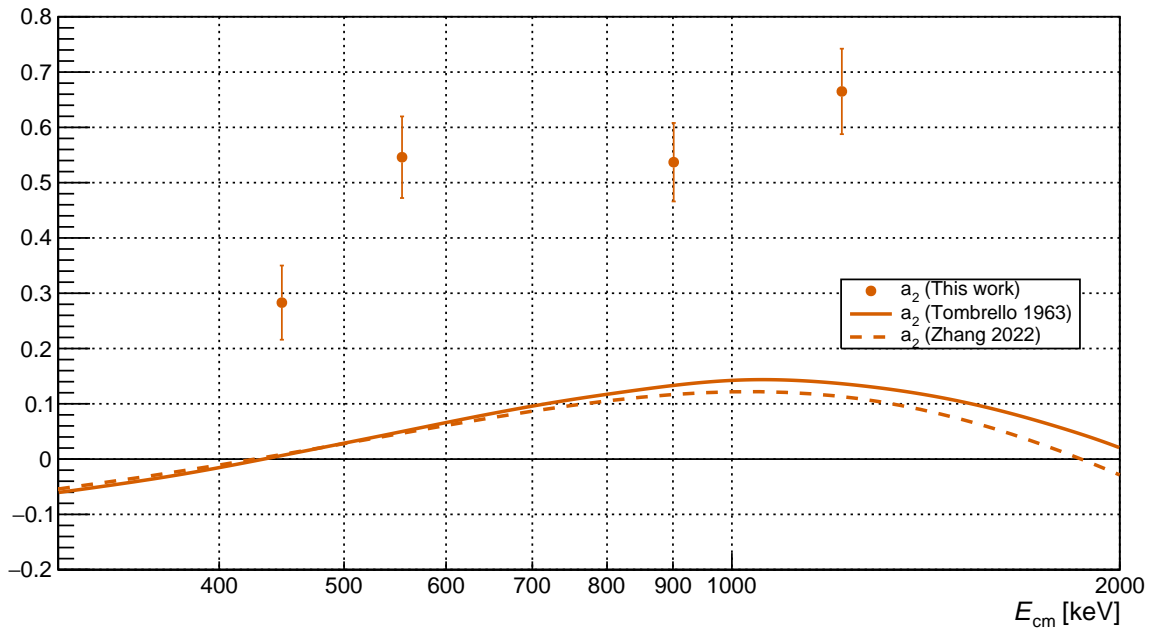


Figure D.21: Energy dependent ‘Legendre polynomials’ for the ground state transition during the FK-V campaign using approach 2 (cf. section 6.3.6), which only takes into account the a_2 component. The corresponding experimental results are compared to the theoretical expectation by Tombrello and Zhang.

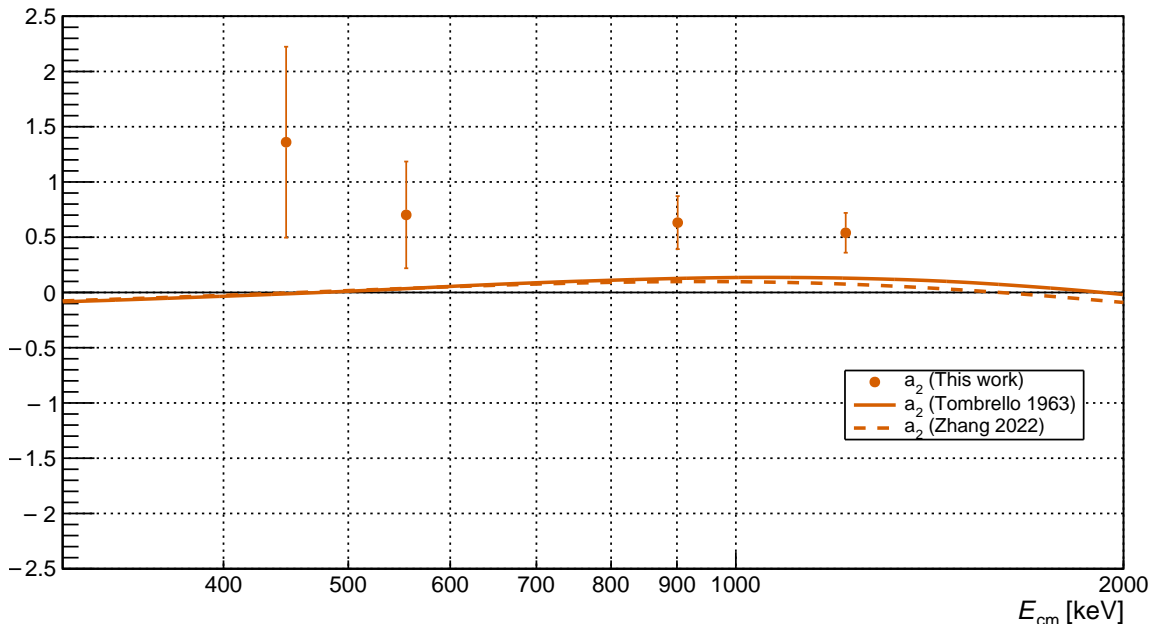


Figure D.22: Energy dependent ‘Legendre polynomials’ for the excited state transition of the ${}^3\text{He}(\alpha,\gamma){}^7\text{Be}$ reaction during the FK-V campaign using approach 2 (cf. section 6.3.6), which only takes into account the a_2 component. The corresponding experimental results are compared to the theoretical expectation by Tombrello and Zhang.

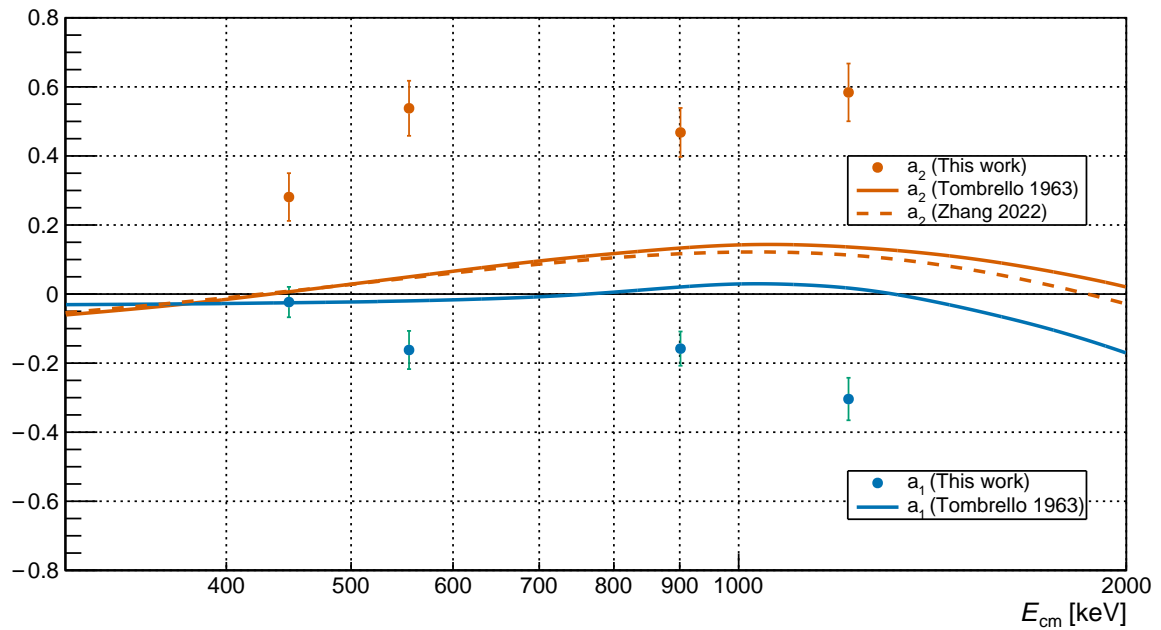


Figure D.23: Energy dependent ‘Legendre polynomials’ for the ground state transition of the ${}^3\text{He}(\alpha,\gamma){}^7\text{Be}$ reaction during the FK-V campaign using approach 3 (cf. section 6.3.6), which takes into account the a_1 component (blue) and the a_2 component (orange). The corresponding experimental results are compared to the theoretical expectation by Tombrello and Zhang.

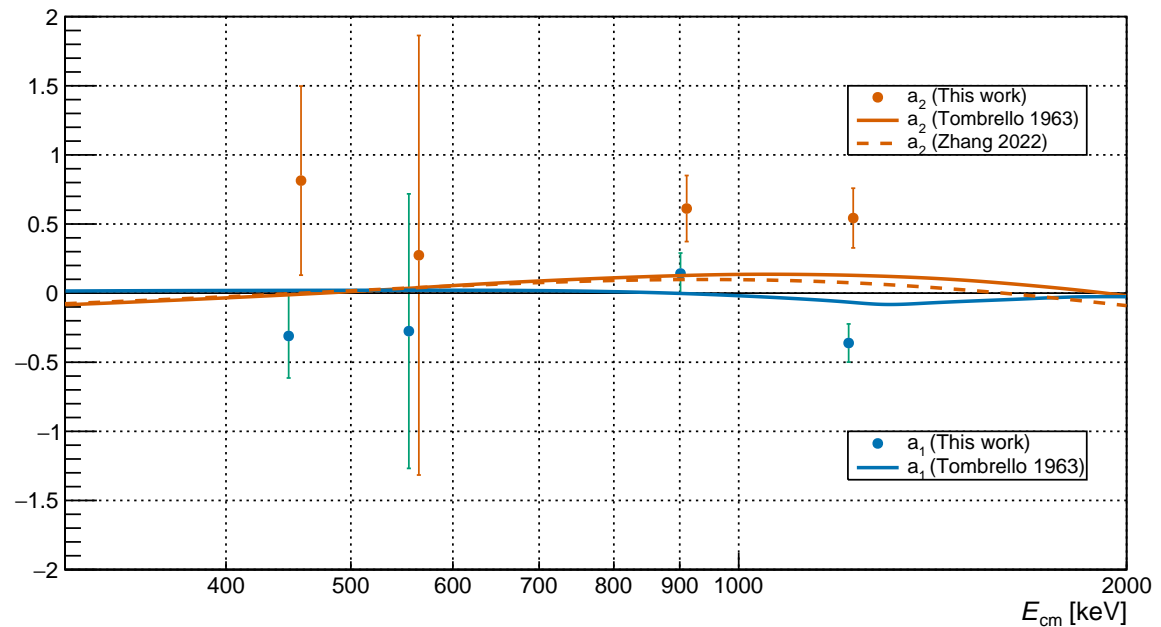


Figure D.24: Energy dependent ‘Legendre polynomials’ for the excited state transition of the ${}^3\text{He}(\alpha,\gamma){}^7\text{Be}$ reaction during the FK-V campaign using approach 3 (cf. section 6.3.6), which takes into account the a_1 component (blue) and the a_2 component (orange). The corresponding experimental results are compared to the theoretical expectation by Tombrello and Zhang.

D.9 The γ -ray angular distribution for ${}^3\text{He}(\alpha,\gamma){}^7\text{Be}$

The γ -ray angular distribution for the ${}^3\text{He}(\alpha,\gamma){}^7\text{Be}$ reaction within the region of interest has been discussed in section 1.4.2. While the figure for the coefficients of the angular distribution span the entire available energy range, the corresponding actual distributions in section 1.4.2 only cover the region of interest for sake of clarity. Their analogon for the entire available energy range up to approximately $E_{\text{lab}} = 8 \text{ MeV}$ ($E_{\text{cm}} \approx 3.5 \text{ MeV}$) is shown in the following in figure D.25 and figure D.26. Due to their identical energy range, these figures here are more suitable to be directly compared to the plot of the angular distribution coefficients in figure 1.7 in order to understand the impact of the $7/2^-$ resonance at $E_{\text{cm}} \approx 2.7 \text{ MeV}$ (stemming from second excited state of ${}^7\text{Be}$ at $E = 4570(50) \text{ keV}$).

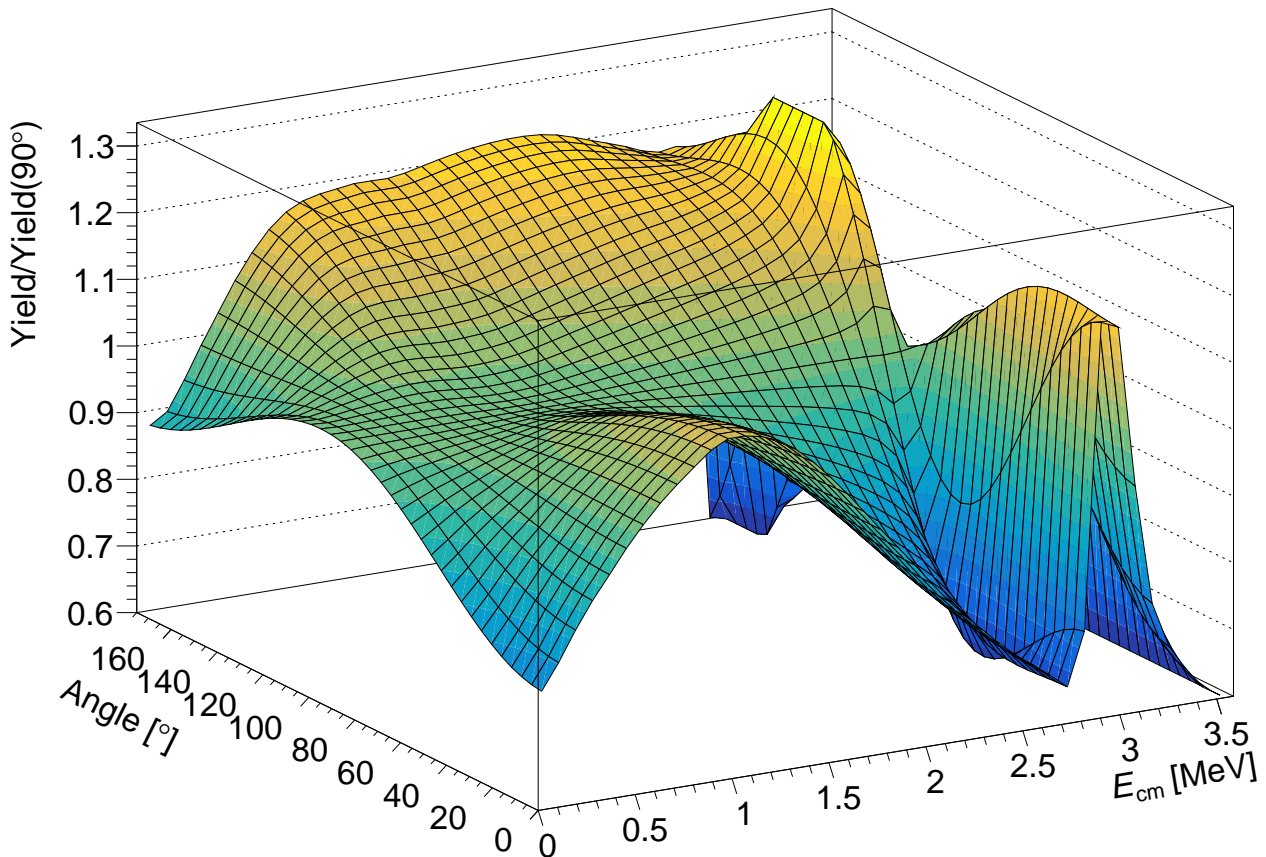


Figure D.25: Comprehensive theoretical γ -ray angular distribution for the ground state transition of the ${}^3\text{He}(\alpha,\gamma){}^7\text{Be}$ reaction. The normalized yield is shown with respect to the E_{cm} of the reaction and the angle of the emitted photons. The data is based on [60] and the energy is shown in linear scale (in contrast to the corresponding figure in section 1.4.2).

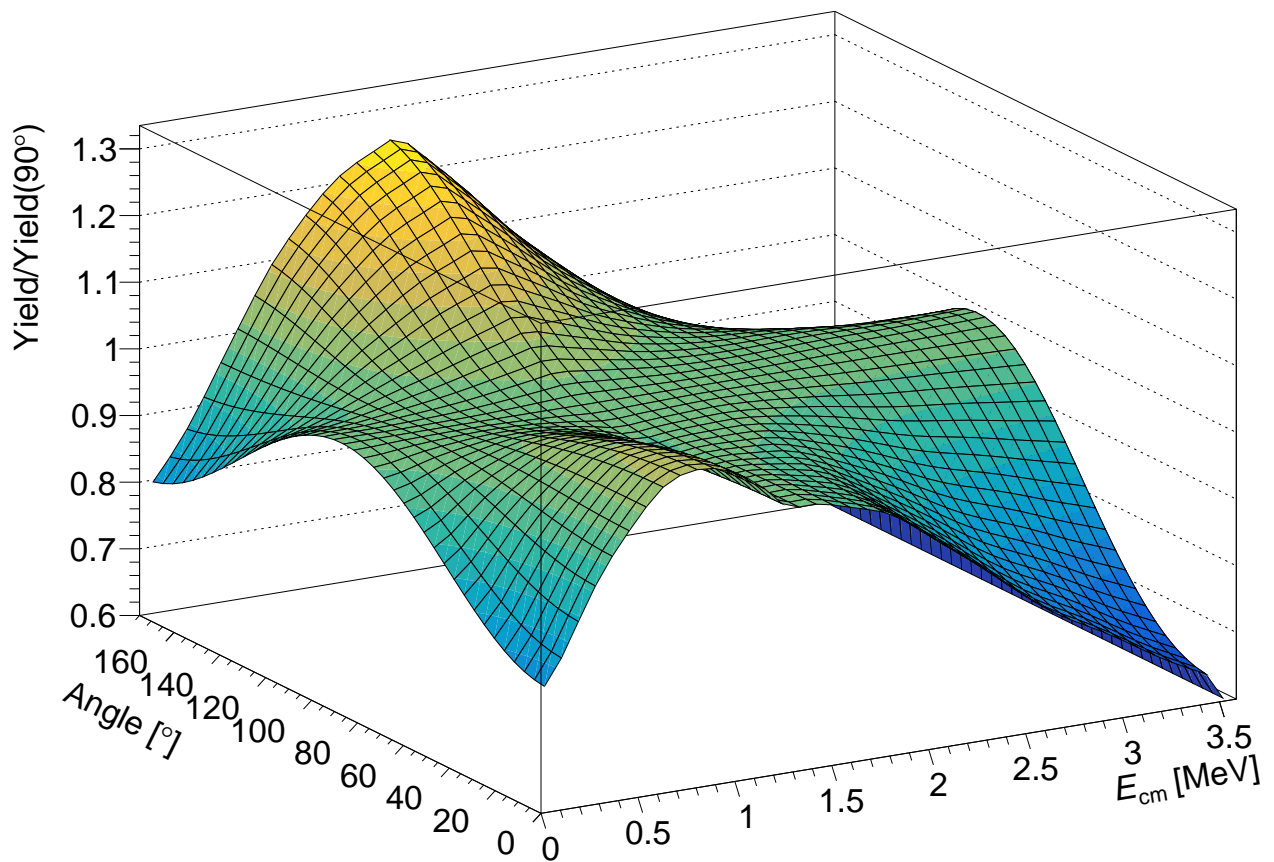


Figure D.26: Comprehensive theoretical γ -ray angular distribution for the transition into the first excited state of the ${}^3\text{He}(\alpha,\gamma){}^7\text{Be}$ reaction. The normalized yield is shown with respect to the E_{cm} of the reaction and the angle of the emitted photons. The data is based on [60] and the energy is shown in linear scale (in contrast to the corresponding figure in section 1.4.2).

Acknowledgement / Danksagung

Due to the fact, that my era as a PhD student took quite a considerable amount of time, there are undoubtedly a lot of people, who paved my way, supported me and have a significant impact on this thesis. Initially, this section was supposed to be rather short until I realized to how many people my gratitude is actually devoted to.

First of all, I want to thank my supervisor and first referee Prof. Kai Zuber for providing me the opportunity to work, study and scientifically grow based on his continuous support during the last years. Kai, I really owe you a lot and I honestly appreciate your ability to simultaneously act as a mentor and a pal. However, also Prof. Daniel Bemmerer has a great share on my scientific development. I'm not only grateful that he acts as my second referee, but also that he became my co-mentor over the last years and introduced me to the world of nuclear astrophysics. I would also like to thank Prof. René Reifarth in particular, who agreed to act as an external referee for my thesis. In addition, my gratitude also is also devoted to the Konrad-Adenauer-Stiftung, and the Deutsche Forschungsgemeinschaft. Their financial and ideational assistance is greatly appreciated and acknowledged.

In general, it is a great gift to work in an environment, which offers you the ability to show your own inabilities. However, I somehow had the luck of calling two of such (equally important) places my scientific home, namely IKTP and Felsenkeller. First of all I would like to thank all members of the neutrino group from IKTP, namely Juliane, Marie, Yingjie, Andy, Christoph, Hans, Johann, Jonas, and Xianke, as well as former group members, like Heinrich, Birgit, Stefan, Jan, and Alex (to name just a few of them). I'm honestly proud to be part of a group that creates an environment of equality, altruism and respect for each other, and furthermore provides such a rather untypical broad variety of physics fields to benefit from. A special thanks goes to my friends Heinrich and Andy. You guys basically shared everything with me: Your office, your scientific curiosity and even your vacations. It was truly a privilege and I deeply hope, that the future holds an empty office somewhere with our name tags on the front door. In addition, a very special thanks also goes to Marie who also became way more than a colleague, but a close friend. In general, I would also like to thank all members of the IKTP, with special emphasis on Nicole, Birgit and Kristin, who are literally the heart of IKTP in both ways of interpretation: empathy and irreplaceability. No matter how desperate some of our situations were, you always provided both a solution and a smile. In addition, I'm also grateful to the entire team from Netzwerk Teilchenwelt, i.e. Uta, Carmen, Philipp and Michael, who taught me the great value and joy of outreach activities.

While the order of appearance might indicate otherwise, I certainly won't call the Felsenkeller my 'second' scientific home, because this would immensely underestimate its importance to me. My long-lasting gratitude goes to the current Felsenkeller team of Daniel B., Bernd R.,

Konrad S., Axel B., Eliana M., Simon R., Thomas H., Anup Y., Max O., Till L., Peter H., Simon V., Noel H., Johannes W., Bruno P., Sebastian F. and Lena B., but also to former colleagues, i.e. Sebastian H. and Felix L. However, a special thanks goes to Simon, Max and Till, who escorted, supported and encouraged me for a considerably long time. Your impact on me as a scientist, but more importantly on my character might be way larger than you imagine. Thank you friends!

After passing the physics exam of theoretical electrodynamics, you might have the feeling that you could basically also apply now for a job as an electrical engineer. However, reality rather quickly lets you know, that you basically know nothing at all. A huge thanks to Toralf D., Bernd R. and Andreas H., who accepted my naivety and persistently tried to teach me 'real-life' engineering skills. But also the support of Maik G., David W., Daniel S., Martin S., and Falk F. in this matter is greatly appreciated.

Special thanks for their continuous assistance, encouragement and their great collegiality also goes to Detlev D., Ronald S., as well as Thomas K. and his group. However, I certainly won't close these acknowledgments without also appreciating the support of countless other people, i.e. Tamás S., Marcel G., Lisa H., Beatrice V., Marielle W., Max M., Klaus S., Armin F., Conrad M., Axel K., Roland B., Arnd J., Andreas W., Stefan R., Louis W., Marian S., Jürgen H., Steffen T., Shavkat A., Oliver B., Jan W., Baris A., Bernd S., Claudia N., Frans M., and all of the great people from the LUNA collaboration.

Despite mentioning all of you already earlier, a huge thanks also goes again to Marie, Heinrich, Simon, Max and Till for investing their time and resources in order to read this work and provide me with valuable comments. I reaaaally appreciate your enormous effort. In addition, I'm also grateful for the continuous support by the council of cakes: A truly pioneering and apple-aworthy institution which took my appreciation into custody.

Abschließend möchte ich gern noch meinen Eltern, meinen Großeltern, meinen Freund:innen und meiner gesamten Familie aus tiefstem Herzen danken. Ihr habt maßgeblich dafür gesorgt, dass ich überhaupt an diesem Punkt angelangt bin und diese Arbeit jetzt endlich gleich drucken werde. #WegMitDemBart! Ich bin jeder Einzelnen und jedem Einzelnen von Euch unermesslich dankbar!

Selbstständigkeitserklärung

Hiermit versichere ich, dass ich die vorliegende Arbeit ohne unzulässige Hilfe Dritter und ohne Benutzung anderer als der angegebenen Hilfsmittel angefertigt habe; die aus fremden Quellen direkt oder indirekt übernommenen Gedanken sind als solche kenntlich gemacht. Die Arbeit wurde bisher weder im Inland noch im Ausland in gleicher oder ähnlicher Form einer anderen Prüfungsbehörde vorgelegt.

Die Promotion wurde an der Technischen Universität Dresden, am Institut für Kern- und Teilchenphysik unter der wissenschaftlichen Betreuung von Prof. Dr. Kai Zuber durchgeführt.

Ich erkenne die Promotionsordnung des Bereichs Mathematik und Naturwissenschaften der TU Dresden vom 23.02.2011 an.

Steffen Turkat

Dresden, 05.04.2023



Bautzner Landstr. 400
01328 Dresden, Germany
Phone +49 351 260-358 1
Fax +49 351 260-1358 1
Email d.bemmerer@hzdr.de
<http://www.hzdr.de>